



**From top antitop production cross section
measurements to the top-quark pole mass
extraction and the MicroMegas upgrade
project for the ATLAS experiment**

DOTTORATO DI RICERCA IN FISICA

XXXIII CICLO

Dottorando

Luca Martinelli

Tutor

Prof. Giuseppe Salamanna

Dipartimento di Matematica e Fisica
Università degli studi di Roma Tre

Contents

Table of Contents	i
Introduction	v
1 The Standard Model of particle physics	1
1.1 Introduction to the Standard Model	1
1.2 Physics at hadron colliders	6
1.3 Top-quark	8
1.3.1 Top-quark production	9
1.3.2 Top-quark decay	14
1.3.3 Top-quark mass	17
2 The Large Hadron Collider and the ATLAS detector	21
2.1 The Large Hadron Collider	21
2.1.1 LHC future programme	24
2.2 The ATLAS detector	25
2.2.1 Magnetic system	26
2.2.2 Inner Detector	27
2.2.3 Calorimeter system	30
2.2.4 Muon spectrometer	31
2.2.5 Trigger system	35
2.2.6 ATLAS upgrade	36
3 The New Small Wheel project and the MicroMegas chambers	37
3.1 The New Small Wheel upgrade project	37
3.1.1 The current Small Wheel	37
3.1.2 Limitations of the present Small Wheel	37
3.1.3 Upgrade requests	40
3.1.4 The New Small Wheel layout	41
3.2 The small Strip Thin Gas chambers	45
3.3 The MicroMegas chambers	46
3.3.1 The MicroMegas technology	47
3.3.2 The MicroMegas gain	48
3.3.3 Resistive strip MicroMegas	48
3.3.4 MicroMegas position reconstruction	50
3.3.5 MicroMegas layout in the New Small Wheel	53

3.3.6	MicroMegas modules in the New Small Wheel	55
3.3.7	MicroMegas readout board and high voltage sections	57
3.3.8	MicroMegas electronics: the VMM3a	59
3.4	Construction and testing of the SM1 MicroMegas chambers	59
3.4.1	SM1 drift panels	60
3.4.2	SM1 mesh stretching	60
3.4.3	SM1 readout panels	62
3.4.4	SM1 final assembling	62
3.5	First results on the modules	66
3.6	Results from test beam on the first SM2 production module	68
3.6.1	Noise levels	69
3.6.2	Resolutions for perpendicular tracks	69
3.6.3	Amplification voltage scan using perpendicular tracks	72
3.6.4	Inclined track runs	76
3.6.5	Gas mixture studies	80
3.7	Validation and integration of the MicroMegas chambers in BB5	84
3.7.1	MicroMegas integration in BB5	84
3.7.2	The cosmic rays stand	84
3.7.3	High voltage maps	86
3.7.4	Double-wedge performance studies	91
4	Object reconstruction	109
4.1	Tracks and vertices reconstruction	109
4.2	Electrons	110
4.2.1	Reconstruction	110
4.2.2	Identification	112
4.2.3	Isolation	112
4.2.4	Efficiency and scale factors	113
4.3	Muons	114
4.3.1	Reconstruction	114
4.3.2	Identification	116
4.3.3	Isolation	117
4.3.4	Efficiency and scale factors	117
4.4	Jets	118
4.4.1	Reconstruction	118
4.4.2	Position and energy calibration	119
4.4.3	Jet energy resolution	120
4.4.4	Jet cleaning from pile-up	121
4.5	<i>b</i> -tagging	121
5	Top antitop cross section measurements	123
5.1	Analysis motivations	123

5.2	Monte Carlo samples	123
5.3	Event selection	126
5.4	Analysis strategy	128
5.4.1	Double tagging technique	128
5.4.2	Total fiducial cross section	130
5.4.3	Total inclusive cross section	131
5.4.4	Fiducial differential cross section	132
5.4.5	Fiducial double differential cross section	139
5.5	Background modelling	144
5.5.1	Mis-identified leptons background	144
5.5.2	$Z \rightarrow \tau\tau$ +jets background	151
5.6	Lepton isolation measurements	153
5.7	Data-Monte Carlo comparison at detector level	161
5.8	Analysis method validation	167
5.8.1	Internal bias tests	167
5.8.2	Stress tests	169
5.8.3	Ratio stress tests	169
5.8.4	Closure tests	169
5.9	Measurements uncertainty	172
5.9.1	Data and Monte Carlo statistics	173
5.9.2	Detector and reconstructed objects	174
5.9.3	Modelling of $t\bar{t}$ process	180
5.9.4	Background	183
5.9.5	Luminosity	186
5.9.6	LHC beam energy	186
5.9.7	Uncertainty breakdown	187
5.10	Results	194
5.10.1	Total fiducial cross section	194
5.10.2	Total inclusive cross section	194
5.10.3	Differential cross section	195
6	Top-quark pole mass extraction	203
6.1	Top-quark pole mass extraction from total inclusive $t\bar{t}$ cross section	203
6.2	Top-quark pole mass extraction from differential $t\bar{t}$ cross section	204
6.2.1	Analysis technique	204
6.2.2	Analysis validation	210
6.2.3	Single results combinations	210
	Conclusions	215
	Appendix	231
A	Double-wedges HV maps and extected efficiencies	231

B	Double-wedges efficiency maps	237
C	Comparison between test beam and cosmics data and MM simuation	253
D	Analysis validation tests	265
E	Analysis uncertainties breakdown	275
Acknowledgements		301

Introduction

This thesis is focused on two main arguments. The MicroMegas chambers in the context of the ATLAS muon spectrometer upgrade and the measurements of the total and differential cross sections of top-quark pairs production.

After the Large Hadron Collider shutdown in 2019-2022 and 2025-2027, the instantaneous luminosity will be increased by a factor 7.5 with respect to the design value. To still be able to operate in the higher background environment and to maintain its current excellent performance, the ATLAS detector will need some important upgrades. The MicroMegas chambers will replace the current tracking chambers in the forward inner region of the ATLAS muon spectrometer. After the construction phase in the construction sites, the validation and the study of the performances of all MicroMegas chambers are essential to ensure their correct operation once they are installed inside the ATLAS detector.

In this work, the MicroMegas chambers construction, and validation of the SM1 module type, in which the Italian collaboration has been deeply involved since the beginning of the project, are presented, together with the first studies on the high voltage stability of the chambers. Besides, the studies performed on the first non-prototype module during a test beam and the final validation of the chambers at CERN before their installation on the New Small Wheel are described.

The top-quark is the up-type quark of the third generation and the heaviest known elementary particle. Good knowledge of the properties of the top-quark, such as its production cross section and its mass, is essential because the top-quarks affect many electroweak parameters resulting in sizeable corrections. After the first observation of the top-quark by the CDF and DØ experiments at the Tevatron proton - anti-proton collider at Fermilab in 1995, its properties were studied with up to 10 fb^{-1} of data at the centre-of-mass energies of 1.8 and 1.96 TeV . A comprehensive set of measurements confirmed that the newly discovered particle behaved accordingly to the Standard Model predictions for the top-quark with a precision that, in most cases, was limited by the available statistics and by the difficulty in the estimation of different background sources. With the start of the Large Hadron Collider at CERN in 2009, much larger samples of top-quark events have become available, allowing the measurement of the top-quark properties with unprecedented precision. The high instantaneous luminosity of the collider and the centre-of-mass energy of $\sqrt{s} = 13 \text{ TeV}$ reached during the Run 2 data taking (2015-2018) allowed the acquisition of a large amount of a top-quark - antitop pair, $t\bar{t}$ for short, events.

In this thesis the measurement of the $t\bar{t}$ production cross section is performed in the dileptonic channel, using proton-proton collision data collected by the ATLAS experiment at a centre-of-mass energy of 13 TeV . The total cross section is measured in the full phase space, and in a fiducial phase space defined following the detector acceptance. In addition,

Introduction

the absolute and normalised single and double differential cross section as a function of several lepton kinematic variables are presented.

The measurement of the top-quark pole mass is performed using two different methods: from the $t\bar{t}$ inclusive cross section measurement, and from normalised differential cross section measurements.

The structure of the thesis is the following. In Chapter 1 an overview of the Standard Model and of the top-quark physics is presented, together with the latest experimental results of the measurement of the $t\bar{t}$ production cross section. In Chapter 2 a general overview of the Large Hadron Collider and of the ATLAS experiment is given. Starting from the work done on the MicroMegas detectors for the ATLAS upgrade, Chapter 3 introduces the New Small Wheel project and the MicroMegas working principle. It contains the first part of the author's original work: the construction of the SM1 MicroMegas modules, the first results of the SM2 module at the test beam (2018), and the study of the performances of the chambers at CERN, before their installation on the New Small Wheel. Chapter 4 contains the description of the reconstruction and calibration of the physics objects. Chapter 5 presents the second part of the author's original work: the measurements of the $t\bar{t}$ total absolute and fiducial cross section and the $t\bar{t}$ single and double absolute and normalised differential cross sections as a function of several lepton kinematic variables. Chapter 6 explains the methods to extract the top-quark pole mass using either the $t\bar{t}$ total inclusive cross section and the normalised differential cross sections.

The Standard Model of particle physics

1

1.1 Introduction to the Standard Model

The Standard Model (SM) of particle physics is a renormalisable quantum field theory based on the gauge¹ symmetry $SU(3)_C \times SU(2)_L \times U(1)_Y$ that describes the elementary particles and their interactions, explained in terms of exchange of bosons. This symmetry can be divided into $SU(3)_C$, which is related to the strong sector and where the conserved charge is the colour (C), while $SU(2)_L \times U(1)_Y$ describes the electro-weak sector, which conserves the weak isospin (the L means that only left-handed particles participate to the interaction) and the hypercharge (Y).

One of the first bases for the Standard Model was placed in 1964 by Murray Gell-Mann and George Zweig [1, 2] when they introduced the idea of nucleons composed of charged particles of spin 1/2, called quarks. Initially, only three types of quarks were found to be necessary (up u , down d and strange s) to describe the particles known so far. But many other particles were in time observed at experiments, requiring a reformulation of the so-called “quark model”.

The prediction of the quark charm c was confirmed, during the so-called “November revolution” (in 1974)². This new quark was discovered at the Stanford Linear Accelerator Center [3] and the Brookhaven National Laboratory [4] with the observation of the J/ψ resonance, the $c\bar{c}$ bound state. In 1977 at Tevatron (Fermilab) another heavy meson state was observed as a $b\bar{b}$ bound state [5], with the first evidence of a new quark: the bottom quark (b). The last quark, the top-quark t , was finally observed in 1995 at Tevatron by both the CDF and DØ experiments [6, 7].

Besides the quarks, the Standard Model includes particles called leptons. The electron, the first charged lepton, was discovered by J.J. Thomson in 1897, while the muon (μ) and the tau particle (τ) were observed respectively in cosmic rays experiments in 1937 (and confirmed in 1946) [8, 9] and at the Stanford Linear Accelerator Center (SLAC) in 1975 [10]. The first neutrino (ν_e) was postulated by Pauli in 1930, to solve the problem of the energy and momentum distributions in the β -decay. The second ν_μ and the third generation ν_τ neutrinos were discovered in 1962 [11] and 2000 [12], respectively. Neutrinos are considered to be massless in the Standard Model scenario, but there are experimental evidence of their massive nature [13].

Leptons and quarks are fermions of spin 1/2 and they are grouped into doublets, as shown in Table 1.1.

¹A theory is gauge invariant when it is invariant under local phase transformation in the space of the internal degrees of freedom of the theory.

²The importance of this discovery is highlighted by the fact that the subsequent, rapid changes in high-energy physics at the time have become collectively known as the “November Revolution”.

$$\begin{array}{l} \text{Quarks} \quad \begin{pmatrix} u \\ d \end{pmatrix} \quad \begin{pmatrix} c \\ s \end{pmatrix} \quad \begin{pmatrix} t \\ b \end{pmatrix} \\ \text{Leptons} \quad \begin{pmatrix} \nu_e \\ e \end{pmatrix} \quad \begin{pmatrix} \nu_\mu \\ \mu \end{pmatrix} \quad \begin{pmatrix} \nu_\tau \\ \tau \end{pmatrix} \end{array}$$

Table 1.1: Particle doublets of the Standard Model theory.

Quarks carry several internal charges: the flavour charge (*up, down, charm, strange, top, bottom*) and the colour charge (*red, green and blue*). The quarks have fractional electric charge, $+2/3e$ ³ for the *up*-type (first row in Table 1.1) and $-1/3e$ for the *down*-type (second row in Table 1.1).

The leptons are e, μ and τ and their three associated neutrinos complete the families. The neutrinos (first row of leptons) are neutral in electric charge while the other three leptons bring an integer electric charge of $1e$. All the leptons carry an internal charge, called leptonic number, that is different for each family (l_e, l_μ and l_τ).

Leptons and quarks interact with each other through four fundamental interactions: electromagnetic, weak, strong and gravitational. Table 1.2 shows the relative strength and range of different interactions⁴.

Interaction type	Strength (a.u.)	Range (m)	Mediator
Electromagnetic	10^{36}	∞	photon (γ)
Weak	10^{25}	10^{-18}	W and Z bosons
Strong	10^{38}	10^{-15}	gluon (g)
Gravitational	1	∞	graviton (hypothetical)

Table 1.2: Conceptual scheme of the relative strength and range for the four different fundamental interactions. The graviton, indicated as gravity mediator, is an hypothetical spin 2 boson introduced in quantum field theory, but not included yet in the Standard Model.

The modern quantum mechanical view of the fundamental forces other than gravity is that particles do not directly interact with each other but they exchange virtual particles (gauge bosons), which are the interaction carriers or force mediators, as shown in Table 1.2.

The electromagnetic and weak forces were described in a unified way in the '70s, mainly thanks to the work of Glashow, Weinberg, and Salam [14–16] while the strong force was included in the Standard Model only later, through the quantum chromodynamics (QCD) theory.

The electromagnetic interaction is described by quantum electrodynamics (QED). The quantum of the electromagnetic field is the photon (γ) that is a massless, chargeless boson of spin 1. The strength of the electromagnetic interaction is proportional to the coupling constant, expressed in Equation 1.1, and to the inverse of the square of the distance between the particles.

³ $e = 1.60217662 \cdot 10^{-19} \text{ C}$

⁴The strength comparison of the four basic forces is determined as the force between two particles placed on a certain distance, it has a meaning only in relative terms.

$$\alpha_{em}(q^2) = \frac{\alpha_{em}(q_0^2)}{1 - \frac{\alpha_{em}(q_0^2)}{3\pi} \ln\left(\frac{q^2}{q_0^2}\right)}, \text{ where } \alpha_{em}(q_0^2) = \frac{e^2}{4\pi\epsilon_0\hbar c} = \frac{1}{137.035999084(21)} \quad (1.1)$$

where q^2 indicates the transferred momentum of the interaction, q_0^2 is a fixed reference value of q^2 while ϵ_0 ⁵, \hbar ⁶ and c ⁷ are constants.

Quantum Chromodynamics (QCD) is a SU(3) gauge field theory that describes the strong interactions between coloured quarks and gluons. The mediators of the interaction are an octet of colour-charged bosons, called gluons (g), each carrying a colour and an anti-colour charge. These particles, like the photons, are massless and have spin 1. The intensity of the strong interactions depends on the α_S coupling which is expressed in Equation 1.2.

$$\alpha_S(q^2) = \frac{\alpha_S(q_0^2)}{1 + \alpha_S(q_0^2) \frac{11N_c - 2N_f}{12\pi} \ln\left(\frac{q^2}{q_0^2}\right)} \quad (1.2)$$

where $N_c = 3$ is the number of colours and N_f is the number of flavours which participate in the interactions at a given q^2 (e.g. $q^2 < 2m_b^2 \rightarrow N_f = 4$).

The behaviour of α_S as a function of the energy scale (q^2) is shown in Figure 1.1.

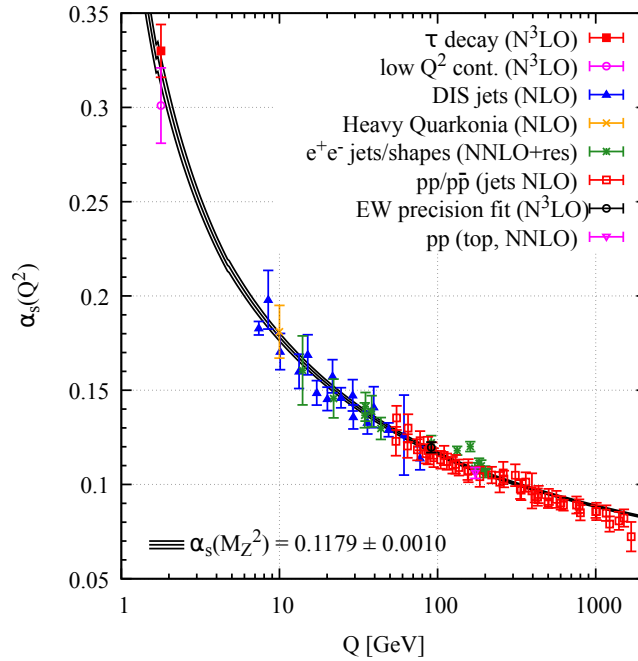


Figure 1.1: Measurements of α_S as a function of the energy scale. The respective degree of QCD perturbation theory used in the extraction of α_S is indicated in brackets [17].

From Equation 1.2 and from Figure 1.1, if $q^2 \rightarrow \infty$, then $\alpha_S \rightarrow 0$ which means that the quarks behave as free particles. This characteristic is known as “*asymptotic freedom*” and is the only condition in which the QCD can be described as a perturbative theory. This

⁵ $\epsilon_0 = 55.26349406 e^2 \cdot GeV^{-1} \cdot fm^{-1}$ is the vacuum permittivity.

⁶ $\hbar = 6.582119569 \cdot 10^{-16} eV \cdot s$ is the Planck constant.

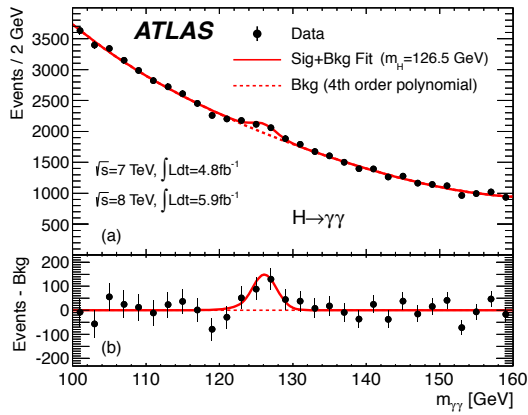
⁷ $c = 299792458 m/s$ is the speed of light.

behaviour implies also the presence of vertexes of self-interaction among the gluons while this effect not present in electromagnetic interactions. On the other side, when $q^2 \rightarrow 0$, then $\alpha_S \rightarrow \infty$, which is the reason for the so-called *confinement*: it is impossible to observe free coloured states. In the Standard Model, the quarks can combine to produce two different singlets: mesons (quark and anti-quark bound state) and baryons (three quarks/anti-quarks bound states). This property is observed in high-energy scattering processes where the strong interaction generates a process called hadronisation, where a bundle of colour singlet hadrons are the outcome of the gluon radiation and branching produced by the scattered coloured particle. The experimental signature of this “hadron shower” is called jet.

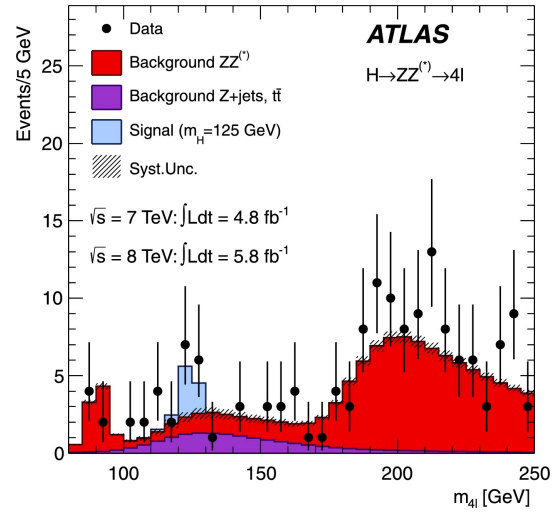
Since the lifetime of pions ($\sim 10^{-8}$ s), muons ($\sim 10^{-6}$ s), and especially neutrons (~ 880 s) is relatively big while the time scale of an electromagnetic or strong decay is respectively 10^{-16} s and 10^{-23} s, it is implied that there is another type of interaction: the weak interaction (with $\alpha_w \ll \alpha_S, \alpha_{em}$). The characteristic of this interaction is that it can break symmetries that are conserved by the strong and electromagnetic interactions, such as the quark flavour conservation, but it is also the only interaction in which the neutrinos can take part. The weak interaction is mediated by massive, spin 1 bosons: the W^\pm , responsible for charge currents, and Z bosons, responsible for neutral currents.

In order to explain the masses of the mediators of the weak force, and at the same time to unify the weak and electromagnetic interactions into a unique theory (Standard Model), a new internal gauge symmetry must be added. This is solved in 1964 with the introduction of the mechanism of the spontaneous symmetry breaking proposed by Higgs, Englert and Brout [18–20]. This addition to the Standard Model predicts also a new massive, neutral boson: the Higgs boson.

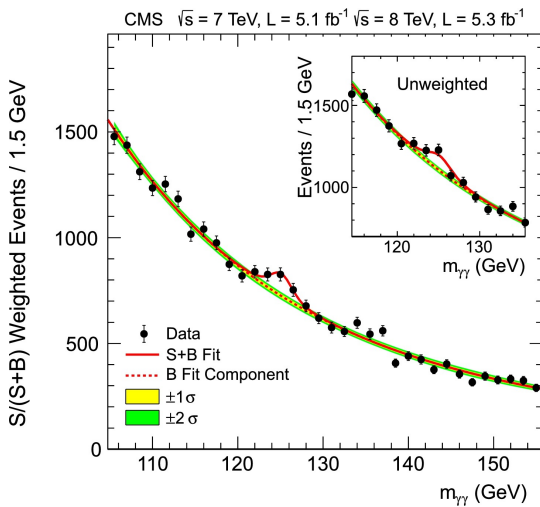
On July 4th, 2012, the ATLAS [21] and CMS [22] experiments at the Large Hadron Collider (LHC) provided further confirmation of the Standard Model theory through the observation of a particle highly compatible with the predicted Higgs boson. As shown in Figure 1.2, the channels which most contribute to the discovery were the four leptons and the di-photons.



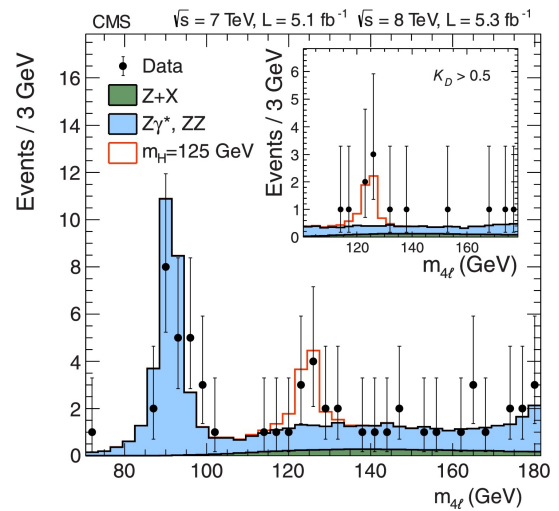
(a) Distribution of the invariant mass of diphoton candidates after all selections for the combined $\sqrt{s} = 7 \text{ TeV}$ and $\sqrt{s} = 8 \text{ TeV}$ data sample collected by the ATLAS experiment. The result of a fit to the data of the sum of a signal component fixed to $m_H = 125 \text{ GeV}$ and a background component described by a fourth-order Bernstein polynomial is superimposed [21].



(b) Distribution of the four-lepton invariant mass compared to the background expectation. The data were collected by the ATLAS experiment with a centre-of-mass energy of $\sqrt{s} = 7 - 8 \text{ TeV}$. The signal expectation for a Standard Model Higgs with $m_H = 125 \text{ GeV}$ is also shown [21].



(c) The diphoton invariant mass distribution with each event weighted by the $S/(S+B)$ value of its category. The lines represent the fitted background and signal, and the coloured bands represent the ± 1 and ± 2 standard deviation uncertainties in the background estimate. The inset shows the central part of the unweighted invariant mass distribution [22].



(d) Distribution of the four-lepton invariant mass compared to the background expectation. The data were collected by the CMS experiment with a centre-of-mass energy of $\sqrt{s} = 7 - 8 \text{ TeV}$. The signal expectation for a Standard Model Higgs with $m_H = 125 \text{ GeV}$ is also shown [22].

Figure 1.2

1.2 Physics at hadron colliders

One of the observables that can be used to test the Standard Model is the *cross section* which is defined as the probability for two initial particles i and j to interact and produce the final state X . It can be written in the following way according to the Fermi rules:

$$\sigma_{ij \rightarrow X} \propto \int \frac{1}{F} \cdot |\mathcal{M}_{ij \rightarrow X}|^2 d\Phi \quad (1.3)$$

where F is the incident flux, $|\mathcal{M}_{ij \rightarrow X}|^2$ is the squared matrix element and Φ is the phase space.

However, contrary to the Large Electron-Positron Collider (LEP) [23], the e^+e^- collider present at CERN before the current LHC, in a pp machine the colliding particles are not fundamental objects. At low energy, the proton can be considered as a uud bound state composed only by the valence quarks while, increasing its momentum, the contribution of the sea quarks (virtual pairs of quarks) and of the gluons, that are continuously created and reabsorbed due to quantum fluctuations, becomes significant. A pp (or $p\bar{p}$) collision can thus be thought of as the incoherent superposition of the interactions between any two constituents of the two protons, each of them carrying a fraction $x_i(x_j)$, also called x of Bjorken, of the proton incoming momentum.

To properly take into account that protons are colliding at LHC, it is necessary to consider the *parton density function* (PDF) of the partons inside the hadrons. The PDF represents the probability of finding the parton $i(j)$ inside the hadron $P_1(P_2)$, with a momentum fraction $x_i(x_j)$ and they are usually obtained from Deep Inelastic Scattering (DIS) cross section measurements. Several sets of PDFs are available and are determined at a given energy scale while the extrapolation to a different energy regime is obtained through the so-called DGLAP [24, 25] equations, which describe the evolution of the α_S coupling constant and the radiation branching properties with energy. Figure 1.3 shows an example of the parton density function for different type of protons constituents.

The cross section of any QCD process can be written, according to the *factorization theorem* as a convolution between calculable parts (hard scattering coefficients) and not-calculable parts (PDFs), as follows:

$$\sigma_{P_1 P_2 \rightarrow X} = \sum_{i,j=q,\bar{q},g} \int_0^1 dx_i dx_j \cdot f_i(x_i, \mu_F^2) f_j(x_j, \mu_F^2) \cdot \hat{\sigma}_{ij \rightarrow X}(\hat{s}, \mu_F, \mu_R) \quad (1.4)$$

where $\hat{\sigma}_{ij \rightarrow X}$ is the hard parton-parton cross section, $\hat{s} = x_i x_j s$ is a centre-of-mass energy in the partonic system and μ_F and μ_R are respectively the factorization and re-normalization scales, the two cut-offs needed to deal with the infrared and ultraviolet divergences that appear in the finite order calculations.

All these factors are taken into account when events are simulated thanks to Monte Carlo methods [27, 28] that describe the different steps of the interaction. As shown in Figure 1.4, the pp interaction at LHC is divided into different parts: *hard scattering*, *parton shower*, *hadronisation*, *underlying event* and *decay of unstable particles*.

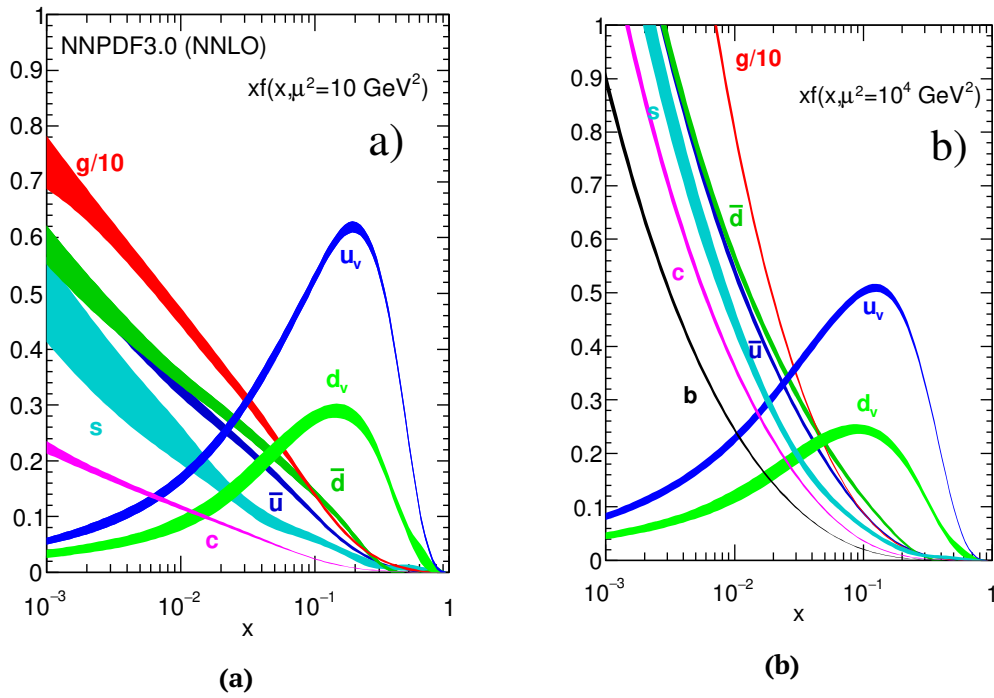


Figure 1.3: Parton distributions $f(x)$ at scales of $\mu^2 = 10 \text{ GeV}^2$ (Figure 1.3a) and $\mu^2 = 10^4 \text{ GeV}^2$ (Figure 1.3b) [26]. Valence quarks carry most of the momentum of the proton so they represent the dominant contribution at high values of x . At lower values of x , gluons and sea quark become increasingly more abundant.

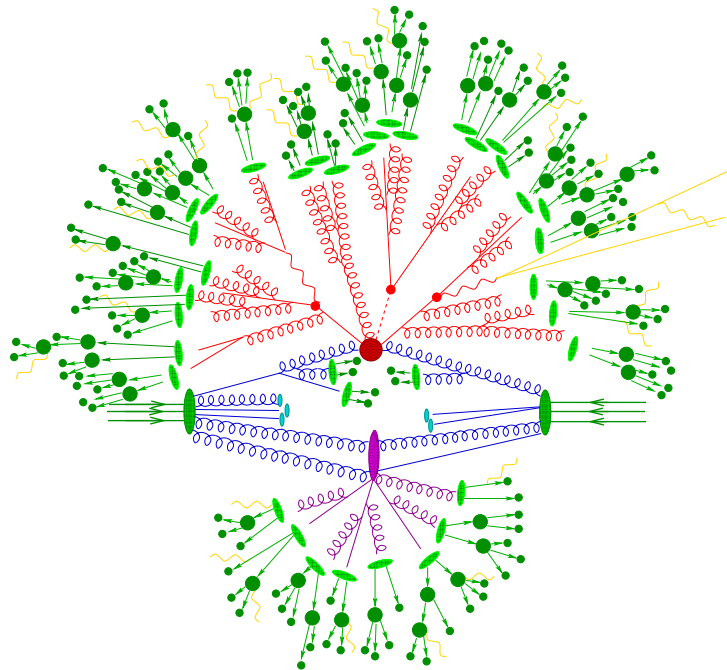


Figure 1.4: Schematic view of the interaction at a pp collider. The hard interaction (big red blob) is followed by the decay of both top-quarks and the Higgs boson (small red blobs). Additional hard QCD radiation is produced (red) and a secondary interaction takes place (purple blob) before the final-state partons hadronise (light green blobs) and hadrons decay (dark green blobs). Photon radiation occurs at any stage (yellow) [29].

The simulation of the parton interactions is called hard-scattering (red) and consider also some possible radiation coming from the partons or the final state themselves. It is called *initial state radiation* (ISR) if the emission is from the incoming partons while emissions from the final state partons are defined as *final state radiation* (FSR). The emission of a parton is encoded in the so-called Sudakov form factors [30], at the parton shower level, describing the probability for a parton to not radiate in the interval Δt . The evolution of the final state continues until the energy regime reaches the order of the Λ_{QCD} . At this stage, the quark/gluons combine into colour-less states (green, hadronisation) creating hadrons that can decay into stable particles (dark green, decay of unstable particles). The last two processes are responsible for the evolution of the partons into collimated spray of hadrons called “jets”. The interactions between the partons not involved in the hard scattering are described in the underlying events or multi-parton interactions (purple, underlying event).

1.3 Top-quark

The top-quark is the third generation up-type quark and it is the heaviest known elementary particle. Good knowledge of the properties of the top-quark is essential because it enters in many parameters of the electroweak theory with sizeable corrections.

After the discovery of the fifth quark (the bottom), due to the absence of flavour-changing neutral currents in the decay of b -quark⁸ and after the measurements of its isospin ($-1/2$), the presence of a further up -type quark was required. Early searches for the top-quark at SLAC (Stanford University) and DESY (in Hamburg) were inconclusive. When the Super Proton Synchrotron (SPS) at CERN arrived at the discovery for the W and Z bosons, it was felt that the discovery of the top-quark was imminent. However, analysing the data collected, it was possible to put only an upper limit on its mass: $m_t > 61 \text{ GeV}$ for UA1 and $m_t > 67 \text{ GeV}$ for UA2 [31]. Only in 1995, the CDF and DØ collaborations, at the Tevatron proton - anti-proton collider, were able to announce the discovery of this “elusive” particle.

One of the characteristics of the top-quark is that it has a short lifetime ($\tau_t \sim 4 \cdot 10^{-25} \text{ s}$), and since hadronisation time is longer ($\tau_{had} \sim 10^{-24} \text{ s}$), it decays before it hadronises into a toponium bound state. Since it does not hadronise, the top-quark can be reconstructed from its decay products and this peculiarity offers a unique opportunity to study directly the properties of this quark.

After the first observation of top-quarks, its properties were studied with up to $10fb^{-1}$ of data at centre-of-mass energies of 1.8 and 1.96 TeV . A comprehensive set of measurements confirmed that the new particle behaved accordingly to the Standard Model predictions, with a precision that in most cases was limited by the available statistics in the data samples and by the difficulty in the estimation of W +jets and multi-jet backgrounds. With

⁸Flavour-changing neutral currents (FCNC) are interaction in which the flavour of fermions change without altering its electric charge. In the Standard Model, they are forbidden at the tree level. In particular for the b -quark, the process $B_s^0 \rightarrow l^+l^-$ is a particular FCNC and its branching ratio is suppressed $BR(B_s^0 \rightarrow l^+l^-) \sim 3 \cdot 10^{-9}$ [17].

the start of the Large Hadron Collider (LHC) at CERN in 2009, much larger samples of top-quark events have become available (both in data and Monte Carlo), and this has allowed measuring the top-quark properties with unprecedented precision. Given the high cross section ($\sigma_t \simeq 0.9 \text{ nb}$) at a centre-of-mass energy of 13 TeV , LHC is considered a “top-factory”.

The top-quark production is the main background of many Standard Model analyses and beyond Standard Model (bSM). For these reasons, a precise understanding of this particle is very important. Moreover, thanks to its special properties described above, the top-quark is considered also to be a good candidate to probe for physics bSM. In this direction, it is crucial to measure all the production, decay and coupling properties of this particle with the highest achievable precision.

1.3.1 Top-quark production

Top-quarks are primarily produced as quark anti-quark pairs ($t\bar{t}$) via gluon-gluon-fusion, but also single top-quark can be produced in the Wt associated production (also referred as Wt), t -channel, and s -channel.

1.3.1.1 Top-quark pair

The partonic cross section $\hat{\sigma}_{ij \rightarrow X}$ in Equation 1.4, can be expanded in fixed order series in α_S as follows:

$$\hat{\sigma}_{ij \rightarrow X} = \alpha_S^2 \cdot \left[\hat{\sigma}_{ij \rightarrow X}^{(LO)} + \alpha_S \hat{\sigma}_{ij \rightarrow X}^{(NLO)} + \alpha_S^2 \hat{\sigma}_{ij \rightarrow X}^{(NNLO)} + \mathcal{O}(NNNLO) \right] \quad (1.5)$$

with NLO referring to next-to-leading order, NNLO to next-to-next-to-leading order and so on.

In a hadronic collisions the top-quark can be produced via two different mechanisms at leading order (LO): quark anti-quark annihilation, whose Feynman diagram is shown in Figure 1.5a, and gluon-gluon fusion, whose Feynman diagrams are shown in Figure 1.5b, Figure 1.5c and Figure 1.5d.

The analytic expressions at LO for the cross section of the two partonic processes are shown in Equation 1.6 (quark anti-quark annihilation) and Equation 1.7 (gluon gluon fusion) [32].

$$\frac{d\hat{\sigma}_{q\bar{q} \rightarrow t\bar{t}}}{dz} = \frac{\pi\alpha_S^2}{9s} \beta (2 - (1 - z^2) \beta) \quad (1.6)$$

$$\frac{d\hat{\sigma}_{gg \rightarrow t\bar{t}}}{dz} = \frac{\pi\alpha_S^2}{96s} \beta \frac{7 + 9z^2\beta^2}{(1 - z^2\beta^2)^2} (1 + 2\beta^2 - 2z^2\beta^2 - 2\beta^4 + 2z^2\beta^4 - z^4\beta^4) \quad (1.7)$$

where $\beta = \sqrt{1 - 4m_t^2/s}$ is the top-quark speed in a centre-of-mass system, s is the energy of a centre-of-mass system, m_t is the top-quark mass, $z = \cos(\theta)$ and θ is the angle between the incoming parton and the outgoing top-quark.

The size of the contribution of the two $t\bar{t}$ production mechanisms (light quark annihila-

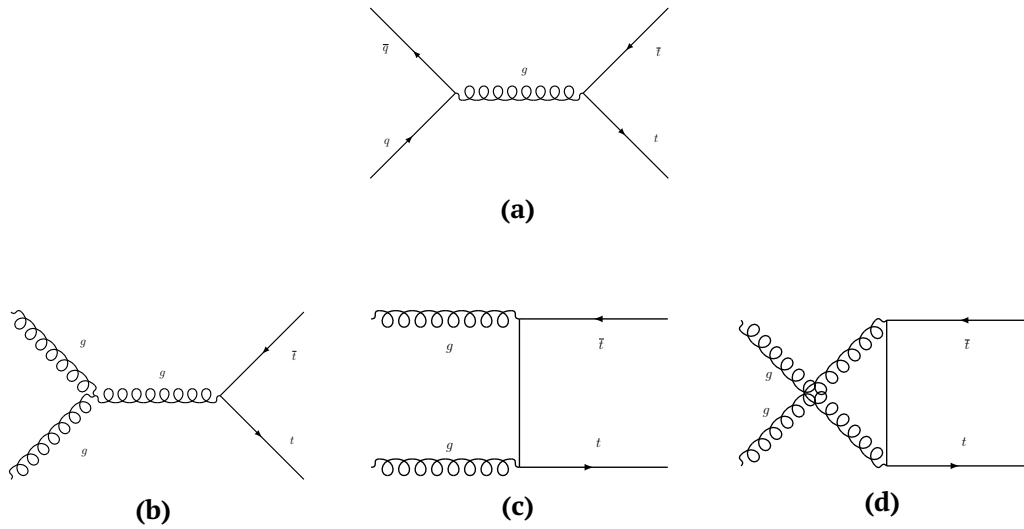


Figure 1.5: Top-quark pairs production Feynman diagrams at LO. Figure 1.5a shows the quark anti-quark annihilation while Figure 1.5b, Figure 1.5c and Figure 1.5d show the gluon gluon production.

tion and gluon gluon fusion) depends on the PDFs inside the hadrons. The light quark annihilation is the main contribution at low energy ($\sqrt{s} \sim 2m_t$) because the interaction takes place through valence quarks. This is confirmed by the fact that 85% of the top-quarks produced at Tevatron were originated from this production mode, while at the LHC ($\sqrt{s} = 13 \text{ TeV}$) this fraction is only 10%. The gluon gluon fusion, instead, becomes more relevant when $\sqrt{s} \gg 2m_t$ since the gluons and the sea quarks start to dominate (with a fraction of $\sim 90\%$ at the LHC and $\sim 15\%$ at the Tevatron).

In $t\bar{t}$ production higher order calculations (NLO) are considered since they give sizeable contributions to the evaluation of the total production cross section. Some example of $t\bar{t}$ production diagrams at NLO are shown in Figure 1.6.

As said above, the $t\bar{t}$ process is the dominant background in many new physics research analyses and precise knowledge of its modelling is necessary. In fact, a large Monte Carlo $t\bar{t}$ modelling uncertainty may hide the presence of rare bSM processes in some corner of the phase space. To improve the knowledge of the $t\bar{t}$ process in all the phase space, many differential measurements ($\frac{d\sigma_{t\bar{t}}}{dX}$ where X is a particular variable) of the $t\bar{t}$ cross section need to be done.

Much progress has been made today but discrepancies still remain between observed data and theoretical predictions. These discrepancies could be due to missing electroweak corrections which, although suppressed due to small coupling ($\alpha_S^2 \cdot \alpha_{em/w}$), can make a significant contribution to the total cross section. In addition, a big difference between NLO predictions and data could also come from higher order corrections (NNLO), as shown in Figure 1.7 where the differential $t\bar{t}$ cross section is expressed as a function of the top-quark p_T .

The $t\bar{t}$ inclusive cross section has been experimentally measured for the first time at Tevatron by the CDF and DØ collaborations at a centre-of-mass energy of $\sqrt{s} = 1.96 \text{ GeV}$.

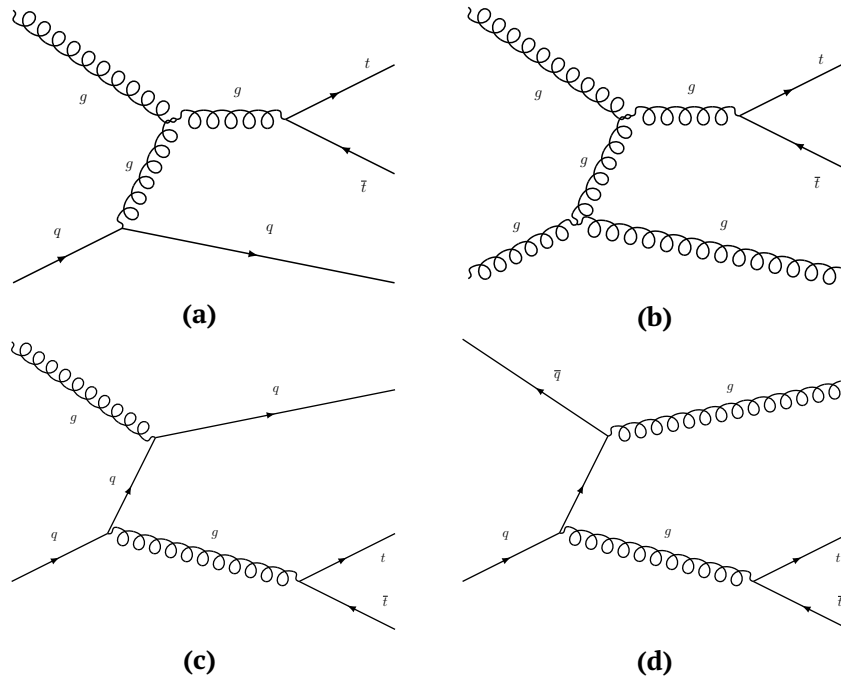


Figure 1.6: Examples of top-quark pairs production Feynman diagrams at NLO.

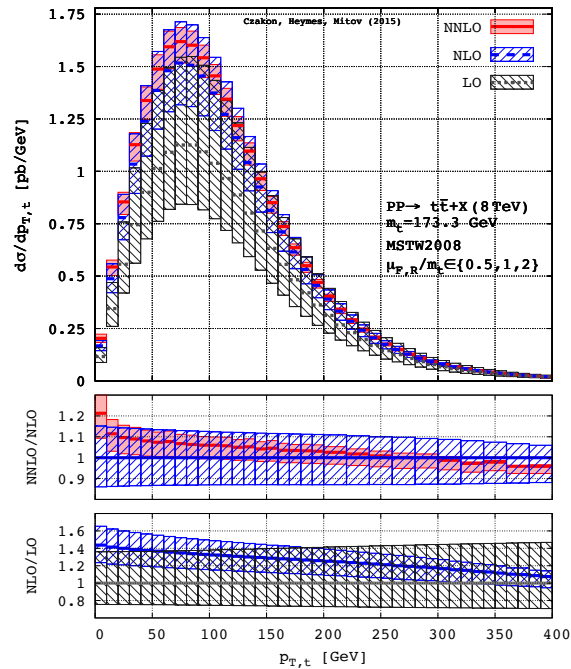


Figure 1.7: Comparison among LO, NLO and NNLO predictions on the $\frac{d\sigma_{t\bar{t}}}{dp_{T,t}^2}$. The bands represent the scale uncertainty associated to the three predictions [33]. A not negligible difference between NLO and NNLO is visible at low and high top-quark p_T .

The combined measured value is [34]:

$$\sigma_{t\bar{t}}(\sqrt{s} = 1.96 \text{ GeV}) = 7.60 \pm 0.20 \text{ (stat)} \pm 0.29 \text{ (syst)} \pm 0.21 \text{ (lumi)} \text{ pb [unc. of 5.4%]} \quad (1.8)$$

in good agreement with the Standard Model expectation of $\sigma_{t\bar{t}}^{th}(\sqrt{s} = 1.96 \text{ GeV}) = 7.35^{+0.28}_{-0.33} \text{ pb}$ at NNLO+NNLL⁹ in perturbative QCD for a top mass of 172.5 GeV .

The $t\bar{t}$ inclusive cross section were measured also by the ATLAS and CMS experiments at a centre-of-mass energy of $\sqrt{s} = 7 - 8 \text{ TeV}$ [35, 36]. The combined results are:

$$\sigma_{t\bar{t}}(\sqrt{s} = 7 \text{ GeV}) = 173.3 \pm 2.3 \text{ (stat)} \pm 7.6 \text{ (syst)} \pm 6.3 \text{ (lumi)} \text{ pb [unc. of 5.8%]} \quad (1.9)$$

$$\sigma_{t\bar{t}}(\sqrt{s} = 8 \text{ GeV}) = 241.5 \pm 1.4 \text{ (stat)} \pm 5.7 \text{ (syst)} \pm 6.2 \text{ (lumi)} \text{ pb [unc. of 3.5%]} \quad (1.10)$$

while the predicted $t\bar{t}$ production cross section is $\sigma_{t\bar{t}}^{th}(\sqrt{s} = 7 \text{ GeV}) = 177.3^{+4.6}_{-6.0} \text{ (scale)} \pm 9.0 \text{ (PDF}+\alpha_S) \text{ pb}$ and $\sigma_{t\bar{t}}^{th}(\sqrt{s} = 8 \text{ GeV}) = 252.9^{+6.4}_{-8.6} \text{ (scale)} \pm 11.7 \text{ (PDF}+\alpha_S) \text{ pb}$ as calculated with the Top++2.0 program to a NNLO order in perturbative QCD [37].

The latest results at LHC at a centre-of-mass energy of $\sqrt{s} = 13 \text{ TeV}$ are for the ATLAS collaboration [38, 39]:

- lepton+jets channel with the Full Run 2 dataset

$$\sigma_{t\bar{t}} = 830.4 \pm 0.4 \text{ (stat)} \pm 36 \text{ (syst)} \pm 14 \text{ (lumi)} \text{ pb [unc. of 4.6%]} \quad (1.11)$$

- di-lepton channel with the partial Run 2 dataset¹⁰

$$\sigma_{t\bar{t}} = 826.4 \pm 3.6 \text{ (stat)} \pm 11.5 \text{ (syst)} \pm 15.7 \text{ (lumi)} \pm 1.9 \text{ (beam)} \text{ pb [unc. of 2.40%]} \quad (1.12)$$

while for the CMS collaboration [40, 41]:

- lepton+jets channel with the partial Run 2 dataset (data collected from 2015 to 2016)

$$\sigma_{t\bar{t}} = 888 \pm 2 \text{ (stat)} \pm_{-28}^{+26} \text{ (syst)} \pm 20 \text{ (lumi)} \text{ pb [unc. of 3.8%]} \quad (1.13)$$

- di-lepton channel with the partial Run 2 dataset

$$\sigma_{t\bar{t}} = 803 \pm 2 \text{ (stat)} \pm 25 \text{ (syst)} \pm 20 \text{ (lumi)} \text{ pb [unc. of 4.0%]} \quad (1.14)$$

The theoretical calculation of the cross section at 13 TeV is made using the Top++2.0 program:

$$\sigma_{t\bar{t}} = 831.76^{+19.77}_{-29.20} \text{ (scale)} \pm 35.06 \text{ (PDF}+\alpha_S) \text{ pb} \quad (1.15)$$

assuming a top-quark mass of $m_t = 172.5 \text{ GeV}$, corresponding to a relative precision of $\begin{matrix} +4.8\% \\ -5.5\% \end{matrix}$.

Figure 1.8 shows the complete picture of the top-quark pair inclusive cross section measurements as a function of \sqrt{s} and compared with the latest NNLO+NNLL predictions.

⁹next-to-next-to-leading logarithmic

¹⁰The analysis of the Full Run 2 dataset (data collected from 2015 to 2018) in the di-lepton channel is the object of this thesis.

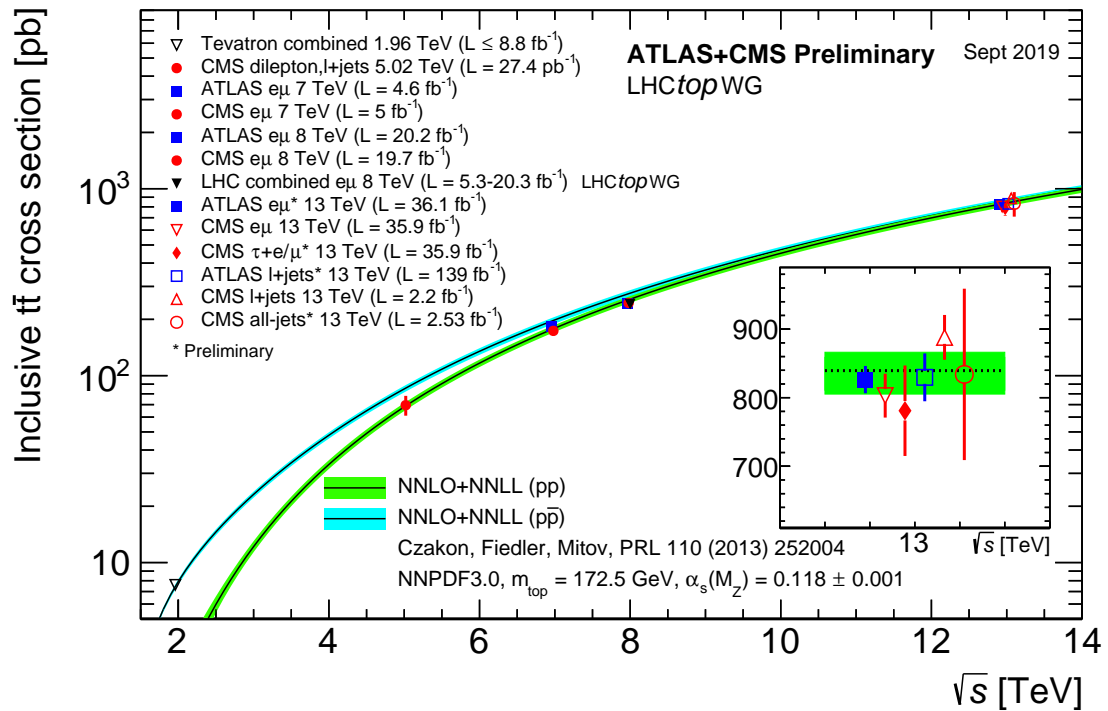


Figure 1.8: Summary of LHC and Tevatron measurements of the top-pair production cross section as a function of a centre-of-mass energy compared to the NNLO QCD calculation. The theory band represents uncertainties due to renormalisation and factorisation scale, parton density functions and the strong coupling. The measurements and the theory calculation are quoted at $m_t = 172.5 \text{ GeV}$ [42].

Both ATLAS and CMS provided an exceptional number of interesting results in measuring $\sigma_{t\bar{t}}/dx$ for a lot of variables, in many channels, at the different centre-of-mass energies and luminosity. In Figure 1.9, only the latest ATLAS and CMS measurements in the $e\mu$ channel, the one studied in this work, are shown.

1.3.1.2 Single Top

The single top-quark production rate is much smaller (around a factor 4) than in the $t\bar{t}$ production since the single top-quark process is mediated by weak interaction. The leading order Feynman diagrams of the single top-quark production are shown in Figure 1.10. The single top-quark processes are divided into:

- t-channel, shown in Figure 1.10a;
- Wt shown in Figure 1.10c and Figure 1.10d;
- s-channel shown in Figure 1.10b.

The dominant process is the t-channel as shown in Table 1.3, followed by Wt, and s-channel. Figure 1.11 shows the theoretical and measured inclusive cross sections by ATLAS and CMS experiments and the combined results for the three channels.

Process	$\sigma_{single\ top}(\sqrt{s} = 13\ TeV)$
t-channel	$216.99^{+9.04}_{-7.71}\ pb$
Wt	$71.70 \pm 3.80\ pb$
s-channel	$10.32^{+0.40}_{-0.36}\ pb$

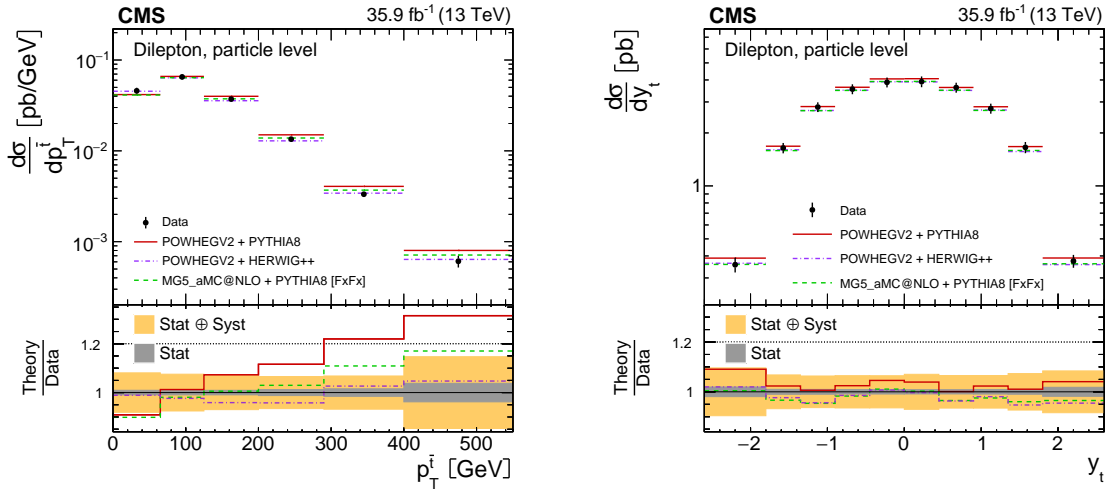
Table 1.3: Predicted single top-quark cross section at 13 TeV calculated for a top-quark mass of 172.5 GeV at next-to-leading order (NLO) in QCD with Hathor v2.1 [44, 45].

The single top-quark production in Wt represents the most important background in the measurements of the top-quark pair production cross section since the final state of this process is similar to the $t\bar{t}$ final state. In addition, the NLO Wt Feynman diagrams are identical to the LO $t\bar{t}$ Feynman diagrams and this overlap needs to be threaded to avoid double counting. Two different techniques were developed [46, 47]:

- Diagram removal (DR) in which the amplitudes of doubly-resonant diagrams are set to zero, removing the interference term from the total amplitude;
- Diagram subtraction (DS) which preserves the interference trying to remove the $t\bar{t}$ terms but causing an enhancement of the uncertainties related to the theoretical calculation.

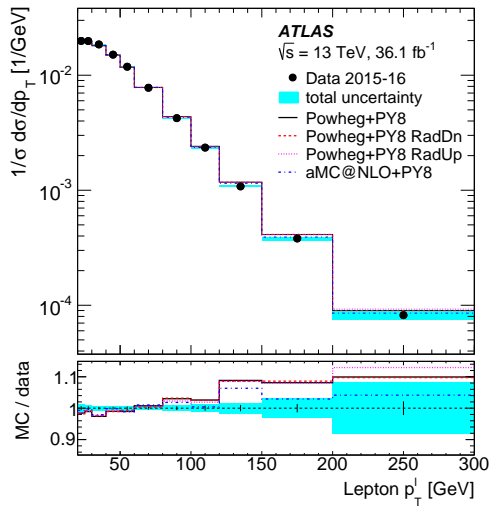
1.3.2 Top-quark decay

The top-quark decays into a W boson and a quark (in more than 99% of cases it is a b-quark) so the signature of the $t\bar{t}$ process is dictated by the decay of the W bosons. Therefore, the final state for the $t\bar{t}$ process can be divided into three classes:

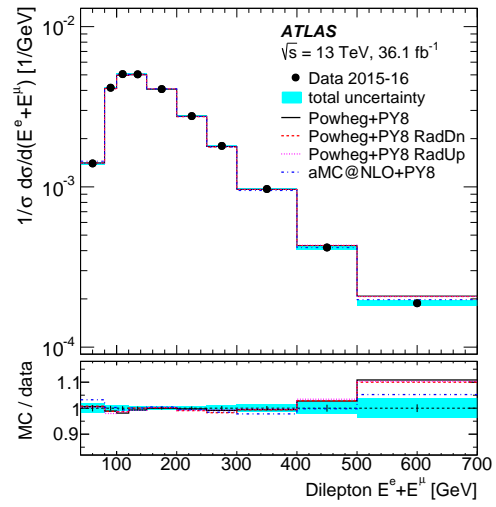


(a) The absolute differential $t\bar{t}$ production cross sections as a function of p_T^l are shown for the data (points) and the Monte Carlo predictions (lines). The vertical lines on the points indicate the total uncertainty in the data. The lower panel in each plot shows the ratios of the theoretical predictions to the data. The dark and light bands show the relative statistical and total uncertainties in the data, respectively [43].

(b) The absolute differential $t\bar{t}$ production cross sections as a function of y^l are shown for the data (points) and the Monte Carlo predictions (lines). The vertical lines on the points indicate the total uncertainty in the data. The lower panel in each plot shows the ratios of the theoretical predictions to the data. The dark and light bands show the relative statistical and total uncertainties in the data, respectively [43].



(c) Normalised differential cross sections as a function of p_T^l . The measured values are shown by the black points with error bars corresponding to the data statistical uncertainties and cyan bands corresponding to the total uncertainties in each bin. The data points are placed at the centre of each bin. The results are compared to the different theoretical predictions. The lower plots show the ratios of predictions to data, with the error bars indicating the data statistical uncertainties and the cyan bands indicating the total uncertainties in the measurements [39].



(d) Normalised differential cross sections as a function of $E^e + E^\mu$. The measured values are shown by the black points with error bars corresponding to the data statistical uncertainties and cyan bands corresponding to the total uncertainties in each bin. The data points are placed at the centre of each bin. The results are compared to the different theoretical predictions. The lower plots show the ratios of predictions to data, with the error bars indicating the data statistical uncertainties and the cyan bands indicating the total uncertainties in the measurements [39].

Figure 1.9: Most recent differential $t\bar{t}$ cross section measurements using the $e\mu$ channel.

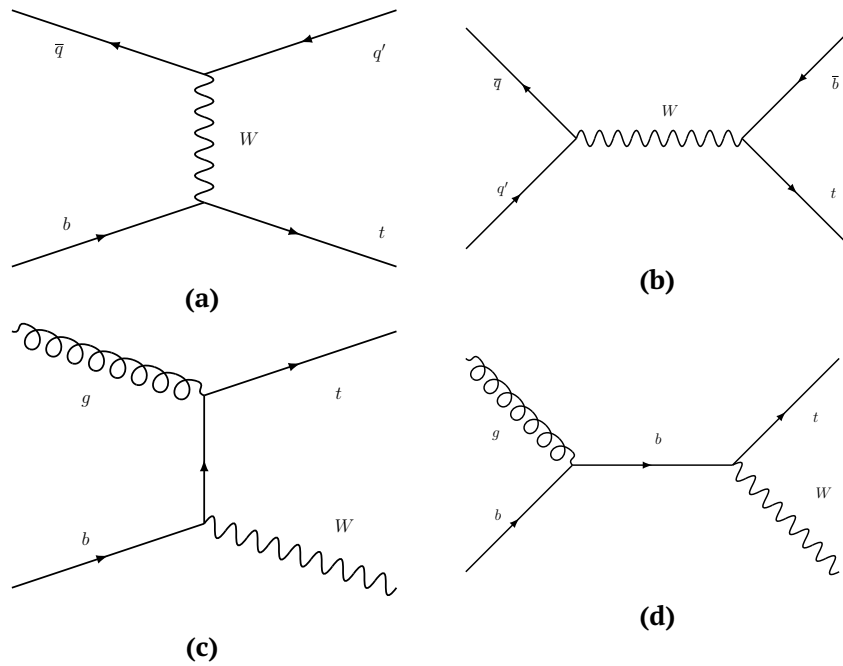


Figure 1.10: Single top-quark Feynman diagrams at LO. Figure 1.10a shows the t-channel, Figure 1.10b shows the s-channel while Figure 1.10c, and Figure 1.10d show the Wt.

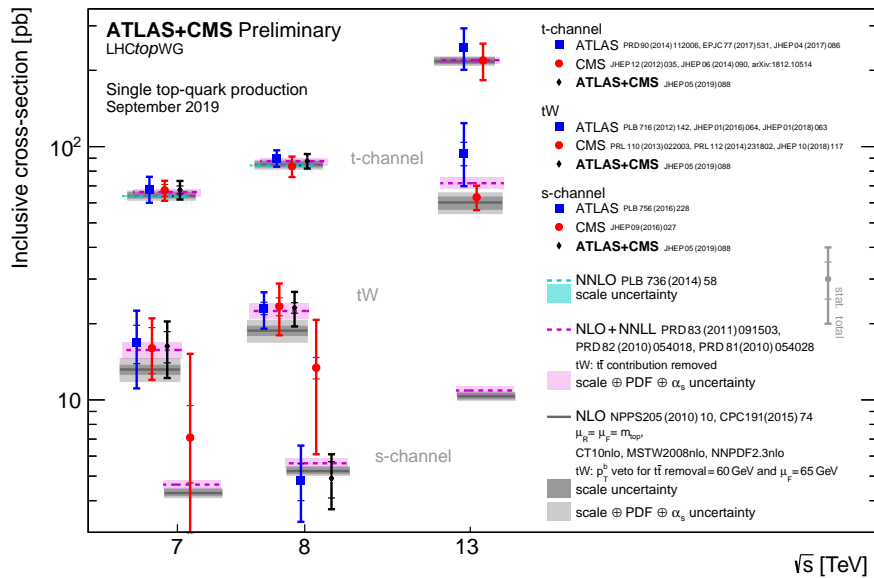


Figure 1.11: Summary of ATLAS, CMS and combined measurements of the single top-quark production cross sections in various channels as a function of a centre-of-mass energy. The measurements are compared to theoretical calculations based on NLO QCD (NNLO QCD for t-channel only) [42].

- *all hadronic channel*: $t\bar{t} \rightarrow W^+bW^-b \rightarrow q\bar{q}'bq''\bar{q}'''b$ with a branching ratio of 45.7%;
- *semi leptonic channel*: $t\bar{t} \rightarrow W^+bW^-b \rightarrow q\bar{q}'bl^-\bar{\nu}_l b + l^+\nu_l b\bar{q}\bar{q}'b$ with a branching ratio of 43.8%;
- *di leptonic channel*: $t\bar{t} \rightarrow W^+bW^-b \rightarrow l^+\nu_l b l^-\bar{\nu}_l b$ with a branching ratio of 10.5%.

The quarks in the final state evolve into jets of hadrons. Their relative contributions, including hadronic corrections, are given assuming lepton universality [17]. While l in the above processes refers to $e, \mu, \text{ or } \tau$, most of the analyses prefer the e and μ with respect to the τ channel, which is more difficult to reconstruct. Typically, the $e\mu$ channel include the di-leptonic channel in which $l = e, \mu$ and also where $l = \tau$ and $\tau \rightarrow l\bar{\nu}_l\nu_\tau$. In this case, the branching ratio is equal to 1.53% considering $BR(\tau \rightarrow l\bar{\nu}_l\nu_\tau) \sim 17\%$.

Figure 1.12 shows the different percentage for all the $t\bar{t}$ decay channels.

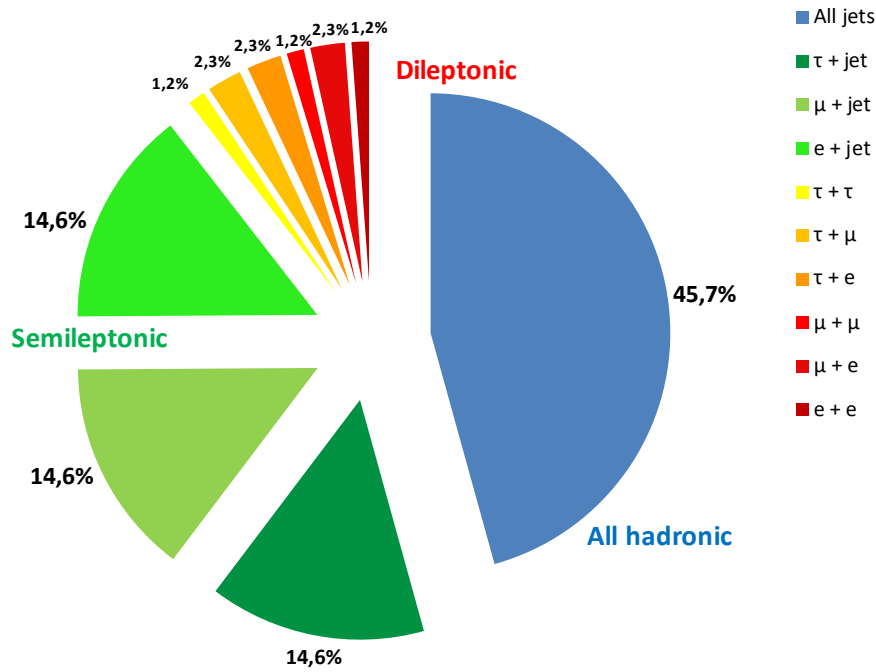


Figure 1.12: $t\bar{t}$ decay channels.

1.3.3 Top-quark mass

In Figure 1.13 are shown the most recent top-quark mass measurements from ATLAS and CMS experiment and the current average value of the top-quark mass is $m_t = 172.76 \pm 0.30 \text{ GeV}$ from direct measurements while $m_t^{\text{pole}} = 172.4 \pm 0.7 \text{ GeV}$ from cross section measurements [17]. This huge mass makes the top-quark the heaviest particle so far known in the Standard Model.

Good knowledge of the m_t together with m_W is an important consistency check of the Standard Model and can lead to a better knowledge of the Standard Model electroweak parameters, as shown in Figure 1.14.

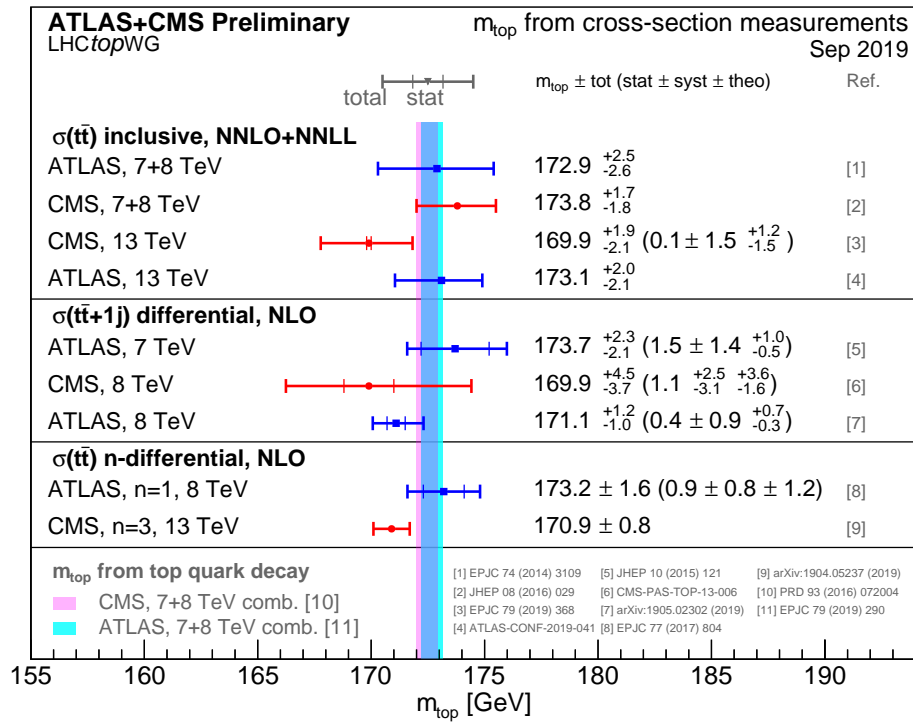


Figure 1.13: Summary of the ATLAS and CMS measurements of the top-quark mass from $t\bar{t}$ production observables. The breakdown of uncertainties is reported only for the analyses that provide such information. The results are compared with the ATLAS and CMS combination of measurements from top-quark decay [42].

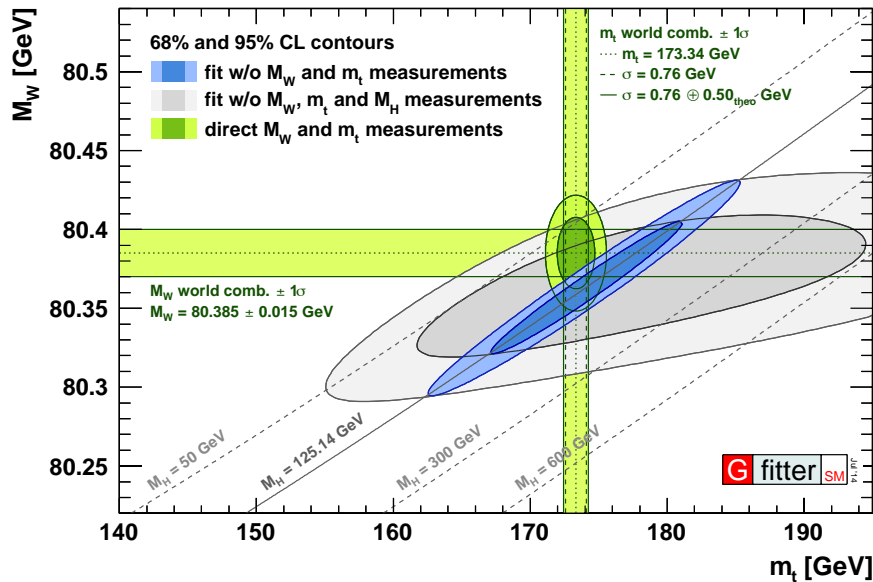


Figure 1.14: Contours of 68% and 95% confidence level obtained from scans of fits with fixed variable pairs m_W versus m_t . The narrower blue and larger grey allowed regions are the results of the fit including and excluding the m_H measurements, respectively. The horizontal bands indicate the 1σ regions of the m_W and m_t measurements (world averages) [48].

In fact, the mass of the W boson can be written as follows:

$$m_W^2 = (m_Z \cdot \cos(\theta_W))^2 = \frac{\pi\alpha_{em}}{\sqrt{2}G_F} \cdot \frac{1}{\sin^2(\theta_W)} \cdot \frac{1}{1 - \Delta r} \quad (1.16)$$

where m_W and m_Z are the masses of the W and Z bosons, respectively, θ_W is the Weinberg angle, G_F is the Fermi constant and Δr represent the radiative term contributions. These terms contain contributions from higher order electroweak loop and depend quadratically from the top-quark mass and logarithmically from the Higgs boson mass. For this reason, a precise measurement of m_t could set constraints on all electroweak parameters.

The Large Hadron Collider and the ATLAS detector

2

The “*Conseil Européen pour la Recherche Nucléaire*” (CERN) is the largest centre for high energy physics research and is also one of the leading institutions driving the development of new detector technologies and computing facilities. Established in 1954, CERN is located in Switzerland and in France near the city of Geneva.

2.1 The Large Hadron Collider

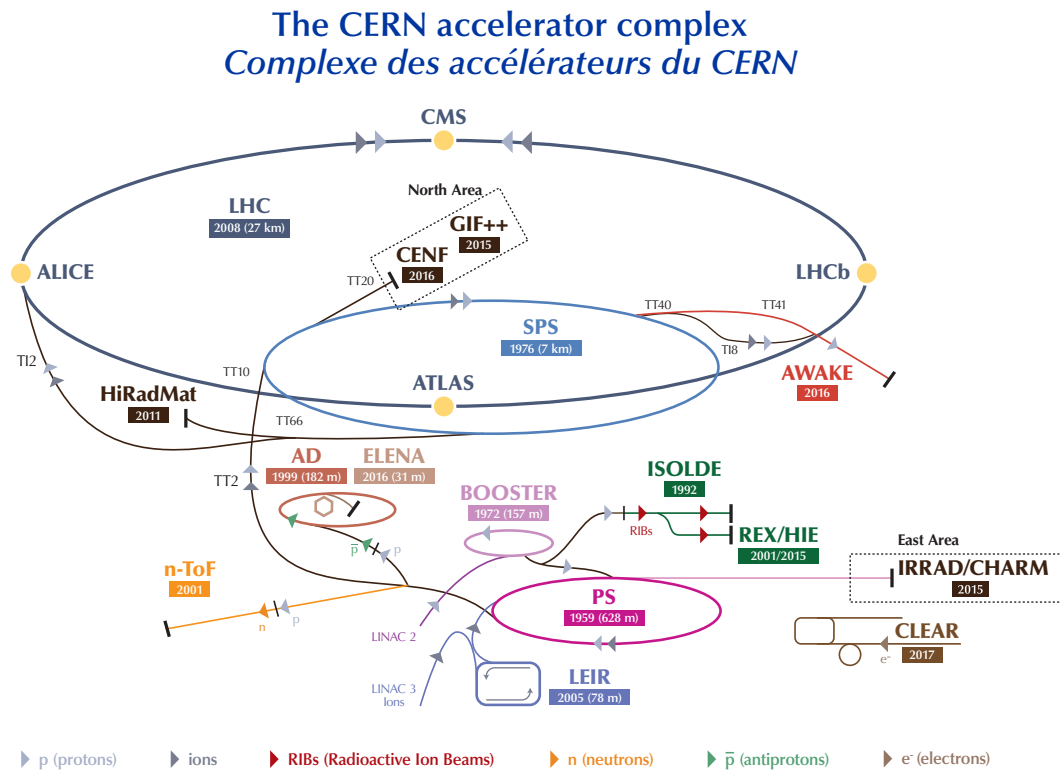
The Large Hadron Collider [49, 50] is currently the biggest and most powerful particle accelerator in the world. It is located at CERN and the first protons collided in 2008. It is a circular machine hosted inside the tunnel that was constructed between 1984 and 1989 for the Large Electron-Positron Collider (LEP) machine [23]. The LHC was built in order to investigate the fundamental structure of the matter and to search for new particles or physics phenomena at unprecedented high energy scales.

It is a 26.7 km circumference ring located 100 m on average below the surface, and it consists of superconducting magnets (cooled to 2°K) producing a magnetic field of $\sim 8 T$ and radio-frequency cavities necessary to bend and accelerate the particles during their path. The LHC was designed to collide either protons or heavy-ions which are circulating in opposite directions in two different beam pipes at high energy and frequency.

The beams are allowed to collide in four interaction points called IP1 - IP8, where the main experiments are located. ATLAS [51], an acronym for “A Toroidal LHC ApparatuS” is located in IP1. In IP2 there is ALICE [52] (“A Large Ion Collider Experiment”), then there is CMS [53] (“Compact Muon Solenoid”) which can be seen as the complementary partner to ATLAS at IP5, and LHCb [54] which stands for “LHC beauty” in IP8. ATLAS and CMS are multi-purpose detectors designed to discover the Higgs boson and to explore the high energy scale; LHCb was designed for physics measurements concerning the b-quark sector, especially focusing on CP violation, while ALICE is intended to first directly prove the existence of and to further investigate quark-gluon plasma in heavy-ion collisions.

Before being injected into the LHC, the particles are accelerated step by step up to the injection energy of 450 GeV, by a series of accelerators shown in Figure 2.1. After the protons have been produced, they are accelerated by the LINAC 2 up to 50 MeV and injected into the booster PS. The booster accelerates the protons until they reach an energy of 1.4 GeV and then it injects them into the Proton Synchrotron (PS) that brings them up to 26 GeV. The last step before the main ring of the LHC is the Super Proton Synchrotron (SPS) which can accelerate the protons up to 450 GeV. Finally, when the protons reach the LHC, the centre-of-mass energy of 13 TeV is achieved, 6.5 TeV for each beam.

The main parameters of a particle accelerator are the centre-of-mass energy and the



LHC - Large Hadron Collider // SPS - Super Proton Synchrotron // PS - Proton Synchrotron // AD - Antiproton Decelerator // CLEAR - CERN Linear Electron Accelerator for Research // AWAKE - Advanced WAKEfield Experiment // ISOLDE - Isotope Separator OnLine // REX/HIE - Radioactive EXperiment/High Intensity and Energy ISOLDE // LEIR - Low Energy Ion Ring // LINAC - LINear ACcelerator // n-ToF - Neutrons Time Of Flight // HiRadMat - High-Radiation to Materials // CHARM - Cern High Energy AcceleraTOR Mixed field facility // IRRAD - proton IRRADiation facility // GIF++ - Gamma Irradiation Facility // CENF - CERN Neutrino platForm

Figure 2.1: Schematic view of the LHC, its pre-accelerators and experiments. Until they reach their final energy of 6.5 TeV , the protons are successively boosted by different accelerators before being injected into the next sequential module. The protons, obtained by ionising hydrogen atoms, start at the linear accelerator LINAC2 after which they are injected into the PS booster followed by the proton synchrotron (PS). After the PS, the protons are transferred to the super proton synchrotron before finally reaching the LHC ring [55].

instantaneous luminosity, which is defined as:

$$\mathcal{L} = \frac{N_b^2 n_b f_r \gamma}{4\pi \epsilon_n \beta^*} \cdot \left(1 + \frac{\theta_c \sigma_z}{2\sigma^*}\right)^{1/2} \quad (2.1)$$

and a definition of each parameter and its design value is reported below:

- N_b is the number of particles per bunch ($\sim 1.67 \cdot 10^{11}$),
- n_b is the number of bunches per beam (2808),
- f_r is the revolution frequency (11245 Hz),
- γ_r is the relativistic gamma factor (~ 7000),
- ϵ_n is the transverse normalised beam emittance (3.75 μm),
- β^* is the beam squeeze at the ATLAS collision point (0.55 m),
- θ_c is the crossing angle between the beams at the interaction point ($\pm 142.5 \mu\text{rad}$),
- σ_z is the Root Mean Square (RMS) of the bunch length (7.55 cm),
- σ^* is the RMS of the beam size at the interaction point.

All these parameters have been optimised to ensure maximal luminosity.

The expected number of events N_{expected} for a process having a production cross section σ is given in terms of the integrated luminosity as

$$N_{\text{expected}} = \sigma \int \mathcal{L} dt \quad (2.2)$$

The high density of the beam bunches and the high frequency of collisions increase the number of events of interest but, on the other hand, they increase also the number of “pile-up” events. Pile-up is a challenge for the detectors and for the acquisition and analysis of the data. In particle physics, pile-up refers to the situation where the detector is being affected by several events at the same time. It can be generated both by the superimposition of particles interactions coming from previous or following bunch crossing (the so-called out-of-time pile-up) or by different interactions in the considered bunch crossing (in-time pile-up). Due to the pile-up, the mean number of interactions for bunch crossing is not equal to one and it increases, and thus the detector must be able to separate particles from multiple simultaneous interactions. The distribution of the mean number of interaction per bunch crossing is shown in Figure 2.2 for the four years of data taking of the Run 2.

The design centre-of-mass energy for pp collisions is 14 TeV (7 TeV per beam) but due to machine safety concerns, the LHC ran at a centre-of-mass energy of 7 TeV and an instantaneous luminosity of $\mathcal{L} = 6 \cdot 10^{33} \text{ cm}^{-2} \text{ s}^{-1}$ with a bunch crossing every 50 ns until the end of 2011 and at 8 TeV during the 2012 run. Since 2015, after the first Long Shutdown (LS1), the data from proton-proton collisions at $\sqrt{s} = 13 \text{ TeV}$ are taken with a maximum instantaneous luminosity of $2.1 \cdot 10^{34} \text{ cm}^{-2} \text{ s}^{-1}$ and an inter bunch of 25 ns.

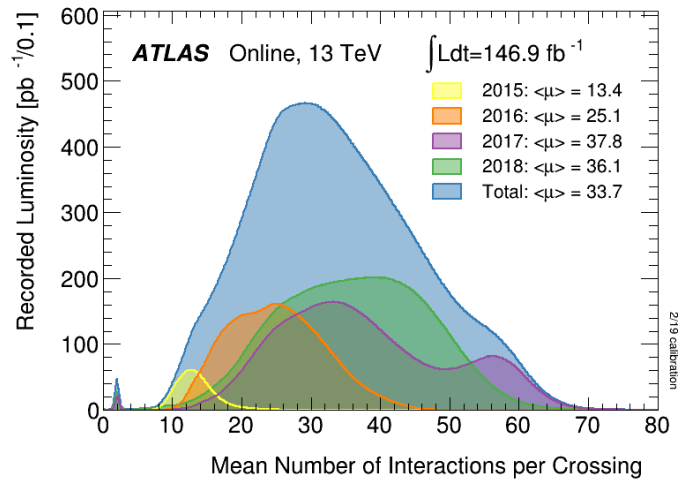


Figure 2.2: Mean number of interactions per crossing for the 2015, 2016, 2017, 2018 and Full Run 2 in pp collision data at 13 TeV centre-of-mass energy [56].

2.1.1 LHC future programme

In order to further increase its discovery potential around the mid-2020s (see Figure 2.3), an upgrade of the LHC will be necessary to increase the luminosity by a factor of 5-7.5. With an increase of the luminosity, more statistics will become available and would provide more accurate measurements of new particles and enable observation of rare processes that occur below the current sensitivity level. This would make it possible to detect rare events not previously witnessed and increase our understanding of the energy frontier. How this should be done is at the heart of the High Luminosity LHC project (HL-LHC) [57]. HL-LHC relies on a number of key innovative technologies, representing exceptional technological challenges, such as cutting-edge 13 Tesla superconducting magnets.

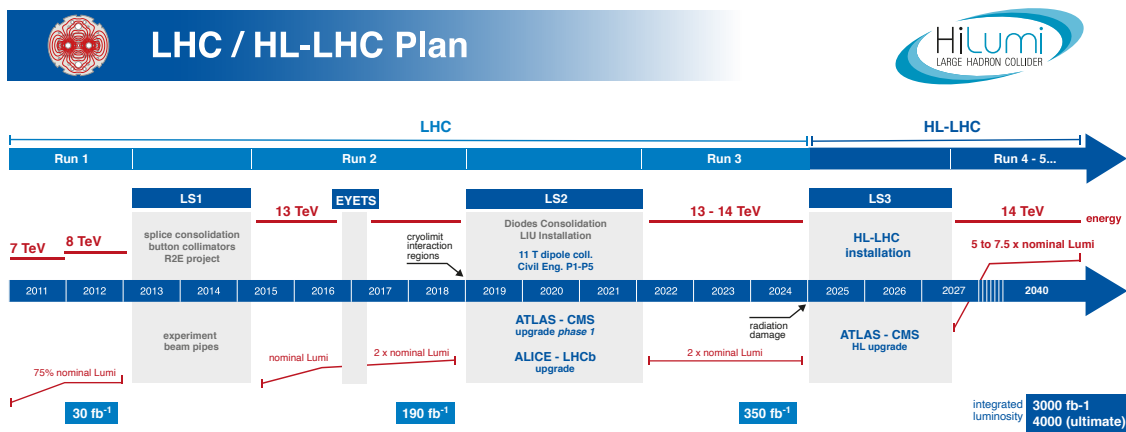


Figure 2.3: This is the LHC plan since 2011, when LHC started to work. Run II ended at the end of 2018 but already since Run III, an increase of a factor 2 of instantaneous luminosity is expected until a new increase to a factor 5-7.5 after HL-LHC installation [57].

2.2 The ATLAS detector

ATLAS is a general purpose detector and it is the biggest experiment along the LHC ring, with a diameter of 25 m, a length of 44 m and a weight of 7000 tons. A schematic view of the ATLAS detector is shown in Figure 2.4. It aims to exploit the full discovery potential of LHC, to perform precise Standard Model measurements, and to investigate the characteristics of the recently discovered Higgs boson. ATLAS has a cylindrical symmetry and is designed to be totally hermetic and to handle high pile-up and luminosity conditions.

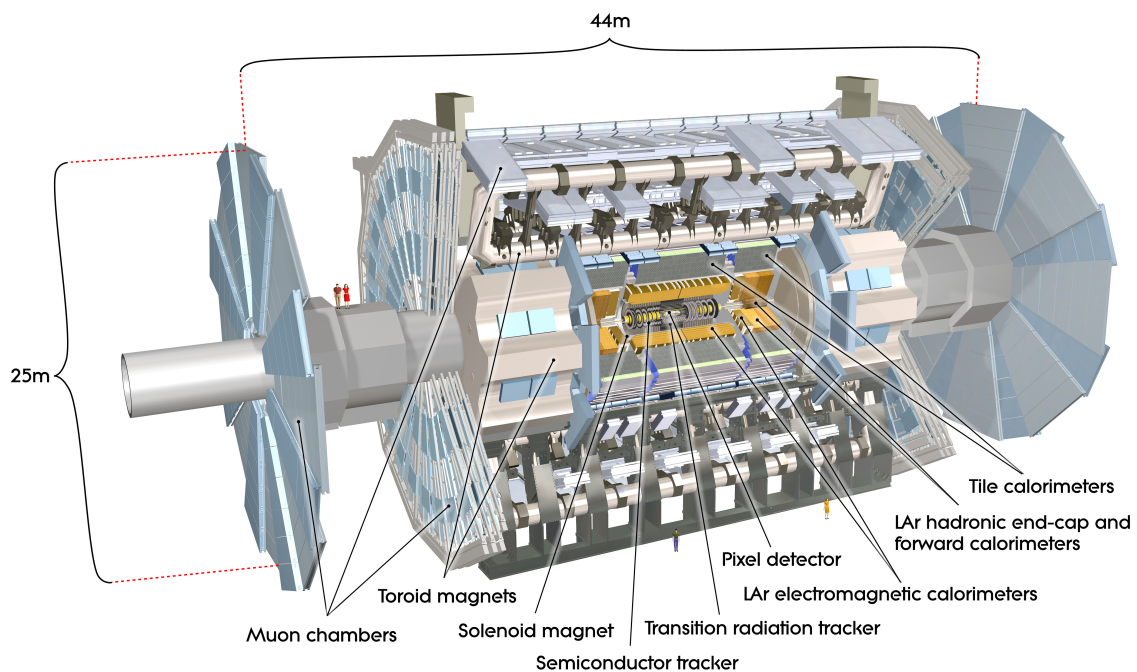


Figure 2.4: Schematic view of the ATLAS experiment with its main components [51].

In detail, it is composed of a magnetic system and many main sub-detectors. Starting from the beam line going outwards there are the Inner Detector, the Calorimeters and the Muon Spectrometer.

The innermost layers compose the Inner Detector (ID) that serves as tracking system. It is immersed in a magnetic field generated by a solenoid. The middle section of ATLAS is filled with the calorimetric system (electromagnetic and hadronic) which measures the energy of most of the particles and prevents them to enter in the outermost layer, the muon spectrometer (MS) dedicated to the identification and reconstructions of muons.

The ATLAS detector uses a right-handed coordinate system [51] shown in Figure 2.5. The beam direction defines the z -axis, and the x - y plane is transverse to the beam direction. The positive x -axis is defined pointing to the centre of the LHC ring and the positive y -axis is defined pointing upwards. The transverse momentum p_T ¹ is defined in the x - y plane.

As in many other experiments at a hadron collider, cylindrical coordinates are used

¹The component of momentum perpendicular to the beam line.

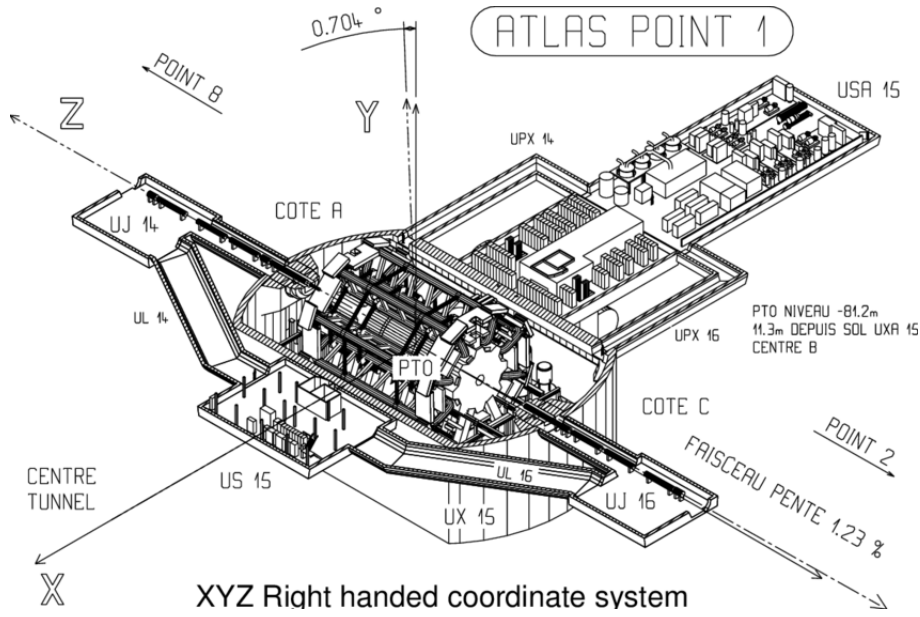


Figure 2.5: The coordinate system in the ATLAS detector [51].

instead of xyz coordinates: in cylindrical coordinates the azimuthal angle ϕ is used and, instead of the polar angle θ , the rapidity y , defined in Equation 2.3 (left), for a massive particle, or pseudo-rapidity η , defined in Equation 2.3 (right), in case the mass particle can be neglected.

$$y = \frac{1}{2} \log \left(\frac{E + P_z}{E - P_z} \right) \quad \text{and} \quad \eta = -\log \left(\tan \frac{\theta}{2} \right) \quad (2.3)$$

This choice is driven by the fact that, at a hadron collider, the total momentum of the initial system along the z -axis is unknown (since the collision takes place between the partons, not at the proton level); for this reason, since longitudinal boosts do not affect the azimuthal angle ϕ and the differences in rapidity are invariant under Lorentz transformation, a useful quantity to measure is the angular distance in the transverse plane:

$$\Delta R = \sqrt{\Delta\eta^2 + \Delta\phi^2} \quad (2.4)$$

In the ATLAS coordinate system, the two end-caps of ATLAS are called the “A-side” and the “C-side” (“B” is the central barrel). The A-side is along the positive z -axis and points towards IP8 which is the direction to the airport and the Saleve, while the C-side is along the negative z -axis and points towards IP2 which is in the direction of the Jura, as shown in Figure 2.5.

2.2.1 Magnetic system

To determine the momentum of charged particles it is essential to measure the curvature of their trajectory through the detector. For this reason, all sub-detectors must be surrounded by a magnetic field. The ATLAS Magnet System is made up of superconducting magnets of three different kinds [58]:

- **Central solenoid:** a solenoidal magnet is placed around the Inner Detector and it has been designed to provide a magnetic field of $\sim 2 T$ along the beam axis [59]. The layout was carefully optimised to minimise the amount of material in front of the calorimetric system.
- **Barrel Toroid:** the ATLAS Barrel Toroid systems consist of eight coils assembled radially and symmetrically around the beam axis; the peak field provided by the Barrel Toroid coils is $3.9 T$, providing 2 to $6 T \cdot m$ of bending power in the pseudo-rapidity range from 0 to 1.3 (the central region of the detector) [60].
- **Endcap Toroids:** the toroidal field, provided by two air-core toroids, characterizes the exterior region of the muon spectrometer [61]. The magnetic field provided inside the toroid muon spectrometer is on average around $1 T$ and peaks at $4 T$.

A schematic view of the ATLAS magnetic system is shown in Figure 2.6.

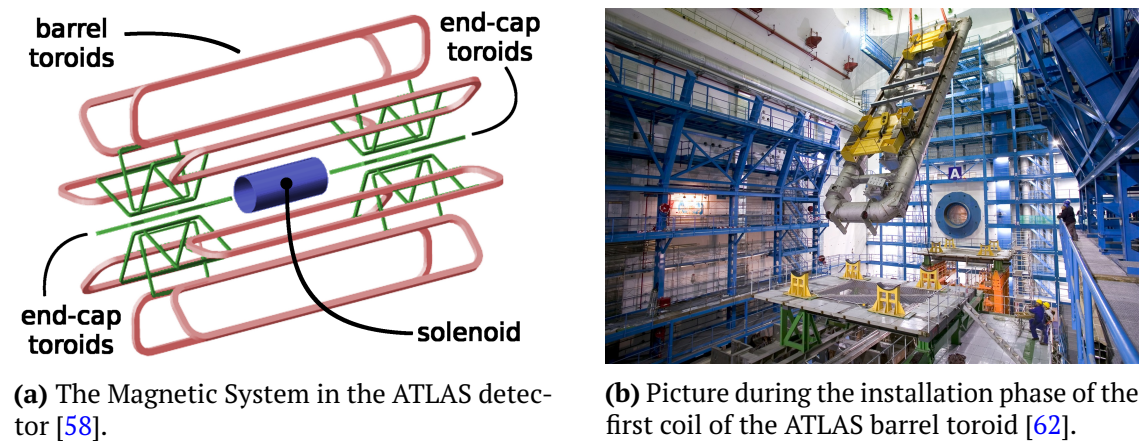


Figure 2.6

2.2.2 Inner Detector

The ATLAS Inner Detector [63, 64] is an ensemble of three precision tracking detectors, as shown in Figure 2.7: the pixel detector, the SemiConductor Tracker (SCT) and the Transition Radiation Tracker (TRT). The ATLAS ID provides high precision track information of charged particles, allows for a reconstruction of primary and secondary vertices through the measurements of the longitudinal (z_0) and transverse (d_0) impact parameters of the tracks and discriminates electrons, muons and heavier charged mesons utilising their specific transition radiation in the TRT. The detectors with higher granularity (pixels and SCT) are based on silicon technology while the TRT is a straw-tube tracking detector. Table 2.1 shows the parameters of the three type of detector of the ATLAS ID.

2.2.2.1 Pixel detector and the Insertable B-Layer

The Pixel detector [67] is the component closest to the beam pipe and it, therefore, has to cope with a higher particle flux than any other detector in ATLAS. This requires a high

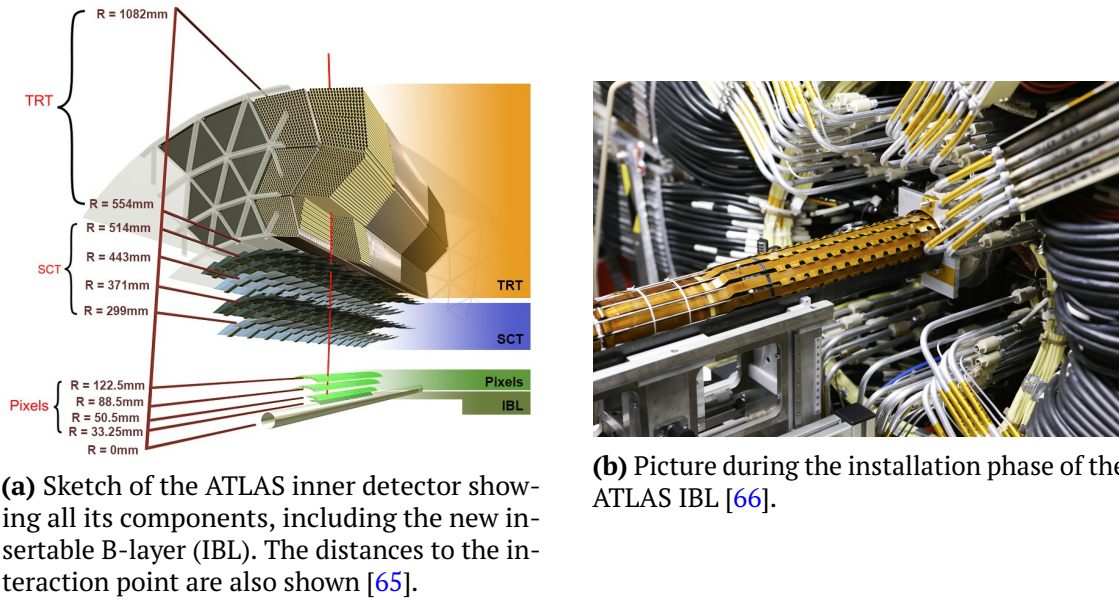


Figure 2.7

Type	Position	Area [m^2]	Resolution [$\sigma(\mu m)$]	Channels (10^6)	η coverage
Pixels	IBL	0.2	$R\phi = 12, z = 66$	16	± 2.5
	3 barrel layers	1.4	$R\phi = 12, z = 66$	81	± 1.7
	3 end-cap disks	0.7	$R\phi = 12, z = 77$	43	1.7 - 2.5
SCT	4 barrel layers	34.4	$R\phi = 16, z = 580$	3.2	± 1.4
	9 end-cap wheels	26.7	$R\phi = 16, z = 580$	3.0	1.4-2.5
TRT	Axial barrel layers		170 (per straw)	0.1	± 0.7
	Radial end-cap layers		170 (per straw)	0.32	0.7-2.0

Table 2.1: Parameters of the ID. The resolutions quoted are typical values.

granularity to disentangle tracks from individual charged particles and to identify primary and secondary vertices. The Pixel detector is composed of three cylindrical layers three disks on each end-cap regions to cover the full tracking pseudo-rapidity range of $|\eta| < 2.5$. It is 1.4 m long and has a diameter of 0.43 m. The active part of the pixel detector consists of a module composed of silicon sensors, front-end electronics and flex-hybrids with control circuits. There are 1744 modules resulting in a total active area of silicon of approximately 2.3 m² and 80.4 million readout channels (this is about 50% of all the readout channels in the entire detector). The size of each pixel is $50 \times 400 \mu\text{m}^2$, allowing to achieve spatial resolutions of 12 μm in the $R - \phi$ plane and 77 μm in z .

During the first Long Shutdown (LS1), between Run 1 and Run 2, a new innermost pixel detector has been added to the configuration and it is called “Insertable B-layer” (IBL) [68]. It is placed at a radius beam pipe of $\sim 33 \text{ mm}$ to cope with the high luminosity expected to be delivered by the LHC during Run 2. With the new layer, the reconstruction of the secondary vertex of decay of B-hadrons is improved and it is less than 10 μm .

2.2.2.2 SemiConductor Tracker

The SCT [69] is built around the pixel detector and it is designed to provide a reconstruction of track in the intermediate radial range, contributing to the measurement of momentum, impact parameter and vertex position, as well as providing good pattern recognition by the use of high granularity. The SCT tracker is composed of four cylindrical layers of modules of silicon micro-strips and nine disks on each end-cap regions to cover the full tracking pseudo-rapidity range of $|\eta| < 2.5$. It has 4088 modules covering an area of approximately 61 m². Including all active readout strips, the SCT layers have more than 6.3 million readout channels in total. The spatial resolution is about 16 μm in the transverse plane and 580 μm in the longitudinal z direction. The system is operated at temperatures between -10°C and -5°C in order to attenuate different types of electronic noise.

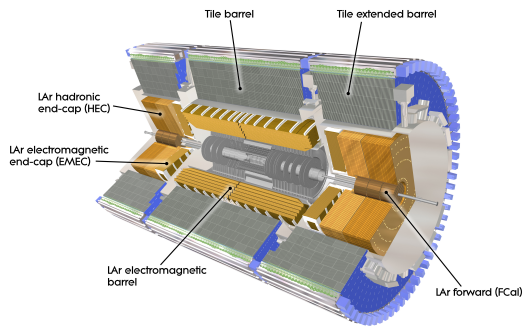
2.2.2.3 Transition Radiation Tracker

The ATLAS TRT [70] is the outermost system of the ID. It provides electron identification capability through the detection of transition radiation X-ray photons. It gives information also during the track reconstruction together with the Pixel and SCT detectors. The detector is a straw-tube tracker; it consists of proportional drift tubes (straws) with a diameter of 4 mm made of Kapton and carbon fibres. Each tube has at its centre a tungsten wire of 31 μm of diameter. The tubes are filled with a gas mixture of $Xe : CO_2 : O_2$ (70% – 27% – 3%). The TRT barrel region is organised in three cylindrical layers and has a total of 52544 straw tubes of 150 cm length, parallel to the beam axis. They cover a pseudo-rapidity range of $|\eta| < 0.7$. Each side of the end-cap consists of 122880 straws with a pseudo-rapidity range of $0.7 < |\eta| < 2.5$. The total number of electronic channels is 420000. Each channel provides a drift-time measurement, giving a spatial resolution of 170 μm per straw.

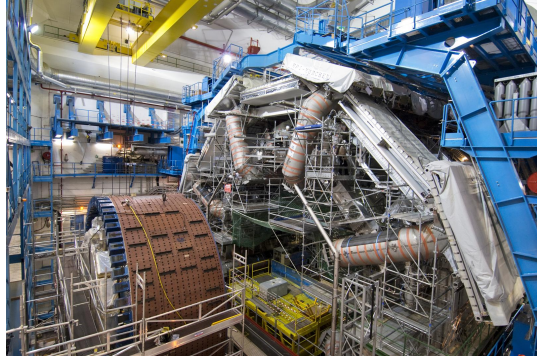
2.2.3 Calorimeter system

The ATLAS solenoid is surrounded by the calorimeters which cover the range $|\eta| < 4.9$ and have a total diameter of 8.46 m and a length of 13.4 m . All the particles exiting the ID, except muons and neutrinos, are stopped in the ATLAS calorimeters which thus measure their energy. It also detects missing transverse energy (the so-called MET, produced by particles that escape the detector undetected such as neutrinos) by summing all the measured energy deposits: $E_T^{miss} = \sqrt{(\sum E_T \cos\phi)^2 + (\sum E_T \sin\phi)^2}$. More precisely, E_T^{miss} is defined as the momentum imbalance in the transverse plane: the resultant of the negative vectorial sum of the momenta of all the particles.

The ATLAS calorimeter, as shown in Figure 2.8, is divided into an electromagnetic part (ECAL), explained in Section 2.2.3.1 and an hadronic part (HCAL), explained in Section 2.2.3.2.



(a) Sketch of the ATLAS calorimetric system [71].



(b) Picture during the installation phase of the ATLAS Tile Calorimeter [72].

Figure 2.8

The total thickness of the ECAL is more than 22 radiation lengths² in the barrel and 24 in the end-caps, while the length of the HCAL is 9.7 interaction lengths³ and 10 in the end-caps), sufficient to provide good resolution also for high-energy jets.

The calorimeter resolution is expressed as follows:

$$\frac{\sigma_E}{E} = \frac{a}{\sqrt{E}} \oplus \frac{b}{E} \oplus c \quad (2.5)$$

where E is usually considered in GeV, a is the coefficient which expresses the dependence of the noise fluctuation plus the radioactivity fluctuation, b represents the coefficient of the sampling fluctuation (fluctuations in photo-statistics, longitudinal and transversal losses and also includes the presence of external passive materials) while c represents the calibration errors, ageing or radiation damaging. All these terms are added in quadrature to obtain the fractional resolution.

²The radiation length is the mean distance over which a high-energy electron loses all but $1/e$ of its energy by bremsstrahlung and $7/9$ of the mean free path for pair production by a high-energy photon.

³The nuclear interaction length is the mean distance travelled by a hadronic particle before undergoing an inelastic nuclear interaction.

2.2.3.1 Electromagnetic calorimeter

The ECAL [73] is a sampling calorimeter made of Liquid-Argon (LAr) as scintillating material and lead as absorbing material, totally immersed in a cryostat at a temperature of $88^\circ K$. This detector was designed with an accordion geometry which provides complete coverage in the azimuthal angle ϕ and leads to a very uniform performance in terms of linearity and resolution as a function of ϕ . It consists of a barrel part with an $|\eta|$ coverage up to 1.475 and two end-caps with the pseudo-rapidity range $1.375 < |\eta| < 3.2$, each part with its own cryostat.

The transition region between the barrel and end-cap ECAL, $1.37 < |\eta| < 1.52$, is expected to have a poorer performance due to the higher amount of passive material in front; this region is referred to as “*crack region*”.

The design resolution of the ATLAS ECAL is:

$$\frac{\sigma_E}{E} = \frac{10\%}{\sqrt{E}} \oplus \frac{170 \text{ MeV}}{E} \oplus 0.7\% \quad (2.6)$$

2.2.3.2 Hadronic calorimeter

The central part of the HCAL is the tile calorimeter (TileCal) [74], placed directly outside the ECAL envelope with the inner radius of 2.28 m and the outer radius of 4.23 m . Two types of end-caps complete the HCAL system of the ATLAS detector: a liquid Argon hadronic end-cap calorimeter (HEC) and a liquid Argon forward calorimeter (FCal).

The TileCal covers the central region ($|\eta| < 1.7$) and uses plastic scintillator plates (called tiles) as active material and steel as absorber. The HEC extends up to $|\eta| < 3.2$ and relies on liquid-argon as active material and copper as absorber material. In this region ($|\eta| < 3.2$), the hadronic calorimeter has a design resolution of:

$$\frac{\sigma_E}{E} = \frac{50\%}{\sqrt{E}} \oplus 3\% \quad (2.7)$$

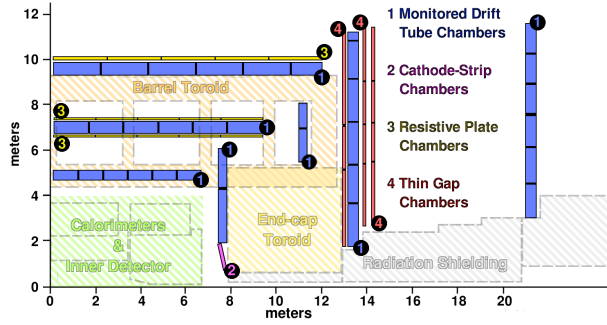
The FCal provides coverage in the very forward region of $3.1 < |\eta| < 4.9$ to improve the measurement of the missing transverse energy. Again liquid-argon was chosen as active material while the absorbing material is composed of copper and tungsten. The design resolution of the FCal is:

$$\frac{\sigma_E}{E} = \frac{100\%}{\sqrt{E}} \oplus 10\% \quad (2.8)$$

2.2.4 Muon spectrometer

The muon spectrometer [75] defines the overall dimensions of the ATLAS detector. It is located outside the calorimeter modules and covers the space between approximately 4.5 m and 11 m in radius and 7 m and 23 m longitudinally. It has the task of detecting charged particles out of the barrel and end-cap calorimeters and measuring their momenta and trajectories which are deflected in the magnetic field up to $|\eta| < 2.7$. It is also designed to

trigger these particles in the region $|\eta| < 2.4$. The muon spectrometer layout is shown in Figure 2.9.



(a) Sketch of the ATLAS muon spectrometer system [75].

(b) Picture during the installation phase of the ATLAS Small Wheel [76].

Figure 2.9

In the barrel region ($|\eta| < 1$), muon tracks are measured in chambers arranged in three concentric cylindrical layers (stations) around the beam axis, with a 5 m, 7.5 m and 10 m radius respectively (inner, medium and outer stations). In the two end-cap regions ($1.0 < |\eta| < 2.7$) the chambers are arranged into three large wheels, perpendicular to the z -axis, at distances of 7.4 m (Small Wheel, SW), 14 m (Big Wheel, BW) and 21.5 m (Outer Wheel, OW) from the interaction point.

The overall momentum resolution provided by the muon system is shown in Table 2.2.

p_T (GeV)	σ_{p_T}/p_T	Comments
20 GeV	$\sim 2.5\%$	Muon spectrometer only limited by energy loss and multiple scattering
	$\sim 1.6\%$	Combined with inner tracker
75 GeV	$\sim 2.4\%$	Muon spectrometer only limited by energy loss and multiple scattering
	$\sim 2.0\%$	Combined with inner tracker
1 TeV	$\sim 11\%$	Limited by charge determination

Table 2.2: Design parameters of the ATLAS muon spectrometer [75].

Designed to measure high-momentum final-state muons, among the most promising signatures of physics at the Large Hadron Collider, the ATLAS Muon Spectrometer is instrumented with separate-function trigger and high-precision tracking chambers that belong to four different detector technologies:

- Cathode Strip Chambers (CSC);
- Monitored Drift Tubes (MDT);
- Resistive Plate Chambers (RPC);
- Thin Gap Chambers (TGC).

Type	Function	Chamber resolution (RMS)			Measurements/track		Number of	
		z/R	ϕ	time	barrel	end-cap	chambers	channel
MDT	Tracking	$35 \mu\text{m}$ (z)	—	—	20	20	1088 (1150)	339k (354k)
CSC	Tracking	$40 \mu\text{m}$ (R)	5 mm	7 ns	—	4	32	30.7k
RPC	Triggering	10 mm (z)	10 mm	1.5 ns	6	—	544 (606)	359k (373k)
TGC	Triggering	$2-6 \text{ mm}$ (R)	$3-7 \text{ mm}$	4 ns	—	9	3588	318k

Table 2.3: Parameters of the sub-systems of the MS. The quoted spatial resolutions (columns 3, 4) do not include chamber-alignment uncertainties. Column 5 shows the intrinsic time resolution of each chamber type. Numbers in brackets refer to the complete detector configuration as planned for 2009 [75].

2.2.4.1 Monitored Drift Tubes

The Monitored Drift Tubes (MDTs) chambers are made of drift tubes with a diameter of 30 mm . The surface of the tube is made using aluminium and is $400 \mu\text{m}$ in thickness. A tungsten-rhenium wire of $50 \mu\text{m}$ in diameter is located at the centre of the tube. The tubes are operated with a non-flammable gas mixture $Ar : CO_2$ (93% : 7%) with a small amount of water vapour at a pressure of 3 bar . The electric field inside the tube is proportional to the inverse of the wire distance so the electrons, produced by the ionisation of the gas by the charged particle passing through it, drift towards the anode wire while the ions drift towards the cathode wall of the tube, with a maximum drift time of 700 ns . Near the wire, the field is sufficiently high to produce the avalanche multiplication of the electrons with a gain of $\sim 2 \cdot 10^4$. The position of the track is determined by measuring the drift time and knowing the drift velocity, the drift time is converted into the distance from the wire.

The MDTs cover almost the full rapidity region of the ATLAS MS $|\eta| \leq 2.7$ apart from the high rapidity region of the SW where CSCs are used. The basic structure consists of two multi-layers of drift tubes separated by a support frame. Each multi-layer combines three layers of tubes except for the inner stations of the muon spectrometer (small radius) where one additional layer of tubes is used in each multi-layer enhancing the pattern recognition performance in the high background rates of this region.

2.2.4.2 Cathode Strip Chambers

The Cathode Strip Chambers (CSCs) are located in the two innermost regions of the end caps, the so-called “Small Wheels”, covering the largest rapidity region $2 \leq |\eta| \leq 2.7$ that is characterised by the highest particle flux among the muon spectrometer stations. They are operated with a gas mixture of $Ar : CO_2$ (80% : 20%) while the voltage is tuned individually per chamber layer ($\sim 1800 - 1900 \text{ V}$) in order to achieve uniform gain throughout the whole CSC system.

They are Multi-Wire Proportional Chambers with the wires serving as the detector anodes. The CSCs host two cathode layers of readout strips measuring the principal (η) and the perpendicular to it (second) coordinates (ϕ). The principal coordinate is obtained by a charge interpolation on the segmented cathode, with strips running perpendicularly with respect to the anodes. A second layer of readout strips, running parallel to the wires, provide the second coordinate measurement. Apart from the precise tracking, the CSCs,

due to the small gap, collect all the ionisation electrons in less than 30 ns; this ensures efficient operation in the forward region (high background) of the muon spectrometer.

2.2.4.3 Resistive Plate Chambers

The Resistive Plate Chambers (RPC) is a parallel-plane gas detector consisting of two resistive planes, made of high resistivity plastic sheets, placed at a distance of 2 mm through insulating spacers. The electrical field between the planes is about 4.9 kV/mm and allows the formation of avalanches to the anode along the ionising tracks. The signal is read by capacitive coupling on metal strips mounted on the outer face of the resistive plane. An RPC chamber is composed of two rectangular detectors called units. Each unit is composed of two independent layers read out by two groups of orthogonal strip (η and ϕ).

The chambers are filled with a gas mixture of $C_2H_2F_4 : C_4H_{10} : SF_6$ (94.7% : 5% : 0.3%) which meets the requirements for a relatively low working voltage, non-flammability and low cost.

In the muon barrel region ($|\eta| \leq 1.05$) the RPC system is responsible for providing the trigger signals. The RPC chamber is able to provide a timing measurement with an accuracy of the order of 1.5 ns fulfilling the requirements of the ATLAS trigger system.

Moreover, being a fast detector technology the RPCs are also characterised by bunch crossing identification capability. Additionally, their fast and coarse tracking can be used to identify the hits of the precision chambers that are related to the detected muon track.

2.2.4.4 Thin Gap Chambers

The trigger information in the muon end-cap region is provided by the Thin Gap Chambers (TGCs). They are also able to provide a measurement of the azimuthal coordinate to complement the bending coordinate measured by the end-cap MDT chambers. The middle end-cap station of the MDTs is complemented by seven layers of TGC which provide both triggering and azimuthal coordinate measurement. The TGC are similar to the Multi-Wire Proportional Chambers with anode wires enclosed by two graphite cathode layers and two layers of readout strips running perpendicularly to the wires. They are operated with a highly quenching gas mixture of $CO_2 + n-C_5H_{12}$ (55% and 45%) and a very intense electric field (3200 V) to satisfy the time, momentum, and azimuthal coordinate resolution requirements while making the performance of large surface chambers insensitive to mechanical deformations. The very good timing resolution guarantees the bunch crossing identification capability of the TGC.

2.2.4.5 Denomination of the muon spectrometer sectors

The eight cryostats of the barrel toroid magnet impose a division into 16 sectors for the muon instrumentation in the barrel region. Eight so-called large sectors are located in the angular regions between the coils, spanning about 29° in ϕ and eight so-called small sectors are located in the angular regions which include a barrel toroid coil each, spanning about 20° in ϕ . Between each large and each small sector, there is an overlap of about 2°

in ϕ .

The sectors are numbered consecutively, starting from sector 1 which contains the positive x-axis ($\phi = 0$). The sector numbers increase with increasing ϕ , see Figure 2.10. This numbering scheme implies that the large sectors have odd numbers, and the small sectors even numbers.

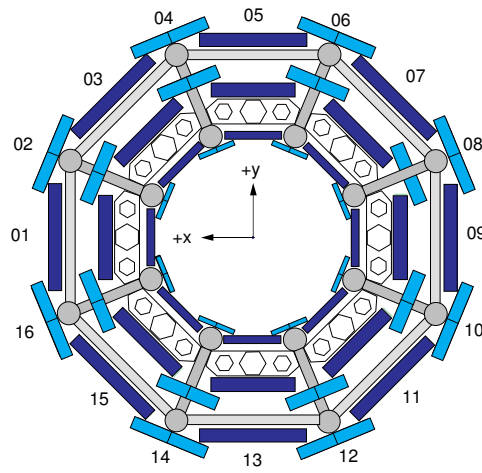


Figure 2.10: Definition of the 16 sectors of the ATLAS muon spectrometer [75].

2.2.5 Trigger system

In ATLAS, the storage size of each digitised event is around 1 MB. Due to the constraint from data storage capacity and rates, it is impossible to store all the events produced in the collisions, therefore, a trigger system is employed to rapidly decide with high efficiency potential interesting events produced in a given bunch-crossing interaction to record for later analysis.

At the LHC design luminosity, the proton-proton collisions take place every 25 ns (40 MHz). The goal of the ATLAS trigger system [77] is to reduce the rate of candidate collisions from 40 MHz to 1 kHz without a loss of interesting physics events. In Run 2, the trigger system consists of two levels of event selections: a Level-1 trigger (L1) reducing event rate to 100 kHz and a high-level trigger (HLT) [78] further reducing event rate to 1 kHz.

2.2.5.1 Level 1 Trigger

There are three L1 subsystems. One is the Level-1 calorimeter trigger (*L1Calo*), which uses calorimeter information of reduced granularity to trigger electrons, photons, hadronic τ decays, jets and (missing) transverse energy. The other system with a direct detector interface is the Level-1 muon trigger (*L1Muon*), which primarily uses TGC and RPC information to make fast decisions on muon trigger items. The last L1 subsystem is the Level-1 topological trigger (*L1Topo*) that combines information from multiple *L1Calo* and *L1Muon* objects as well as their kinematics (e.g. angular separation, invariant mass). The

Central Trigger Processors uses the information from the L1 subsystems to define regions of interest (RoI) in the detector and perform an initial selection on the events.

2.2.5.2 High Level Trigger

Events accepted by L1 trigger, are passed to the HLT which operates on the information from the RoI and from the full event. While the L1 trigger uses custom-made electronics based on FPGAs, the HLT runs on a conventional computer cluster and has about ~ 200 ms on average to decide. The target average HLT rate is 1 kHz, a significant improvement compared to 0.6 kHz of the Run 1. The set of active triggers usually changes during the data taking, as the intensity of the beam changes.

2.2.6 ATLAS upgrade

The LHC will be upgraded in several phases extending the reach of its physics program as discussed in Section 2.1.1. Already after the end of the first long shutdown (LS1) during 2013-2014 the accelerator's energy was increased at the value of 6.5 TeV per beam with an instantaneous luminosity of the order of $10^{34} \text{ cm}^{-2} \text{ s}^{-1}$. With the intermediate upgrades, that will follow in the next years, ATLAS foresees a luminosity increase by a (safe) factor 7.5 with respect to the design value. In order to maintain its current excellent performance, the ATLAS detector will need some important upgrades.

Major upgrades provided by ATLAS for the LS2 [79] are:

- the New Small Wheel;
- integrating the NSW into the L1 trigger;
- new LAr calorimeter electronics for better use in the L1 trigger (to cope with the higher pile-up).

Even during the LS3 there will be other upgrades of the ATLAS detector to ensure that its performance does not crawl with the installation of HL-LHC.

- the main activity will be the construction of a new inner detector (ITk);
- the Calorimeter readouts will need a substantial upgrade (new photo-detector), part of it will be done in a staged way in the LS2;
- most of the existing electronics/computing/TDAQ will need to be upgraded and modernised to face additional 8-10 years of running in extreme conditions;
- finally, also the MDT/RPC electronic will be upgraded.

The New Small Wheel project and the MicroMegas chambers

3

3.1 The New Small Wheel upgrade project

3.1.1 The current Small Wheel

The current Small Wheel (SW) structure, shown in Figure 3.1, is composed of two wheels each one consisting of two parts:

- the *Detector Wheel* where the tracking detectors (MDT and CSC chambers) and the alignment system are installed; the mechanical structure consists of a massive central hub from which the various rays, all interlinked to each other like petals around the corolla of a flower, extend radially;
- the shielding (*JD shielding*), i.e. a disk-shaped structure that covers the entire surface of the SW with, in the more interior radius, a protruding cylindrical extension (plug) around the beam pipe. Thin Gas Gap Chambers (TGC) are located in the outer part of the disk shield and pointing in the opposite direction with respect to the interaction vertex.

The detector wheel with the precision chambers shows the segmentation into 8 small (on the IP side¹) and 8 large sectors (on the HO side) with a small overlap region between the two types.

3.1.2 Limitations of the present Small Wheel

With the instantaneous luminosity increase predicted by the LHC upgrade, two fundamental aspects must be taken into account for the ATLAS muon spectrometer.

1. The performance of the muon tracking (especially in end-cap regions) worsens due to the increase of the expected background rate in the ATLAS cavern. Background hits in the muon spectrometer originate predominantly from low energy photons and neutrons: these particles are generated by proton collisions, either synchronous ones with bunch crossings that mislead the ATLAS trigger (*in-time background*) or by collisions that occur one or more bunch crossings before (*out-of-time background*). Regardless of the mode of production, such particles are referred to as the *cavern background*. By extracting the future high luminosity and high energy conditions, using the rates observed for the 2012 luminosity conditions, there is a significant degradation of performance in terms of both efficiency and resolution in the inner

¹IP is the direction pointing to the interaction point while HO is the direction pointing to the blue support structures at the ends of the main cavern called HO.

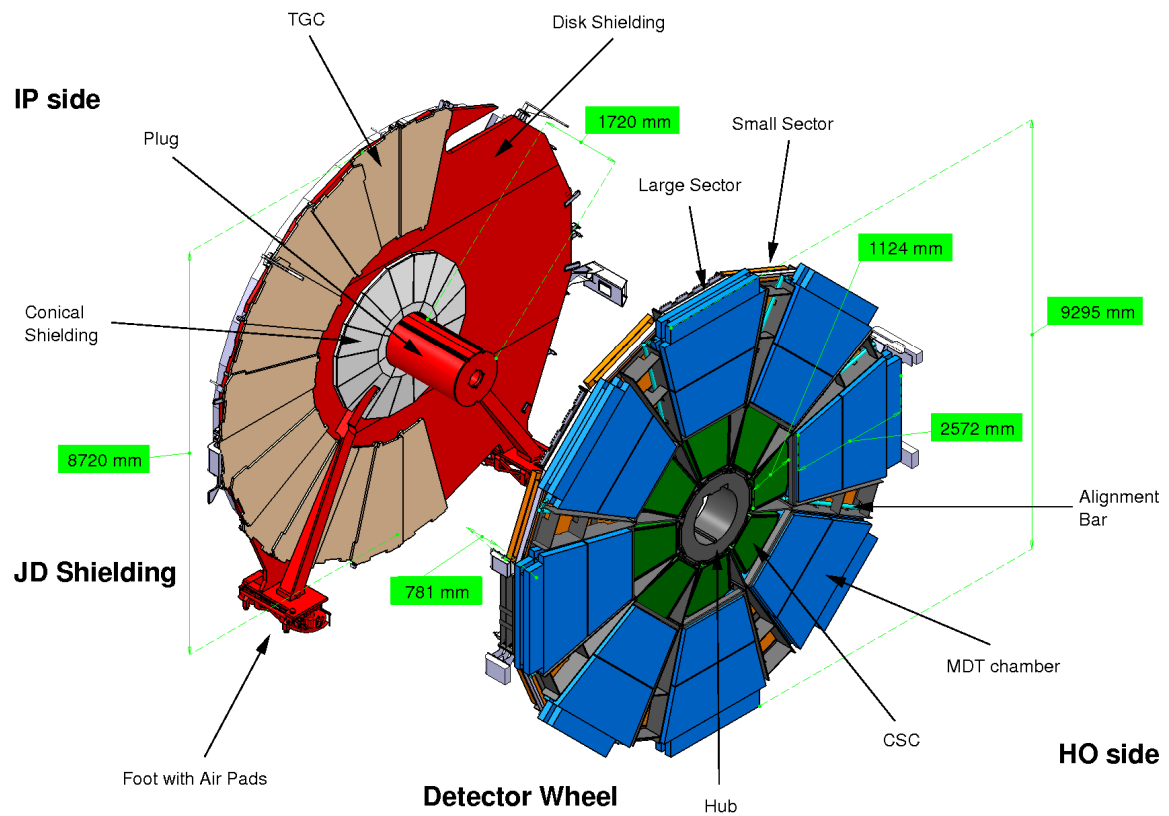


Figure 3.1: Schematic structure of the actual SW. The arrangement of the CSC and MDT chambers on the wheel can be seen in the picture [75]. The CSC chambers are inclined respect the plane of the MDT chambers and are not orthogonal to the beam line.

station of the spectrometer in the end-cap, the Small Wheel. As can be seen in Figure 3.2, the efficiency of the current MDT decreases linearly with the rate increase and with 300 kHz per tube, which is the one expected for the design luminosity of $10^{34} \text{ cm}^{-2} \text{ s}^{-1}$, the MDT already has inefficiencies of about 35%. This inefficiency can be recovered at the chamber level (only a subset of all available hits is required by the segment finding algorithm), but beyond this rate, also the chamber efficiency starts to decrease dramatically. LHC has already managed to take data at this luminosity with a hit rate recorded on MDTs lower than expected. This would allow MDTs to be used also Run 3, but an upgrade would still be necessary for future runs (HL-LHC). Considering that the resolution of the muon momenta depends heavily on the presence of the hits in the SW, the degradation of its performance is highly detrimental to the overall performance of the detector.

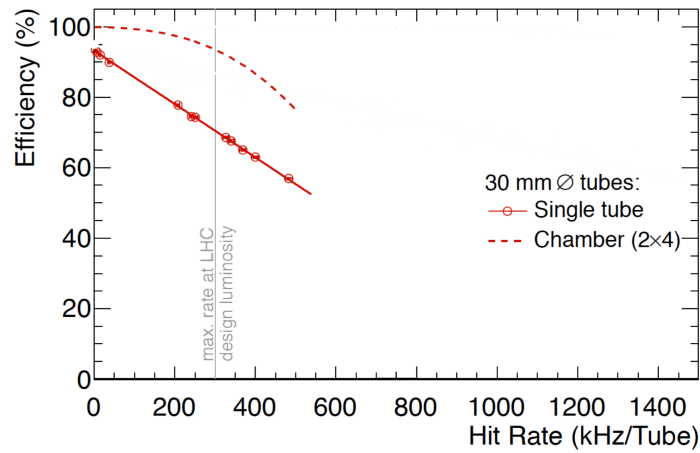


Figure 3.2: Reconstruction efficiency for a single MDT tube hit (continuous line) and segment track efficiency (dotted line) for a MDT chamber as a function of the estimated rate from data and simulations. With the expression “designed luminosity” refers to the already exceeded instantaneous luminosity $\mathcal{L} = 1 \times 10^{34} \text{ cm}^{-2} \text{ s}^{-1}$ [80].

2. The first level trigger rate for muons increases proportionally to instantaneous luminosity. The first level trigger in the end-cap regions is based on track segments reconstructed by the TGCs. The transverse momentum of the muons is determined by the angle of the track segment with respect to the direction pointing towards the interaction point. A significant part of the end-cap trigger rate is due to backgrounds such as low energy particles, mainly protons, generated inside the material between the interaction point and the end-cap muon station, and particles that are scattered in the material and can produce false triggers having an angle similar to the real high- p_T -shaped muons, as shown in Figure 3.3. A 2012 data analysis shows that around 90% of the muon trigger in the end-caps are coming from fake leptons as shown in Figure 3.4. This is due to the fact that only the Big Wheel is used to trigger the events, as shown in Figure 3.3. Consequently, the rate of the first level trigger for muons in end-cap regions is 8 to 9 times higher than that in the barrel. In fact, as can

be seen in Figure 3.4, more than 90% of the first level trigger rate for muons comes from the end-caps, and most of the triggered objects are not reconstructed off-line. The maximum rate allowed by the first level trigger is 100 kHz, determined by the experiment readout system and it is only 20 kHz for a single muon. At a luminosity of $3 \times 10^{34} \text{ cm}^{-2} \text{ s}^{-1}$ the expected rate, extrapolated from the data with the current small wheel configuration, is 60 kHz for $p_T > 20 \text{ GeV}$ and then is three times larger than the one bearable by the readout system. Increasing the threshold to 40 GeV reduces the rate of only a factor two, which is therefore even greater than the bearable one at the cost of a substantial loss of efficiency.

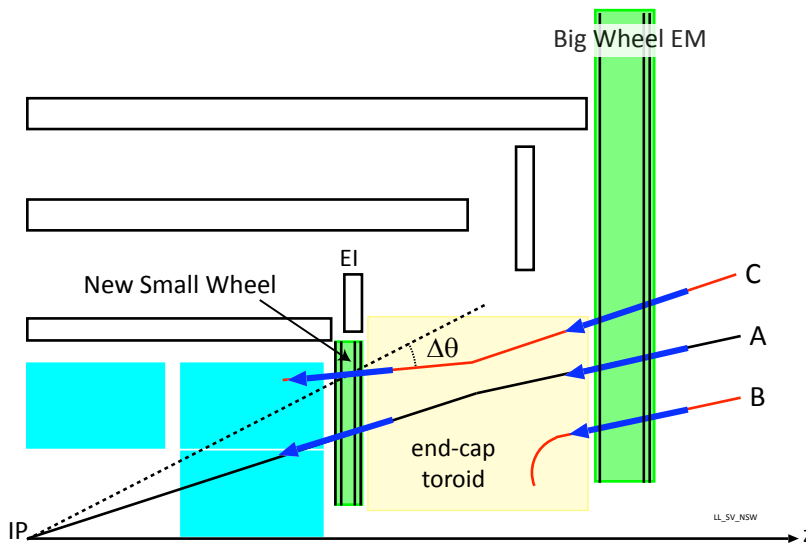


Figure 3.3: Muon trigger scheme in end-caps. The current trigger system, relying only on the Big Wheel, would accept all three tracks shown. With NSW only track A, as confirmed by the systems placed on both wheels, will be accepted. Track C will be discarded because the track in the NSW does not point in the direction of the interaction vertex and the same fate will have the track B [80].

3.1.3 Upgrade requests

The main requirement of the upgraded SW is to have at least equal performance as the current SW at both low and high luminosity conditions [80]. In particular, it must be able to measure the muon transverse momentum with a precision of 15% at 1 TeV for all η coverage of the SW (up to $|\eta| < 2.7$). For this reason, the new detectors must satisfy the following requirements:

- ability to reconstruct the track segments with a resolution of $\sim 40 \mu\text{m}$ on the bending plane to match the performance of the current MDT chambers. The chamber resolution includes contributions from readout strip position accuracy ($30 \mu\text{m}$ in the precision coordinate) and planarity of readout and drift planes accuracy ($80 \mu\text{m}$ in the z -coordinate). This will ensure that the spectrometer has a better momentum

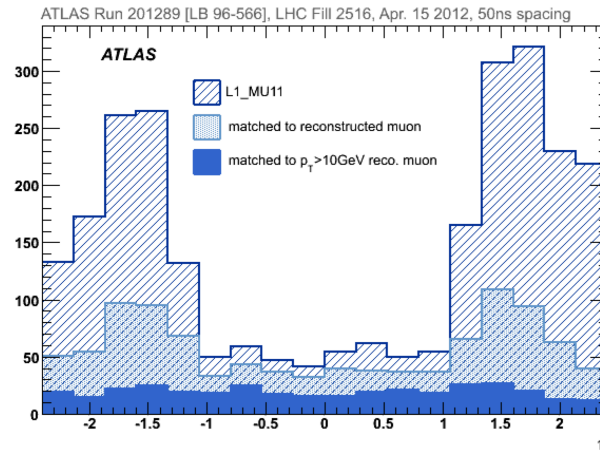


Figure 3.4: Distributions in η of muons ($p_T > 10 \text{ GeV}$) coming from the I level trigger (L1_MU11) with the subset of those for which there is a well-reconstructed track (combining information on tracks from the inner detector and the muon spectrometer for $p_T > 3 \text{ GeV}$). Finally, it is also shown the distribution of triggered muons for which there is a reconstructed muon with $p_T > 10 \text{ GeV}$ [80].

resolution of 10% at $p_T \sim 1 \text{ TeV}$. When including the mis-alignment the momentum resolution can grow until 15%. To comply with this request, a resolution of at least $100 \mu\text{m}$ is required for each layer of a future multilayer detector that will be installed in the upgraded wheel;

- segment finding efficiency greater than 97% for muons with $p_T > 10 \text{ GeV}$;
- efficiency and resolution must not degrade at high p_T ;
- capability to measure the second coordinate (ϕ) with a resolution of $\sigma \sim 1 - 2 \text{ mm}$ to facilitate the reconstruction of muons.

The environment in which the upgrade will work will be characterised by numerous spurious hits generated by δ rays², neutrons, or other background particles. In addition, a multilayer detector with great redundancy is required and it needs to be durable so as not to require repairs over time. Any new detector installed in place of the current Small Wheel must be operational for ATLAS's entire activity time, and to be able to acquire up to 3000 fb^{-1} of collision data.

3.1.4 The New Small Wheel layout

The New Small Wheel (NSW) is the inner end-cap station of the ATLAS muon spectrometer that will replace the current SW. The NSW system [80] will consist of sixteen planes of detectors arranged in two multi-layers, each comprising eight small-strip TGC (sTGC) and as many Micro-Mesh Gaseous Structures (MicroMegas, MM). sTGCs will be mainly used for the trigger, given their ability to identify products from single bunch crossing while

²Electrons generated during primary ionisation having such energy to produce other electron-ion pairs and generate a fake additional track in the detector.



Figure 3.5: Images of the two mechanical structures of the ATLAS New Small Wheels ready to host the chambers.

the MicroMegas will be mainly used as tracker. The detectors will be arranged (sTGC - MM - MM - sTGC) to maximise the distance between the sTGCs of the two multi-layers. Between the two MicroMegas chambers, a spacer frame of 5 cm will be inserted as shown in Figure 3.6.

The choice of having eight planes per detector is dictated by the need to provide a robust and fully functional detection system for the entire operating period because if some detectors may have malfunctions over the years the repair would be rather problematic. Furthermore, neutrons, background photons, and also δ rays, change the number of hits compared to that of the real tracks. With eight levels of detectors, the tracks will be reliably reconstructed even under these conditions.

A naming scheme has been defined to refer to the chambers and their parts. In this thesis, the standard nomenclature is used and it is described below:

- **Plane** or **Layer**: single detector gas gap with the readout structures;
- **Multiplet** or **Quadruplet** or **Module** : assembly of four layers of a single technology (sTGC or MicroMegas) in z direction which constitute a single independent object produced as a unit;
- **Wedge**: assembly of modules of a single technology type (sTGC or MicroMegas) in the z -direction, covering a full sector in the $r-\phi$ plane;

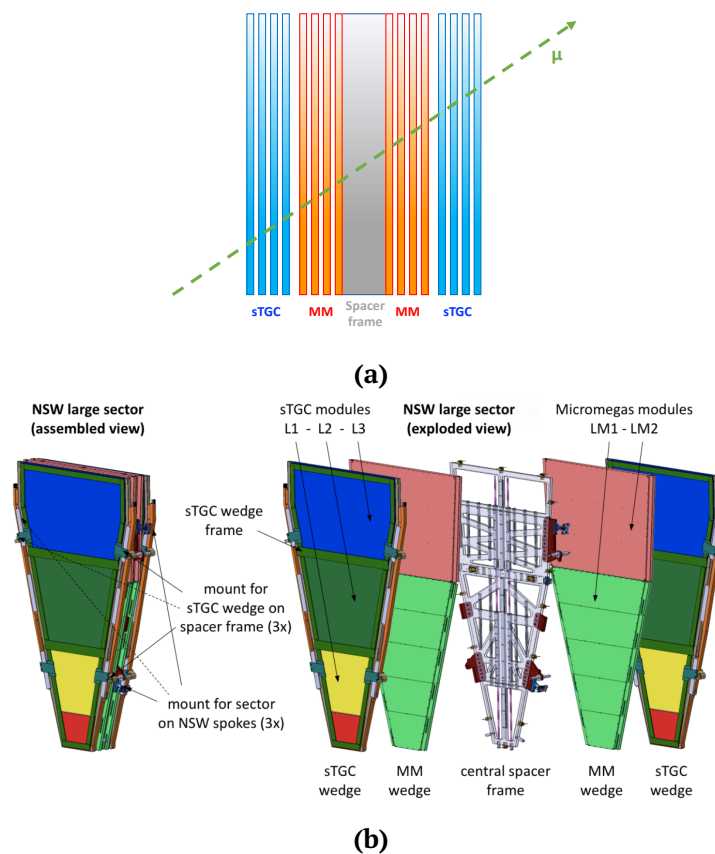


Figure 3.6: Schematic view of the detectors disposition in the New Small Wheel (sTGC - MM - spacer frame - MM - sTGC) from the interaction point. Different radial segmentation is shown for the sTGC and MicroMegas detectors in Figure 3.6b [80].

- **Double-wedge:** assembly of two wedges of a single technology type (in particular MicroMegas) in the z direction, covering a full sector in the $r - \phi$ plane;
- **Sector:** $1/16^{th}$ of the NSW on side A or C (corresponding to a large or small geometric sector), comprised of two sTGC wedges and two MicroMegas wedges. A sector is named using the side of the NSW and the number following the ATLAS muon spectrometer sector scheme, as described in Sec. 2.2.4.

Each wedge has a radial segmentation in modules of different sizes and shapes. For the MicroMegas layer four types of MicroMegas quadruplets are distributed along r and in small/large sectors, while each sTGC sector is composed of three different quadruplet types, as shown in Figure 3.7:

MicroMegas

LM1, lower radius of the large sectors

LM2, larger radius of the large sectors

SM1, lower radius of the small sectors

SM2, larger radius of the small sectors

sTGC

QL1, lower radius of the large sectors

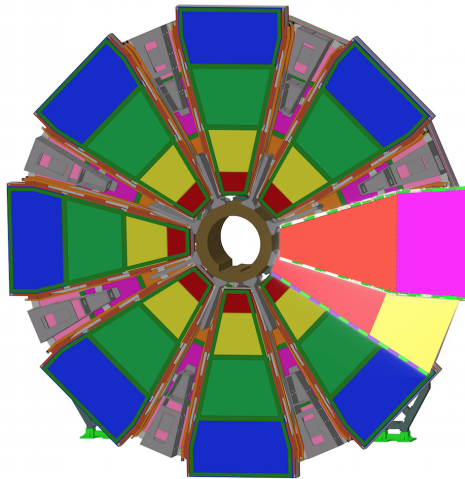
QL2, medium radius of the large sectors

QL3, larger radius of the large sectors

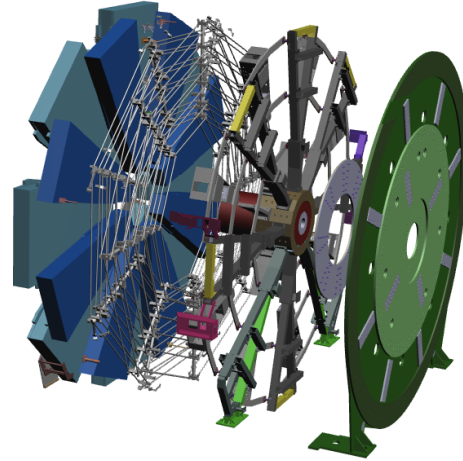
QS1, lower radius of the small sectors

QS2, medium radius of the small sectors

QS3, larger radius of the small sectors



(a) Two MicroMegas sectors, one small and one large, are also shown. In reality, the MicroMegas will not be visible sitting in between the two sTGC quadruplets.



(b) Components of one New Small Wheel. From left to right: large and small sectors; alignment bars and rays; the mechanical support; the NJD shielding

Figure 3.7: Graphical representation of an assembled NSW [80].

The detectors selected for NSW, the sTGC and the MicroMegas are planar gas detectors. While the internal structure of the two detectors is different, the position measurement is based in both cases on precision strips located on printed circuit boards (PCBs). To stiffen each layer of the detector without making the structure too heavy, the aluminium honeycomb panels, that have hexagonal cells structure, high stiffness and low density, are glued to the PCBs. Detector units of each detector type assembled in multiplerts and generally have a trapezoidal shape. The two technologies used in the NSWs are complementary to tracking: sTGCs can also contribute to off-line precision tracking, as these chambers can measure track hits at a resolution of better than $150 \mu m$, (this value largely depends on the angle of the incident track), while MicroMegas detectors will also be used for the trigger, providing additional robustness and coverage of the device in the end-caps region. Based on the issues and needs outlined, one can define the general layout features of the NSW and its detectors:

- sTGC chambers are the primary trigger system and MicroMegas chambers are the main precision tracking detectors;

- trigger acceptance in $1.3 < |\eta| < 2.5$;
- accuracy of precision tracking in $1.3 < |\eta| < 2.7$;
- detectors are located in eight small sectors, and as many large sectors, covering in η the corresponding MDT chambers in end-cap stations;
- wheel consisting of planar detectors, unlike current CSCs that are inclined;
- a total of eight layers of sTGC detection and as many MicroMegas in each sector; the arrangement of the layers in the z direction consists of four layers of sTGC, four MicroMegas, an optional spacer and a supporting structure, four other layers of MicroMegas and the last four of sTGC(s).

As shown in Figure 3.8a, the sTGC(s) are built by institutions from 4 different countries: Canada (QS3 and QL2), Chile (QS1), China (QS2) and Israel (QL1 and QL3). The MicroMegas chambers are built by the institutions of 5 different countries as shown in Figure 3.8b : Germany (SM2), Italy (SM1), Russia and Greece (LM2) and France (LM1).

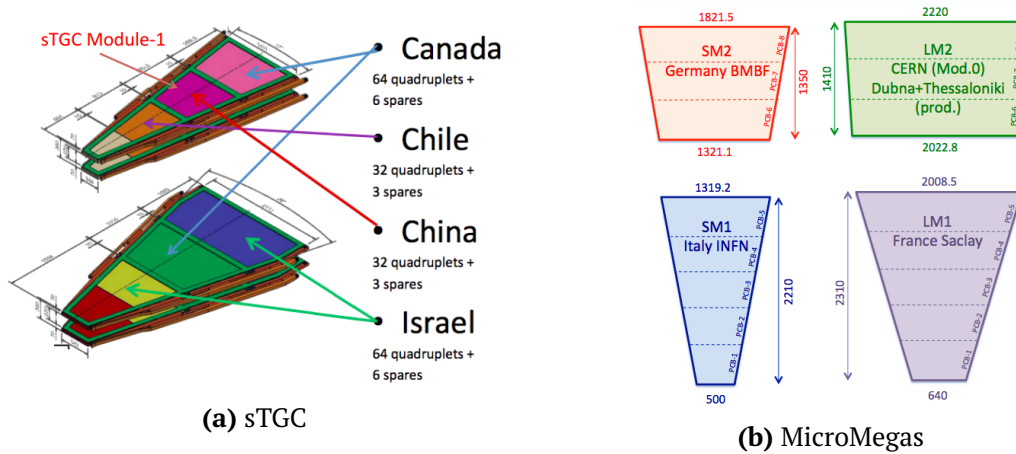


Figure 3.8: Shape of quadruplets that are under construction with the name of the institution that will be in charge of the construction and validation of the sTGC (Figure 3.8a) and MicroMegas (Figure 3.8b) [80].

3.2 The small Strip Thin Gas chambers

The sTGC are the detectors selected to perform the trigger function. Trigger detectors must provide bunch crossing identification, good timing resolution, and good angular resolution, better than 1 mrad , for on-line track reconstruction that translates into good spatial online resolution.

The basic structure of a sTGC is shown in Figure 3.9. It consists of a grid of $50 \mu\text{m}$ thickness tungsten wires plated in gold with a 1.8 mm pitch, placed between two cathode planes at a distance of 1.4 mm from the wire plane. The cathodic planes are made of a compound of graphite and resin (0.1 mm thick) and behind one of the two, there are strips

running perpendicular to the wire while behind the other, there are pads that cover a large rectangular surface. The strips have a 3.2 mm pitch, much smaller than the strip pitch of the ATLAS TGC, hence the name “small-strip TGC” for this technology. The chamber is filled with a gas mixture of 55% CO_2 and 45% n-pentane, which has an electron drift velocity of about $3\text{ cm}/\mu\text{s}$ under an electric field of $2.9\text{ kV}/\text{cm}$.

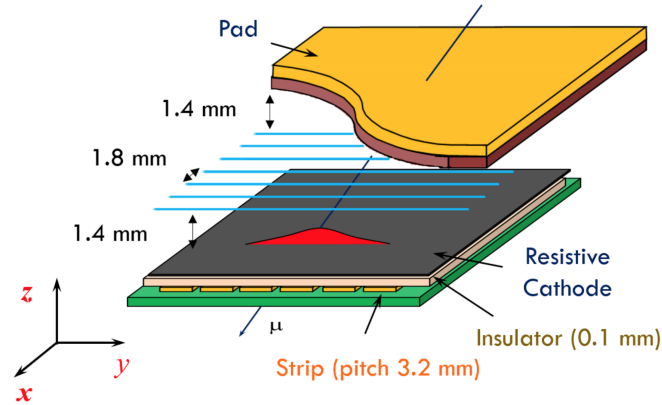


Figure 3.9: Graphical representation of the sTGC internal structure. The signal due to the drifting of the ionisation charges and their multiplication is induced on the anode wires, readout pads and strips sitting behind the cathode planes [80].

The project for NSW has two quadruplets separated by 5 cm in z . Each quadruplet contains four sTGC(s), each with pads, wires and readout strips. Pads are used to produce a coincidence of 3/4 or 4/4 per module to identify tracks of muons pointing roughly toward the point of interaction. They are also used to define what the readout strips should read to obtain a precise measurement in the bending coordinate for the on-line selection of muons. The azimuthal coordinate, for which a precision of about 10 mm is required, is obtained from the readout of the wires. Charge of all strips, pads, and wires is read for off-line reconstruction.

The position resolution required by the trigger has been optimised by constructing small prototype detectors and studying it according to the strip pitch, keeping the number of readout channels at a minimum. The results led to the following results:

- sTGC chambers can work smoothly, even under high radiation (up to hit rates of $\sim 20\text{ kHz}/\text{cm}^2$) exposure, with high efficiency for Minimum Ionising Particles (MIPs);
- using a pitch of 3.2 mm and the centroid charge method, the position resolution changes from $\sim 100\text{ }\mu\text{m}$ with zero incidence angles (corresponding to particles perpendicular to the readout system) to $\sim 200\text{ }\mu\text{m}$ for angles of incidence of 30° .

3.3 The MicroMegas chambers

The MicroMegas (*Micro-MEsh GAsEous structure*) chambers are gas detectors born from the development of the wire chambers invented by G. Charpak in the '70s. They were

first proposed in 1992 by Charpak and I. Giomataris to improve the spatial resolution of multiwire chambers and their ability to quickly release the detector from the positive ions generated by gas ionisation at the passage of charged particles [81]. MicroMegas belong to the family of Micro Pattern Gas Detectors (MPGDs) based on the printed circuit board (PCB) technology combined with photo-lithography and thin layer polyamide deposition. Due to the fast ion collection MicroMegas detectors can achieve stable operation at high gains and at high particle fluxes like the ones required from the ATLAS NSW upgrade project.

3.3.1 The MicroMegas technology

MicroMegas chambers are characterised mainly by their two very asymmetric regions. Standard MicroMegas detectors consist of a planar electrode, a gas gap of a few millimetres thickness acting as conversion and drift region, and a thin metallic mesh at $\sim 100 \mu\text{m}$ distance from the readout electrode, creating the amplification region. A structure of cylindrical spacers (pillars), made of insulating material and placed with a pitch of $\sim 400 \div 500 \mu\text{m}$, defines the height of the amplification region. The typical internal structure and operational parameters of a MicroMegas are shown in Figure 3.10.

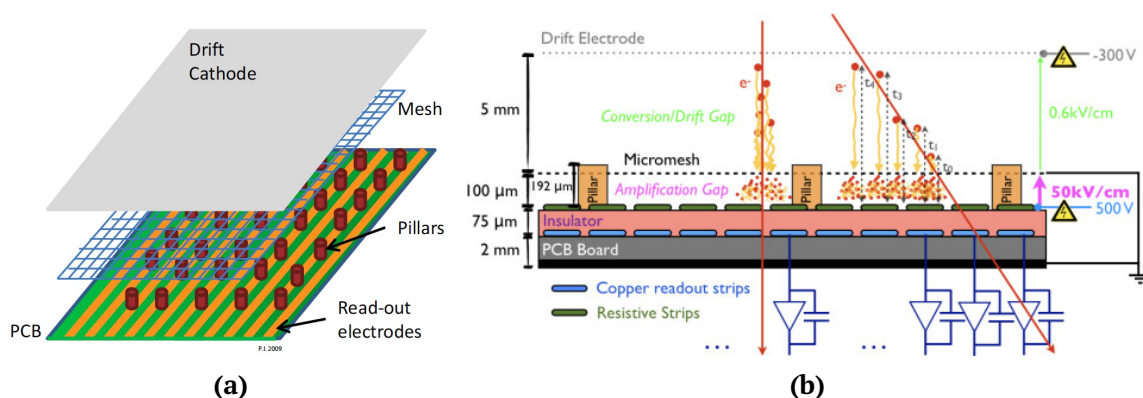


Figure 3.10: Sketch of the layout and operating principle of a MicroMegas detector [80, 82]. In Figure 3.10a a standard MicroMegas is shown while in Figure 3.10b the ATLAS MicroMegas with the resistive strips is shown. The drift region is the one between the cathode (drift electrode) and the mesh while the amplification region is the one enclosed between the mesh and the readout PCB. The height of the amplification region is dictated by the height of the pillars which support the mesh.

The high voltage potentials are chosen such that the electric field in the drift region is a few hundred of V/cm , and $40 \div 50 kV/cm$ in the amplification region, achieving gas gain values of the order of 10^4 . When a charged particle passes through the gas gap, it ionises the atoms and the electrons liberated by this ionisation process drift towards the mesh which is connected to the ground. Between the mesh and the anode strips, the value of the electric field reached in the amplification region is 50-100 times higher than the drifting field. The electron avalanche takes place in the thin amplification region, immediately above the readout electrode. The drift of the electrons in the conversion gap is a relatively slow process; depending on the drift gas, the drift distance, and the drift field it typically

takes several tens of nanoseconds ($v_d^e = 4 \div 5 \text{ cm}/\mu\text{s}$). On the other hand, the amplification process happens in a fraction of a nanosecond, resulting in a fast pulse on the readout strip. The ions that are produced in the avalanche process move, in the opposite direction of the electrons, back to the amplification mesh. Most of the ions are produced in the last avalanche step and therefore close to the readout strip. Given the relatively low drift velocity of the ions ($v_d^{ions} = 4 \div 5 \cdot 10^{-2} \text{ cm}/\mu\text{s}$), it takes them about 100 ns to reach the mesh, still very fast compared to other detectors. It is the fast evacuation of the positive ions which makes the MicroMegas particularly suited to operate at very high particle fluxes.

3.3.2 The MicroMegas gain

The electric fields in the conversion (or drift) and in the amplification region have very different intensity and are roughly uniform in both regions. Multiplication of electrons occurs in the amplification region with a high electric field between the mesh and readout electrode. The multiplication factor M of the electrons in a gas, under a pressure P between two flat-plane electrodes at distance d , with a uniform electric field E , is described by Equation 3.1:

$$M = e^{\alpha d} \quad (3.1)$$

where α is the Townsend coefficient, which represents the inverse of the free average path of an electron between two ionisations. A good approximation of the coefficient is given by the formula of Rose-Korff written in Equation 3.2:

$$\alpha = A \cdot P \cdot e^{-\frac{BP}{E}} \quad (3.2)$$

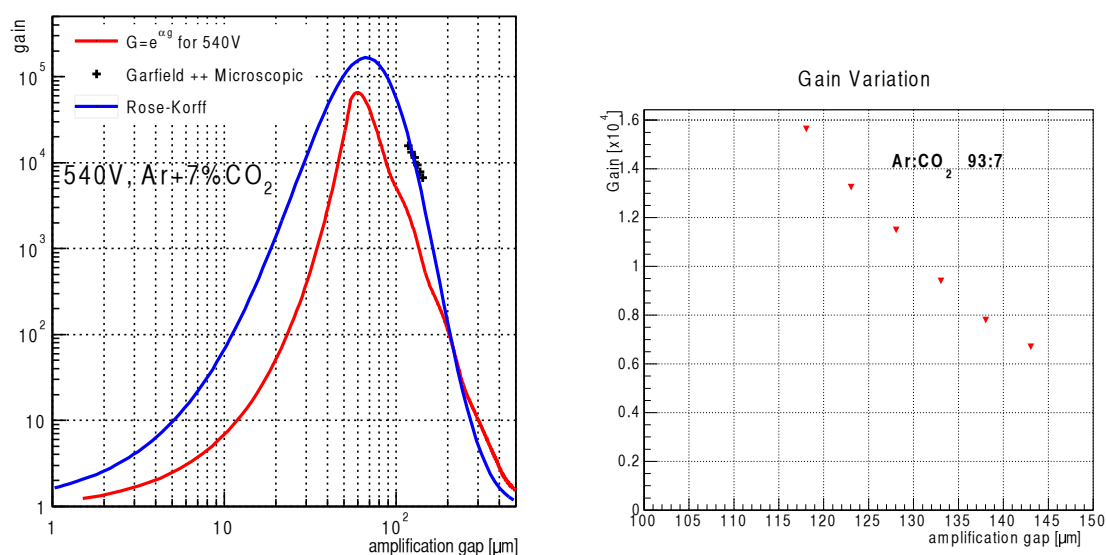
where A and B are two parameters that depend on the gas mixture. By substituting, in Equation 3.1, the expression of the Townsend coefficient given from 3.2 and the expression of the electric field $E = V/d$, where V is the applied voltage:

$$\log M = A \cdot P \cdot d \cdot e^{-\frac{BPd}{V}} \quad (3.3)$$

Figure 3.11 shows the gain factor as a function of the width of the amplification gap; in the small gap region, the leading contribution is given by the linear term d in Equation 3.3 until the gain reaches the peak in the region between 50 and $100 \mu\text{m}$ where the decreasing exponential becomes the main contribution. Black dots show the work area where the MicroMegas chambers are located, so for small increases in the size of the gap the gain decreases and vice versa increases for small reductions.

3.3.3 Resistive strip MicroMegas

Despite the excellent characteristics of the MicroMegas technology, the very thin amplification region along with the finely sculpted readout structure makes them particularly vulnerable to discharges (sparks). Sparks occur when the total number of electrons in the



(a) The red curve shows the shape obtained from Equation 3.1 while the blue curve is obtained with the approximation of Rose-Korff from Equation 3.2. Black dots were obtained from simulations made with GARFIELD++ [83] and show the working area of the MicroMegas chambers.

(b) Microscopic simulation of the gas gain for $Ar + 7\%CO_2$ versus the height of the amplification gap.

Figure 3.11: Gain as a function of the amplification gap size for a mixture of $Ar - CO_2$ at 93% - 7% with amplification voltage of 540 V [84].

avalanche reaches $\sim 10^{7-8}$ (Raether limit [85]).

In order to obtain, however, high detection efficiencies for MIP muons, amplification factors of the order of 10^4 must be obtained. Therefore, ionisation processes that produce more than a thousand electrons (due for example to photons or neutrons or α particles) at comparable distances to the lateral extension of an avalanche (some hundreds of μm) can produce dangerous discharges that can damage the detector or reading electronics or cause long dead times. Moreover, for large area MicroMegas small defects can likely occur in the very thin amplification gap that can easily induce discharges.

Since, in the NSW region of the ATLAS muon system, during the LHC Run 3 and beyond, particle rates can reach the order of $15 \text{ kHz}/\text{cm}^2$, the risk of sparking for the MicroMegas operated at high gas multiplication values can increase. Therefore, since 2008, the resistive anode Micromegas was developed by the MAMMA (Muon Atlas MicroMegas Activity) Collaboration [86] at CERN in the context of the RD-51 Collaboration [87]. The developed anti-spark protection system involves the addition of a layer of resistive strips whose resistivity should be in the order of a few tens of $M\Omega/\text{cm}$, placed on the top of a thin layer of insulating material directly above the readout electrodes. Geometrically, resistive strips are arranged to follow the pattern of the readout strip and are electrically isolated from them, as shown in Figure 3.10b. Signals are induced through capacitive couplings with readout strips that are no longer directly exposed to the charge produced in the

amplification region. In the case of discharges, the resistive strips are charged and, locally, the electric field falls to block the spark process. In this way, the detector becomes much more “robust”.

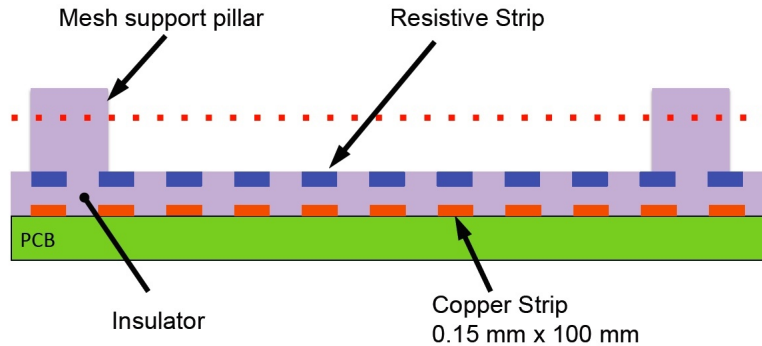


Figure 3.12: Spark protection principle. Resistive and readout strips are coupled together and are separated between them by a small insulator layer [80].

The constructive principle just described is shown schematically in Figure 3.12. Adding this protective device, the structure can operate with a higher gain factor and have at the same time discharges whose intensity is reduced by three orders of magnitude.

3.3.4 MicroMegas position reconstruction

Each incoming charged particle induces a signal in a few strips per event. A simple clusterisation algorithm is used to merge the adjacent strips with a signal, into a single cluster (hit). The goal of this type of detector is to reconstruct the hits of the particles that pass through it in order to determine the momentum and the charge of the particles. For this reason, the position reconstruction is an important point for the correct use of these chambers. This can be done in two ways:

- using the “Charge centroid method”;
- using the micro - Time Projection Chamber method (“ μTPC method”) [82].

When the particle is orthogonal to the chamber readout plane, the charge centroid method is used to provide a very accurate hit reconstruction in absence of a magnetic field. When the particle is inclined with respect to the readout plane, the μTPC method is used in a MicroMegas chamber.

3.3.4.1 Charge centroid reconstruction

In the case of gaseous detectors, for a charged particle passing through the active volume of the detector, the ionisation charge is shared among several readout strips due to different phenomena:

- the movement (drifting) of the ionisation electrons (ions) towards the anode (cathode);

- the diffusion of the ionisation electrons and ions governed by the gas mixture properties and the drift electric field;
- the charge sharing between capacitively coupled neighbouring readout strips.

For tracks perpendicular to the anode plane, the cluster (or hit) position using the charge centroid method is calculated by weighting the position of each strip with its signal charge and taking the average as shown in Equation 3.4:

$$x_{centroid} = \frac{\sum_{i=1}^N q_i \cdot x_i}{\sum_{i=1}^N q_i} \quad (3.4)$$

with x_i being the positions of the strips. An example of a reconstructed cluster in a event is shown in Figure 3.13.

This method performs well for tracks approximately perpendicular to the chamber due to the reduced cluster dimension.

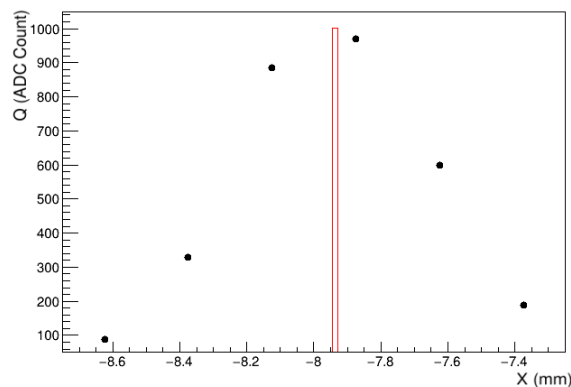


Figure 3.13: Example of a reconstructed cluster in a event: the dots represent the strip charge (q_i) and the position (x_i) for a reconstructed cluster while in red the cluster x position calculated using the centroid method (eq. 3.4) is shown.

In the case of inclined tracks, the primary ionisation clusters are distributed along several readout strips and consequently, the single strip signal amplitude becomes sensitive to the primary cluster charge fluctuations. As a result, the accuracy of the charge centroid method deteriorates with increasing track inclination angles, as shown in Figure 3.16.

3.3.4.2 μ TPC

For perpendicular tracks, the timing information is not accurate. However, when the tracks are inclined, there is a higher possibility that the signal of each strip is induced by the drifting of a single primary cluster allowing for an accurate measurement of its drift time. This information along with the strip position allows for a two-dimensional reconstruction of the primary cluster initial position inside the drift gap. For the translation of the measured time into distance, the precise knowledge of the drift velocity value is supposed. As shown in Figure 3.14, a drift velocity of $v_{drift} = 4.7 \text{ cm}/\mu\text{s}$ for $\text{Ar} - \text{CO}_2$ mixture (93% – 7%) with a drift electric field of $0.6 \text{ kV}/\text{cm}$ in the absence of magnetic field is expected. Note

that this value of the electric drift field is in the drift velocity plateau zone for the selected gas mixture. With this value, the maximum drift time in the gap of 5 mm is ~ 100 ns.

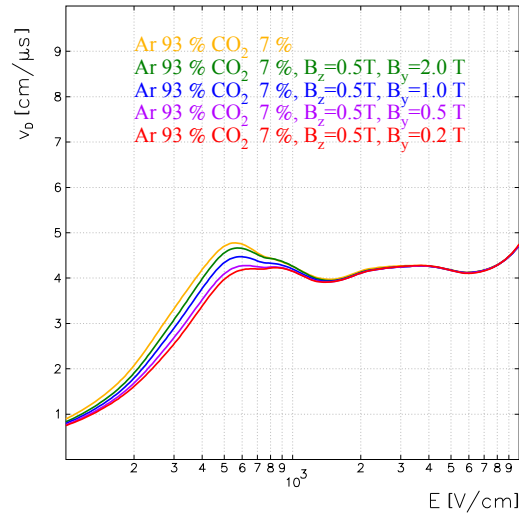


Figure 3.14: Drift velocity as a function of the electric field applied, for different gas mixtures, obtained by simulations carried out with GARFIELD [83]. Drift velocity with magnetic field $B = 0.5$ T are also shown because in the NSW of the ATLAS experiment the MicroMegas chambers will have to work in the presence of a magnetic field [84].

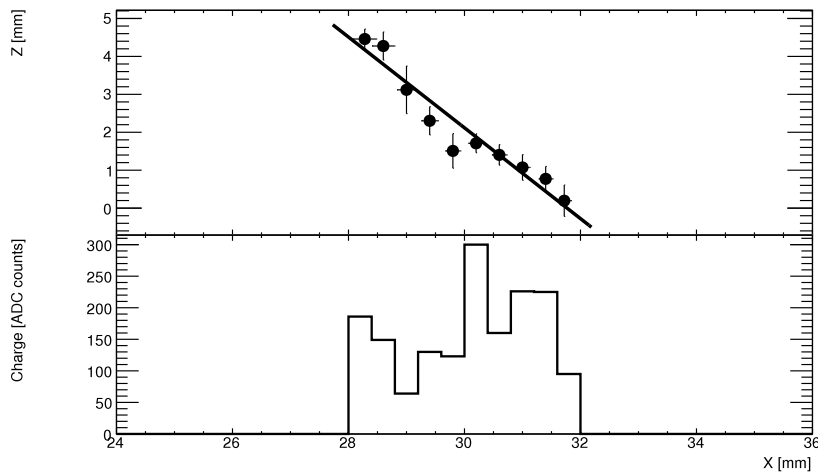


Figure 3.15: Example of a 10-strip cluster in a small prototype MicroMegas chamber with the beam inclined with 40° deg respect to the readout plane. *Upper:* Coordinate z measured using the drift time as a function of the strip position with the μ TPC fit superimposed; *Lower:* the charges detected by the 10 strips [82].

As can be seen in Figure 3.15, once the $x-z$ coordinates from each strip within the cluster are obtained, the track inside the drift gap can be reconstructed by selecting clusters with at least three strips and making a linear fit $z = mx + q$. From the fit parameters, the angular coefficient m of the straight line and therefore the inclination angle of the track $\theta = \arctan(m)$ can be obtained. The best measurement of the position of the cluster, in this case, is given by the coordinate x_{half} which corresponds to the intersection between the

fit and the height at half-gap ($z_{half} = 2.5 \text{ mm}$), as described from the Equation 3.5.

$$x_{half} = \frac{z_{half} - q}{m} = \frac{2.5 \text{ mm} - q}{m} \quad (3.5)$$

where m and q are the two fit parameters.

3.3.4.3 Centroid and μTPC method combination

The two reconstruction methods are complementary as the charge centroid method provides better spatial resolution for perpendicular tracks or for tracks with low inclination angles while the μTPC method is ideal for tracks with incidence angles greater than 10° that light up more strips. In order to improve the measurement accuracy, in particular in the small-angle region, the two algorithms can be combined by taking a weighted average of the corresponding reconstructed positions, x_c and $x_{\mu TPC}$ using the cluster size as weight:

$$x_{comb} = \frac{(n_{strips}/n_{cut})^2 \cdot x_{\mu TPC} + (n_{cut}/n_{strips})^2 \cdot x_c}{(n_{strips}/n_{cut})^2 + (n_{cut}/n_{strips})^2} \quad (3.6)$$

where n_{strips} is the cluster multiplicity (number of strip used to reconstruct the cluster) and $n_{cut} = 4$ [82]. In this way, the position determined with the charge centroid method is heavily weighted for small clusters. For extended clusters, as for inclined tracks, the μTPC result is dominant as shown in Figure 3.16. When the NSW will be installed in the ATLAS detector, tracks will have incidence angles between 7.5° and 30.5° and, combining the two methods, a resolution of $100 \mu\text{m}$ throughout the range can be obtained.

3.3.5 MicroMegas layout in the New Small Wheel

The MicroMegas to be installed in the NSW differ from their original configuration. The first important change from the original project [88] is the application of a positive High Voltage (HV) to the resistive strips, placing the mesh at ground. This arrangement allows a more stable operation of the entire detector. Moreover, the problem of any discharges is reduced thanks to the fact that the current, produced in this new configuration, is quickly discharged to the ground through the mesh.

One main change concerns the construction method. The first prototypes of MicroMegas have been built according to the “bulk” technology, where the mesh is directly integrated in the readout board structure. A change has been made necessary to overcome the limitations imposed by bulk technology for PCBs.

In the new scheme the mesh is part of the panel containing the cathode plane; in this way, the drift gap, being separated from the reading PCB, is no longer dependent on its size. This, together with connecting the high voltage to the strips instead of on having it connected to the mesh, is a huge advantage: the high voltage, in this new configuration, can be segmented giving the possibility to connect one section to a different amplification voltage with respect to the other sections.

Figure 3.17 shows a diagram of this new MicroMegas assembly method, known as the

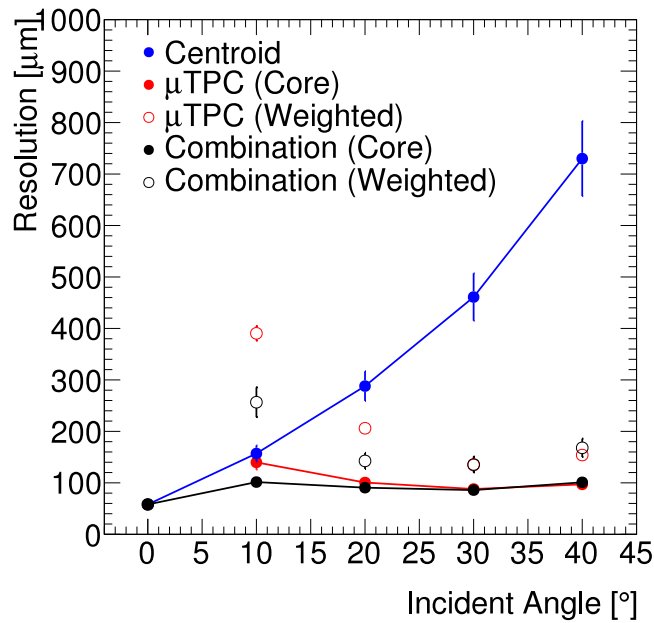


Figure 3.16: MicroMegas spatial resolution as a function of the track inclination angle using charge centroid method (blue curve), the μTPC method (red curve) and the combination of the two (black curve). The resolutions are calculated through the fit of a double Gaussian on the difference between the reconstructed track and cluster position residuals. The final resolution is expressed in two ways: full circles are the σ of the core Gaussian, while empty circles are the weighted average (using the integral of the respective Gaussian) of the σ . The data were acquired at the SPS/H4 test beam facility with a $150 \text{ GeV}/c \mu/\pi$ beam [82].

“floating mesh” technique.

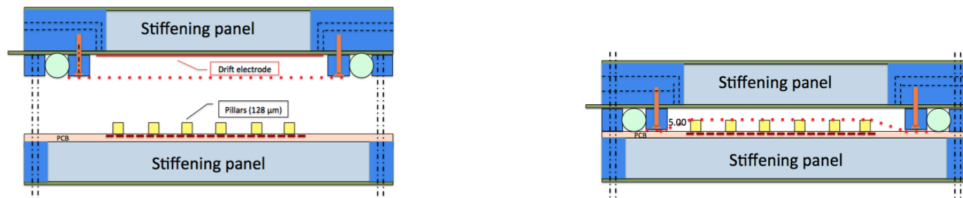


Figure 3.17: Assembly diagram of a single MicroMegas plane. *Left:* the drift and readout panels are opened and separated, and the mesh and the mesh is integrated to the first one gluing it to an aluminium frame (mesh frame). *Right:* the drift panel is hooked to the readout [88].

As shown in Figure 3.17, the pillars (mesh supports) are arranged at the top of the readout panel. The mesh is integrated into the drift panel: it is first stretched and then glued to the aluminium frame surrounding the rigid panel (stiffening panel). Once the two panels have been hooked up with a high precision mechanical process, the mesh is placed above the supporting pillars. The advantages of this new technique are above all constructive since mesh sizes are now independent from PCBs and therefore production can take place in different places and times; the opening and cleaning operations of the detector are also facilitated.

The MicroMegas performance has been extensively studied since the beginning of the

Item/Parameter	Characteristics	Value
Mesh	Stainless steel separate from readout board	250 lines/inch
Amplification gap		128 μm
Drift/conversion gap		5 mm
Resistive strips	Interconnected	$\rho = 10 \div 20 M\Omega/cm$
readout strip pitch		0.425 – 0.450 mm
Stereo angle	4/8 layers	$\pm 1.5^\circ$
Total number of strips		2.1 M
Gas	Ar : CO ₂	93 : 7
HV on resistive strips	positive polarity	570 V
Amplification field		45 kV/cm
Drift field		600 V/cm

Table 3.1: Main MicroMegas detector and operating parameters.

MAMMA project. The first results showed a spatial resolution of down to 40 μm , well below the ATLAS requirements, employing a prototype of MicroMegas with strip pitch of 250 μm and a mixture of Ar : CF₄ : C₄H₁₀ (88% : 10% : 2%). Nevertheless, two points must be taken into account: a too fine granularity implies a high number of channels for the required electronics, resulting in increased costs, and the gas mixture must be safe from the point of view of ageing. Therefore, after testing various gas mixtures, ATLAS has opted for the reuse of the Ar : CO₂ (93% 7%) mixture, already used in existing MDT chambers, which has proved to be suitable for meeting the operational requirements for the NSW. Finally, concerning the readout strips, the option of a strip pitch of $\sim 400 \mu m$ was adopted, a choice that translates into $\sim 2 \cdot 10^6$ channels of electronics for the NSW system, which, although large, is still reasonable. In summary, the main constructive and operational parameters of MicroMegas that will be used for NSWs in ATLAS are reported in Table 3.1.

3.3.6 MicroMegas modules in the New Small Wheel

The different dimensions of the MicroMegas modules (SM1, SM2, LM1, LM2) that have to be built are illustrated in Figure 3.8b. The SM1 and SM2 modules together make up the Small Sectors (Figure 3.18a) while the LM1 and LM2 the Large Sectors (Figure 3.18b). The overlap region between the Small and Large Sectors on the NSW is shown in Figure 3.18c.

Depending on the type (large/small sector and radial position) each trapezoidal module consists of several PCBs precisely glued together. The readout boards (or PCB) are produced with standard printed circuit boards techniques with a 0.5 ± 0.05 mm thick FR4³ base material on which the copper readout strips 300 μm wide and 17 μm thick are produced. On top of the readout strips, a 50 μm thick Kapton® foil carrying the resistive strips are glued (produced by a screen-printing technique). Geometrically, the resistive strips match

³The FR4 or Fiberglass is a composite material made of glass fibres arranged orthogonally between two layers in an epoxy matrix, widely used as an insulator, present in many electronic devices, including household appliances and power tools.

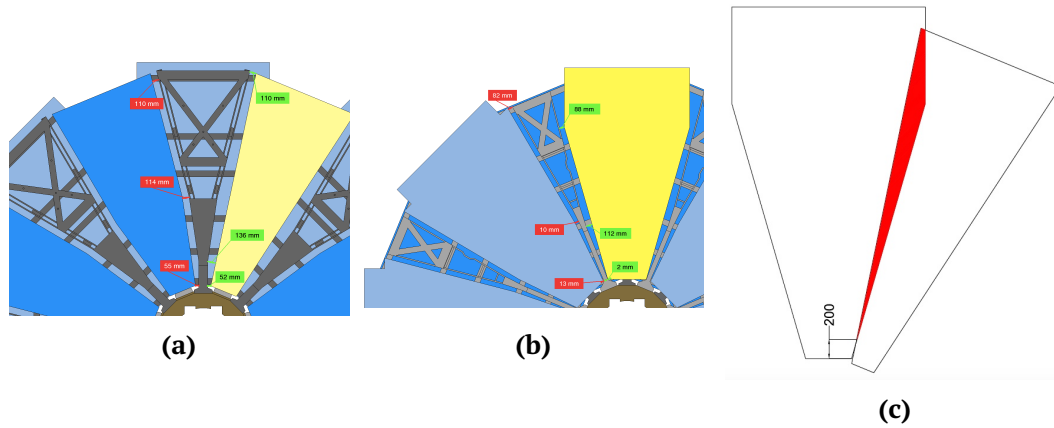


Figure 3.18: Layout (Figure 3.18a and Figure 3.18b) of the MicroMegas detectors with services in the NSW. The distances at various points to the NSW structure are indicated for both Small and Large. The sketch of the overlap region is illustrated in Figure 3.18c [80].

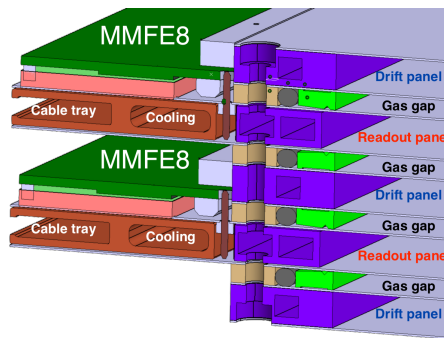


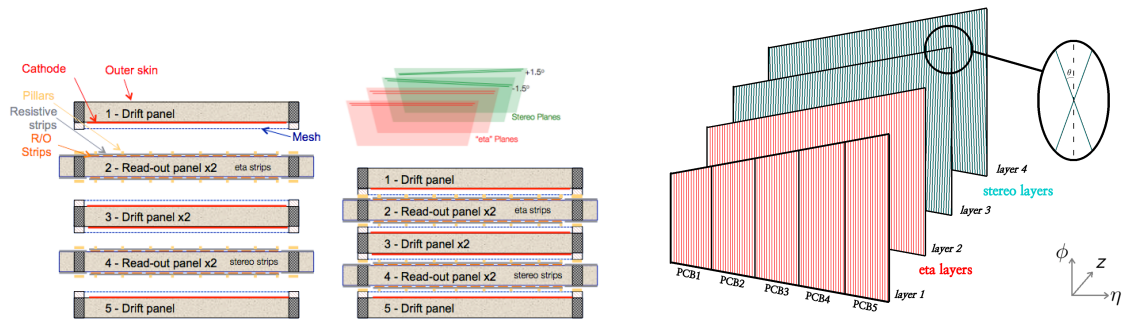
Figure 3.19: 3D drawing of the quadruplet edge showing the guide for the alignment pin and the electronics and services placement on the readout PCB surplus part [80].

the pattern of the readout strips. Both readout and resistive strips have a width of $300 \pm 20 \mu\text{m}$ for all the modules with a pitch of $425 \mu\text{m}$ and $450 \mu\text{m}$ for small and large modules respectively. On top of the resistive strips, the mesh support pillars are deposited using a layer of photo-imageable material (pyralux).

Each PCB comprises 1024 readout strips, half of them are read on one side and the other half on the opposite side. This anti-symmetric configuration equalises the heat and weight load of the detector readout boards on the two sides of the detector while it also leaves some extra space for the placement of supplementary electronics and services. There will be three different types of readout PCBs in each MicroMegas module depending on the orientation of the strips. Two will have the strips running perpendicularly to the radial direction (precision strips or η strips) while the other two will have the strips tilted, with respect to the η strips, by a small stereo angle ($+1.5^\circ$ and -1.5° stereo strips respectively) to allow for the reconstruction of the second coordinate (ϕ).

Each MicroMegas module will combine four detection layers (four MicroMegas gaps). A schematic view of a MicroMegas quadruplet consisting of three drift panels and two readout panels is shown in Figure 3.19 and in Figure 3.20.

The outer layers of one MicroMegas quadruplet are two identical one-sided drift panels⁴ that carry the drift cathode structure and the integrated micro-mesh on their inward side. One additional double-sided drift panel carries drift cathode and micro-mesh on both sides occupying the middle of the quadruplet. In between the drift panels, two double-sided readout panels carry the readout PCBs on both sides. One of the two readout panels features two parallel eta-strip readout PCBs while the second one has PCBs with stereo strips tilted by $\pm 1.5^\circ$, with respect to the eta strips, on each side.



(a) Layout of a multiplet of a MicroMegas detector consisting of three drift panels and two double-side readout panels. The first two MicroMegas gap read the precision coordinates (η) and the second two read the second coordinates (ϕ) [88].

(b) Schematic view of the 4 layers of a MicroMegas multiplet. In the picture is shown the orientation of the strip of each layer.

Figure 3.20: Layout of a MicroMegas quadruplet.

3.3.7 MicroMegas readout board and high voltage sections

In the resistive chambers implemented for the ATLAS NSW, neighbouring resistive strips are interconnected between each other every 20 mm along the strips and these interconnection bridges are also shifted by 10 mm from one strip to the next one as shown in Figure 3.21. This design allows for a more homogeneous impedance between the high voltage supply line, the so-called “silver line”, and the resistive strips. Thanks to these interconnections, if a spike occurs, the huge amount of charge is evacuated through a network of strips and not a single strip equalising the effective resistance over the full area of the detector. Another advantage of these interconnections is that defects in the resistive pattern like e.g. broken strips become uncritical unless they are too massive.

The resistive strips are interrupted in the middle of their length dividing the readout PCBs into two “HV section” and therefore the high voltage is supplied independently on each side of each board. This fine segmentation, shown in Figure 3.22, prevent high voltage problems in case of local imperfections inside the amplification gap.

⁴Cathode PCBs have simply a thin layer of copper on the FR4 fibreglass surface.

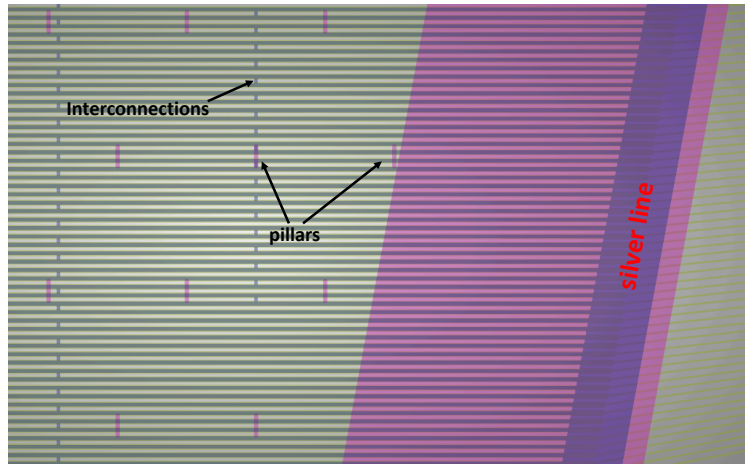


Figure 3.21: Gerber file of a single PCB. The pillars, the silver line and the interconnections between the resistive strip are shown in the figure

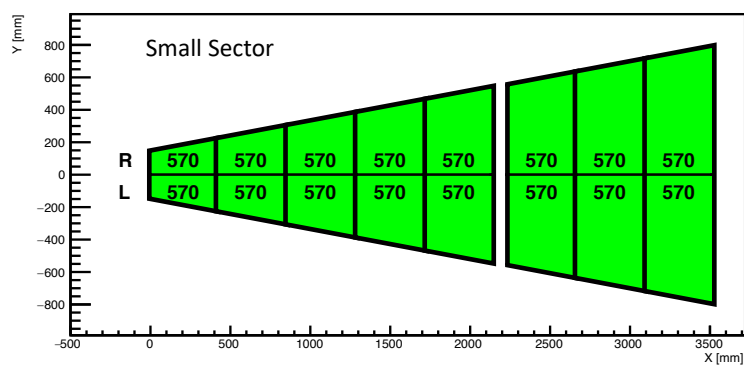


Figure 3.22: High voltage section divisions in a layer of a small sector. The same division is adopted also for the large sectors.



Figure 3.23: Picture of a MMFE8 readout board. Eight VMM3a can be seen on top.

3.3.8 MicroMegas electronics: the VMM3a

In 2009 studies started to find the best electronics for the NSW chambers. A custom front-end Application Specific Integrated Circuit (ASIC) was developed to be used to read both the sTGC and the MicroMegas detectors of the ATLAS NSW. The ASIC is named “VMM” and the version for the NSW production modules is the *VMM3a* [89]. Both NSW detectors require precision amplitude and time measurement, for position reconstruction and trigger, by charge interpolation and these requirements are fully met by the VMM3a due to its highly configurable parameters.

Each PCB of a MicroMegas chamber board is connected at two readout boards, called MMFE8 and shown in Figure 3.23, carrying eight front-end chips (VMM3a) of 64 channels each.

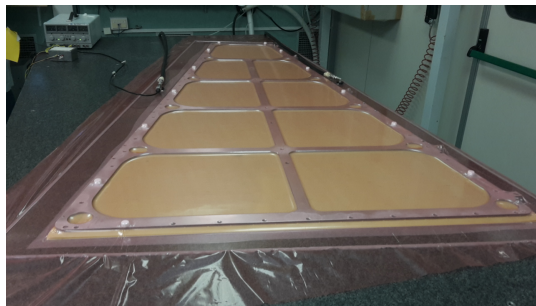
For each channel, there is a discriminator with neighbour enabling logic, and individual threshold trimming, the peak detector, and the time detector. The threshold is adjusted by a global 10-bit Digital to Analogue Converter (DAC) and an individual channel 5-bit trimming DAC. The neighbour channel logic forces the measurements of channels neighbouring a triggered one, even those channels did not exceed the set threshold. The peak detector measures the peak amplitude and stores it in an analogue memory. The time detector measures the timing using a time-to-amplitude converter (TAC), i.e., a voltage ramp that starts either at threshold crossing or at the time of the peak and stops at a clock cycle of the bunch-crossing (BC) clock (every 25 ns). The VMM3a has four values of adjustable peaking time: 25, 50, 100, and 200 ns.

3.4 Construction and testing of the SM1 MicroMegas chambers

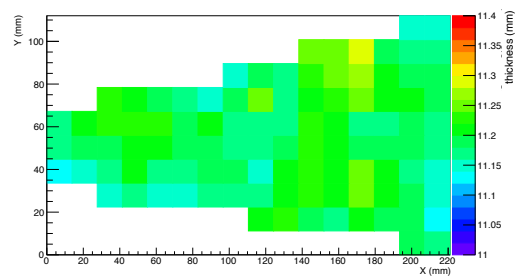
As shown in Figure 3.8b, the Italian INFN collaboration, composed by the Cosenza, Lecce, Laboratori Nazionali di Frascati (LNF), Napoli, Roma1, Roma3, and Pavia, is engaged in the construction of the SM1 Modules [90, 91].

3.4.1 SM1 drift panels

The bare drift panels (without the mesh) are constructed at the Roma1 INFN section, in the cleanroom using the so-called vacuum bag technique [92]. The cathode PCB boards are glued on the “drift” panels. One cathode layer is segmented into five cathodes PCBs, each composed by a uniform layer of $17\ \mu\text{m}$ thick copper on a substrate of $500\ \mu\text{m}$ of FR4. The “outer” single side drift panels are made with a sandwich of cathode PCB, aluminium honeycomb and internal aluminium frames, and a “skin” of FR4 on the outer side. For the central double-sided panels, the external skin is replaced by another set of 5 cathode PCBs. All layers are glued together with Araldite 2011®, adopting the vacuum bag technique [92] on a granite table that guarantees the flatness below $37\ \mu\text{m}$ required, as shown in Figure 3.24.



(a) Picture of one drift panel after its assembly. The mask and the vacuum bag are shown in this photo.



(b) Example of a drift panel thickness map made in Roma1.

Figure 3.24

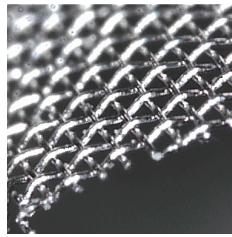
After construction, the panels are sent to Cosenza for gas tightness tests and for glue and connection finishing.

3.4.2 SM1 mesh stretching

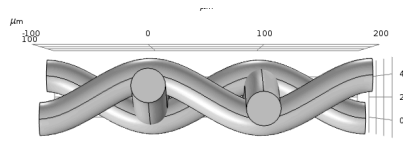
The meshes are prepared in the cleanroom at the Roma3 INFN section and they are shipped to the Laboratori Nazionali di Frascati of the INFN where they will be integrated to the bare drift panels coming from Cosenza. The mesh is a stainless steel wire mesh with a diameter of $30 \pm 2\ \mu\text{m}$, an opening width equal to $71\ \mu\text{m}$ and a pitch of $101\ \mu\text{m}$ as shown in Figure 3.25.

To ensure that the mesh does not deform inside the gap, due to the strong electric field, and does not decrease by more than a few micrometres the amplification gap (to keep a constant gain and avoid sparks), it must be stretched and brought to tension between 7 and $10\ \text{N/m}$. In order to reach this tension, the mesh is placed on a stretching table and it is held with 28 clamps that are gradually moved away increasing its tension. The mesh tension is continuously measured by sensors placed on each clamp and, at the end, using a mesh tension measuring gauge (textitSEFAR Tensocheck 100®).

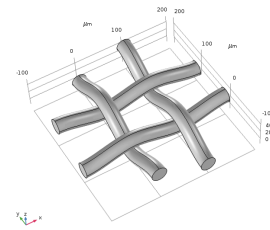
Once the optimal tension is reached, the mesh is glued on a trapezoidal aluminium



(a) Picture of the mesh made using the DinoLite microscope.



(b) 3D drawing of the longitudinal view of the MicroMegas mesh.



(c) 3D drawing of the frontal view of the MicroMegas mesh.

Figure 3.25

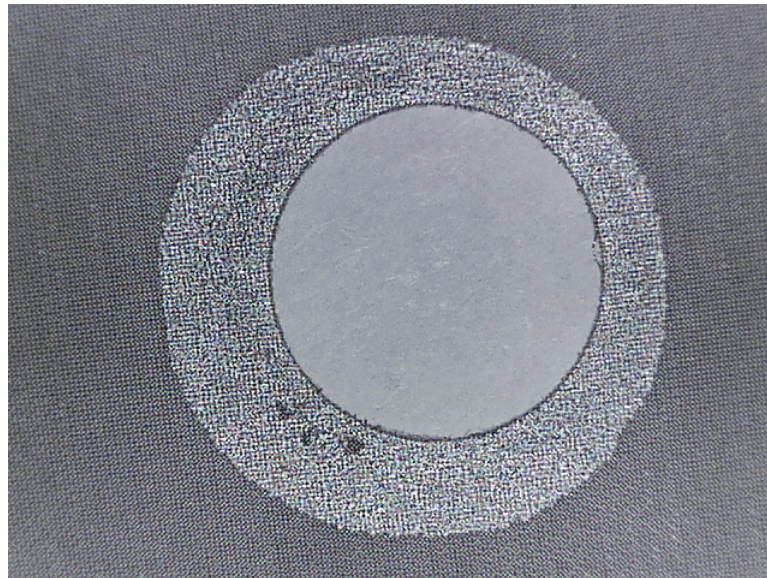


Figure 3.26: Mesh after the drilling in the interconnection position. This procedure does not reveal any free wires that could create discharges within the amplification gap.

structure called transfer frame, as shown in Figure 3.27, which is used to transport the mesh without losing its tension. The mesh is also drilled in the interconnections regions (where screws will be positioned to hold all the MicroMegas panels together) with a particular technique to ensure that the mesh does not fray. A Tedlar foil with a circular glue spot of Araldite 2011[®] (8.5 mm of diameter) is positioned on the mesh in the interconnection regions and, with the help of 5 kg weights, the glue is pressed and left to cure. Then it is drilled (see Figure 3.26) and the last quality control measurement is made on the height of the cut mesh plus the glue spot in order to be sure that the thickness of the glue is as expected.

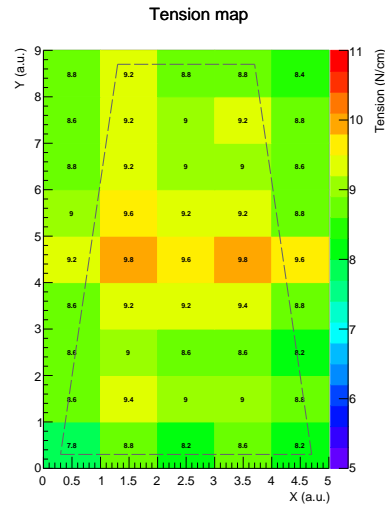
In the end, the meshes are shipped to the Laboratori Nazionali di Frascati of the INFN to be integrated with the bare drift panels. The average tension for all the 155⁵ stretched

⁵Not all stretched meshes have been used. 136 meshes were finalised on the drift panels in order to complete 32(+2 spare) SM1 modules, some were damaged during the procedures (12) while the others are kept as spares.

mesh and for the three stretching steps is shown in Figure 3.28.



(a) Picture of one mesh during the glue curing on the transfer frame.



(b) Example of a mesh tension map made in Roma3.

Figure 3.27

It has been observed that for some meshes there are small metallic deformations that can alter the uniformity of the electric field inside the amplification gap, as shown in Figure 3.29, and can cause sparks. To correct these imperfections, a polishing technique has been introduced which, by passing over the mesh an ultra-fine grain sandpaper ($10\ \mu\text{m}$), removes these imperfections without damaging the mesh.

After all these steps, the mesh is glued on the bare drift panel where it reaches the final stretching tension, as shown in Figure 3.30b.

3.4.3 SM1 readout panels

The readout panels for the SM1 chambers are constructed in the Pavia clean room using the stiff-back technique [90, 92]. As for the SM1 drift panels, the readout panels have 5 PCBs for each side, as shown in Figure 3.31. The assembly starts placing the first set of PCBs on the granite table, precisely positioned using reference pins and sucked on this with a vacuum pump while a second set is placed on the stiff-back. Then, as for the drift, the frames and the honeycomb are glued over the first set of PCBs and after the stiff-back is rotated upside-down and moved over the table to put the second set on top of the assembled panel. As for the drift panels, the planarity of the readout panels is required to be lower than $37\ \mu\text{m}$.

3.4.4 SM1 final assembling

Once all the panels are in the INFN Frascati section, the cleaning procedure with specific micro polishing detergents, de-mineralised water and an oven to dry the panels before the assembly is made. This must be done since during the panels and the board production it

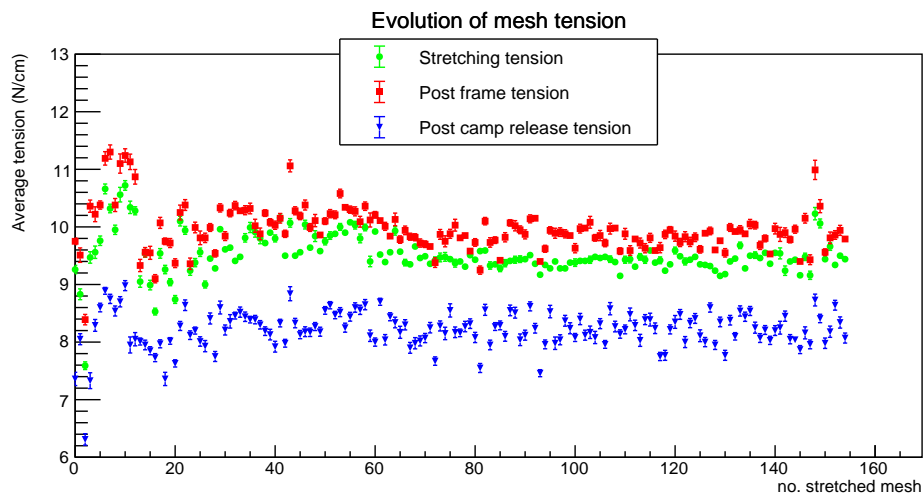
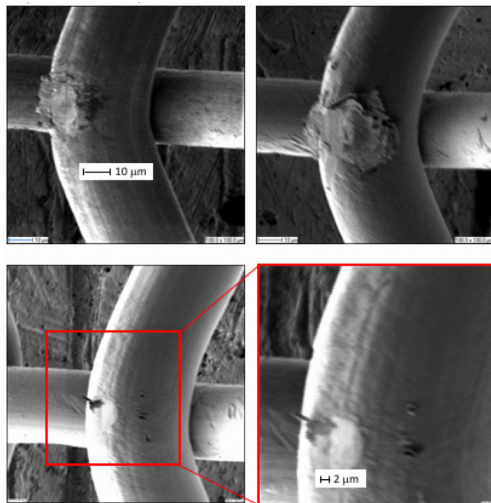
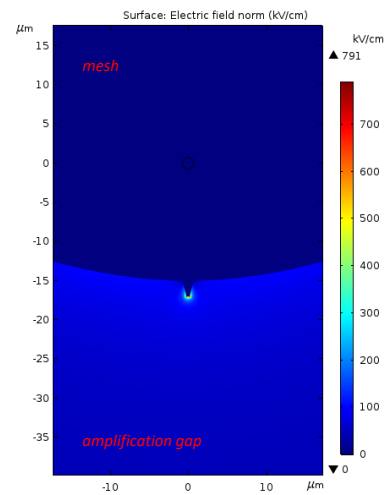


Figure 3.28: Average mesh tension during the first stretching phase (blue triangles), after the transfer frame is lifted until it is in contact with the mesh (red squared) and after the gluing process (green circles).



(a) Picture of the wire of the mesh. Small defects of few μm can be seen and can create problems inside the amplification gap.

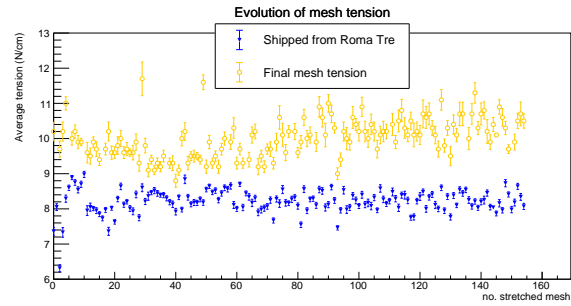


(b) Simulation made using COMSOL showing how small defects in the mesh can alter the electric field within the amplification gap by increasing it locally by more than 100 times the nominal one.

Figure 3.29



(a) Picture of one finalised drift panel at LNF. The mesh can be seen on top of the drift panel.



(b) Average mesh tension shipped from Roma3 and after the finalisation in the drift panel at LNF.

Figure 3.30

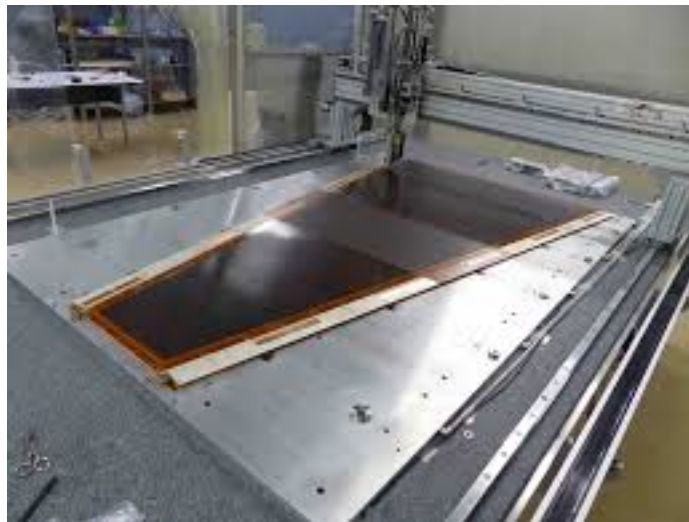


Figure 3.31: Picture of a SM1 readout panel in Pavia on the granite table.

is possible that some organic residuals remain on the surfaces, compromising the high voltage stability of the chambers. The vertical assembly procedure made in the cleanroom at LNF, shown in Figure 3.32, guarantees the alignment of the readout strips and also a validation of the functioning of the single planes.



(a) Picture during the closure of the first gas gap of a quadruplet.



(b) Picture of one SM1 Modules on the granite plane after the construction.

Figure 3.32

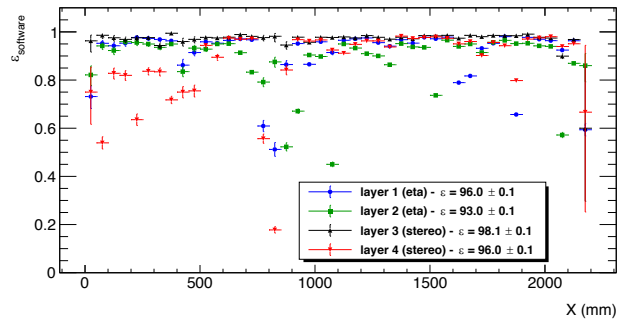
The assembly starts from the closure of the first gap with a drift panel and the stereo readout panel. Then the high voltage test is performed to be sure that everything is working well. Once the test is completed, the procedure continues with the assembly of the central drift, the other readout panel and the last outer drift panel. After the construction and assembly of the MicroMegas quadruplet, several validation measurements are required to ensure the correct functioning of the chambers:

- the planarity of each face of the chamber;
- inter-alignment of readout planes through optical measurements;
- gas tightness;
- high voltage stability.

In the end, the modules need to be validated at the Cosmic Ray Stand to estimate the efficiency and gain uniformity. The experimental setup is shown in Figure 3.33a and consists of two scintillators, placed below the chamber, for the trigger coincidence separated by 35 cm of iron and achieving a trigger rate of 50 Hz. Using a self-tracking method (each chamber is composed of four layers) the track can be reconstructed and the efficiencies as a function of the extrapolated position can be measured as shown in Figure 3.33b.



(a) Picture of the LNF Cosmic Ray Stand.



(b) Efficiencies of each layers as a function of the precision coordinate (η or x). The efficiency is measured fitting a constant line per each layer and the final efficiency value is written in the plot. The layer efficiency is well above the 90% and in some cases there are efficiency drops due to a problematic channels in the readout electronics (APVs).

Figure 3.33

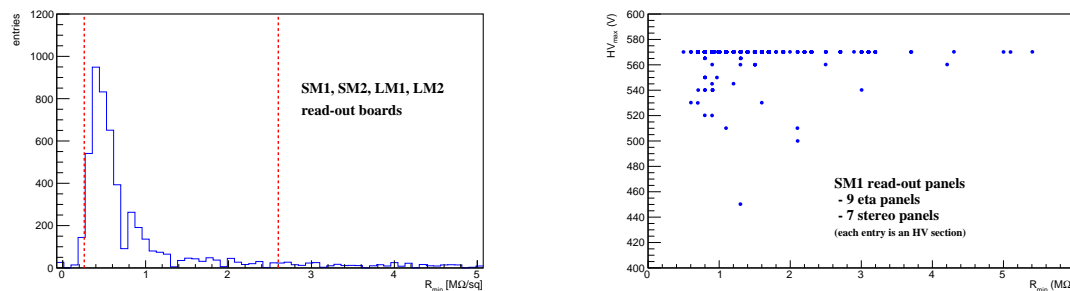
3.5 First results on the modules

After the construction and the first tests of the first modules, problems with the high voltage stability of the high voltage sectors emerged. After several tests, it was decided to take some measures that improved the behaviour of these chambers. In particular, the polishing of the meshes, described in the Section 3.4.2, which is necessary to eliminate small imperfections, and also the washing of the panels (both readout and drift) and the meshes with special detergents that are used to eliminate both dust and possible organic residues as well as ionic contamination, i.e. the remains of the products used during the production of PCBs. With these measures, the high voltage stability of the chambers has improved but was still not fully acceptable for certain high voltage sections.

Besides a very accurate cleanliness of the panels, and all the elements composing the modules, another key element to safely and stably operate the MicroMegas is the effectiveness of the resistive spark protection system. In MicroMegas, as well as in other MPGD, sparks regularly occur if the detectors are operated at high gain (and under high particle flow). This is why the resistive layer has been implemented for the ATLAS NSW MicroMegas, having the properties to greatly quench the intensity of the sparks. The highest the resistivity, the highest the quenching capability. On the other hand, a very high resistance is incompatible with the detection of high particles flow (rate capability). The required range for the resistive foils produced for the ATLAS MicroMegas was in the range of $0.26 \div 2.6 M\Omega/sq$. From the experience done after launching the production, the lowest acceptable values resulted to be at the limit of the effectiveness to quench sparks. This also has non-trivial dependencies on the geometry and on the layout with interconnections. Unfortunately, a large production of resistive foils has values close to the lower limit and even lower (see Figure 3.34a), resulting in a significant number of RO boards (high voltage sections) suffering for instabilities when operated at nominal

gain/voltage. Such a correlation between unstable (“weak”) high voltage sections and the low resistivity can be seen in Figure 3.34b where most sectors that do not reach the nominal voltage of 570 V have a minimum value of the resistance (measured with a 1 cm long probe) of less than 1 M Ω .

The occurrence of sparks for weak high voltage sections was mostly localised at the edges of the active area, at the start of the resistive strips that is at the locations of closest approach to the silver-line (the power supply lines). These locations of minimal resistance are, therefore, the points with minimal spark quenching capability.



(a) Minimum value of the resistance per square of the resistive strip on each MicroMegas read-out board. The red line represents the minimum limit below which the board has a high probability of causing spark within the amplification gap.

(b) Correlation of the minimal resistance measured using a 1 cm probe.

Figure 3.34

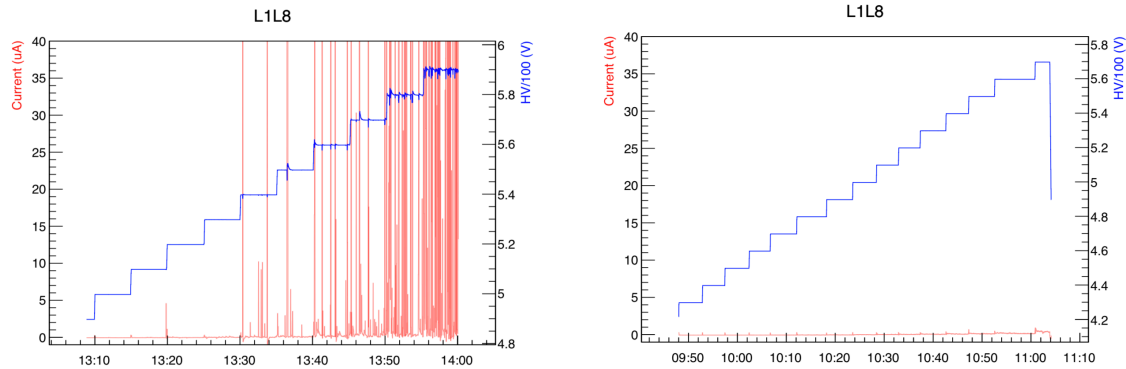
An effective solution was then implemented by masking the area of lowest resistance, by effectively slightly reducing the active area at the two sides of the boards. This was done by putting, 1 – 5 cm long depending on the resistance level of the board, of Araldite 2011® at the edges of the PCBs (where the resistance of the strips is less). This procedure eliminated most of the weak points of the gap.

In order to further improve the stability of the detectors and operation for a long time with a safer margin, the stability was also investigated as a function of the gas mixture. These studies are still ongoing. In particular, different gas mixtures with more quencher were tested at the construction sites, CERN Gamma Irradiation Facility (GIF++) [93] and during the test beams in order to find one that would improve the high voltage stability. Different percentage of Ar : CO₂ were used at the construction sites (Saclay and Frascati) and at the test beam (as described below in Section 3.6) without highlighting major changes in terms of high voltage stability.

Definitely better results are instead obtained with a gas mixture containing a small amount of isobutane: Ar : CO₂ : C₄H₁₀ (93 : 5 : 2). First results obtained at Saclay and later confirmed at Frascati and at CERN (GIF++ and BB5 on double-wedge finalised, as described in Section 3.7.4.8), have shown that sparks are greatly reduced with this mixture, as for example reported in Figure 3.35 where current and high voltage are reported during the

test at GIF++ during the exposition of the chamber to a large flux of particles.

However, mixtures with isobutane can give problems of ageing (which is why they were not considered until now) and therefore studies are still ongoing to ensure safe operation for a long time under high irradiation at HL-LHC.



(a) Behaviour of the voltage and current of a LM2 high voltage section with a nominal gas mixture of $Ar : CO_2$ (93 : 7) at GIF++ during the exposition to a large flux of particles. High values of current are shown highlighting the bad behaviour of this high voltage section.

(b) Behaviour of the voltage and current of a LM2 high voltage section with a different gas mixture of $Ar : CO_2 : C_4 : H_{10}$ (93 : 5 : 2) at GIF++ during the exposition to a large flux of particles. The current is perfectly under control.

Figure 3.35: Behaviour of the same high voltage section with the nominal gas mixture and with the alternative gas mixture.

These studies are going to be finalised in the next few months and are discussed later.

3.6 Results from test beam on the first SM2 production module

The first production module (SM2 chamber built by the German cluster composed of Munich, Wurzburg, Mainz) was also tested for the first time at CERN in July 2018 during a test beam at H8 beam line of SPS. The beam is composed by 180 GeV/c pions or muons with a spot size of $\sim 10 \times 10 \text{ cm}^2$, as shown in Figure 3.37. The aim of this test was:

- verify the good performances of the chamber and the electronics;
- find a good configuration of the VMM parameters;
- find the high voltage working point from the efficiency curves;
- try different gas mixtures from the $Ar + CO_2$ (93 : 7) in order to find a possible alternative working point.

The test beam setup is shown in Figure 3.36, and it is composed by three one view $10 \text{ cm} \times 10 \text{ cm}$ TZ chambers⁶ used as reference for the external track reconstruction, the SM2

⁶The TZ chambers are bulk resistive MicroMegas with $10 \text{ cm} \times 10 \text{ cm}$ active area, with strips $150 \mu\text{m}$ wide with a pitch of $250 \mu\text{m}$.

Module 1 chamber equipped with four MMFE8 boards (only half of a PCB is instrumented, 512 strips per layer) and two scintillators as a trigger. The other chambers shown in the Figure 3.36 are different MicroMegas prototypes with a different readout system and they are not used for the track reconstruction. In this test beam, the VMM3 version of the electronic was used which is a previous version with respect to the final one (the VMM3a).

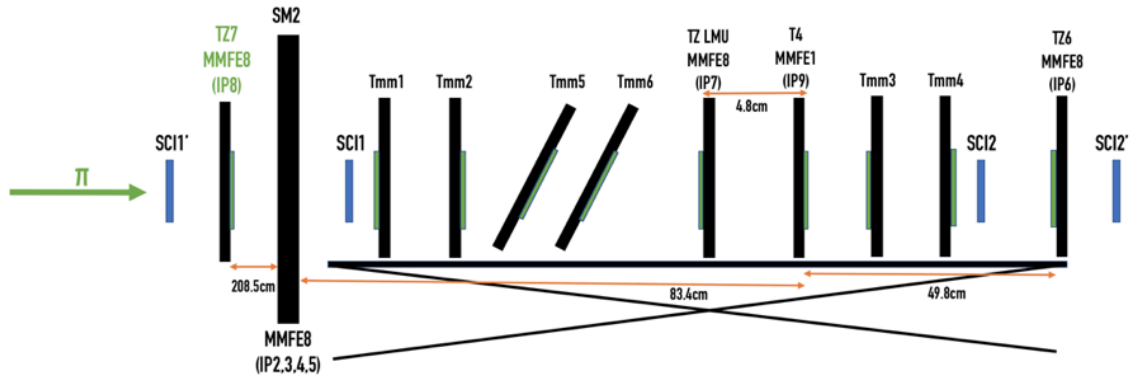


Figure 3.36: Experimental setup of the 2018 test beam. Only the TZ chambers equipped with an MMFE8 were used as reference chambers and only half PCB of SM2 was equipped with the electronics.

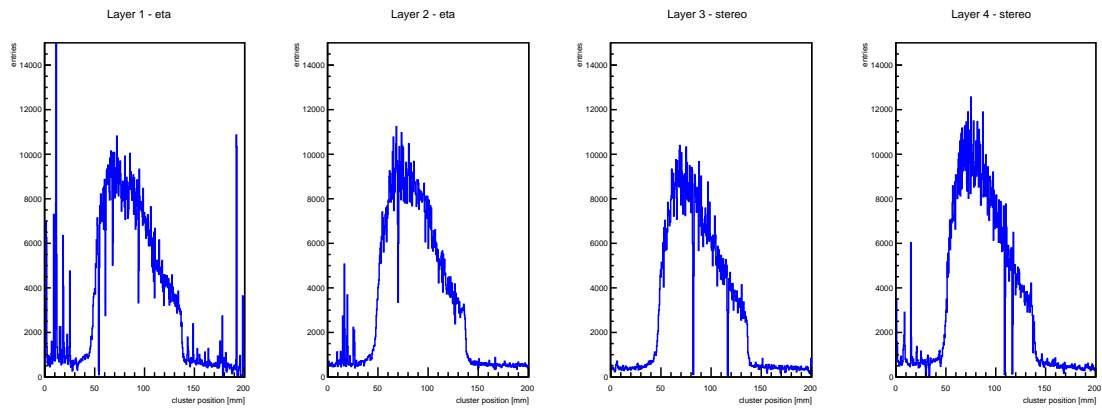
3.6.1 Noise levels

One of the fundamental parameters of the VMM is the charge threshold for each strip. Therefore, runs without the beam have been taken to measure the baseline of each channel and its fluctuations. The hardware threshold must be selected to be low enough to get a signal but also high enough to keep the noise below the predicted hit rate at HL-LHC ($1 \text{ kHz}/\text{strip}$). Furthermore, the noise is not Gaussian and therefore it is necessary to raise the thresholds to avoid selecting non-physical events. However, it has been found that MicroMegas intrinsic noise, due to the high strip capacitance (due to their length $> 1 \text{ m}$), is not as low as expected (Figure 3.38) and, having to keep the noise hit-rate below the $1 \text{ kHz}/\text{strip}$, the minimum usable threshold is $6 \times \sigma$ (σ being the fluctuation of the baseline). This high-level of threshold can impact all the standard distributions (like cluster charge and then gain but also the efficiency).

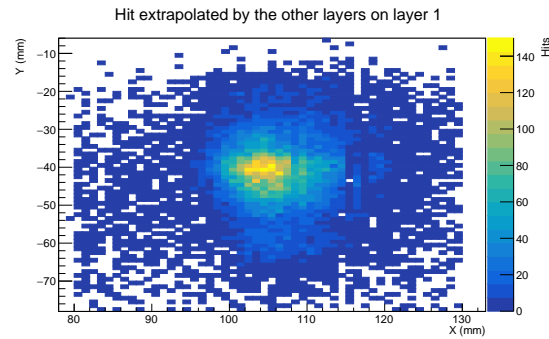
3.6.2 Resolutions for perpendicular tracks

The distribution of the difference between the reconstructed cluster positions (also called residuals) of the first two layers of the SM2 chamber can be found. This distribution contains information on the resolution of the layers. In the test beam studies, a cluster is reconstructed if there are at least 2 strips (with charge greater than 30 PDO counts ⁷ in order to remove noise) with at most 1 hole and a charge greater than 100 PDO counts .

⁷PDO is an acronym for Peak Detector Output.



(a) Beam profile reconstructed by all the layers. The beam spot can be seen with some noisy reconstructed cluster. The holes are due to consecutive dead electronic channels.



(b) Beam spot in 2D reconstructed the tracks using layer 2,3 and 4 and extrapolating the position on the first layer.

Figure 3.37

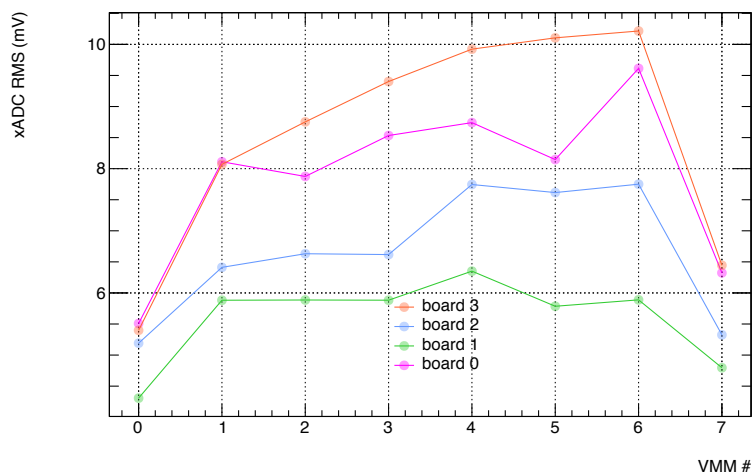


Figure 3.38: Noise level, in terms of xADC count per each board of each layer. The measurement was done on the PCB8 (the one with the longest strip of the small NSW sectors) with a gain of $9 \text{ mV}/fC$ for each VMM3. This means that a threshold of $6 \times \sigma$ is equivalent of $\sim 6 fC \approx 37 ke^-$.

The distributions, shown in Figure 3.39 are fitted with double Gaussian functions to describe also the tails. The mean parameter has the meaning of the shift between the two readout planes and gives information about how well the chamber is constructed, in terms of alignment between the layers. For what concerns the spatial resolution, it is often expressed in two ways:

- using the σ_{core} which is the σ of the core Gaussian which give the spatial resolution for good events;
- using the $\sigma_{weighted} = \frac{\sqrt{I_{core} \cdot \sigma_{core}^2 + I_{tail} \cdot \sigma_{tail}^2}}{\sqrt{I_{core} + I_{tail}}}$, where I is the integral of the single core/tail Gaussian, which takes into account also the tails due to delta rays (in small percentage) but mostly due to bad position reconstructions (hole inside the clusters, fake strip included in the clusters reconstruction).

To reconstruct the eta/phi coordinate using the stereo's planes, the following geometrical formulas were used:

$$\eta = \frac{\eta'_{i3} + \eta''_{i4}}{2} \quad \phi = \frac{\eta'_{i3} - \eta''_{i4}}{2 \cdot \tan(\theta)} \quad (3.7)$$

where η'_{i3} and η''_{i4} are the position reconstructed in the local coordinate system of the layer while $\theta = 1.5^\circ$ is the tilt angle of the stereo strip.

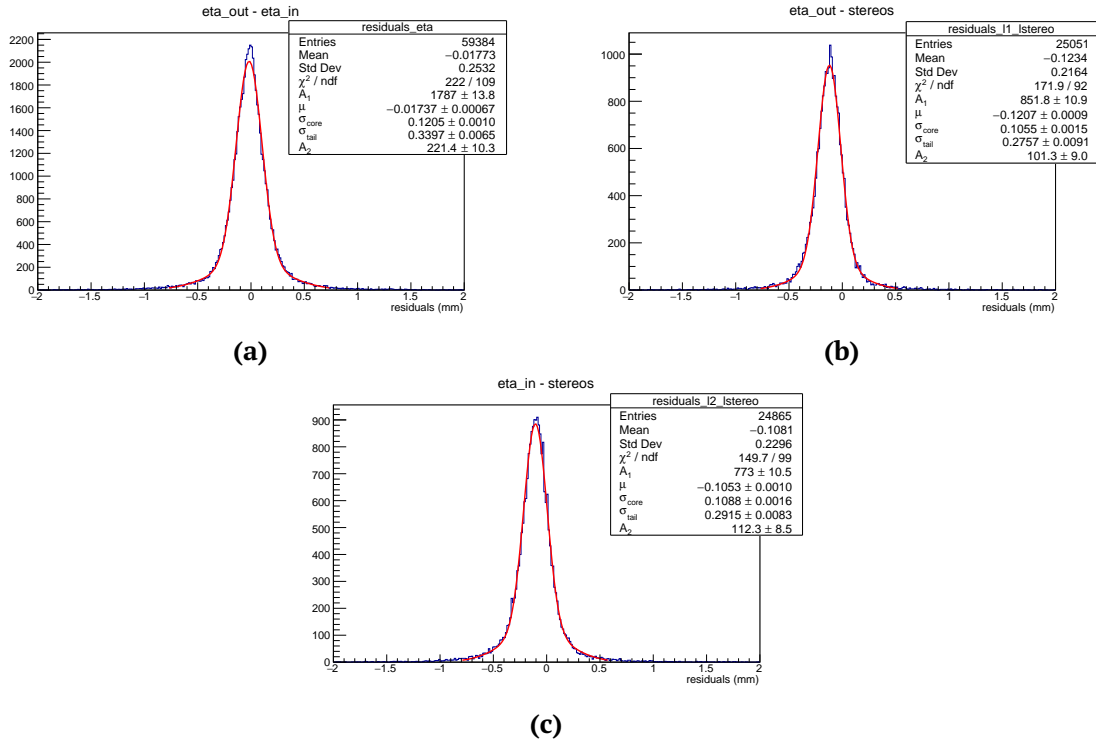


Figure 3.39: Residuals fitted with a double Gaussian. Figure 3.39a shows the difference between the cluster positions of the first “eta_out” layer and the second “eta_in” layer, Figure 3.39b shows the difference between the cluster positions of the first “eta_out” layer and of the stereo combination and in Figure 3.39c shows the difference between the cluster positions of the first “eta_in” layer and of the stereo combination. The amplification voltage for all layers was 600 V.

Assuming the resolution of two layers equal between them, the σ obtained from the fit is equal to $\sigma_{fit} = \sqrt{2}\sigma_{layer}$ which means that the achieved resolution for perpendicular tracks of all the layers is well below the $100\ \mu\text{m}$ required. The mean parameter of the fit (μ) is the shift between the layers; $17\ \mu\text{m}$ of shift between the two eta layers (see Figure 3.39a) means that the construction was done really well since the alignment requirement is at most $60\ \mu\text{m}$ while the alignment between the eta layers and the stereo combination shows values a bit out of the requirement but still acceptable if known and measured, in order to be corrected off-line.

In Figure 3.40 the resolution using the σ_{core} and the $\sigma_{weighted}$ as a function of the amplification voltage for the four layers is shown. The values of the resolutions are constant as a function of the amplification voltage.

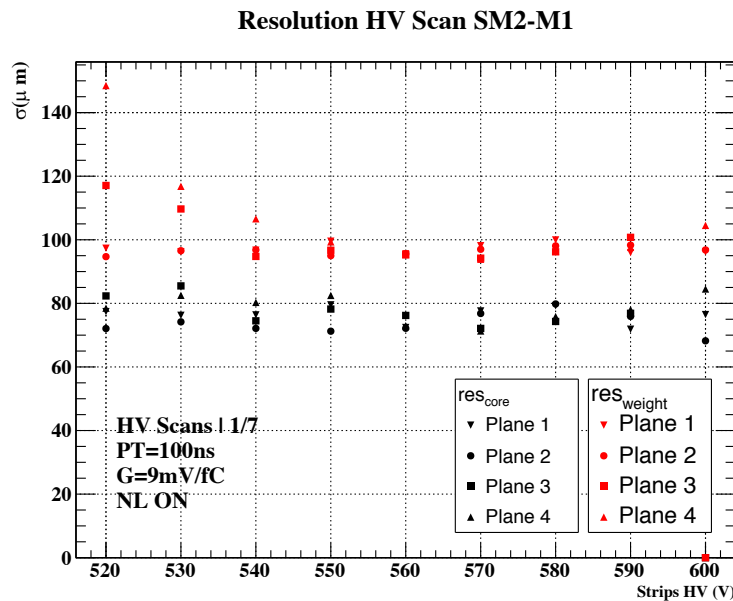


Figure 3.40: Resolution using the σ_{core} and the $\sigma_{weighted}$ as a function of the amplification voltage for the four layers. Most of the values are well below the required $100\ \mu\text{m}$.

3.6.3 Amplification voltage scan using perpendicular tracks

During the duration of the test beam, several runs were recorded changing the voltage of one layer at a time in order to scan the typical distributions and the efficiency as a function of the amplification voltage. In particular, different definitions of efficiency were used.

- The *hardware efficiency* is the fraction of events where there is at least one strip in the analysed chamber compared to the total number of selected events. This kind of efficiency is the most basic analysis that can be made and helps to figure out if, in general, the chamber is working properly.
- The *cluster efficiency* is the fraction of events where there is at least one reconstructed cluster in the analysed chamber compared to the total number of selected events.

This kind of efficiency is the less basic respect of the hardware efficiency and, in principle, should remove all the noisy hits and it gives a more realistic value of the efficiency of the chamber. In this efficiency calculation, the cluster reconstruction efficiency can play a role.

- The *software efficiency* is the fraction of events where a cluster was found in a selected window (± 1 mm for perpendicular tracks) with respect to the total number of selected events. With respect to the cluster efficiency, this calculation eliminates also the reconstructed clusters with neighbour noisy strips.

These three types of efficiencies were measured by reconstructing the track using the telescope chambers (external-tracking), and by reconstructing the track using information from the other 3 layers (self-tracking). The plots of these efficiencies are shown in Figure 3.41, and no visible difference can be found between external-tracking and self-tracking method. As expected by construction, hardware efficiency is greater than cluster efficiency, which in turn is greater than software efficiency.

The difference between the curves of the four layer could be due to drops of the voltage due to sparks happened in the layer during the recording.

The cluster distributions were also used to study the behaviour of the chamber: the cluster multiplicity and the cluster charge. The cluster multiplicity, shown in Figure 3.42a, is the number of strips composing a cluster and depends on many VMM parameters, such as neighbour logic. The gas mixture also plays an important role since different gas mixture implies different longitudinal and transverse dispersion of the avalanche. The cluster charge measured in the test beam is shown in Figure 3.42b.

As explained in Section 3.3.8, the VMM chip has different parameters that can be tuned. Fixing the amplification voltage to 580 V, different combination of the parameters were studied and in Figure 3.44 the software efficiency values for seven different combinations of three parameters are shown: neighbour logic, charge threshold (in terms of RMS of baseline fluctuation) and peak time. Figure 3.44 shows that the neighbour logic has an important role in the efficiency since enabling this feature, many under-threshold strips can be recovered also having a high value of the threshold. It does not have on the other hand a significant impact on the cluster charge, as shown in Figure 3.43.

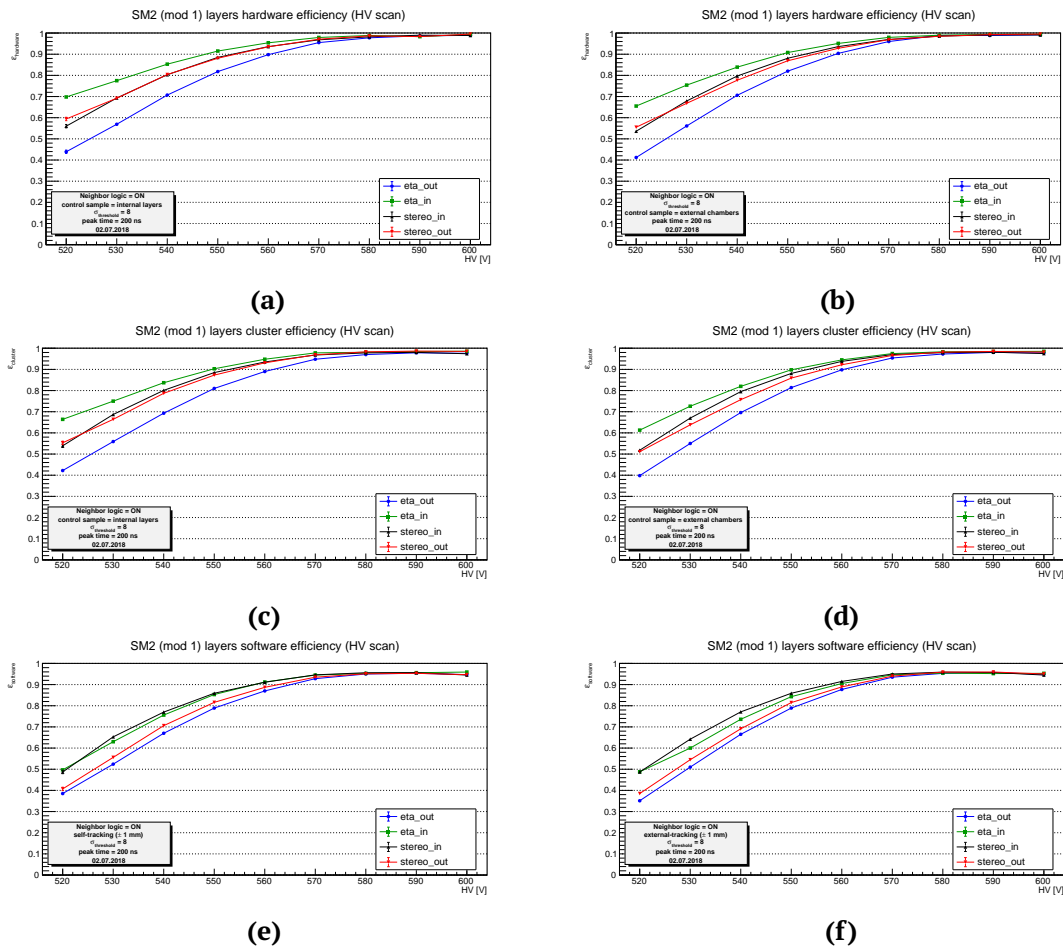


Figure 3.41: Efficiency curves as a function of the amplification voltage. Figure 3.41a and Figure 3.41b show the hardware efficiencies with the external-tracking and the self-tracking, Figure 3.41c and Figure 3.41d show the cluster efficiencies with the external-tracking and the self-tracking while Figure 3.41e and Figure 3.41f show the hardware efficiencies with the external-tracking and the self-tracking for all the four layers of the SM2 chamber.

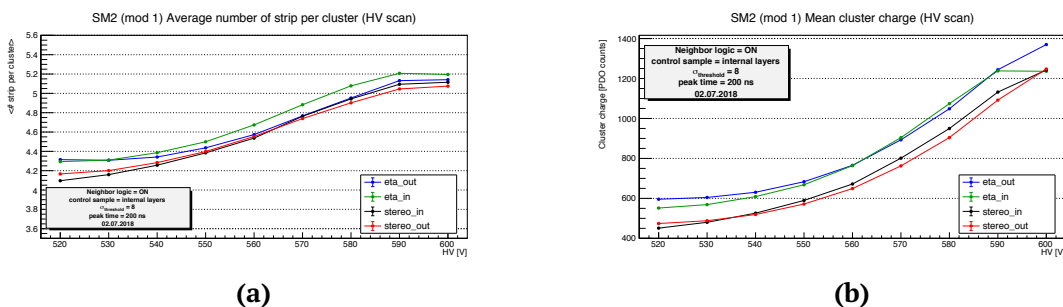


Figure 3.42: Cluster multiplicity, Figure 3.42a, and cluster charge, Figure 3.42b, as a function of the amplification voltage. As expected with the increase of the applied voltage, the charge on the strips (and consequently also the cluster charge) increases and this increase the number of strips above the threshold. The “eta_in” cannot stay stable at 600 V then the voltage was decreased during the run to 590 V but also the others layer were drawing current so the point at 600 V don’t follow the shape of the previous.

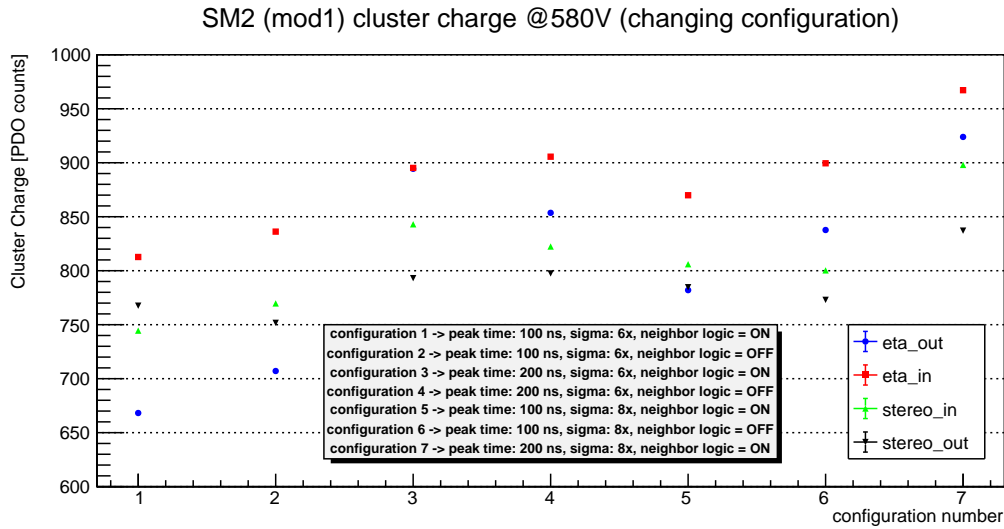


Figure 3.43: Cluster charge for the four SM2 layers measured using different combinations of the VMM3 parameters (neighbour logic, peak time and charge threshold). As expected, the best configuration is the one with neighbour logic ON, low threshold ($6 \times \sigma$) and biggest peak time (200 ns).

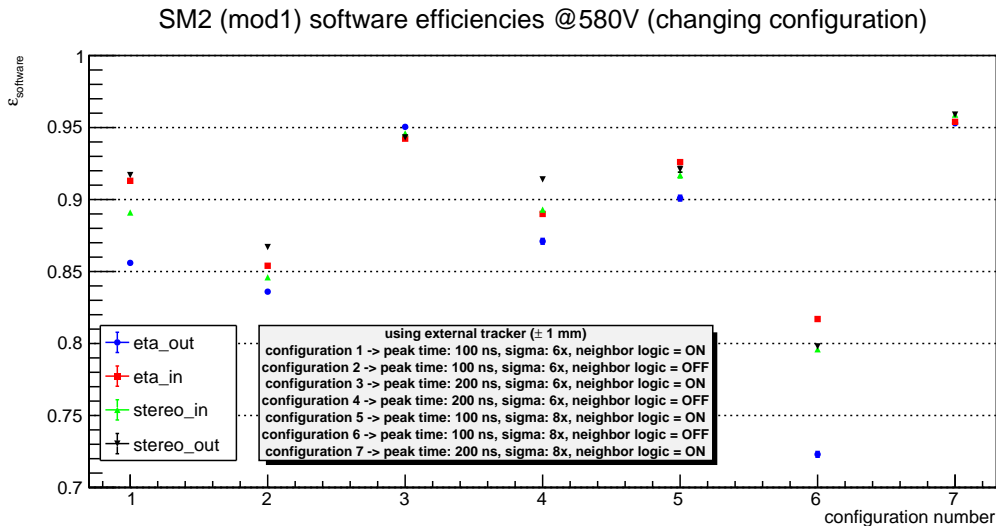


Figure 3.44: Software efficiency for the four SM2 layers measured using different combinations of the VMM3 parameters (neighbour logic, peak time and charge threshold). The neighbour logic has a big impact on the efficiency calculation since recovering the strip below the threshold helps to reconstruct real clusters. As expected, the best configuration is the one with neighbour logic ON, low threshold ($6 \times \sigma$) and biggest peak time (200 ns).

3.6.4 Inclined track runs

The setup used to study the detector performance with inclined tracks is identical to the setup used for the perpendicular tracks analysis with the only difference that the MicroMegas chambers were rotated by 30 degrees with respect to the x-axis, as shown in Figure 3.45. Both charge centroid and μTPC were used to reconstruct the position and to study the MicroMegas performances in terms of resolutions.

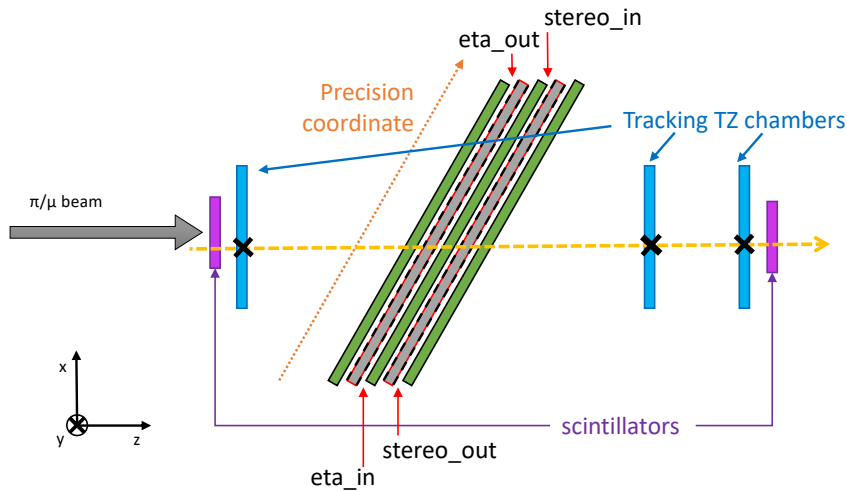


Figure 3.45: Schematic representation of the experimental setup of the 2018 test beam with inclined tracks. The SM2 module is tilted while the reference chambers are in the same position with respect to the runs with perpendicular tracks.

Figure 3.46 shows the efficiency curve for three different combinations of the VMM parameters and using the centroid method (increasing to ± 5 mm the window in which the cluster is searched). By tilting the chamber, the avalanche charge is distributed among several strips, as shown in Figure 3.47, and therefore the neighbour logic plays an increasingly important role in the presence of high thresholds.

Using the external telescope to reconstruct the track, the difference between the expected track position and the cluster position can be found. Figure 3.48 show the residuals of the position of the clusters obtained using the charge centroid method with respect to the predicted position of the track. A double Gaussian function was fitted to the distribution. Instead, Figure 3.49 show the residuals of the position of the clusters obtained using the μTPC method with respect to the predicted position of the track. A double Gaussian function was fitted to the distribution covering 95% of the entries. To achieve the resolution of the layer, the extrapolation error of the track was taken into account.

As shown in Figure 3.48 the resolution achieved with the charge centroid method is comparable with the ones obtained from the previous test beam using the small MicroMegas prototype (see Figure 3.16) while for the μTPC the resolution are worse than expected and this is still under study.

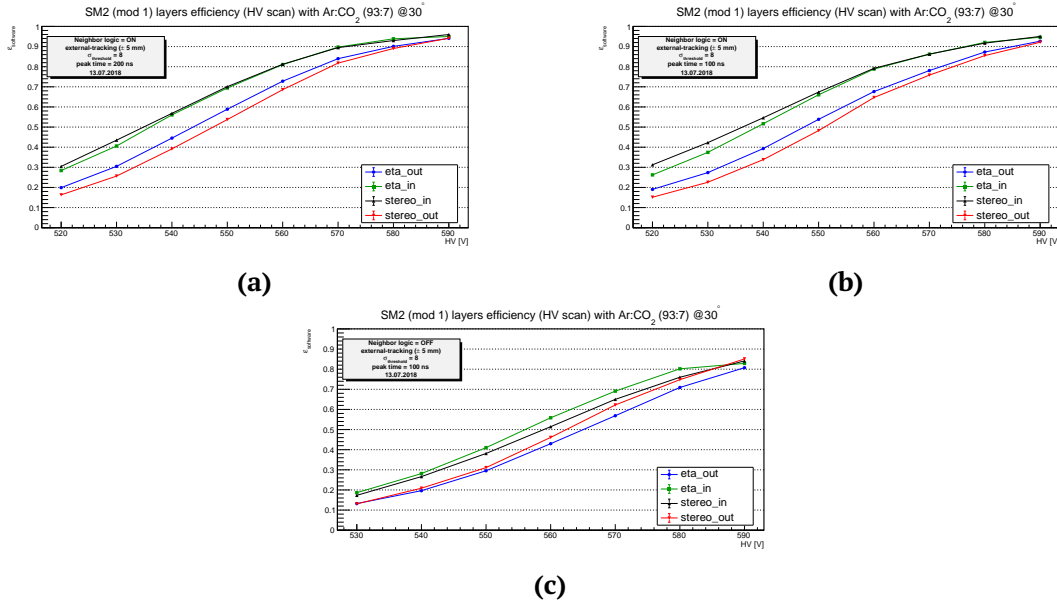


Figure 3.46: Efficiency curves as a function of the amplification voltage for three different VMM parameters configuration.

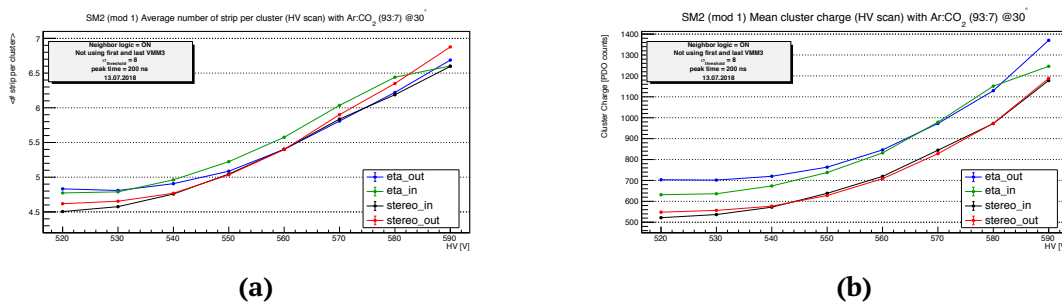


Figure 3.47: Cluster multiplicity, Figure 3.47a, and cluster charge, Figure 3.47b, as a function of the amplification voltage for tracks with an inclination of 30°.

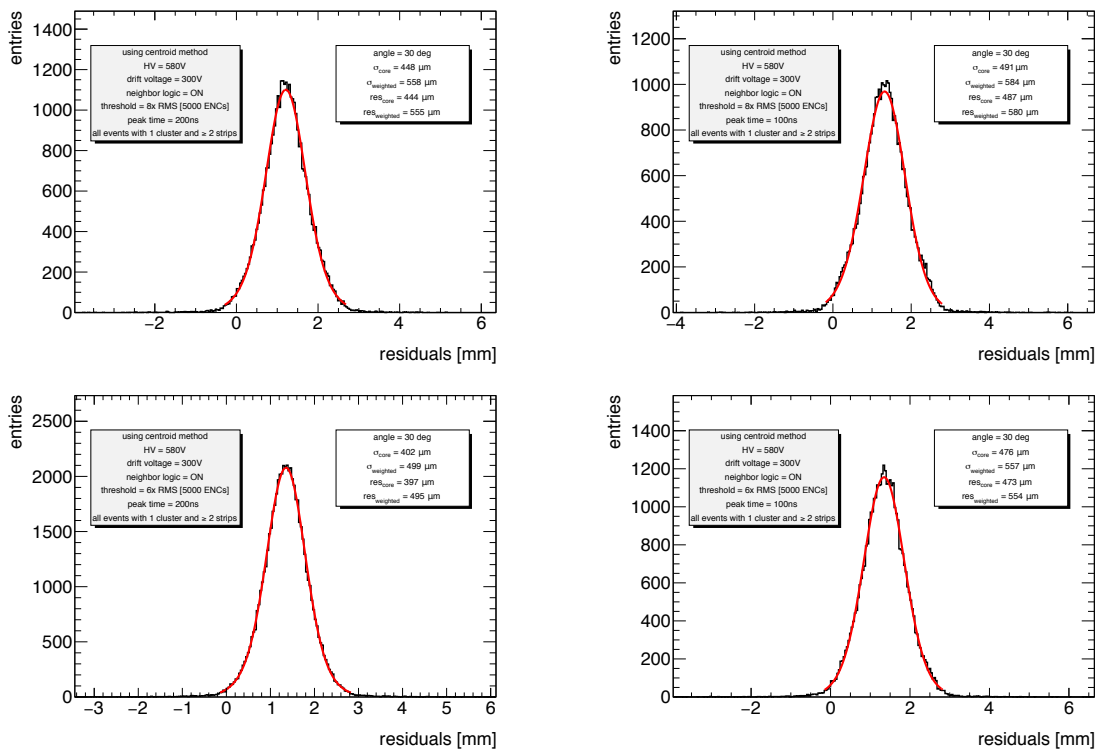


Figure 3.48: Residuals between expected track position and cluster position reconstructed using the charge centroid method for four different combinations of the VMM3 parameters. Both the σ_{core} and $\sigma_{weighted}$ from the fit results are shown in the plots while res_{score} and $res_{weighted}$ is the results after the subtraction of the extrapolation error of the track.

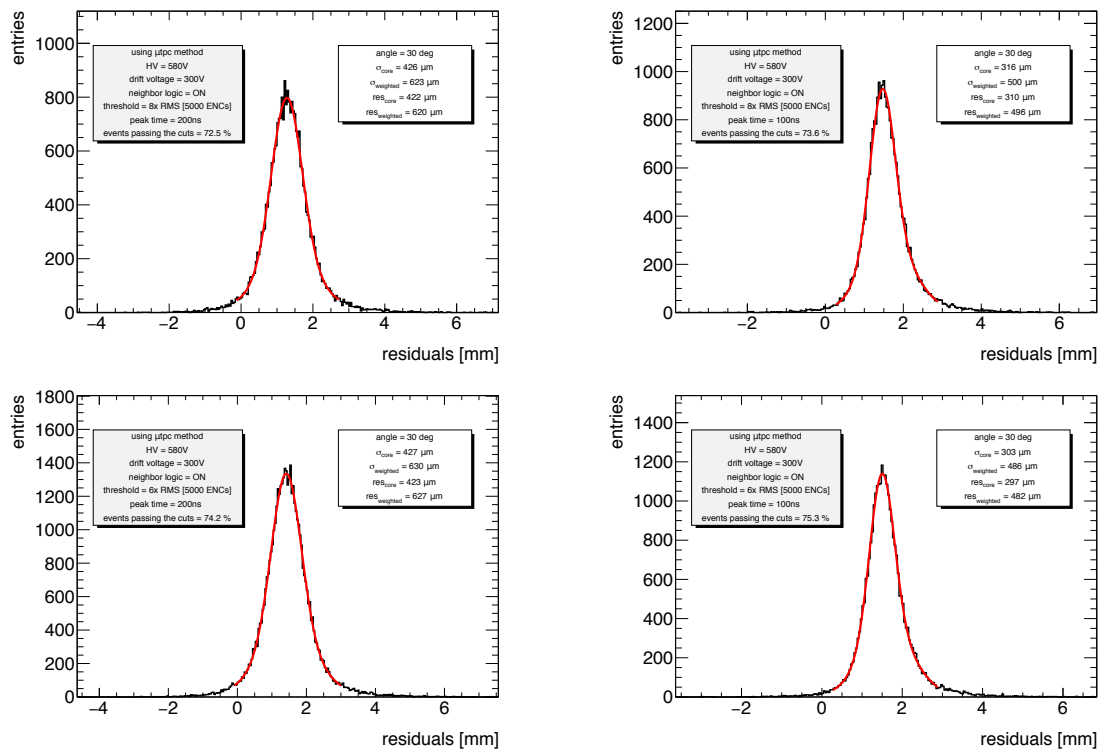


Figure 3.49: Residuals between expected track position and cluster position reconstructed using the μ TPC method for four different combinations of the VMM3 parameters. Both the σ_{core} and $\sigma_{weighted}$ from the fit results are shown in the plots while res_{core} and $res_{weighted}$ is the results after the subtraction of the extrapolation error of the track.

3.6.5 Gas mixture studies

Three different compositions of argon and carbon dioxide were studied during the test beam to see if there was room for improvement by changing the gas mixture:

- $Ar + CO_2$ (93 : 7) (nominal);
- $Ar + CO_2$ (70 : 30);
- $Ar + CO_2$ (85 : 15).

For the two new mixtures, the drift and amplification voltages have been chosen in order to have the same electrons drift velocity ($v_d \sim 5 \text{ cm}/\mu\text{s}$) and the similar transverse diffusion ($\sigma \sim 100 \mu\text{m}/5 \text{ mm}$).

3.6.5.1 $Ar + CO_2$ (70 : 30)

Various runs have also been recorded for the $Ar + CO_2$ (70 : 30) gas mixture. The Figure 3.50a and Figure 3.50b show the values of efficiency, cluster average charge (Figure 3.50c and Figure 3.50d) and cluster multiplicity (Figure 3.50e and Figure 3.50f) for runs with perpendicular and 30 degree inclined tracks. Comparing the average charge distributions obtained with the nominal mixture, the equivalent voltage for the new mixture is obtained. A voltage of 570 V with the 93 : 7 gas mixture is equivalent to a voltage of 710 V for the 70 : 30 gas mixture. Furthermore, at the same gain the average cluster multiplicity is 4.7 for $Ar + 30\% CO_2$ while 4.9 for $Ar + 7\% CO_2$. These two numbers are compatible with the difference in transverse diffusion coefficient between the two mixtures: 185 $\mu\text{m}/5 \text{ mm}$ and 100 $\mu\text{m}/5 \text{ mm}$ respectively.

3.6.5.2 $Ar + CO_2$ (85 : 15)

Different scans were also measured for the gas mixture of $Ar + CO_2$ (85 : 15). The Figure 3.51a and Figure 3.51b show the values of efficiency, cluster average charge (Figure 3.51c and Figure 3.51d) and cluster multiplicity (Figure 3.51e and Figure 3.51f) for runs with perpendicular and 30 degree inclined tracks. Comparing the average charge distributions obtained with the nominal mixture, the equivalent voltage for the new mixture is obtained. A voltage of 570 V with the 93 : 7 gas mixture is equivalent to a voltage of 620 V for the 85 : 15 gas mixture.

3.6.5.3 Gas mixture comparisons

In Figure 3.52 the efficiency, cluster charge and cluster multiplicity for perpendicular tracks at the same gain for the three different gas mixture are shown. The comparisons were made using a hardware threshold of $6 \times \sigma$, neighbour logic ON and two different settings of peak time (100 and 200 ns). There is no big difference between these three combinations of $Ar + CO_2$.

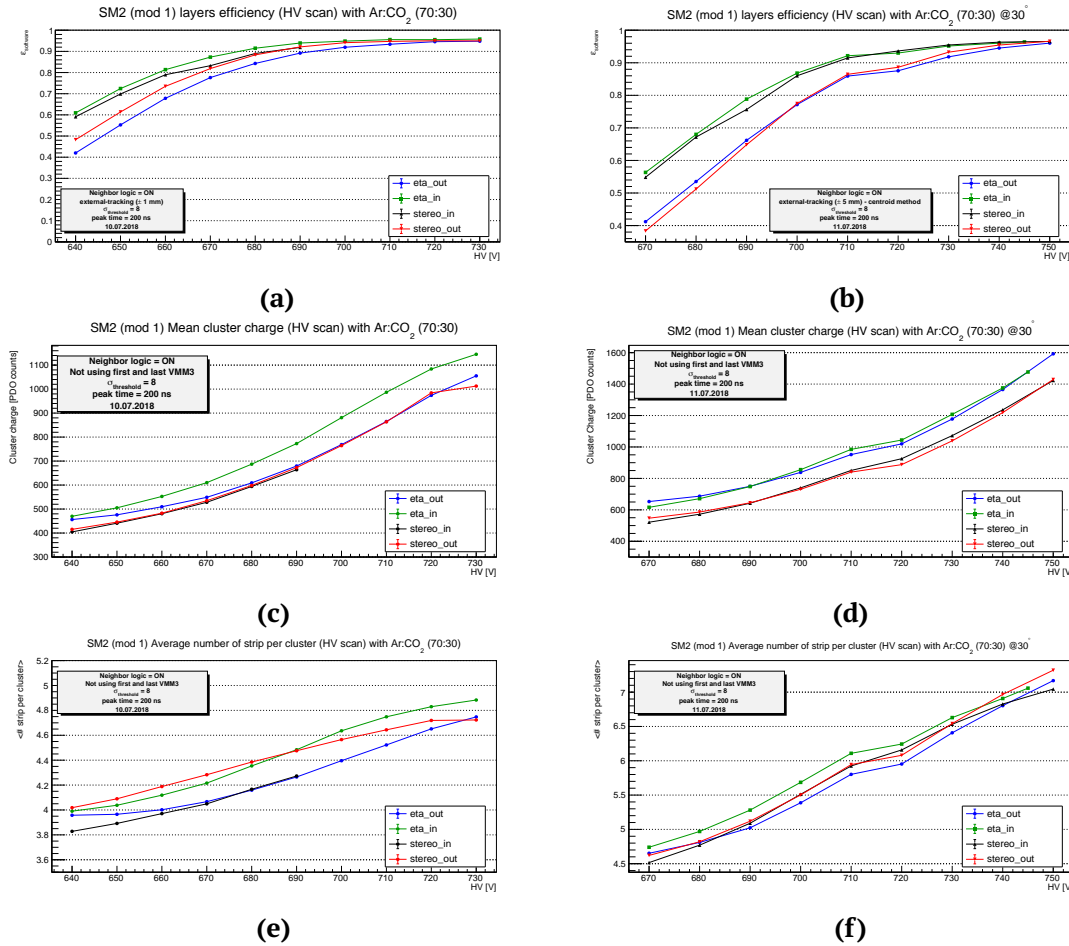


Figure 3.50: Efficiency (Figure 3.50a and Figure 3.50b), cluster charge (Figure 3.50c and Figure 3.50d) and cluster multiplicity (Figure 3.50e and Figure 3.50f) as a function of the amplification voltage using the Ar + CO₂ (70 : 30) gas mixture. “Stereo_in” layer starts to draw current after 690 V so the points at higher voltage were not measured. The gap between 710 V and 720 V is due to the fact that the point below 720 V were measured the day before when all the layers were drawing less current and this has brought to have a better behaviour respect to the day after.

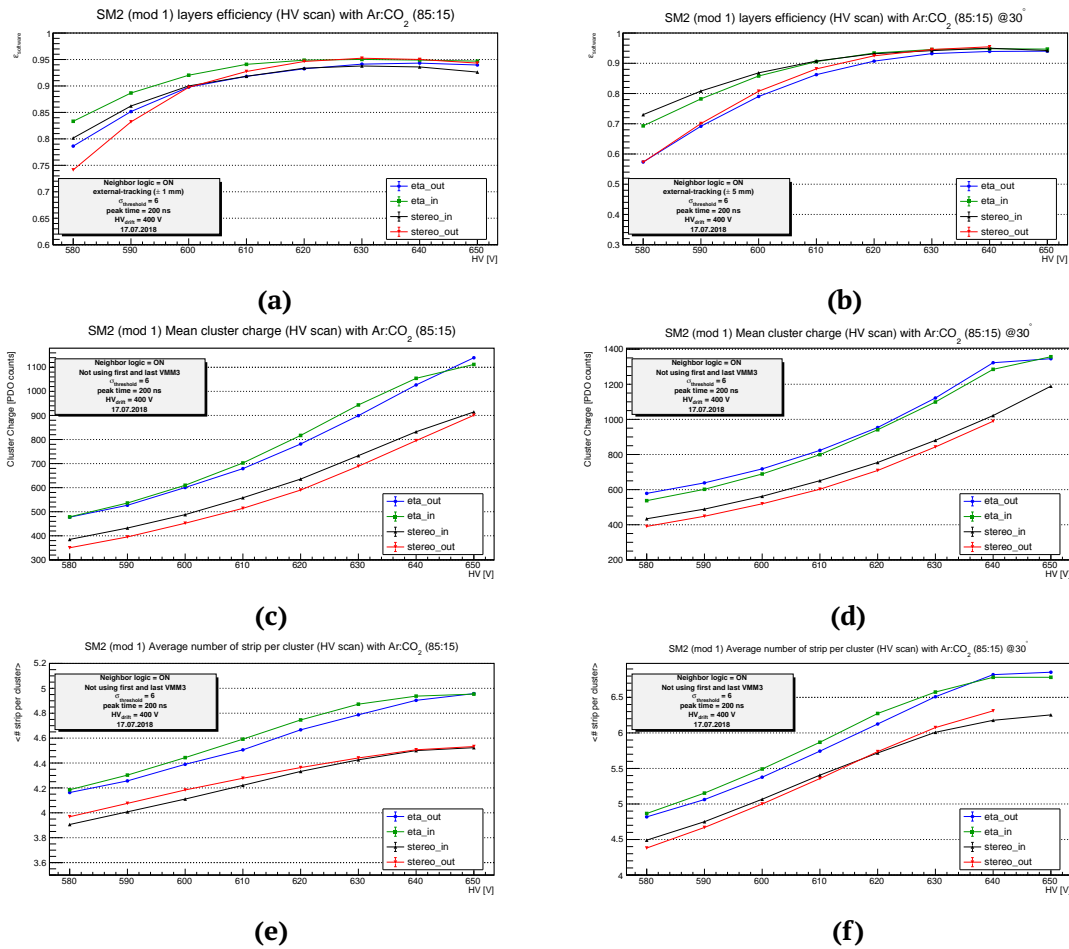


Figure 3.51: Efficiency (Figure 3.51a and Figure 3.51b), cluster charge (Figure 3.51c and Figure 3.51d) and cluster multiplicity (Figure 3.51e and Figure 3.51f) as a function of the amplification voltage using the Ar + CO₂ (85 : 15) gas mixture. “Stereo_out” layer cannot stay at 650 V in a stable condition so the point was not measured.

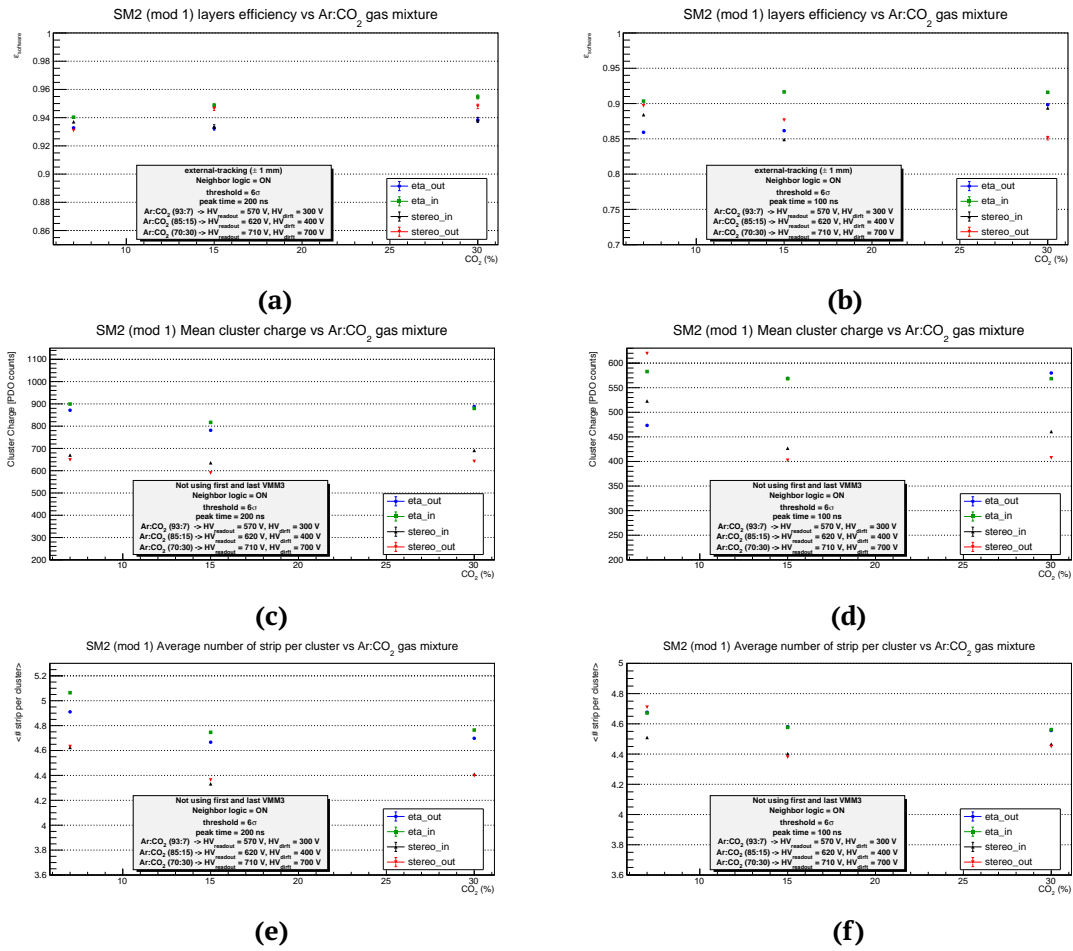


Figure 3.52: Efficiency (Figure 3.52a and Figure 3.52b), cluster charge (Figure 3.52c and Figure 3.52d) and cluster multiplicity (Figure 3.52e and Figure 3.52f) for the three different percentage of CO_2 .

3.7 Validation and integration of the MicroMegas chambers in BB5

Once the modules have been constructed and have been passed all the quality criteria in terms of high voltage stability, alignment between layers, gas leak, efficiency, and so on, they are shipped to CERN, in particular to the building BB5, where the MicroMegas chambers are integrated in sectors (“MicroMegas double-wedges”), equipped with the electronics and services (cables, readout, HV, LV, gas, cooling, ...) and validated with cosmic rays.

3.7.1 MicroMegas integration in BB5

The work in BB5 is divided into different groups, each dealing with a specific task.

Once the modules arrive in BB5, the reception team performs some acceptance tests to be sure that nothing is changed/damaged during the shipping. New gas leak and high voltage stability tests for each high voltage section are performed. Some chambers are also sent to the GIF++ where the behaviour of voltages and currents are studied when the chambers are subjected to a large flow of particles. In parallel, the spacer frame with all the services (Cooling and gas interconnections, HV cables, LV cables, optic fibre, ...) is prepared. Two type 1 modules and two type 2 modules, together with the spacer frame, are integrated into a double-wedge, checking after each step the alignment between the modules.

The completed double-wedge is moved into a rotation station (a mechanical support that allows the double-wedge to rotate) on which the electrical connections are tested (in order to find out some bad welds or short-cuts) and then the double-wedge is moved again into a second rotation station to equip it with the full readout electronics.

At this point, the double-wedge is ready to be finally validated and it is moved to the cosmic ray stand.

The Figure 3.53 shows the view of the BB5 building. The two rotation stations and the cosmic ray stand in the background are visible.

3.7.2 The cosmic rays stand

A dedicated Cosmic Ray Stand is installed in building BB5 at CERN. As shown in Figure 3.54, four scintillators, grouped in two up+down pairs (of different dimensions), are used to trigger good events. The trigger logic consists of taking the OR condition between the coincidences (AND) of the up+down scintillator pairs. The double-wedge is placed under the two scintillator pairs with the IP wedge facing the floor. The final expected rate is $\sim 105 \text{ Hz}$.

The first step of the validation is the check of the dead channels and the validation of the readout path. In order to do this, few runs are taken using the internal pulser of each VMM. The baseline and the noise level of each channel can be measured in this way,

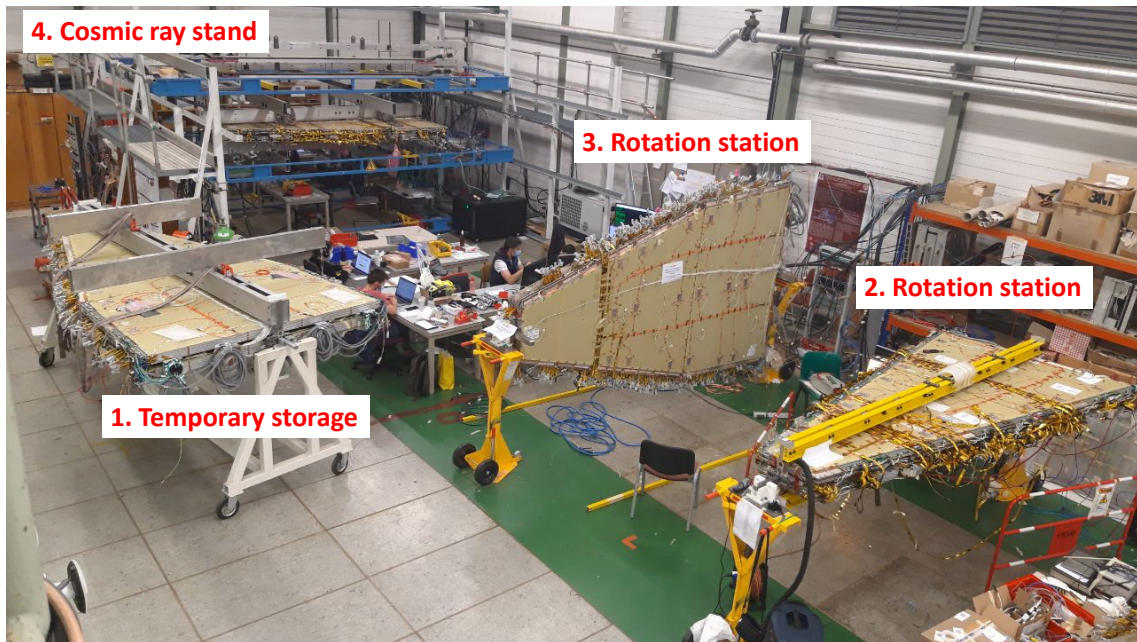
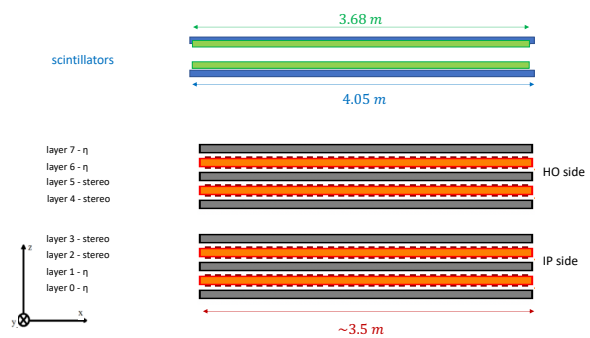


Figure 3.53: View from above inside the BB5 building. A large double-wedge is stored temporarily on a mechanical support (1.), a small double-wedge is on one rotation station and the electrical connections are going to be tested (2.), another large double-wedge is on a second rotation station and it is ready to be fully equipped with the electronic (3.) while on the background it is visible the cosmic ray stand (4.) with another large double-wedge during the final validation process.



(a) Picture of one small double-wedge at the cosmic ray stand in BB5.



(b) Scheme of the cosmic ray stand. Two sets of pairs of scintillators (green and blue) are used to trigger the event while under them, the 8 layer of the double-wedge are shown.

Figure 3.54

hence the charge thresholds and the trimmers calibrations are decided⁸. The noise level for each channel is shown in Figure 3.55. The noise increases as a function of the channel number (the first strip is the shortest) since the noise due to the capacitance of the strips increases with the length of the strips themselves.

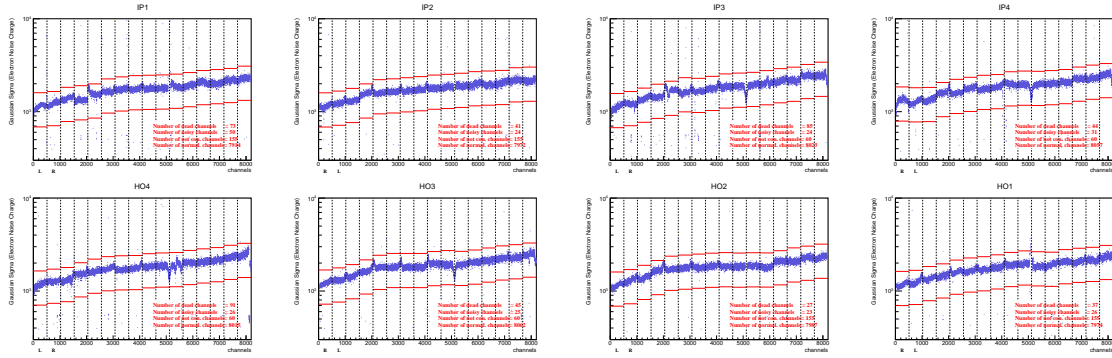


Figure 3.55: Noise level in terms of RMS of the baseline per each channel of each layer of the double-wedge. The σ of the baseline fluctuation grows as a function of the strip length (strip number). The red lines are $0.6\times$ and $1.4\times$ the σ of the baseline. The channels that have a baseline fluctuation not between the two red lines are marked as noisy (more than $1.4\times\sigma$) or dead (less than $0.6\times\sigma$). The total number of noisy/dead or not connected are written in the bottom right part of the canvas.

3.7.3 High voltage maps

Once the double-wedge arrives at the cosmic ray stand, the high voltage behaviour is checked. This is needed to test all the final configuration, from the detector to the cables and to see if there is something that has changed (worsened) during the integration works.

The current high voltage distribution scheme is done through a “splitter box” which consists of one channel per layer per module (i.e. 16 channels in total) plus 4 additional channels (one per module) called “hospital line” (HOL) in which all sectors that cannot reach the nominal voltage can be connected. For this reason, it is important to make a first scan to try to match the problems seen at the construction sites and during the reception of the chambers and to understand which sections can be connected to the main channel of the layer (usually $HV_{layer} = 570\text{ V}$). The scan is carried out by slowly increasing the voltage of each section until the maximum “stable” voltage is reached. It is defined by the three main parameters:

- I_{below} which is the average current below a set threshold (i.e. 40 nA) and tells if the section has a baseline in current;
- $spike/rate$ which is the rate per minute in which the current goes above the threshold;
- I_{above} which is the average current above the threshold and tells how big are the current spike.

⁸Each VMM chip has a common threshold for all the channels plus a trimmer per each channel to fine-tune the charge threshold.

Parameters combinations	Goodness
$I_{below} > 30 \text{ nA}$ or $I_{above} > 200 \text{ nA}$ or $spike/rate > 3 \text{ spike/min}$	Bad
$20 \text{ nA} < I_{below} \leq 30 \text{ nA}$ or [$100 < I_{above} \leq 200 \text{ nA}$ or $0.5 < spike/rate \leq 1 \text{ spike/min}$] or $1.5 < spike/rate \leq 3 \text{ spike/min}$	Ok
$I_{below} \leq 20 \text{ nA}$ or [$I_{above} \leq 100 \text{ nA}$ or $spike/rate \leq 0.5 \text{ spike/min}$] or $spike/rate \leq 1.5 \text{ spike/min}$	Good

Table 3.2: Combination of the parameters used to define a stable section. The orange sections are defined stable but can deteriorate their behaviour since the test is done in a limited time window and they may not have shown strong instability yet.

The stability of a section has been defined according to the Table 3.2.

Once the high voltage sections are tested alone, these are connected through the splitter box (shown in Figure 3.56) to the layer channel if their behaviour is considered stable at the nominal voltage of 570 V while the others are grouped (per module) and connected to the hospital line.



Figure 3.56: Picture of the splitter box. The cables coming from each module of the double-wedge are connected to the splitter box as for the cables coming from the high voltage power supply. The gold jumpers are used to connect the sections to their channel.

The voltage applied to the HOL is dictated by the maximum voltage reached by the section with the worst behaviour. In Figure 3.57 the final map obtained for the double-wedge A12 (the second validated) is shown while the other maps are in Appendix A. As shown in Figure 3.57a some sections are disconnected (OFF) and this is because the maximum voltage reached is less or equal to 500 V and, since the expected efficiency for a voltage $< 500 \text{ V}$ is less than 30%, to avoid that also the other sections connected to the HOL are compromised in terms of efficiency, it is not connected.

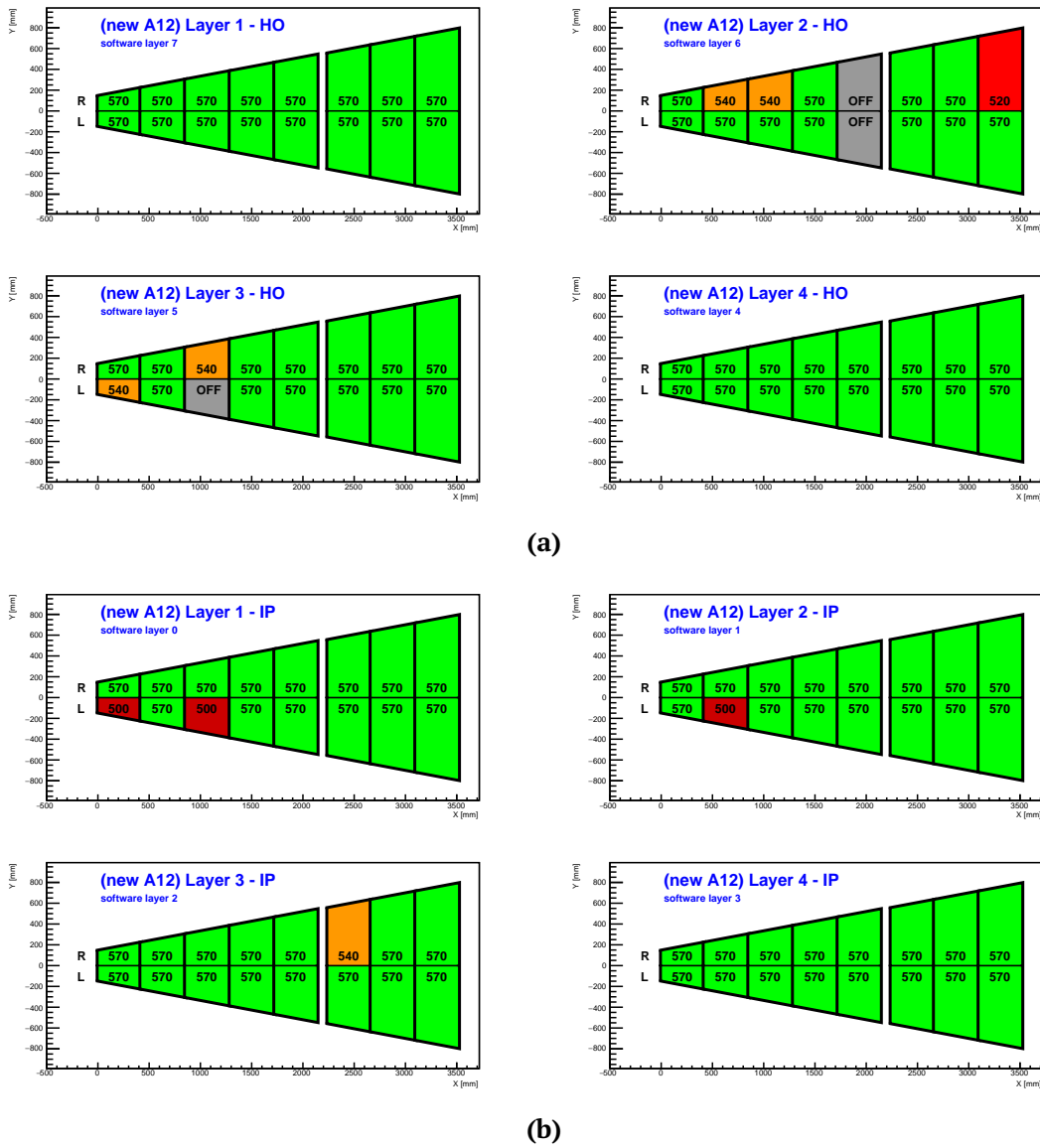


Figure 3.57: Final high voltage map for the double-wedge A12. 9 section are connected to the hospital lines while 3 section needs to be disconnected.

The grouping phase of the sections is very important and the efficiency of the layer must be maximised. Using the dependence of the efficiency as a function of the high voltage obtained from the other validated double-wedge (see Section 3.7.4 and Figure 3.76), the optimal configuration for each double-wedge module can be found, as shown in Figure 3.58.

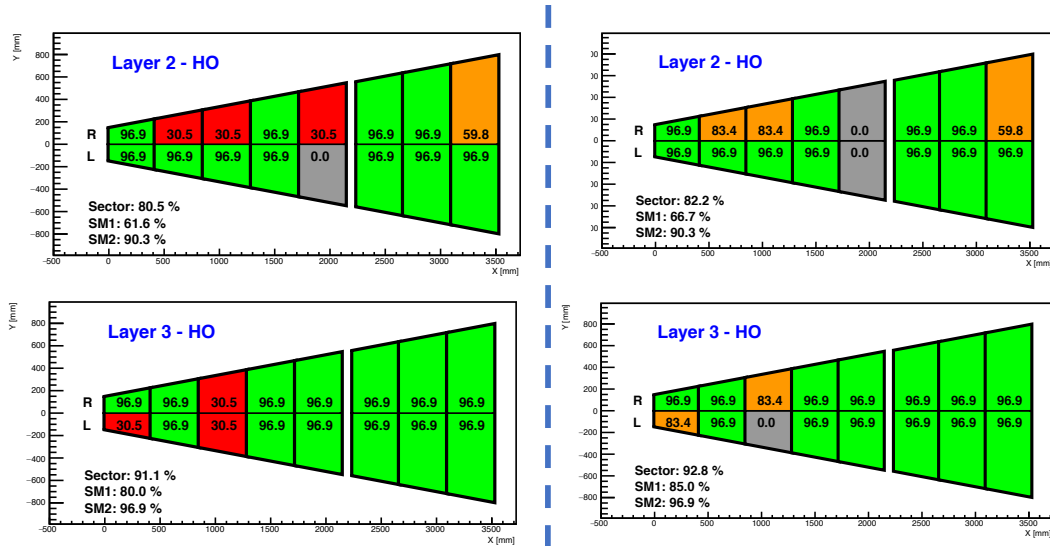


Figure 3.58: Efficiency per each section for layer 2 and 3 (HO chambers). The first configuration (*left*) shows 6 sections connected to the HOL ($HV = 500 V$) and one disconnected for the SM1 module while the second (*right*) shows 4 section connected to the HOL ($HV = 540 V$) and 3 section disconnected. Calculating the expected efficiency from the measured efficiency versus high voltage curves, and reweighting the efficiency of each section using its active area, the expected efficiency of the layer can be estimated. The second configuration shows an increase of the efficiency of $\sim 5\%$ for both layer 2 and layer 3 of the SM1 module, as shown in the bottom-left part of the canvas.

The final check from the high voltage point of view is to study the stability of all the sections connected together during the time. All the chambers are connected to the high voltage once the final mapping is configured and then, the stability of each channel can be monitored using different scripts. The output of the script used to monitor the behaviour of a chamber is shown in Figure 3.59 where the criteria to evaluate the stability of a channel (group of high voltage sections) are reported in Table 3.2 where now the limits on the *spike/rate* are multiplied by N which is the number of connected sections. The final high voltage validation is obtained from a chamber if it has 80% of section connected to the main line and it needs to have good stability (following the same conditions described in Table 3.2 and multiplying the values for the number of connected section in the channel).

In Figure 3.60 is shown the percentage of section connected to the HOL or disconnected, divided per double-wedge. The A04 double-wedge present many problematic sections which are not connected to the main line. For this reason, this double-wedge is not certified as validated and will not be installed on the NSW. The chambers composing the double-wedge A04 will be replaced to pass the validation criteria.

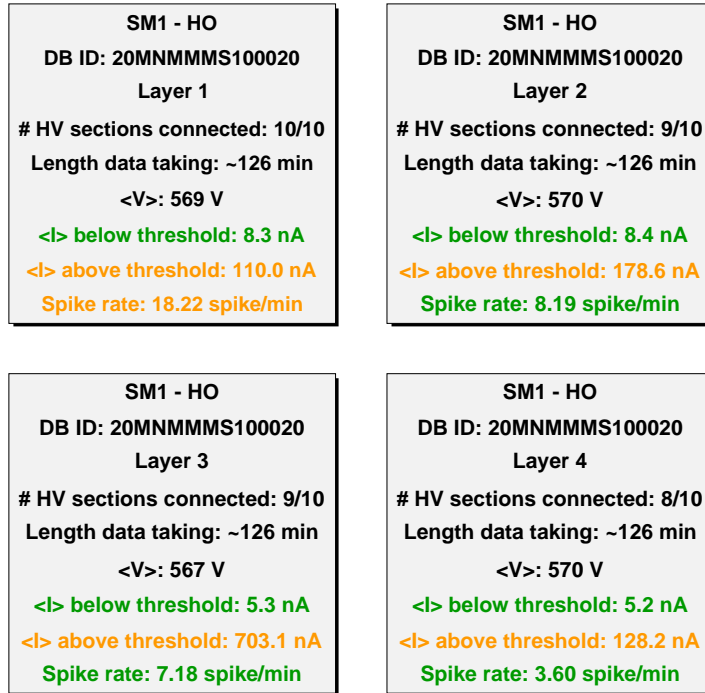


Figure 3.59: Output of one of the scripts used to monitor the high voltage behaviour. The colour code is used in order to highlight the bad/good sections following the Table 3.2.

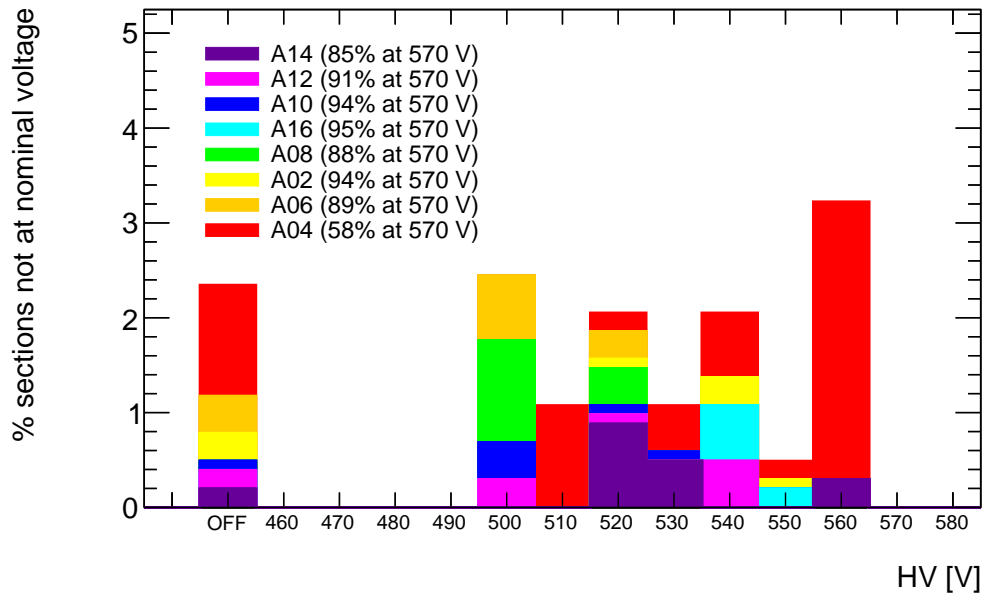


Figure 3.60: Percentage of section connected to the HOL or disconnected, divided per double-wedge.

3.7.4 Double-wedge performance studies

The goal of the studies made at the cosmic ray stand is to validate the entire detector+electronics system. To do that, the different measurements (studies of standard distributions, charge maps, efficiency maps, etc.) are performed on each layer of each double-wedge which will be installed on the New Small Wheel.

Some channels are particularly noisy due to electronic problems. In addition, some channels have low occupancy and this is due to the connectors (“zebra connectors”) which may cause connectivity problems. To ensure that tracks are not badly reconstructed due to these fake hits, strips that have an occupancy greater than three times the average occupancy of the MMFE8 board to which they belong are masked. Strips that are less than 0.2 times the average occupancy of MMFE8 are classified as not good but are not masked in the track reconstruction. An example of the channel occupancy as a function of the channel number is shown in Figure 3.61 where the high-occupancy and low-occupancy limits for each MMFE8 are shown.

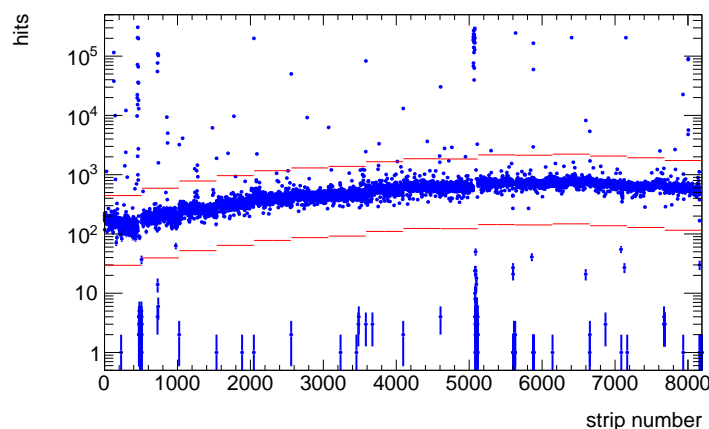
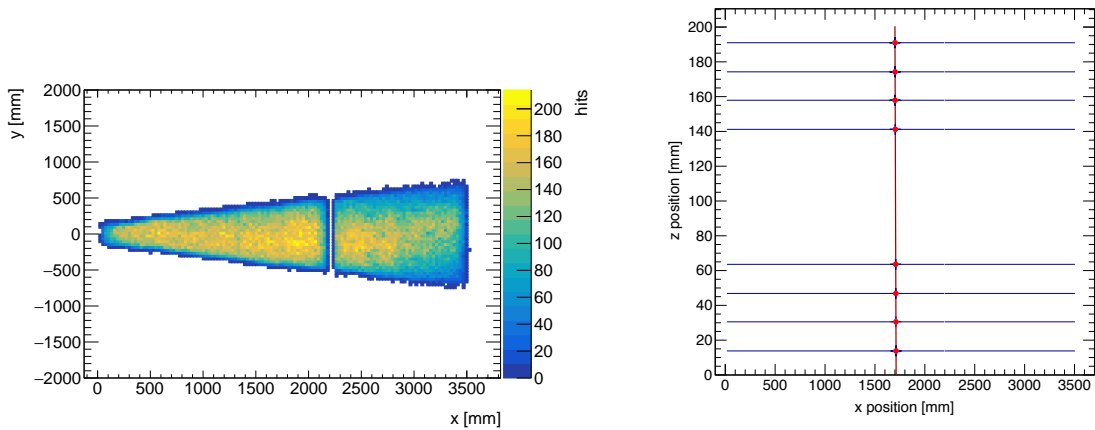


Figure 3.61: Occupancy of each strip for a single layer. Red lines show the 0.2 times and 3 times the average occupancy of the MMFE8. The strips with an occupancy greater than the upper limit are marked as noisy and are masked while the strips with an occupancy less than the lower limit are marked as low-occupancy strip but are not masked.

After the masking, the charge centroid method is used for the position determination of the hit. Since there is not external tracking, a 3D self-tracking method is performed using at least 5 layers (two need to be eta-type and two stereo-type) and excluding the layer under study. The hit map of the reconstructed track on a layer of a small double-wedge is shown in Figure 3.62a and an example of a reconstructed track is shown in Figure 3.62b.

3.7.4.1 Toy Monte Carlo

In order to compare and understand all the spatial and angular distributions of the reconstructed tracks, a toy Monte Carlo simulation is realised to simulate the cosmic ray stand setup with its geometry. In particular, the geometric acceptance of the system has been estimated to understand the accumulated statistics and detector coverage as a function of data taking. In Figure 3.63c are shown all the tracks accepted by the scintillators trigger

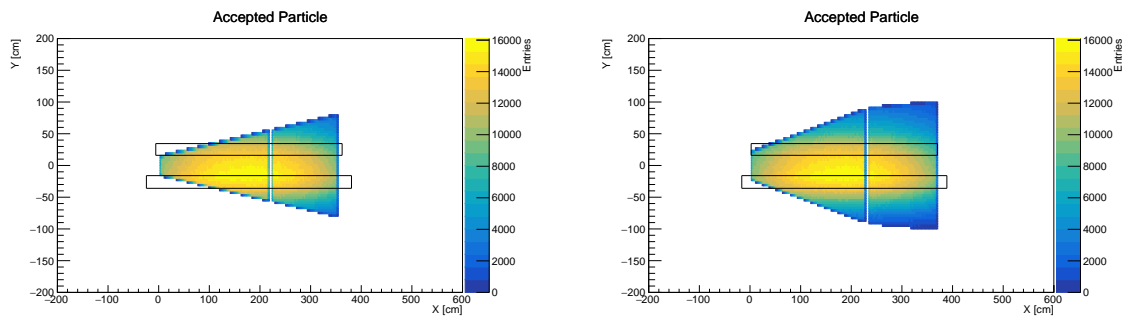


(a) Reconstructed track position at the z coordinate of a layer of a small sector.

(b) Event with 8 clusters and a reconstructed track using the 3D self-tracking method.

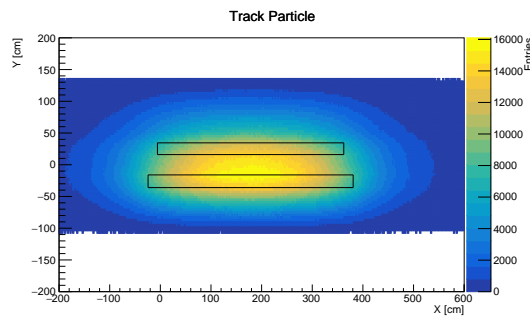
Figure 3.62

logic while in Figure 3.63a and Figure 3.63b are shown all the tracks accepted by the trigger and pass through the double-wedge.



(a) Number of simulated track accepted by the trigger which also pass through the small sector.

(b) Number of simulated track accepted by the trigger which also pass through the large sector.



(c) Number of simulated track accepted by the trigger.

Figure 3.63

The fraction of events in which tracks fall in the acceptance of the small (large) sectors is 0.48 (0.62).

3.7.4.2 Characterisation of the MicroMegas double-wedges response

One of the main measurements to be made on the double-wedges is the measurement of the charge and uniformity of response of each gas gap as shown in Figure 3.64.

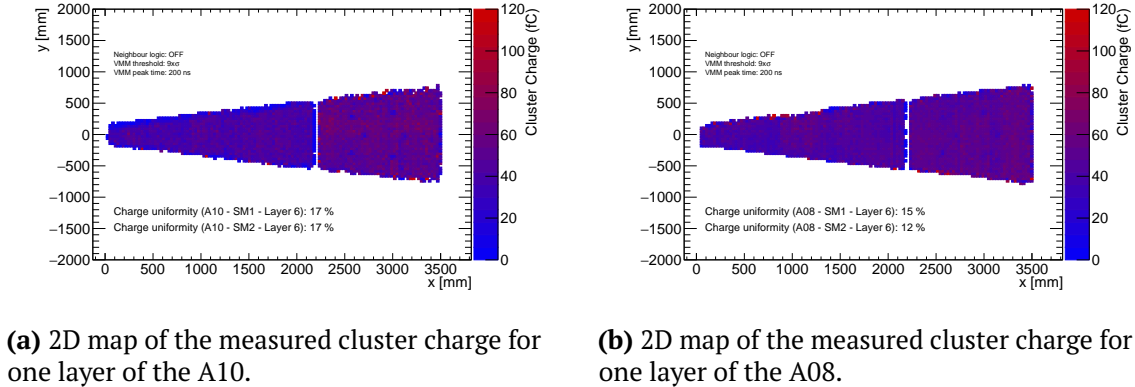


Figure 3.64

As shown in Figure 3.64, the charge uniformity of each individual module layer is in the order of 15%, well below ATLAS requirements ($\sim 50\%$). However, the Figure 3.64a and Figure 3.64b show a difference in the charge of two different double-wedges and especially between layers of type 1 and type 2 chambers (in figure the small sector map is shown), as also shown in Figure 3.65 with the cluster charge as a function of the MMFE8 number. The difference of the mean cluster charge between SM1 modules and SM2 modules has been studied taking runs inverting the gas flow direction from the nominal one (from SM2 to SM1 chambers) to the “reverse” one (from SM1 to SM2 chambers).

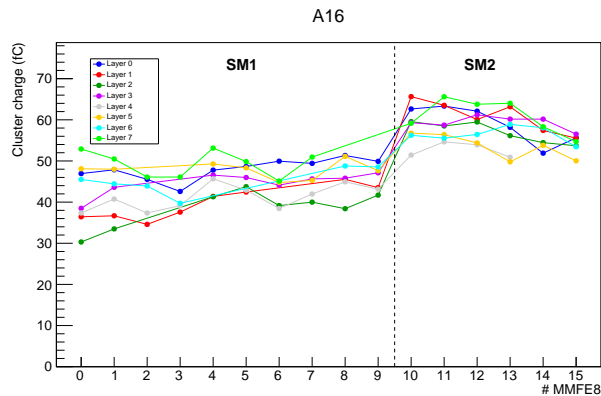


Figure 3.65: Mean cluster charge as a function of the MMFE8. 0–9 is the range of the SM1 chamber while 10–15 for the SM2 chamber. Only MMFE8 connected to a PCB which is completely at nominal voltage (570 V) are used in this plot.

Figure 3.66 is shown the cluster charge as a function of the MMFE8 number for the two runs with the same configurations except for the gas flow direction. The gas plays an important role in cluster charge but it is not the only explanation for the difference in charge between SM1 and SM2. In fact, if it was the only explanation, in the run with reverse gas flow, a higher SM1 charge compared to SM2, should be visible while the two

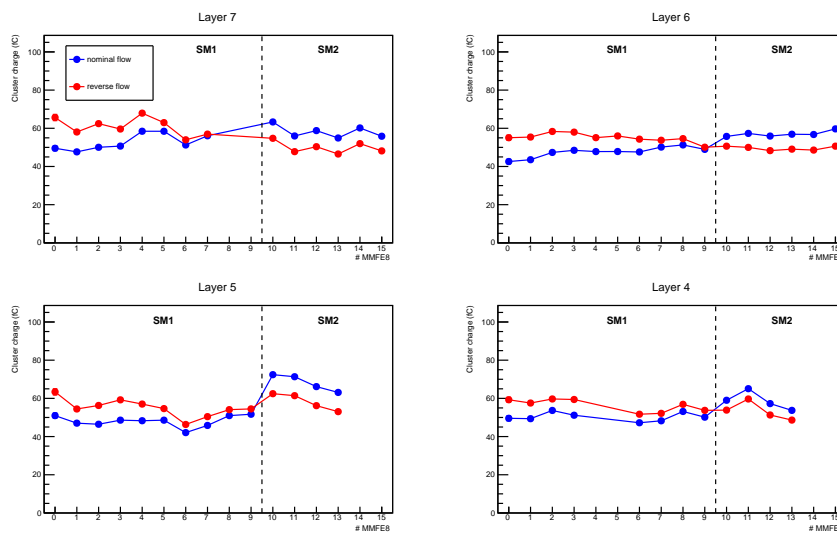


Figure 3.66: Mean cluster charge as a function of the MMFE8 for the nominal gas flow (from SM2 to SM1) and with the inverted one (from SM1 to SM2). 0–9 is the range of the SM1 chamber while 10–15 for the SM2 chamber. Only MMFE8 connected to a PCB which is completely at nominal voltage (570 V) are used in this plot.

are similar.

Pressure within the chambers can also play a key role in the mean cluster charge. The difference in gas pressure between SM1 and SM2 is not such as to explain the two different mean cluster charge. Therefore the effect is intrinsic in these chambers and not in the experimental setup. This effect has also been controlled in large type chambers and the difference between LM1 and LM2 chambers is not present.

3.7.4.3 Characterisation of the MicroMegas double-wedges response as a function of the track angle

Since the particle angles range expected from the MicroMegas chambers inside the ATLAS detector is between $\sim 7.5^\circ$ and $\sim 30.5^\circ$, the study of the standard distributions as a function of the angle is one of the particular characteristics that must be performed. In Figure 3.67 the strip charge is shown; it decreases with the angle since it is subjected to less ionisation charge at large angles than perpendicular tracks, as shown in Figure 3.10b. In Figure 3.68 the mean cluster width (the number of strips plus number of holes composing the cluster) is shown while in Figure 3.69 the mean cluster charge is shown. Although the average strip charge decreases as a function of the angle, as shown in Figure 3.67, the cluster width has the opposite trend as a function of the incidence angle of the particle (shown in Figure 3.68). These two effects balance each other but increasing the path made by the particle within the drift gap (inclined tracks) leads to increased ionisation which brings to higher values of the cluster charge for inclined tracks. There is a significant spread between layers and double-wedge that may indicate appreciable gain differences that are still being studied and it could be due to some differences in the noise level and therefore due to different threshold per channel. In Figure 3.70 the sigma of the narrowest Gaussian

of the double Gaussian fit made on the distributions of residuals as a function of the angle is shown. This parameter of the fit represents the centroid resolution and, as shown in Figure 3.16, it decreases as a function of the angle. The values obtained at the cosmic ray stand are larger than expected but the extrapolation error of the track is not negligible (as can be seen from the fact that the internal layers -aka 1 and 6- have better resolutions than the external ones -aka 0 and 7-) and in addition, the mis-alignment effects between layers but especially between IP and HO wedges have not been considered. In addition, since there is no selection of cosmic muon p_T , multiple scattering is another effect that worsens BB5's cosmic ray stand resolutions.

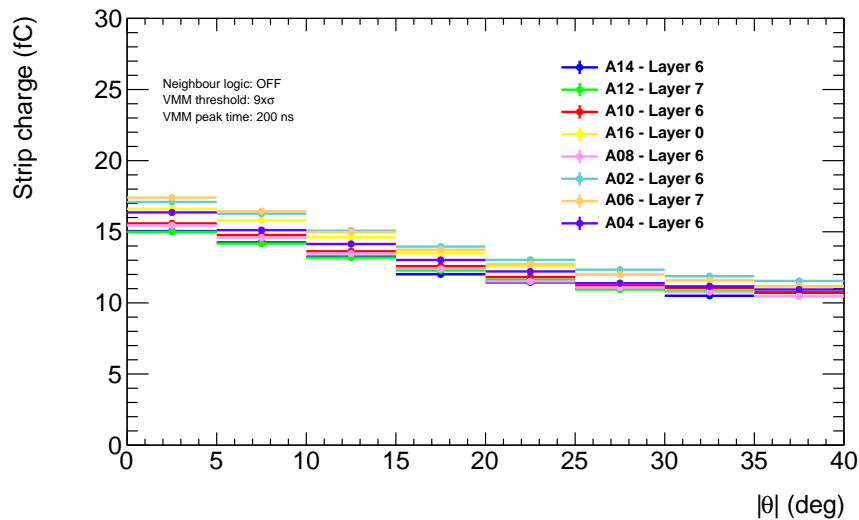


Figure 3.67: Measured mean strip charge of a layer completely connected to the nominal voltage of each small double-wedge as a function of the angle θ taken from the track reconstruction using the other layers of the double-wedge.

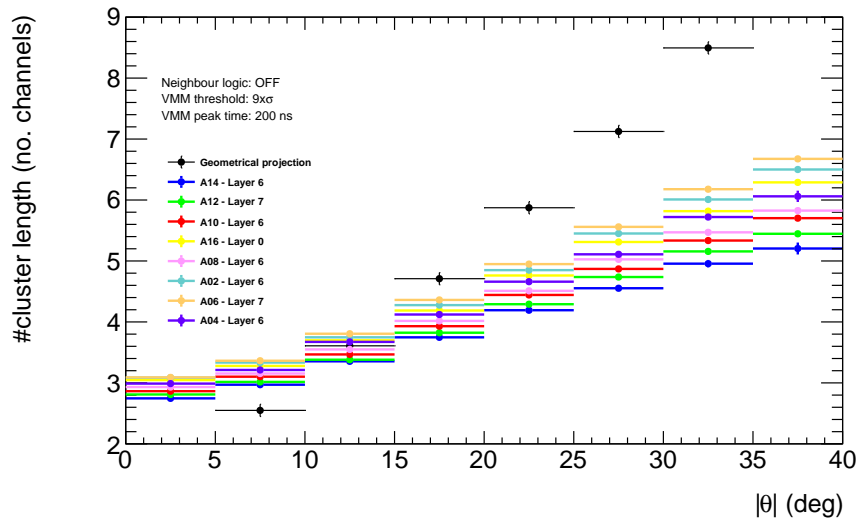


Figure 3.68: Measured mean cluster width (number of hits+holes per cluster) of a layer completely connected to the nominal voltage of each small double-wedge as a function of the angle θ taken from the track reconstruction using the other layers of the double-wedge. The geometrical projection is also shown and it is defined as the number of strips hit by the muon using a simple geometrical projection $(1 + \tan(\theta) * h_{drift\ gap}/pitch)$. The difference between the geometrical projection and the measured cluster width is completely due to the single ionisation electron efficiency in the drift gap.

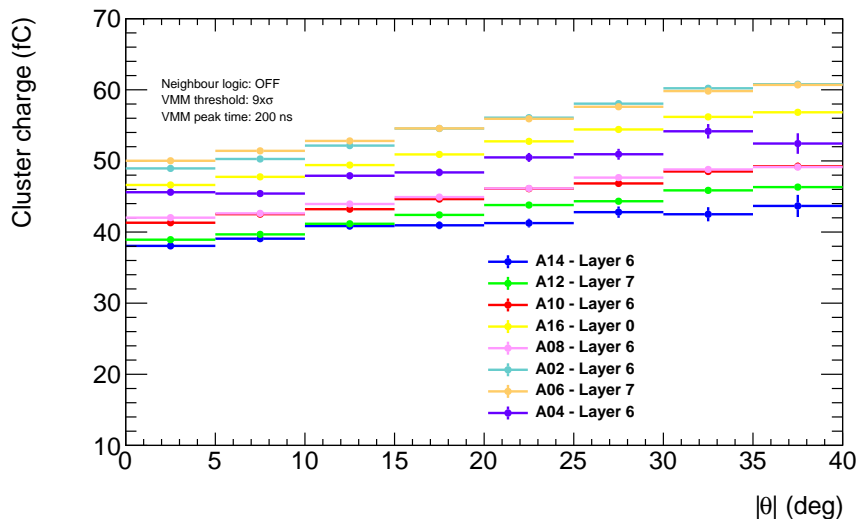


Figure 3.69: Measured mean cluster charge of a layer completely connected to the nominal voltage of each small double-wedge as a function of the angle θ taken from the track reconstruction using the other layers of the double-wedge.

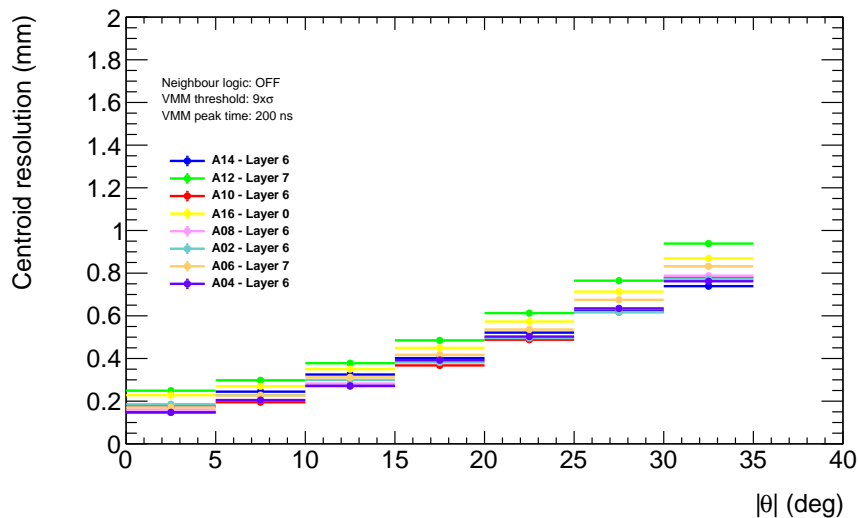


Figure 3.70: Measured centroid resolution (without subtracting the extrapolation error) of a layer completely connected to the nominal voltage of each small double-wedge as a function of the angle θ taken from the track reconstruction using the other layers of the double-wedge. The σ is obtained from the narrowest Gaussian from the double Gaussian fit of the residuals per each angle.

3.7.4.4 Distributions versus amplification voltage

Given the stability problems in the various high voltage sections that arose during the construction phases of the final chambers, it is important to know the performance of MicroMegas detectors as a function of the amplification voltage applied to the resistive strips. In order to do this, runs were taken by fixing the voltages of 7 layers of the double-wedge and varying only the 8th. In this way, it is possible to reconstruct the tracks having 7 layers working at full efficiency while the 8th is used for the study. The layer under analysis is chosen (in each double-wedge) selecting a layer that had no problems keeping the nominal voltage of 570 V on all its high voltage sections. In Figure 3.71, Figure 3.72, Figure 3.73 and Figure 3.74 are shown respectively the measured mean strip charge, mean cluster width, mean cluster charge and the layer efficiency as a function of the amplification voltage. The efficiencies are measured using the extrapolated track position: if a cluster is found within $\pm 5\sigma$ from the expected position on the precision coordinate (where σ is the RMS of the distribution obtained from the residuals between the layer under analysis and the track) the layer is considered efficient. Since the stereo residuals are wider than the eta layer, the 5σ window is different between the two types of layers and in particular, is 5 mm for the eta layers and 10 mm from the stereo layers.

From Figure 3.69 and especially in Figure 3.73 is visible that the mean cluster charge at 570 V is between $45 \div 60$ fC. From the cluster charge, the gain of the MicroMegas chambers can be calculated knowing that $50 e^-$ are produced in the drift gap. The result is a gain of $G = 5.5 \div 7.5 \cdot 10^3$ which is less than the design project value. This effect is expected since the ATLAS MicroMegas community has decided to decrease the working point from 600 V to 570 V in order to avoid high voltage instability problems (that can occur at higher

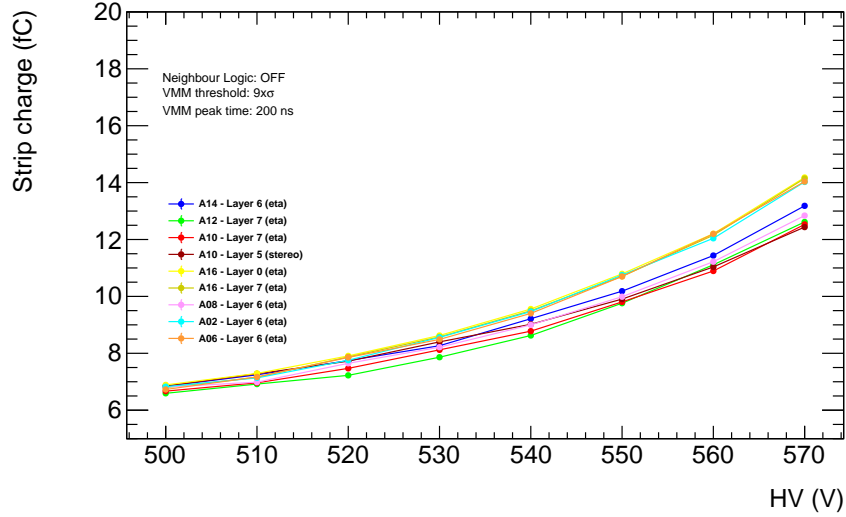


Figure 3.71: Measured mean strip charge as a function of the amplification voltage.

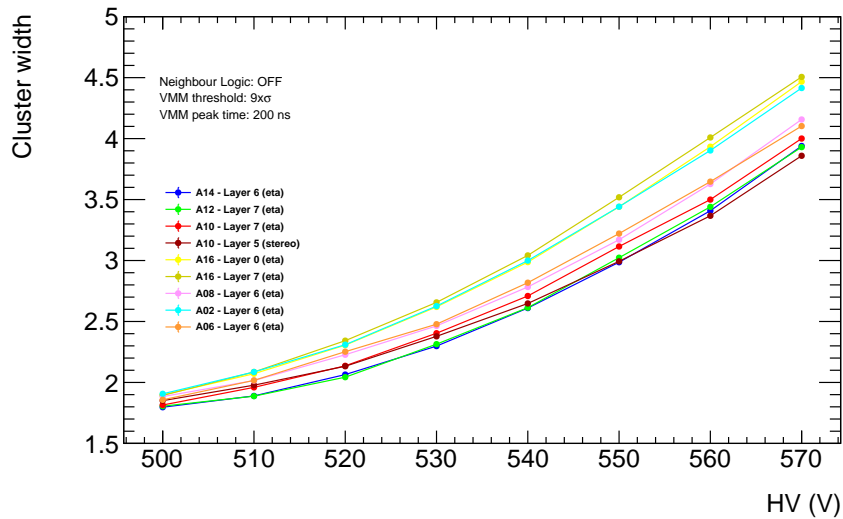


Figure 3.72: Measured mean cluster width as a function of the amplification voltage.

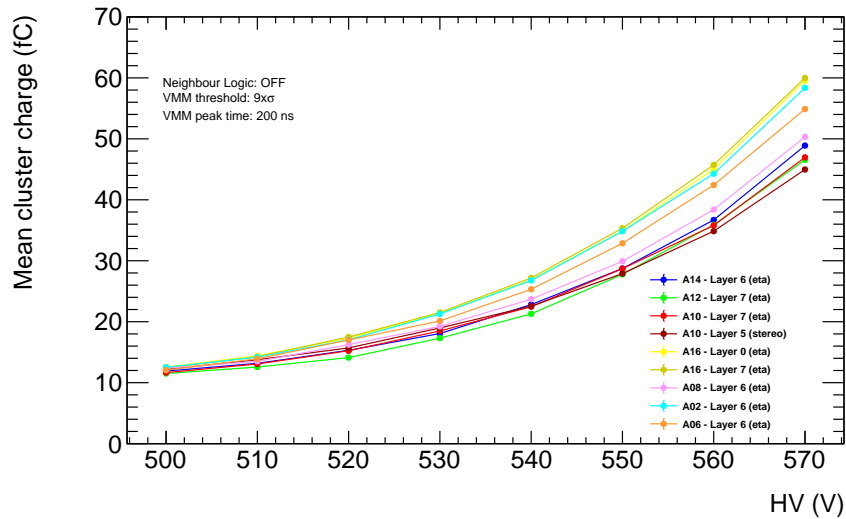


Figure 3.73: Measured mean cluster charge as a function of the amplification voltage.

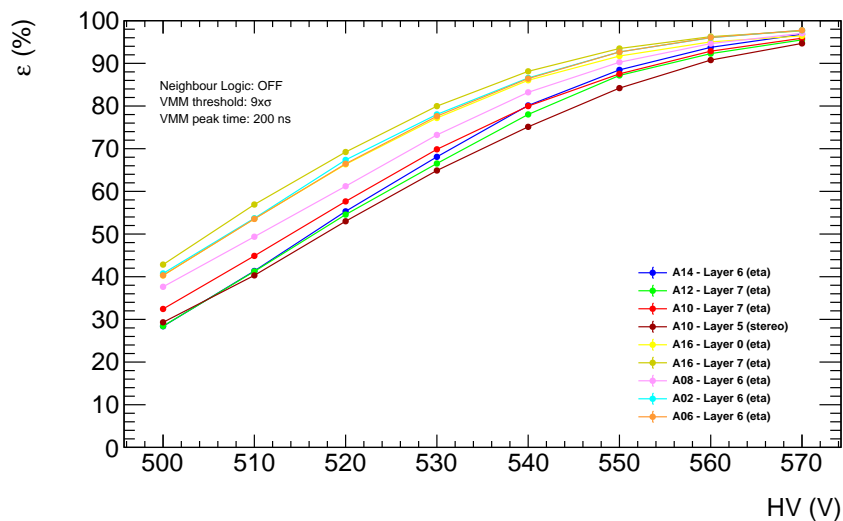


Figure 3.74: Measured layer efficiency as a function of the amplification voltage.

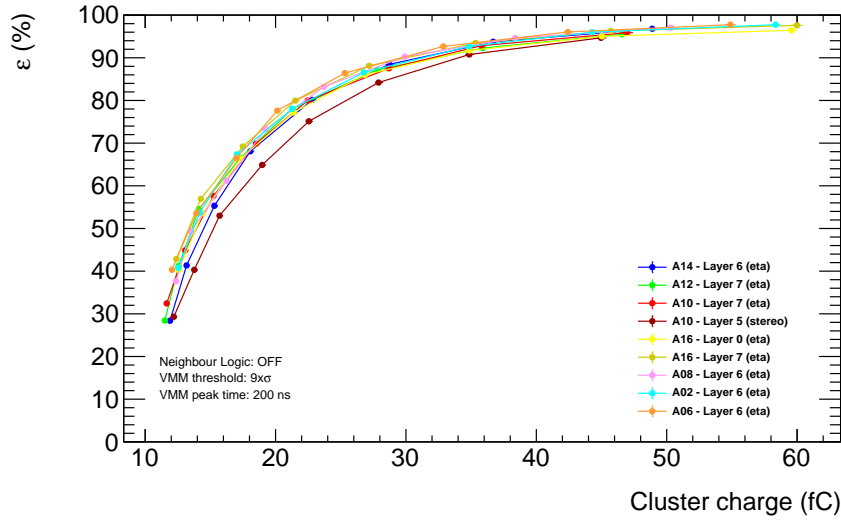


Figure 3.75: Measured layer efficiency as a function of the mean cluster charge.

voltages) and keeping the efficiency to higher values ($\varepsilon > 90\%$ even if it is not yet in the efficiency plateau).

Figure 3.75 is showing the correlation between efficiency and mean cluster charge. Each point represents the efficiency and cluster charge value at fixed voltage (e.g. first point is at 500 V and the others are at step of 10 V until 570 V) obtained from Figure 3.73 and Figure 3.74. As expected the points live on the same curve, meaning that the intrinsic behaviour of all layers is identical. What is changing is the mean cluster charge of the layer which is currently under investigation.

Using all the points coming from all the studied layers shown in Figure 3.74, the average efficiency per each voltage can be obtained and by fitting the sigmoid function the analytical efficiency dependence from the high voltage can be extracted:

$$\varepsilon(HV) = \frac{p_0}{1 + e^{-p_1 \cdot (HV - p_2)}} \quad (3.8)$$

where p_0 is value at the plateau, p_1 is the slope indicating how fast the curve grows and p_2 which is an horizontal offset.

The resulting curve, together with the curve fitted from the test beam data of SM2 are shown in Figure 3.76. The fitted $\varepsilon(HV)$ can be used, as explained in Section 3.7.3, to extract the expected efficiency from a section, knowing the applied high voltage.

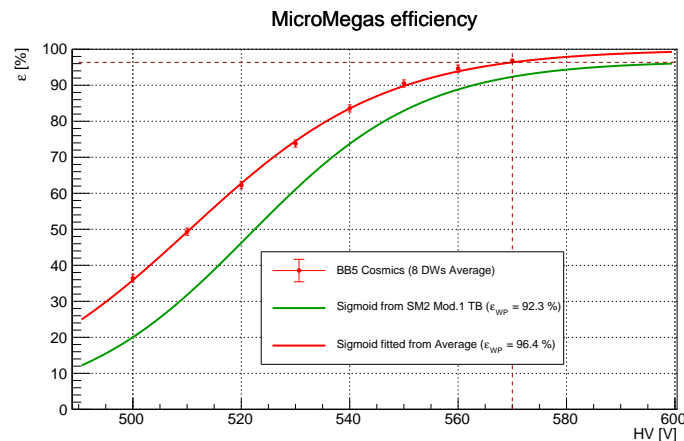


Figure 3.76: Average efficiency as a function of the amplification voltage. The fitted curve (using Equation 3.8) from the BB5 data and from the SM2 test beam is also shown in red and green respectively. The difference between the two curve is completely due to the higher noise level during the test beam with respect to the final VMM3a configuration used in the BB5 cosmic ray stand.

3.7.4.5 Resolutions and alignment studies

To be less dependent by the goodness of the track reconstruction and by external factors such as misalignment between layers and wedges, it is possible to estimate the resolution of a layer by simply subtracting the reconstructed positions between two layers, as was already done during the SM2 test beam and as shown in Figure 3.39. Using the Equation 3.7 the precision and the second coordinate can be reconstructed using two stereo layers. In Figure 3.77 the resolutions are shown as a function of the track angle obtained fitting the residuals between two layers with a Gaussian function and, in the hypothesis that the resolution of the two layers is identical, the following relationship is valid: $\sigma_{layer} = \sqrt{2} \cdot \sigma_{residuals}$. The difference, as a function of the track angle, of the cluster position between layer 0 and 1 (η), between layer 6 and 7 (η) and between the combination of the two stereo's layers of the IP wedge and HO wedge, both precision and second coordinate, is fitted using a Gaussian function and the $\sigma / \sqrt{2}$ as a function of the angle is shown in Figure 3.77. The measured resolution for the η layer is similar to what is found using the difference of the cluster with respect to the track reconstructed (Figure 3.70) except for the small angles.

In Table 3.3 the results using perpendicular track obtained taking the content of the first bin of the plots in Figure 3.77 are shown. The resolution is a bit worst than the one obtained from the test beam but, as said before, the multiple scattering can play a fundamental role in this measurement. The resolution on the precision coordinate obtained using the combination of the stereo layers is better since in this calculation two couple of layers are used to reconstruct the position. The resolution on the second coordinate is as expected and within the NSW requirements.

From the Gaussian fit, the alignment between the two layers can be measured. For perpendicular tracks, the mean of the Gaussian fit takes information about the alignment

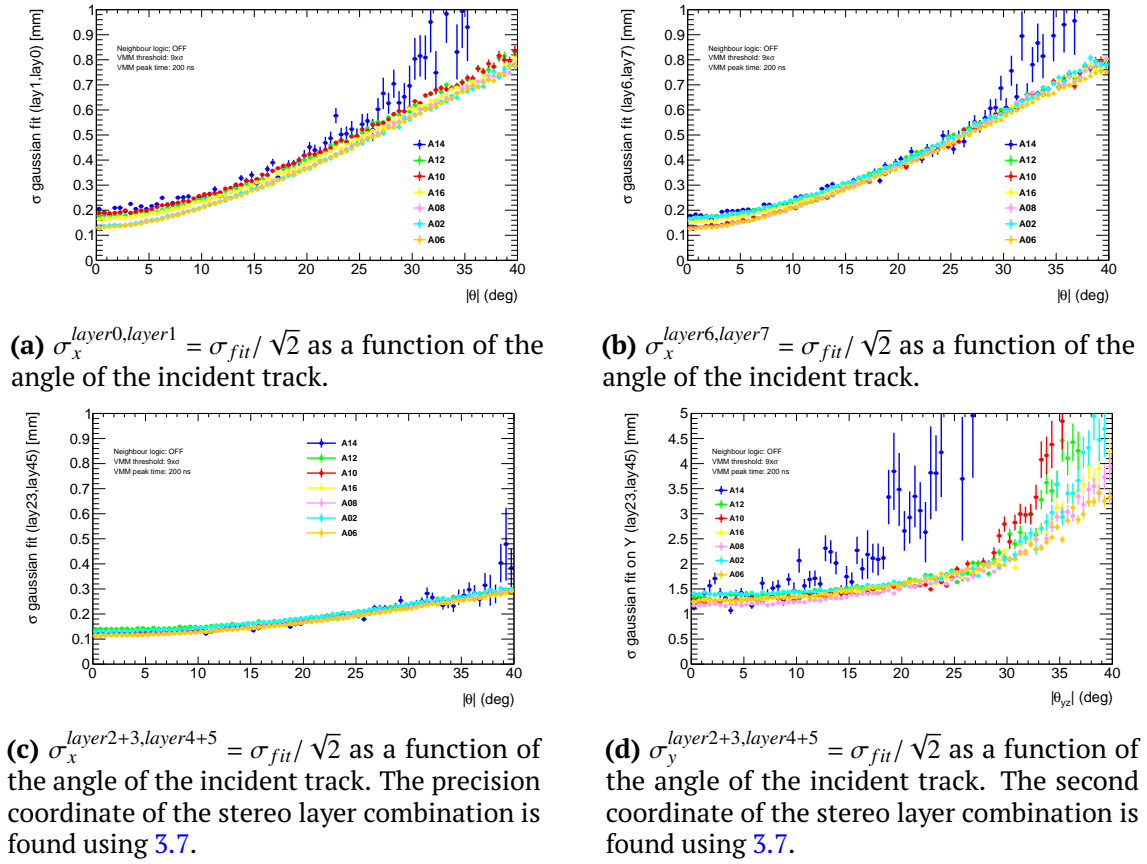


Figure 3.77

Double-wedge	$\sigma_x^{layer0,1}$ [mm]	$\sigma_x^{layer6,7}$ [mm]	$\sigma_x^{layer2+3,4+5}$ [mm]	$\sigma_y^{layer2+3,4+5}$ [mm]
A14	0.198 ± 0.004	0.179 ± 0.004	0.121 ± 0.002	1.26 ± 0.03
A12	0.178 ± 0.001	0.167 ± 0.001	0.140 ± 0.001	1.36 ± 0.01
A10	0.189 ± 0.002	0.134 ± 0.001	0.123 ± 0.001	1.26 ± 0.01
A16	0.166 ± 0.002	0.157 ± 0.001	0.116 ± 0.001	1.26 ± 0.01
A08	0.136 ± 0.001	0.130 ± 0.001	0.115 ± 0.001	1.18 ± 0.01
A02	0.137 ± 0.001	0.171 ± 0.001	0.131 ± 0.001	1.41 ± 0.01
A06	0.132 ± 0.001	0.128 ± 0.001	0.114 ± 0.001	1.27 ± 0.01

Table 3.3: Values of the resolution obtained using the charge centroid method and making the difference between two eta layers or two stereo combination layers. The values are the weighted average of the resolutions obtained with $\theta \leq 2^\circ$. Differences between double-wedge are due to the non perfect HV behaviour which can deteriorate a bit the resolutions.

Double-wedge	$\Delta\eta^{layer0,1}[\mu m]$	$\Delta\eta^{layer6,7}[\mu m]$	$\Delta\eta^{layer2+3,4+5}[\mu m]$	$\Delta\phi^{layer2+3,4+5}[\mu m]$
A14	32	56	43	-107
A12	14	19	43	4
A10	22	8	22	74
A16	15	16	33	-25
A08	18	20	34	46
A02	12	15	34	77
A06	16	10	32	67

Table 3.4: Values of the alignment between two eta layers of the same wedge and between the two stereo combinations of the two wedges, both in the precision and second coordinate.

between two layers. The mean of the fitted Gaussian and for small angle, is shown in Table 3.4. As shown in the table, the mis-alignment between the eta layers are within the requirements while the mis-alignment between the stereo combinations, in the second coordinate, sometimes is a bit out of the requirements but still acceptable.

3.7.4.6 Efficiency measurements

Once the 3D track is reconstructed, the 2D efficiency map can be measured extrapolating the track position at the z of the layer. Only the tracks reconstructed inside the active area of the layer are used. The way to measure the efficiency is described in Sec. 3.7.4.4. In Figure B.31 are shown the 2D efficiency maps of the eight layers of the A08 double-wedge while the others are shown in App B.

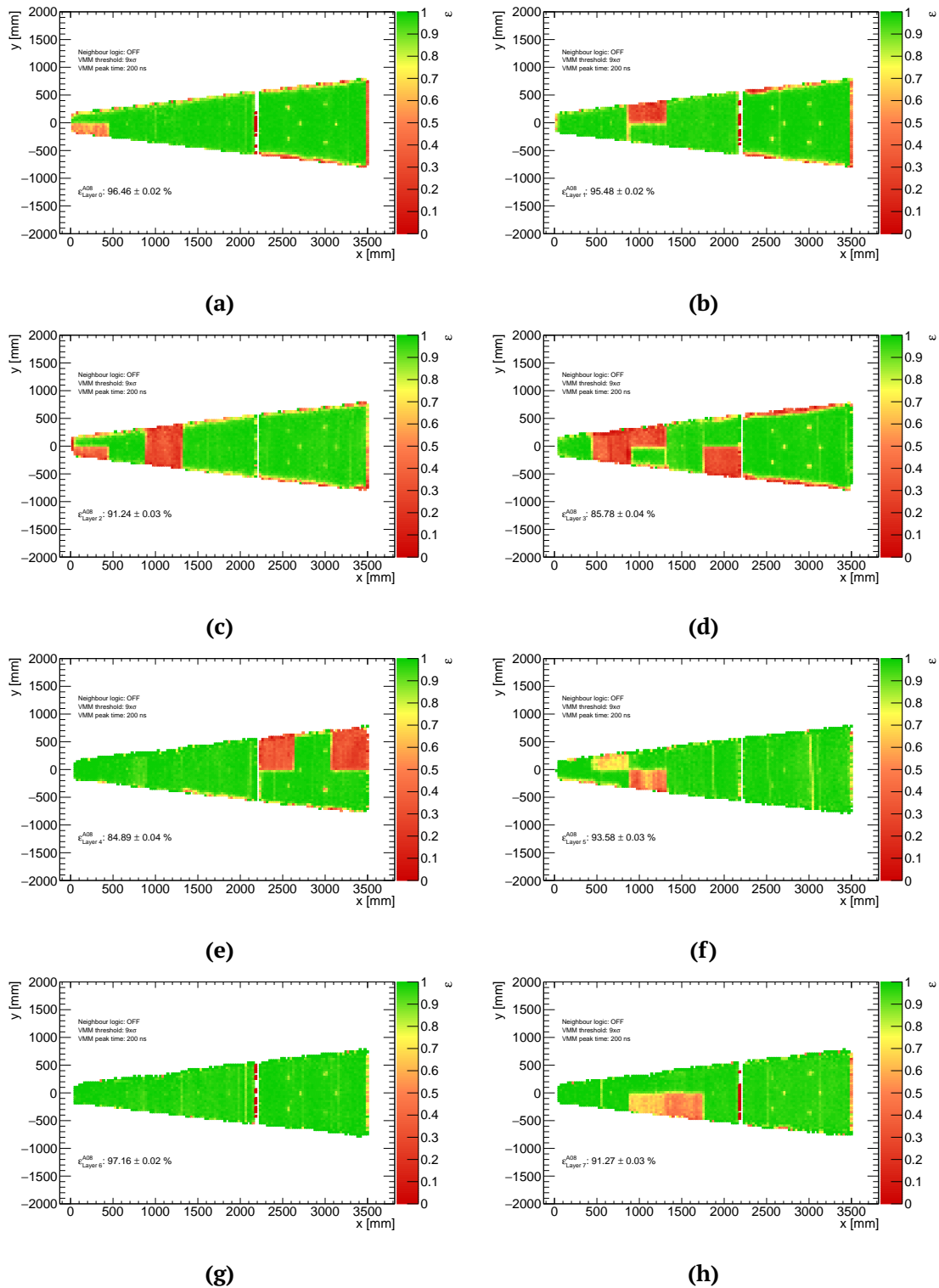


Figure 3.78: 2D efficiency map for the double-wedge A08. On different layers the passivated region on the perimeter of the layer is visible, especially in Figure B.31d where on the SM2 this region is bigger than in other layers. In all the layers are also visible 6 small regions with less efficiency due to the interconnection positions. The regions in red, with low efficiency are completely due to the high voltage map and there is a complete matching between the sections which are at low voltage and the low efficiency regions. The high voltage maps for the double-wedge A08 is shown in Figure A.17 together with the expected efficiency, shown in Figure A.18.

3.7.4.7 Expected segment reconstruction efficiency

As explained above, from the efficiency curve as a function of the high voltage, shown in Figure 3.74 it is possible to construct efficiency maps for all the layer of the double-wedge knowing the voltage applied to each high voltage section. Requiring a particular combination of the layers, it is possible to estimate the efficiency of segment reconstruction in the NSW using only MicroMegas chambers. Three working points have therefore been defined in this way:

- *Loose*: a segment is reconstructed if at least 4 layers (over 8) are efficient. Two eta and two stereo layers must be efficient to have the capability to reconstruct also the second coordinate. The 2D efficiency map of the NSW requiring this combination is shown in Figure 3.79a.
- *Medium*: a segment is reconstructed if at least 5 layers (over 8) are efficient. At least two eta and two stereo layers must be efficient to have the capability to reconstruct also the second coordinate. An additional request is made on stereo layers: one must have the strips tilted by $+1.5^\circ$ and another must have the opposite inclination -1.5° . This request is used since the MicroMegas trigger will ask for this combination. The 2D efficiency map of the NSW requiring this combination is shown in Figure 3.79b.
- *Tight*: a segment is reconstructed if at least 6 layers (over 8) are efficient. At least three eta and three stereo layers must be efficient. The 2D efficiency map of the NSW requiring this combination is shown in Figure 3.79c.

The NSW requirement is a segment reconstruction using at least 5 layers (over 16, considering also the sTGC chambers to reconstruct the tracks) with an overall reconstruction efficiency of 97% [80]. As shown in Figure 3.80 the green region is with at least 95% but using only the MicroMegas chambers. These figures confirm also that the double-wedge A04 is not conform and will not be installed on the NSW.

The same exercise can be done using real data measured at the cosmic ray stand of BB5. Using the average efficiency of each layer, many combinations can be made to calculate the expected segment reconstruction efficiency, as shown in Figure 3.80.

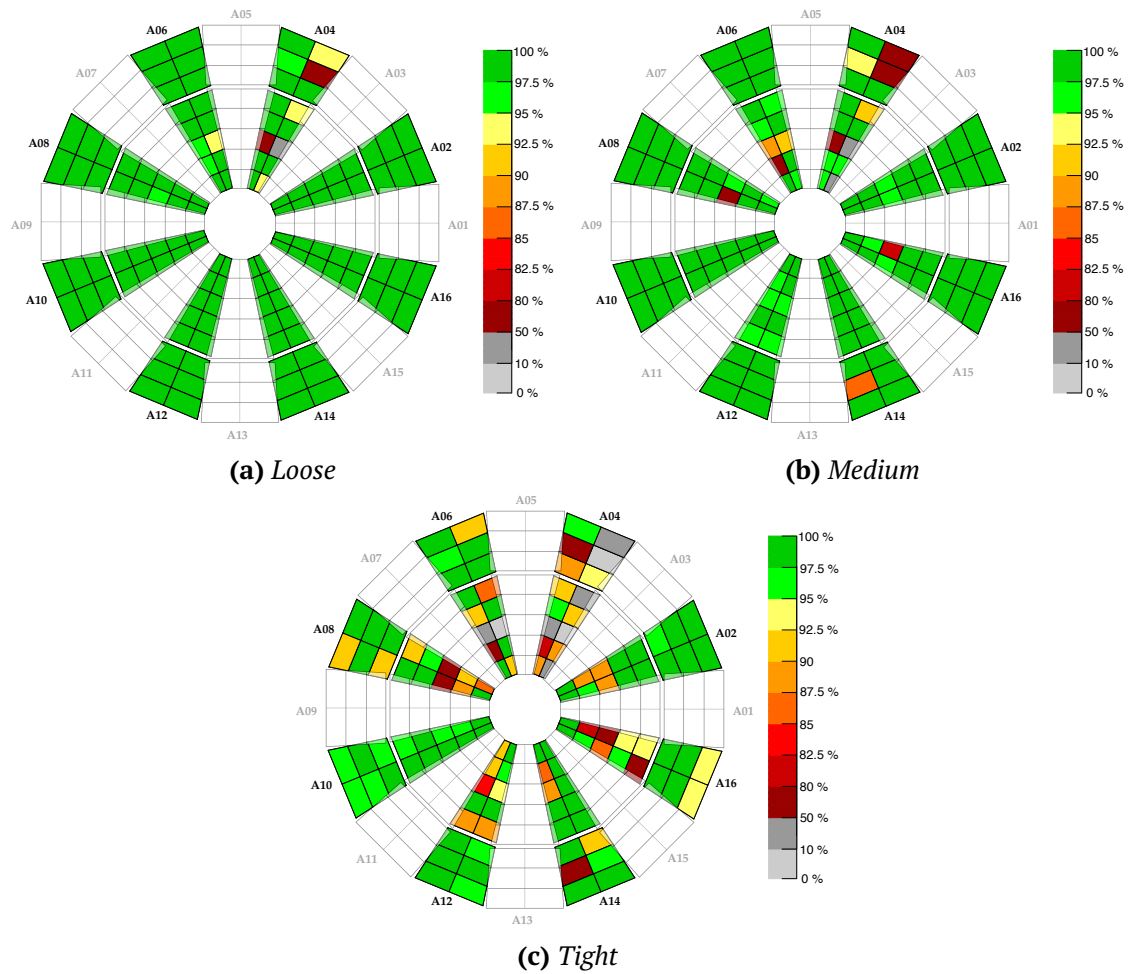


Figure 3.79: 2D map of the NSW with the expected segment reconstruction efficiency requiring *Loose* 3.79a, *Medium* 3.79b or *Tight* 3.79c reconstruction criteria.

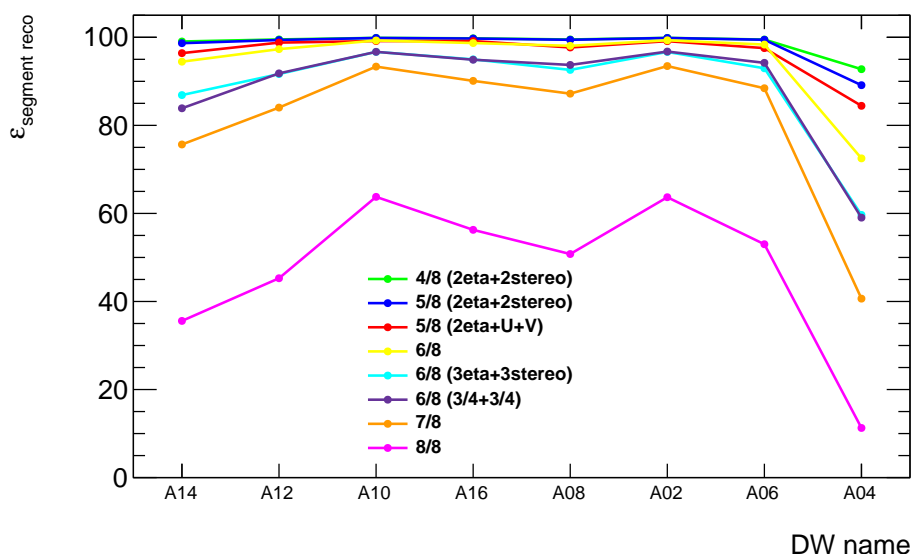


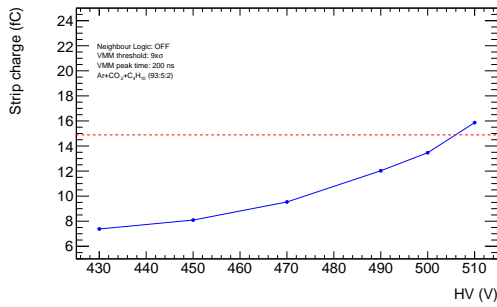
Figure 3.80: Expected segment reconstruction efficiency requiring different combination of layers. The legend describes the required combination and between brackets are expressed the further requests made on the type of layers that must be efficient (e.g. “2eta+2stereo” mean at least two eta layers and two stereo layers must be efficient, “3/4+3/4” means that at least the first wedge, and the second, must have at least 3 layers over 4 efficient).

3.7.4.8 Gas mixture studies: Ar + CO₂ + C₄H₁₀ (93 : 5 : 2)

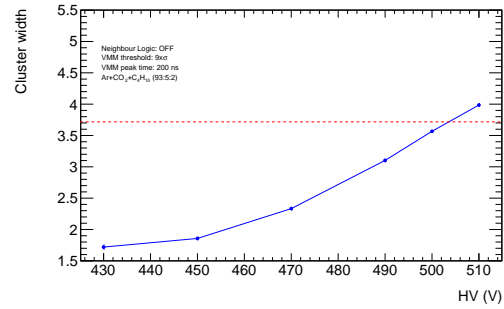
Since the stability in terms of high voltage is not good for the first large double-wedge (A13), as shown in Figure A.25 and Figure A.26, it was decided to test its performance with a different gas mixture that had already been previously used in the various construction sites. The idea of this test is to verify the correct operation, both in terms of high voltage and standard distributions, of the detectors using this new mixture. In Figure 3.81 are shown the standard distributions (mean strip charge, mean cluster width, mean cluster charge and efficiency) as a function of the high voltage. As shown in Figures 3.81a, 3.81b, and 3.81c the amplification voltage that needs to be compared to the 570 V of the nominal gas mixture (red lines) is around 505 V. In order to perform this test, the high voltage on all the other layers was fixed to 490 V while only the one on layer 7 was changed. All the double-wedge (except for 2 sections which were at 480 V) can stay at 490 V in a stable situation without having spikes.

In Figure 3.82 the efficiency as a function of the amplification voltage is shown for both the averaged curve, explained in Section 3.7.4.4, and the curve measured using the isobutane gas mixture. As shown, the working points of the two gas mixtures are ~ 65 V apart from each other.

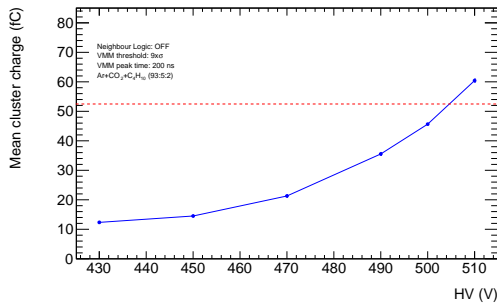
Given the very good high voltage stability shown first by the tests at the construction sites, at GIF++ and by the double-wedge A13, a further test is still in progress to verify the behaviour of this mixture subjected to large particle flow (GIF++) for a very long period and to study its stability over time. If this test will give positive results, the MicroMegs community might consider the change of the gas mixture inside the chambers.



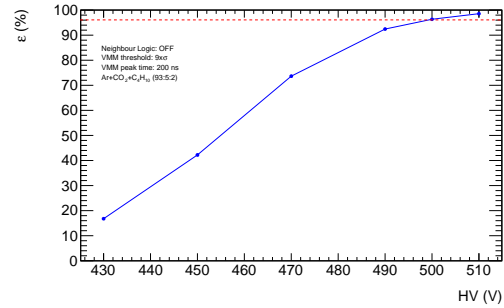
(a) Measured mean strip charge as a function of the amplification voltage using the $Ar + CO_2 + C_4H_{10}$ (93 : 5 : 2) gas mixture. The red line shows the value of the mean strip charge using the nominal gas mixture.



(b) Measured mean cluster width as a function of the amplification voltage using the $Ar + CO_2 + C_4H_{10}$ (93 : 5 : 2) gas mixture. The red line shows the value of the mean cluster width using the nominal gas mixture.



(c) Measured mean cluster charge as a function of the amplification voltage using the $Ar + CO_2 + C_4H_{10}$ (93 : 5 : 2) gas mixture. The red line shows the value of the mean cluster charge using the nominal gas mixture.



(d) Measured layer efficiency as a function of the amplification voltage using the $Ar + CO_2 + C_4H_{10}$ (93 : 5 : 2) gas mixture. The red line shows the value of the efficiency using the nominal gas mixture.

Figure 3.81

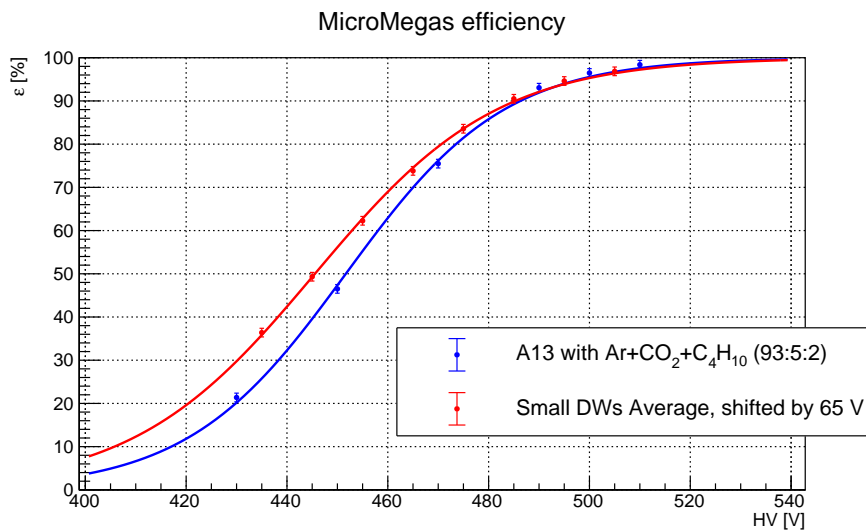


Figure 3.82: Efficiency curve for the nominal $Ar + CO_2$ (93 : 7) gas mixture (red, shifted by 65 V) and the alternative $Ar + CO_2 + C_4H_{10}$ (93 : 5 : 2) gas mixture (blue).

Object reconstruction

Each event collected by the ATLAS detector, described in Section 2.2, undergoes off-line event reconstruction. The output information from all sub-detectors is combined to form basic objects such as tracks and calorimetric clusters. These quantities are then used to reconstruct final physics objects. The reconstruction and identification of $t\bar{t}$ events require the usage of different types of physics objects (electrons, muons, jets) for which a good performance of all the detector components is necessary. Each physics object (muon, electron, ...) is defined by a set of quality criteria and in an appropriate kinematic range, depending on the specific characteristics of the detector.

4.1 Tracks and vertices reconstruction

Track reconstruction: the ATLAS track reconstruction [94] uses information collected by the inner tracker.

The first step is the clusters reconstruction from the deposits in the Pixel detector and in the SCT while the TRT is used to obtain the raw timing information. A combination of at least three points (clusters reconstructed in a 3D location) from the Pixel and SCT layers is used to create track seeds which provide a first estimate of the particle trajectory. A global χ^2 and a combinatorial Kalman filter [95] is then used to extend the seeds to the remaining Pixel and SCT clusters. Several requirements are applied to identify and remove fake tracks:

- $p_T > 400 \text{ MeV}$ and $|\eta| < 2.5$;
- minimum 7 Pixels and SCT cluster (12 are expected per track);
- maximum of either one shared pixel cluster or two shared SCT clusters on the same layer;
- not more than two holes¹ in the combined Pixel and SCT cluster;
- no more than one hole in the Pixel cluster;
- $|d_0^{BL}| < 2.0 \text{ mm}$;
- $|z_0^{BL} \cdot \sin\theta| < 3.0 \text{ mm}$;

where $|d_0^{BL}|$ is the transverse impact parameter calculated with respect to the measured beam line position and $|z_0^{BL}|$ is the longitudinal difference along the beam line between the

¹A hole is defined as a hit expected to be associated with a track but not present.

point where d_0^{BL} is measured and the primary vertex², and θ is the polar angle of the track.

The track reconstruction algorithm described below works well for all hadronic particles, but its performances for the electrons are not good due to the bremsstrahlung radiation. A *Gaussian Sum Filter* (GSF) model is used for the electrons. This model consists of refitting the tracks loosely matched to an ECAL seed cluster to better estimate the track parameters. The GSF method assumes that the trajectory of the electron can be approximated by a weighted sum of n Gaussian functions, each one representing the quantised components of the radiative loss of electrons as they traverse the pixel and SCT trackers.

Vertices reconstruction: the procedure of primary vertex reconstruction is divided into two stages which are the vertex finding and the vertex fitting [96]. The former stage generally denotes the pattern recognition process: the association of reconstructed tracks to vertex candidates. The vertex fitting stage includes the reconstruction of the actual vertex position.

The tracks entering the first stage must fulfil more stringent selection with respect to the track reconstruction step, in order to reduce the pile-up tracks. Only tracks with $p_T > 400 \text{ MeV}$, with at least four (nine) hits in the SCT (SCT or pixel) detector, and no pixel holes, enter the vertex reconstruction algorithms. A dedicated vertex finder is employed to find primary and secondary vertices using an iterative method. Only vertices with at least two associated tracks are retained and among all the vertices reconstructed in a bunch crossing, the primary vertex is defined as the one with the highest scalar sum of squares transverse momenta of the associated tracks ($\sum p_T^2$).

4.2 Electrons

The signature of the electrons consists of a track in the ID matched with a narrow shower in the ECAL. An excellent electron recognition is crucial to reject the large backgrounds typically originating from jets leading to mis-identified (so-called “fake”) electrons.

4.2.1 Reconstruction

The electrons in ATLAS are reconstructed [97] within the region $|\eta| < 2.47$, where the coverage of the ID ends. The region $1.37 < |\eta| < 1.52$, as discussed in Section 2.2.3.1, corresponds to the “crack region” and the material simulation in this part of the detector is very difficult, due to the presence of infrastructures for cooling, support and services, and it is excluded from the electron reconstruction region.

The electron reconstruction is divided into different steps described below.

Cluster reconstruction: the *topo-cluster reconstruction algorithm* begins by forming proto-clusters in the ECAL and HCAL using a set of noise thresholds in which the cell initiating the cluster is required to have significance $\zeta_{cell} = E_{cell} / E_{cell}^{exp. noise} > 4$ where E_{cell} is the energy of the single cell and $E_{cell}^{exp. noise}$ the energy due to the expected noise. The

²The tracks and the seed are used to estimate the best vertex position with an iterative fit rejecting the non-compatible tracks.

proto-clusters then collect neighbouring cells with significance $|\zeta_{cell}| > 2^3$. If two proto-clusters contain the same cell with $|\zeta_{cell}| > 2$ they are merged. After all nearby cells have been collected, a final set of neighbouring cells with $|\zeta_{cell}| \geq 0$ are added to the cluster. Proto-clusters with two or more local maxima are split into separate clusters; a cell is considered a local maximum when it has $E > 0.5 \text{ GeV}$, at least four neighbours, and when none of the neighbours has a larger signal. Topo-clusters are accepted only if they have $E_T > 400 \text{ MeV}$ to suppress clusters from pile-up or from $\pi^0 \rightarrow \gamma\gamma$ decays.

Cluster-track association: the electron is defined by the existence of one or more reconstructed tracks (see Section 4.1) matched to a seed cluster. The match must be within $|\eta| < 0.05$ and $-0.20 < q \cdot (\phi_{track} - \phi_{cluster}) < 0.05$ when using the track energy to extrapolate from the last inner detector hit, or $|\eta| < 0.05$ and $-0.10 < q \cdot (\phi_{track} - \phi_{cluster}) < 0.05$ when using the cluster energy to extrapolate from the track perigee; q refers to the reconstructed charge of the track.

Electron candidate reconstruction: to become an electron super-cluster, a topo-cluster needs to pass the requirement of having at least $E_T > 1 \text{ GeV}$ and must be matched to a track with at least four hits in the silicon tracking detectors. For a photon, different requirements are chosen; a topo-cluster must have $E_T > 1.5 \text{ GeV}$ to qualify as a super-cluster seed, without a match with a track. Electrons are distinguished by converted photons if there is the presence of two close tracks originated from a vertex displaced from the interaction point and by verifying the location of the first hit along the path of the single track. Topo-clusters near the seed candidates is identified as satellite cluster candidates, which may emerge from bremsstrahlung radiation or topo-cluster splitting. For both electrons and photons, a cluster is considered a satellite if it falls within a window of $\Delta\eta \times \Delta\phi = 0.075 \times 0.125$ around the seed cluster barycentre, as these cases tend to represent secondary ECAL showers originating from the same initial electron or photon. For electrons, a cluster is also considered a satellite if it is within a window of $\Delta\eta \times \Delta\phi = 0.125 \times 0.300$ around the seed cluster barycentre and its “best-matched” track is also the best-matched track for the seed cluster.

An additional requirement on the electrons, used by many analysis, is the Track-To-Vertex-Association (TTVA) which requires the track to be compatible with the primary interaction vertex of the hard collision, to reduce the background from conversions and secondary particles. TTVA on the electrons requires for:

- $|d_0/\sigma_{d_0}| < 5$;
- $|\Delta z_0 \cdot \sin\theta| < 0.5 \text{ mm}$;

where d_0 is the transverse impact parameter, σ_{d_0} the associated uncertainty, z_0 is the longitudinal impact parameter and Δz_0 , is the distance between the track and the primary vertex and θ is the polar angle of the track.

³the presence of negative-energy cells induced by the calorimeter noise, the algorithm uses $|\zeta_{cell}|$ instead of ζ_{cell} to avoid biasing the cluster energy upwards, which would happen if only positive-energy cells were used.

Tightness level	Signal (Z, W, J/ ψ)	Non-Iso Bkg.	Conversions	Hadrons	Unclassified Bkg.
Loose	93.027 \pm 0.011%	26.17 \pm 0.33%	2.502 \pm 0.025%	0.4327 \pm 0.0035%	1.368 \pm 0.018%
Medium	87.411 \pm 0.011%	19.56 \pm 0.28%	0.649 \pm 0.013%	0.2190 \pm 0.0025%	0.756 \pm 0.014%
Tight	78.587 \pm 0.010%	14.20 \pm 0.23%	0.406 \pm 0.010%	0.0950 \pm 0.0016%	0.451 \pm 0.010%

Table 4.1: Summary table for signal and background identification efficiency for the three ID working points [98].

4.2.2 Identification

The separation between real electrons and fake ones is reached by applying an identification algorithm that employs a likelihood-based method (LH). It is a multivariate analysis (MVA) technique that simultaneously evaluates several properties of the electron candidates and combines them in a discriminant, used to separate signal and background, e.g. fake tracks due to converted photons, electrons produced in the decay of heavy-flavours hadrons, etc. The properties included in the likelihood are related to track quality, ECAL shower shape, track-cluster matching related quantities and information deriving from the TRT. Three different working points (Tight, Medium, and Loose) corresponding to different levels of signal acceptance and background rejection are defined, depending on the information passed to the discriminant, as shown in Table 4.1.

4.2.3 Isolation

In order to further reject background electrons originating from hadronic decays, isolation requirements are applied to the leptons. The isolation uses the amount of momentum/energy surrounding the particle of interest to determine whether the particle is prompt or not. This surrounding momentum/energy can be either from charged or neutral particles ⁴.

For these reasons, an isolation requirement on the electrons is applied to improve the separation from either fake ones. This is based on the definition of three variables:

- E_T^{cone20} which is the sum of the E_T of ECAL clusters within a cone of $\Delta R = 0.02$ around the electron candidate;
- $p_T^{cone20(30)}$ which is the sum of the p_T of all tracks failing in a cone of $\Delta R = 0.2(0.3)$ around the electron candidate and excluding tracks associated to the electron or converted photons;
- $p_T^{varcone20(30)}$ which is the sum of the p_T of all tracks $\Delta R = \min(0.2(0.3), 10/E_T[GeV])$ around the electron track candidate and excluding the electron associated tracks.

The implementation of isolation criteria is specific to the physics analysis needs, therefore, several operating points are developed; their typical isolation efficiencies are mea-

⁴For charged particles, p_T is generally used while for neutral particles more often E_T is used. They can be easily related to one another by the expression (in natural units): $E^2 = m^2 + p^2$ and for low mass particles with relatively high momentum, E_T and p_T are very similar. Throughout this thesis p_T will be used when it concerns track-based isolation and only when isolation based on calorimeter cells is discussed, E_T will appear.

sured in data and determined from simulation, ranging from approximately 90% for the tightest operating points to nearly 99% for the loosest, as reported in Table 4.2.

Working point		Calo isolation		Track isolation
<i>FCLoose</i>		$E_T^{cone20}/p_T < 0.2$		$p_T^{varcone20}/p_T < 0.15$
<i>FCTight</i>		$E_T^{cone20}/p_T < 0.06$		$p_T^{varcone20}/p_T < 0.06$
<i>Gradient</i>		$\varepsilon = 0.1143 \cdot p_T[GeV] + 92.14$ using E_T^{cone20}/p_T		$\varepsilon = 0.1143 \cdot p_T[GeV] + 92.14$ using $p_T^{varcone20}/p_T$
<i>HighPtCaloOnly</i>		$E_T^{cone20} < \max(0.015 \cdot p_T, 3.5 GeV)$		-
<i>TightTrackOnly</i>		-		$p_T^{varcone30}/p_T < 0.06$
<i>TightTrackOnly_FixedRad</i>		-		$p_T^{varcone30}/p_T < 0.06$ below 50 GeV $p_T^{varcone20}/p_T < 0.06$

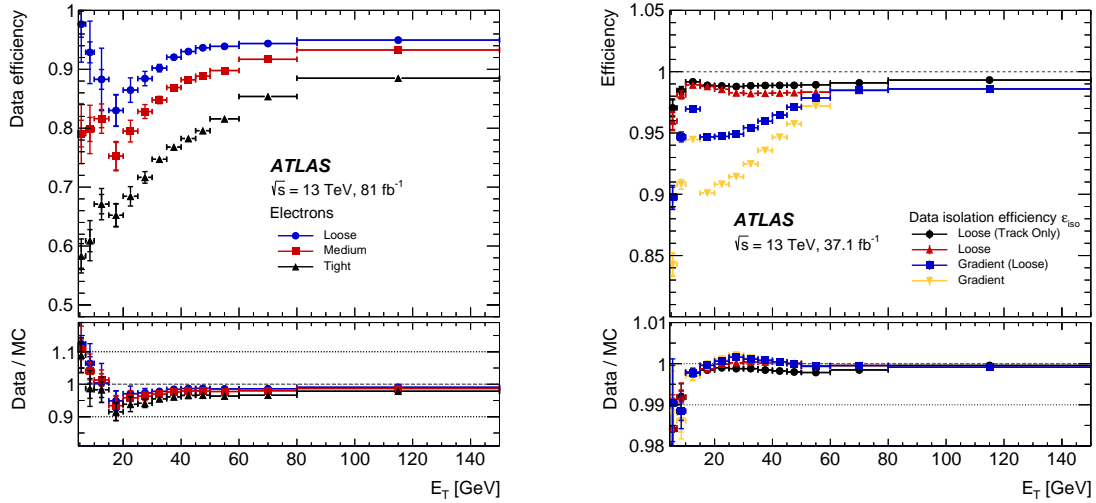
Table 4.2: Definition of the different electron isolation working points. In the *Gradient* working point, the cut on the isolation variables is setted in order to reach predefined level of efficiency.

4.2.4 Efficiency and scale factors

Corrections are applied to Monte Carlo simulations in the form of efficiency scale factors (SF), to match the reconstruction, identification and isolation efficiency in data. These corrections are obtained by comparing Monte Carlo predictions to large samples of $J/\psi \rightarrow ee$ and $Z \rightarrow ee$ data events using the tag-and-probe method. The scale factors for the electrons are defined in this way:

$$SF_e = SF_{trigger} \cdot SF_{reconstruction} \cdot SF_{identification} \cdot SF_{isolation} \quad (4.1)$$

In Figure 4.1 the electron reconstruction and isolation efficiency as a function of the E_T are shown.



(a) The electron identification efficiency in $Z \rightarrow ee$ events in data as a function η for the Loose, Medium and Tight operating points. The efficiencies are obtained by applying data-to-simulation efficiency ratios measured in $J/\psi \rightarrow ee$ and $Z \rightarrow ee$ events to $Z \rightarrow ee$ simulation [97].

(b) Isolation efficiencies for data (in the upper panels) and the ratio to simulation (lower panels) for some working points as a function of candidate electron η in $Z \rightarrow ee$ events. Gradient (Loose) is not used in Full Run 2 analyses [97].

Figure 4.1

4.3 Muons

The reconstruction and identification of the muons are performed independently in the ID and MS [99]. Small deposits of energy in the calorimetric systems can be used to help in the reconstruction of muons. The information from individual sub-detectors is then combined to form the muon tracks that are used in physics analyses.

4.3.1 Reconstruction

The muon spectrometer allows the reconstruction of muons with a p_T above 3 GeV. Muons with momenta lower than that are difficult to reconstruct since they do not reach the spectrometer, as they lose too much energy in the calorimeter and/or do not leave a significant signal over the noise in the muon spectrometer.

The muon reconstruction in the MS starts by searching for hit patterns in each muon chamber to form segments. The Hough transform is used to perform the search of hits of the MDT chambers of the MS which are aligned on a trajectory in the bending plane of the detectors. The RPC or TGC hits measure the coordinate orthogonal to the bending plane. In the CSC chambers, segments are build searching in the η and ϕ planes. After the separated search in each component of the MS, the muon track candidates are reconstructed by fitting together hits of segments of different layers. At least two matching segments are required to accept the track, except in the barrel end-cap transition region where a single high-quality segment with η and ϕ information can be used to build a track. The track

reconstruction in the inner tracker is performed as described in Section 4.1.

Five definitions of muons are derived combining the information of ID, MS and calorimeter in various ways, differing for the fake discrimination and the η coverage:

- **Combined (CB) muons:** this type of muons is characterised by a track reconstruction performed independently in the ID and MS. The particle is identified matching the two reconstructed tracks performing a combined track fit based on the ID and MS hits, taking into account the energy loss in the calorimeters. The larger part of the muons is reconstructed starting from the MS track and then extrapolated inward and matched to a track in the inner detector. These are defined only in the region $|\eta| < 2.5$.
- **Inside-out combined (IO) muons:** the algorithm to reconstruct IO muons is based on an ID reconstructed track and hits in the MS, without requiring a MS reconstructed track and, therefore, recovering some efficiency. The trajectory is reconstructed extrapolating the ID tracks to the MS in order to search for MS hits to be used in a combined track fit.
- **Segment-tagged (ST) muons:** are muons in which the ID track, extrapolated to the MS regions, is matched with at least one track segment in the MDT or CSC chambers. The ST muons are used when muons cross only one layer of MS chambers, either because of their low p_T or because they fall in regions with reduced MS acceptance.
- **Calorimeter-tagged (CT) muons:** are identified by extrapolating ID tracks through the calorimeters to search for energy deposits consistent with a minimum-ionising particle.
- **Extrapolated (ME) or Standalone muons:** are reconstructed in case a MS track cannot be matched to a ID track. The muon trajectory reconstruction is based only on the MS track and a loose requirement on compatibility with originating from the IP. Such muons are used to extend the acceptance outside that of the ID, benefiting from the full MS coverage up to $|\eta| < 2.7$.

As for the electrons, muons have an additional requirement used by many analyses: the Track-To-Vertex-Association (TTVA). The TTVA on the muons requires:

- $|d_0/\sigma_{d_0}| < 3$;
- $|\Delta z_0 \cdot \sin\theta| < 0.5 \text{ mm}$;

where d_0 is the transverse impact parameter, σ_{d_0} the associated uncertainty, z_0 is the longitudinal impact parameter and Δz_0 , is the distance between the track and the primary vertex and θ is the polar angle of the track.

4.3.2 Identification

Five sets of selection criteria are defined with decreasing reconstruction efficiency but increasing purity: *Loose*, *Medium*, *Tight*, *High- p_T* , and *Low- p_T* . The selection working points target the rejection of light hadrons, which in general result in lower quality muon tracks. Bottom and charm decays produce good quality muon tracks which can be distinguished from prompt muons via requirements on the association to the primary vertex and the isolation in the tracker and/or in the calorimeters.

The **Loose** identification criteria include all muon types and they are optimised for the Higgs searches. It accepts CB and ME muons requiring to have at least two precision stations, except in the $|\eta| < 0.1$ region where muons are considered but can have at most one muon precision station. The q/p significance⁵ must be less than 7 to ensure a loose compatibility between the ID and MS measurements. The acceptance is extended outside the ID coverage by including ME muons, required to have at least three precision stations, in the range $2.5 < |\eta| < 2.7$. The loose selection accepts also CT and ST muons restricted to $|\eta| < 0.1$. To increase the efficiency of the Loose criteria for low- p_T muons, IO muons with $p_T < 7 \text{ GeV}$ and only one precision station are accepted in the range $|\eta| < 1.3$, provided they are independently reconstructed also as ST muons. Among prompt muons passing the Loose WP in $t\bar{t}$ events, about 97% are CB or IO muons.

The **Medium** working point accepts only CB and IO muons within the ID acceptance $|\eta| < 2.5$, and ME muons in the range $2.5 < |\eta| < 2.7$. It is a sub-set of Loose muons excluding CT and ST muons and the exception for low- p_T muons in the barrel. Unlike the Loose WP, Medium muons provide a better purity in prompt muons leading to smaller systematics in the efficiency calibrations and it is used in a wide variety of analyses, especially the Standard Model precision measurements. Among prompt muons passing the Medium WP in $t\bar{t}$ events, more than 98% are CB muons.

The **Tight** selection accepts only CB and IO muons with at least two precision stations. It provides the highest purity, offering a substantially improved background rejection at the cost of a few percent efficiency loss. Requirements are placed on the χ^2 of the track, on the q/p significance and on ρ' ⁶ depending on the p_T and $|\eta|$ of the muon.

The **High- p_T** WP ensures an optimal momentum measurement for muons with p_T above 100 GeV . It is optimised for the bSM searches of W' and Z' .

The **Low- p_T** WP targets the lowest- p_T muons, which are less likely to be independently reconstructed as full tracks in the MS, so that identification based on MS segments is necessary. Two versions of the Low- p_T WP have been developed: using a cut-based selection, which reduces the kinematic dependencies of the background efficiencies, simplifying the implementation of data-driven estimates, and a multivariate (MVA) technique, maximis-

⁵ $q/p = \frac{|q/p_{ID} - q/p_{MS}|}{\sqrt{\sigma^2(q/p_{ID}) + \sigma^2(q/p_{MS})}}$ where q/p_{ID} and q/p_{MS} are the measurements in the ID and MS of the ratio between the charge q and the momentum p of the muon, expressed at the IP, while $\sigma^2(q/p_{ID})$ and $\sigma^2(q/p_{MS})$ are the corresponding uncertainties.

⁶ $\rho' = \frac{|p_T^{ID} - p_T^{MS}|}{p_T^{CB}}$ where p_T^{ID} and p_T^{MS} are respectively the muon p_T measured in the ID and in the MS, while p_T^{ID} is the value resulting from the combined track fit.

Working point	Calo isolation	Track isolation
<i>Loose</i>	$E_T^{cone20}/p_T < 0.3$	$p_T^{varcone30}/p_T < 0.15$
<i>Loose_FixedRad</i>	$E_T^{cone20}/p_T < 0.3$	$p_T^{varcone30}/p_T < 0.15$ below 50 GeV $p_T^{cone20}/p_T < 0.15$
<i>Tight</i>	$E_T^{cone20}/p_T < 0.15$	$p_T^{varcone30}/p_T < 0.04$
<i>Tight_FixedRad</i>	$E_T^{cone20}/p_T < 0.15$	$p_T^{varcone30}/p_T < 0.04$ below 50 GeV $p_T^{cone20}/p_T < 0.04$
<i>FixedCutHighPtTrackOnly</i>	-	$p_T^{cone20} < 1.25$ GeV
<i>TightTrackOnly</i>	-	$p_T^{varcone30}/p_T < 0.06$
<i>TightTrackOnly_FixedRad</i>	-	$p_T^{varcone30}/p_T < 0.06$ below 50 GeV $p_T^{varcone20}/p_T < 0.06$

Table 4.3: Definition of the different muon isolation working points.

ing the overall performance. Typical analyses that benefit from the use of the Low- p_T WP are measurements of Standard Model parameters in the quark-mixing sector and searches for SuperSymmetry with compressed mass spectra.

4.3.3 Isolation

As done for the electrons, an isolation requirement on the muons is applied to improve the separation from fake ones. This is based on the same variables defined previously for the electrons. Also for the muons, several working points are defined and are listed in Table 4.3.

4.3.4 Efficiency and scale factors

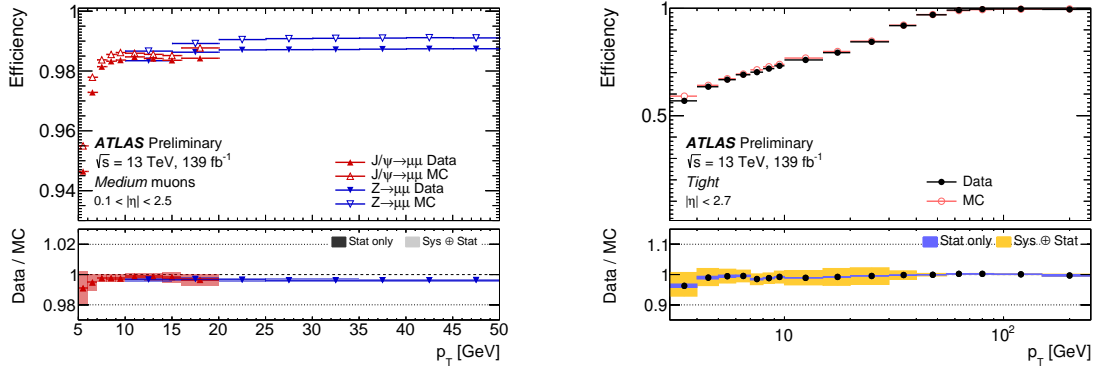
As for the electrons, corrections are applied to Monte Carlo simulations in form of efficiency scale factors (SF), to match the reconstruction, identification and isolation efficiency in data.

Two different methods are used to measure the reconstruction, identification, isolation, and vertex association efficiencies with high precision, depending on the $|\eta|$ region. In the region corresponding to the ID acceptance ($|\eta| < 2.5$), two independent detectors are available and the standard tag-and-probe method is used with the $J/\psi \rightarrow \mu\mu$ and $Z \rightarrow \mu\mu$ events. In the $2.5 < |\eta| < 2.7$ region, muons are reconstructed using only the MS detector. The SF is calculated from the double ratio: $SF_{high-\eta} = [\frac{N_{data}}{N_{MC}}]_{2.5 < |\eta| < 2.7} / [\frac{N_{data}}{N_{MC}}]_{2.2 < |\eta| < 2.5}$.

The scale factors for the muons are defined in this way:

$$SF_{\mu} = SF_{trigger} \cdot SF_{reconstruction} \cdot SF_{identification} \cdot SF_{isolation} \quad (4.2)$$

In Figure 4.2 the muon reconstruction and isolation efficiency as a function of the p_T are shown.



(a) Muon reconstruction and identification efficiencies for the Medium criteria measured in $J/\psi \rightarrow \mu\mu$ and $Z \rightarrow \mu\mu$ events as a function of p_T for muons with $0.1 < |\eta| < 2.5$. The error bars on the efficiencies indicate the statistical uncertainty. The panel at the bottom shows the ratio of the measured to predicted efficiencies, with statistical and systematic uncertainties [99].

(b) Muon isolation efficiency measured in $Z \rightarrow \mu\mu$ events for the Tight isolation criteria, as a function of p_T for muons with $p_T > 3$ GeV. The error bars on the efficiencies indicate the statistical uncertainty. The panel at the bottom shows the ratio of the measured to predicted efficiencies, with statistical and systematic uncertainties [99].

Figure 4.2

4.4 Jets

The jets are collimated showers of hadrons built to collect all the products of the hadronisation of coloured particles (quarks or gluons). Jets tend to preserve part of the momentum of the particles they originate from and are therefore a proxy to measuring quarks or gluons momenta.

4.4.1 Reconstruction

Jets can be reconstructed from a combination of tracks in the detector (*track-jets*), from the energy deposits in the calorimeter (*topological-clusters jets* or *topo-clusters jets*) [100, 101], or using an alternative approach exploiting the measurements from both the tracker and the calorimeter (*particle-flow jet*) [102]. The advantage of this new jet definition is the combination of two complementary measurements with a good high- p_T resolution thanks to the calorimeter and a good low- p_T thanks to the ID. In the following, only topo-cluster jets will be discussed as they represent the default jet definition used in the $t\bar{t}$ analyses.

Topo-clusters are reconstructed using the *anti-kt* algorithm [103]. The clustering proceeds by identifying the smallest of the distances expressed in Equation 4.3-4.4.

$$d_{ij} = \min \left(\frac{1}{k_{ii}^2}, \frac{1}{k_{ij}^2} \right) \frac{\Delta R_{ij}^2}{R^2} \quad (4.3)$$

$$d_{iB} = \frac{1}{k_{ii}^2} \quad (4.4)$$

where $\Delta R_{ij} = \sqrt{(y_i - y_j)^2 + (\phi_i - \phi_j)^2}$ and $k_{ii(j)}$, $y_{i(j)}$ and $\phi_{i(j)}$ are the transverse momentum,

the rapidity and the azimuthal angle respectively of the $i(j)$ cluster while R is a fixed parameter of the algorithm related to the radius of the jet (the standard definition is $R = 0.4$).

The algorithm starts with an iterative process constructing all the combinations of d_{ij} and d_{iB} . If $d_{ij} < d_{iB}$, the two clusters (i and j) are recombined into a unique jet with new $\eta - \phi - p_T$ while if it is $d_{ij} > d_{iB}$ the cluster i is defined as a jet and removed from the list of available topo-clusters. The reconstructed jets have in general a circular shape as shown in Figure 4.3.

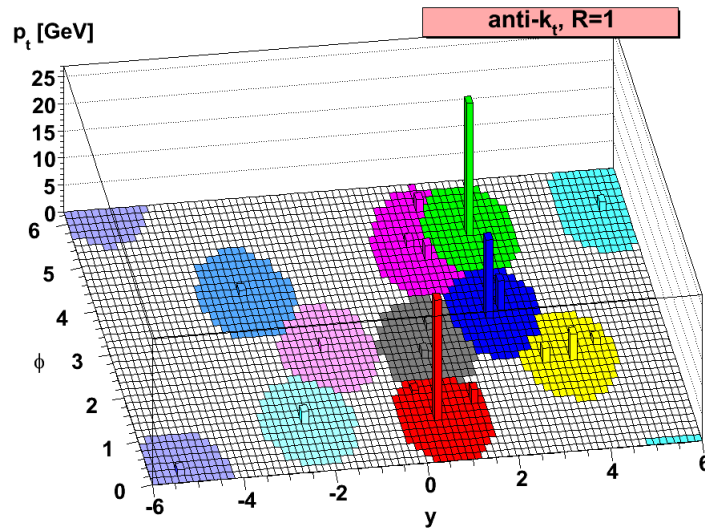


Figure 4.3: Event clustered with the anti-kt jet algorithm, illustrating the circular areas of the resulting hard jets [103].

4.4.2 Position and energy calibration

Different corrections are applied to the jets.

- **Origin correction:** the default jet direction is the centre of the detector but, since the reconstructed jet is expected to originate from the hard scatter, the direction is corrected assuming that the jet points to the primary vertex of the interaction.
- **Pile-up correction:** the pile-up generates additional particles that contaminate jets. This contribution inside a jet is estimated from the median p_T density of the reconstructed jets in the $\eta - \phi$ plane divided by the area of the jet [104].
- **Absolute JES calibration:** the jet energy scale (JES) calibration aims at restoring the energy scale of the reconstructed jets to the one of the truth jets. A factor is applied to the jet energy to correct for this effect [105, 106].
- **Absolute η inter-calibration:** the jet energy response can vary as a function of η , especially in the regions between different calorimeter technologies and granularities. An additional correction is derived from the ratio between the reconstructed

and truth jet η , parametrised as a function of the reconstructed jet η and truth jet energy E^{truth} .

- **Global sequential calibration:** the Global Sequential Calibration (GSC), consists of a track-based post-calibration correction that attempts to reduce the difference in response between quark and gluon jets. In fact, the hadrons contained in a quark-initiated jet carry a large fraction of the jet p_T , whereas a gluon-initiated jet typically includes much softer particles. The GSC includes a punch-through correction to correct high p_T jets whose energy is not fully contained within the calorimeter. The corrections applied to depend on the topology of energy deposits in the calorimeter, the tracking information and the MS information.
- **Residual in-situ calibration:** a final residual calibration is derived using in-situ measurements and is applied only to data. This final step aims to recover the residual differences between the jet energy response measured in simulation and data. Firstly, di-jet events are used to derive an η inter-calibration where the response of forward ($0.8 < |\eta| < 4.5$) jets is calibrated to the response of jets in the central region ($|\eta| < 0.8$). In a second step $Z + jets$ events, in which the Z boson decays into an electron or a muon pair, are used to calibrate the jets p_T using the well reconstructed recoil of the Z boson, up to 500 (950) GeV for electron (muon) pair. Finally, a multi-jet method is used to extend the p_T range of the calibration up to 2 TeV using a system of well calibrated lower p_T jets balanced against a single very high- p_T jet.

4.4.3 Jet energy resolution

Precise knowledge of the jet energy resolution (JER) is important for detailed measurements of Standard Model jet production, measurements and studies of the properties of the Standard Model particles that decay to jets, as well as searches for physics beyond the Standard Model involving jets.

The dependence of JER on the jet p_T can be parametrised with three independent contributions:

$$\frac{\sigma(p_T)}{p_T} = \frac{N}{p_T} \oplus \frac{S}{\sqrt{p_T}} \oplus C \quad (4.5)$$

where N is the noise term due to the electronics as well as that due to pile-up, S is the stochastic term due to statistical fluctuations in the amount of deposited energy, and C is the constant term that contains all the constant contributions to the energy resolution (energy depositions in passive material, the starting point of the hadron showers, and non-uniformities of the response across the calorimeter).

To measure the JER, for the majority of the jet p_T spectrum, the width of the distribution of the balance between jets and well measured photons or reconstructed Z bosons is used. In addition, the energy balance between di-jets (or tri-jets) events can be used to extend these measurements to higher $|\eta|$ and p_T spectrum [106].

Working Point	Average efficiency	Average fake rate
Loose	97%	8%
Medium	92%	2%
Tight	85%	0.6%

Table 4.4: JVT working point and their average efficiency for jet from hard scattering and for fake jet from pile-up.

4.4.4 Jet cleaning from pile-up

The topo-clusters reconstructed in the calorimeter can be contaminated by both *in-time* and *out-of-time* pile-up. The first refers to multiple parton interactions within the same bunch crossing, while the second originates from pile-up interactions from the previous and the following bunch crossing. The jet-vertex-tagger (JVT) is a likelihood discriminant used to reject these fake jets originated from pile-up fluctuations. Three working points, as shown in Table 4.4, are defined depending on the efficiency for hard scattering jets and the fake rate for pile-up jets.

4.5 *b*-tagging

The identification of the presence of a hadron containing a *b*-quark inside the jet is possible thanks to the long decay time (~ 1 ps) of these hadrons. This leads to the existence of a secondary vertex that is well separated from the primary one at which the *b*-hadron was created (a few hundred of μm) that can be exploited to identify the jet as coming from a *b*-quark. Besides, the high decay multiplicity of the *B*-hadrons and the properties of the *b*-quark fragmentation are used as input of the *b*-tagging algorithms.

Three different *b*-tagging algorithms are used in ATLAS [107]. The *IP2D*, *IP3D* are based on a log-likelihood ratio which uses as input the impact parameter significance of the tracks matched to the jet, which represent good discrimination between jets originated from different flavours. The *SV1* is based on the identification and reconstruction of the secondary vertex and its properties making a fit with all the tracks. The *JetFitter* reconstructs the decay chains $IP \rightarrow b \rightarrow c \rightarrow X$ inside the jet using Kalman filters.

The most discriminating variables of the *IPXD*, *SV1* and *JetFitter* algorithms are combined and used as input to a multivariate analysis using a boosted decision tree (BDT) [108] that combines the information in a discriminant called *MV2c10* to enhance the separation of different jet flavours. Four operating points are used in ATLAS and are reported in Table 4.5 with the efficiency and the rejection factors. Figure 4.4 shows the discriminant distribution for the *b*-jets, *c*-jets and light-jets.

$\varepsilon_{b\text{-tagging}}$ (%)	$c\text{-jet}$ RR	$\tau\text{-jet}$ RR	$l\text{-jet}$ RR
61.14	22	150	1204
70.84	8	39	313
77.53	4	16	113
85.23	2	6	28

Table 4.5: b -tagging efficiency and c , τ and light-jets rejection rate (RR) for the four ATLAS MV2c10 working points [107].

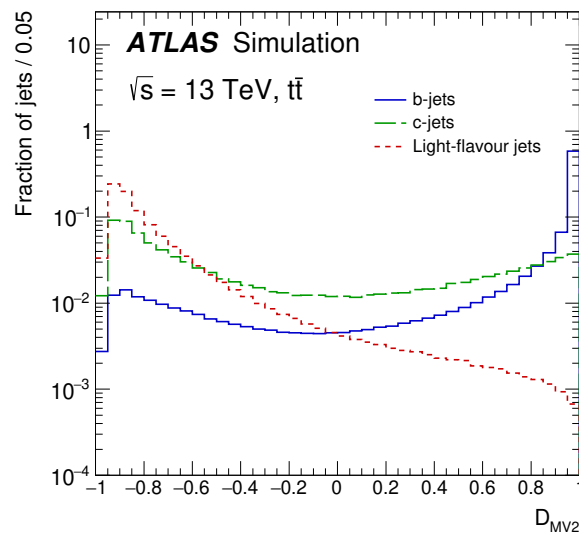


Figure 4.4: Distribution of the output discriminant of the MV2 b -tagging algorithm for b -jets, c -jets and light-flavour jets in the baseline $t\bar{t}$ simulated events [107].

Top antitop cross section measurements

5

5.1 Analysis motivations

The top-quark plays a special role in the Standard Model and in some theories beyond the Standard Model, as discussed in Section 1.3. The top-quark can provide important tests of the Standard Model and any observed deviation from predictions could indicate the presence of new physics. The large top-quark mass and the large $t\bar{t}$ pair production cross section in pp collisions allow for a rich environment to make important measurements that test perturbative QCD to higher order and can constrain:

- kinematics and properties (e.g spin correlations) of the top-quarks;
- matching and merging parameters of matrix element generators;
- modelling of parton shower and hadronisation.

In addition, some of the measured distributions can be used to improve our understanding of parton density functions (PDFs).

For these reasons, this analysis aims to measure both the total and fiducial $t\bar{t}$ cross section and to give measurements of the differential $t\bar{t}$ cross section as a function of several leptonic kinematic variables or as a function of couples of leptonic kinematic variables. In order to perform this measurements, the Full Run 2 ATLAS dataset ($\mathcal{L} = 139 \text{ fb}^{-1}$) is used. Since the top-quark decays almost always to a W boson and a b -quark, the decay of a top-quark pair produces six particles in the final state. The decay channel considered in this analysis is characterised by the leptonic decay of the two W bosons and it is common to refer to as di-leptonic decay mode.

5.2 Monte Carlo samples

Most of the Monte Carlo (MC) samples in this analysis are simulated using the full ATLAS detector simulation [109] (FullSim) based on GEANT4 [110], while a few samples, in particular samples used for evaluating systematic uncertainties, are simulated with a faster ATLAS detector simulation, AtlasFast-II (AFII) [111, 112] package, that uses parametrised shower shapes in the calorimeters to speed up the detector response simulation process.

In this analysis several generators are used to simulate the $t\bar{t}$ signal and the various sources of background:

- POWHEG [113–115], which implements NLO calculation for a large number of processes using a p_T ordered emission. To obtain a full event generation it needs to

be interfaced with a showering generator. This matching could originate an overlap between the hard emissions and the soft/collinear radiations generated at the level of the parton showering. For this reason generator and showering algorithm parameters need to be varied to have good matching and to avoid double counting. The h_{damp} parameter is one of these parameters and it controls the p_T of the first additional emission.

- MADGRAPH5_aMC@NLO [116], as POWHEG, implements NLO calculation with a different procedure which includes negative weights assigned to a small fraction of events.
- PYTHIA 8 [117, 118] is a multi-purpose generator that can be interfaced the output of POWHEG or MADGRAPH5_aMC@NLO to generate the showering, hadronisation and decay of the particles. The showering approach follows a p_T ordering.
- HERWIG [119] which is similar to PYTHIA 8, a multi-purpose generator that can be interfaced with an NLO generator that simulates the showering step. HERWIG uses an angular ordering (first large angles) of the showering, instead of a p_T ordering.
- SHERPA [29] (Simulation of High-Energy Reactions of PArticles) is a particular generator that can handle all the steps together, from the generation to the showering.

The generator used to simulate the $t\bar{t}$ signal is POWHEG+PYTHIA 8, using the NNPDF3.0 [26] set of PDFs and parameter values set according to the A14 [120] tune with PDF NNPDF23 at LO [121]. The h_{damp} parameter is set to $1.5 \cdot m_{top}$, m_{top} is set to 172.5 GeV and a di-leptonic filter is applied to the sample generator, to select only ee , $\mu\mu$ and $e\mu$ events (including events coming from τ decays) which constitute the signal of the analysis. A similar sample, simulated with “non all hadronic filter”¹ is used as well, to estimate the background from mis-identified leptons.

Many alternative generators are used to simulate $t\bar{t}$ signal and evaluate the effects on the measurement of the differences in various simulation steps:

- POWHEG+PYTHIA 8 with a different h_{damp} parameter (2 times nominal), which is used to estimate the variation coming from h_{damp} .
- POWHEG+PYTHIA 8 reweighted to modify the parameter α_S that regulates the Initial State Radiation scenario. The range of the variation is selected accordingly to the dedicated ATLAS PYTHIA 8 tune A14 [120]. This variation is done in conjunction with the variation of the renormalisation and factorisation scales in POWHEG, which are modified in the range [0.5, 2] with respect to the standard value ($\mu_R = \mu_F = \sqrt{m_t^2 + p_T^2}$).
- POWHEG+PYTHIA 8 reweighted with a different μ_R parameter (both up, $\mu_R = 2.0$, and down variation, $\mu_R = 0.5$) which changes α_S to take into account an higher/lower Final State Radiation (FSR).

¹The events simulated and selected with the non all hadronic filter are the ones with at least one W , coming from the top/antitop-quark, decays into a lepton plus neutrino.

- POWHEG+PYTHIA 8 reweighted with 30 components of the Hessian PDF4LHC15_30 error set. These samples are used to evaluate the PDF uncertainty.
- POWHEG+PYTHIA 8 with different top-quark masses, respect to the nominal values of 172.5 GeV , (from $m_{top} = 169 \text{ GeV}$ to $m_{top} = 176 \text{ GeV}$) which are used to evaluate the top-quark mass dependence, to make validation tests and also to extract the top-quark mass.
- POWHEG interfaced with HERWIG 7.0.4 which is used to evaluate the parton shower uncertainty.

The major background in this analysis comes from the single top-quark, with the Wt associated production process, and the samples used to describe it are produced with POWHEG with PDF NNPDF3.0 at NLO interfaced with PYTHIA 8 with the A14 tune and PDF NNPDF2.3 at LO and with a di-lepton filter. Two samples are used to simulate this background: one for the Wt process and one for the $W\bar{t}$ process. The interference between the $t\bar{t}$ and Wt is modelled using the diagram removal scheme [46, 122]. The same samples, produced with the non all hadronic filter, are used for the mis-identified leptons background estimation, as for the $t\bar{t}$. To estimate the systematic uncertainties coming from the modelling of the interference between $t\bar{t}$ and Wt an alternative set of samples is used, where the interference is modelled with the diagram subtraction scheme [46]. To estimate the fragmentation systematic uncertainty in the single top-quark background, the samples produced with POWHEG for the underlying simulation with PDF NNPDF3.0, interfaced with HERWIG 7.0.4 [119] for the fragmentation model and parton shower, are used. The tune used is H7UE [123]. To estimate the hard scattering systematic uncertainty, the samples simulated with MADGRAPH5_aMC@NLO [116], interfaced with PYTHIA 8 with the A14 tune, are generated. A set of Wt samples, with the same set-up as the nominal POWHEG+PYTHIA 8, with the di-lepton filter but with varied top-quark masses, is generated and used to estimate the top-quark mass uncertainty on the cross section (together with the $t\bar{t}$ top-quark mass variation samples). A minor contribution to the single top-quark background comes from the t -channel, which is simulated with POWHEG in the four flavour scheme [124] with PDF NNPDF3.0 at NLO interfaced with PYTHIA 8 with the A14 tune and PDF NNPDF2.3 at LO.

The background generated from di-boson events (WW, WZ and ZZ) is simulated using SHERPA v. 2.2.2 [125] with PDF NNPDF3.0 at NNLO. These samples model loop-induced production from gg , which is not included in the standard di-lepton samples [126]. Di-boson samples generated with SHERPA v. 2.2.1 with PDF NNPDF3.0 at NNLO are used to include final states where one of the leptons is misidentified. Three di-boson samples are included for processes where two gluons produce four leptons via intermediate vector bosons [126].

Another background contribution comes from the Z boson decaying to two τ , which then decay to an e and a μ , and jets. Those samples are simulated with SHERPA v. 2.2.1, for both the matrix element calculation and the parton shower tuning, with PDF NNPDF3.0 at

NNLO in $\max(H_T, p_T^V)$ slices². SHERPA v. 2.2.1 adopts a 5-flavour scheme and the merging of different parton multiplicities is achieved through a matching scheme based on the CKKW-L [127] technique using a matching scale of $Q_{cut} = 20 \text{ GeV}$. Additional $Z \rightarrow ee + \text{jets}$ and $Z \rightarrow \mu\mu + \text{jets}$ samples are used to extract a factor to scale the $Z \rightarrow \tau\tau + \text{jets}$ background to data. To compare the $Z + \text{jets}$ modelling, alternative $Z + \text{jets}$ samples are generated with POWHEG + PYTHIA 8.

The background coming from $t\bar{t}V$ and $t\bar{t}WW$ are described by samples simulated with MADGRAPH + aMC@NLO interfaced with PYTHIA 8 with the A14 tune and PDF NNPDF2.3 at LO.

To evaluate the mis-identified leptons background contribution, the $W \rightarrow l\nu + \text{jets}$ samples, simulated with SHERPA v. 2.2.1 with the same settings of the $Z \rightarrow ll + \text{jets}$ samples, are included.

Additional backgrounds from tZ and $t\bar{t}\bar{t}$ are not included as their contribution is negligible.

Physics process	Generator	Parton Shower	cross section normalisation
$t\bar{t}$	POWHEG	PYTHIA 8	NNLO+NNLL
Single top-quark: Wt	POWHEG	PYTHIA 8	NLO
Single top-quark: t -channel	POWHEG	PYTHIA 8	NLO
Single top-quark: s -channel	POWHEG	PYTHIA 8	NLO
$t\bar{t}V + t\bar{t}VV$	MC@NLO	PYTHIA 8	NLO
$t\bar{t}H$	MC@NLO	PYTHIA 8	NLO
$Z \rightarrow ll + \text{jets}$		SHERPA	NLO(0,1,2 jets) + LO (3,4 jets)
$W \rightarrow l\nu + \text{jets}$		SHERPA	NLO(0,1,2 jets) + LO (3,4 jets)
Di-bosons (VV)		SHERPA	NLO(0,1 jet) + LO (2,3 jets)
Tri-bosons (VVV)		SHERPA	LO (0,1 jet)

Table 5.1: Summary of Monte Carlo samples, showing the generator for the hard-scattering process, parton shower and cross section normalisation precision used in the analysis.

To reproduce the pileup conditions of the real data taking, each simulated sample is produced independently for each year and the distribution of the expected pile-up $\langle \mu \rangle$ is reweighted to match the data distributions, presented in Figure 2.2. In addition, each sample is normalised to the NNLO theoretical prediction.

5.3 Event selection

The selections applied in this analysis are chosen in order to have a great purity³ of events and at the same time to be as insensitive as possible to particular systematic variations. The events cuts applied are listed below:

- *Good Run Lists* (GRL)⁴ is applied to the data samples;

² H_T is the scalar sum of the transverse momenta of all the particles. p_T^V is the transverse momentum of the vector boson V .

³The purity is defined as the ratio between the selected signal events over the total selected events.

⁴The data collected for physics measurements must satisfy the quality constraints. In detail, LHC beam

- *primary vertex* presence: a primary vertex must be reconstructed in the event to discard not interesting events; this is applied to both data and Monte Carlo events;
- the events need to pass at least one of the single lepton trigger chains (only for Monte Carlo to match with the data sample) with a p_T of at least 27 GeV (25 GeV for events from the 2015 data taking year);
- there must be two opposite flavour ($e + \mu$) and opposite sign (OS) leptons with a p_T greater than 25 GeV to select the di-leptonic decay of $t\bar{t}$ process and to suppress the Z background; these requirements bring the signal purity to a value greater than 90%; the same flavour and same sign region are used as control regions;
- there are no requirements on the Missing Energy Transverse (MET) or on number of jets in order to be as insensitive as possible to the systematics uncertainties related to these objects.

The events selection is applied to both detector level object and particle level objects⁵ and is based on the objects defined in Table 5.2. Each event is then categorised according to the number of b -tagged jets in the event⁶.

must be in stable-mode (ready for physics), ATLAS Magnets are on (and not in ramping), Sub-detectors are switched on and there are not too many noisy cells.

⁵The particle level is the set of final particles in the events before the interaction with the detector and after all the decay processes.

⁶The clustering of particle level jets does not include heavy flavour hadrons in the input particle collection, since their lifetimes are shorter than the stable particle definition. However, a heavy flavour hadron can be included in the jet finding as a particle with an infinitely small momentum and the presence of this B -hadron (or C -hadron) in the jet defines then the jet flavour. This procedure is called ghost-association [128].

Object	Detector Level	Particle Level
Electrons	$ d_0/\sigma_{d_0} < 5$ and $ z_0 \cdot \sin(\theta) < 0.5$ ID: “Tight” and Isolation: “Gradient” $p_T > 25 \text{ GeV}$ $ \eta < 1.37$ or $1.52 < \eta < 2.47$	$p_T > 25 \text{ GeV}$ $ \eta < 1.37$ or $1.52 < \eta < 2.47$
Muons	$ d_0/\sigma_{d_0} < 3$ and $ z_0 \cdot \sin(\theta) < 0.5$ ID: “Medium” and Isolation: “FCTight_FixedRad” $p_T > 25 \text{ GeV}$ $ \eta < 2.5$	$p_T > 25 \text{ GeV}$ $ \eta < 2.5$
Jets	<i>anti-k_t</i> , R = 0.4 JVT: “medium” $p_T > 25 \text{ GeV}$ $ \eta < 2.5$	$p_T > 25 \text{ GeV}$ $ \eta < 2.5$
<i>b</i> -tag jets	<i>MV2c10</i> > 0.83 (70% WP)	if it has a ghosted <i>B</i> -hadron
Overlap removal	<i>e</i> removed if share a track with μ <i>jet</i> removed if $\Delta R^{e,jet} < 0.2$ <i>e</i> removed if $\Delta R^{e,jet} < 0.4$ <i>jet</i> with less than 3 track is removed if $\Delta R^{\mu,jet} < 0.2$ μ removed if $\Delta R^{\mu,jet} < 0.4$	<i>e</i> removed if $\Delta R^{e,jet} < 0.4$ μ removed if $\Delta R^{\mu,jet} < 0.4$

Table 5.2: Summary of event selections for detector level and Monte Carlo generated particle level events.

5.4 Analysis strategy

The total and differential $t\bar{t}$ production cross sections are measured in the di-lepton channel of the $t\bar{t}$ decay, where $t\bar{t} \rightarrow W^+W^-b\bar{b}$ and both the two *W* bosons decay to a lepton (electron, muon or tau) and the two leptons have opposite sign and opposite flavour. If there is a τ coming from a *W* boson, only the leptonic decays of the tau are considered.

The additional opposite flavour request removes the need to exclude the *Z* peak region in the ee - and $\mu\mu$ -channels using cuts on the di-lepton mass. The branching ratio of the $t\bar{t}$ system in the di-lepton channel ($e\mu$) is dictated by the branching ratio of the decays of the *W* boson and it is measured to be approximately 2.4% [17]. In this analysis though, the events where the leptons come from an intermediate τ -decay, $W \rightarrow \tau\nu_\tau \rightarrow e\bar{\nu}_e\nu_\tau\nu_\tau$ or $W \rightarrow \tau\nu_\tau \rightarrow \mu\bar{\nu}_\mu\nu_\tau\nu_\tau$, are included as well, which increases the total branching ratio of the signal events increase slightly. This can be calculated by taking into account that the measured branching ratio of a τ to an electron or a muon with their corresponding neutrino and a tau neutrino is roughly 17%. The resulting branching ratio of the $t\bar{t}$ signal taken into consideration in this analysis becomes therefore $\sim 3.2\%$.

The events are furthermore required to contain either exactly one or exactly two *b*-tagged jets in order to finally extract the cross section. The fiducial cross section (both total and differential) are extracted to particle level.

5.4.1 Double tagging technique

The total fiducial cross section can be measured using an event count technique. This technique, also called the “double tagging technique”, subdivides the selected $e\mu$ OS events

into events with one b -jet and events with two b -jets.

The double tagging technique equations can be derived starting from the definition of the cross section:

$$\sigma_{t\bar{t}} = \frac{N}{\mathcal{L} \cdot A \cdot \epsilon_{t\bar{t}} \cdot BR} \quad (5.1)$$

where $\sigma_{t\bar{t}}$ is the cross section, N is the number of events after background subtraction (the number of signal events), \mathcal{L} is the dataset integrated luminosity, A is the fiducial acceptance (detector acceptance plus reconstruction efficiency), $\epsilon_{t\bar{t}}$ is the efficiency of the $t\bar{t}$ events and BR is the branching ratio of the process used to calculate the cross section.

From Equation 5.1, N can be derived:

$$N = \sigma_{t\bar{t}} \cdot \mathcal{L} \cdot A \cdot \epsilon \cdot BR \quad (5.2)$$

where the number of signal events is $N = N_{tot} - N_{bkg}$.

To measure the fiducial cross section, the following equation can be used:

$$\sigma_{t\bar{t}} \cdot A \cdot BR = \sigma_{t\bar{t}}^{fid} \quad (5.3)$$

and the Equation 5.2 becomes:

$$N_{tot} = \sigma_{t\bar{t}}^{fid} \cdot \mathcal{L} \cdot \epsilon + N_{bkg}. \quad (5.4)$$

Since $e\mu$ OS events are selected with either one or two b -tagged jets, two different equations can be set up, where the cross section can be extracted from the number of $e\mu$ OS events with one b -jet and in the other with two b -jets. By doing so, it is needed to introduce the b -tagging efficiency in both equations.

The correlation between the two b -tagged jets needs to be accounted for in both equations, so a coefficient is introduced for that. Furthermore, the reconstruction efficiency needs to be considered, that is a measure of how many $e\mu$ OS events were reconstructed in the detector out of the entire true $e\mu$ OS events generated. This value, as well as the b -tagging correlation coefficient, are entirely evaluated from Monte Carlo simulation samples. By putting together all these elements, the double tagging equations are derived:

$$\begin{aligned} N_1 &= \mathcal{L} \sigma_{t\bar{t}}^{fid} G_{e\mu} 2\epsilon_b (1 - \epsilon_b C_b) + N_{1,bkg} \\ N_2 &= \mathcal{L} \sigma_{t\bar{t}}^{fid} G_{e\mu} (\epsilon_b)^2 C_b + N_{2,bkg} \end{aligned} \quad (5.5)$$

where N_1 and N_2 are the number of data events with either one b -jet or two b -jets, \mathcal{L} is the integrated luminosity of the dataset used for the analysis, $\sigma_{t\bar{t}}^{fid}$ is the total fiducial cross section, $G_{e\mu}$ is the reconstruction efficiency for the $e\mu$ events taken from simulation, ϵ_b is the b -tagging efficiency, C_b is the b -tagging correlation coefficient, also taken from simulation and finally $N_{1,bkg}$ and $N_{2,bkg}$ are the number of background events with either one or two b -jets, calculated using simulation samples and, in some cases, by applying data driven techniques together with the estimates from simulations, as explained in

Section 5.5. The two unknowns in these equations, the cross sections and the b -tagging efficiency can be found by applying the log-likelihood method to these two equations.

The b -tagging efficiency, ϵ_b , in this equation is not the same as the b -tagging working point efficiency used to tag jets as b -jets this parameter expresses the efficiency that a jet is reconstructed in the fiducial region chosen (both regarding η and p_T cut), passes the JVT cut and is also tagged as a b -jet. This efficiency will therefore be lower than the b -tagging working point efficiency chosen. The ϵ_b values could be taken by simulation, this would though introduce higher uncertainties related to jets and b -jets, therefore this value is fitted together with the cross section.

The reconstruction efficiency $G_{e\mu}$ is defined as the ratio between the number of reconstructed $e\mu$ OS events from $t\bar{t}$ and the number of true $e\mu$ OS events from $t\bar{t}$ at particle level, where particle level refers to the true stable particles, present after the parton shower:

$$G_{e\mu} = \frac{N_{e\mu,all}^{t\bar{t},reco}}{N_{e\mu,all}^{t\bar{t},particle}} \quad (5.6)$$

where *all* means that all $e\mu$ OS events in the $t\bar{t}$ signal sample are taken into account, without any requirements on the number of b -tagged jets or matching of the reco level and particle level bins. When calculating $t\bar{t}$ related systematic uncertainties, the reconstruction efficiency is calculated using a different $t\bar{t}$ samples or reweighted $t\bar{t}$ samples.

If the reconstruction of the two b -tagged jets is completely independent from one another, the probability to reconstruct and tag both b -jets is given by $\epsilon_{bb} = (\epsilon_b)^2$, where ϵ_{bb} is the probability of tagging two jets at the same time and ϵ_b is the b -tagging efficiency. In reality, ϵ_{bb} is not equal to $(\epsilon_b)^2$ because there is a small correlation, due to physical and instrumental reasons, between the probability of tagging the second jet after tagging the first one. The b -tagging correlation coefficient C_b takes into consideration these small correlation between the two b -tagged jets and provides a correction to the b -tagging efficiency and is:

$$C_b = \frac{\epsilon_{bb}}{(\epsilon_b)^2} \quad (5.7)$$

By isolating the C_b term in Equation 5.5, it can be derived that:

$$C_b = \frac{4 \cdot N_{e\mu,all}^{t\bar{t}} \cdot N_{e\mu,2}^{t\bar{t}}}{(N_{e\mu,1}^{t\bar{t}} + 2N_{e\mu,2}^{t\bar{t}})^2} \quad (5.8)$$

where $N_{e\mu,all}^{t\bar{t}}$ is the total number of reconstructed $e\mu$ OS events from $t\bar{t}$ while $N_{e\mu,1}^{t\bar{t}}$ and $N_{e\mu,2}^{t\bar{t}}$ are the number of reconstructed $e\mu$ OS events from $t\bar{t}$ with either one or two b -tagged jets. When estimating the $t\bar{t}$ systematic uncertainties, the values of C_b and $G_{e\mu}$ are calculated with the appropriate samples.

5.4.2 Total fiducial cross section

Using the Equation 5.5 and knowing the nominal value of the reconstruction efficiency with the nominal POWHEG + PYTHIA 8 $t\bar{t}$ di-lepton sample, which is $57.06\% \pm 0.02\%$ and the nominal value of the b -tagging correlation coefficient with the nominal POWHEG + PYTHIA 8 $t\bar{t}$ di-lepton sample, which is 1.0058 ± 0.0006 , it is possible to measure the $t\bar{t}$ total fiducial cross section.

Once also the number of background events is calculated, the minimisation of the negative log-likelihood of Equation 5.5 can be performed. The probability to observe N signal events in a collection of signal and background events is by definition Poissonian and can therefore be written as:

$$p(N|s, b) = \frac{(s+b)^N e^{-(s+b)}}{N!} \quad (5.9)$$

where $p(N|s, b)$ is the probability of observing N data events given signal prediction s and background prediction b . In case of two different observations N_1 and N_2 , the probability (or likelihood) of observing them both is the product of the single probabilities. If the signal and background models contain parameters, those can then be found by minimising the negative log of the likelihood:

$$\frac{\partial(-\ln(L(N|s, b)))}{\partial(s, b)} = 0. \quad (5.10)$$

In the case of the double tagging technique, the likelihood becomes:

$$L = p(N_1^{obs}|N_1) \cdot p(N_2^{obs}|N_2) \quad (5.11)$$

where L is the likelihood, N_1^{obs} and N_2^{obs} are the number of observed $e\mu$ OS events with one or two b -jets in data while N_1 and N_2 is the predicted number of events with one or two b -jets from Equation 5.5. The negative log-likelihood takes this form:

$$-\ln(L) = N_1 + N_2 - N_1^{obs} \ln(N_1) - N_2^{obs} \ln(N_2) \quad (5.12)$$

and by substituting the double tagging equations from Equation 5.5 in Equation 5.12, the cross section $\sigma_{t\bar{t}}$ and the b -tagging efficiency ϵ_b can be found by minimisation. Note that in Equation 5.12 the factorial of N_1^{obs} and N_2^{obs} have been removed since they are constants and they would not affect the final minimisation result. In order to carry this out, the TMinuit ROOT class was used with the MINOS minimizer algorithm [129].

5.4.3 Total inclusive cross section

The total inclusive cross section can be found in the same manner as the total fiducial cross section, though with the addition of a factor that takes into account the acceptance between the entirety of the $t\bar{t}$ pair produced in all channels and those chosen in the fiducial region, as shown in Equation 5.3.

In this case the reconstruction efficiency is substituted with the pre-selection efficiency $E_{e\mu} = A_{e\mu} \cdot G_{e\mu}$, where $A_{e\mu}$ is defined as such:

$$A_{e\mu} = \frac{N_{e\mu,all}^{t\bar{t},particle}}{N_{all}^{t\bar{t}}} \quad (5.13)$$

where $N_{e\mu,all}^{t\bar{t},particle}$ is the number of all particle level $e\mu$ OS events (not subdivided according to the number of b -jets), while $N_{all}^{t\bar{t}}$ is the total number of $t\bar{t}$ pairs produced in the Monte Carlo sample used. The acceptance factor comes purely from Monte Carlo $t\bar{t}$ samples (the same sample used to calculate the reconstruction efficiency should be used to calculate the acceptance). However, since the nominal sample and the alternative $t\bar{t}$ samples used in this analysis are produced with a di-lepton filter, it means that $N_{all}^{t\bar{t}}$ is in reality $N_{di-lepton}^{t\bar{t}}$. This needs to be corrected with the branching ratio to obtain the proper $N_{all}^{t\bar{t}}$. The branching ratio for $t\bar{t}$ events to dilepton used in this analysis is 10.61%, which is obtained from the Standard Model measured branching ratio $BR(W \rightarrow \ell\nu) = 10.86\%$ ⁷ [17]. The nominal value of $E_{e\mu}$ (including the branching ratio of $t\bar{t}$ pairs to di-lepton events) with the nominal POWHEG + PYTHIA 8 $t\bar{t}$ di-lepton sample is $0.7301\% \pm 0.0003$, while the value of the acceptance $A_{e\mu}$ also calculated with the nominal POWHEG + PYTHIA 8 $t\bar{t}$ di-lepton sample is $1.2795\% \pm 0.0004\%$.

When extracting the total inclusive cross section the double tagging equations become:

$$\begin{aligned} N_1 &= \mathcal{L}\sigma_{t\bar{t}}E_{e\mu}2\epsilon_b(1 - \epsilon_b C_b) + N_{1,bkg} \\ N_2 &= \mathcal{L}\sigma_{t\bar{t}}E_{e\mu}(\epsilon_b)^2 C_b + N_{2,bkg} \end{aligned} \quad (5.14)$$

5.4.4 Fiducial differential cross section

Eight leptonic differential distributions are taken into consideration in this analysis: the vectorial ($p_T^{e\mu}$) and the scalar sum of the lepton momentum ($p_T^e + p_T^\mu$), the eta ($|\eta^l|$) and momentum of the leptons (p_T^l), the sum of the lepton energies ($E^e + E^\mu$), the $e\mu$ invariant mass ($m^{e\mu}$), the difference in azimuthal angle between the two leptons ($\Delta\phi^{e\mu}$) and the rapidity of the $e\mu$ system ($|y^{e\mu}|$). Each distribution is unfolded to particle level in the fiducial region by applying the double tagging technique on each bin of each distribution, as done in Ref. [39, 130–132].

The double tagging equations for the differential measurements are as follows:

$$\begin{aligned} N_1^i &= \mathcal{L}\sigma_{t\bar{t}}^i G_{e\mu}^i 2\epsilon_b^i (1 - \epsilon_b^i C_b^i) + N_{1,bkg}^i \\ N_2^i &= \mathcal{L}\sigma_{t\bar{t}}^i G_{e\mu}^i (\epsilon_b^i)^2 C_b^i + N_{2,bkg}^i \end{aligned} \quad (5.15)$$

where N_1^i and N_2^i are the number of data events with either one b -jet or two b -jets in bin i , \mathcal{L} is the integrated luminosity of the dataset used for the analysis, $\sigma_{t\bar{t}}^i$ is the fiducial cross section in bin i , $G_{e\mu}^i$ is the reconstruction efficiency for $e\mu$ OS events taken from simulation, ϵ_b^i is the b -tagging efficiency in bin i , while C_b^i is the b -tagging correlation coefficient in

⁷ $BR(t\bar{t} \rightarrow \ell\nu b\ell\nu b) = (3 \cdot b)^2$, with $b = 10.86\%$, assuming $BR(t \rightarrow Wq) = 100\%$

bin i also taken from simulation and finally $N_{1,bkg}^i$ and $N_{2,bkg}^i$ are the number of background events in bin i with either one or two b -jets, calculated using simulation samples and, in some cases, by applying data driven techniques together with the estimates from simulations, as explained in Section 5.5. The two unknowns in these equations, the cross sections and the b -tagging efficiency, can be found by applying the log-likelihood method to these two equations.

The reconstruction efficiency $G_{e\mu}^i$ is defined as above, though one value per bin i per distribution is found:

$$G_{e\mu}^i = \frac{N_{e\mu,all}^{i,\bar{t}\bar{t},reco}}{N_{e\mu,all}^{i,\bar{t}\bar{t},particle}} \quad (5.16)$$

where *all* means that all $e\mu$ OS events from $\bar{t}\bar{t}$ events are taken into account, without subdividing them according to how many b -tagged jets they have. The i bin for $N_{e\mu,all}^{i,\bar{t}\bar{t},reco}$ refers to the reco-level bin (without requirement on the particle level) while for $N_{e\mu,all}^{i,\bar{t}\bar{t},particle}$ it refers to the particle level bin (without requirement on the reco level). The $N_{e\mu,all}^{i,\bar{t}\bar{t},reco}$ and $N_{e\mu,all}^{i,\bar{t}\bar{t},particle}$ in the last bin of each distribution contain the overflow events as well, except for angular variables ($|\eta^l|$, $\Delta\phi^{e\mu}$ and $|y^{e\mu}|$) that have no entries in the overflow. This value is calculated for each bin in each distribution using the nominal POWHEG + PYTHIA 8 $\bar{t}\bar{t}$ sample and the results can be seen in Figure 5.1. It is important to note, that in Figure 5.1a and 5.1b both leptons in the event are entered, meaning that there are two entries per event.

As in Equation 5.8, the b -tagging correlation coefficient C_b^i takes into consideration the correlation between the two b -tagged jets for each bin i of each distribution and provides a correction to the b -tagging efficiency and is:

$$C_b^i = \frac{4N_{e\mu,all}^i N_{e\mu,2}^i}{(N_{e\mu,1}^i + 2N_{e\mu,2}^i)^2} \quad (5.17)$$

where $N_{e\mu,all}^i$ is the total number of $e\mu$ OS events while $N_{e\mu,1}^i$ and $N_{e\mu,2}^i$ are the number of $e\mu$ OS events with either one or two b -tagged jets. The overflow events are added to the counts of the last bin in each distribution. The results for the nominal POWHEG + PYTHIA 8 $\bar{t}\bar{t}$ simulation sample can be seen in Figure 5.2.

In order to ensure, that the double tagging technique, which is a bin-by-bin unfolding technique, is valid and works, the data needs to be binned such that most of the reconstructed $e\mu$ OS events are in the same bin as the corresponding particle level events. To check for this, migration matrices have been built to check that around 90% of the events lie in the diagonal. Even though a finer binning could in principle be used on the spatial/angular variables ($|\eta^l|$, $\Delta\phi^{e\mu}$ and $|y^{e\mu}|$), it was chosen to use 30 bins being a good compromise between fine binning and computational time (each bin requires a fit). In a second iteration, the binning of the variable $|\eta^l|$ (for $|\eta^l| > 2$) has been modified to take into account the binning used for the electron scale factor.

In fact, in a bin-by-bin unfolding from reconstruction level to particle level, the un-

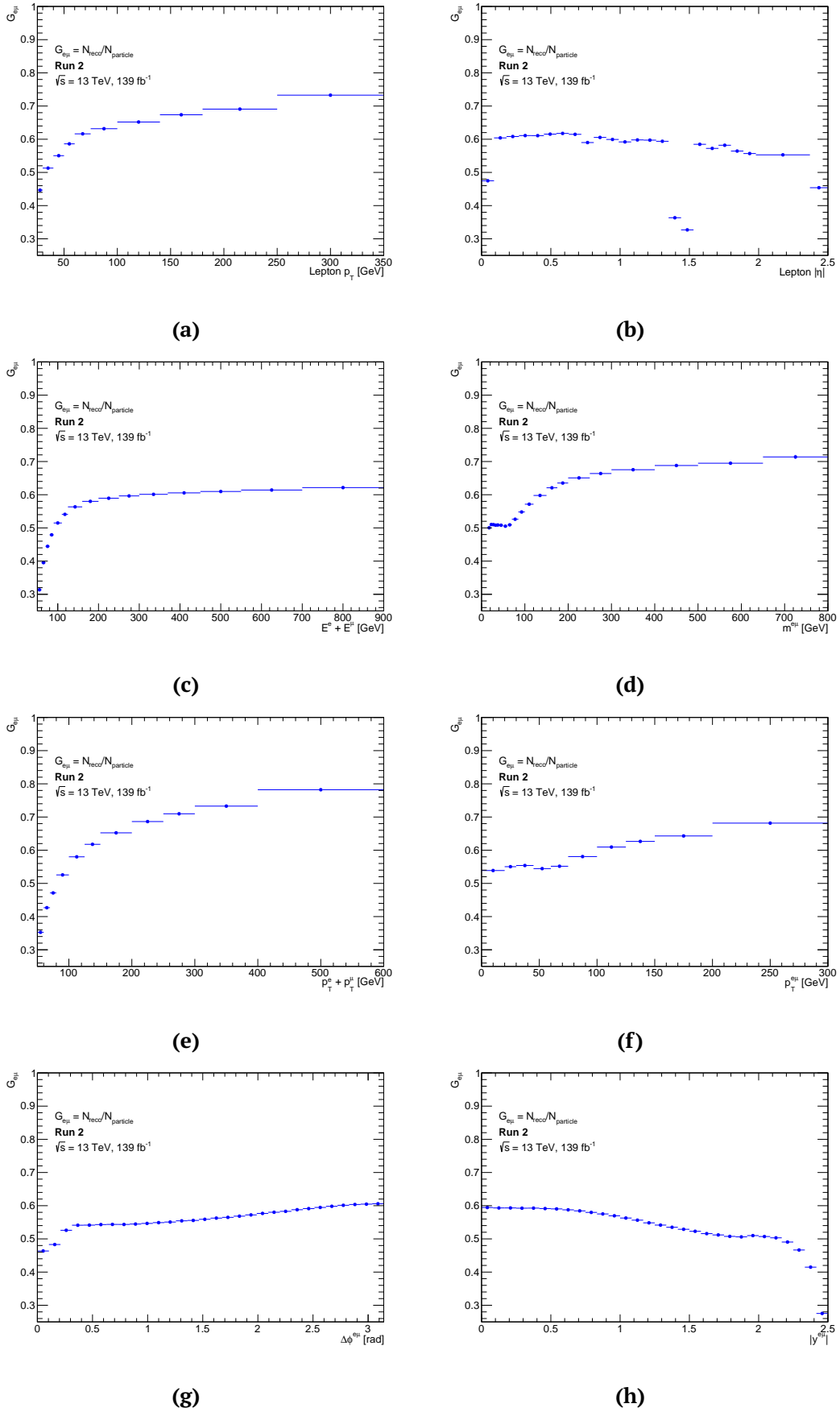


Figure 5.1: Reconstruction efficiency for each bin of each distributions calculated using Equation 5.16 with the baseline di-lepton POWHEG + PYTHIA 8 sample. The drop in Figure 5.1b at $|\eta| \sim 1.4$ is due to the ECAL crack-region which is excluded from the electron reconstruction.

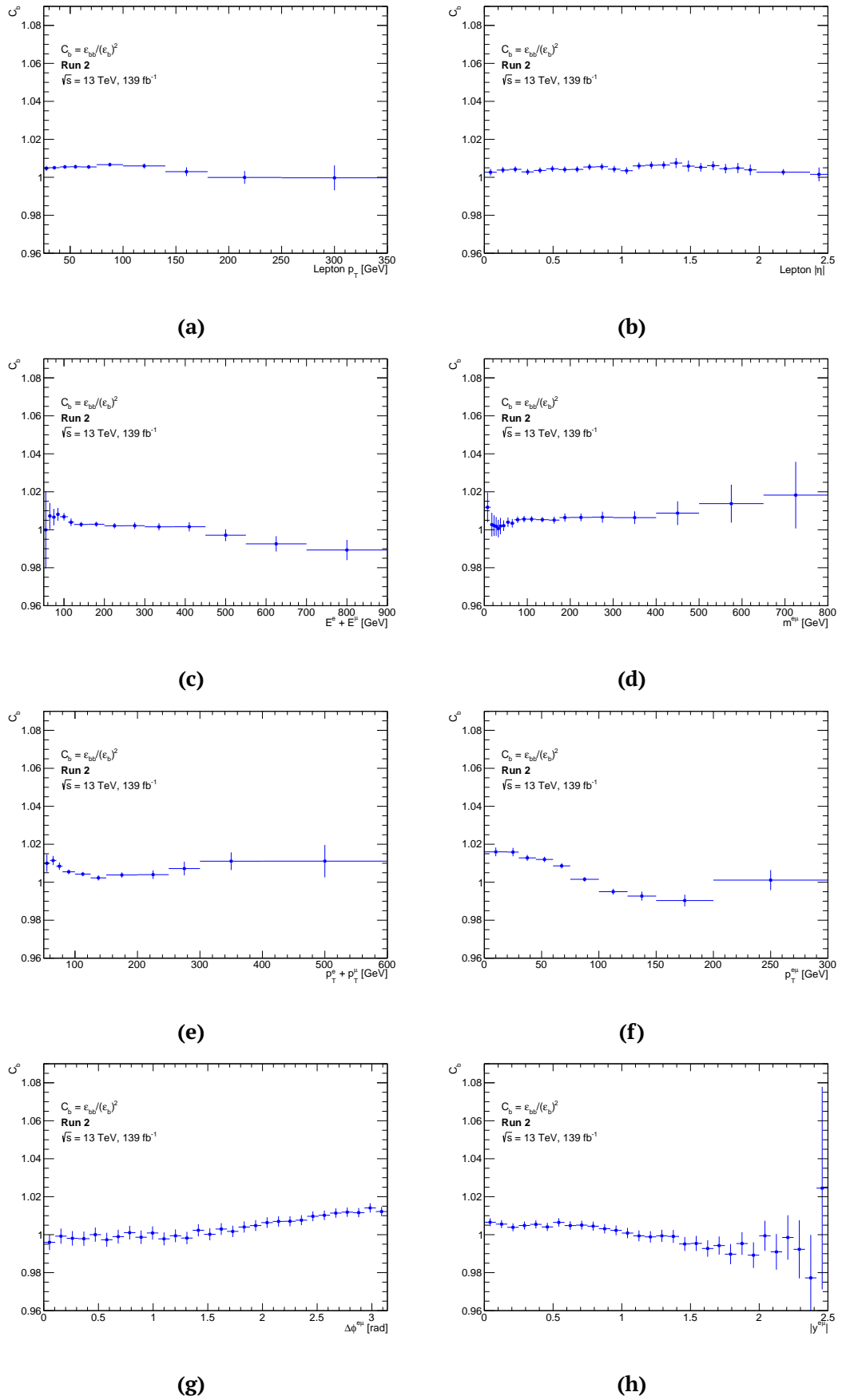


Figure 5.2: b -tagging correlation coefficient for each bin of each distributions calculated using Equation 5.17 with the baseline di-lepton POWHEG + PYTHIA 8 sample.

folding itself it just a correction factor applied to every bin, and this can only be done if the migration from particle level bins to reconstruction level bins does not branch to too many bins.

The migration matrices for the eight variables, calculated with the nominal POWHEG + PYTHIA 8 $t\bar{t}$ di-lepton sample, are seen in Figure 5.3 and 5.4 and they are obtained by matching the reconstructed $e\mu$ OS events with the corresponding $e\mu$ events at particle level and plotting the variables at reconstruction and particle level in a 2D histogram.

Besides the 90% migration, the binning needs to ensure statistical and systematic stability of the results. The high p_T regions in the $p_T^{e\mu}$, $p_T^e + p_T^\mu$, p_T^l are quite problematic due to two issues, i.e. the lower statistics and the high impact of the $t\bar{t}/Wt$ systematic uncertainty, which limited the possible range achievable in these variables.

For better visualisation of the migration matrices, one-dimensional histograms are shown in Figure 5.5, where the bins contain the values of the diagonal element of each migration matrix. As can be seen, most reconstructed events have a match with the particle level at the 90% level with small exceptions.

Once the reconstruction efficiency, b -tagging correlation coefficient and the number of background events are calculated, the b -tagging equations can be minimised for each bin in each distribution adapting the negative log-likelihood from Equation 5.12 to the following:

$$-\ln(L) = N_1^i + N_2^i - N_1^{i,obs} \ln(N_1^i) - N_2^{i,obs} \ln(N_2^i) \quad (5.18)$$

where again the factorial of N_1^{obs} and N_2^{obs} are not included. The overflow events in each distribution are added to the last bin of each distribution, both for $G_{e\mu}^i$, C_b^i , $N_1^{i,obs}$ and $N_2^{i,obs}$, but also for $N_{1,bkg}^i$ and $N_{2,bkg}^i$. Finally, in order to present the results in standard units, the differential cross section from bin i is divided by the width of the corresponding bin i . The normalised differential cross section can be found by normalising the absolute differential cross section. The normalised differential cross section for bin i is therefore:

$$\sigma_{t\bar{t},norm}^i = \frac{\sigma_{t\bar{t}}^i}{\sum_j \sigma_{t\bar{t}}^j} \quad (5.19)$$

The normalisation is applied before dividing the cross section with the bin width.

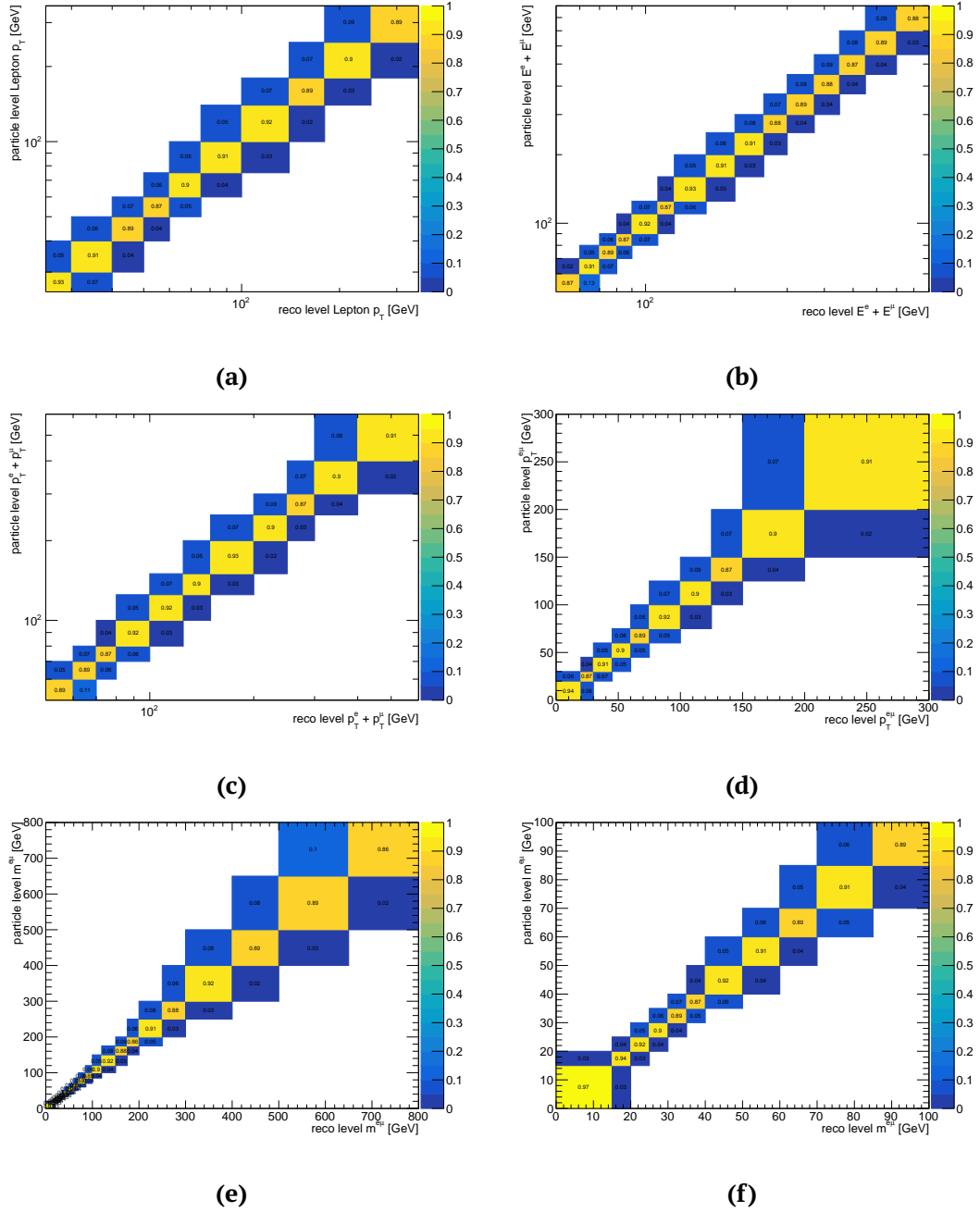


Figure 5.3: Migration matrices for each distributions calculated with the baseline di-lepton POWHEG + PYTHIA 8 sample. The $m^{e\mu}$ distribution is plotted for the total range (Figure 5.3e) and for a portion of the range, due to the high granularity at low values (Figure 5.3f).

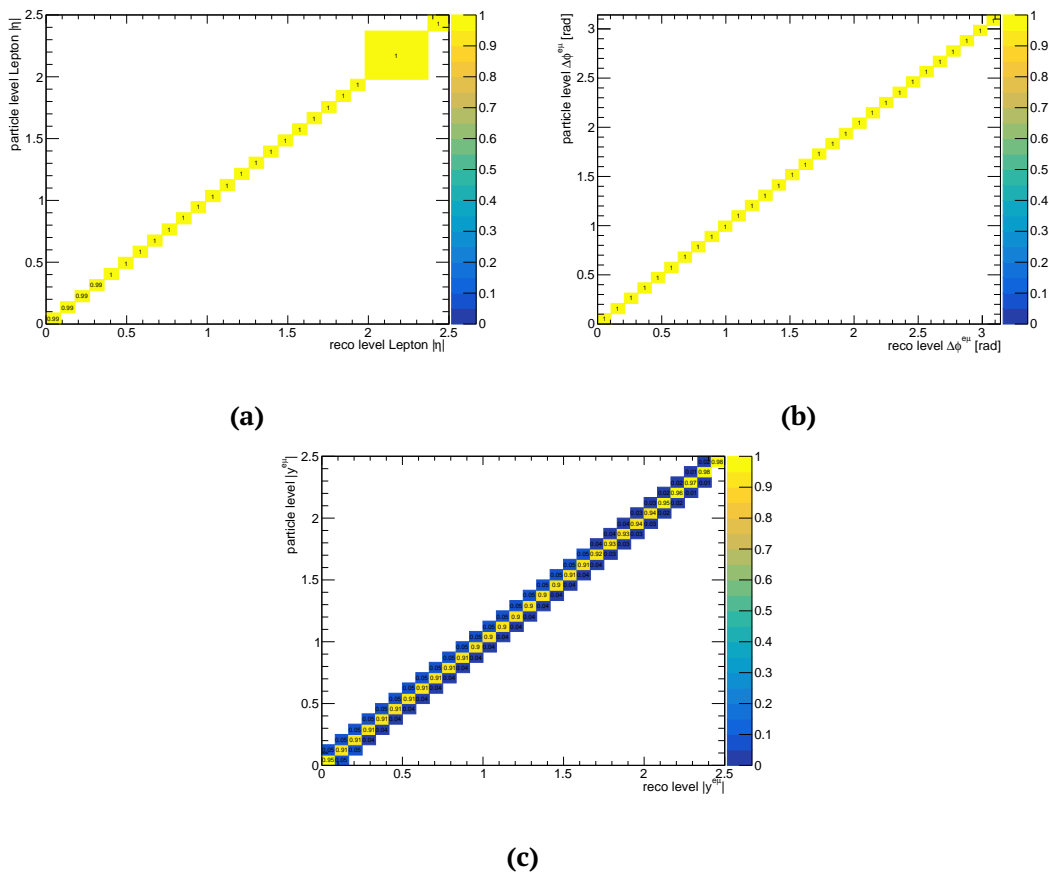


Figure 5.4: Migration matrices for each distributions calculated with the baseline di-lepton POWHEG + PYTHIA 8 sample.

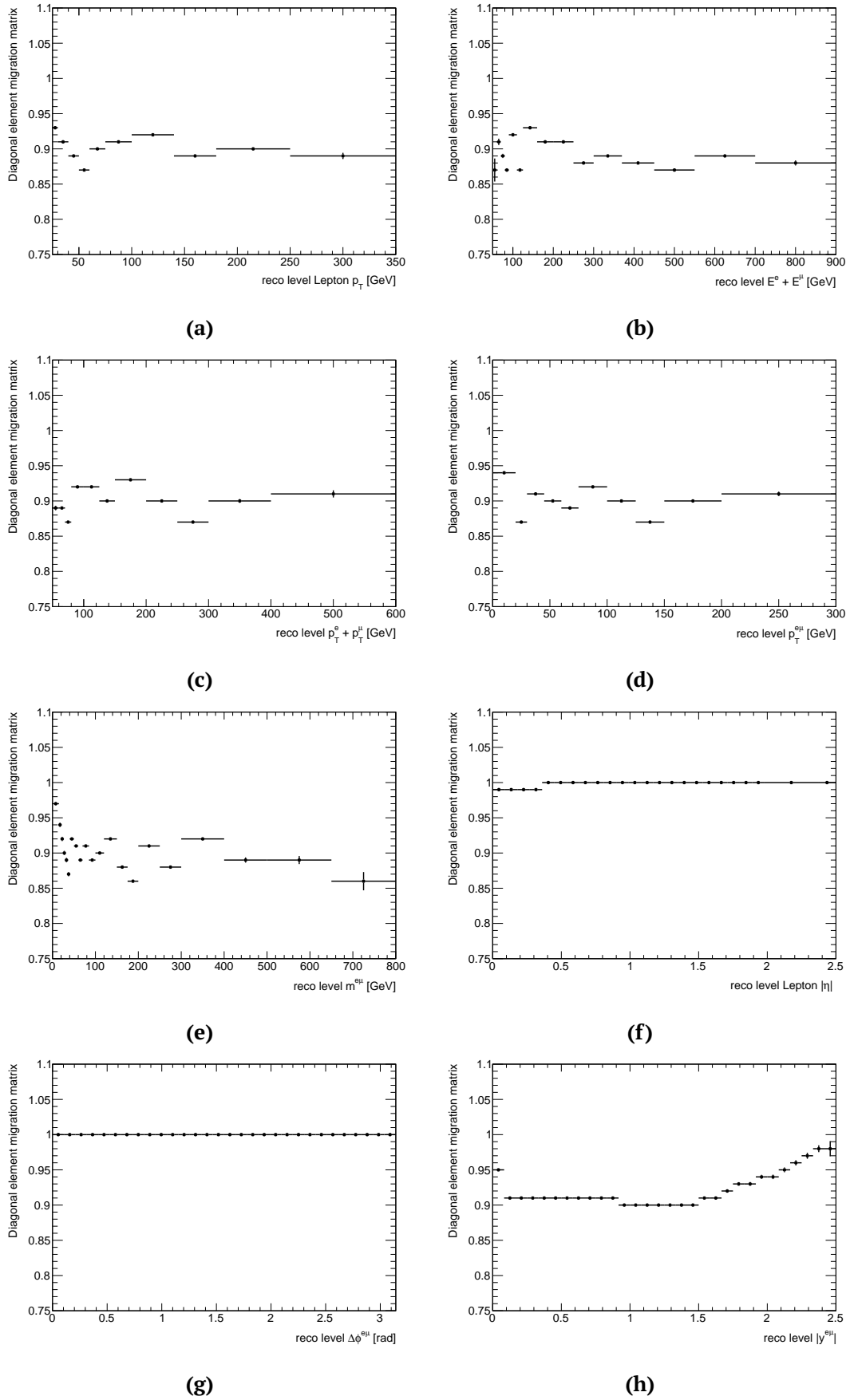


Figure 5.5: Diagonal elements of the migration matrices for each distributions calculated with the baseline di-lepton POWHEG + PYTHIA 8 sample. The $m^{e\mu}$ distribution is plotted for the total range and for a portion of the range, due to the high granularity at low values.

5.4.5 Fiducial double differential cross section

The phase space of the fiducial cross section measurements can be divided in bins as a function of one of the lepton kinematics variables as described in Section 5.4.4. Given the huge statistical power of this analysis with the Run 2 dataset, the phase space of the cross section measurement can be further divided as a function of two different leptonic variables. The possibility to do this has been explored in this analysis by performing measurements in bins of some angular leptonic variables (X) in steps of other different kinematic variables (Y).

The kinematic variables (Y) chosen are $m^{e\mu}$, $p_{\text{T}}^{e\mu}$ and $E^e + E^\mu$, where the angular variables (X) chosen are $|y^{e\mu}|$ and $\Delta\phi^{e\mu}$. $m^{e\mu}$ is chosen as one of the Y variables because it is correlated to the invariant mass of the $t\bar{t}$ system, while $p_{\text{T}}^{e\mu}$ and $E^e + E^\mu$ are chosen because they can be used as a starting point to improve the predictions of Monte Carlo generators.

Four double differential distribution are measured:

- $|y^{e\mu}|$ in bins of $m^{e\mu}$ with boundaries at $[0, 70, 100, 130, 200, \infty]$ GeV,
- $\Delta\phi^{e\mu}$ in bins of $m^{e\mu}$ with boundaries at $[0, 70, 100, 130, 200, \infty]$ GeV,
- $\Delta\phi^{e\mu}$ in bins of $p_{\text{T}}^{e\mu}$ with boundaries at $[0, 40, 65, \infty]$ GeV,
- $\Delta\phi^{e\mu}$ in bins of $E^e + E^\mu$ with boundaries at $[0, 110, 140, 200, 250, \infty]$ GeV,

The two-dimensional distributions are considered as one-dimensional with $N = M \times M'$ bins where M is the number of bins of the angular variable ($|y^{e\mu}|$, $\Delta\phi^{e\mu}$) while M' is the number of bins of the second variable ($m^{e\mu}$, $p_{\text{T}}^{e\mu}$, $E^e + E^\mu$).

For display purpose, the double differential cross section measurements are unrolled. Considering m as the bin number of the angular distribution and m' as the bin number of the other kinematic variable used for the 2D distribution, the corresponding bin in the unrolled distribution is equal to $m + m' \cdot r$ where r is the range of the angular variable and its value is $r_{|y^{e\mu}|} = 2.5$ and $r_{\Delta\phi^{e\mu}} = \pi$.

Apart from the initial assignment of the events to the correct bins, these double differential fiducial cross section distributions are treated as one-dimensional. Each double differential distribution is unfolded to particle level in the fiducial region as done with the one dimensional in Section 5.4.4 by applying the double tagging technique equations (Equation 5.15) on each bin of each distribution.

The reconstruction efficiency $G_{e\mu}^i$, as defined in Equation 5.16, is calculated for each bin in each double differential distribution using the nominal POWHEG + PYTHIA 8 $t\bar{t}$ sample and the results can be seen in Figure 5.6.

As in Equation 5.17, the b -tagging correlation coefficient C_b^i takes into consideration the correlation between the two b -tagged jets for each bin i of each distribution. The results for the nominal POWHEG + PYTHIA 8 $t\bar{t}$ simulation sample can be seen in Figure 5.7.

The migration matrices of the double differential distribution are shown in Figure 5.8. The migration in the angular variables is negligible, so the only migration is due to the

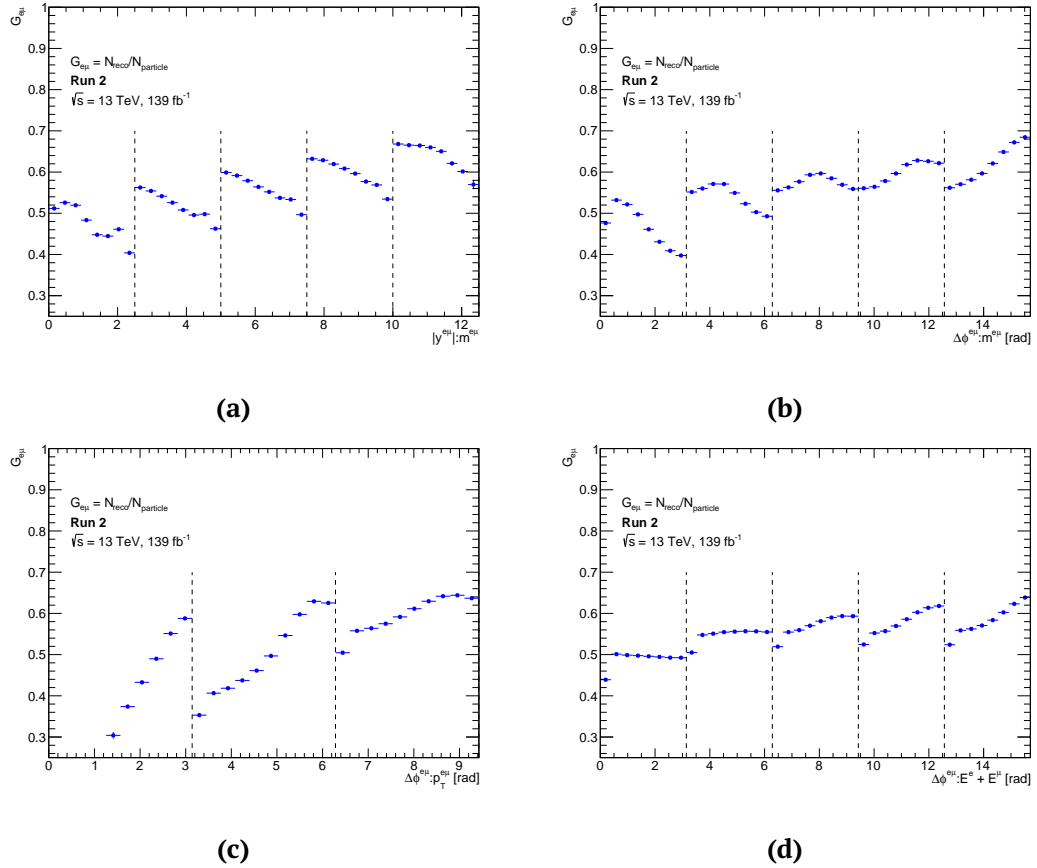


Figure 5.6: Reconstruction efficiency for each bin of each double differential distributions calculated using Equation 5.16 with the baseline di-lepton POWHEG + PYTHIA 8 sample. For display purpose, the double differential cross section measurements is unrolled. Considering m as the bin number of the angular distribution and m' as the bin number of the other kinematic variable used for the 2D distribution, the corresponding bin in the unrolled distribution is equal to $m + m' \cdot r$ where r is the range of the angular variable. The lines represent the range edges of the second variable.

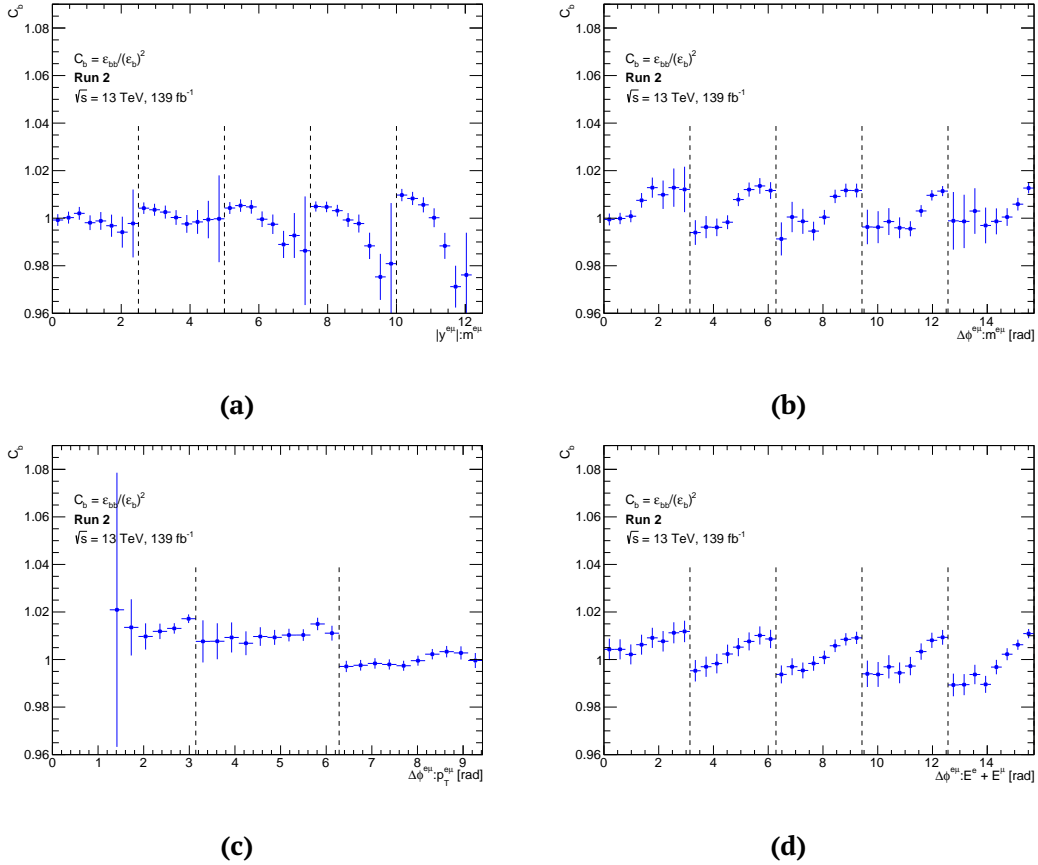


Figure 5.7: b -tagging correlation coefficient for each bin of each double differential distributions calculated using Equation 5.17 with the baseline di-lepton POWHEG + PYTHIA 8 sample. For display purpose, the double differential cross section measurements is unrolled. Considering m as the bin number of the angular distribution and m' as the bin number of the other kinematic variable used for the 2D distribution, the corresponding bin in the unrolled distribution is equal to $m + m' \cdot r$ where r is the range of the angular variable. The lines represent the range edges of the second variable.

other kinematic variables, and this leads to the formation of bands parallel to the main diagonal. The binning of the variables are chosen in order to obtain, as for the one-dimension differential cross section distributions, a fraction on the diagonal around 90% for all bins. As for the single differential distributions, one-dimensional histograms are shown in Figure 5.9, containing the elements of the diagonal of each migration matrix.

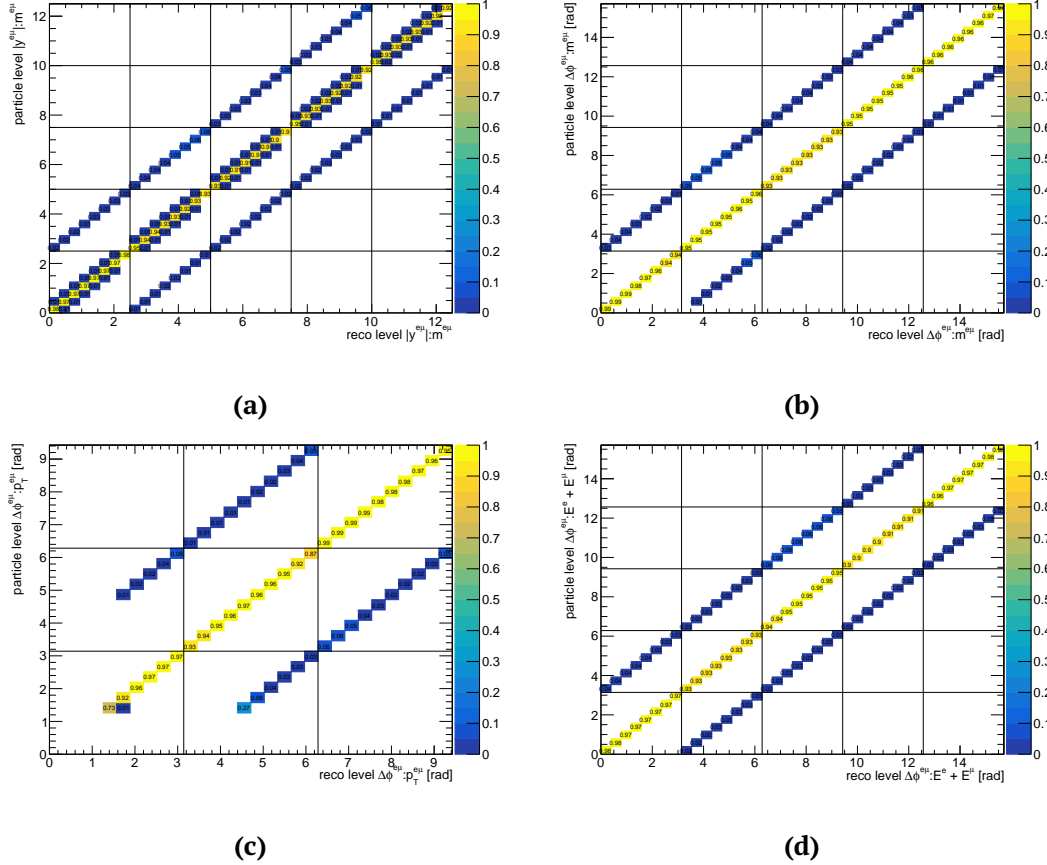


Figure 5.8: Migration matrices for each double distributions calculated with the baseline dilepton POWHEG + PYTHIA 8 sample. For display purpose, the double differential cross section measurements is unrolled. Considering m as the bin number of the angular distribution and m' as the bin number of the other kinematic variable used for the 2D distribution, the corresponding bin in the unrolled distribution is equal to $m + m' \cdot r$ where r is the range of the angular variable. The lines represent the range edges of the second variable.

As done for the single differential distributions, the normalised double differential cross section distributions can be found by normalising the absolute double differential cross section applying Equation 5.19.

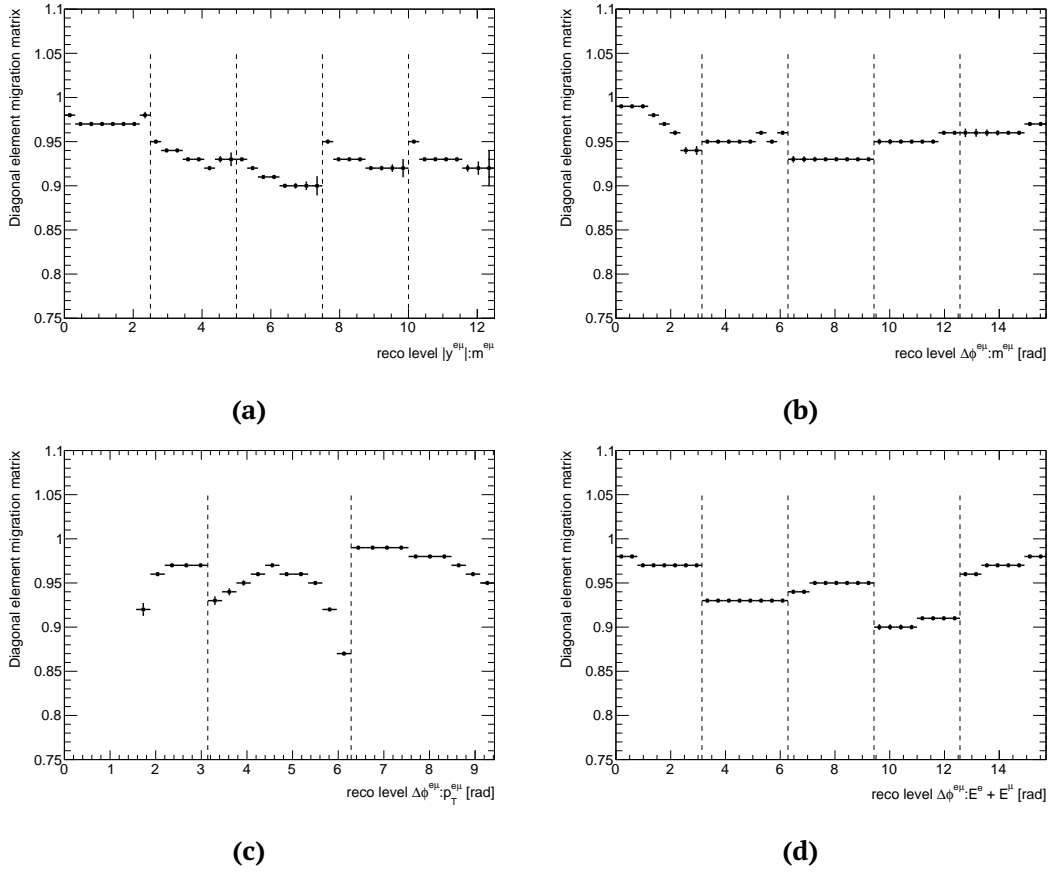


Figure 5.9: Diagonal elements of the migration matrices for each double distributions calculated with the baseline di-lepton POWHEG + PYTHIA 8 sample. For display purpose, the double differential cross section measurements is unrolled. Considering m as the bin number of the angular distribution and m' as the bin number of the other kinematic variable used for the 2D distribution, the corresponding bin in the unrolled distribution is equal to $m + m' \cdot r$ where r is the range of the angular variable. The lines represent the range edges of the second variable.

5.5 Background modelling

Different background sources are estimated with Monte Carlo based techniques. In some cases, due to imprecision or inaccuracies in theoretical modelling, the background does not match data correctly. In these cases, the predictions are compared to data in a region where such backgrounds dominate (the so-called control regions), in order to correct the normalisation of the background to the data.

The $t\bar{t}$ signal is extremely pure in the signal region (89% in the one b -tag region and 96% in the two b -tags region). However, a precise estimate of the background is essential given the sensitivity that this analysis aims to achieve. The background from electroweak single top-quark production is the largest background contribution in both considered regions; it amounts to 82% (71%) of the total background for the one (two) b -tag region. The second most significant source of background is the mis-identified leptons which is the 9% (19%) of the total amount of background in the one (two) b -tag region. The mis-identified leptons background is estimated using a data-driven technique as explained in Section 5.5.1. Other sources of background in this analysis are the $Z \rightarrow \tau\tau$ +jets based on Monte Carlo and corrected using a data-driven technique (see Section 5.5.2), the di/tri-boson processes and the $t\bar{t}V$ and $t\bar{t}H$, which are present although very small.

5.5.1 Mis-identified leptons background

Events with “*non-prompt*” leptons or non-leptonic particles identified as leptons, may satisfy the analysis selection criteria giving rise to the so-called mis-identified leptons background.

The mis-identified leptons background is estimated with a partially data-driven technique using the $e\mu$ same sign (SS) control region, since the majority of the leptons in this region are mis-identified (84% for both one and two b -tags regions), as shown in Table 5.3. The agreement is very good in all regions, except for the SS $e\mu$ region (this excess in data is coming from the events with zero associated b -jets) which is not used in this analysis. This disagreement is due to Monte Carlo mis-modelling of some of the background contributions as, for example, the di-boson with addition jets process, also seen in Ref. [133].

For the mis-identified leptons background estimation, the $t\bar{t}$ and Wt samples with a non all hadronic filter⁸ are used in order to consider the case in which a mis-identified lepton is originated by a jet coming from the W bosons.

For almost all of the cases, only one of the leptons is mis-identified or is non-prompt, while only in very few events both leptons are mis-identified.

Each Monte Carlo SS and opposite sign (OS) $e\mu$ event is categorised depending on the origin of the leptons (derived from the Monte Carlo) in one of those six categories:

- *prompt right sign (RS)* in which both leptons are prompt and both are reconstructed with the correct charge (which is checked by looking at the sign of truth pdgID of

⁸These samples include the di-lepton events plus the single leptons events ($l + jets$ channel).

the leptons);

- *prompt wrong sign (WS)* in which both leptons are prompt, but the electron was reconstructed with the wrong charge (again checked against the truth pdgID of the truth electron);
- *e from photon conversion* where the muon is prompt, while the electron comes from a photon conversion, which can both originate from a photon emitted by the electron from the top-quark ($t \rightarrow e \rightarrow \gamma \rightarrow e$) or from a background conversion. This is the dominant category in each variable;
- *e from heavy-flavour* where the muon is prompt, while the electron is produced in the decay of a bottom or charm hadron;
- μ *from heavy-flavour* where the electron is prompt, while the muon is produced in the decay of a bottom or charm hadron;
- *other*, which includes all the other cases: the electron is prompt and the muon is a background muon, coming from an in-flight decay of a pion or kaon; the electron is prompt and the muon is non-prompt but the source is unknown; the muon is prompt while the electron is non-prompt but the source is unknown; both leptons are non-prompt.

When all the events are categorised, the different lepton pair contributions are summed for all the signal and background samples for both the OS and SS channels and they are plotted against the data collected in those same channels. The different contributions in the OS and SS regions can be seen in Table 5.3, where N_1 is the number of $e\mu$ events with one b -jet, N_2 is the number of $e\mu$ events with two b -jets and $N_{e\mu}$ is number of all $e\mu$ events, and in Figure 5.10- 5.11 for one and two b -jets selections.

It can be noticed that in the SS channel (shown in Table 5.3) the majority of the events have one (or more) mis-identified lepton, as mentioned before, while in the OS channel only few events have mis-identified leptons. The biggest contribution to the mis-identified leptons in the SS channel comes from the events with a mis-identified electron, in particular from events where the electron comes from a conversion process or the charge of the electron has been mis-identified, as shown in Table 5.3 and Figure 5.10- 5.11. Another thing to note is that the heavy flavour contribution to the mis-identified leptons background lies mostly in a low p_T region, due to either low energetic deposits in the calorimeter that are reconstructed as leptons, or due to low energetic semi-leptonic b -decays, as shown in Table 5.3 and Figure 5.10 - 5.11.

The number of mis-identified leptons events in the OS channel can be computed as:

$$N_b^{i,mis-ID,OS} = R_b^i \cdot (N_b^{i,data,SS} - N_b^{i,MC-prompt,RS,SS}) \quad (5.20)$$

Run 2	N_1	OS N_2	$N_{e\mu}$
Prompt RS	$(4620.7 \pm 2.7) \cdot 10^2$	$(2417.6 \pm 1.8) \cdot 10^2$	$(1116.1 \pm 1.1) \cdot 10^3$
Prompt WS	1.89 ± 0.14	0.608 ± 0.060	30.06 ± 0.92
Conversion	3637 ± 24	1684 ± 15	$(93.1 \pm 1.6) \cdot 10^2$
Heavy flavour e	456.0 ± 8.8	46.1 ± 2.5	1256 ± 55
Heavy flavour μ	326.0 ± 7.7	53.7 ± 2.7	1286 ± 76
Other	492 ± 12	219.2 ± 5.4	$(31.1 \pm 2.5) \cdot 10^2$
Total	$(4669.8 \pm 2.7) \cdot 10^2$	$(2437.6 \pm 1.8) \cdot 10^2$	$(1131.1 \pm 1.2) \cdot 10^3$
Data	$(4685.7 \pm 6.8) \cdot 10^2$	$(2485.7 \pm 5.0) \cdot 10^2$	$(1150.3 \pm 1.1) \cdot 10^3$
Data/MC	1.0031 ± 0.0015	1.0197 ± 0.0020	1.01943 ± 0.00095

Run 2	N_1	SS N_2	$N_{e\mu}$
Prompt RS	625.5 ± 2.9	246.5 ± 1.3	10141 ± 31
Prompt WS	851 ± 11	361.1 ± 7.0	2031 ± 37
Conversion	1819 ± 17	826 ± 11	$(51.1 \pm 1.7) \cdot 10^2$
Heavy flavour e	412.1 ± 8.0	25.5 ± 1.9	934 ± 21
Heavy flavour μ	212.2 ± 6.8	14.9 ± 1.5	525 ± 23
Other	88.5 ± 9.0	32.9 ± 2.1	$(6.1 \pm 1.5) \cdot 10^2$
Total	4009 ± 25	1507 ± 13	$(193.5 \pm 2.3) \cdot 10^2$
Data	3995 ± 63	1501 ± 39	$(271.6 \pm 1.6) \cdot 10^2$
Data/MC	0.997 ± 0.016	0.996 ± 0.025	1.4037 ± 0.0085

Table 5.3: Event counts divided into mis-identified leptons categories for the Full Run 2 dataset. N_1 is the region with one b -tagged jet, N_2 is the region with two b -tagged jets while $N_{e\mu}$ is the region with no b -jets requirements.

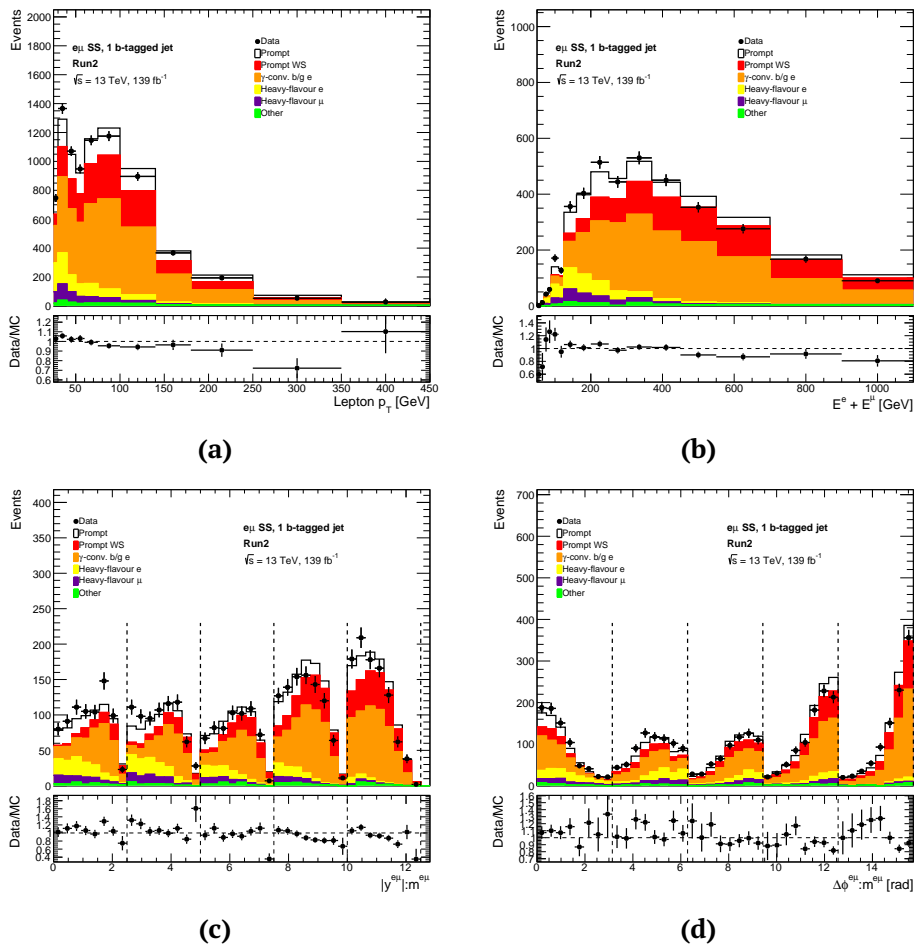


Figure 5.10: Unrolled single and double differential distributions for $e\mu$ SS events with one b -jet. The dotted vertical lines show the regions of the Y variable for each distribution.

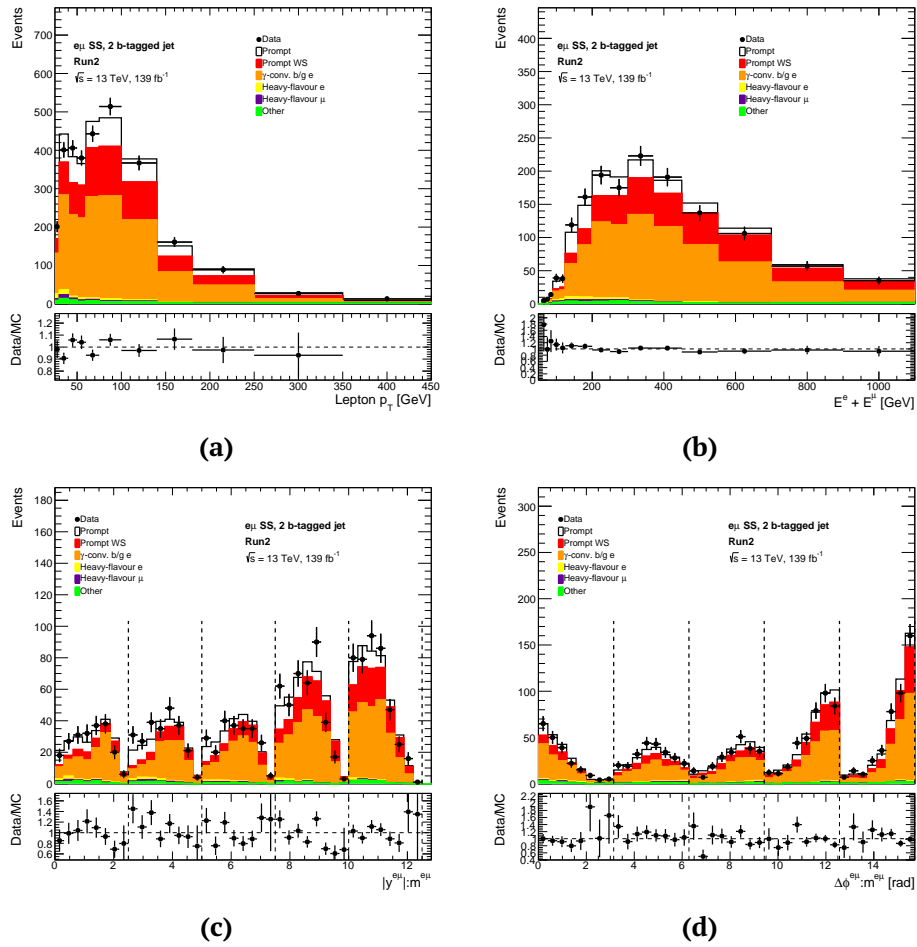


Figure 5.11: Unrolled single and double differential distribution for $e\mu$ SS events with two b -jets. The dotted vertical lines show the regions of the Y variable for each distribution.

with

$$R_b^i = \frac{N_b^{i,MC-mis-ID,OS}}{N_b^{i,MC-mis-ID,SS}} \quad (5.21)$$

where b is the number of b -jets used in the selection, i is the bin number, $N_b^{i,mis-ID,OS}$ is the number of estimated mis-identified leptons events from Monte Carlo and data in the OS channel for a b -jet selection in bin i , $N_b^{i,data,SS}$ is the number of data events in the SS channel with b -jet selection b , $N_b^{i,MC-prompt,RS,SS}$ is the number of prompt with right sign lepton pairs from Monte Carlo in the SS channel for a b -jet selection and R_b^i is the ratio between the number of mis-identified leptons in the OS and SS channels, derived from Monte Carlo. Using the above equations, the mis-identified leptons background can be computed for each bin of each distribution.

The R_b^i factor for the one and two b -jet distributions can be seen in Figure 5.12, where it is seen that the factor is above one for all distributions and generally around 1.5, indicating, that generally in Monte Carlo simulated samples, there are more mis-identified leptons background events predicted in the OS channel than in the SS channel. This is independent on the number of b -jets.

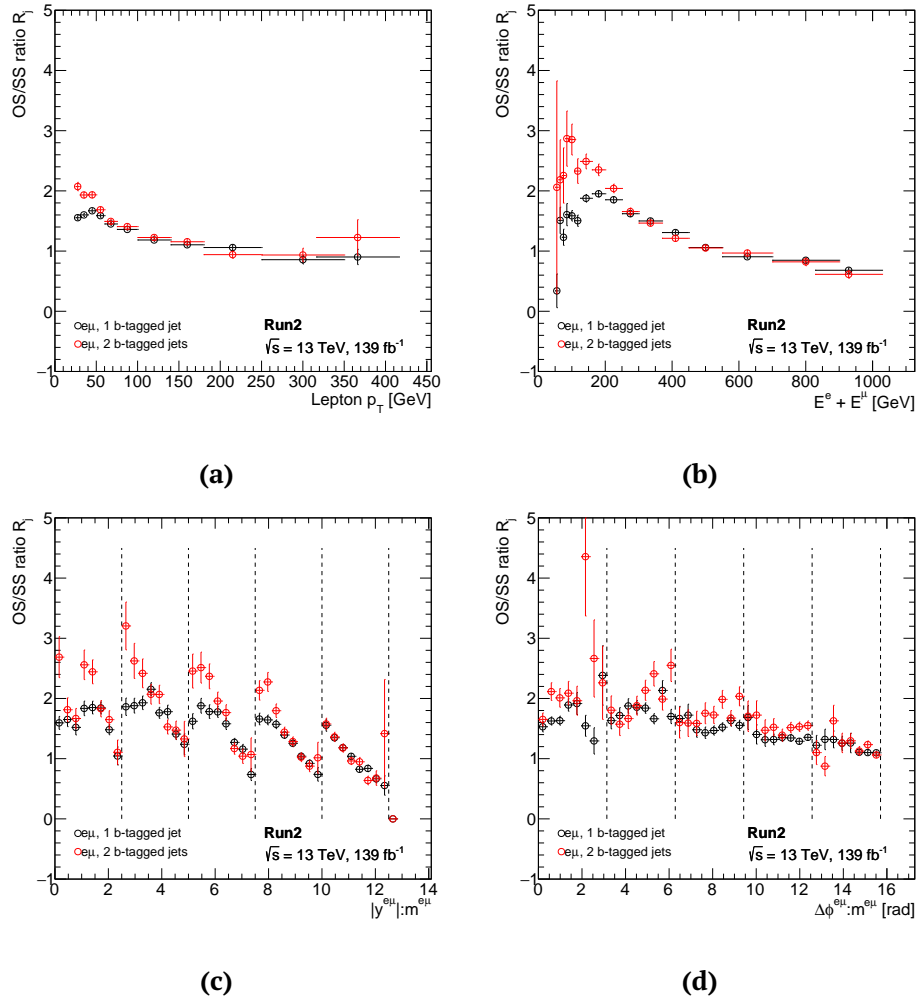


Figure 5.12: R factor from Equation 5.21 for each bin of single/double differential distributions for different selections.

5.5.2 $Z \rightarrow \tau\tau + \text{jets}$ background

The $Z \rightarrow \tau\tau + \text{jets}$ background is simulated with SHERPA 2.2.1. The event yield of this background has large theoretical QCD uncertainties [134] leading to unreliable Monte Carlo simulation. In order to correct for this mis-modelling, the inconsistencies between the $Z + \text{jets}$ background and the data is measured in two control regions and a correction factor is derived from this procedure and applied then to the $Z \rightarrow \tau\tau + \text{jets}$ background in the signal region, assuming lepton universality. The two control regions are the ee OS and the $\mu\mu$ OS channels around the Z pole mass and the scale factors are derived separately for events with one and two b -jets.

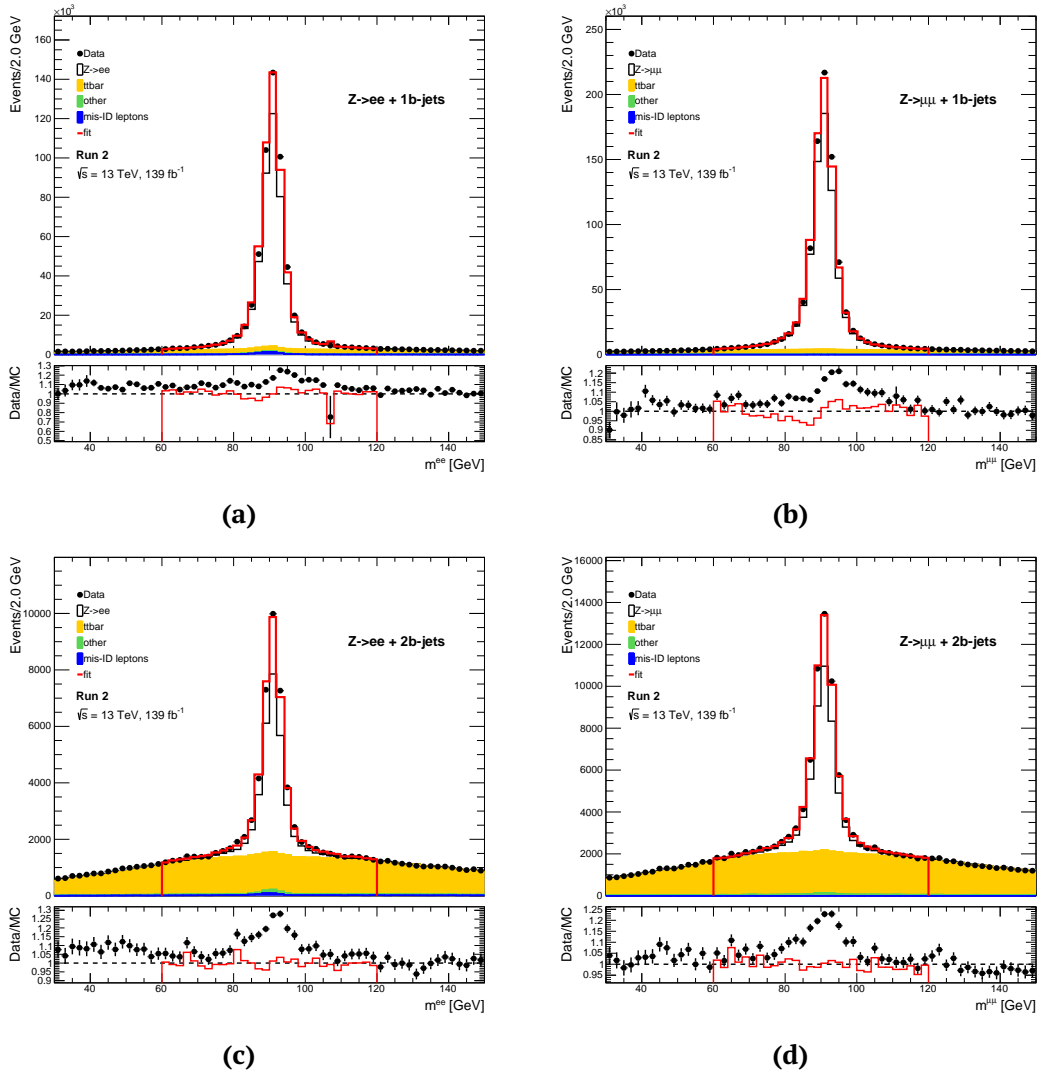


Figure 5.13: Control regions used to extract the Z scale factor that normalises the SHERPA simulated samples to data. Different components, as $t\bar{t}$, di-boson and mis-identified leptons are also included as part of the background. The fit to extract the Z scale factor is performed between 60 GeV and 120 GeV.

In order to derive the correction factors, the invariant mass of the two leptons, $m^{\ell\ell}$ is calculated for each event in the control regions, both for the $Z \rightarrow \ell\ell + \text{jets}$ samples and for

Run 2 OS	$ee + 1 b\text{-jet}$	$\mu\mu + 1 b\text{-jet}$	$ee + 2 b\text{-jets}$	$\mu\mu + 2 b\text{-jets}$
$t\bar{t}$	65623 ± 95	$(963.9 \pm 1.6) \cdot 10^2$	37653 ± 70	56037 ± 86
Other	8189 ± 47	11844 ± 52	1464 ± 13	2059 ± 15
mis-IDs	$(76.2 \pm 1.5) \cdot 10^2$	379 ± 21	839 ± 17	61.9 ± 3.3
Z+jets	$(451.9 \pm 2.3) \cdot 10^3$	$(735.4 \pm 1.8) \cdot 10^3$	$(233.7 \pm 1.3) \cdot 10^2$	$(360.1 \pm 1.7) \cdot 10^2$
Total	$(532.9 \pm 2.3) \cdot 10^3$	$(835.0 \pm 1.8) \cdot 10^3$	$(633.2 \pm 1.5) \cdot 10^2$	$(941.9 \pm 1.9) \cdot 10^2$
Data	$(6129.1 \pm 7.8) \cdot 10^2$	$(9534.8 \pm 9.8) \cdot 10^2$	$(722.2 \pm 2.7) \cdot 10^2$	$(1052.5 \pm 3.2) \cdot 10^2$
Data/MC	1.1502 ± 0.0015	1.1298 ± 0.0012	1.1405 ± 0.0042	1.1175 ± 0.0034

Table 5.4: Event counts for $Z \rightarrow ee + \text{jets}$ and the $Z \rightarrow \mu\mu + \text{jets}$ the Full Run 2 dataset in the range between 60 and 120 GeV.

the background samples ($t\bar{t}$, $t\bar{t}V$, single top-quark, di-boson). The mis-identified lepton contribution is in this case taken directly from Monte Carlo, by categorising each di-lepton event as either prompt or mis-identified in the same way as in Section 5.5.1. The invariant mass of the leptons is then plotted for all the contributions around the Z-peak value, which is clearly visible both in data and in Monte Carlo around 90 GeV. The difference between data and Monte Carlo is clear from Figure 5.13, where there is an excess of data events compared to Monte Carlo events. The event counts for the plots can be seen in Table 5.4, where it is shown that the data excess is between 12 – 15%.

The correction scale factors for each region are extracted by fitting the Monte Carlo $Z \rightarrow \ell\ell + \text{jets}$ contribution and background contributions to the data. The fitting function contains two normalisation factors, one for the $Z \rightarrow \ell\ell + \text{jets}$ contribution and one for the total background contributions. Those two normalisation parameters are fitted, so that the entire Monte Carlo $Z \rightarrow \ell\ell + \text{jets} + \text{background}$ contribution is fitted to the data. The function fitted to data is:

$$f = n_Z \cdot \text{hist}(Z \rightarrow \ell\ell) + n_{bkg} \cdot \text{hist}(\text{bkg}) \quad (5.22)$$

where f is the fitting function, n_Z and n_{bkg} are the fitted normalisation parameters for the Monte Carlo $Z \rightarrow \ell\ell$ contribution and for the background contribution respectively, while $\text{hist}(Z \rightarrow \ell\ell)$ and $\text{hist}(\text{bkg})$ are the Monte Carlo $Z \rightarrow \ell\ell$ and background histogram contributions, respectively. The fit is performed with a log likelihood in a range between 60 GeV and 120 GeV. The normalisation factor of the $Z \rightarrow \ell\ell$ contribution is then taken as the scale factor for that specific control region. The normalisation factor for the background contribution diverges from 1 by a maximum of 4% for every region, without any need to constrain this parameter, meaning that the background contribution is well simulated within 4%.

After this procedure, four scale factors are found in total, two for each signal region, both for the events with one b -tagged jet and for the events with two b -tagged jets. The results can be seen in Table 5.5. A total scale factor for the $Z \rightarrow \tau\tau + \text{jets}$ background for the one b -jet and two b -jets sub-samples are found by taking the weighted average of

the two scale factors derived from the $Z \rightarrow ee + \text{jets}$ and from the $Z \rightarrow \mu\mu + \text{jets}$ regions, assuming that the two regions are uncorrelated from each other. The final results can be seen also in Table 5.5.

Channel	SF 1 b -jet region	SF 2 b -jets region
$Z \rightarrow ee + \text{jets}$	1.177 ± 0.002	1.31 ± 0.01
$Z \rightarrow \mu\mu + \text{jets}$	1.151 ± 0.001	1.273 ± 0.008
Total	1.161 ± 0.001	1.287 ± 0.006

Table 5.5: Factors extracted from the $Z \rightarrow ee + \text{jets}$ and the $Z \rightarrow \mu\mu + \text{jets}$ control regions.

5.6 Lepton isolation measurements

The standard ATLAS lepton isolation efficiency is measured using a sample of $Z \rightarrow \ell\ell$ events. The $t\bar{t}$ events may, due to their different intrinsic nature involving the presence of two or more jets, have a different isolation efficiency. Given the large statistics available (Monte Carlo and data) it is possible to make an *in situ* measurement on a sample of $t\bar{t}$ events.

In order to do that, the cuts on the isolation and on the TTVA⁹ for leptons are removed. A tag and probe method is then applied, whereby the events with two opposite sign $e\mu$ are selected. One of the leptons, defined as the tag, is requested to have a match with the trigger, to pass the standard isolation cut and to pass the cut on the TTVA in order to select a good control sample. The second lepton, the probe, is used to study isolation efficiency. If both leptons pass the requirement, they are both taken as probe and tag.

Considering electrons and muons separately, the Monte Carlo and data isolation efficiency cut ε_j can be expressed, in the sample with j b -tagging jets, as:

$$\varepsilon_j = \frac{N_j^{p,p}}{N_j^p} = 1 - \zeta_j \quad (5.23)$$

where $N_j^{p,p}$ is the number of prompt leptons which pass the isolation request, N_j^p is the total number of prompt leptons and ζ_j is the fraction of prompt probe leptons which fail the lepton isolation cut. For the data measurements, it may be useful to define ζ_j as:

$$\zeta_j = \frac{N_j^{p,f}}{N_j^p} = \frac{N_j^{d,f} - N_j^{d,ff} - B_j^{MC,pf}}{N_j^d - N_j^{d,ff} - N_j^{d,fp} - B_j^{MC,p}} \quad (5.24)$$

where $N_j^{d,f}$ is the number of data leptons which fail the isolation request, N_j^d is the total number of leptons in the data sample, $N_j^{d,ff}$ and $N_j^{d,fp}$ are respectively the number of mis-identified (mis-ID) leptons in data which fail and pass the isolation cuts, $B_j^{MC,pf}$ is the

⁹ $|\frac{d_0}{\sigma_{d_0}}| < 5$ and $|z \cdot \sin(\theta)| < 0.5$ for the electrons, as described in Section 4.2.1, and $|\frac{d_0}{\sigma_{d_0}}| < 3$ and $|z \cdot \sin(\theta)| < 0.5$ for the muons, as described in Section 4.3.1

number of prompt background leptons which fail the isolation request and $B_j^{MC,p}$ is the total number of prompt background leptons. Both $B_j^{MC,pf}$ and $B_j^{MC,p}$ are evaluated using the yield obtained from the Monte Carlo samples.

Lepton isolation scale factors are obtained as a function of the number of b -tagging jets (j), lepton type, p_T and barrel/end-cap region:

$$SF_{p_T,\eta}^{j,lepton} = \frac{\varepsilon_{p_T,\eta}^{data}}{\varepsilon_{p_T,\eta}^{MC}} \quad (5.25)$$

where $\varepsilon_{p_T,\eta}^{MC}$ and $\varepsilon_{p_T,\eta}^{data}$ are respectively the Monte Carlo and data isolation efficiency.

Electron and muon scale factors are measured separately using $t\bar{t}$ events and are referred to as $t\bar{t} \rightarrow e\mu$ scale factors.

Monte Carlo and data efficiencies and the scale factors are calculated as a function of the lepton p_T and are categorised according to whether the lepton fell within the barrel ($|\eta| \leq 1.5$) or end-cap ($|\eta| > 1.5$) region. Eight bins of lepton p_T (from 25 to 150 GeV) are used in the barrel. Leptons with $p_T > 65$ GeV for the end-cap and $p_T > 150$ GeV for the barrel are included in the last bin of the end-cap and of the barrel respectively. In the end-cap region, three bins are used (from 25 to 65 GeV) and for display purpose they are shown in this way:

- bin from -35 to -15 GeV means $p_T \in [25, 45] \text{ GeV}$ and $|\eta| > 1.5$;
- bin from -15 to 5 GeV means $p_T \in (45, 65] \text{ GeV}$ and $|\eta| > 1.5$;
- bin from 5 to 25 GeV means $p_T \in (65, \infty) \text{ GeV}$ and $|\eta| > 1.5$;

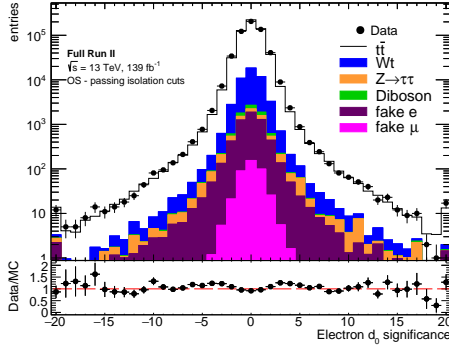
This arrangement is referred to as “extended lepton p_T ” in the text and figures below.

The measurements of the data isolation efficiencies in the Equation 5.24 are sensitive to the mis-identified leptons background contamination. These are estimated using two methods:

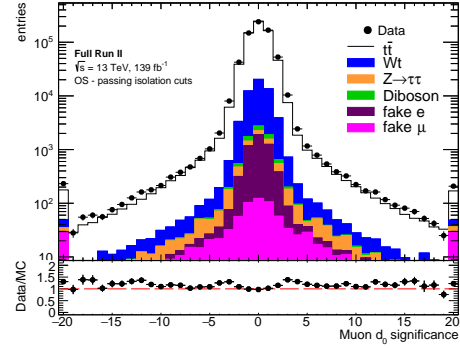
- $N_j^{d,fp}$, which is a marginal term to the total yield and it is evaluated using the same method described in Section 5.5.1;
- $N_j^{d,ff}$, which is a dominant term in the failing isolation region and it is evaluated using the $high - |\frac{d_0}{\sigma_{d_0}}|$ method [133, 135]. This is based on the measurements of the number of data events in the OS high-d0 region rescaled to the ratio between the events SS in the “high-d0 region” and the total number of events, as shown in Equation 5.27. This method is more accurate because high-d0 regions are populated only by mis-identified leptons.

The high-impact parameter significance sub-samples (high-d0) of the opposite and same sign samples failing the isolation requirements are defined by requiring $|\frac{d_0}{\sigma_{d_0}}| > 5$ for electrons and $|\frac{d_0}{\sigma_{d_0}}| > 3$ for muons. The $\frac{d_0}{\sigma_{d_0}}$ distributions for the events with more than zero b -tagging jets are shown in Figure 5.14. The inclusive, failing isolation and high-d0

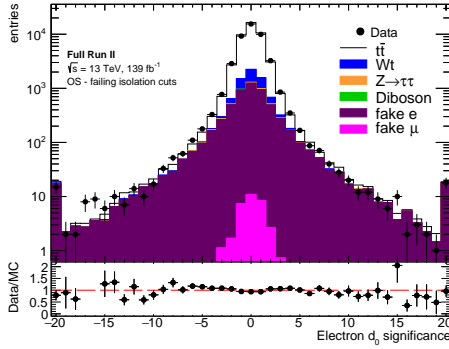
numbers of events for data and simulation in the opposite sign and region are reported in Table 5.6, together with the number of predicted mis-identified leptons from simulation and the percentage of mis-identified leptons per region.



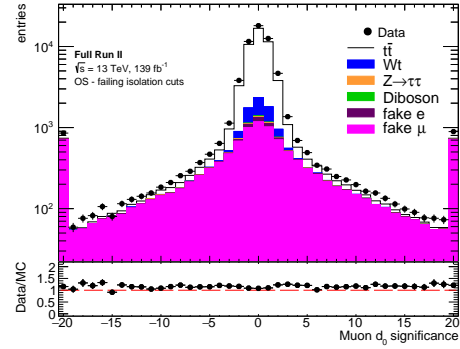
(a) Impact parameter significance for electrons passing the isolation cut in opposite sign for events with at least one b -tagged jet.



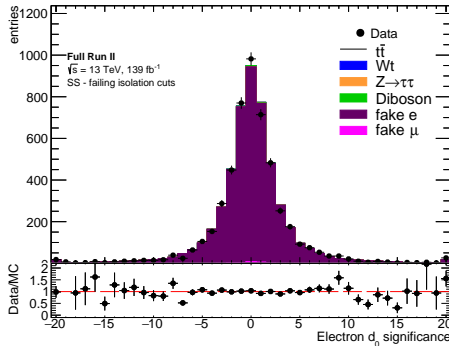
(b) Impact parameter significance for muons passing the isolation cut in opposite sign for events with at least one b -tagged jet.



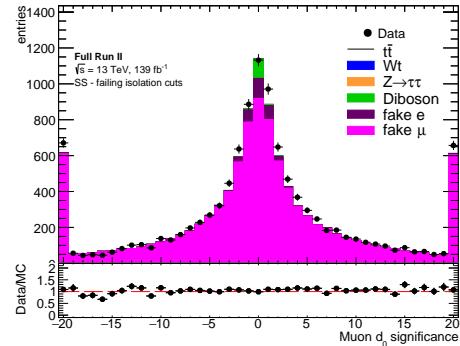
(c) Impact parameter significance for electrons failing the isolation cut in opposite sign for events with at least one b -tagged jet.



(d) Impact parameter significance for muons failing the isolation cut in opposite sign for events with at least one b -tagged jet.



(e) Impact parameter significance for electrons failing the isolation cut in same sign for events with at least one b -tagged jet.



(f) Impact parameter significance for muons failing the isolation cut in same sign for events with at least one b -tagged jet.

Figure 5.14: Impact parameter significance for electron and muons in three different regions. The Full Run 2 data is shown compared to the simulation prediction using the $t\bar{t}$ and background events, normalised to the same number of selected leptons as the data.

The opposite sign fail-isolation region is not sufficiently pure in mis-identified leptons

Selection	Sample	Electron 1 b -tag	Electron 2 b -tag	Muon 1 b -tag	Muon 2 b -tag
Inclusive OS	Data	393291	206889	483562	254822
	Simulation	430016	217666	494782	249610
	mis-IDs from sim.	9049 (2 %)	2332 (1 %)	15020 (3 %)	2780 (1 %)
Inclusive SS	Data	7902	1656	13522	2096
	Simulation	7599	1528	12465	1708
	mis-IDs from sim.	7407 (97 %)	1519 (99 %)	12138 (97 %)	1696 (99 %)
Fail-Iso OS	Data	30337	13376	43020	18144
	Simulation	32643	14063	40652	16660
	mis-IDs from sim.	5006 (15 %)	669 (4 %)	11030 (27 %)	1188 (7 %)
Fail-Iso SS	Data	4541	430	10014	804
	Simulation	4555	431	9502	713
	mis-IDs from sim.	4537 (99 %)	431 (99 %)	9375 (98 %)	711 (99 %)
High-d0 OS	Data	2562	1031	10830	3209
	Simulation	2196	811	9818	2688
	mis-IDs from sim.	666 (30 %)	56 (6 %)	5050 (51 %)	442 (16 %)
High-d0 SS	Data	729	82	4615	324
	Simulation	710	82	4352	292
	mis-IDs from sim.	708 (99 %)	82 (99 %)	4345 (99 %)	292 (99 %)

Table 5.6: Event counts for data, simulation and number of predicted mis-identified leptons from simulation (and the corresponding fraction of mis-identified leptons) for opposite sign and same sign region. High-d0 regions are with $|d_0/\sigma_{d_0}| > 5$ for electrons and $|d_0/\sigma_{d_0}| > 3$ for muons.

background as shown in Figure 5.14c, Figure 5.14d, and in Table 5.6. The same sign fail-isolation regions, instead, are composed almost entirely of mis-identified leptons as shown in Figure 5.14e, and 5.14f and can be used as a template for the mis-identified leptons $|d_0/\sigma_{d_0}|$ distribution in the opposite sign fail-isolation samples, allowing the mis-identified leptons contribution in this latter sample to be normalised using the number of events in the high-d0 region. The $N_j^{d,ff}$ can be therefore determined as:

$$N_j^{d,OS,ff} = N_j^{d,OS,ff,high-d0} \cdot (H_j)^{-1} \quad (5.26)$$

where $N_j^{d,OS,ff,high-d0}$ is the number of mis-identified leptons in the opposite sign high-d0 region in data and H_j is the fraction of mis-identified leptons failing isolation cut that also have high-d0. These two are calculated as:

$$N_j^{d,OS,ff,high-d0} = N_j^{d,OS,f,high-d0} - N_j^{MC,OS,f,high-d0,p} \quad (5.27)$$

$N_j^{d,OS,ff,high-d0}$ is measured from the number of opposite sign leptons failing the isolation cut and that have high-d0 ($N_j^{d,OS,f,high-d0}$), from which it is subtracted the number of prompt leptons obtained from Monte Carlo ($N_j^{MC,OS,f,high-d0,p}$).

$$H_j = \frac{N_j^{d,SS,f,high-d0}}{N_j^{d,SS,f}} \quad (5.28)$$

H_j is measured from $N_j^{d,SS,f,high-d0}$ and $N_j^{d,SS,f}$ which are the number of leptons in the same sign region than have failed the isolation cut and are respectively in the high-d0 region or in all the $|d_0/\sigma_{d_0}|$ spectrum. The number of mis-identified leptons which fail the isolation cut is shown in Figure 5.15.

The uncertainty on the efficiency isolation measured using the data depends on the mis-identified uncertainties, and in particular, it is affected by the uncertainties on the fail mis-identified leptons. The uncertainty on the data efficiency isolation has three contributions coming from mis-identified leptons:

- uncertainty on $N_j^{d,OS,f,high-d0}$, which is the opposite sign data statistical uncertainty;
- uncertainty on $N_j^{MC,OS,f,high-d0,p}$, which is set to 25% based on the level of agreement between data and simulation in Figure 5.14c, 5.14d;
- uncertainty on H_j , which depends on the data statistics in the same sign selection.

The fraction of data events with high-d0 to its total number is similar for events with one and two b -tagged jets.

Figure 5.15 shows that in the failing-cut sample the mis-identified leptons contribution is not negligible compared to the total number of events passing the isolation requirements.

Using equations 5.23, and 5.24 the data isolation efficiencies are obtained and, they are shown in Figure 5.16 together with the Monte Carlo isolation efficiencies.

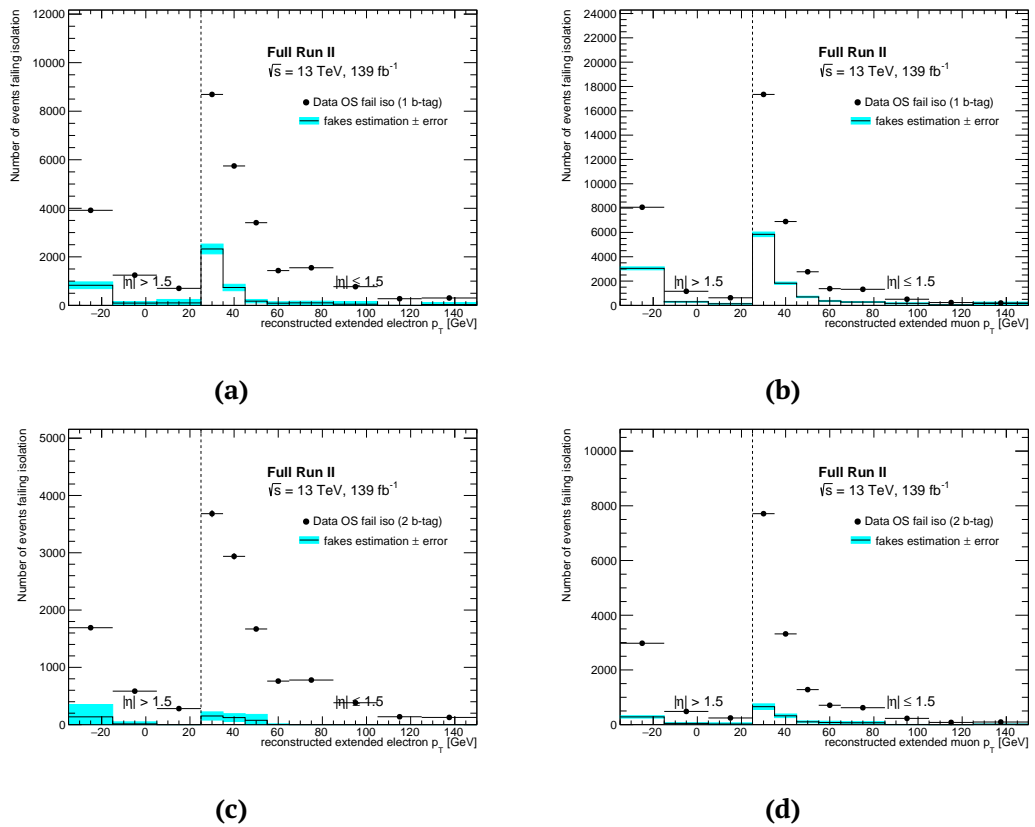


Figure 5.15: The plots show the number of events in the opposite sign failing isolation cut as a function of the extended p_T (see text for details). The left plots are for the electrons while the right for the muons. The dots are the total number of events while with the black line the estimated contribution from mis-identified leptons with its uncertainty indicated by the blue band.

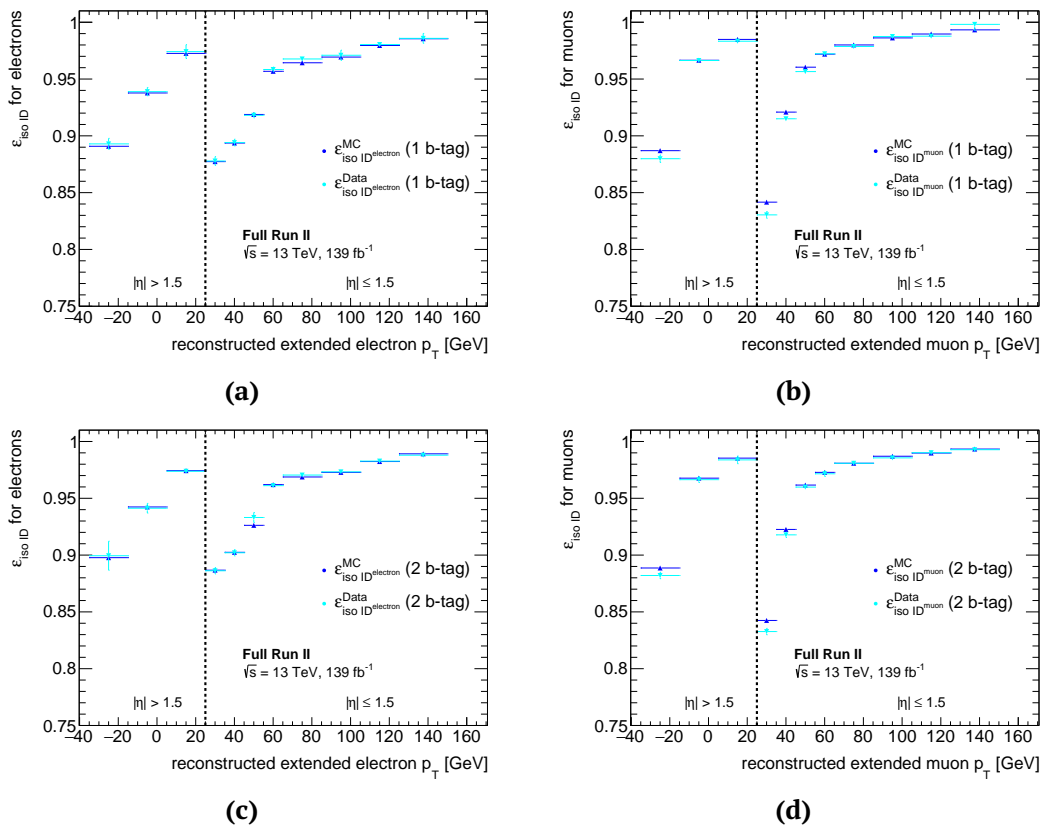


Figure 5.16: Data and Monte Carlo isolation efficiencies measured as a function of the extended p_T (see text for details) for electron (left plots) and muons (right plots).

The $t\bar{t} \rightarrow e\mu$ scale factors are obtained using Equation 5.25 and compared to the scale factors measured from $Z \rightarrow \ell\ell$ events, as shown in Figure 5.17. The error bars in this plot are calculated using the up and down variation for the $Z \rightarrow \ell\ell$ scale factors, while for the $t\bar{t}$ scale factors errorbars are calculated using the data and Monte Carlo efficiency errors propagation. The efficiencies, however, have an asymmetric error and therefore, for the estimation of the error associated to the scale factors, the error is propagated using the maximum variation between up/down for both Monte Carlo and data efficiency. The plots in Figure 5.17, show that the scale factors (obtained from $t\bar{t} \rightarrow e\mu$ events) are perfectly compatible within errors with the ones obtained from $Z \rightarrow \ell\ell$.

The nominal isolation $Z \rightarrow \ell\ell$ scale factors are in this analysis substituted with isolation scale factor measured with $t\bar{t} \rightarrow e\mu$.

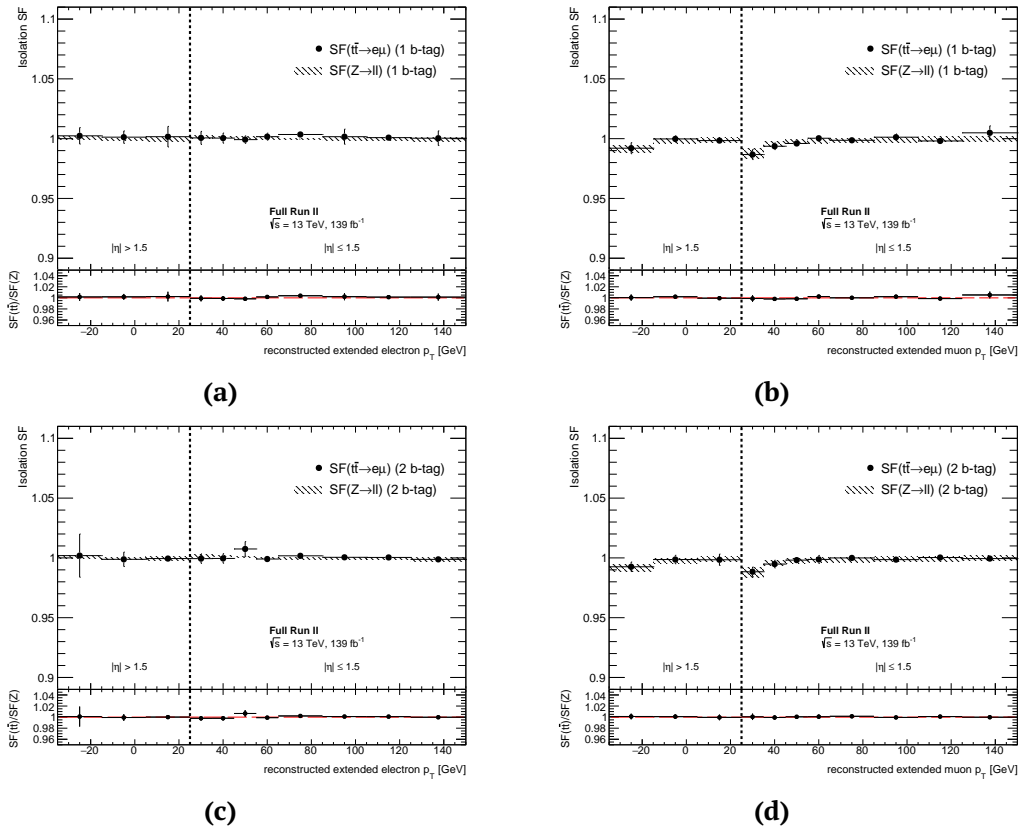


Figure 5.17: Scale factors measured in situ using $t\bar{t}$ events (dots) for electrons and muons as a function of the extended p_T (see text for details) for one (up) and two (down) b -tagged jets. The scale factor obtained from $Z \rightarrow \ell\ell$ events and its error are also shown as hatched band. The ratio is showing the relative differences between $SF(t\bar{t} \rightarrow e\mu)$ and the $SF(Z \rightarrow \ell\ell)$. In all the regions, the two scale factor types are perfectly compatible within errors.

Using the technique described above it is possible to obtain scale factors ad-hoc for different $t\bar{t}$ samples. To derive these scale factors for alternative Monte Carlo $t\bar{t}$ samples, the nominal POWHEG + PYTHIA 8 sample is replaced by the alternative one. Therefore to obtain the Monte Carlo efficiency per each $t\bar{t}$ samples, the terms $N_j^{p,p}$ and N_j^p of the Equation 5.23 will change, while to measure the data efficiency only the mis-identified lepton background

estimation will change. In particular the terms $N_j^{MC,OS,f,high-d0,p}$ of Equation 5.27, and $N_b^{i,MC-promptRS,SS}$ of Equation 5.20 will change in reference to the estimation of the number of mis-identified passing the isolation cut ($N_j^{data,fp}$) and failing the isolation cut ($N_j^{data,ff}$) which enters in the Equation 5.24. These scale factors are used instead of the nominal ones (from POWHEG + PYTHIA 8) to reweight the corresponding $t\bar{t}$ samples.

5.7 Data-Monte Carlo comparison at detector level

The event count for the Full Run 2 dataset is presented in Table 5.7, and the number of events for different b -jet multiplicities can be seen in Figure 5.18. The Monte Carlo contribution has been normalised to the same integrated luminosity as the data and corrected with the appropriate lepton, pileup, b -tagging and JVT scale factors. In the region with more than 2 b -tagging jets, the discrepancy is due to the mis-modelling of the $t\bar{t}$ + heavy flavour.

The kinematic variables derived with the selected $e\mu$ events with either one or two b -jets are shown in Figure 5.19-5.22. In all the distributions of the number of events as a function of a single kinematic quantity, except for the η^l , $\Delta\phi^{e\mu}$ and $|y^{e\mu}|$ distributions, the last bin contains the overflow events. The four two dimensional distributions are shown in Figures 5.20, 5.22. The two dimensional distributions ($X : Y$) are named respectively $|y^{e\mu}| : m^{e\mu}$, $\Delta\phi^{e\mu} : m^{e\mu}$, $\Delta\phi^{e\mu} : p_T^{e\mu}$ and $\Delta\phi^{e\mu} : E^e + E^\mu$ and are unrolled into one dimensional distribution. The dotted vertical lines show the regions of the Y variable for each distribution. In all distributions the grey shaded area both in the histogram and in the ratio plot is an uncertainty band that contains the detector, background and luminosity uncertainties, but not the $t\bar{t}$ modelling uncertainties.

The backgrounds included in the figures are the ones from Wt and t -channel single top-quark events in blue, from di-boson events in green, from $Z \rightarrow \tau\tau$ + jets events in purple, from misidentified leptons in light blue and from $t\bar{t}V$ and $t\bar{t}H$ events in orange and brown respectively. The ratio plots show the data/Monte Carlo agreement.

In the kinematic variables in Figure 5.19a and 5.21a the mis-modelling of the lepton p_T is clear, and it come from the mis-modelling of the p_T of the top-quark in the current Monte Carlo generators due to missing higher order QCD effects in $t\bar{t}$ pair production [33, 136, 137] (see Figure 1.7).

Process	OS - 1 b-tag	OS - 2 b-tags	OS - all $e\mu$ events
$t\bar{t}$	$(4155.4 \pm 1.3) \cdot 10^2$	234117 ± 94	$8388.7 \pm 1.8) \cdot 10^2$
Single top-quark	42604 ± 76	7238 ± 31	$(810.7 \pm 1.1) \cdot 10^2$
Z+jets	1577 ± 65	100.6 ± 7.5	$(90.7 \pm 1.0) \cdot 10^3$
di-boson	1395.3 ± 9.4	49.5 ± 1.1	$(1034.4 \pm 1.5) \cdot 10^2$
mis-ID leptons	$(48.9 \pm 1.0) \cdot 10^2$	1994 ± 67	$(277.0 \pm 9.3) \cdot 10^2$
$t\bar{t}V + t\bar{t}H$	1181.3 ± 4.1	799.7 ± 3.3	2663.7 ± 6.1
Total	$(4671.9 \pm 1.9) \cdot 10^2$	$(2443.0 \pm 1.2) \cdot 10^2$	$(1144.4 \pm 1.4) \cdot 10^3$
Data	$(4684.7 \pm 6.8) \cdot 10^2$	$(2485.7 \pm 5.0) \cdot 10^2$	$(1153.1 \pm 1.1) \cdot 10^3$
Data/MC	1.003 ± 0.015	1.017 ± 0.020	1.008 ± 0.030

Table 5.7: Event counts for the Full Run 2 dataset.

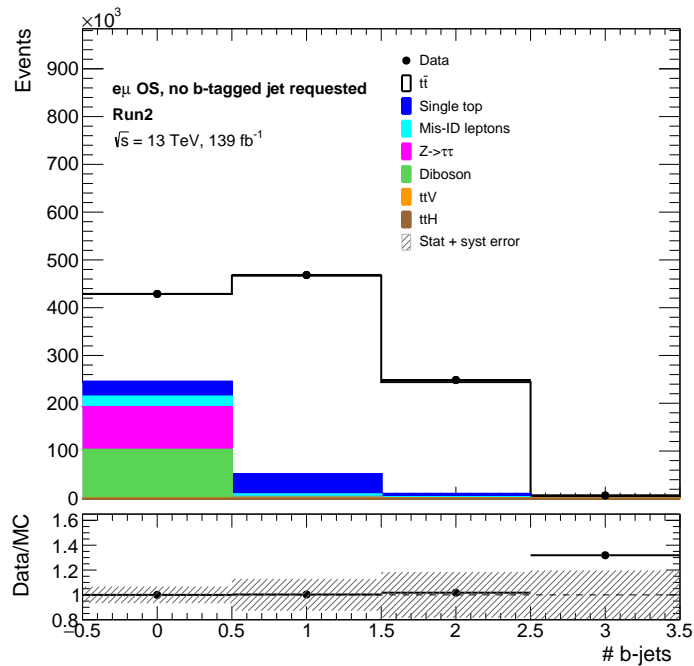


Figure 5.18: Event count for different b -jet multiplicities in the $e\mu$ OS region. The uncertainty band contains the statistical uncertainty, all the experimental and background uncertainties, but no $t\bar{t}$ uncertainties. The blue background comes from single top-quark (Wt and t -channel), the light blue from the misidentified leptons, the purple from the $Z \rightarrow \tau\tau + \text{jets}$, the green from di-boson events, the orange from $t\bar{t}V$ and the brown from $t\bar{t}H$. The lower plot shows the ratio between the number of data events and the predicted events from Monte Carlo.

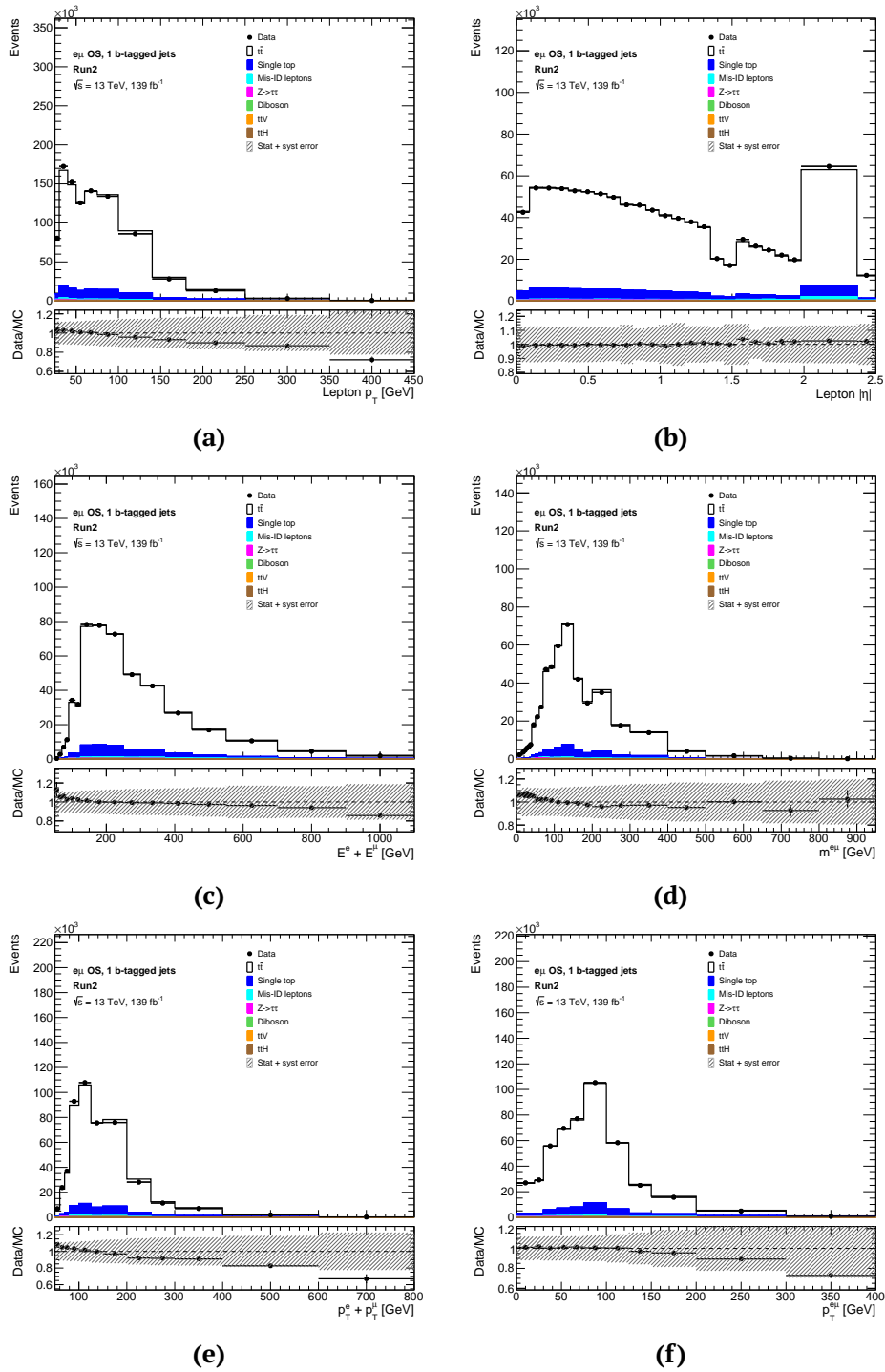


Figure 5.19: Single lepton kinematic variables for $e\mu$ events with one b -jet. The uncertainty band contains the statistical uncertainty, all the experimental and background uncertainties, but no $t\bar{t}$ uncertainties. The backgrounds from single top-quark (Wt and t -channel), misidentified leptons, from $Z \rightarrow \tau\tau + \text{jets}$, from di-boson, from $t\bar{t}V$ and from $t\bar{t}H$ are also plotted. The last bin in the p_T variables contains the overflow events. The lower plots show the ratio between the number of data events and the predicted events from Monte Carlo.

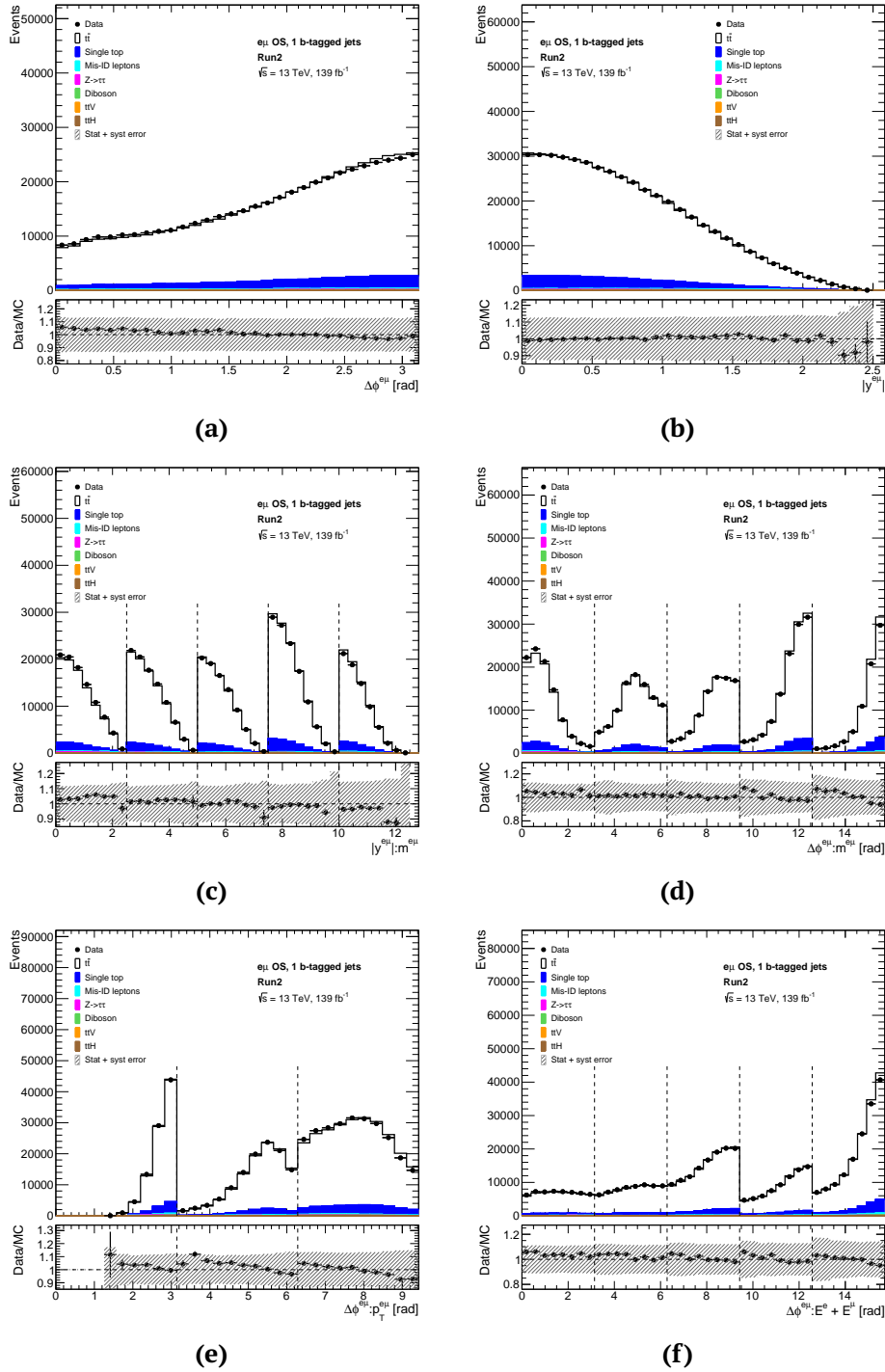


Figure 5.20: Single lepton kinematic variables for $e\mu$ events and unrolled double distribution ($X : Y$) for four combinations of the kinematic variables for $e\mu$ events with one b -jet. The dotted vertical lines show the regions of the Y variable for each distribution. The uncertainty band contains the statistical uncertainty, all the experimental and background uncertainties, but no $t\bar{t}$ uncertainties. The backgrounds from single top-quark (Wt and t -channel), misidentified leptons, from $Z \rightarrow \tau\tau + \text{jets}$, from di-boson, from $t\bar{t}V$ and from $t\bar{t}H$ are also plotted. The lower plots show the ratio between the number of data events and the predicted events from Monte Carlo.

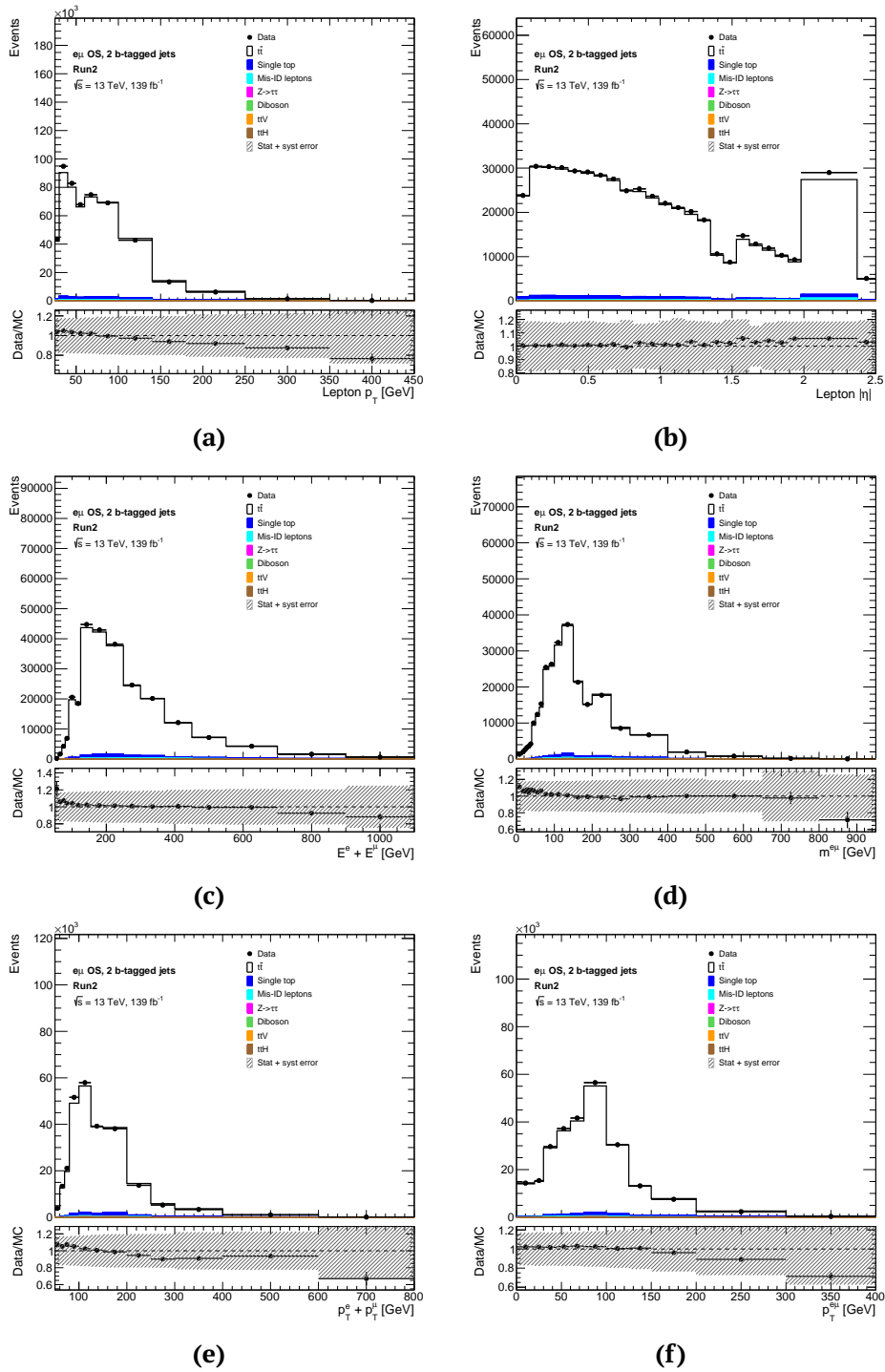


Figure 5.21: Single lepton kinematic variables for $e\mu$ events with two b -jets. The uncertainty band contains the statistical uncertainty, all the experimental and background uncertainties, but no $t\bar{t}$ uncertainties. The backgrounds from single top-quark (Wt and t -channel), misidentified leptons, from $Z \rightarrow \tau\tau + \text{jets}$, from di-boson, from $t\bar{t}V$ and from $t\bar{t}H$ are also plotted. The last bin in the p_T variables contains the overflow events. The lower plots show the ratio between the number of data events and the predicted events from Monte Carlo.

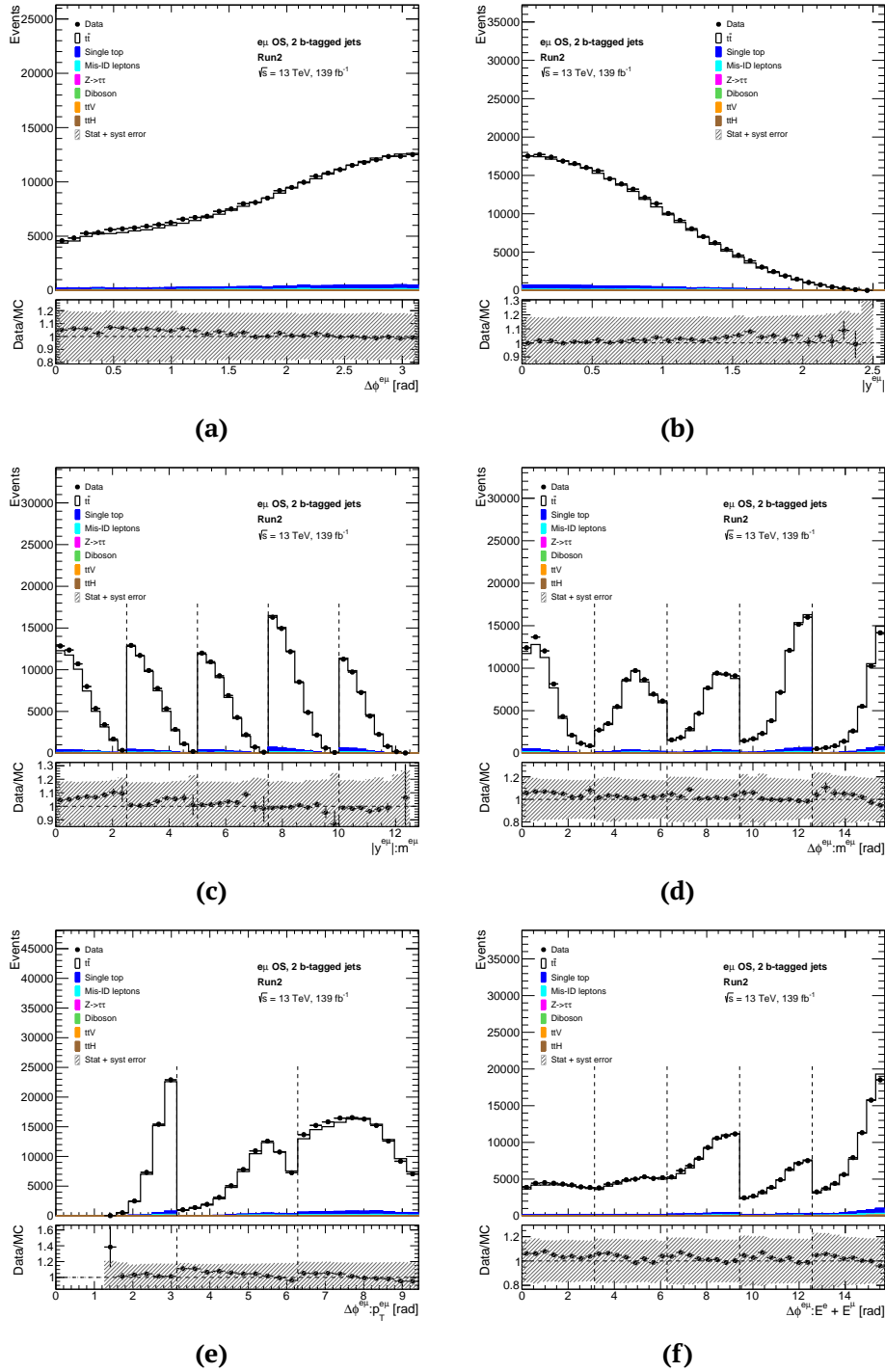


Figure 5.22: Single lepton kinematic variables for $e\mu$ events and unrolled double distribution ($X : Y$) for four combinations of the kinematic variables for $e\mu$ events with two b -jets. The dotted vertical lines show the regions of the Y variable for each distribution. The uncertainty band contains the statistical uncertainty, all the experimental and background uncertainties, but no $t\bar{t}$ uncertainties. The backgrounds from single top-quark (Wt and t -channel), misidentified leptons, from $Z \rightarrow \tau\tau + \text{jets}$, from di-boson, from $t\bar{t}V$ and from $t\bar{t}H$ are also plotted. The lower plots show the ratio between the number of data events and the predicted events from Monte Carlo.

5.8 Analysis method validation

In order to make sure that the analysis technique is not biased, validation tests have been carried out using different strategies based on toy experiments. Many different validation tests are performed:

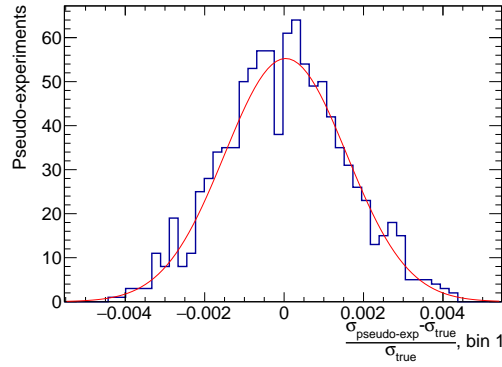
- *Internal bias tests* with a Poissonian fluctuation, to measure the bias of the fit implementation with respect to the statistical sensibility. These are performed using the nominal $t\bar{t}$ POWHEG + PYTHIA 8 sample both to calculate the parameters of the fit (reconstruction efficiency and b -tagging correlation coefficient), and as signal sample to construct the pseudo-data.
- *Stress tests*, to measure the bias of the fit changing the underlying truth distribution of the Monte Carlo sample. These are performed using the nominal $t\bar{t}$ POWHEG + PYTHIA 8 sample to calculate the parameters of the fit (reconstruction efficiency and b -tagging correlation coefficient) and a sample with a different top-quark mass as a pseudo-data sample.
- *Ratio stress tests*, to measure the bias of the fit when the data/Monte Carlo agreement is not equal to unity. The nominal $t\bar{t}$ POWHEG + PYTHIA 8 sample is used to calculate the parameters of the fit (reconstruction efficiency and b -tagging correlation coefficient), but a reweighted sample with the data/Monte Carlo ratio is used to construct the pseudo-data.
- *Closure tests*, to measure the bias using a statistically independent reference and pseudo-data samples. These are performed using half of the nominal $t\bar{t}$ POWHEG + PYTHIA 8 sample to calculate the parameters of the fit (reconstruction efficiency and b -tagging correlation coefficient) and the other half as signal sample to construct the pseudo-data;

5.8.1 Internal bias tests

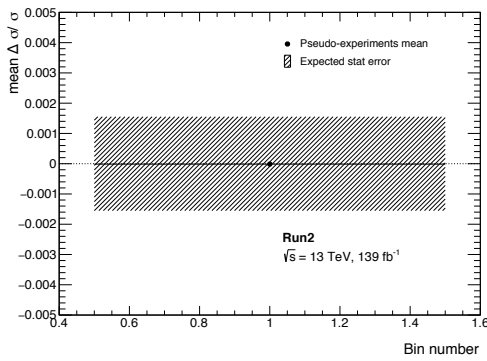
The internal bias tests are carried out using toy Monte Carlo samples as pseudo-data, which are constructed by using the nominal $t\bar{t}$ POWHEG + PYTHIA 8 sample as signal and the nominal estimated background as background. The values of the reconstruction efficiency and b -tagging correlation coefficient are also taken from the nominal $t\bar{t}$ sample. The N_1^i and N_2^i in Equation 5.5 or in Equation 5.15, derived in this case from the Monte Carlo pseudo-data, are fluctuated 1000 times, with the fluctuations being generated as a random number extracted from a Poissonian distribution with N_1^i or N_2^i as parameters. This is done for the total fiducial cross section and repeated for each bin in each differential distribution.

The double tagging fit is performed on all 1000 variations (of each bin independently for the single and double differential variables) and the results are shown in Figure 5.23a. Here the relative difference between the extracted cross section of each experiment ($\sigma_{pseudo-exp}$) and the cross section of the particle level (σ_{true}) is plotted for the total cross section but it

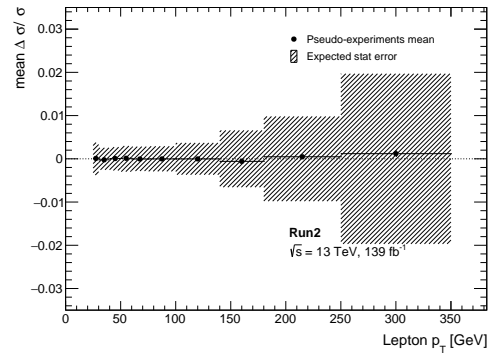
is done for each bin in each distribution. The normalised residuals are then each fitted to a Gaussian, to extract the mean and its error which is then plotted in Figure 5.23b and in Figure 5.23c (black dots). The grey shaded region is the expected statistical error of the Full Run 2. The results for the internal bias tests for all the variables are shown in Appendix D.1.



(a) Results of the 1000 internal bias tests pseudo-experiments where the Monte Carlo pseudo-data bin content is fluctuated 1000 times. The normalised residuals, $(\sigma_{pseudo-exp} - \sigma_{true}) / \sigma_{true}$, are plotted for each experiment and the final results are fitted with a Gaussian function.



(b) Mean extracted from the Poissonian fluctuations fitted to the 1000 internal bias tests pseudo-experiments results. The mean is in all cases consistent with zero within the standard deviation, demonstrating that the double tagging technique has no internal bias within the expect statistical sensitivity.



(c) Mean extracted from the Poissonian fluctuations fitted to the 1000 internal bias tests pseudo-experiments results for each bin in the absolute differential distribution as a function of p_T^l . The mean is in all bins consistent with zero within the standard deviation, demonstrating that the double tagging technique has no internal bias within the expect statistical sensitivity.

Figure 5.23

5.8.2 Stress tests

Stress tests are performed again in the same manner as for the internal bias tests, but instead of using the nominal $t\bar{t}$ POWHEG + PYTHIA 8 sample as signal sample, a sample with a different underlying truth distribution is used.

The aim of these tests is to assess the stability of the double tagging fit by changing the underlying truth distribution of the pseudo-data N_1^i and N_2^i counts, to see if the fit converges towards the truth even when using different samples/underlying distributions. In particular the tests are performed with two samples with varied top-quark mass, one with $m_{\text{top}} = 169$ GeV and another with $m_{\text{top}} = 176$ GeV. The background used is the same as the nominal background. The results for the total cross section are shown in Figure 5.24a and in Figure 5.24c for $m_{\text{top}} = 169$ GeV and in Figure 5.24b and in Figure 5.24d for $m_{\text{top}} = 176$ GeV. The gray shaded region is the expected statistical error of the Full Run 2. In this test a small evidence of bias is present for the total cross section measurement but considering the Monte Carlo statistical uncertainty of the alternative sample the point results compatible with 1 at level of $\sim 1\sigma$. All the results for the single and double differential distributions are shown in Appendix D.2. These tests are called stress tests, since they change the underlying distribution to be tested, without changing the parameters used to unfold to the particle level true cross section, and they aim to assess whether the technique works even if there are unexpected behaviours in the data.

5.8.3 Ratio stress tests

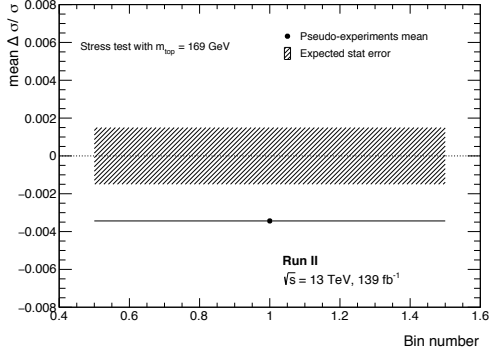
The ratio stress tests are performed using a pseudo-data sample constructed with the nominal samples reweighted. The reweighting is made using the data/Monte Carlo ratio obtained from the one and two b -tagging regions or with 0 weight in case there is no match between particles and reco-level.

These tests aim to assess the stability of the double tagging fit in presence of non-perfect data/Monte Carlo agreements. The only values changed are therefore the N_1^i and N_2^i , while the rest of the parameters remain unchanged and are taken from the nominal values. The reconstruction efficiency and b -tagging correlation coefficient are taken from the nominal $t\bar{t}$ POWHEG + PYTHIA 8 sample with $m_{\text{top}} = 172.5$ GeV and the true cross section is evaluated using the true $t\bar{t} \rightarrow e\mu$ events from the nominal sample.

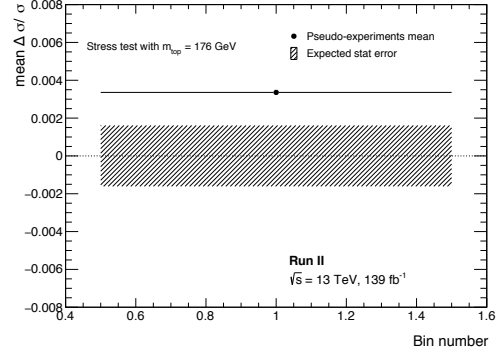
1000 pseudo-experiments are carried out, the $\sigma_{\text{pseudo-exp}} - \sigma_{\text{true}} / \sigma_{\text{true}}$ distributions of the pseudo-experiments are fitted with Gaussian and the result of these are seen in Figure 5.25 (black dots) with the gray shaded region is the expected statistical error of the Full Run 2. The tests for the other variables are shown in Appendix D.3.

5.8.4 Closure tests

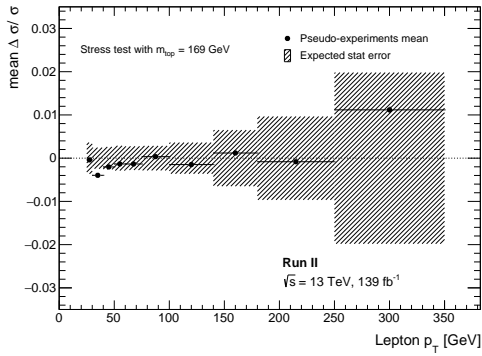
The last tests are the closure tests which are performed to assess the ability of the double tagging fit to converge on the correct answer within the computed uncertainty, using only a part of the Monte Carlo events available. The closure tests aim to test whether the



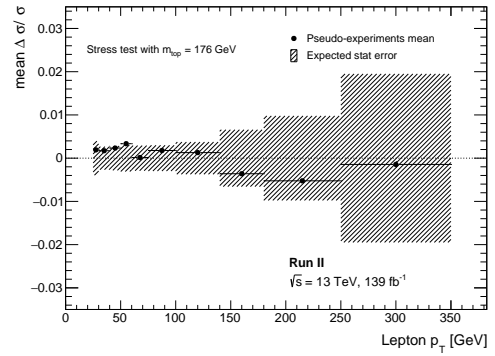
(a) Results of the 1000 pseudo-experiments where the Monte Carlo pseudo-data with $m_{\text{top}} = 169$ GeV is fluctuated 1000 times. The normalised residuals, $(\sigma_{\text{pseudo-exp}} - \sigma_{\text{true}}) / \sigma_{\text{true}}$, are plotted for each experiment and the final results are fitted with a Gaussian function. In this test a small evidence of bias is present but considering the Monte Carlo statistical uncertainty of the alternative sample the point results compatible with 1 at level of $\sim 1\sigma$.



(b) Results of the 1000 pseudo-experiments where the Monte Carlo pseudo-data with $m_{\text{top}} = 176$ GeV is fluctuated 1000 times. The normalised residuals, $(\sigma_{\text{pseudo-exp}} - \sigma_{\text{true}}) / \sigma_{\text{true}}$, are plotted for each experiment and the final results are fitted with a Gaussian function. In this test a small evidence of bias is present but considering the Monte Carlo statistical uncertainty of the alternative sample the point results compatible with 1 at level of $\sim 1\sigma$.

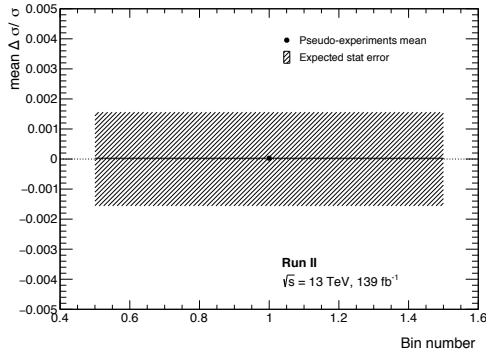


(c) Results of the 1000 pseudo-experiments where the Monte Carlo pseudo-data with $m_{\text{top}} = 169$ GeV is fluctuated 1000 times for each bin in the absolute differential distribution as a function of p_T^l . The mean is in all bins consistent with zero within the standard deviation, demonstrating that the double tagging technique has no bias changing the underlying truth distribution within the expect statistical sensitivity.

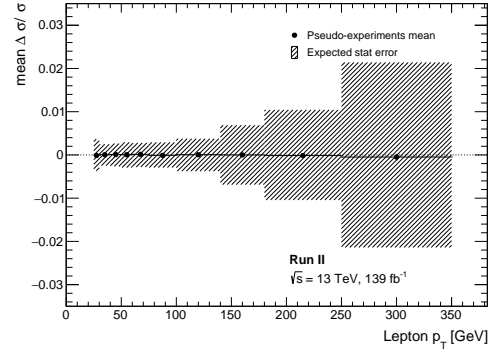


(d) Results of the 1000 pseudo-experiments where the Monte Carlo pseudo-data with $m_{\text{top}} = 176$ GeV is fluctuated 1000 times for each bin in the absolute differential distribution as a function of p_T^l . The mean is in all bins consistent with zero within the standard deviation, demonstrating that the double tagging technique has no bias changing the underlying truth distribution within the expect statistical sensitivity.

Figure 5.24



(a) Mean extracted from the Poissonian fluctuations fitted to the 1000 ratio stress tests pseudo-experiments results. The mean is in all cases consistent with zero within the standard deviation, demonstrating that the double tagging technique has no bias with a non-perfect data/MC ratio within the expected statistical sensitivity.



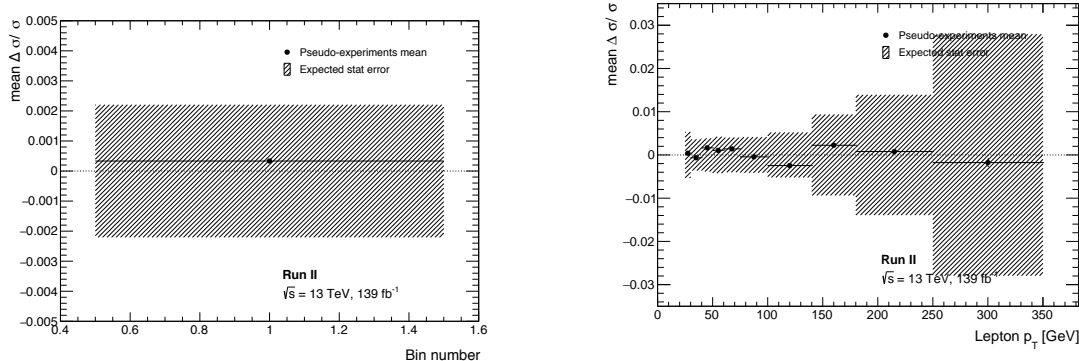
(b) Mean extracted from the Poissonian fluctuations fitted to the 1000 ratio stress tests pseudo-experiments results for each bin in the absolute differential distribution as a function of p_T^l . The mean is in all cases consistent with zero within the standard deviation, demonstrating that the double tagging technique has no bias with a non-perfect data/Monte Carlo ratio within the expected statistical sensitivity.

Figure 5.25

technique works with a statistically independent sample.

The $t\bar{t}$ and background samples are divided into two independent parts by using the Monte Carlo event number, events with an even event number went to one sub-sample and events with an odd event number to the other. One part is used to calculate the $G_{e\mu}^i$, C_b^i , $N_{1,bkg}^i$ and $N_{2,bkg}^i$, while the other is used to calculate the pseudo-data N_1^i and N_2^i values, which are fluctuated 1000 times using a Poissonian distribution with N_1^i and N_2^i as parameter.

The cross section extracted from each pseudo-experiment is compared to the true cross section evaluated using true $t\bar{t} \rightarrow e\mu$ events. The results are shown in Figure 5.26 and in Appendix D.4



(a) Mean extracted from the Poissonian fluctuations fitted to the 1000 closure tests pseudo-experiments results. The mean is in all cases consistent with zero within the standard deviation, demonstrating that the double tagging technique has no bias using an independent sample.

(b) Mean extracted from the Poissonian fluctuations fitted to the 1000 closure tests pseudo-experiments results for each bin in the absolute differential distribution as a function of p_T^l . The mean is in all cases consistent with zero within the standard deviation, demonstrating that the double tagging technique has no bias using an independent sample.

Figure 5.26

5.9 Measurements uncertainty

The measurements of the inclusive and differential cross section are affected by uncertainties deriving from multiple sources. The effect of each uncertainty has been determined by recalculating each parameter of the double tagging technique with new inputs changed according to corrections and resolving the equations to find the shifted cross section. Depending on the systematic uncertainty though, only some of the elements of Equation 5.5 and Equation 5.15 need to be recalculated and therefore the systematic uncertainties have been divided into five major families:

- *Data and MC statistics*: this category is due to the limited statistics of data and Monte Carlo samples and it affects all the elements of the double tagging equations.
- *Detector and reconstructed objects*: this category collects all the systematic uncertainties related to the reconstructed objects, like electrons, muons, jets, b -jets, and the systematic uncertainties related to the detector, such as the pileup. These systematic uncertainties affect all the elements of the double tagging equations.
- *Modelling of $t\bar{t}$ process*: this category is for all the systematic uncertainties connected to the $t\bar{t}$ production, such as ISR and FSR, PDF, parton shower or variation of the Monte Carlo parameters. Since the $t\bar{t}$ sample is not part of the background, these systematic uncertainties affect only the reconstruction efficiency, the acceptance factor and the b -tagging correlation coefficient.
- *Background*: this category is connected to the variation of the different backgrounds, which bring possible variations in the measured cross sections. The background

uncertainties include variations of the background due to Monte Carlo modelling or estimation of data-driven backgrounds. These systematic uncertainties affect only the count of background events in Equation 5.5 and Equation 5.15.

- *Integrated luminosity*: this category is only for the systematic uncertainty on the integrated luminosity. This affects the value of the integrated luminosity in Equation 5.5 and Equation 5.15 and the number of background events.

5.9.1 Data and Monte Carlo statistics

The bootstrapping technique is a re-sampling technique that makes it possible to evaluate statistical uncertainties as well as to uncover correlations between bins of the same and of different distributions [138, 139]. To create toy experiments with bootstrapping, each event used in the analysis (this applies both to data and Monte Carlo events) is assigned a series of weights, each of which is drawn from a Poissonian distribution with mean 1. The event is then filled in the nominal histogram and in a series of replica histograms, where for each replica the event weight is multiplied by the corresponding Poissonian weight for that replica.

The bootstrapping technique is used on data events in order to construct 1000 replicas, meaning that for each bin in each distribution the double tagging technique is solved 1000 times, each time with a bootstrapped number of data events N_1^i and N_2^i . The reconstruction efficiency and b -tagging correlation coefficient are taken from the nominal $t\bar{t}$ POWHEG + PYTHIA 8 sample, while the number of background events is taken from the nominal background estimates (and are not bootstrapped). The 1000 replicas are then used to find the covariance matrix, which contains information about the bin-to-bin correlation within one variable and amongst bins of different variables and, in the diagonal elements, contains the data statistical uncertainty. The correlation matrix can be extracted and it is shown in Figure 5.27 for both the absolute and normalised differential cross section.

The correlation matrix for the absolute differential cross section shows that there are almost no correlations between bins of one distribution as expected since each bin is filled independently from the other bins in the same distribution, except for the p_T^l variable, since this is filled twice per event, once for the electron and once for the muon (if the electron has a low p_T , the muon has a high probability of having a low p_T as well). There are instead correlations between bins of different distributions and those are mostly positive, especially for $p_T^{e\mu}$, $p_T^e + p_T^\mu$, p_T^l , $E^e + E^\mu$, $m^{e\mu}$, because, for example, an event with high p_T leptons will likely have a high $p_T^{e\mu}$, $p_T^e + p_T^\mu$, $E^e + E^\mu$ and $m^{e\mu}$, $|\eta^l|$, $\Delta\phi^{e\mu}$ and $|y^{e\mu}|$ are not as strongly correlated with other variables as decays are assumed to occur in the hole phase space. When looking at the correlation matrix for the normalised differential cross section the positive correlations between bins of different distributions are still there, and new negative correlations arise between the bins of one distribution, due to the normalisation condition, where all bins are shifted.

The bootstrapping technique is used also on Monte Carlo events (as pseudo-data) in

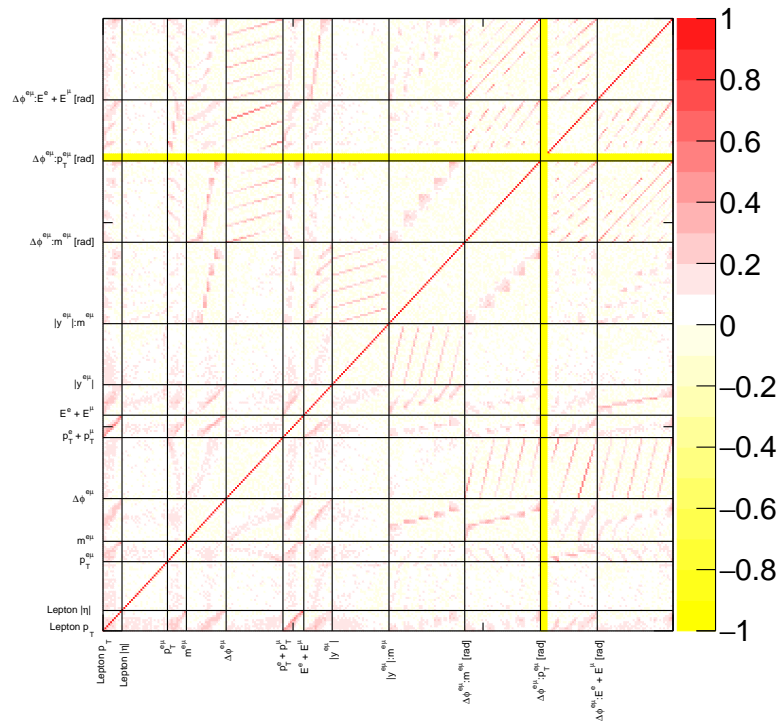
order to construct other 1000 replicas of the nominal $t\bar{t}$ POWHEG + PYTHIA 8 sample as signal and of the background samples. The sum of the signal and background bootstrapped counts are used as pseudo-data in the double tagging technique's N_1^i and N_2^i . In this case, the mis-identified lepton background is not estimated as in the nominal background, but it is taken directly from Monte Carlo by adding all the bootstrapped mis-identified lepton contributions in the OS region. The reconstruction efficiency and b -tagging correlation coefficient are taken from the nominal $t\bar{t}$ POWHEG + PYTHIA 8 sample, while the number of background events is taken from the nominal samples. The double tagging equations are solved 1000 times for each bin in each differential distribution.

The correlation matrix, extracted from these experiments, is shown in Figure 5.28 for both the absolute and normalised differential cross section. The same tendencies are seen as in the data bootstrapping experiments. Again here, the diagonal elements of the covariance matrices for the differential distributions can be used as the Monte Carlo statistical uncertainty.

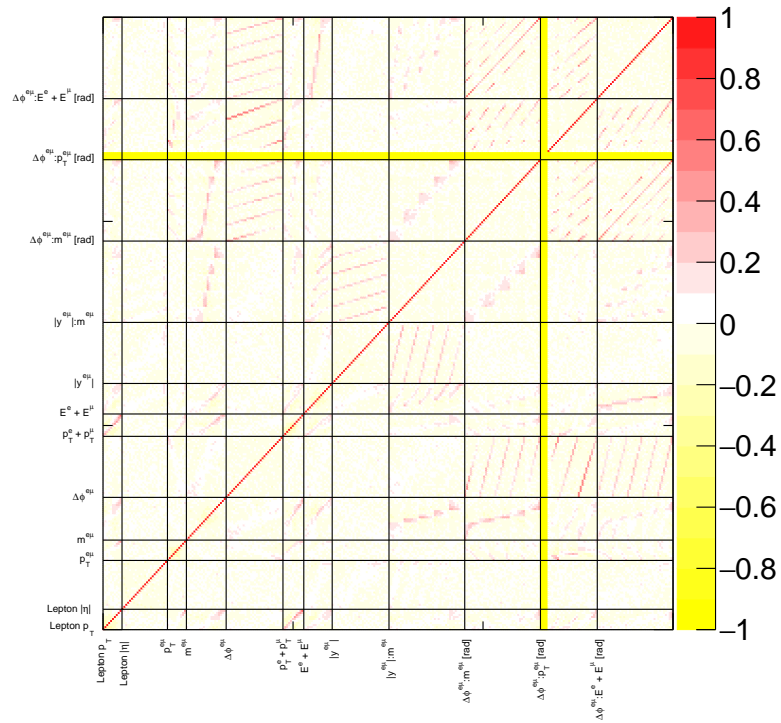
5.9.2 Detector and reconstructed objects

Since the events are reconstructed in the detector, the systematic uncertainties that can arise due to features of the detector itself, as event triggering, object reconstruction (electron, muons and jets) and pileup need to be considered. To calculate the effect of a single variation, the ATLAS performance groups provide several packages to calculate the up and down variations or modified weights for each event in Monte Carlo, allowing for the calculation of the cross section for each systematic variation. The considered variation in this analysis are:

- *Electron scale and resolution:* The energy scale and resolution of electrons are calculated using $Z \rightarrow ee$ events and $J/\Psi \rightarrow ee$ events. The uncertainties due to the electron energy scale and energy resolution are calculated by shifting the objects (electrons in this case) in energy [97].
- *Electron efficiency:* The trigger [140], reconstruction [97] and identification efficiencies [141] for electrons are derived with the tag-and-probe technique using $Z \rightarrow ee$ events and $J/\Psi \rightarrow ee$ events and using electrons with $\Delta R(e, jet) > 0.4$ in different η and p_T bins. Scale factors are computed to account for the difference in efficiency in Monte Carlo samples and data. The systematic uncertainties for these scale factors are calculated by shifting them up and down with $\pm 1\sigma$ variation independently. For all the efficiencies the up and down variations are calculated by assuming that the systematic uncertainties on all η and p_T bins are fully correlated, to approximate the up and down variations to one single variation.
- *Muon scale and resolution scale:* The systematic uncertainties related to the μ scale and resolution are a $\pm 1\sigma$ variation of the momentum of the inner detector track, of the muon spectrometer track and of the momentum scale based on different techniques [99]. All these variations are considered separate sources of uncertainty.

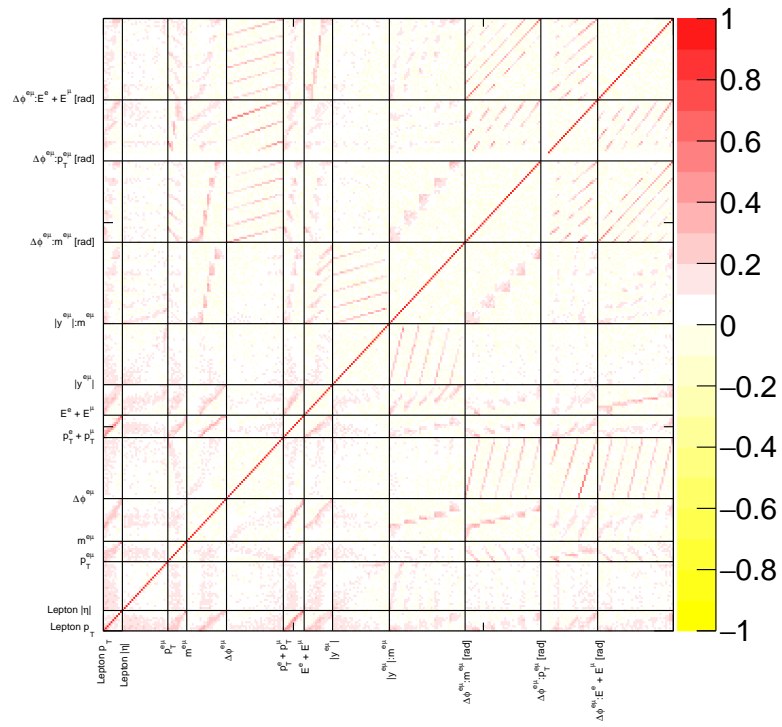


(a)

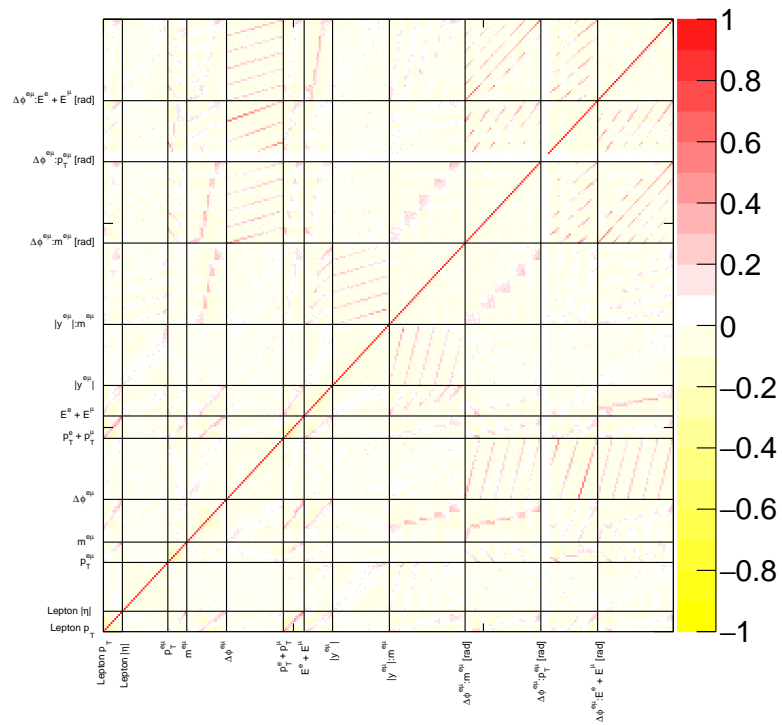


(b)

Figure 5.27: Correlation matrices for the absolute (Figure 5.27a) and normalised (Figure 5.27b) differential cross section from data bootstrapping experiments.



(a)



(b)

Figure 5.28: Correlation matrices for the absolute (Figure 5.28a) and normalised (Figure 5.28b) differential cross section from Monte Carlo bootstrapping experiments.

- *Muon reconstruction efficiency*: The scale factors, to take the muon identification efficiency into account, are derived from J/Ψ and $Z \rightarrow \mu\mu$ events using the tag-and-probe technique [99]. The systematic uncertainties on these scale factors are calculated by shifting the factors up and down with $\pm 1\sigma$ statistic and systematic variations, separately for the low p_T region ($p_T < 15$ GeV) and for the remaining p_T region.
- *Muon trigger and TTVA efficiency*: The scale factors to correct the Monte Carlo to data for μ trigger efficiency and track-to-vertex associations efficiencies are varied up and down with $\pm 1\sigma$ statistical and systematic variations independently [99].
- *Lepton isolation efficiency*: The lepton isolation efficiency scale factors are calculated using $t\bar{t} \rightarrow WbWb \rightarrow e\nu b\mu\nu b$ events as described in Section 5.6. The uncertainties on the cross section due to these scale factors is found by varying them one sigma up/down.
- *JVT*: The jet vertex tagger efficiency scale factor weight is used to correct for the JVT efficiency and hence match Monte Carlo and data. The corresponding systematic uncertainty is found by varying the scale factor weight with its $\pm 1\sigma$ variation, this method though affects the reconstruction efficiency in the total fiducial (and inclusive) cross section with a 0.45% uncertainty. Since the reconstruction efficiency is a purely leptonic variable and does not depend on the number of jets in each event, logically the uncertainty from the JVT cut on this should be zero and the total uncertainty on the cross section should be dictated by the uncertainties on the b -tagging correlation coefficient and on the number of background events.

Before putting the uncertainty from JVT on the reconstruction efficiency to zero, tests need to be done to assess whether this is a fair assumption. In fact, in the reconstruction and selection code, the JVT cut could in principle affect the number of electrons and muons at the reconstruction level, because of the overlap removal procedure. JVT failing jets (so jets probably not coming from a primary vertex) participate in the overlap removal objects, but they cannot remove other objects in the procedure, so electrons and muons within a specific cone of the JVT failing jets are not removed with the rules explained in Table 5.2. This could therefore mean, that there could be a different number of $e\mu$ events at reconstruction level depending on the JVT working point used, which would change the $G_{e\mu}$ with the JVT working point.

In particular, a factor that could contribute to the uncertainty on $G_{e\mu}$ is that JVT failing jets participate in the overlap removal of objects, but they cannot remove other objects. This could lead to a difference in the number of $e\mu$ events at the reconstruction level depending on the JVT working point used, hence changing $G_{e\mu}$ with the JVT working point. Therefore, to have an idea of the actual size of the JVT uncertainty, another method is used to estimate the impact of the JVT cut on $G_{e\mu}$.

For each reconstructed $e\mu$ event used for the analysis, the fraction of leptons removed by overlap removal to the total original number of leptons in the event is calculated. In most of the cases, the fraction of leptons removed in overlap removal is zero, only in 0.1% of the selected $e\mu$ events this is different from zero. This overlap-removed lepton fraction (fraction of leptons removed by overlap removal to the total number of leptons in an event) is multiplied by the relative difference between the JVT efficiency and its up and down variations for each jet in the event. Again, in most of the events this resulted in a zero uncertainty, while in the events where the fraction of leptons removed by overlap removal is bigger than zero, the JVT uncertainty estimated with this method amounted on average to approximately 0.03%, as visible in Figure 5.29. As a further check, the reconstruction efficiency for the three available JVT working points, Tight, Medium (the one used in this analysis) and Loose, is calculated and the relative difference in $G_{e\mu}$ between Medium and Tight and Medium and Loose is of the order of 0.0001%, underlying the fact that the systematic uncertainty coming from JVT on the reconstruction efficiency is very close to zero.

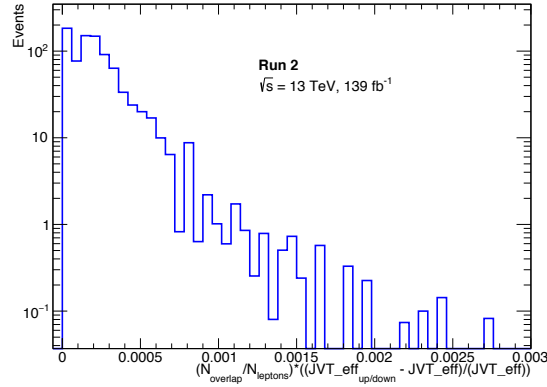


Figure 5.29: Estimation of the JVT uncertainty. The ratio of the number of leptons removed by overlap removal over the total number of leptons multiplied by the relative difference between the JVT efficiency and its up and down variations for each jet in the event is shown.

Given the results of the test above, the error on the reconstruction efficiency in the total and differential cross section can be safely assumed as negligible, so the error from the JVT uncertainty can be calculated by varying the b -tagging correlation coefficient and number of background events with the up and down variations of the JVT scale factor uncertainty, while assuming no variation on $G_{e\mu}$ from the JVT cut.

- *JES effective NPs:* The uncertainties in the jet energy scale are derived using $Z + \text{jet}$, $\gamma + \text{jet}$ and multijet samples at $\sqrt{s} = 13$ TeV with data or simulation calibration corrections [142]. In total 15 nuisance parameters are varied up and down, where all variations are orthogonal to each other and are assumed uncorrelated.

- *JES¹⁰ EtaInterCalibration*: The η intercalibration is a way to calibrate the jet energy scale from jets in the forward region ($0.8 < |\eta| < 4.5$) from jets in the barrel ($|\eta| < 0.8$) [142]. The uncertainty due to this calibration is performed by shifting the energy of the physics objects with the up and down variations of the calibration. The systematic uncertainties components include a statistical component, a modelling component (that accounts for different Monte Carlo generators modelling of the physical objects and pileup modelling) and a non-closure component of the technique in the $2.0 < |\eta| < 2.6$ region.
- *JES flavour*: Jets contain different quark flavours and gluons, but when reconstructing the jet, uncertainties arise on their actual composition. Additionally, the jet energy scale calorimetric response poses a systematic uncertainty [142]. Both those uncertainties are found by shifting the physics objects' energy and momentum with their up and down variations.
- *JES b -jes response*: The uncertainty due to the calorimetric response to b -jets is found by shifting the appropriate physics objects' energy with up and down variations [142].
- *JES pileup*: The jet energy scale pileup uncertainty comes mainly from Monte Carlo simulation modelling, in particular the number of average interactions μ , number of primary vertices N_{pV} and the modelling of the p_T distributions. These uncertainties are found by shifting the physics objects' energy and momentum with the up and down variations of these uncertainties.
- *JES punch-through*: When a jet has such a high p_T , that the jet is no longer contained in the calorimeter, but crosses over to the muon spectrometer, it is denoted as a punch-through jet. Up and down variations due to the correction of these jets are applied to all relevant physics objects to find the corresponding uncertainty.
- *JES high- p_T* : This uncertainty is due to high p_T jets response in the detector and is calculated by shifting the physics objects' energy and momentum with the up and down variations of these uncertainties.
- *MET soft term*: The uncertainties related to missing energy $E_{T,miss}$ receives contributions from the presence of low- p_T jets and calorimeter cells not included in reconstructed objects (the so-called "soft terms"). It is evaluated using $Z \rightarrow \mu\mu$ events from $E_{T,miss}$ data/Monte Carlo in events without jets and from the balance between soft terms and hard objects.
- *JER¹¹*: The jet energy resolution uncertainty is found by using the 7 orthogonal nuisance parameter model, where the object is recalculated for each parameter's up and down variations. Besides the 7 parameters, another uncertainty taking the data

¹⁰Jet Energy Scale

¹¹Jet Energy Resolution

versus Monte Carlo disagreement into consideration is calculated using symmetrised variations.

- *b-tagging*: The *b*-tagging efficiency scale factor for a specific working point is applied to Monte Carlo events through a weight and therefore the uncertainties on the *b*-tagging are calculated by varying this scale factor weight. The uncertainty on *b*-jets efficiency is found with nine eigenvectors (with up and down symmetrisation), the uncertainty on *c*-jets efficiency is found with four eigenvectors and the uncertainty on light jets efficiency is found with five eigenvectors [143].

5.9.3 Modelling of $t\bar{t}$ process

The $t\bar{t}$ related uncertainties have an impact on the reconstruction efficiency and of the *b*-tagging correlation coefficient of the double tagging technique, see Equation 5.5, and on the acceptance factor of Equation 5.13. Most of these uncertainties can be calculated with alternative $t\bar{t}$ samples, others require a reweighting of the nominal sample to generate the variations of the parton shower. The systematic uncertainties considered in this analysis are:

- *h_{damp} variation*: The h_{damp} variation is used as generator systematic uncertainty since it changes the parameters configuration of the Monte Carlo event generation. The variation is found using another $t\bar{t}$ POWHEG+PYTHIA 8 AFII sample, where the h_{damp} parameter is shifted to $3 \cdot m_{top}$, and it is compared with the nominal $t\bar{t}$ POWHEG+PYTHIA 8 AFII sample. The difference between the cross sections obtained with the two samples is taken as up and down uncertainty.
- *Parton shower*: The systematic uncertainty related to the different fragmentation or hadronisation models can be assessed using a different fragmentation model than the one used in the PYTHIA samples, the Lund model. In particular, the HERWIG model is used as an alternative one. Therefore the nominal AFII sample is compared to a sample using the same events, which are showered with HERWIG 7.0.4 instead of PYTHIA 8. The difference between the cross sections obtained with the two samples is taken as up and down uncertainty.
- *ISR*: The initial state radiation systematic uncertainty is used to simulate events with more/less ISR and it is found by reweighting, which adapts the sample to a varied renormalisation and/or factorisation scale.
- *FSR*: The final state radiation systematic uncertainty is used to simulate events with more/less FSR and it is also found by reweighting using internal weights (as previously done for ISR).
- *PDF*: The PDF uncertainty is used to see the impact of changing the PDF during the Monte Carlo event generator and it is again extracted through reweighting of the nominal sample. The default PDF for the nominal sample is NNPDF3.0,

which is one of the PDF's included in PDF4LHC15. In Ref. [144] a recipe is given on how to determine the uncertainty on the PDF for a cross section measurement, and these guidelines are followed. First of all the cross section is calculated with the PDF4LHC15 PDF, by reweighing the nominal sample by changing the Monte Carlo weight with the appropriate weight. The value of the cross section found is then the central value. Afterwards, the cross section is calculated for each of the components of the Hessian PDF4LHC15_30 error set, where each component is orthogonal to the others, again by changing the Monte Carlo weight with the appropriate Hessian PDF4LHC15_30 weight in the nominal $t\bar{t}$ sample. When the cross section is determined both with the central value and with the error set, the PDF uncertainty is found with:

$$\delta^{PDF} \sigma = \sqrt{\sum_{k=1}^{30} (\sigma^{(k)} - \sigma^{(0)})^2} \quad (5.29)$$

where 30 is the number of the vectors of the error set, $\sigma^{(k)}$ is the cross section found with each of the error set weights and $\sigma^{(0)}$ is the cross section found with the central value.

- *Top-quark mass dependence:* Changing the top-quark mass value, several parameters of the double tagging technique change, in particular the reconstruction efficiency, the acceptance factor and the number of background events, since the major background comes from Wt , where the mass of the top-quark mass plays a role. In order to estimate the effect it has on the cross section, the dependence of the different double tagging equations' parameters on the top-quark mass has been studied by varying the yields of $t\bar{t}$ and Wt samples together using samples at top-quark mass values of 169, 171, 172, 172.25, 172.5, 172.75, 173, 174 and 176 GeV.

Figure 5.30a shows the dependence of $G_{e\mu}$ for the total fiducial cross section, where each point is found by $\Delta G_{e\mu}/G_{e\mu} = [G_{e\mu}(m_{\text{top}}) - G_{e\mu}(172.5 \text{ GeV})]/G_{e\mu}(172.5 \text{ GeV})$ and the graph is fitted with a second order polynomial. At the top-quark mass of 172.5 GeV, which is the value used for all the Monte Carlo samples in this analysis, the derivative of the efficiency with respect to m_{top} is found in order to have an estimate of the dependence of the reconstruction efficiency on the mass of the top, and its value is $0.096 \pm 0.005 \text{ \%/GeV}$, as reported in Table 5.8 (the uncertainty on the value is found by calculating the derivative at 173.5 and 171.5 GeV and finding the difference with the central value). In the same way, the dependence of C_b on the top-quark mass is $0.001 \pm 0.004 \text{ \%/GeV}$, the dependence of the number of background events with one b -jet on the top-quark mass is $-0.77 \pm 0.02 \text{ \%/GeV}$ and the dependence of the number of background events with two b -jets is $-0.55 \pm 0.04 \text{ \%/GeV}$, as reported in Table 5.8 and shown in Figure 5.30. The total effect of these dependencies on the total fiducial cross section amounts to $d\sigma_{fid}^{t\bar{t}}/dm_{\text{top}} = -0.004 \pm 0.003 \text{ \%/GeV}$. The same procedure can be applied to the total inclusive cross section, where $dE_{e\mu}/dm_{\text{top}}$

is $0.470 \pm 0.005 \%/GeV$ and its effect on the total inclusive cross section leads to $d\sigma_{tt}/dm_{top} = -0.379 \pm 0.005 \%/GeV$. These values are not considered as a source of uncertainty for the total fiducial and inclusive cross section and the top-quark mass uncertainty is set to zero by convention as the cross section is quoted for a fixed $m_{top} = 172.5 GeV$.

For the single and double differential cross section the uncertainty is calculated by finding the single and double differential cross section with the varied parameters ($G_{e\mu}^i, C_b^i, N_{1,bkg}^i, N_{2,bkg}^i$) at $\pm 1 GeV$ (from $172.5 GeV$) and symmetrising the difference between the nominal cross section and the ones with varied mass parameters.

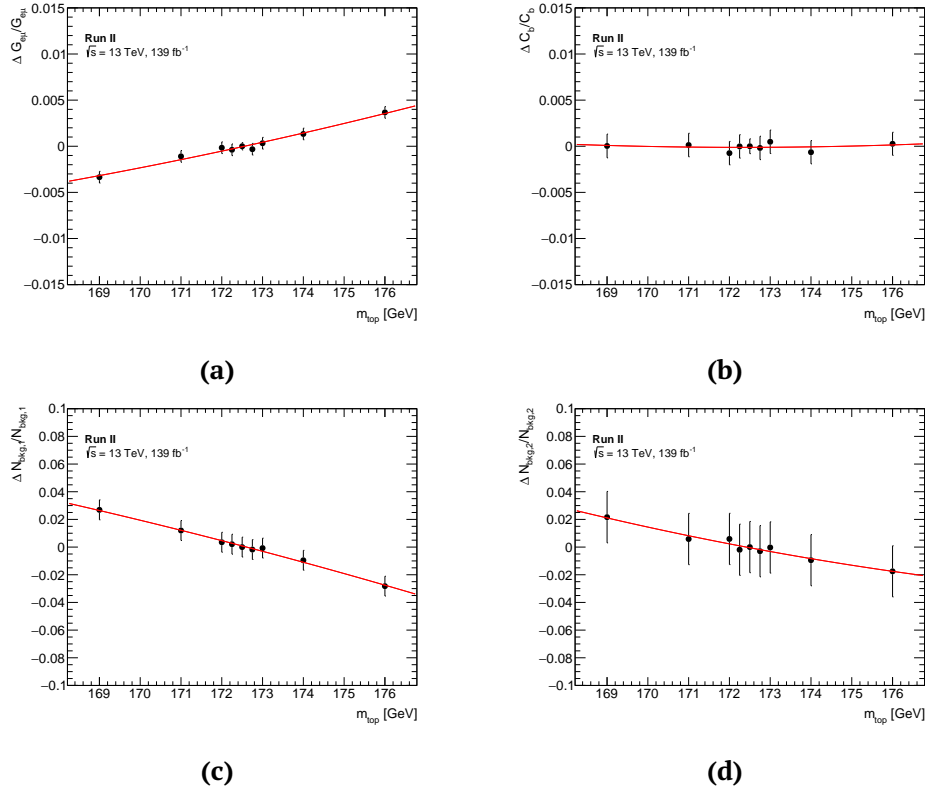


Figure 5.30: Dependence of the double tagging technique parameters on the top-quark mass value.

Quantity	Derivative [%/GeV]
$dG_{e\mu}/dm_{top}$	0.096 ± 0.004
$dE_{e\mu}/dm_{top}$	0.470 ± 0.005
dC_b/dm_{top}	0.001 ± 0.004
$dN_{bkg,1}/dm_{top}$	-0.77 ± 0.02
$dN_{bkg,2}/dm_{top}$	-0.55 ± 0.04
dN/dN_{events}	-0.005 ± 0.003
$dN_{inclusive}/dN_{events}$	-0.379 ± 0.005

Table 5.8: Derivative of the double tagging technique parameters with respect to m_{top} , evaluated at $m_{top} = 172.5 GeV$.

5.9.4 Background

The background related uncertainties are calculated for each different background independently, and they affect only the total number of background events in the double tagging technique, see Equation 5.5. The list of background systematic uncertainties taken into consideration is described below.

- *Wt cross section*: The relative uncertainty on the Wt background theoretical cross section is 5.3% and it is calculated by [145], where the theoretical cross section uncertainty is determined in case of $\sqrt{s} = 7$ or 8 TeV. The theoretical uncertainty at $\sqrt{s} = 13$ TeV is derived with the same methods as for the $\sqrt{s} = 7$ or 8 TeV case [130, 132, 133, 146]. The total Wt background is scaled up and down with 1 ± 0.053 in order to find the up and down variations of this systematic uncertainty.
- *Wt/t \bar{t} interference, DR vs DS*: The interference between $t\bar{t}$ and Wt is handled in the nominal samples using the diagram removal scheme. However, this is not the only choice, as another scheme has been developed, the diagram subtraction scheme, as discussed in Section 1.3.1.2 and in [46]. The difference between the cross section obtained using the two samples to estimated the background is taken as uncertainty.
- *Wt ISR/FSR*: The uncertainty due to initial and final state radiation in the Wt background is derived by reweighting the nominal samples, in the same way as the $t\bar{t}$ samples above.
- *Wt matrix element*: The uncertainty in the matrix element generation is determined by comparing the nominal Wt background with the one generated using the MADGRAPH5_aMC@NLO generator interfaced with PYTHIA 8.
- *Wt parton shower*: The systematic uncertainty due to the hadronisation or fragmentation model is assessed by comparing the nominal Wt background to the one produced with POWHEG interfaced with HERWIG 7, as done for the $t\bar{t}$ parton shower uncertainty.
- *Di-boson cross section*: The uncertainty on the di-boson background theoretical cross section is 6% following [147]. The total di-boson background (derived from the sum of all the sub-sample contributions) is scaled up and down with 1 ± 0.06 in order to find the up and down variations of this systematic uncertainty.
- *Di-boson modelling*: The modelling uncertainty of the di-boson background is assessed through reweighting of the SHERPA sample in order to change the factorisation (μ_F) and renormalisation (μ_R) scale used to generate the SHERPA samples. The seven point scale variation are changed: $(\mu_{R,var}, \mu_{F,var}) \times (0.5\mu_R, 0.5\mu_F)$, $(0.5\mu_R, 1\mu_F)$, $(1\mu_R, 0.5\mu_F)$, $(1\mu_R, 1\mu_F)$, $(1\mu_R, 2\mu_F)$, $(2\mu_R, 1\mu_F)$, $(2\mu_R, 2\mu_F)$. The uncertainty on the di-boson modelling is the envelope of the scale variations.

- *Z+jets scale factor*: The scale factors derived in Section 5.5.2 have a statistical uncertainty due to the limited Monte Carlo events. Several functions have been used to test the fit stability (double Gaussian, crystal ball plus Gaussian, crystal ball plus second-degree polynomial) and the resulting scale factors are compatible with each other. The uncertainty from the fit amounts to less than 1%. To take into account possible errors due to high Monte Carlo weights or variations of these scale factors during the estimation of the lepton systematics (the scale factor is fixed when evaluating the other systematics), a conservative systematic uncertainty of 5% is assigned, both in the one b -jet and the two b -jets region.
- *Z+jets modelling*: The systematic uncertainty due to the shape of the $Z + \text{jets}$ background is estimated using an alternative sample. In particular the nominal SHERPA 2.2.1 samples are compared to POWHEG + PYTHIA 8 samples. The scaling factors to be applied to the $Z \rightarrow \tau\tau + \text{jets}$ sample are recalculated using the alternative $Z \rightarrow ee + \text{jets}$ samples and $Z \rightarrow \mu\mu + \text{jets}$ samples as done for the nominal sample (described in Section 5.5.2) and as shown in Figure 5.31 and Table 5.9. The POWHEG + PYTHIA 8 samples in the two b -jets selection, see Figure 5.31c and 5.31d have a larger Monte Carlo/data discrepancy than the corresponding selection with the SHERPA 2.2.1 samples. This could be caused by the fact, that POWHEG + PYTHIA 8 does not have the matrix elements for $Z + b\bar{b}$ production, generating the two b -jet final state only via the parton shower. This means, that the normalisation factor extracted for these samples is higher than for the SHERPA 2.2.1. samples, as shown in Table 5.9. This difference leads to an uncertainty of approximately 0.05% on the total fiducial cross section.

Selection/number of b -jets	1 b -jet	2 b -jets
$Z \rightarrow ee + \text{jets}$	1.154 ± 0.002	2.15 ± 0.02
$Z \rightarrow \mu\mu + \text{jets}$	1.314 ± 0.002	2.42 ± 0.02
Total	1.244 ± 0.001	2.30 ± 0.01

Table 5.9: Factors extracted from the $Z \rightarrow ee + \text{jets}$ and the $Z \rightarrow \mu\mu + \text{jets}$ control regions for the POWHEG + PYTHIA 8 samples.

- *Mis-identified lepton background*: When performing the estimate of the number of mis-identified leptons in the OS region using Equation 5.20, the R_b^i factor derived from Monte Carlo and the $N_b^{i,promptRS,SS}$, the number of SS prompt events from Monte Carlo estimations, are affected by systematic uncertainties. The origin of these systematic uncertainties is the fact that several assumptions are made both on the mechanisms to produce the secondary or mis-identified leptons, and on instrumental effects that result in mis-identified leptons. The number of data events $N_b^{i,data,SS}$ has also a statistical uncertainty, and this contribution is also included. For each detector, systematic uncertainty, the values of R_b^i and $N_b^{i,prompt,SS}$ are recalculated and a new estimate of the mis-identified lepton background is performed, while for the

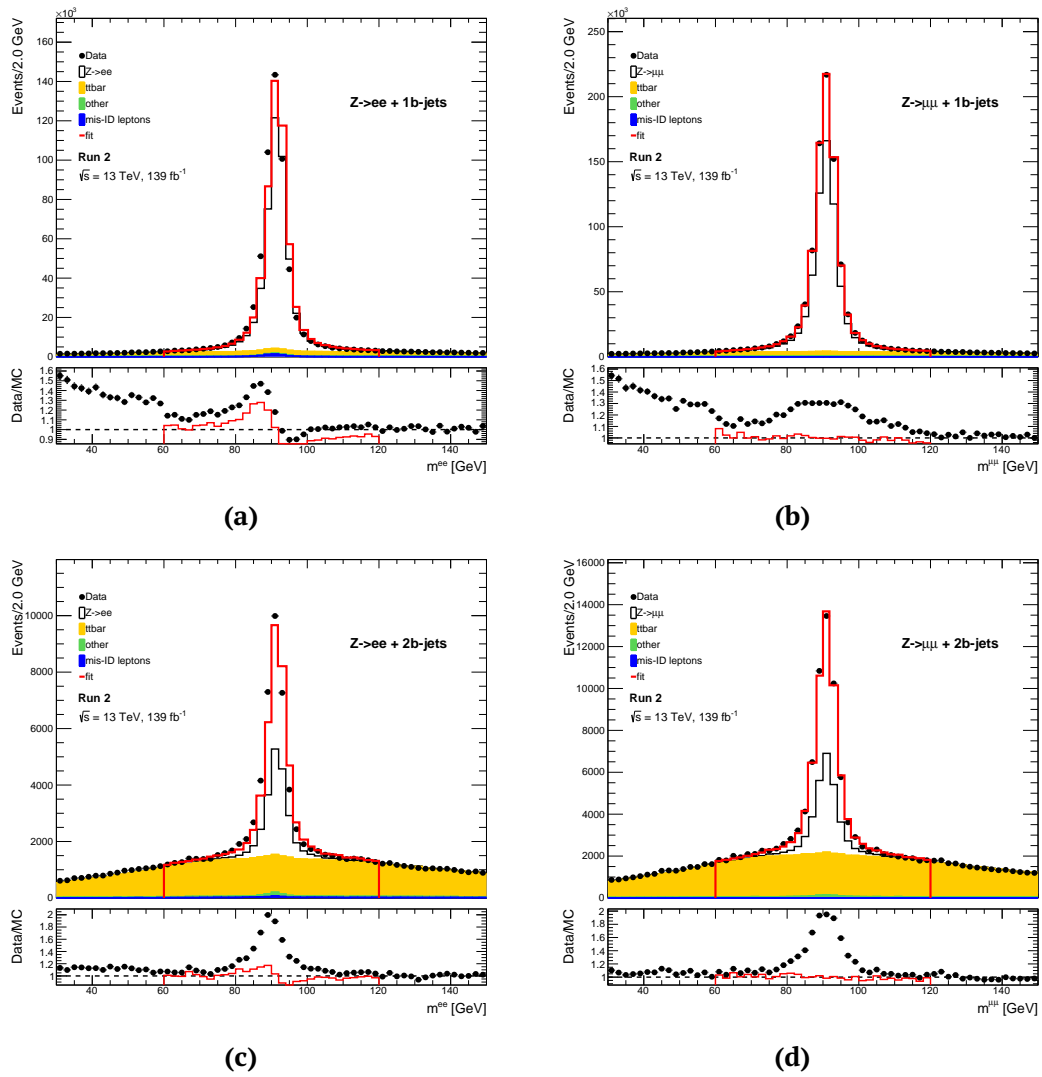


Figure 5.31: Control regions to extract the Z scale factor that normalises the POWHEG + PYTHIA 8 simulated $Z \rightarrow ee$ and $Z \rightarrow \mu\mu$ signals to data. Different components, as $t\bar{t}$, di-boson and mis-identified leptons are also included as part of the background. The fit to extract the Z scale factor is performed between 60 GeV and 120 GeV.

rest of the $t\bar{t}$ and background uncertainties, these numbers are taken as their nominal values. This does not mean though, that these values could not be affected by a different fragmentation model, for example, or by one of the background samples. For this reason, instead of recalculating the mis-identified lepton background each time, a conservative 50% systematic uncertainty on the number of prompt RS events in the SS region is applied, both for the one and two b -jets selections, while the R_b^i are varied up and down, with 25% for the one b -jet sample and with 50% for the two b -jet sample [130, 132, 133, 148]. where the up variation is defined as $R_b^i + \sigma_{R_b^i}$ and the down variation is $R_b^i - \sigma_{R_b^i}$, where the $\sigma_{R_b^i}$ is calculated using error propagation of Equation 5.21.

- *$t\bar{t}V$ cross section*: The uncertainty on the $t\bar{t}V$ cross section is 13% following [149]. The total $t\bar{t}V$ background is scaled up and down with 1 ± 0.13 in order to find the up and down variations of this systematic uncertainty.

5.9.5 Luminosity

The integrated luminosity uncertainty affects two parts of the double tagging technique, one is the value itself of the integrated luminosity, which is included in Equation 5.5 and in Equation 5.15, the other is the number of background events. The reconstruction efficiency and the b -tagging correlation coefficient are not affected, as they are ratios and are hence not affected by normalisation uncertainties.

The uncertainty in the combined 2015 – 2018 integrated luminosity is 1.7% [150], obtained using the LUCID-2 detector [151]. It is derived from the calibration of the luminosity scale using x - y beam-separation scans, following a methodology similar to that detailed in Ref. [152], and using the LUCID-2 detector for the baseline luminosity measurements [151].

The \mathcal{L} and the total background are scaled up and down with 1 ± 0.017 in order to find the up and down variations of this systematic uncertainty.

5.9.6 LHC beam energy

The beam energy value is one of the parameters the theoretical value of the cross section depends on and therefore it needs to be taken into consideration in the systematic uncertainty evaluation. The uncertainty on the cross section due to the LHC beam energy is considered as an experimental uncertainty and added to the rest of the systematic uncertainties. The uncertainty on the LHC beam energy is evaluated to be 0.1% [153]. Given this value, the beam energy uncertainty is parametrised in [154] and the recommendation for $\sqrt{s} = 13$ TeV analyses is to use an uncertainty of 0.23% on the cross section. This value is used for the uncertainty on the total fiducial and inclusive cross section.

To extract the uncertainty on each bin of the normalised and absolute differential and double differential cross section, a reweighting method is used on the MC@NLO + PYTHIA 8 sample, using the nominal value for the uncertainty on the LHC beam energy of 0.1%, as mentioned. Each Monte Carlo event weight is reweighted with a ratio to correct the

PDF for the higher or lower beam energy using the LHAPDF library [155]. The reweighting ratio is:

$$R = \frac{f(x_1^{mod}, Q^2) \cdot f(x_2^{mod}, Q^2)}{f(x_1, Q^2) \cdot f(x_2, Q^2)} \quad (5.30)$$

where x_1 and x_2 are the momentum fractions of the partons (also called Bjorken- x values), x_1^{mod} and x_2^{mod} are the shifted momentum fractions and Q^2 is the energy scale of the collision. The x_1^{mod} and x_2^{mod} are found as: $x_i^{mod} = x_i \cdot (1 \pm 0.001)$, where 0.001 comes from the LHC beam energy uncertainty of 0.1% [153]. The sum of weights used for normalisation is changed correspondingly, to take the new weights into consideration. The method to calculate the beam energy uncertainty is taken from Ref. [39, 148].

The comparison at particle level between the up and down variation is taken as a systematic uncertainty on the LHC beam energy. The impact of this systematic uncertainty is shown in Figure 5.32. As \sqrt{s} increases, the leptons become slightly harder in p_T and more forward in $|\eta|$, leading to changes of 0.03 – 0.05% at the edges of the distributions. These changes are generally very small compared to the other systematic and statistical uncertainties on the measurements in these regions.

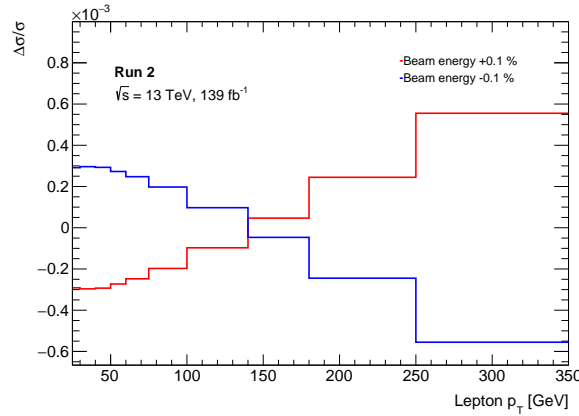


Figure 5.32: Relative change $\Delta\sigma/\sigma$ on the predicted differential fiducial cross sections as a function of the lepton p_T , due to a $\pm 0.1\%$ change in the LHC collision energy from the nominal $\sqrt{s} = 13 \text{ TeV}$.

5.9.7 Uncertainty breakdown

5.9.7.1 Total cross section

The uncertainty breakdown for the total fiducial and inclusive cross section is shown in Figure 5.10. As shown for both the fiducial and inclusive total cross section, the main source of uncertainty is the luminosity, which is 3 times greater than the sub-leading source of uncertainty which is the Wt cross section, followed by the uncertainty on the electron isolation.

In addition to the more impactful uncertainties listed above, there are a few of them which have a non-negligible impact on this measurement: one coming from Wt DR vs DS since the Wt process is the main background and the uncertainties related to the leptons

(electron and muon reconstruction efficiency and muon isolation).

The jet and missing energy related uncertainties are very small or even zero, as expected, since no cuts on the jets have been applied. Slightly higher uncertainty is observed for the b -tagging, which comes from the up and down variations of the b -tagging scale factors applied to Monte Carlo events.

Finally, the result is affected by the $t\bar{t}$ uncertainties, in particular by the PDF uncertainty (for the inclusive cross section), ISR and h_{damp} variation.

5.9.7.2 Differential and double differential cross section

The results for the (double) differential absolute cross section are presented in Figure 5.33-5.34 and more in detail in Appendix E.

The statistical uncertainty increases with increasing p_T , combined mass or energy, reaching a maximum of 6%, while it is constant for $|\eta|^l$ and $|\Delta\phi|^{e\mu}$ bins. For $|y^{e\mu}|$ the total uncertainty is stable and constant until 1.5 and then start to increase up to approximately $\sim 20\%$. The luminosity uncertainty is still one of the dominating uncertainties in most bins, as it ranges between 1.9–2.3%, but especially in the high p_T bins, the Wt uncertainty dominates the total uncertainty. This is mostly due to the $t\bar{t}/Wt$ interference uncertainty, the modelling of which disagrees with the data at high p_T values [156]. The rest of the uncertainties follow the same trend as for the total fiducial cross section.

The results for the normalised differential cross section are presented in this section in in Figure 5.35-5.36 and more in detail in Appendix E.

The statistical uncertainty follows the same trends as for the absolute differential cross section, while on the systematic side, the uncertainty due to the luminosity decreases and it is no longer one of the dominating uncertainties. Instead, the interference between $t\bar{t}/Wt$ becomes one of the most important uncertainties, and it dominates especially the high p_T regions, combined mass and energy distributions. The $t\bar{t}$ uncertainties are also amongst the biggest ones, while the lepton and jets uncertainties are very small.

	$\sigma_{fiducial}$	$\sigma_{inclusive}$
Data statistics (%)	0.15	0.15
MC statistics (%)	0.15	0.15
hdamp variation (%)	0.27	0.27
Parton shower (%)	0.16	0.14
Top-quark mass dependence (%)	0.00	0.00
PDF (%)	0.04	0.43
ISR (%)	0.12	0.38
FSR (%)	0.15	0.21
Electron scale and resolution (%)	0.10	0.10
Electron efficiency (%)	0.37	0.37
Electron isolation (in situ) (%)	0.51	0.51
Muon scale and resolution scale (%)	0.13	0.13
Muon reconstruction efficiency (%)	0.35	0.35
Muon trigger and TTVA efficiency (%)	0.06	0.05
Muon isolation i(n situ) (%)	0.33	0.33
JVT (%)	0.03	0.03
JES b -jes response (%)	0.05	0.05
JES effective NPs (%)	0.01	0.01
JES EtaInterCalibration (%)	< 0.01	< 0.01
JES flavour (%)	0.08	0.08
JES pileup (%)	0.02	0.02
JES PunchThrough (%)	< 0.01	< 0.01
JES HighPt (%)	< 0.01	< 0.01
MET soft term (%)	< 0.01	< 0.01
JER (%)	< 0.01	< 0.01
b -tagging (%)	0.07	0.07
$t\bar{t}/Wt$ interference (%)	0.35	0.35
Wt background (%)	0.53	0.53
Wt matrix element (%)	0.22	0.22
Wt parton shower (%)	0.30	0.30
Di-boson background (%)	0.05	0.05
ttV background (%)	0.03	0.03
Z+jets background (%)	0.06	0.06
mis-ID background (%)	0.32	0.32
Beam energy (%)	0.23	0.23
Luminosity (%)	1.90	1.90
Total uncertainty (%)	2.28	2.35

Table 5.10: Results for the total fiducial and inclusive cross section. All the sources of uncertainty (statistical and systematics) are listed with their relative impact on the final measurement.

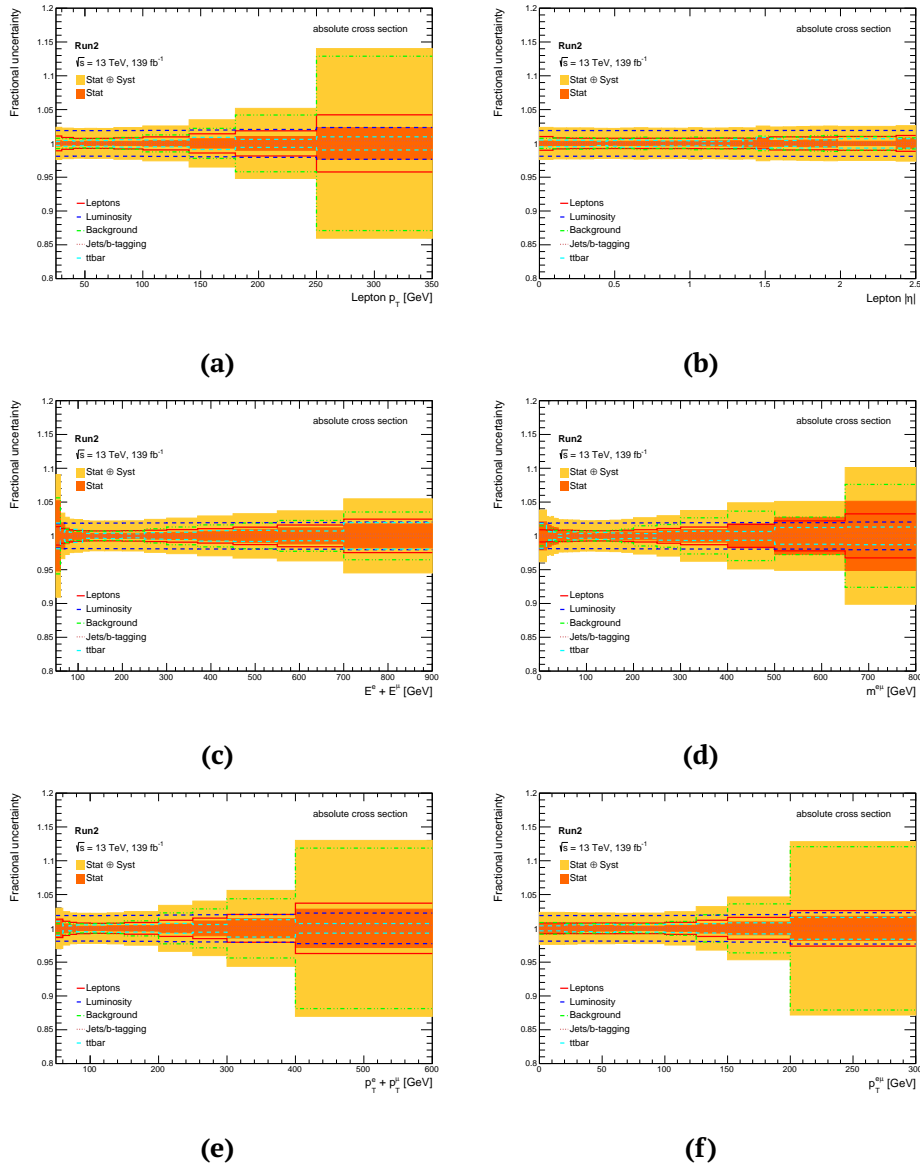


Figure 5.33: Statistical and total systematic error and contributions from different categories of systematic uncertainties for the absolute differential cross section.

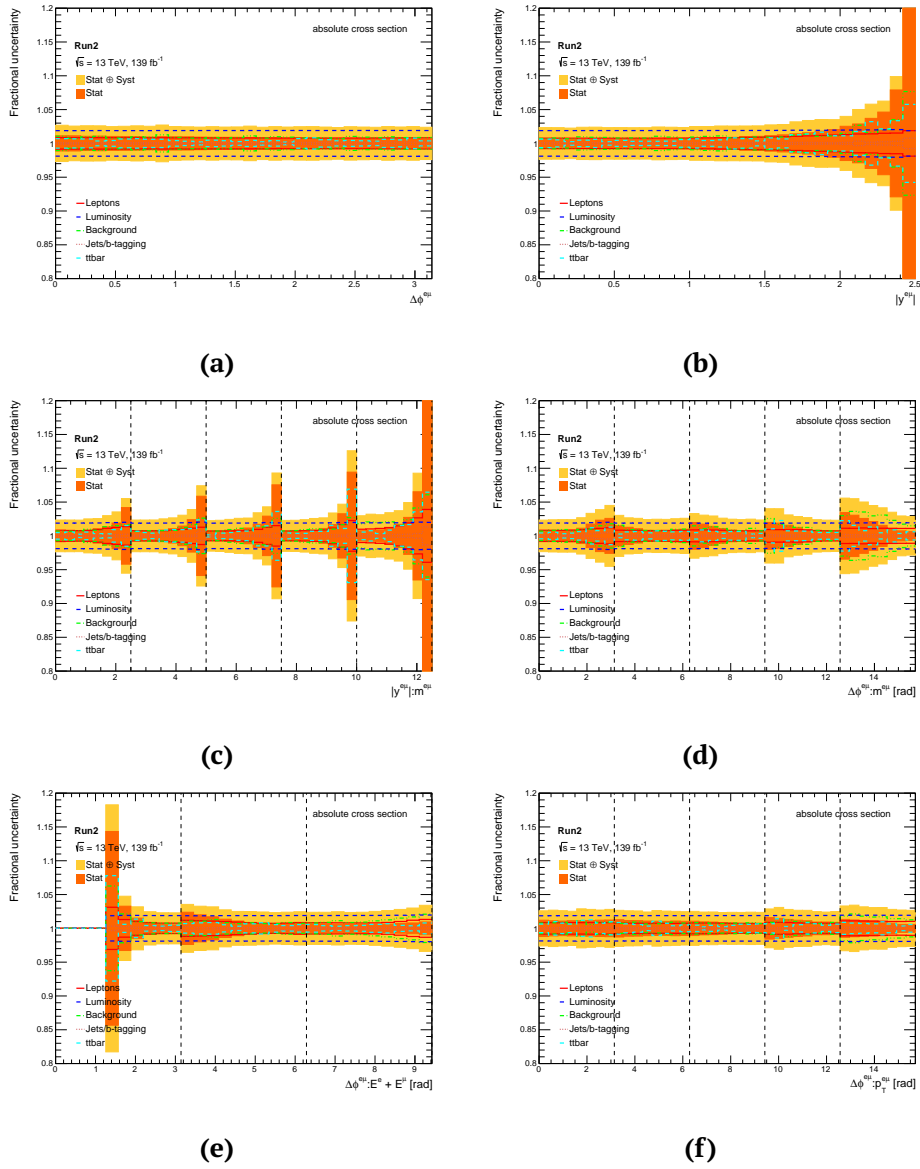


Figure 5.34: Statistical and total systematic error and contributions from different categories of systematic uncertainties for the absolute differential cross section.

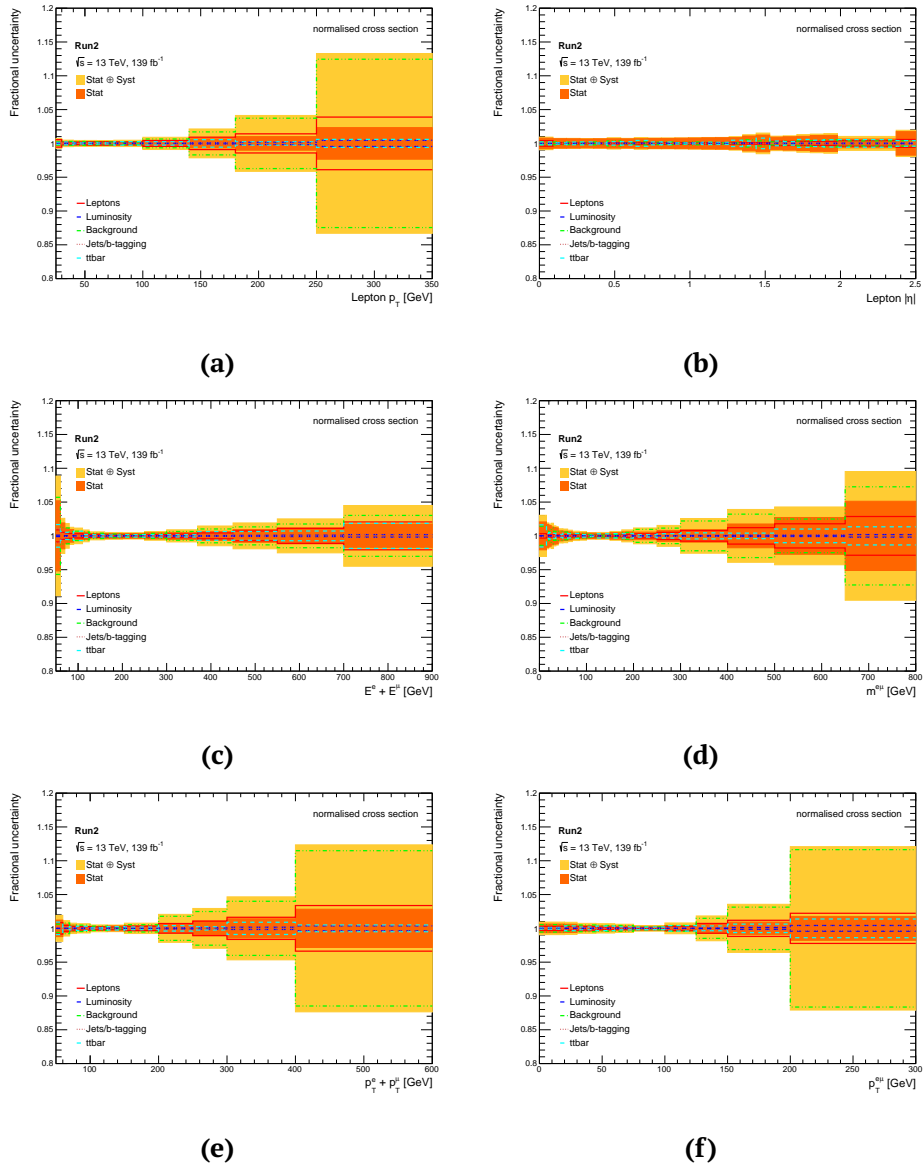


Figure 5.35: Statistical and total systematic error and contributions from different categories of systematic uncertainties for the absolute differential cross section.

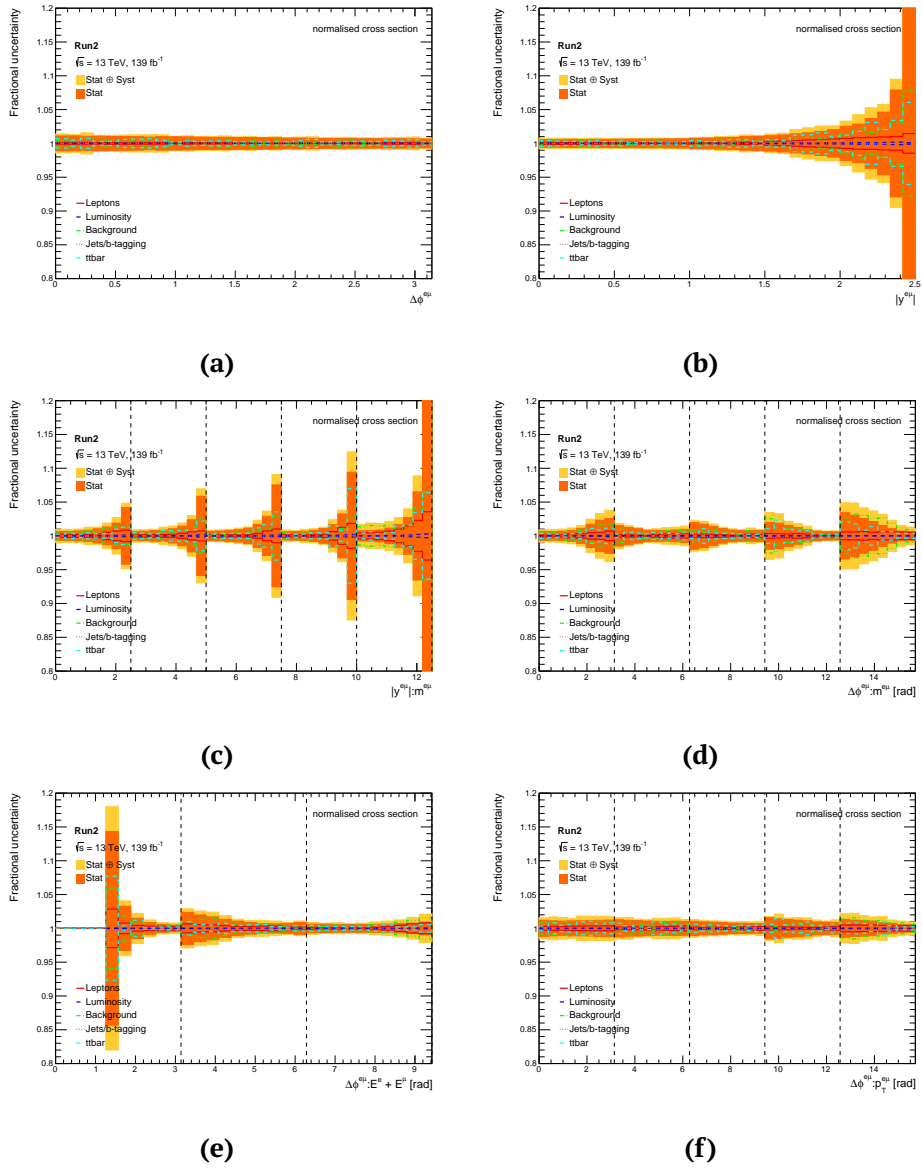


Figure 5.36: Statistical and total systematic error and contributions from different categories of systematic uncertainties for the absolute differential cross section.

5.10 Results

5.10.1 Total fiducial cross section

The total fiducial cross section for the Full Run 2 dataset is found to be:

$$\sigma_{fid,t\bar{t}} = 10.62 \pm 0.02 \pm 0.20 \pm 0.13 \text{ pb}$$

where the first uncertainty is the statistical one, the second is the luminosity uncertainty and the last is the systematic uncertainty from all of the other sources with a total relative uncertainty of 2.28%.

Compared to the results, in the same channel, obtained in Run 1 in Ref. [130, 133], where the relative total uncertainty on the total inclusive cross section amounts to 3.9% and 3.6% for the measurement at $\sqrt{s} = 7 \text{ TeV}$ and 8 TeV respectively (the uncertainties on the total fiducial cross section are approximately the same size), the current measurement from Run 2 shows a definite improvement, both due to higher statistics, but also thanks to improved reconstruction algorithms and Monte Carlo modelling. When comparing this result with the latest published result with the data collected in the period 2015 – 2016 [39], where the measurement of the total fiducial cross section has a relative total uncertainty of 2.36%, it can be seen that using the Full Run 2 dataset yield a small improvement on the total uncertainty. The statistical improvement due to the bigger size of the dataset impacts the measurement only slightly because in both this analysis and in Ref. [39] the result is completely dominated by systematic uncertainties and in particular by the luminosity uncertainty. Also, even if one of the other biggest systematic uncertainties presented in this analysis is reduced ($t\bar{t}/Wt$ interference and $t\bar{t}$ modelling), to get a relative total uncertainty below 2% the knowledge on the luminosity measurement needs to be improved to decrease its impact on the total uncertainty.

5.10.2 Total inclusive cross section

The total inclusive cross section for the Full Run 2 dataset is found to be:

$$\sigma_{t\bar{t}} = 830.3 \pm 1.2 \pm 15.9 \pm 11.2 \text{ pb}$$

where then the first uncertainty is the statistical one, the second is the luminosity uncertainty and the last is the systematic uncertainty from all of the other sources with a total relative uncertainty of 2.35%.

The reason there is an increase in the $t\bar{t}$ uncertainties is due to the acceptance factor, which is based fully on Monte Carlo and hence can change significantly depending on the simulation setup and assumptions.

The predicted NNLO value of the total inclusive cross section for $\sqrt{s} = 13 \text{ TeV}$, and for a top-quark mass of 172.5 GeV , is reported in Equation 1.3.1.1 and it is $\sigma_{t\bar{t}} = 831.76^{+19.77}_{-29.20} \text{ (scale)} \pm 35.06 \text{ (PDF}+\alpha_S) \text{ pb}$ and the value found in this analysis results to be compatible with the theoretical predictions.

The total uncertainty is lower compared to the one from Run 1 [130, 133], due to an improvement in detector modelling and $t\bar{t}$ simulation and this slightly below the one obtained in the measurement with the 2015 – 2016 data [39], where the total relative uncertainty on the relative total inclusive cross section is 2.4%.

5.10.3 Differential cross section

A comparison between the absolute and normalised fiducial single and double differential cross section results with the theoretical predictions of different $t\bar{t}$ generators is carried out to make more stringent tests on perturbative QCD calculations.

The results are shown in Figure 5.37-5.39 for the absolute single and double differential cross section and in Figure 5.40-5.42 for the normalised single and double differential cross sections.

When comparing the results obtained in this analysis with the ones from the Full Run 1 in Ref. [131, 135], it is clear that the uncertainties on all bins, both statistical and systematic, are very much improved in the same way as the uncertainty on the total fiducial cross section. The uncertainties on the results with the data collected from 2015 – 2016 [39] are instead very close to the ones found in this analysis, again underlying the fact that the measurement is dominated by systematic uncertainties and their calculations have not improved drastically between 2015 – 2016 and the Full Run 2. For the normalised differential cross sections though, the large statistics of the Full Run 2 sample represent a significant gain over previous measurements, since the systematic uncertainty on the luminosity, for the most part, cancels out in the ratio, but the results for the normalised differential distributions cannot be directly compared to the ones in Ref. [39], due to the different binning.

A thing to note regarding this analysis though is that the granularity of the binning of most of the variables is finer, without losing in statistical precision on each bin, this is possible thanks to the high statistical power of the Run 2 dataset. Having precise and finer distributions is an advantage for many reasons: these distributions can be used for top-quark pole mass extraction, and the more bins there are, the higher the number of degrees of freedom will be when comparing the measured differential cross section with the template distributions with a χ^2 . Also, the lower uncertainties on the normalised differential distributions will translate to lower systematic uncertainties on the top-quark mass value as well.

These distributions can also be used to study the theoretical and simulation modelling of top-quark processes, by comparing the predicted top-quark distributions with respect to the measured ones, one example being the $t\bar{t}/Wt$ interference or the top-quark p_T spectrum, as done in Ref. [33] for example. Certainly, the low uncertainty on each bin would help in discerning viable models to non-viable ones when doing a comparison between the data and the alternative modelled distributions.

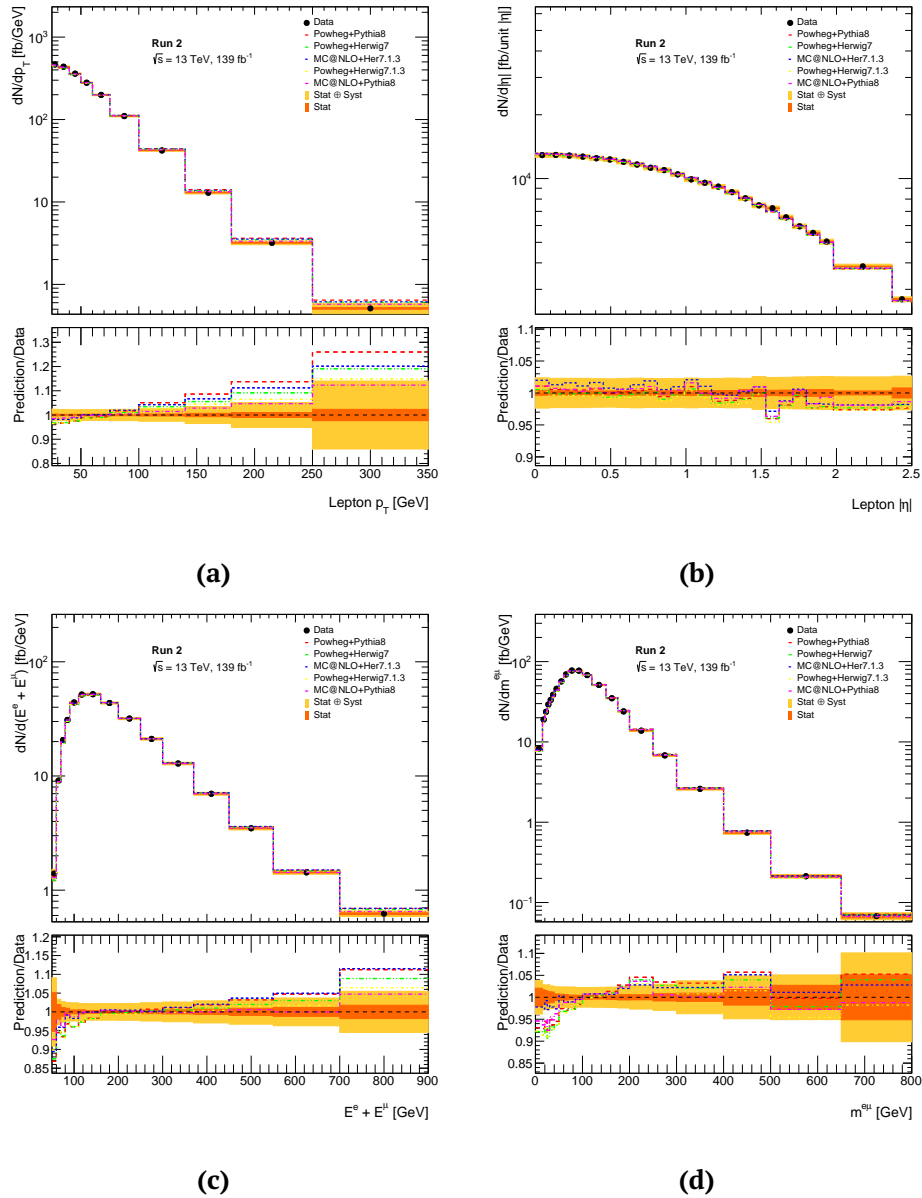


Figure 5.37: Absolute differential cross section with statistical and systematic error plotted together with predictions from different Monte Carlo generators.

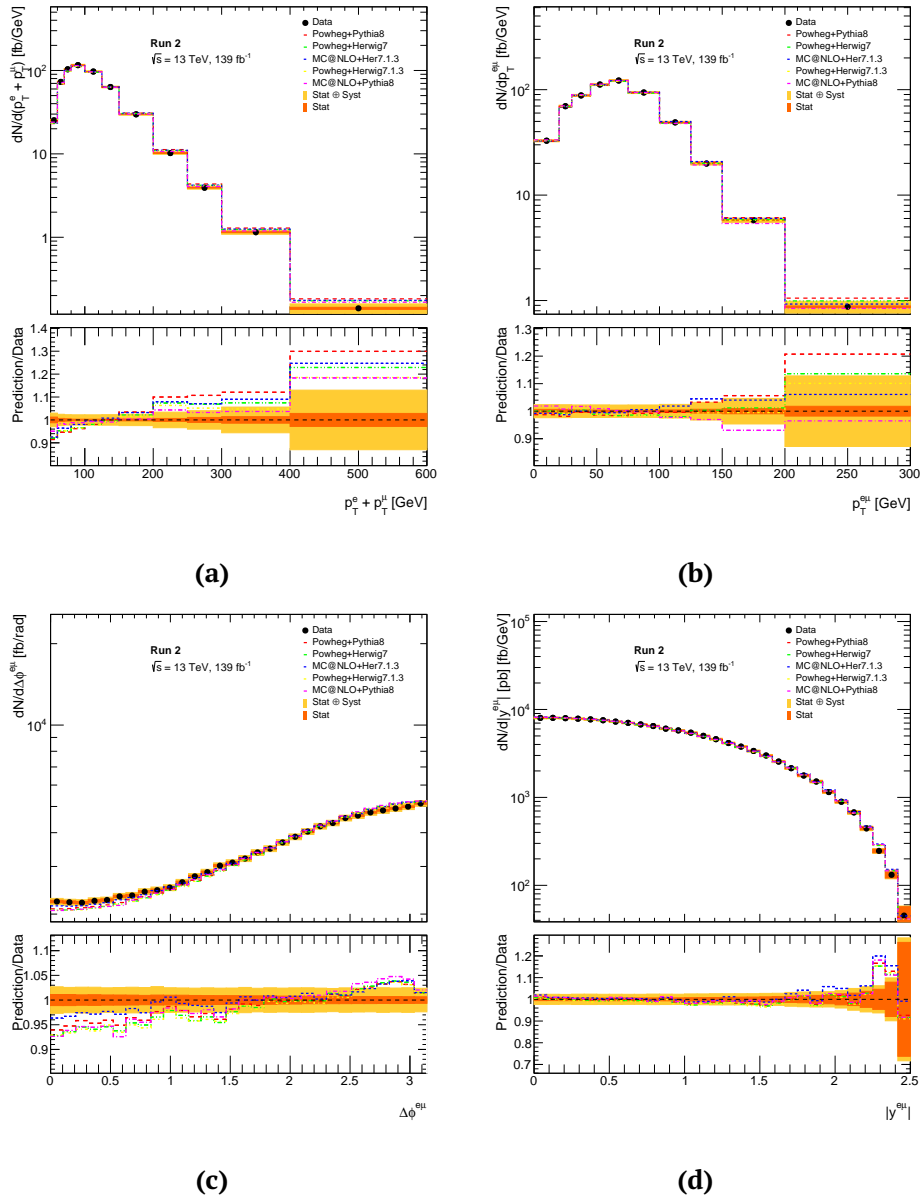


Figure 5.38: Absolute differential cross section with statistical and systematic error plotted together with predictions from different Monte Carlo generators.

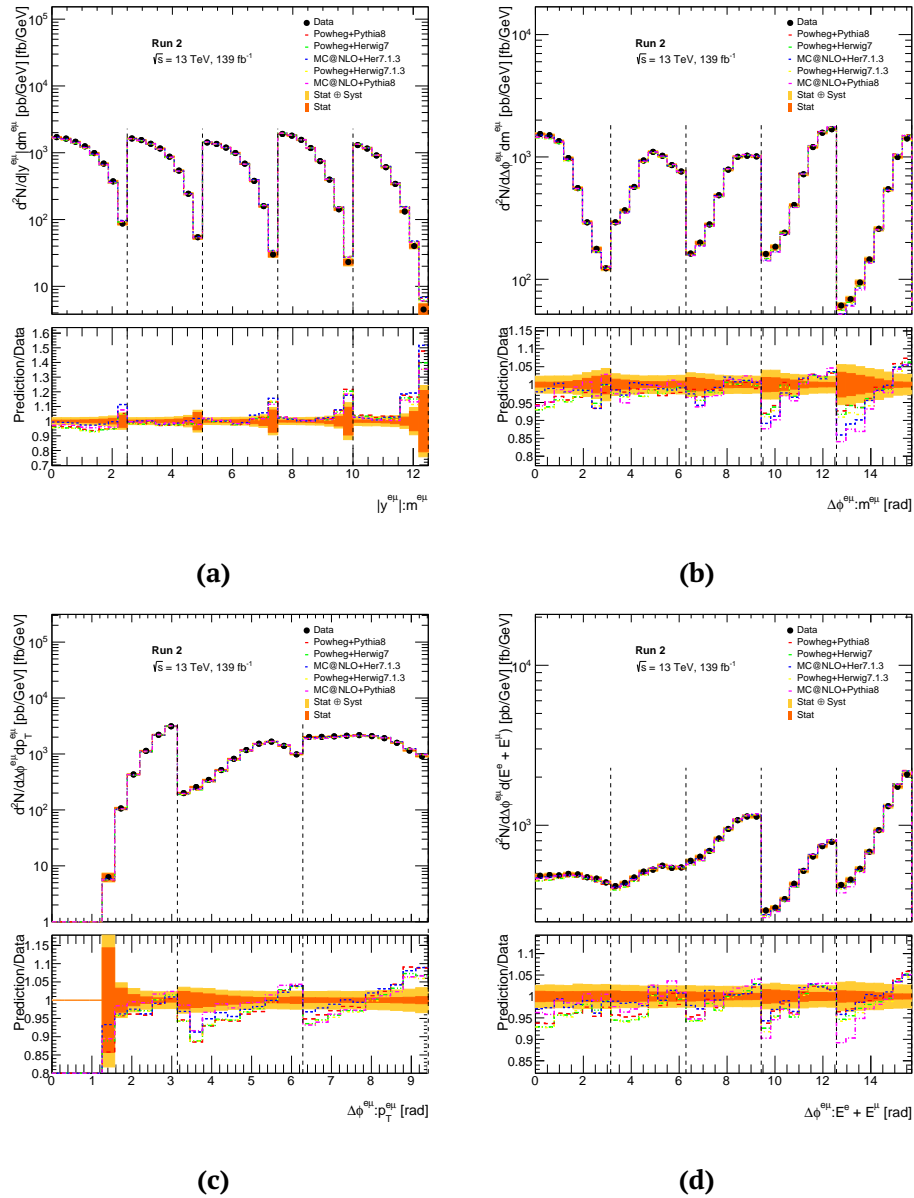


Figure 5.39: Absolute differential cross section with statistical and systematic error plotted together with predictions from different Monte Carlo generators.

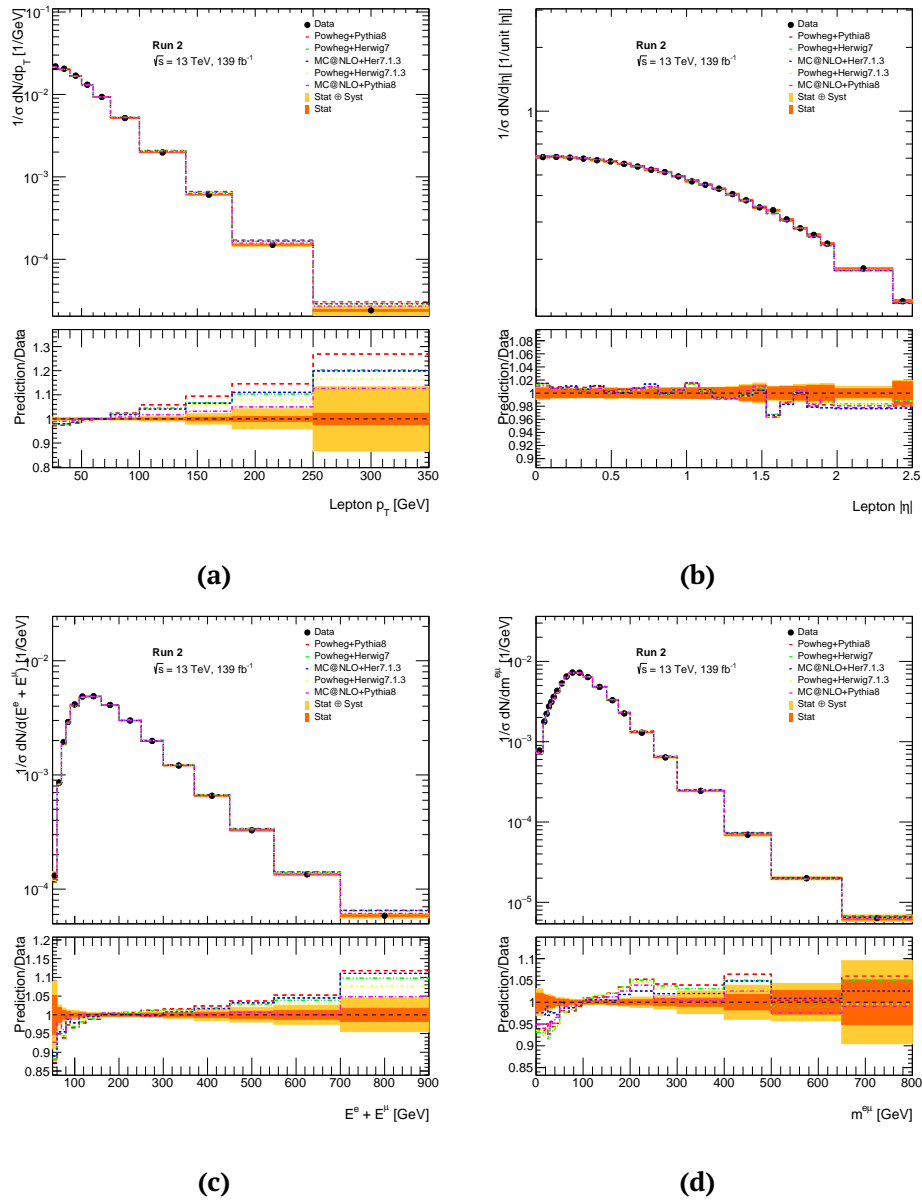


Figure 5.40: Normalised differential cross section with statistical and systematic error plotted together with predictions from different Monte Carlo generators.

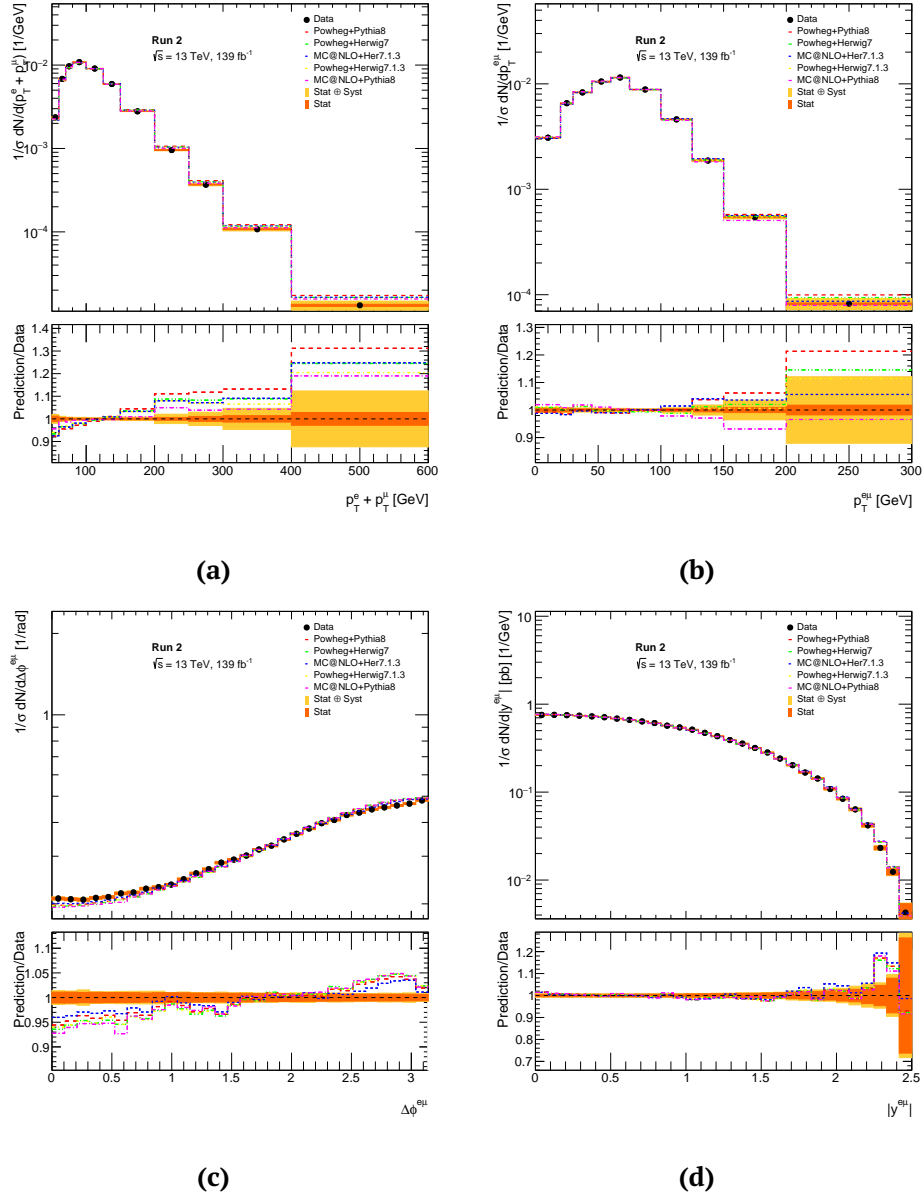


Figure 5.41: Normalised differential cross section with statistical and systematic error plotted together with predictions from different Monte Carlo generators.

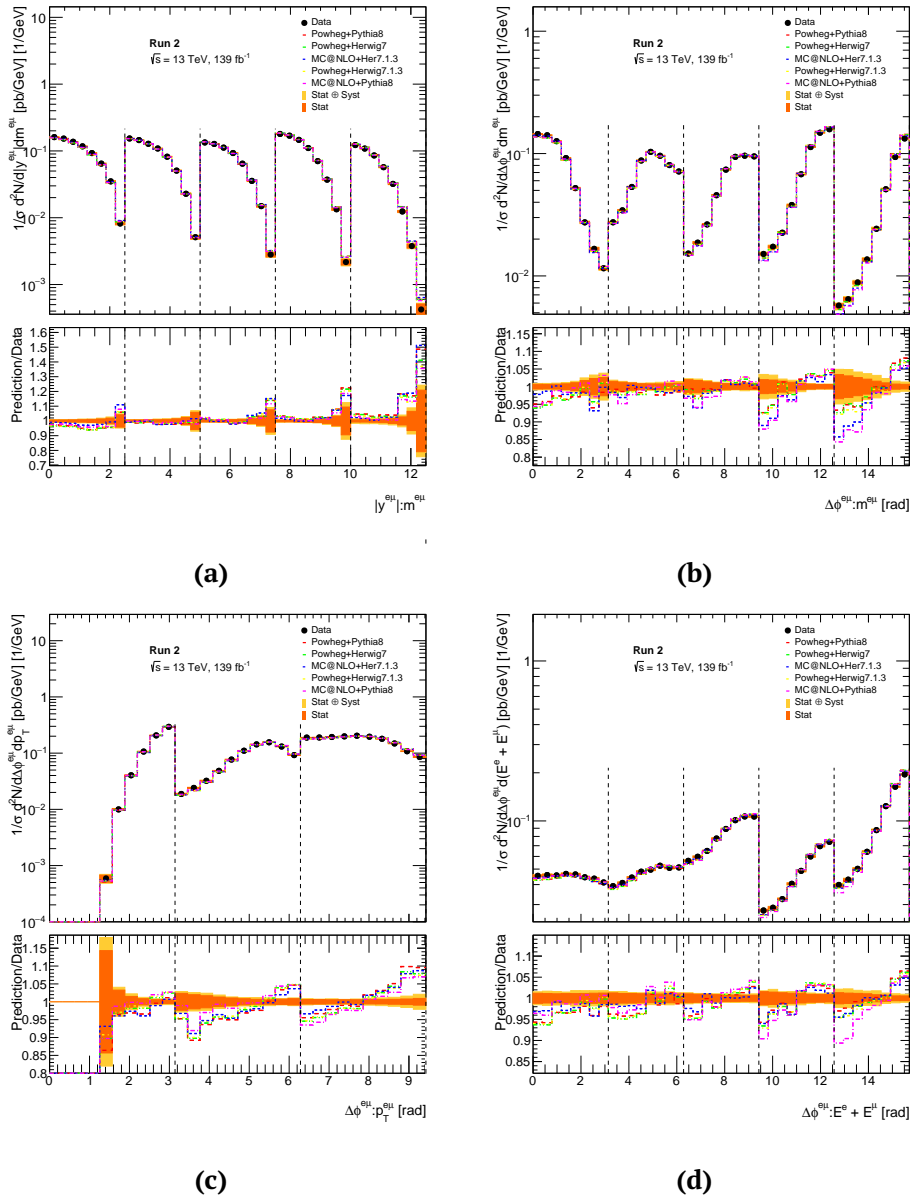


Figure 5.42: Normalised differential cross section with statistical and systematic error plotted together with predictions from different Monte Carlo generators.

Top-quark pole mass extraction

6.1 Top-quark pole mass extraction from total inclusive $t\bar{t}$ cross section

The interplay between the top-quark mass and the inclusive $t\bar{t}$ cross section offers the possibility of interpreting measurements of $\sigma_{t\bar{t}}$ as measurements of m_t^{pole} .

The predicted cross section $\sigma_{t\bar{t}}^{theo}$ was parametrised using the Equation 6.1, originally proposed in Ref. [154, 157].

$$\sigma_{t\bar{t}}^{theo}(m_t^{pole}) = \sigma_{t\bar{t}}(m_t^{ref}) \left(\frac{m_t^{ref}}{m_t^{pole}} \right)^4 (1 + a_1 x + a_2 x^2) \quad (6.1)$$

where $m_t^{ref} = 172.5 \text{ GeV}$, $x = (m_t^{pole} - m_t^{ref})/m_t^{ref}$, while $\sigma_{t\bar{t}}(m_t^{ref})$, a_1 and a_2 are free parameters. The values of the free parameters at $\sqrt{s} = 13 \text{ TeV}$ are given in Table 9 of Ref. [154] for the NNPDF3.0 PDF set used for this study.

The m_t^{pole} appearing in Equation 6.1 is the pole mass corresponding to the definition of a free particle, which may differ from the top-quark mass measured through direct reconstruction of its decay products by $\mathcal{O}(1 \text{ GeV})$ [158].

As discussed in Section 5.9.3, the experimentally measured cross section does have a little dependence on the top-quark mass m_t , with which the Monte Carlo template is generated. The measured cross section at any value of m_t can be evaluated as a variation of $-0.379\%/GeV$ with respect to the one measured at $m_t = 172.5 \text{ GeV}$ (see Table 5.8). Given the small dependence of the cross section on m_t , one can assume that $\sigma_{t\bar{t}}(m_t) \simeq \sigma_{t\bar{t}}(m_t^{pole})$, as long as the differences between m_t and m_t^{pole} are of few GeV.

The $\sigma_{t\bar{t}}^{measured}$ and the $\sigma_{t\bar{t}}^{theoretical}$ together with their uncertainties as a function of the m_t^{pole} are shown in Figure 6.1. The value of m_t^{pole} can be extracted from the intersections of the two cross sections (red and blue in Figure 6.1) and results to be:

$$m_t^{pole} = 173.2_{-2.6}^{+2.9} \text{ GeV}. \quad (6.2)$$

The uncertainties are dominated by those on the theoretical cross section prediction, such as the PDF, α_S and scale uncertainties, and the total experimental uncertainty (dominated by the uncertainty on the integrated luminosity) plays a relatively minor role. The small dependence of the inclusive cross section on the top-quark pole mass and the large uncertainty on the theoretical predictions lead to a final error on the measured top-quark pole mass of $1.5 - 1.6\%$. This value is compatible with the value reported in Ref. [17]: $m_t = 172.4 \pm 0.7 \text{ GeV}$.

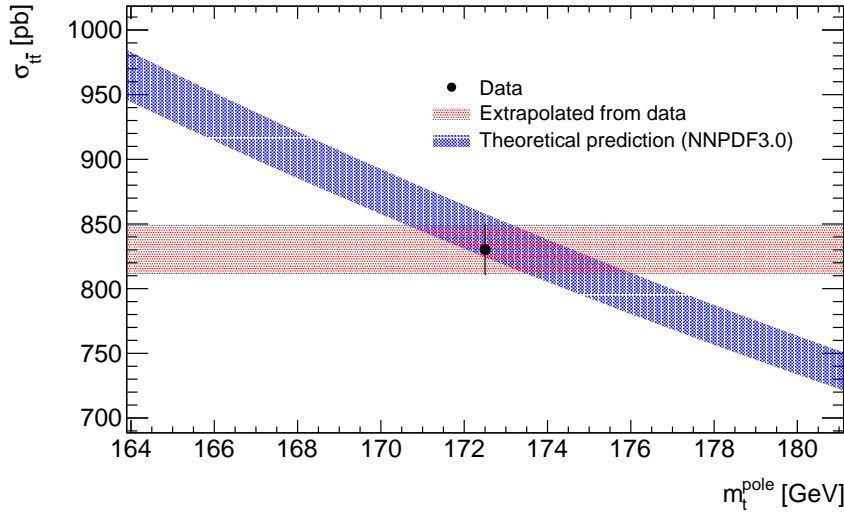


Figure 6.1: $\sigma_{t\bar{t}}$ as a function of the top-quark pole mass at $\sqrt{s} = 13 \text{ TeV}$. Both the predicted inclusive $t\bar{t}$ production cross sections, using the NNPDF3.0 PDF set, and the experimental measurement from Full Run 2 ATLAS dataset are shown. The blue band shows the total uncertainty on the predictions from PDF, α_S and QCD scale variations while the red band shows the experimental total uncertainty of the measured inclusive cross section extrapolated at any m_t^{pole} with respect to the one measured at 172.5 GeV (black point).

6.2 Top-quark pole mass extraction from differential $t\bar{t}$ cross section

The measured normalised p_T^l , $p_T^{e\mu}$, $p_T^e + p_T^\mu$, $m^{e\mu}$ and $E^e + E^\mu$ differential cross sections are sensitive to the top-quark pole mass, as shown in Figure 6.2. Furthermore, as explained in Ref. [159], they are less sensitive to the modelling of perturbative and non-perturbative QCD, and a measurement performed using these distributions is closer to the one predicted by the Standard Model, with respect to the one obtained by fully reconstructing the top-quark decay products.

The main advantage of this technique is that there is no need to reconstruct the top-quark decay products, allowing the measurement to be insensitive to the large uncertainties associated with the missing transverse energy of the neutrinos and to the jets (JER, JES, ...). On the other hand, a mis-modelling in the Monte Carlo prediction for these distributions can directly impact this measurement. In particular, the well known Monte Carlo mis-modelling of the top-quark p_T , due to missing NNLO corrections, can impact the extracted m_t^{pole} (see Figure 1.7 and Ref. [33]). This effect could be potentially mitigated with a better understanding of the top-quark production and decay processes, and hence an improved Monte Carlo prediction.

6.2.1 Analysis technique

The top-quark mass is extracted using a template fit method: the distributions are parametrised as a function of m_t , and the value of the top-quark mass is found as the

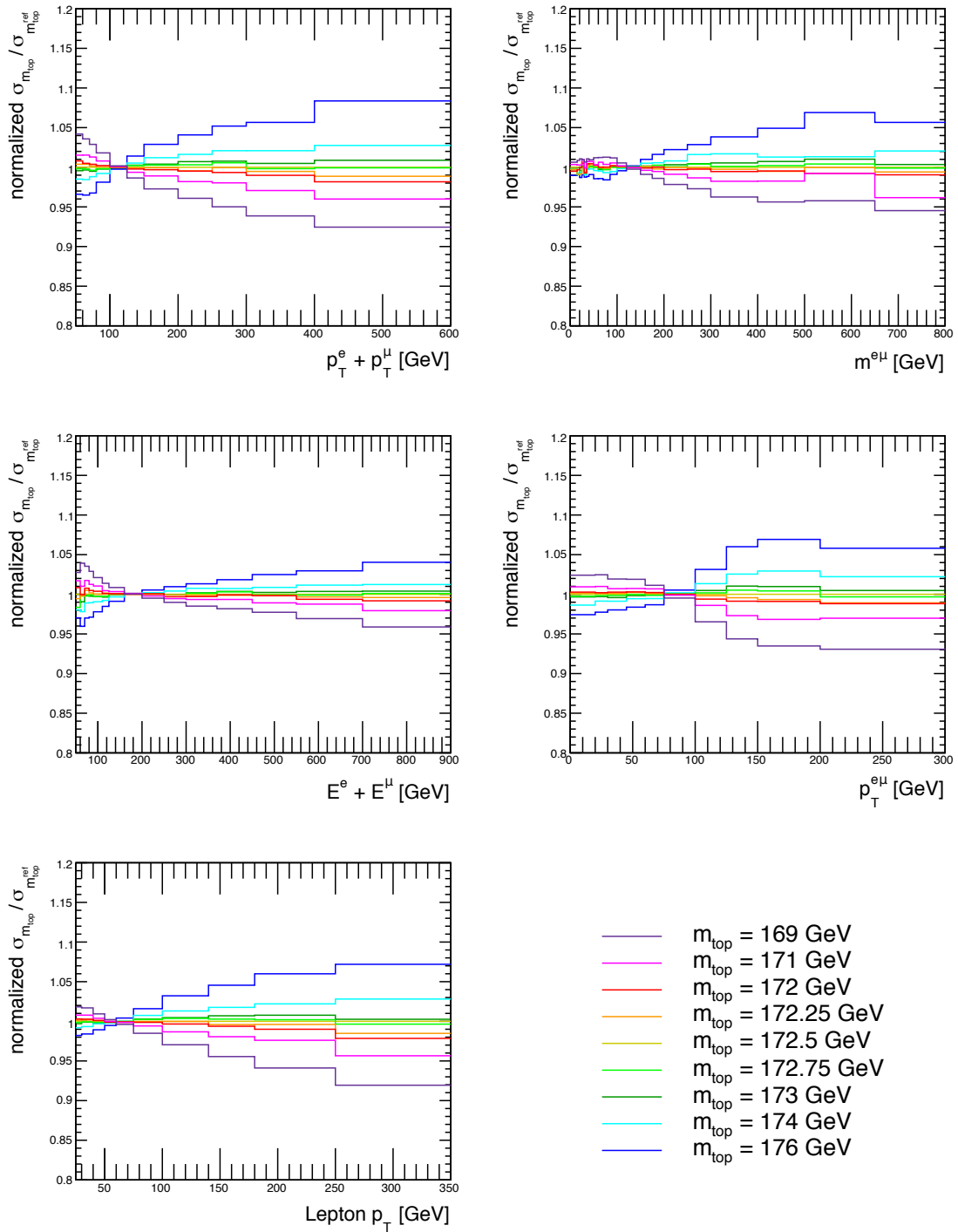


Figure 6.2: Ratio of top-quark mass templates respect to the nominal top-quark mass template with $m_t = 172.5$ GeV for the five variables used for the m_t^{pole} extraction.

one which minimises the χ^2 with respect to the measured data shown in Section 5.10. Five variables are considered (p_T^l , $p_T^{e\mu}$, $p_T^e + p_T^\mu$, $m^{e\mu}$ and $E^e + E^\mu$) and, for each of them, the distribution in data is compared to the Monte Carlo prediction from POWHEG+PYTHIA 8, generated for nine different values of the top-quark mass (169, 171, 172, 172.25, 172.5, 172.75, 173, 174 and 176 GeV). The template fit uses the information on the shape of the distribution, taking into account the uncertainty in each bin. In Figure 6.3, the measured normalised cross sections compared the Monte Carlo predictions for different values of the top-quark mass as a function of the $p_T^{e\mu}$ variable are shown.

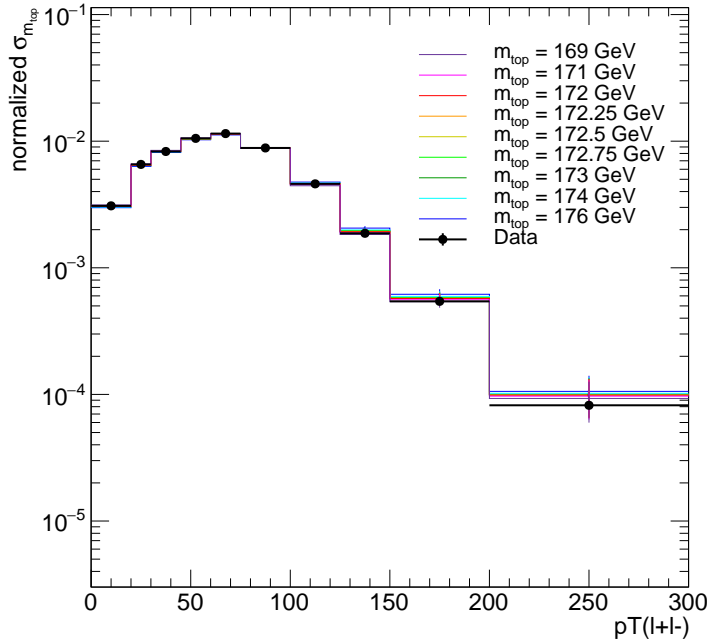


Figure 6.3: Top-quark mass predicted distributions together with the measured normalised differential cross section as a function of the $p_T^{e\mu}$ variable.

In order to smooth out statistical fluctuations in the Monte Carlo templates, the value of the normalised cross section in each bin of the five distributions is plotted as a function of the nine top-quark masses used to generate the Monte Carlo templates, and a second order polynomial fit is performed. As a consequence, the value of the cross section in each bin associated to a given top-quark mass value is now taken as the one extracted from the fit at that mass. An example of fit is shown in Figure 6.4 where for each bin, the fit of the second order polynomial function is also shown.

For each of the five distributions and each top-quark mass value, the χ^2 value is computed using the following equation:

$$\chi^2(m_t) = \Delta_{(n-1)}^T(m_t) \cdot C_{(n-1) \times (n-1)}^{-1} \cdot \Delta_{(n-1)}(m_t) \quad (6.3)$$

where n is the number of bins of a particular distribution, $\Delta_{(n-1)}(m_t)$ represents the

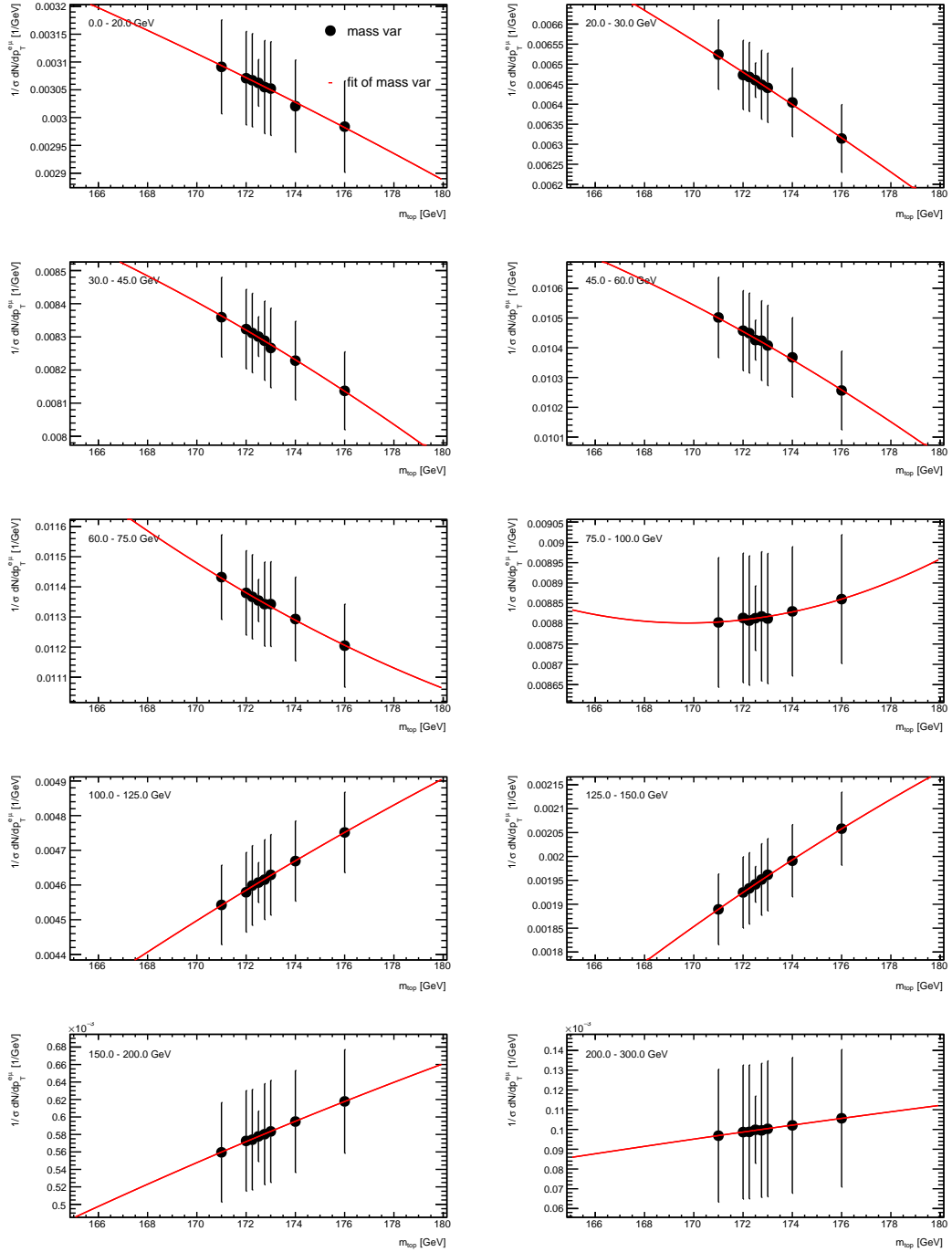


Figure 6.4: Values of the normalised cross section for each top-quark mass template divided per bins of the $p_T^{e\mu}$ variable. The second order polynomial function used for the fit is shown in red.

vector of differences between the measured normalised differential cross section value and the prediction of a sample calculated with a particular value of m_t , while $C_{(n-1)\times(n-1)}$ represent the total covariance matrix between the bins. Both the data statistical uncertainty and experimental systematic uncertainties on the measurements of the differential distributions are included in the $C_{(n-1)\times(n-1)}$ matrix. The determination of the statistical covariance matrices (from data and Monte Carlo) is done with the bootstrapping technique as explained in Section 5.9.1.

To construct the covariance matrices for the systematic variations, the uncertainties are assumed to be fully correlated between bins i and j , with a correlation factor of $\rho_{ij} = 1$. Each systematic covariance matrix is then constructed in this way:

$$C^{(s)} = u_i^{(s)} u_j^{(s)} \rho_{ij}^{(s)} \quad (6.4)$$

where (s) is the single systematic uncertainty, $u_i^{(s)}$ and $u_j^{(s)}$ are the values of this uncertainty in bin i and bin j respectively, and $\rho_{ij}^{(s)}$ is the correlation factor between two bins of a systematic uncertainty. In addition, since the distributions are normalised, the covariance matrices for each systematic variation is corrected using the following formula:

$$C'^{(s)} = G \cdot C^{(s)} \cdot G^T \quad (6.5)$$

where $C^{(s)}$ is the covariance matrix of the uncertainties constructed using Equation 6.4 for the systematic variation (s) , $C'^{(s)}$ is the corrected covariance matrix which takes into account the fact that the distributions are normalised, and G is the matrix of the partial derivatives which expresses the dependence of the normalised cross section in bin i^{th} on the absolute cross section in bin j^{th} and it is defined as:

$$G_{ij} = \left(\frac{\partial \sigma_{i\bar{i},norm}^i}{\partial \sigma_{i\bar{i}}^j} \right); \quad (6.6)$$

$$G_{ii} = \frac{1}{\sigma_{i\bar{i},fid}} - \frac{\sigma_{i\bar{i}}^i}{\sigma_{i\bar{i},fid}^2}, \quad G_{ij,i \neq j} = -\frac{\sigma_{i\bar{i}}^i}{\sigma_{i\bar{i},fid}^2} \quad (6.7)$$

The total covariance matrix for the measurement of each distribution is evaluated as the sum of the contributions from the statistical and all systematic contributions, which is equivalent to adding all the uncertainties in quadrature while keeping track of the total bin-to-bin correlations arising from both statistical and systematic uncertainties.

In order to make sure that the covariance matrix can be inverted, one of the bins is removed from the covariance matrix and from the vector differences $\Delta_{(n-1)}(m_t)$. For simplicity, the last bin is removed but equal results are obtained if another bin other than the last is removed.

In order to derive the value of the top-quark mass giving the best agreement between data and Monte Carlo prediction for each distribution, the $\chi^2/ndof$ distribution is plotted as a function of the top-quark mass values and a parabolic fit is used to extract the

minimum. The total uncertainty on m_t is found by extracting the mass values at $\chi^2_{min} \pm 1$.

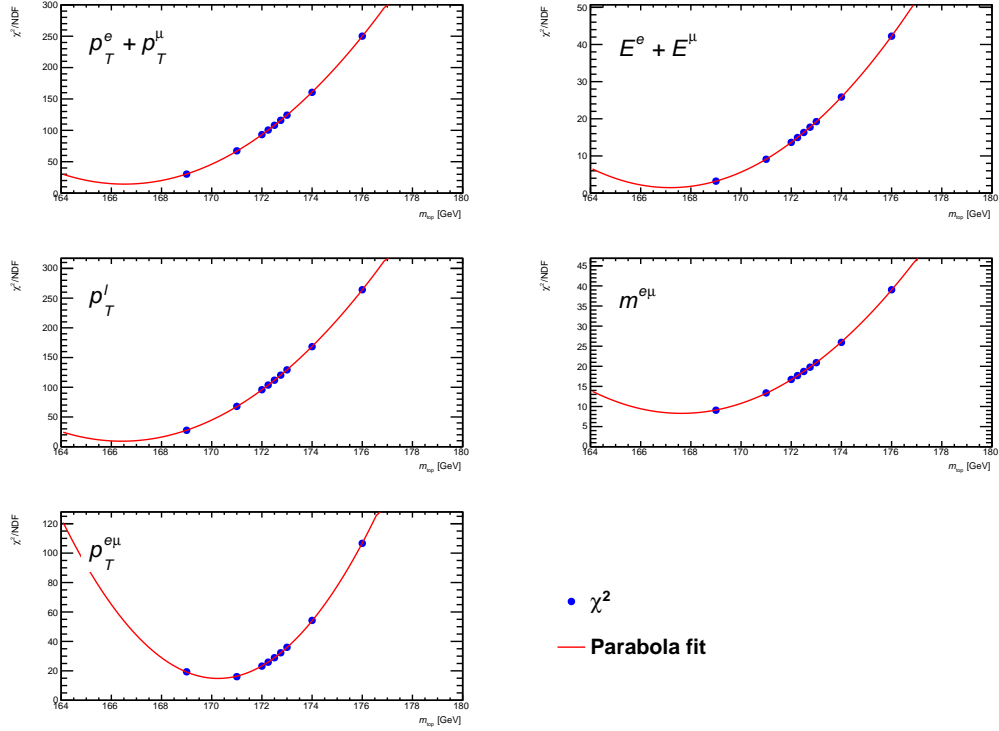


Figure 6.5: $\chi^2/ndof$ distributions for the variables used to extract m_t . Each distribution is fitted with a second degree polynomial.

The values of the mass extracted with this procedure for the five distributions are reported in Table 6.1, together with the corresponding value of the $\chi^2/ndof$ and the statistical, systematic, and total uncertainties. The most sensitive and precise variable is the $p_T^{e\mu}$ as shown in Figure 6.5 and in Table 6.1. The total uncertainty (statistical plus systematic uncertainties) for each mass value is evaluated using $\sigma_{m_t}^{up} = m_t(\chi^2_{min} + 1)$ and $\sigma_{m_t}^{down} = m_t(\chi^2_{min} - 1)$. To evaluate the impact of the statistical part alone, the normalised differential cross sections found with the data bootstrapping experiments are used to extract 1000 values of top-quark mass for each variable. The top-quark mass statistical uncertainty is the RMS of these 1000 values from bootstrapping experiments.

The extracted values of the top-quark mass result to be several standard deviations below the results obtained with the method described in Section 6.1.

This is due to the fact that the top-quark p_T spectrum predicted by the Monte Carlo generators is harder than the one observed in data, which can be related to missing NNLO QCD and NLO EW corrections. This is reflected also in the leptonic p_T variables shown in Figure 5.19 and in Figure 5.21 in which it can be observed that the data/Monte Carlo disagreement becomes more pronounced at increasing values of the lepton p_T , of the scalar and vectorial sum of the leptonic p_T and have a non-negligible effect also on the $m^{e\mu}$ and $E^e + E^\mu$ variables.

Looking at the Monte Carlo predicted normalised cross section for different top-quark

mass values as a function of the $p_T^{e\mu}$ (for example) shown in Figure 6.4, it can be observed that the distribution is very sensitive to the value of the top-quark mass, especially from 100 GeV and above, which corresponds to the region of the $p_T^{e\mu}$ mis-modelling. In this region, the Monte Carlo distributions having the smallest differences with the data are those generated with smaller values of the top-quark mass.

Variable	p_T^l	$p_T^{e\mu}$	$p_T^e + p_T^\mu$	$m^{e\mu}$	$E^e + E^\mu$
Central value (GeV)	166.32	170.27	166.48	167.19	167.14
$\chi^2/ndof$	7.4/8	14.9/8	13.6/9	7.2/19	1.4/13
Stat uncertainty (%)	0.03	0.03	0.05	0.03	0.06
Syst uncertainty (%)	0.60	0.60	0.62	1.56	1.38
Total uncertainty (%)	0.60	0.60	0.62	1.57	1.39

Table 6.1: Measurements of the top-quark mass from individual template fits to the p_T^l , $p_T^{e\mu}$, $p_T^e + p_T^\mu$, $m^{e\mu}$ and $E^e + E^\mu$ distributions. The central value associated to the χ_{min}^2 is shown together with the impact of the statistical and systematics uncertainties.

6.2.2 Analysis validation

In order to check the validity of the method used to extract the top-quark mass, the 1000 pseudo-experiments produced and explained in Section 5.9.1 are used. The top-quark mass value is extracted 1000 times for each variable as shown in Figure 6.6. The relative difference between the mean of the 1000 extracted top-quark mass and the nominal mass values (172.5 GeV) is shown in Figure 6.7. The mean in the five variables is consistent with zero within the expected statistical uncertainty, demonstrating that the technique has no bias. The $E^e + E^\mu$ variable shows a slightly greater deviation with respect to the other variables. The Monte Carlo statistic of the top-quark mass templates has a double number of events with respect to the data then the expected Monte Carlo statistical error is equal to $\sigma_{stat}^{MC} = \sigma_{stat}^{data} / \sqrt{2} \simeq 0.04\%$. Therefore, considering also the Monte Carlo statistical error, also the variable $E^e + E^\mu$ is within 1 standard deviation.

6.2.3 Single results combinations

The results from the template fit methods are combined using the “Best Linear Unbiased Estimate” (BLUE) technique [160]. The five values of the top-quark mass are measurements of the same quantity, performed with different distributions but using from the same data. For this reason, these measurements are correlated with each other and these correlations need to be taken into account in the combination.

Statistical correlations are evaluated using the 1000 pseudo-experiments described in Section 5.9.1. For each normalised differential cross section $\sigma_i^{v_m}$ evaluated from the i^{th} pseudo-experiment and for the variable v_m ($m = 1 \div 5$), a value of $m_{top}^{v_m, i}$ can be extracted. From these 1000 values of $m_{top}^{v_m}$, the correlation matrix among the variables can be built. Each matrix element ρ^{v_m, v_n} can be calculated in this way:

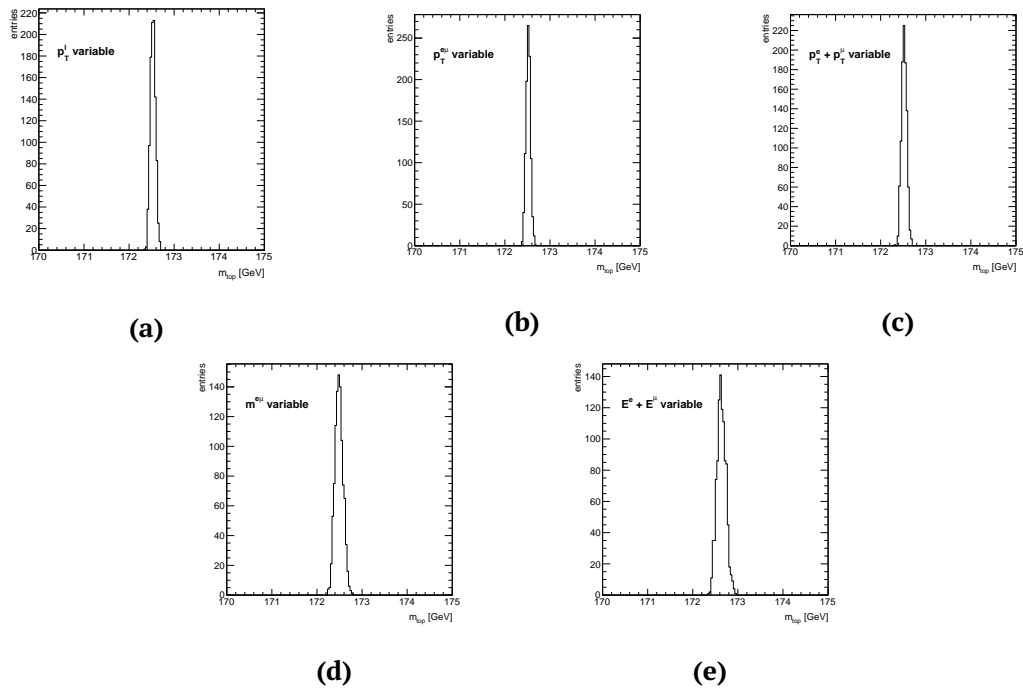


Figure 6.6: Results of the 1000 top-quark mass extracted from the pseudo-experiments using the p_T^l (6.6a), $p_T^{e\mu}$ (6.6b), $p_T^e + p_T^\mu$ (6.6c), $m^{e\mu}$ (6.6d) and $E^e + E^\mu$ (6.6e) normalised differential cross sections.

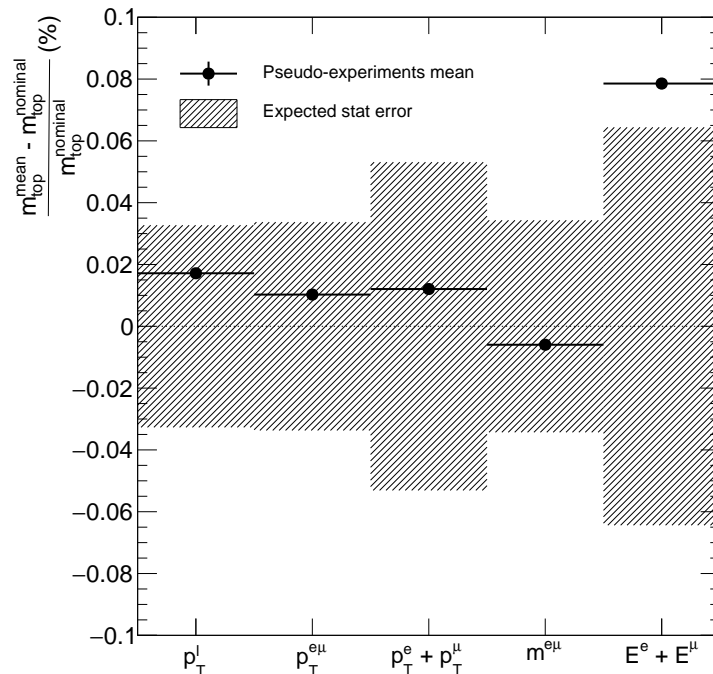


Figure 6.7: Relative difference between the mean extracted from 1000 pseudo-experiments and the nominal top-quark mass value (172.5 GeV). The mean is in all cases consistent with zero within the expected statistical error, demonstrating that the technique has no internal bias.

$$\rho^{v_m, v_n} = \frac{\langle m_{top}^{v_m} \rangle \cdot \langle m_{top}^{v_n} \rangle - \langle m_{top}^{v_m} \cdot m_{top}^{v_n} \rangle}{\sigma(m_{top}^{v_m}) \cdot \sigma(m_{top}^{v_n})} \quad (6.8)$$

where $\langle m_{top}^{v_m} \rangle$ ($\langle m_{top}^{v_n} \rangle$) is the average value over the 1000 top-quark masses extracted from all the pseudo-experiments for the variable v_m (v_n) and $\sigma(m_{top}^{v_m})$ ($\sigma(m_{top}^{v_n})$) is the associated standard deviation. In case m is equal to n , $\rho^{v_m, v_n} = 1$. The values of the statistical correlation between the five variables are shown in Figure 6.8. As expected, the variables are highly correlated.

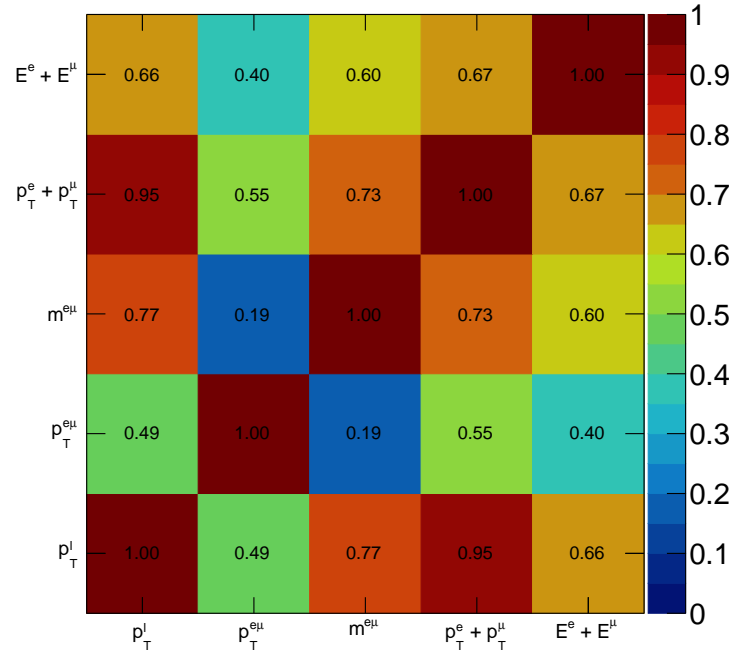


Figure 6.8: Correlation matrix between the five variables used to extract the top-quark mass.

Correlations between systematic uncertainties are determined by assuming the effect on m_t from each individual experimental or theoretical component to be fully correlated between distributions.

Given the five estimated values of m_t reported in Table 6.1 and their correlations, the error matrix E can be constructed. The diagonal elements of the matrix are the variances of the individual m_t estimates while the off-diagonal terms describe the correlation between pairs of estimates. Each element of the error matrix is calculated as in the following equation:

$$E^{v_m, v_n} = \rho^{v_m, v_n} \cdot \sigma_{stat}^{v_m} \sigma_{stat}^{v_n} + \sum_s 1 \cdot \sigma_{syst, s}^{v_m} \sigma_{syst, s}^{v_n} \quad (6.9)$$

where ρ^{v_m, v_n} is the statistical correlation coefficient described in Equation 6.8, $\sigma_{stat}^{v_m}$ ($\sigma_{stat}^{v_n}$) is the statistical error of the v_m (v_n) variable while $\sigma_{syst, s}^{v_m}$ ($\sigma_{syst, s}^{v_n}$) is the systematic error of

the s^{th} uncertainty of the variable v_m (v_n).

The BLUE technique ensures that the estimator \hat{m}_{top} is a linear combination of the individual estimates, it provides an un-biased estimate of m_{top} , and it has the minimum possible variance ($\sigma_{m_{top}}^2$). This estimator can be written as:

$$\hat{m}_{top} = \sum_{m=1}^5 \alpha^{v_m} \cdot m_{top}^{v_m} \quad (6.10)$$

where α^{v_m} and $m_{top}^{v_m}$ are the weight and the top-quark mass estimates, respectively, obtained using the variable v_m . The variance $\sigma_{m_{top}}^2$ of the combined mass is:

$$\sigma_{m_{top}}^2 = \alpha^T \cdot E \cdot \alpha \quad (6.11)$$

where α is the vector of weights and E is the error matrix. The five weights are found so that they minimise the variance of the combined estimate:

$$\alpha = \frac{E^{-1} U}{U^T E^{-1} U} \quad (6.12)$$

where U is a vector of dimension $d = 5$ with all unity components, and E^{-1} is the inverse of the error matrix. The values of α^{v_m} obtained from this equation are reported below.

$$\begin{aligned} \alpha^{p_T^l} &= -1.82 & \alpha^{p_T^{e\mu}} &= 0.57 & \alpha^{p_T^e + p_T^\mu} &= 3.18 \\ \alpha^{m^{e\mu}} &= 0.11 & \alpha^{E^e + E^\mu} &= -1.04 \end{aligned}$$

These can be used in Equation 6.10 together with the $m_{top}^{v_m}$ values, reported in Table 6.1, to derive the value of \hat{m}_{top} . The final combined top-quark mass is:

$$m_{top} = 168.32 \pm 0.04 \text{ (stat)} \pm 1.19 \text{ (syst)} \text{ GeV} \quad (6.13)$$

This value is 2.2σ away from the one reported in Ref. [17]. This is due to the fact that this methodology uses the full information from the shape of variables that are sensitive to the top-quark mass but, at the same time, suffer from data/Monte Carlo mis-modelling which causes a shift in the measured top-quark mass central value. On the other hand, the final uncertainty on the top-quark pole mass is very small, demonstrating the level of accuracy this methodology can achieve. Including an additional uncertainty to cover for the data/Monte Carlo mis-modelling in the variables would spoil this feature, therefore, it was decided not to add it. Nevertheless, this is already encoded in the distance between the measured top-quark mass central value and the one in Ref. [17].

In order to make the two values compatible with each other, NNLO corrections need to be added to the cross section calculation, as they would consequently lead to a better description of the variables and, therefore, to a more precise estimation of the top-quark mass.

Conclusions

In this thesis, the challenging New Small Wheel ATLAS upgrade project has been presented focusing on the MicroMegas chambers construction and on the studies of its performance. Currently, the MicroMegas chambers are subject to a large number of tests both to understand and to validate their behaviour before their installation of the two NSW (NSW-A and NSW-C) during the LS2.

Before being mounted inside the MicroMegas chamber at the “Laboratori Nazionali di Frascati”, the metallic mesh undergoes a stretching procedure which has been developed by the Roma Tre INFN group. 155 meshes were stretched to complete 32 (+2 spare) SM1 modules and have some spares. The high voltage stability is crucial for the MicroMegas, therefore, several studies have been performed to identify and solve different sources of instability. The cleaning procedure was adopted to remove residuals from PCBs production and manipulation. Different studies were made to understand and remove mesh imperfections. The passivation of the readout boards edges was adopted to increase the resistance of the resistive strips. All these operations allowed to reduce the probability of having a spark inside the amplification gap and to increase the high voltage stability of the MicroMegas chambers.

In 2018, a test beam on the first non-prototype chamber (of SM2 type) was carried out and the chambers performances in terms of efficiencies and resolutions have been studied together with studies with different electronic settings to find the best configuration to operate them.

Once the modules are assembled and validated at the construction sites, they are shipped to the building BB5 at CERN, where they are integrated to form the double-wedge. Eight small MicroMegas double-wedges were studied at the Cosmic Ray Stand (only seven were validated) in terms of response as a function of track angle and amplification voltage. For all of them, the final high voltage configuration was found using the “splitter-boxes” and the final efficiency maps were produced. Different gas mixtures were used, both during the test beam and at BB5, to find a new mixture that ensures a better high voltage stability.

The second part of this work is focused on the $t\bar{t}$ production cross section measurements. Inclusive and fiducial cross section, together with single and double differential cross section, were measured using the 139 fb^{-1} collected by the ATLAS experiment during the Run 2 period (2015-2018). The measured $t\bar{t}$ cross section in the fiducial volume is:

$$\sigma_{fid,t\bar{t}} = 10.62 \pm 0.02 (stat) \pm 0.20 (lumi) \pm 0.13 (syst) \text{ pb}$$

while the total inclusive $t\bar{t}$ production cross section is:

$$\sigma_{t\bar{t}} = 830.3 \pm 1.2 \text{ (stat)} \pm 15.9 \text{ (lumi)} \pm 11.2 \text{ (syst)} \text{ pb}$$

which has a smaller error with respect to the previous analysis [39] and it is in agreement with the NNLO prediction of $831.76^{+19.77}_{-29.20}$ (scale) ± 35.06 (PDF+ α_S) pb. The present measurement is systematically limited. The main systematic uncertainty comes from the luminosity which gives a contribution of 1.9% with respect to a total relative uncertainty of 2.35%.

The large quantity of $t\bar{t}$ events produced due to the high value of the luminosity reached by the LHC has allowed performing differential measurements with a very high precision which will help to improve the prediction of the simulations for the future Monte Carlo generators. With respect to the previous ATLAS analysis [39], a finer binning and an extended range of the differential distributions was adopted keeping the uncertainty at the level of 2–3% in the majority of the bins.

The inclusive $t\bar{t}$ production cross section is used together with the parametrisation in Ref. [154, 157] to extract the top-quark pole mass. This was found to be $m_t^{pole} = 173.2^{+2.9}_{-2.6}$ GeV which is consistent with the values reported in Ref. [17].

Some of the measured normalised differential cross sections are sensitive to the top-quark pole mass. A combination of measurements performed in the single distributions yields a top-quark mass value of $m_t^{pole} = 168.32 \pm 0.04$ (stat) ± 1.19 (syst) GeV which differs from the value of 172.4 ± 0.7 GeV of Ref. [17] mainly due to the missing NNLO corrections in the adopted Monte Carlo samples.

Bibliography

- [1] M. Gell-Mann, *A schematic model of baryons and mesons*, *Physics Letters* **8** (1964) 214 – 215, <http://www.sciencedirect.com/science/article/pii/S0031916364920013>.
- [2] G. Zweig, *An SU(3) model for strong interaction symmetry and its breaking. Version 2*. <https://inspirehep.net/files/a752aea6bc476e4f50c506481b414337>.
- [3] J. E. Augustin et al., *Discovery of a Narrow Resonance in e^+e^- Annihilation*, *Phys. Rev. Lett.* **33** (1974) 1406–1408, <https://link.aps.org/doi/10.1103/PhysRevLett.33.1406>.
- [4] J. J. Aubert et al., *Experimental Observation of a Heavy Particle J*, *Phys. Rev. Lett.* **33** (1974) 1404–1406, <https://link.aps.org/doi/10.1103/PhysRevLett.33.1404>.
- [5] W. R. Innes et al., *Observation of Structure in the Υ Region*, *Phys. Rev. Lett.* **39** (1977) 1240–1242, <https://link.aps.org/doi/10.1103/PhysRevLett.39.1240>.
- [6] CDF Collaboration, *Observation of Top Quark Production in $\bar{p}p$ Collisions with the Collider Detector at Fermilab*, *Phys. Rev. Lett.* **74** (1995) 2626–2631, <https://link.aps.org/doi/10.1103/PhysRevLett.74.2626>.
- [7] D0 Collaboration, *Observation of the Top Quark*, *Phys. Rev. Lett.* **74** (1995) 2632–2637, <https://link.aps.org/doi/10.1103/PhysRevLett.74.2632>.
- [8] S. H. Neddermeyer and C. D. Anderson, *Note on the Nature of Cosmic-Ray Particles*, *Phys. Rev.* **51** (1937) 884–886, <https://link.aps.org/doi/10.1103/PhysRev.51.884>.
- [9] M. Conversi, E. Pancini, and O. Piccioni, *On the Disintegration of Negative Mesons*, *Phys. Rev.* **71** (1947) 209–210, <https://link.aps.org/doi/10.1103/PhysRev.71.209>.
- [10] M. L. Perl et al., *Evidence for Anomalous Lepton Production in $e^+ - e^-$ Annihilation*, *Phys. Rev. Lett.* **35** (1975) 1489–1492, <https://link.aps.org/doi/10.1103/PhysRevLett.35.1489>.

- [11] G. Danby, J.-M. Gaillard, K. Goulianos, L. M. Lederman, N. Mistry, M. Schwartz, and J. Steinberger, *Observation of High-Energy Neutrino Reactions and the Existence of Two Kinds of Neutrinos*, *Phys. Rev. Lett.* **9** (1962) 36–44, <https://link.aps.org/doi/10.1103/PhysRevLett.9.36>.
- [12] DONUT Collaboration, K. Kodama et al., *Observation of tau neutrino interactions*, *Phys. Lett. B* **504** (2001) 218–224, [arXiv:hep-ex/0012035](https://arxiv.org/abs/hep-ex/0012035).
- [13] Super-Kamiokande Collaboration, Y. Fukuda et al., *Measurements of the solar neutrino flux from Super-Kamiokande's first 300 days*, *Phys. Rev. Lett.* **81** (1998) 1158–1162, [arXiv:hep-ex/9805021](https://arxiv.org/abs/hep-ex/9805021), [Erratum: *Phys. Rev. Lett.* **81**, 4279 (1998)].
- [14] S. L. Glashow, *Partial Symmetries of Weak Interactions*, *Nucl. Phys.* **22** (1961) 579–588.
- [15] S. Weinberg, *A Model of Leptons*, *Phys. Rev. Lett.* **19** (1967) 1264–1266, <https://link.aps.org/doi/10.1103/PhysRevLett.19.1264>.
- [16] A. Salam, *Weak and Electromagnetic Interactions*, *Conf. Proc. C* **680519** (1968) 367–377.
- [17] P. D. Group, *Review of Particle Physics*, *Progress of Theoretical and Experimental Physics* **2020** (2020), <https://academic.oup.com/ptep/article-pdf/2020/8/083C01/33653179/ptaa104.pdf>, <https://doi.org/10.1093/ptep/ptaa104>, 083C01.
- [18] P. W. Higgs, *Broken symmetries, massless particles and gauge fields*, *Phys. Lett.* **12** (1964) 132–133.
- [19] P. W. Higgs, *Broken Symmetries and the Masses of Gauge Bosons*, *Phys. Rev. Lett.* **13** (1964) 508–509.
- [20] F. Englert and R. Brout, *Broken Symmetry and the Mass of Gauge Vector Mesons*, *Phys. Rev. Lett.* **13** (1964) 321–323.
- [21] G. Aad et al., *Observation of a new particle in the search for the Standard Model Higgs boson with the ATLAS detector at the LHC*, *Physics Letters B* **716** (2012) 1 – 29, <http://www.sciencedirect.com/science/article/pii/S037026931200857X>.
- [22] S. Chatrchyan et al., *Observation of a new boson at a mass of 125 GeV with the CMS experiment at the LHC*, *Physics Letters B* **716** (2012) 30 – 61, <http://www.sciencedirect.com/science/article/pii/S0370269312008581>.
- [23] *LEP design report*. CERN, Geneva, 1984. <https://cds.cern.ch/record/102083>. Copies shelved as reports in LEP, PS and SPS libraries.

- [24] G. Altarelli and G. Parisi, *Asymptotic freedom in parton language*, *Nuclear Physics B* **126** (1977) 298 – 318, <http://www.sciencedirect.com/science/article/pii/0550321377903844>.
- [25] Y. L. Dokshitzer, *Calculation of the Structure Functions for Deep Inelastic Scattering and e^+e^- Annihilation by Perturbation Theory in Quantum Chromodynamics.*, *Sov. Phys. JETP* **46** (1977) 641–653, http://www.jetp.ac.ru/cgi-bin/dn/e_046_04_0641.pdf.
- [26] NNPDF Collaboration, R. D. Ball et al., *Parton distributions for the LHC Run II*, *JHEP* **04** (2015) 040, [arXiv:1410.8849](https://arxiv.org/abs/1410.8849) [hep-ph].
- [27] A. Buckley et al., *General-purpose event generators for LHC physics*, *Physics Reports* **504** (2011) 145 – 233, <http://www.sciencedirect.com/science/article/pii/S0370157311000846>.
- [28] S. Alioli et al., *Monte Carlo event generators for high energy particle physics event simulation*, [arXiv:1902.01674](https://arxiv.org/abs/1902.01674) [hep-ph].
- [29] T. Gleisberg, S. Höche, F. Krauss, M. Schönherr, S. Schumann, F. Siegert, and J. Winter, *Event generation with SHERPA 1.1*, *Journal of High Energy Physics* **2009** (2009) 007–007, <https://doi.org/10.1088/2F1126-6708/2F2009/2F02/2F007>.
- [30] J. C. Collins, *Sudakov form-factors*, pp. , 573–614. 1989. [arXiv:hep-ph/0312336](https://arxiv.org/abs/hep-ph/0312336).
- [31] UA1 Collaboration, *Search for the top quark in UA1 and in the other hadron collider experiments*, *Acta Phys. Polon. B* **21** (1990) 327–343, <https://inspirehep.net/files/f1aaebd26af2cf63bd75defd0fa43be8>.
- [32] K. Kröninger, A. Meyer, and P. Uwer, *Top-Quark Physics at the LHC.*, Springer, Cham. (2015).
- [33] M. Czakon, D. Heymes, and A. Mitov, *High-precision differential predictions for top-quark pairs at the LHC*, *Phys. Rev. Lett.* **116** (2016) 082003, [arXiv:1511.00549](https://arxiv.org/abs/1511.00549) [hep-ph].
- [34] CDF Collaboration and D0 Collaboration, *Combination of measurements of the top-quark pair production cross section from the Tevatron Collider*, *Phys. Rev. D* **89** (2014) 072001, <https://link.aps.org/doi/10.1103/PhysRevD.89.072001>.
- [35] ATLAS Collaboration and CMS Collaboration, *Combination of ATLAS and CMS top-quark pair cross section measurements using up to 1.1 fb⁻¹ of data at 7 TeV*, Tech. Rep. ATLAS-CONF-2012-134, CERN, Geneva, Sep, 2012. <https://cds.cern.ch/record/1478422>.

- [36] ATLAS Collaboration and CMS Collaboration, *Combination of ATLAS and CMS top quark pair cross section measurements in the $e\mu$ final state using proton-proton collisions at $\sqrt{s}=8$ TeV*, Tech. Rep. ATLAS-CONF-2014-054, CERN, Geneva, Sep, 2014. <https://cds.cern.ch/record/1951322>.
- [37] M. Czakon and A. Mitov, *Top++: A program for the calculation of the top-pair cross-section at hadron colliders*, *Comput. Phys. Commun.* **185** (2014) 2930, [arXiv:1112.5675](https://arxiv.org/abs/1112.5675) [hep-ph].
- [38] ATLAS Collaboration, *Measurement of the $t\bar{t}$ production cross-section in the lepton+jets channel at $\sqrt{s}=13$ TeV with the ATLAS experiment*, [arXiv:2006.13076](https://arxiv.org/abs/2006.13076) [hep-ex].
- [39] ATLAS Collaboration, *Measurement of the $t\bar{t}$ production cross-section and lepton differential distributions in $e\mu$ dilepton events from pp collisions at $\sqrt{s}=13$ TeV with the ATLAS detector*, *Eur. Phys. J. C* **80** (2020) 528, [arXiv:1910.08819](https://arxiv.org/abs/1910.08819) [hep-ex].
- [40] CMS Collaboration, *Measurement of the $t\bar{t}$ production cross section using events with one lepton and at least one jet in pp collisions at $\sqrt{s}=13$ TeV*, *JHEP* **09** (2017) 051, [arXiv:1701.06228](https://arxiv.org/abs/1701.06228) [hep-ex].
- [41] CMS Collaboration, *Measurement of the $t\bar{t}$ production cross section, the top quark mass, and the strong coupling constant using dilepton events in pp collisions at $\sqrt{s}=13$ TeV*, *Eur. Phys. J. C* **79** (2019) 368, [arXiv:1812.10505](https://arxiv.org/abs/1812.10505) [hep-ex].
- [42] LHCTopWG, *LHC Top WG Summary Plots*, <https://twiki.cern.ch/twiki/bin/view/LHCPhysics/LHCTopWGSummaryPlots>.
- [43] CMS Collaboration, *Measurements of $t\bar{t}$ differential cross sections in proton-proton collisions at $\sqrt{s}=13$ TeV using events containing two leptons*, *JHEP* **02** (2019) 149, [arXiv:1811.06625](https://arxiv.org/abs/1811.06625) [hep-ex].
- [44] P. Kant, O. Kind, T. Kintscher, T. Lohse, T. Martini, S. Mölbitz, P. Rieck, and P. Uwer, *HatHor for single top-quark production: Updated predictions and uncertainty estimates for single top-quark production in hadronic collisions*, *Comput. Phys. Commun.* **191** (2015) 74–89, [arXiv:1406.4403](https://arxiv.org/abs/1406.4403) [hep-ph].
- [45] M. Aliev, H. Lacker, U. Langenfeld, S. Moch, P. Uwer, et al., *HATHOR: Hadronic Top and Heavy quarks cross section calculator*, *Comput.Phys.Commun.* **182** (2011) 1034–1046, [arXiv:1007.1327](https://arxiv.org/abs/1007.1327) [hep-ph].
- [46] C. D. White, S. Frixione, E. Laenen, and F. Maltoni, *Isolating Wt production at the LHC*, *Journal of High Energy Physics* **2009** (2009) 074–074, <https://doi.org/10.1088%2F1126-6708%2F2009%2F11%2F074>.

- [47] S. Frixione, E. Laenen, P. Motylinski, C. White, and B. R. Webber, *Single-top hadroproduction in association with a W boson*, *Journal of High Energy Physics* **2008** (2008) 029–029, <https://doi.org/10.1088%2F1126-6708%2F2008%2F07%2F029>.
- [48] Gfitter Group Collaboration, M. Baak, J. Cúth, J. Haller, A. Hoecker, R. Kogler, K. Mönig, M. Schott, and J. Stelzer, *The global electroweak fit at NNLO and prospects for the LHC and ILC*, *Eur. Phys. J. C* **74** (2014) 3046, [arXiv:1407.3792](https://arxiv.org/abs/1407.3792) [[hep-ph](#)].
- [49] L. Evans and P. Bryant, *LHC Machine*, *JINST* **3** (2008) S08001.
- [50] O. S. Brüning, P. Collier, P. Lebrun, S. Myers, R. Ostojic, J. Poole, and P. Proudlock, *LHC Design Report*. CERN Yellow Reports: Monographs. CERN, Geneva, 2004. <https://cds.cern.ch/record/782076>.
- [51] ATLAS Collaboration, *The ATLAS Experiment at the CERN Large Hadron Collider*, *JINST* **3** (2008) S08003.
- [52] ALICE Collaboration, *The ALICE experiment at the CERN LHC*, *JINST* **3** (2008) S08002.
- [53] CMS Collaboration, *The CMS experiment at the CERN LHC*, *JINST* **3** (2008) S08004.
- [54] LHCb Collaboration, *The LHCb Detector at the LHC*, *JINST* **3** (2008) S08005.
- [55] CERN, *Facts and figures about the LHC*, <https://home.cern/resources/faqs/facts-and-figures-about-lhc>.
- [56] ATLAS Collaboration, *Luminosity Public Results Run2*, <https://twiki.cern.ch/twiki/bin/view/AtlasPublic/LuminosityPublicResultsRun2>.
- [57] L. Rossi and O. Brüning, *High Luminosity Large Hadron Collider: A description for the European Strategy Preparatory Group*, Tech. Rep. CERN-ATS-2012-236, CERN, Geneva, Aug, 2012. <https://cds.cern.ch/record/1471000>.
- [58] H. J. Herman, *The superconducting magnet system for the ATLAS Detector at CERN*, *IEEE Transactions on Applied Superconductivity* **10** (2000) 347–352.
- [59] A. Yamamoto, Y. Makida, R. Ruber, Y. Doi, T. Haruyama, F. Haug, H. Ten Kate, M. Kawai, T. Kondo, Y. Kondo, et al., *The ATLAS Central Solenoid*, Nuclear Instruments and Methods in Physics Research Section A: Accelerators, Spectrometers, Detectors and Associated Equipment **584** (2008) 53–74, <https://www.sciencedirect.com/science/article/pii/S0168900207020414>.
- [60] ATLAS Collaboration, *ATLAS Barrel Toroid: Technical design report*, Cern-lhcc-97-19, <https://cds.cern.ch/record/331065/files/cer-000254565.pdf>.

- [61] ATLAS Collaboration, *ATLAS Endcap Toroids: Technical design report*, Cern-lhcc-97-20, 1997, <https://cds.cern.ch/record/331066>.
- [62] M. Brice, *Lowering the first ATLAS toroid. Le 26 octobre, des ponts ont descendu dans le hall souterrain d'ATLAS la première des huit bobines toroïdales du tonneau.*, tech. rep., Oct, 2004. <https://cds.cern.ch/record/802466>.
- [63] ATLAS Collaboration, *ATLAS Inner Detector: Technical design report. Vol. 1*, Cern-lhcc-97-16, atlas-tdr-4, 1997, <https://cds.cern.ch/record/331063>.
- [64] ATLAS Collaboration, *ATLAS Inner Detector: Technical design report. Vol. 2*, Cern-lhcc-97-17, 1997, <https://cds.cern.ch/record/331064>.
- [65] ATLAS Collaboration, *Track Reconstruction Performance of the ATLAS Inner Detector at $\sqrt{s} = 13$ TeV*, ATL-PHYS-PUB-2015-018, 2015, <https://cds.cern.ch/record/2037683>.
- [66] C. Marcelloni De Oliveira, *IBL installation into the inner detector of the ATLAS Experiment side C*, tech. rep., May, 2014. <https://cds.cern.ch/record/1702006>. General Photo.
- [67] ATLAS Collaboration, *ATLAS Pixel Detector: Technical design report*, Cern-lhcc-98-13, 1998, <https://cds.cern.ch/record/2285585>.
- [68] ATLAS Collaboration, *ATLAS Insertable B-Layer Technical Design Report*, Cern-lhcc-2010-013, atlas-tdr-19, 2010, <https://cds.cern.ch/record/1291633>.
- [69] ATLAS Collaboration, *The ATLAS semiconductor tracker (SCT)*, *Nucl. Instrum. Meth. A* **541** (2005) 89–95.
- [70] ATLAS Collaboration, *The ATLAS Transition Radiation Tracker (TRT) proportional drift tube: Design and performance*, *JINST* **3** (2008) P02013.
- [71] J. Pequenaó, *Computer Generated image of the ATLAS calorimeter*, tech. rep., Mar, 2008. <https://cds.cern.ch/record/1095927>.
- [72] M. Brice, *Installation of the last module of the Hadronic Tile Calorimeter side A in ATLAS cavern*, tech. rep., May, 2006. <https://cds.cern.ch/record/1049117>.
- [73] ATLAS Collaboration, *ATLAS Liquid Argon Calorimeter: Technical design report*, Cern-lhcc-96-41, 1996, <https://cds.cern.ch/record/331061>.
- [74] ATLAS Collaboration, *ATLAS Tile Calorimeter: Technical design report*, Cern-lhcc-96-42, 1996, <https://cds.cern.ch/record/331062>.

- [75] ATLAS Collaboration, *ATLAS Muon Spectrometer: Technical design report*, Cern-lhcc-97-22, atlas-tdr-10, 1997, <https://cds.cern.ch/record/331068>.
- [76] C. Marcelloni, *Lowering the second small wheel down the 100 m shaft into the ATLAS cavern*, tech. rep., Feb, 2008. <https://cds.cern.ch/record/1091947>.
- [77] ATLAS Collaboration, *ATLAS Trigger Performance: Status report*, Cern-lhcc-98-15, 1998, <http://cdsweb.cern.ch/record/381430/files/cer-0307031.pdf>.
- [78] ATLAS Collaboration, *ATLAS high-level trigger, data-acquisition and controls: Technical Design Report*, Cern-lhcc-2003-022, 2003, <https://cds.cern.ch/record/616089>.
- [79] ATLAS Collaboration, *Letter of Intent for the Phase-II Upgrade of the ATLAS Experiment*, Tech. Rep. CERN-LHCC-2012-022. LHCC-I-023, CERN, Geneva, Dec, 2012. <https://cds.cern.ch/record/1502664>.
- [80] T. Kawamoto, S. Vlachos, L. Pontecorvo, J. Dubbert, G. Mikenberg, P. Iengo, C. Dallapiccola, C. Amelung, L. Levinson, R. Richter, and D. Lellouch, *New Small Wheel Technical Design Report*, Tech. Rep. CERN-LHCC-2013-006. ATLAS-TDR-020, Jun, 2013. <https://cds.cern.ch/record/1552862>.
- [81] Y. Giomataris, P. Rebourgeard, J. Robert, and G. Charpak, *MICROMEGAS: a high-granularity position-sensitive gaseous detector for high particle-flux environments*, *Nuclear Instruments and Methods in Physics Research Section A: Accelerators, Spectrometers, Detectors and Associated Equipment* **376** (1996) 29 – 35, <http://www.sciencedirect.com/science/article/pii/0168900296001751>.
- [82] T. Alexopoulos et al., *Performance studies of resistive-strip bulk micromegas detectors in view of the ATLAS New Small Wheel upgrade*, *Nuclear Instruments and Methods in Physics Research Section A: Accelerators, Spectrometers, Detectors and Associated Equipment* **937** (2019) 125 – 140, <http://www.sciencedirect.com/science/article/pii/S0168900219305194>.
- [83] R. Veenhof, *Simulation of gaseous detectors (Garfield++)*, <http://garfieldpp.web.cern.ch/garfieldpp/>.
- [84] G. Iakovidis, *Research and Development in Micromegas Detector for the ATLAS Upgrade*, CERN-THESIS-2014-148, <https://cds.cern.ch/record/1955475>.
- [85] H. Raether, *Die Entwicklung der Elektronenlawine in den Funkenkanal*, *Zeitschrift für Physik* **112** (1939) 464 – 489, <https://link.springer.com/content/pdf/10.1007/BF01340229.pdf>.
- [86] T. Alexopoulos et al., *Development of large size Micromegas detector for the upgrade of the ATLAS Muon system*, *Nuclear Instruments and Methods in Physics Research*

- Section A: Accelerators, Spectrometers, Detectors and Associated Equipment **617** (2010) 161 – 165, <http://www.sciencedirect.com/science/article/pii/S0168900209013485>.
- [87] M. Alfonsi et al., *Development of Micro-Pattern Gas Detectors Technologies*, CERN-LHCC-2008-011 / LHCC-P-001, <https://cds.cern.ch/record/1120459>.
- [88] M. Iodice, *Micromegas detectors for the Muon Spectrometer upgrade of the ATLAS experiment*, *Journal of Instrumentation* **10** (2015) C02026–C02026.
- [89] G. Iakovidis, *VMM3a, an ASIC for tracking detectors*, *Journal of Physics: Conference Series* **1498** (2020) 012051.
- [90] C. Arcangeletti, *Assembly of the SM1 MicroMegas chambers for the muon spectrometer upgrade of the ATLAS experiment at LHC*, *Il Nuovo Cimento C* **043 - Issue 02-03** (2020), <https://cds.cern.ch/record/1120459>.
- [91] L. Martinelli, *Micromegas chambers performance studies for the ATLAS upgrade*, *Nuovo Cim. C* **43** (2020) 60.
- [92] *Construction techniques and performances of a full-size prototype Micromegas chamber for the ATLAS muon spectrometer upgrade*, *Nuclear Instruments and Methods in Physics Research Section A: Accelerators, Spectrometers, Detectors and Associated Equipment* **955** (2020) 162086.
- [93] *The radiation field in the Gamma Irradiation Facility GIF++ at CERN*, *Nuclear Instruments and Methods in Physics Research Section A: Accelerators, Spectrometers, Detectors and Associated Equipment* **866** (2017) 91 – 103.
- [94] ATLAS Collaboration, *Performance of the ATLAS Track Reconstruction Algorithms in Dense Environments in LHC Run 2*, *Eur. Phys. J. C* **77** (2017) 673, [arXiv:1704.07983](https://arxiv.org/abs/1704.07983) [hep-ex].
- [95] R. Fruhwirth, *Application of Kalman filtering to track and vertex fitting*, *Nucl. Instrum. Meth. A* **262** (1987) 444–450.
- [96] ATLAS Collaboration, *Reconstruction of primary vertices at the ATLAS experiment in Run 1 proton–proton collisions at the LHC. Reconstruction of primary vertices at the ATLAS experiment in Run 1 proton-proton collisions at the LHC*, *Eur. Phys. J. C* **77** (2016) 332. 52 p, <https://cds.cern.ch/record/2235651>.
- [97] ATLAS Collaboration, *Electron and photon performance measurements with the ATLAS detector using the 2015–2017 LHC proton-proton collision data*, *JINST* **14** (2019) P12006, [arXiv:1908.00005](https://arxiv.org/abs/1908.00005) [hep-ex].

- [98] ATLAS Collaboration, *Background rejection study in the context of the electron reconstruction and identification: Background rejection for genuine electrons (from prompt decays)*, Tech. Rep. ATL-COM-PHYS-2020-092, CERN, Geneva, Jan, 2020. <https://cds.cern.ch/record/2709125>.
- [99] ATLAS Collaboration, *Muon reconstruction and identification efficiency in ATLAS using the full Run 2 pp collision data set at $\sqrt{s} = 13$ TeV*, Tech. Rep. ATLAS-CONF-2020-030, CERN, Geneva, Aug, 2020. <https://cds.cern.ch/record/2725736>.
- [100] W. Lampl, S. Laplace, D. Lelas, P. Loch, H. Ma, S. Menke, S. Rajagopalan, D. Rousseau, S. Snyder, and G. Unal, *Calorimeter clustering algorithms: Description and performance*, <https://cds.cern.ch/record/1099735>.
- [101] ATLAS Collaboration, *Topological cell clustering in the ATLAS calorimeters and its performance in LHC Run 1*, *Eur. Phys. J. C* **77** (2017) 490, [arXiv:1603.02934](https://arxiv.org/abs/1603.02934) [hep-ex].
- [102] ATLAS Collaboration, *Jet reconstruction and performance using particle flow with the ATLAS Detector*, *Eur. Phys. J. C* **77** (2017) 466, [arXiv:1703.10485](https://arxiv.org/abs/1703.10485) [hep-ex].
- [103] M. Cacciari, G. P. Salam, and G. Soyez, *The anti- k_t jet clustering algorithm*, *JHEP* **04** (2008) 063, [arXiv:0802.1189](https://arxiv.org/abs/0802.1189) [hep-ph].
- [104] M. Cacciari and G. P. Salam, *Pileup subtraction using jet areas*, *Phys. Lett.* **B659** (2008) 119–126, [arXiv:0707.1378](https://arxiv.org/abs/0707.1378) [hep-ph].
- [105] ATLAS Collaboration, ATLAS Collaboration, *Jet energy scale measurements and their systematic uncertainties in proton-proton collisions at $\sqrt{s} = 13$ TeV with the ATLAS detector*, [arXiv:1703.09665](https://arxiv.org/abs/1703.09665) [hep-ex].
- [106] ATLAS Collaboration, ATLAS Collaboration, *Jet energy scale and resolution measured in proton-proton collisions at $\sqrt{s} = 13$ TeV with the ATLAS detector*, [arXiv:2007.02645](https://arxiv.org/abs/2007.02645) [hep-ex].
- [107] ATLAS Collaboration, *ATLAS b-jet identification performance and efficiency measurement with $t\bar{t}$ events in pp collisions at $\sqrt{s} = 13$ TeV*, *Eur. Phys. J. C* **79** (2019) 970, [arXiv:1907.05120](https://arxiv.org/abs/1907.05120) [hep-ex].
- [108] A. Hocker et al., *TMVA - Toolkit for Multivariate Data Analysis*, [arXiv:physics/0703039](https://arxiv.org/abs/physics/0703039).
- [109] ATLAS Collaboration, *The ATLAS Simulation Infrastructure*, *Eur. Phys. J. C* **70** (2010) 823, [arXiv:1005.4568](https://arxiv.org/abs/1005.4568) [physics.ins-det].
- [110] GEANT4 Collaboration, S. Agostinelli et al., *GEANT4: A Simulation toolkit*, *Nucl.Instrum.Meth.* **A506** (2003) 250–303.

- [111] ATLAS Collaboration, *The simulation principle and performance of the ATLAS fast calorimeter simulation FastCaloSim*, ATL-PHYS-PUB-2010-013, 2010, <https://cds.cern.ch/record/1300517>.
- [112] W. Lukas, *Fast Simulation for ATLAS: Atlfast-II and ISF*, 2012. <http://cdsweb.cern.ch/record/1458503/files/ATL-SOFT-PROC-2012-065.pdf>.
- [113] P. Nason, *A New method for combining NLO QCD with shower Monte Carlo algorithms*, *JHEP* **11** (2004) 040, [arXiv:hep-ph/0409146](https://arxiv.org/abs/hep-ph/0409146) [hep-ph].
- [114] S. Frixione, P. Nason, and C. Oleari, *Matching NLO QCD computations with Parton Shower simulations: the POWHEG method*, *JHEP* **11** (2007) 070, [arXiv:0709.2092](https://arxiv.org/abs/0709.2092) [hep-ph].
- [115] S. Alioli, P. Nason, C. Oleari, and E. Re, *A general framework for implementing NLO calculations in shower Monte Carlo programs: the POWHEG BOX*, *JHEP* **06** (2010) 043, [arXiv:1002.2581](https://arxiv.org/abs/1002.2581) [hep-ph].
- [116] J. Alwall, R. Frederix, S. Frixione, V. Hirschi, F. Maltoni, O. Mattelaer, H. S. Shao, T. Stelzer, P. Torrielli, and M. Zaro, *The automated computation of tree-level and next-to-leading order differential cross sections, and their matching to parton shower simulations*, *JHEP* **07** (2014) 079, [arXiv:1405.0301](https://arxiv.org/abs/1405.0301) [hep-ph].
- [117] T. Sjostrand, S. Mrenna, and P. Z. Skands, *A Brief Introduction to PYTHIA 8.1*, *Comput. Phys. Commun.* **178** (2008) 852–867, [arXiv:0710.3820](https://arxiv.org/abs/0710.3820) [hep-ph].
- [118] T. Sjostrand, S. Mrenna, and P. Z. Skands, *PYTHIA 6.4 Physics and Manual*, *JHEP* **05** (2006) 026, [arXiv:hep-ph/0603175](https://arxiv.org/abs/hep-ph/0603175) [hep-ph].
- [119] J. Bellm et al., *Herwig 7.0/Herwig++ 3.0 release note*, *Eur. Phys. J. C* **76** (2016) 196, [arXiv:1512.01178](https://arxiv.org/abs/1512.01178) [hep-ph].
- [120] *ATLAS Run 1 Pythia8 tunes*, Tech. Rep. ATL-PHYS-PUB-2014-021, CERN, Geneva, Nov, 2014. <https://cds.cern.ch/record/1966419>.
- [121] R. D. Ball et al., *Parton distributions with LHC data*, *Nucl. Phys.* **B867** (2013) 244–289, [arXiv:1207.1303](https://arxiv.org/abs/1207.1303) [hep-ph].
- [122] E. Re, *Single-top Wt -channel production matched with parton showers using the POWHEG method*, *Eur. Phys. J.* **C71** (2011) 1547, [arXiv:1009.2450](https://arxiv.org/abs/1009.2450) [hep-ph].
- [123] S. Gieseke, C. Rohr, and A. Siodmok, *Colour reconnections in Herwig++*, *Eur. Phys. J.* **C72** (2012) 2225, [arXiv:1206.0041](https://arxiv.org/abs/1206.0041) [hep-ph].
- [124] R. Frederix, E. Re, and P. Torrielli, *Single-top t -channel hadroproduction in the four-flavour scheme with POWHEG and aMC@NLO*, *JHEP* **09** (2012) 130, [arXiv:1207.5391](https://arxiv.org/abs/1207.5391) [hep-ph].

- [125] T. Gleisberg et al., *Event generation with SHERPA 1.1*, *JHEP* **02** (2009) 007, [arXiv:0811.4622](https://arxiv.org/abs/0811.4622) [hep-ph].
- [126] F. Cascioli, S. Höche, F. Krauss, P. Maierhöfer, S. Pozzorini, and F. Siegert, *Precise Higgs-background predictions: merging NLO QCD and squared quark-loop corrections to four-lepton + 0,1 jet production*, *JHEP* **01** (2014) 046, [arXiv:1309.0500](https://arxiv.org/abs/1309.0500) [hep-ph].
- [127] L. Lonnblad, *Correcting the color dipole cascade model with fixed order matrix elements*, *JHEP* **05** (2002) 046, [arXiv:hep-ph/0112284](https://arxiv.org/abs/hep-ph/0112284) [hep-ph].
- [128] M. Cacciari and G. P. Salam, *Dispelling the N^3 myth for the k_t jet-finder*, *Phys. Lett. B* **641** (2006) 57–61, [arXiv:hep-ph/0512210](https://arxiv.org/abs/hep-ph/0512210).
- [129] R. Brun and F. Rademakers, *ROOT: An object oriented data analysis framework*, *Nucl. Instrum. Meth. A* **389** (1997) 81–86.
- [130] ATLAS Collaboration, *Measurement of the $t\bar{t}$ production cross-section using $e\mu$ events with b -tagged jets in pp collisions at $\sqrt{s} = 7$ and 8 TeV with the ATLAS detector*, *Eur. Phys. J. C* **74** (2014) 3109, [arXiv:1406.5375](https://arxiv.org/abs/1406.5375) [hep-ex].
- [131] ATLAS Collaboration, *Measurement of lepton differential distributions and the top quark mass in $t\bar{t}$ production in pp collisions at $\sqrt{s} = 8$ TeV with the ATLAS detector*, *Eur. Phys. J. C* **77** (2017) 804, [arXiv:1709.09407](https://arxiv.org/abs/1709.09407) [hep-ex].
- [132] ATLAS Collaboration, *Measurement of the $t\bar{t}$ production cross-section using $e\mu$ events with b -tagged jets in pp collisions at $\sqrt{s} = 13$ TeV with the ATLAS detector*, *Phys. Lett. B* **761** (2016) 136, [arXiv:1606.02699](https://arxiv.org/abs/1606.02699) [hep-ex].
- [133] R. Hawkings, *Measurement of the $t\bar{t}$ production cross-section in pp collisions at $\sqrt{s} = 7-8$ TeV using $e\mu$ events with b -tagged jets*, Tech. Rep. ATL-PHYS-INT-2014-025, CERN, Geneva, Oct, 2014. <https://cds.cern.ch/record/1952814>.
- [134] A. V. Lipatov, G. I. Lykasov, M. A. Malyshev, A. A. Prokhorov, and S. M. Turchikhin, *Hard production of a Z boson plus heavy flavor jets at LHC and the intrinsic charm content of a proton*, *Phys. Rev. D* **97** (2018) 114019, [arXiv:1802.05085](https://arxiv.org/abs/1802.05085) [hep-ph].
- [135] R. Hawkings, *Measurement of lepton differential distributions in $t\bar{t}$ production in pp collisions at $\sqrt{s} = 8$ TeV using $e\mu$ events with b -tagged jets*, Tech. Rep. ATL-COM-PHYS-2015-002, CERN, Geneva, Jan, 2015. <https://cds.cern.ch/record/1979932>.
- [136] ATLAS Collaboration, *Further studies on simulation of top-quark production for the ATLAS experiment at $\sqrt{s} = 13$ TeV*, ATL-PHYS-PUB-2016-016, 2016, <https://cds.cern.ch/record/2205262>.

- [137] ATLAS Collaboration, *Improvements in $t\bar{t}$ modelling using NLO+PS Monte Carlo generators for Run 2*, ATL-PHYS-PUB-2018-009, 2018, <https://cds.cern.ch/record/2630327>.
- [138] R. Barlow, *Application of the Bootstrap resampling technique to Particle Physics experiments*, MAN/HEP/99/4 (2000), <http://www.hep.manchester.ac.uk/preprints/manhep99-4.ps>.
- [139] R. Barlow, *SLUO Lectures on Statistical and Numerical Methods in HEP. Lecture 6: Resampling and the Bootstrap*, https://www-group.slac.stanford.edu/sluo/Lectures/stat_lecture_files/sluolec6.pdf.
- [140] ATLAS Collaboration, *Performance of electron and photon triggers in ATLAS during LHC Run 2*, *Eur. Phys. J. C* **80** (2020) 47, [arXiv:1909.00761](https://arxiv.org/abs/1909.00761) [[hep-ex](#)].
- [141] ATLAS Collaboration, *Electron identification measurements in ATLAS using $\sqrt{s} = 13$ TeV data with 50 ns bunch spacing*, ATL-PHYS-PUB-2015-041, 2015, <https://cds.cern.ch/record/2048202>.
- [142] ATLAS Collaboration, *Jet energy scale measurements and their systematic uncertainties in proton–proton collisions at $\sqrt{s} = 13$ TeV with the ATLAS detector*, *Phys. Rev. D* **96** (2017) 072002, [arXiv:1703.09665](https://arxiv.org/abs/1703.09665) [[hep-ex](#)].
- [143] ATLAS Collaboration, *Measurements of b -jet tagging efficiency with the ATLAS detector using $t\bar{t}$ events at $\sqrt{s} = 13$ TeV*, *JHEP* **08** (2018) 089, [arXiv:1805.01845](https://arxiv.org/abs/1805.01845) [[hep-ex](#)].
- [144] J. Butterworth et al., *PDF4LHC recommendations for LHC Run II*, *J. Phys. G* **43** (2016) 023001, [arXiv:1510.03865](https://arxiv.org/abs/1510.03865) [[hep-ph](#)].
- [145] N. Kidonakis, *Two-loop soft anomalous dimensions for single top quark associated production with a W - or H -*, *Phys.Rev.* **D82** (2010) 054018, [arXiv:1005.4451](https://arxiv.org/abs/1005.4451) [[hep-ph](#)].
- [146] *NLO single-top channel cross section*, <https://twiki.cern.ch/twiki/bin/view/LHCPhysics/SingleTopRefXsec>.
- [147] ATLAS Collaboration, *Single Boson and Diboson Production Cross Sections in pp collisions at $\sqrt{s} = 7$ TeV*, <https://cds.cern.ch/record/1287902>.
- [148] R. Hawkings, *Measurement of the $t\bar{t}$ production cross-section and lepton differential distributions in pp collisions at $\sqrt{s} = 13$ TeV with 2015-16 ATLAS data*, Tech. Rep. ATL-COM-PHYS-2018-1163, CERN, Geneva, Aug, 2018. <https://cds.cern.ch/record/2634819>.
- [149] ATLAS Collaboration, *Measurement of the $t\bar{t}Z$ and $t\bar{t}W$ production cross sections in multilepton final states using 36.1 fb^{-1} of pp collisions at 13 TeV at the LHC*, <https://cds.cern.ch/record/2235582>.

- [150] ATLAS Collaboration, *Luminosity determination in pp collisions at $\sqrt{s} = 13$ TeV using the ATLAS detector at the LHC*, Tech. Rep. ATLAS-CONF-2019-021, CERN, Geneva, Jun, 2019. <https://cds.cern.ch/record/2677054>.
- [151] G. Avoni et al., *The new LUCID-2 detector for luminosity measurement and monitoring in ATLAS*, *JINST* **13** (2018) P07017.
- [152] ATLAS Collaboration, *Luminosity determination in pp collisions at $\sqrt{s} = 8$ TeV using the ATLAS detector at the LHC*, *Eur. Phys. J. C* **76** (2016) 653, [arXiv:1608.03953](https://arxiv.org/abs/1608.03953) [hep-ex].
- [153] E. Todesco and J. Wenninger, *Large Hadron Collider momentum calibration and accuracy*, *Phys. Rev. Accel. Beams* **20** (2017) 081003, <https://link.aps.org/doi/10.1103/PhysRevAccelBeams.20.081003>.
- [154] J. Ferrando and D. Wendland, *Reference $t\bar{t}$ production cross sections for use in ATLAS analyses*, Tech. Rep. ATL-COM-PHYS-2014-112, CERN, Geneva, Feb, 2014. <https://cds.cern.ch/record/1662536>.
- [155] A. Buckley, J. Ferrando, S. Lloyd, K. Nordström, B. Page, M. Rüfenacht, M. Schönherr, and G. Watt, *LHAPDF6: parton density access in the LHC precision era*, *Eur. Phys. J.* **C75** (2015) 132, [arXiv:1412.7420](https://arxiv.org/abs/1412.7420) [hep-ph].
- [156] ATLAS Collaboration, *Probing the quantum interference between singly and doubly resonant top-quark production in pp collisions at $\sqrt{s} = 13$ TeV with the ATLAS detector*, *Phys. Rev. Lett.* **121** (2018) 152002, [arXiv:1806.04667](https://arxiv.org/abs/1806.04667) [hep-ex].
- [157] M. Czakon, P. Fiedler, and A. Mitov, *Total Top-Quark Pair-Production Cross Section at Hadron Colliders Through $\alpha(\frac{4}{3})$* , *Phys. Rev. Lett.* **110** (2013) 252004, [arXiv:1303.6254](https://arxiv.org/abs/1303.6254) [hep-ph].
- [158] A. H. Hoang and I. W. Stewart, *Top Mass Measurements from Jets and the Tevatron Top-Quark Mass*, *Nucl. Phys. B Proc. Suppl.* **185** (2008) 220–226, [arXiv:0808.0222](https://arxiv.org/abs/0808.0222) [hep-ph].
- [159] S. Frixione and A. Mitov, *Determination of the top quark mass from leptonic observables*, *JHEP* **09** (2014) 012, [arXiv:1407.2763](https://arxiv.org/abs/1407.2763) [hep-ph].
- [160] L. Lyons, D. Gibaut, and P. Clifford, *How to Combine Correlated Estimates of a Single Physical Quantity*, *Nucl. Instrum. Meth.* **A270** (1988) 110.

A Double-wedges HV maps and extected efficiencies

This appendix shows all the final HV maps of each double-wedge validated so far with the expected efficiencies. The following colour code is used in the plots below: gray if the HV is equal to 0 V, dark red if $0 V < HV < 510 V$, red if $510 V \leq HV < 530 V$, three different shades of orange (from darkest to lightest) if $530 V \leq HV < 560 V$, yellow if $560 V \leq HV < 570 V$ while green if the high voltage is equal to 570 V.

A.1 Double-wedge A14

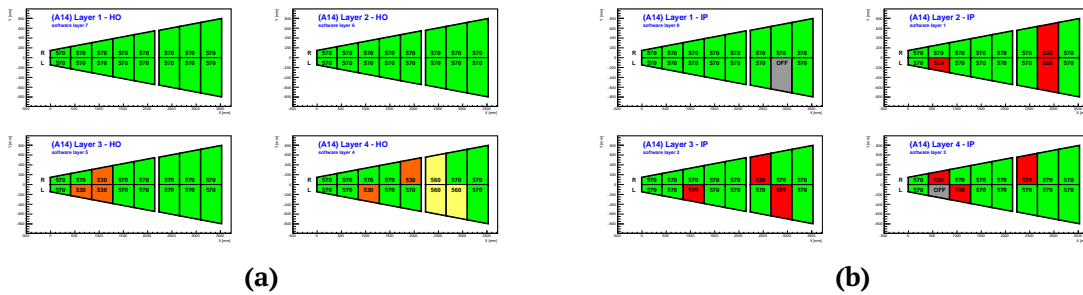


Figure A.9: Final HV map for the double-wedge A14.

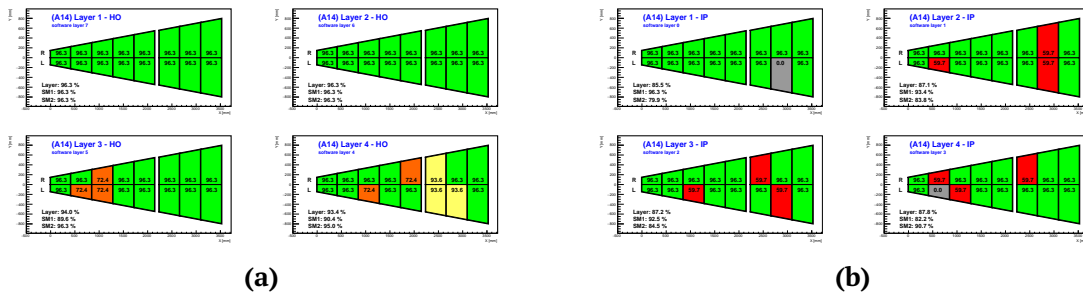


Figure A.10: Final expected efficiency for the double-wedge A14.

A.2 Double-wedge A12

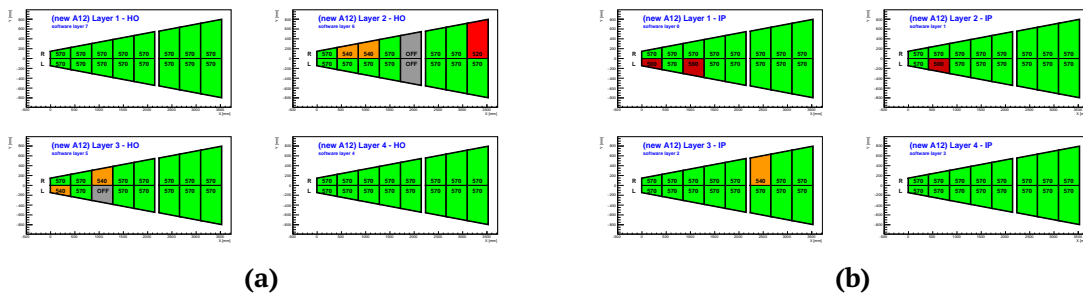


Figure A.11: Final HV map for the double-wedge A12.

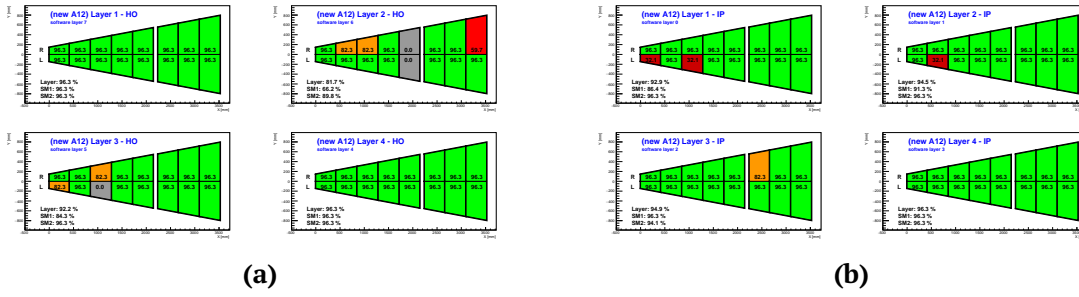


Figure A.12: Final expected efficiency for the double-wedge A12.

A.3 Double-wedge A10

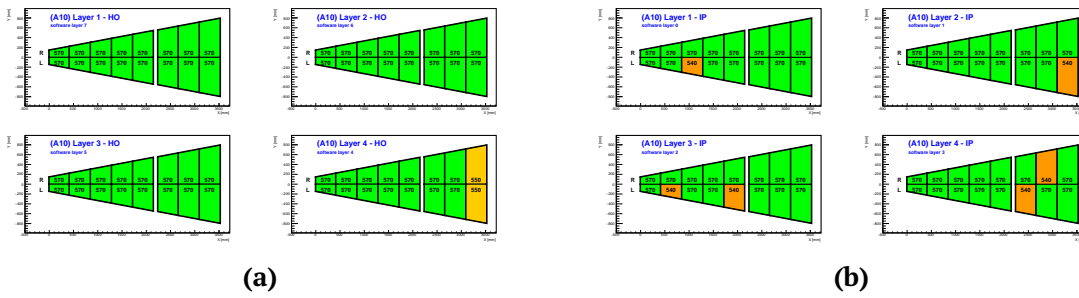


Figure A.13: Final HV map for the double-wedge A10.

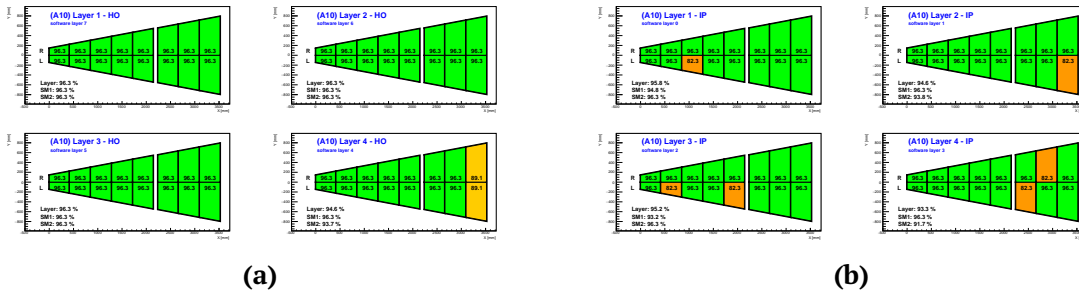


Figure A.14: Final expected efficiency for the double-wedge A10.

A.4 Double-wedge A16

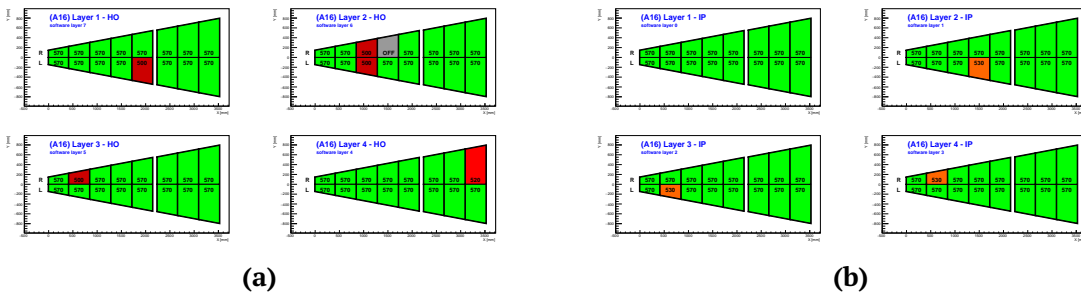


Figure A.15: Final HV map for the double-wedge A16.

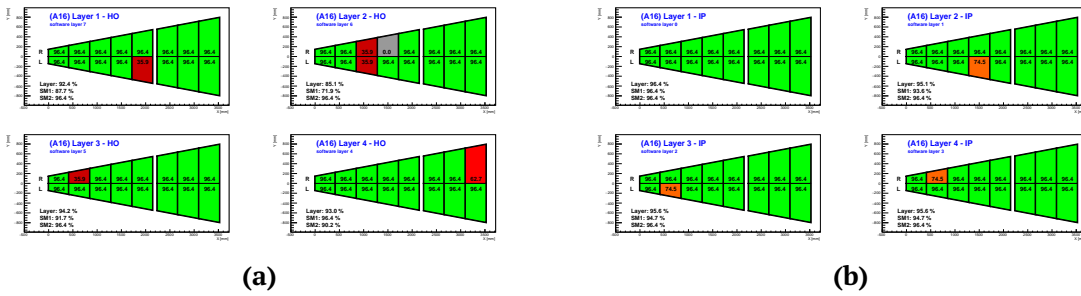


Figure A.16: Final expected efficiency for the double-wedge A16.

A.5 Double-wedge A08

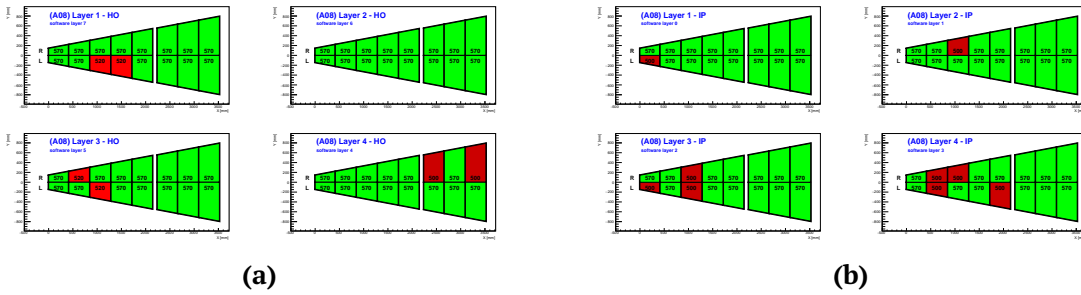


Figure A.17: Final HV map for the double-wedge A08.

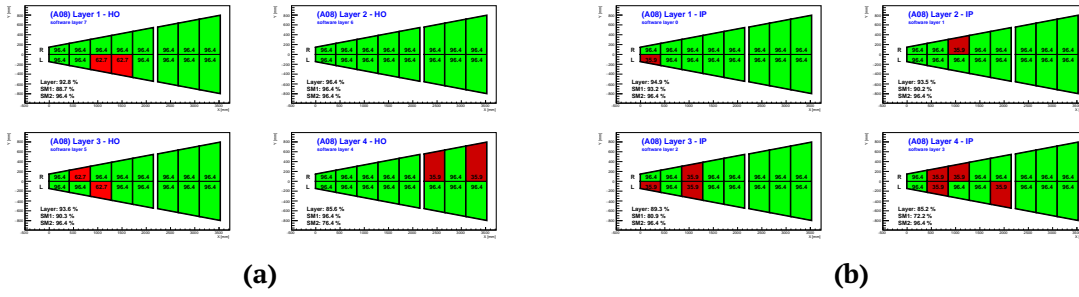


Figure A.18: Final expected efficiency for the double-wedge A08.

A.6 Double-wedge A02

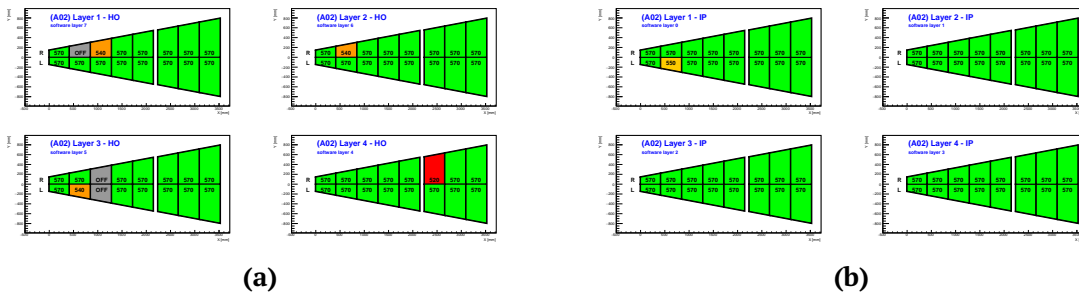


Figure A.19: Final HV map for the double-wedge A02.

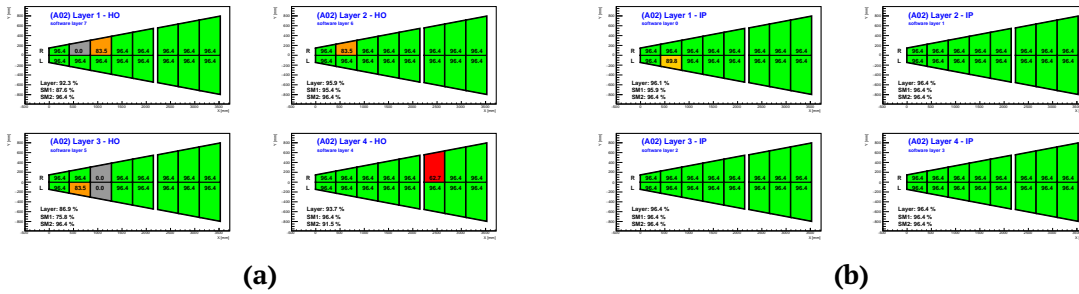


Figure A.20: Final expected efficiency for the double-wedge A02.

A.7 Double-wedge A06

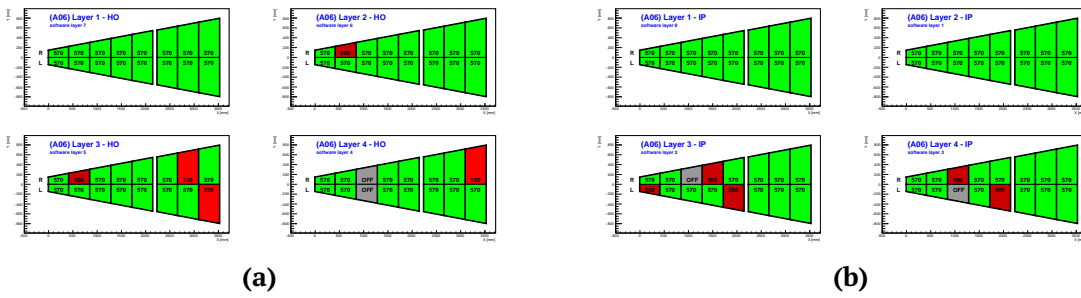


Figure A.21: Final HV map for the double-wedge A06.

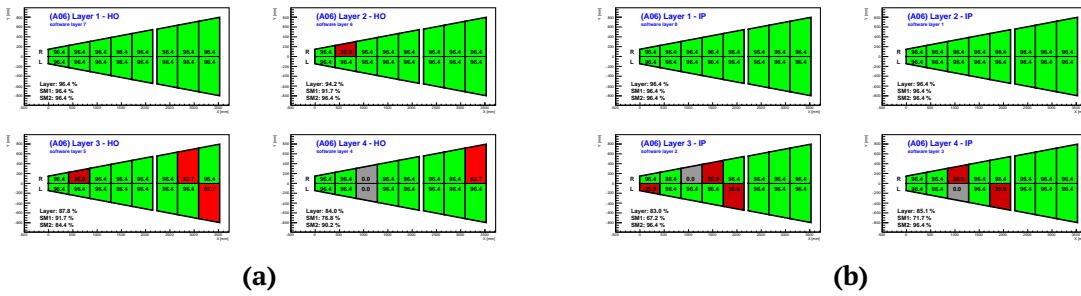


Figure A.22: Final expected efficiency for the double-wedge A06.

A.8 Double-wedge A04

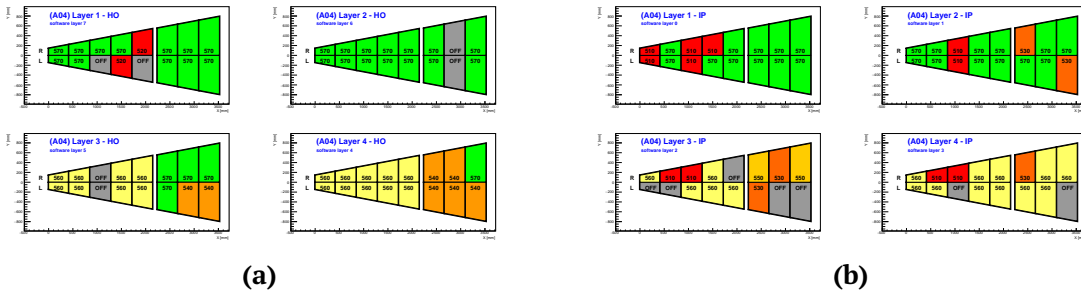


Figure A.23: Final HV map for the double-wedge A04.

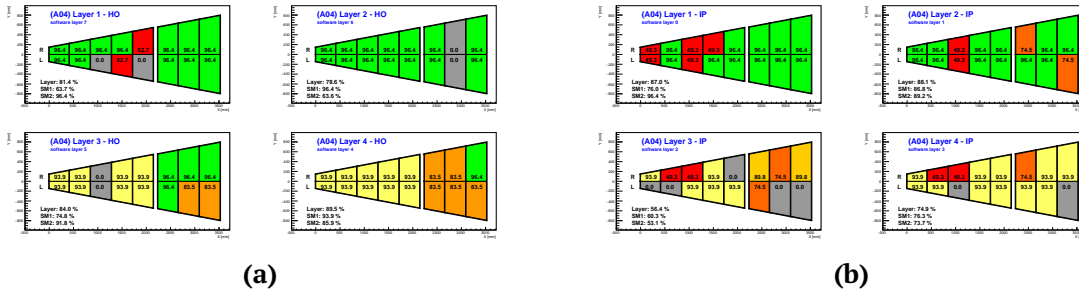


Figure A.24: Final expected efficiency for the double-wedge A04.

A.9 Double-wedge A13

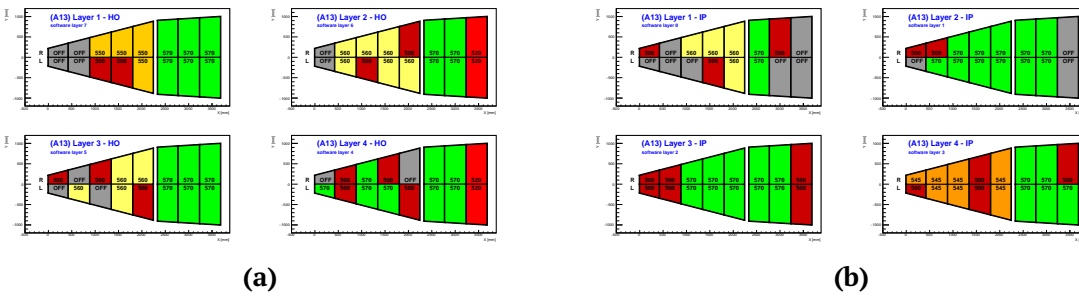


Figure A.25: Final HV map for the double-wedge A13.

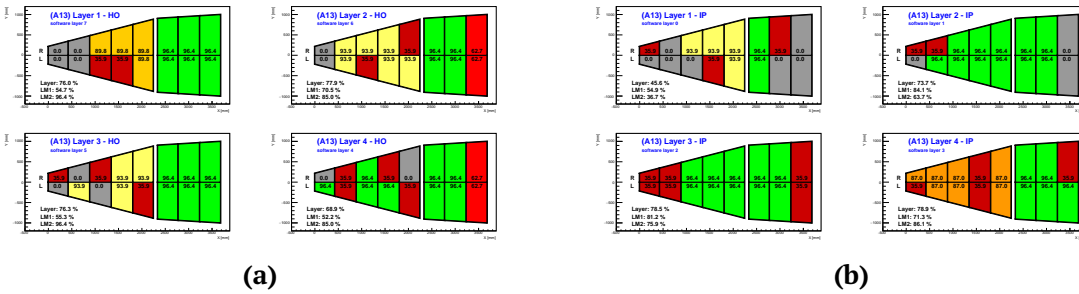


Figure A.26: Final expected efficiency for the double-wedge A13.

B Double-wedges efficiency maps

This appendix shows all the final 2D efficiency maps of each double-wedge validated so far.

B.1 Double-wedge A14

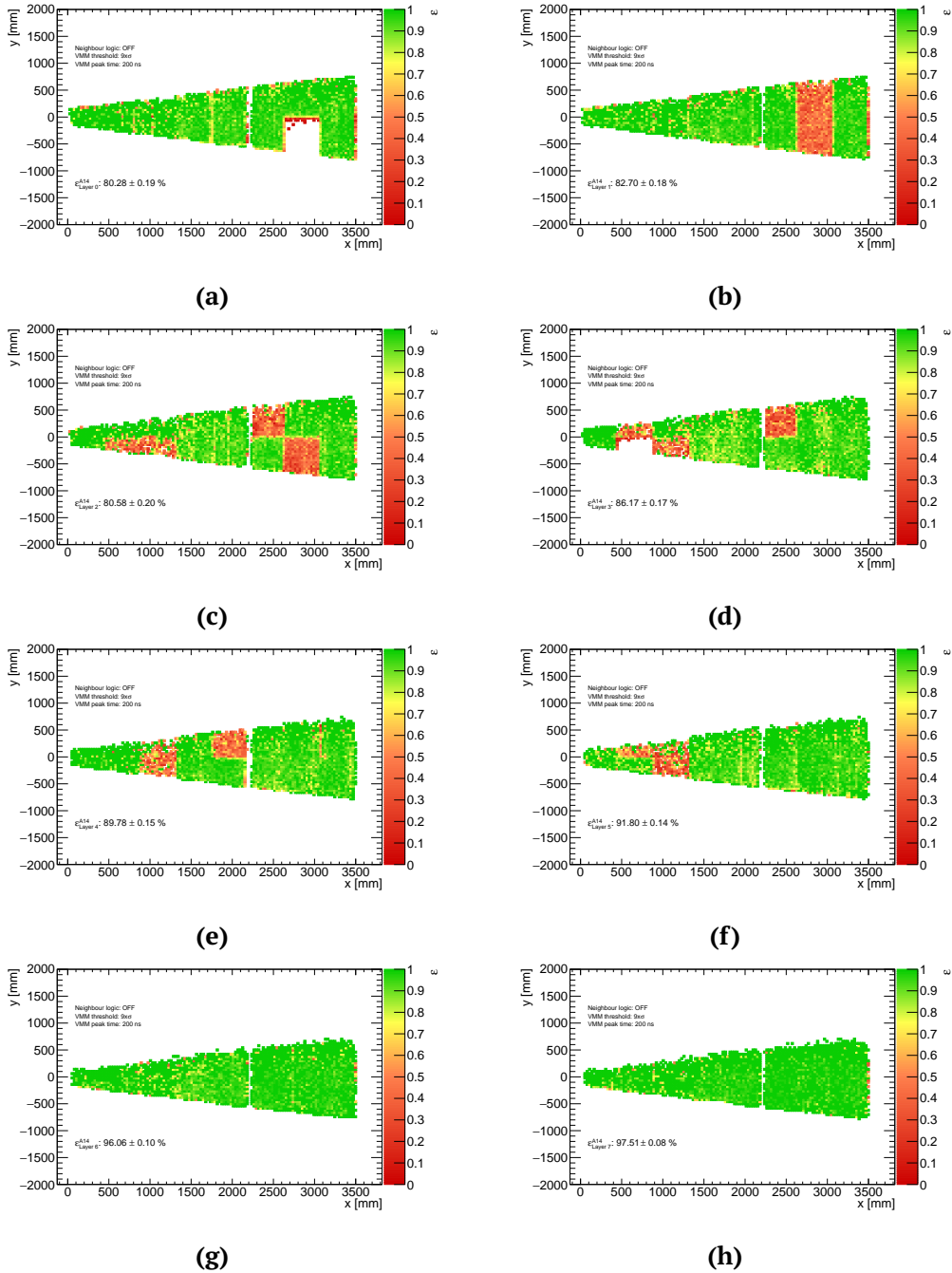


Figure B.27: 2D efficiency map for the double-wedge A14.

B.2 Double-wedge A12

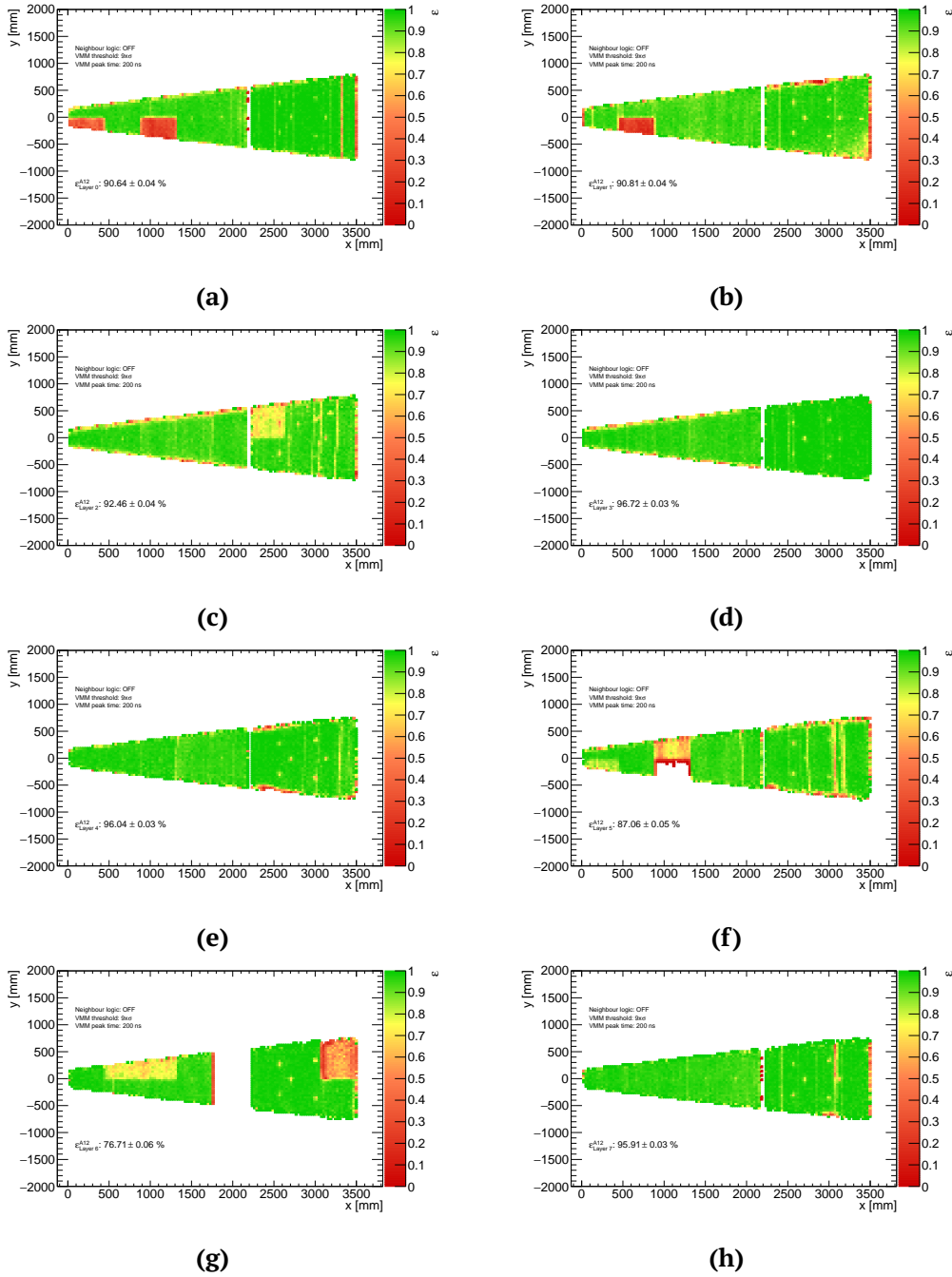


Figure B.28: 2D efficiency map for the double-wedge A12.

B.3 Double-wedge A10

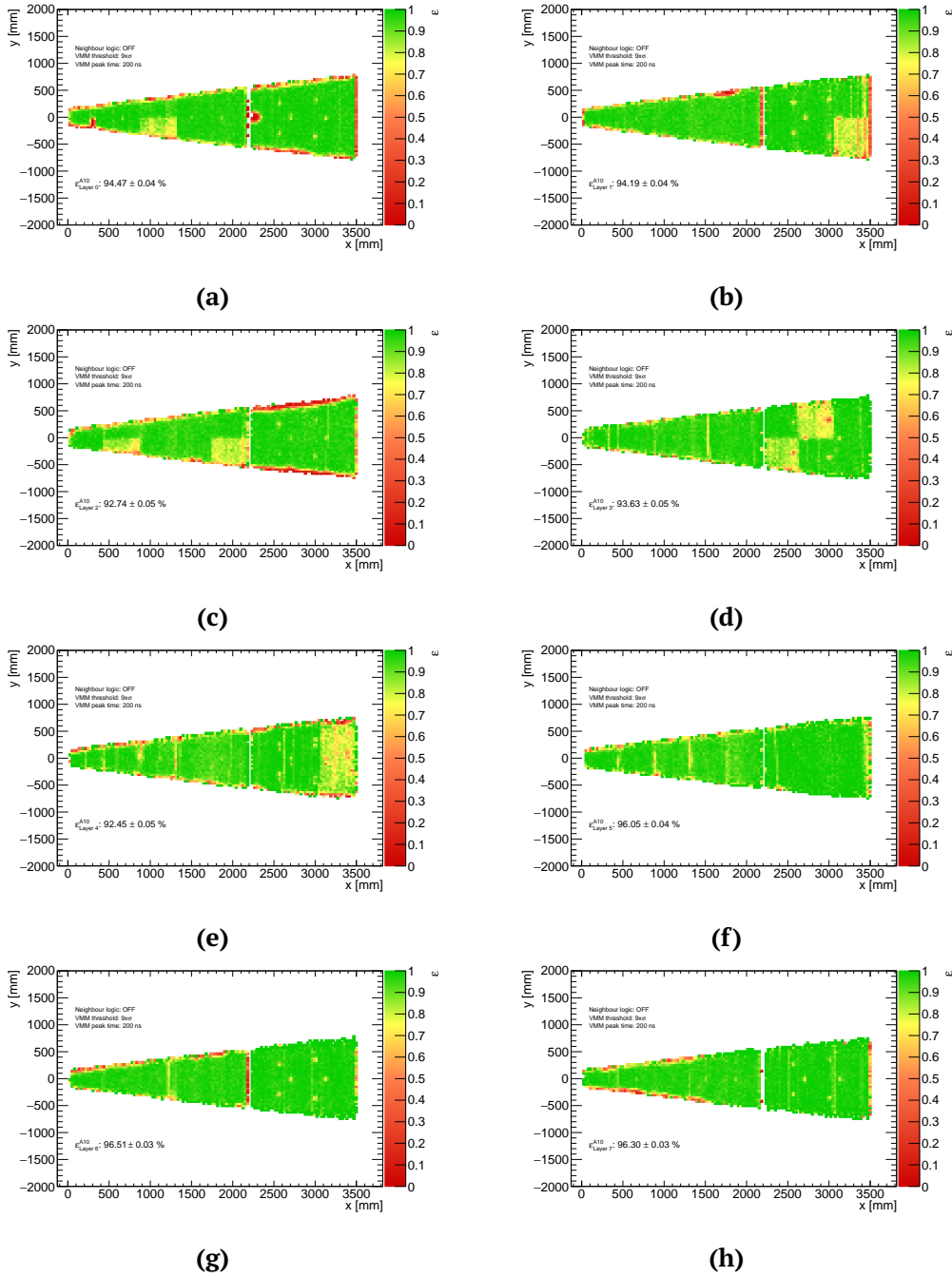


Figure B.29: 2D efficiency map for the double-wedge A10.

B.4 Double-wedge A16

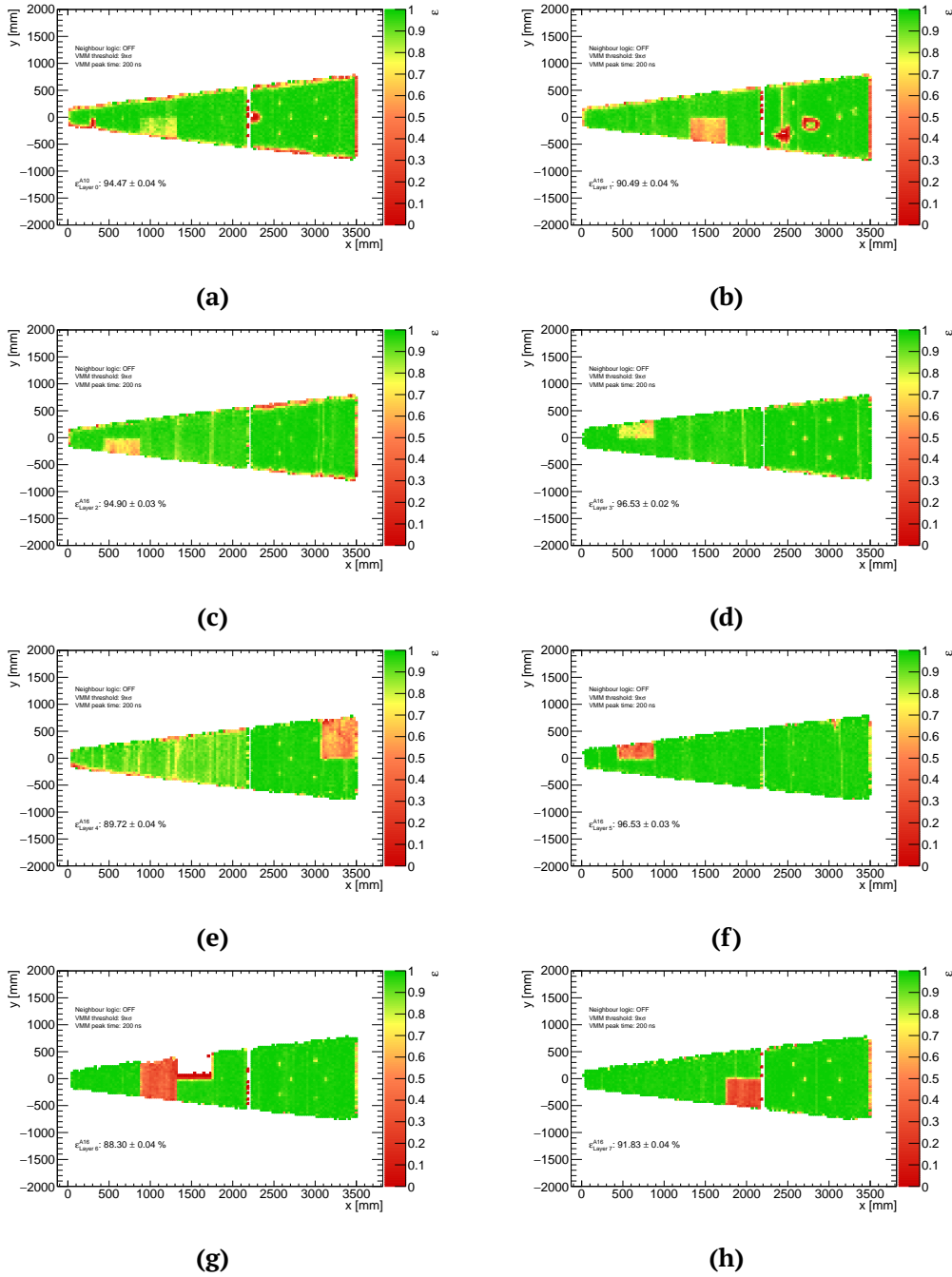


Figure B.30: 2D efficiency map for the double-wedge A16.

B.5 Double-wedge A08

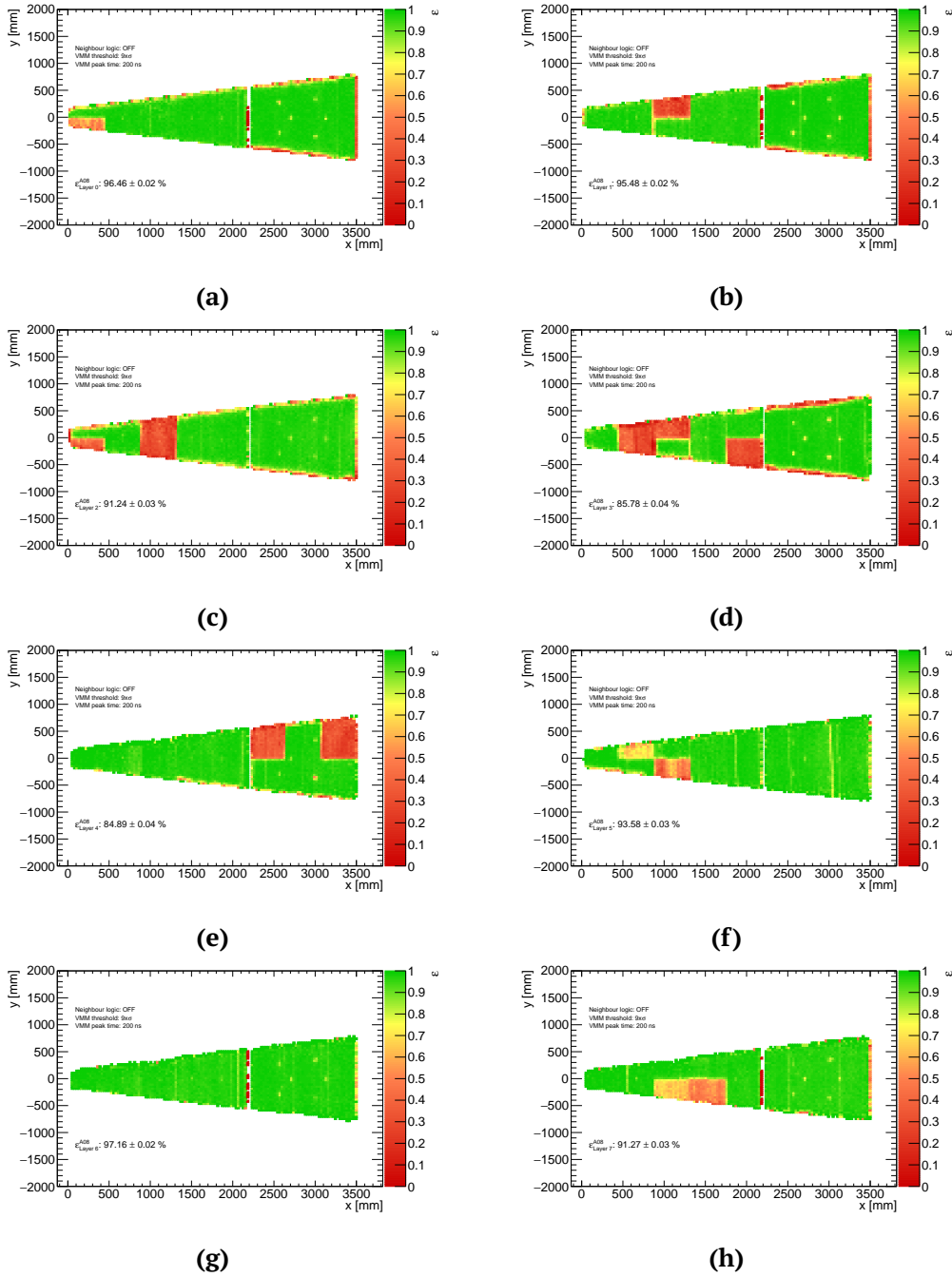


Figure B.31: 2D efficiency map for the double-wedge A08.

B.6 Double-wedge A02

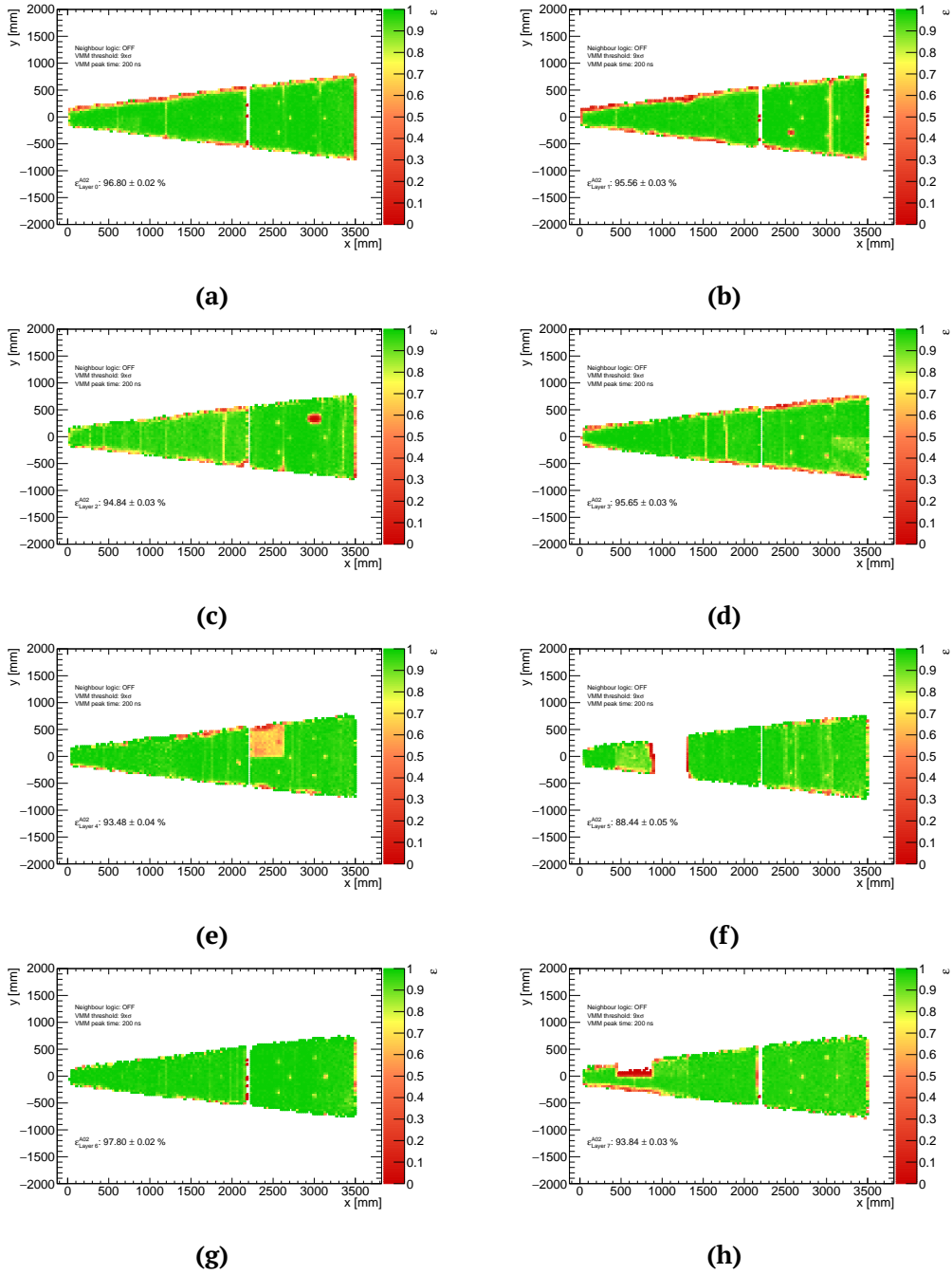


Figure B.32: 2D efficiency map for the double-wedge A02.

B.7 Double-wedge A06

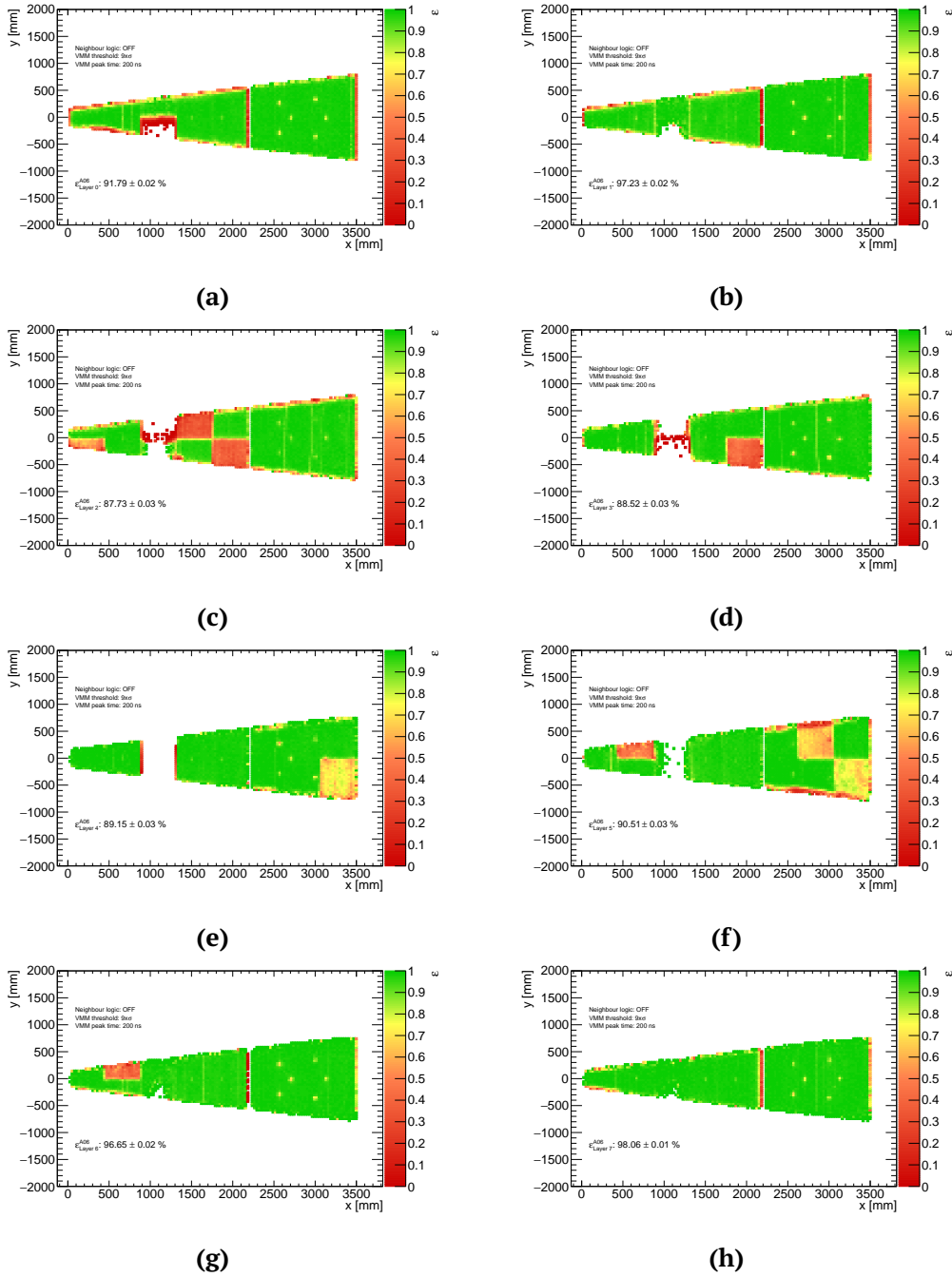


Figure B.33: 2D efficiency map for the double-wedge A06.

B.8 Double-wedge A04

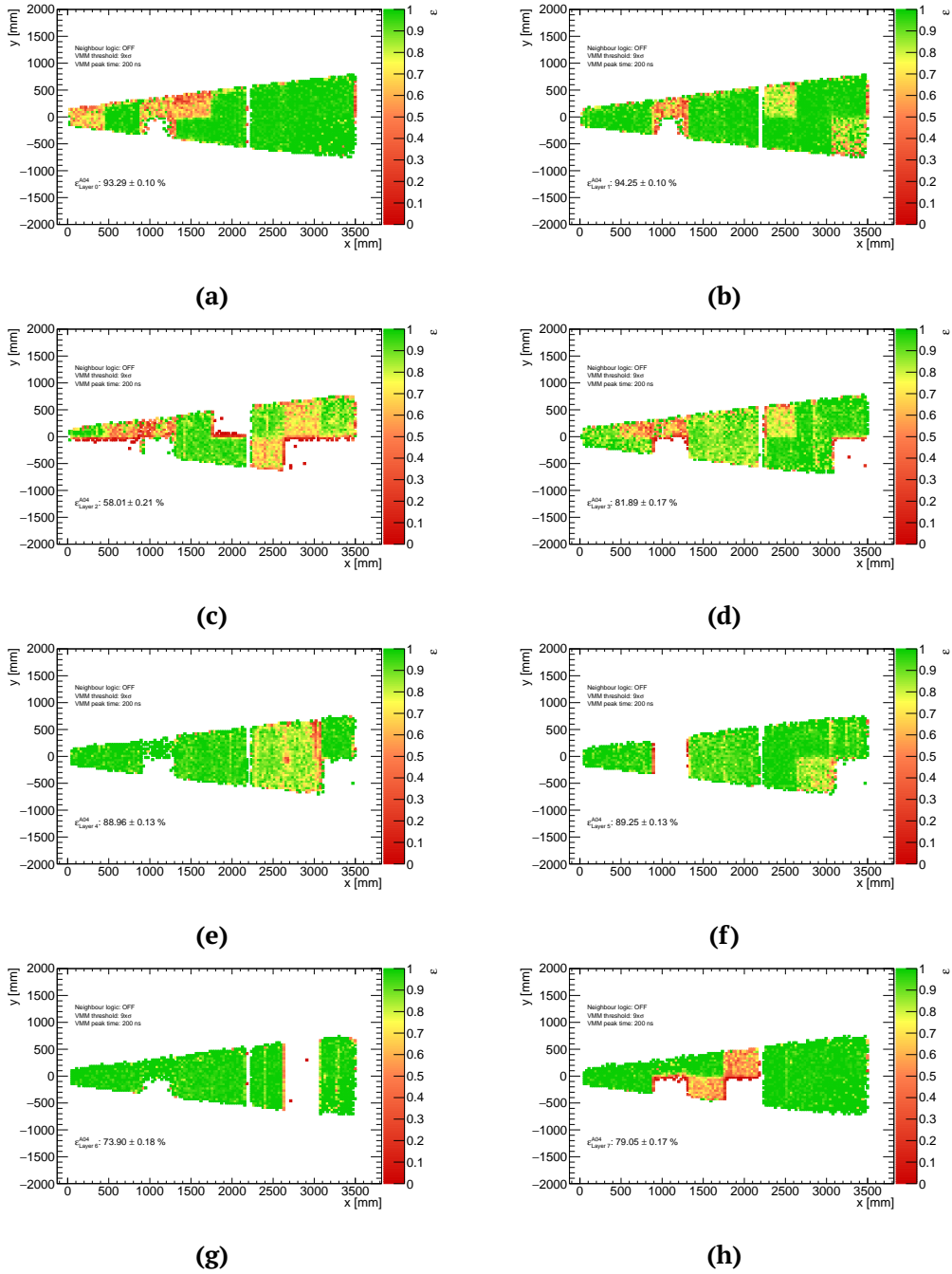


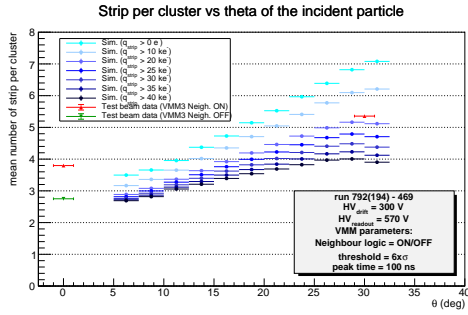
Figure B.34: 2D efficiency map for the double-wedge A04.

C Comparison between test beam and cosmic data and MM simulation

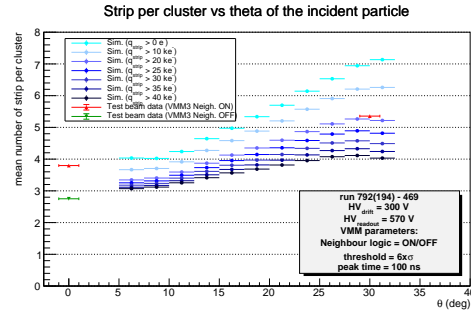
Once the NSW is installed inside the ATLAS detector, a realistic and detailed simulation of the MicroMegas will be essential in order to emulate how the muons interact with the real detector. A comparison between samples of muons that interacted in the ATLAS NSW and real data (from test beam data and from cosmic stand at the construction sites data) was made by changing different parameters of the VMM. Using these comparisons, it was possible to understand how the simulation deviated from the data collected using real detectors.

Below are shown different standard distributions for using different muon sample ($p_T \in [10, 100] \text{ GeV}$ and $p_T \in [100, 1000] \text{ GeV}$) compared with the distributions obtained using different VMM parameters (or a different read-out electronics).

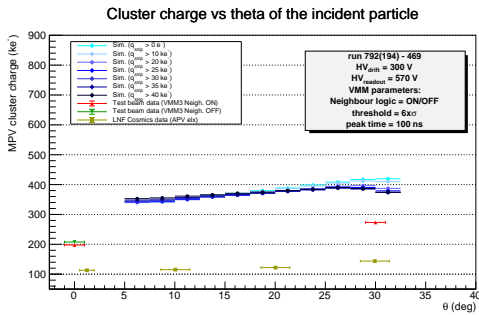
C.1 Threshold: 6x, Peak time: 100 ns



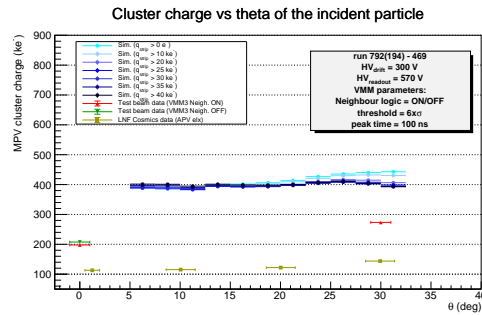
(a) Cluster multiplicity for a simulated sample of muons with $p_T \in [10, 100] \text{ GeV}$. The data sample are collected using a threshold of $6 \times \sigma$ and peak time of 100 ns at the test beam.



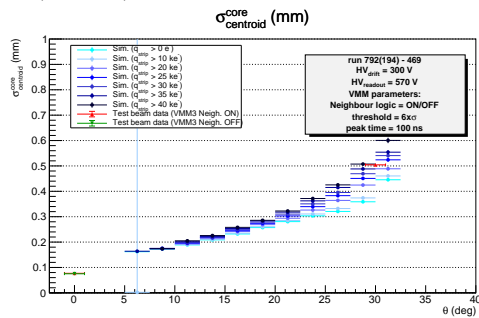
(b) Cluster multiplicity for a simulated sample of muons with $p_T \in [100, 1000] \text{ GeV}$. The data sample are collected using a threshold of $6 \times \sigma$ and peak time of 100 ns at the test beam.



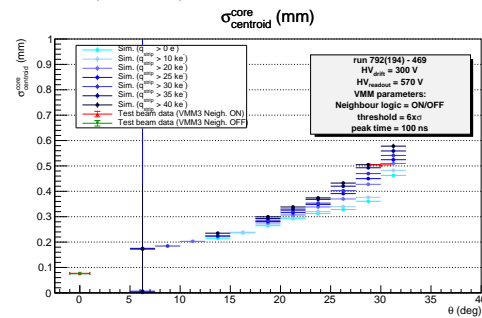
(c) Cluster charge for a simulated sample of muons with $p_T \in [10, 100] \text{ GeV}$. The data sample are collected using a threshold of $6 \times \sigma$ and peak time of 100 ns at the test beam. Results from the cosmic stand of Frascati (LNF) are also shown (using a different type of electronics (APV25)).



(d) Cluster charge for a simulated sample of muons with $p_T \in [100, 1000] \text{ GeV}$. The data sample are collected using a threshold of $6 \times \sigma$ and peak time of 100 ns at the test beam. Results from the cosmic stand of Frascati (LNF) are also shown (using a different type of electronics (APV25)).

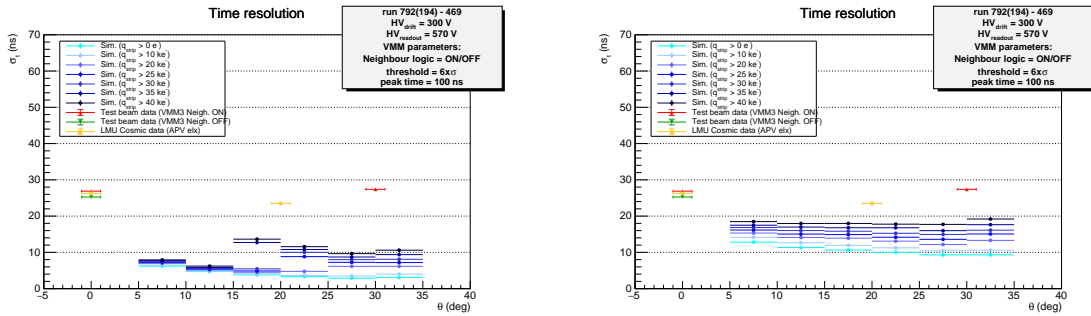


(e) Centroid core resolution for a simulated sample of muons with $p_T \in [10, 100] \text{ GeV}$. The data sample are collected using a threshold of $6 \times \sigma$ and peak time of 100 ns at the test beam.



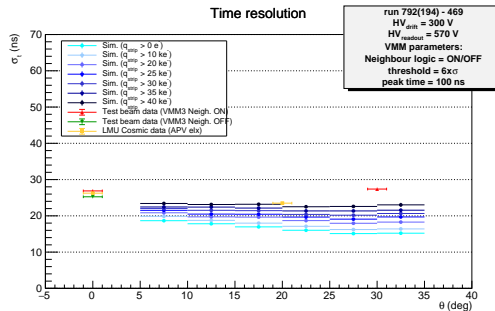
(f) Centroid core resolution for a simulated sample of muons with $p_T \in [100, 1000] \text{ GeV}$. The data sample are collected using a threshold of $6 \times \sigma$ and peak time of 100 ns at the test beam.

Figure C.35: Standard distributions for a MicroMegas chamber. In blue shades are indicated the simulations values with different cuts on the strip charge while in the other colours are indicated the values obtained from data measured at the test beam and/or at the cosmic ray stands of the construction sites. On the left is shown the simulation sample with the muons p_T between 10 and 100 GeV while on the right with muons p_T between 100 and 1000 GeV .



(a) Time resolution for a simulated sample of muons with $p_T \in [10, 100] GeV$. The data sample are collected using a threshold of $6 \times \sigma$ and peak time of 100 ns at the test beam. Results from the cosmic stand of Munich (LMU) are also shown (using a different type of electronics (APV25)).

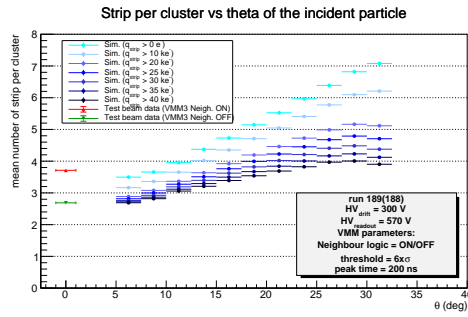
(b) Time resolution for a simulated sample of muons with $p_T \in [10, 100] GeV$ and a time smearing of 10 ns. The data sample are collected using a threshold of $6 \times \sigma$ and peak time of 100 ns at the test beam. Results from the cosmic stand of Munich (LMU) are also shown (using a different type of electronics (APV25)).



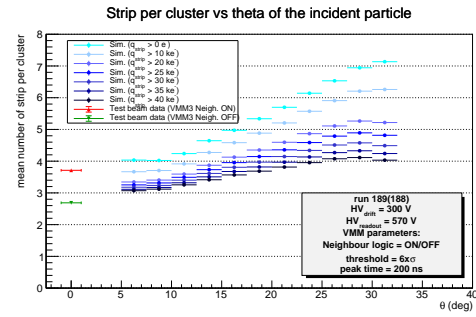
(c) Time resolution for a simulated sample of muons with $p_T \in [10, 100] GeV$ and a time smearing of 20 ns. The data sample are collected using a threshold of $6 \times \sigma$ and peak time of 100 ns at the test beam. Results from the cosmic stand of Munich (LMU) are also shown (using a different type of electronics (APV25)).

Figure C.36: Time resolutions for a MicroMegas chamber as a function of the track angle. In blue shades are indicated the simulations values with different cuts on the strip charge while in the other colours are indicated the values obtained from data measured at the test beam and/or at the cosmic ray stands of the construction sites.

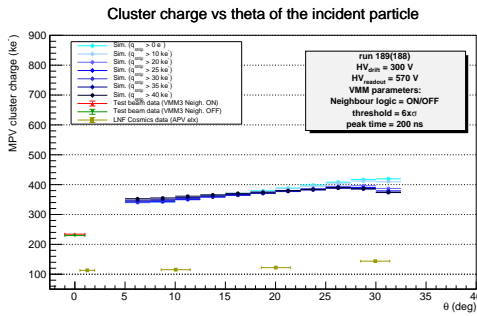
C.2 Threshold: 6x, Peak time: 200 ns



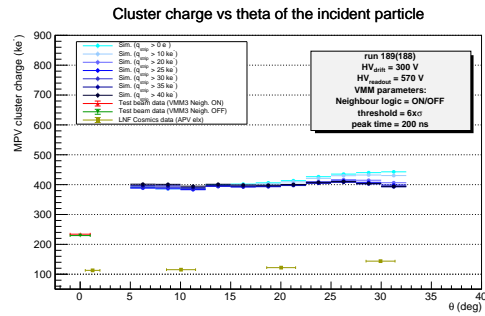
(a) Cluster multiplicity for a simulated sample of muons with $p_T \in [10, 100] \text{ GeV}$. The data sample are collected using a threshold of $6 \times \sigma$ and peak time of 200 ns at the test beam.



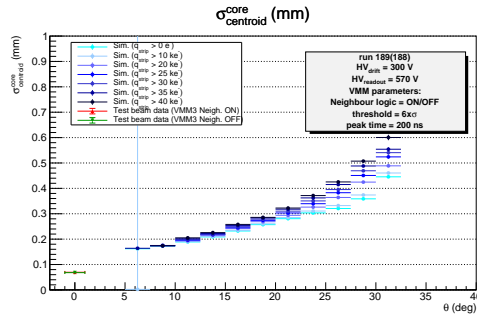
(b) Cluster multiplicity for a simulated sample of muons with $p_T \in [100, 1000] \text{ GeV}$. The data sample are collected using a threshold of $6 \times \sigma$ and peak time of 200 ns at the test beam.



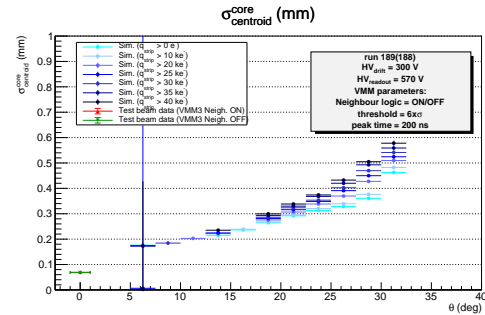
(c) Cluster charge for a simulated sample of muons with $p_T \in [10, 100] \text{ GeV}$. The data sample are collected using a threshold of $6 \times \sigma$ and peak time of 200 ns at the test beam. Results from the cosmic stand of Frascati (LNF) are also shown (using a different type of electronics (APV25)).



(d) Cluster charge for a simulated sample of muons with $p_T \in [100, 1000] \text{ GeV}$. The data sample are collected using a threshold of $6 \times \sigma$ and peak time of 200 ns at the test beam. Results from the cosmic stand of Frascati (LNF) are also shown (using a different type of electronics (APV25)).

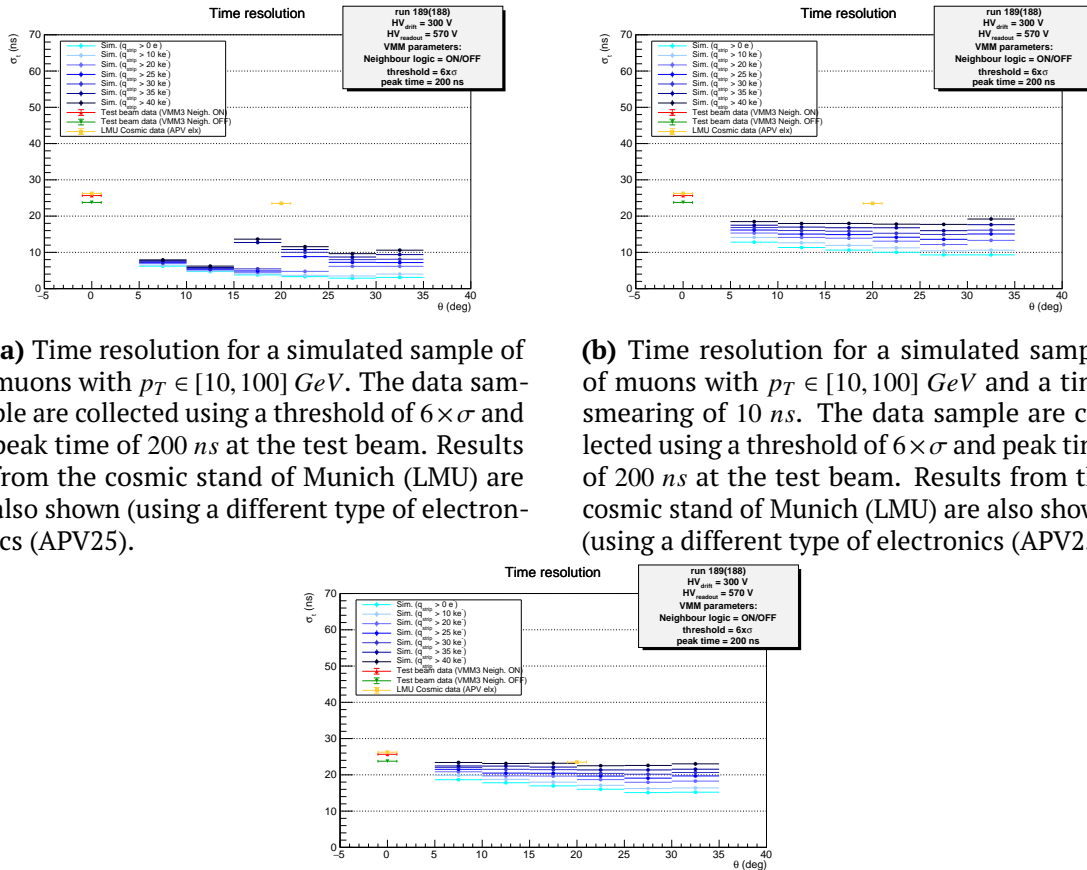


(e) Centroid core resolution for a simulated sample of muons with $p_T \in [10, 100] \text{ GeV}$. The data sample are collected using a threshold of $6 \times \sigma$ and peak time of 200 ns at the test beam.



(f) Centroid core resolution for a simulated sample of muons with $p_T \in [100, 1000] \text{ GeV}$. The data sample are collected using a threshold of $6 \times \sigma$ and peak time of 200 ns at the test beam.

Figure C.37: Standard distributions for a MicroMegas chamber as a function of the track angle. In blue shades are indicated the simulations values with different cuts on the strip charge while in the other colours are indicated the values obtained from data measured at the test beam and/or at the cosmic ray stands of the construction sites. On the left is shown the simulation sample with the muons p_T between 10 and 100 GeV while on the right with muons p_T between 100 and 1000 GeV .



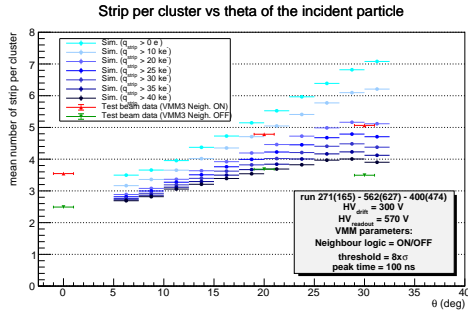
(a) Time resolution for a simulated sample of muons with $p_T \in [10, 100] \text{ GeV}$. The data sample are collected using a threshold of $6 \times \sigma$ and peak time of 200 ns at the test beam. Results from the cosmic stand of Munich (LMU) are also shown (using a different type of electronics (APV25)).

(b) Time resolution for a simulated sample of muons with $p_T \in [10, 100] \text{ GeV}$ and a time smearing of 10 ns. The data sample are collected using a threshold of $6 \times \sigma$ and peak time of 200 ns at the test beam. Results from the cosmic stand of Munich (LMU) are also shown (using a different type of electronics (APV25)).

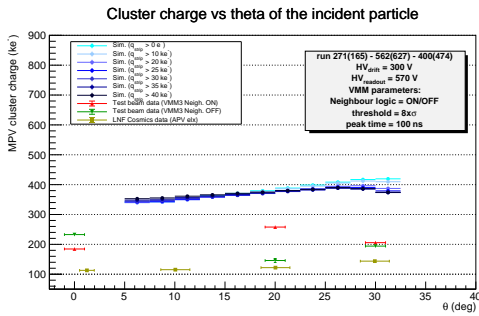
(c) Time resolution for a simulated sample of muons with $p_T \in [10, 100] \text{ GeV}$ and a time smearing of 20 ns. The data sample are collected using a threshold of $6 \times \sigma$ and peak time of 200 ns at the test beam. Results from the cosmic stand of Munich (LMU) are also shown (using a different type of electronics (APV25)).

Figure C.38: Time resolutions for a MicroMegas chamber as a function of the track angle. In blue shades are indicated the simulations values with different cuts on the strip charge while in the other colours are indicated the values obtained from data measured at the test beam and/or at the cosmic ray stands of the construction sites.

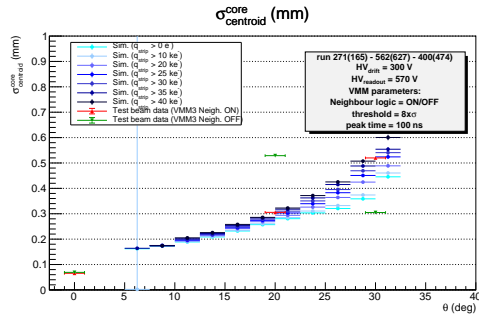
C.3 Threshold: 8x, Peak time: 100 ns



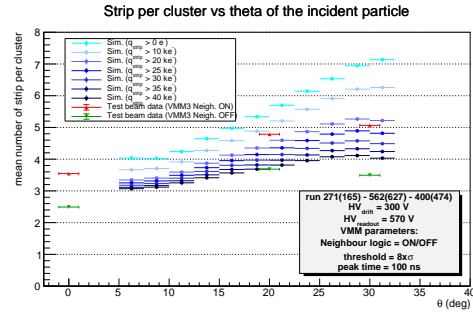
(a) Cluster multiplicity for a simulated sample of muons with $p_T \in [10, 100] \text{ GeV}$. The data sample are collected using a threshold of $8 \times \sigma$ and peak time of 100 ns at the test beam.



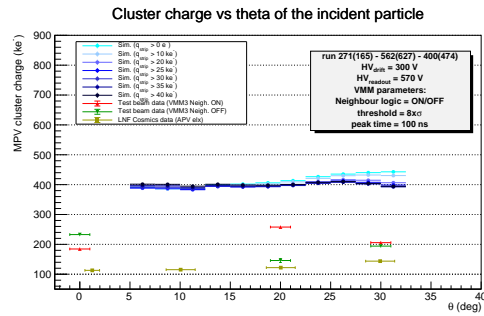
(c) Cluster charge for a simulated sample of muons with $p_T \in [10, 100] \text{ GeV}$. The data sample are collected using a threshold of $8 \times \sigma$ and peak time of 100 ns at the test beam. Results from the cosmic stand of Frascati (LNF) are also shown (using a different type of electronics (APV25)).



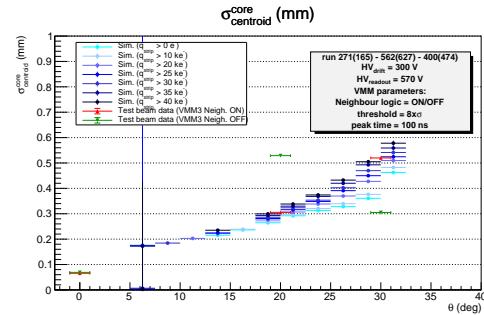
(e) Centroid core resolution for a simulated sample of muons with $p_T \in [10, 100] \text{ GeV}$. The data sample are collected using a threshold of $8 \times \sigma$ and peak time of 100 ns at the test beam.



(b) Cluster multiplicity for a simulated sample of muons with $p_T \in [100, 1000] \text{ GeV}$. The data sample are collected using a threshold of $8 \times \sigma$ and peak time of 100 ns at the test beam.

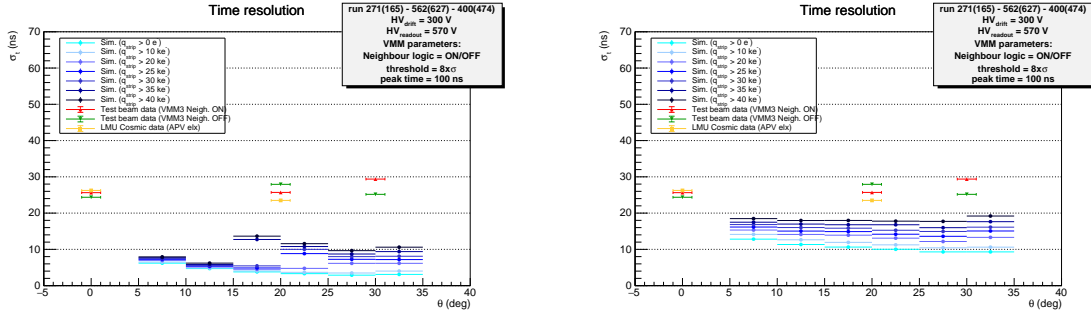


(d) Cluster charge for a simulated sample of muons with $p_T \in [100, 1000] \text{ GeV}$. The data sample are collected using a threshold of $8 \times \sigma$ and peak time of 100 ns at the test beam. Results from the cosmic stand of Frascati (LNF) are also shown (using a different type of electronics (APV25)).



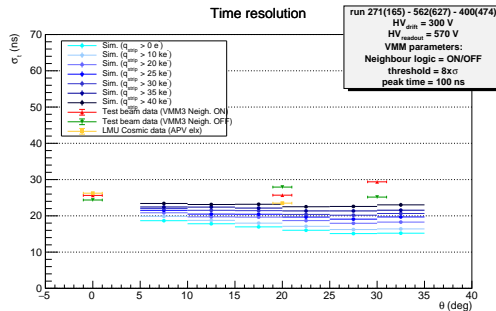
(f) Centroid core resolution for a simulated sample of muons with $p_T \in [100, 1000] \text{ GeV}$. The data sample are collected using a threshold of $8 \times \sigma$ and peak time of 100 ns at the test beam.

Figure C.39: Standard distributions for a MicroMegas chamber as a function of the track angle. In blue shades are indicated the simulations values with different cuts on the strip charge while in the other colours are indicated the values obtained from data measured at the test beam and/or at the cosmic ray stands of the construction sites. On the left is shown the simulation sample with the muons p_T between 10 and 100 GeV while on the right with muons p_T between 100 and 1000 GeV .



(a) Time resolution for a simulated sample of muons with $p_T \in [10, 100] \text{ GeV}$. The data sample are collected using a threshold of $8 \times \sigma$ and peak time of 100 ns at the test beam. Results from the cosmic stand of Munich (LMU) are also shown (using a different type of electronics (APV25)).

(b) Time resolution for a simulated sample of muons with $p_T \in [10, 100] \text{ GeV}$ and a time smearing of 10 ns . The data sample are collected using a threshold of $8 \times \sigma$ and peak time of 100 ns at the test beam. Results from the cosmic stand of Munich (LMU) are also shown (using a different type of electronics (APV25)).



(c) Time resolution for a simulated sample of muons with $p_T \in [10, 100] \text{ GeV}$ and a time smearing of 20 ns . The data sample are collected using a threshold of $8 \times \sigma$ and peak time of 100 ns at the test beam. Results from the cosmic stand of Munich (LMU) are also shown (using a different type of electronics (APV25)).

Figure C.40: Time resolutions for a MicroMegas chamber as a function of the track angle. In blue shades are indicated the simulations values with different cuts on the strip charge while in the other colours are indicated the values obtained from data measured at the test beam and/or at the cosmic ray stands of the construction sites.

C.4 Threshold: 8x, Peak time: 200 ns

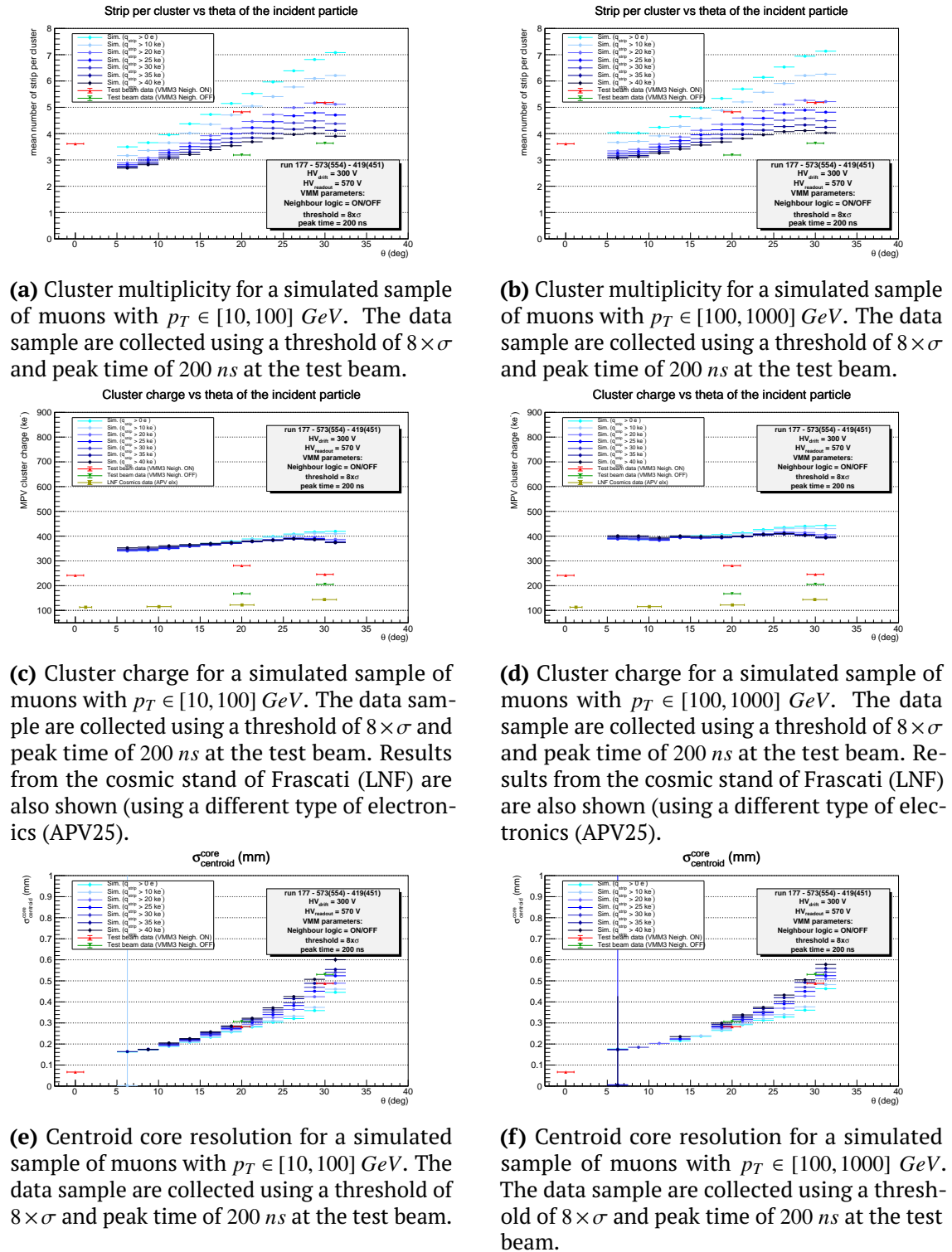
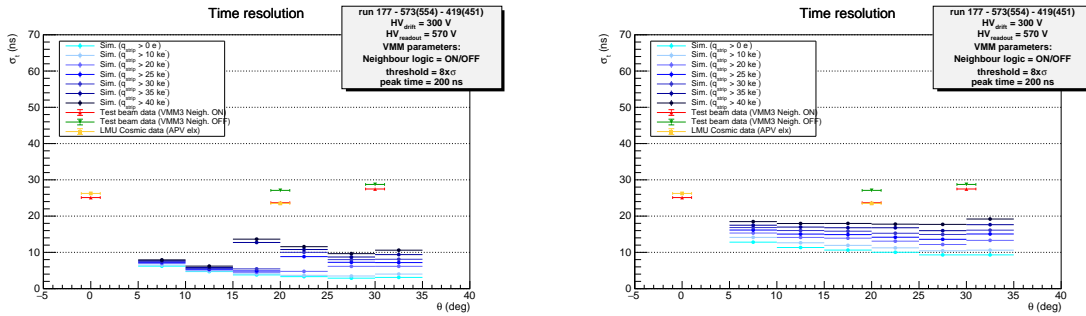
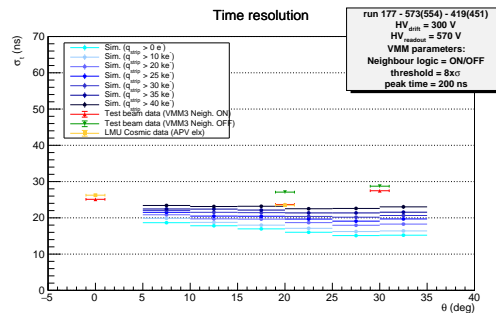


Figure C.41: Standard distributions for a MicroMegas chamber as a function of the track angle. In blue shades are indicated the simulations values with different cuts on the strip charge while in the other colours are indicated the values obtained from data measured at the test beam and/or at the cosmic ray stands of the construction sites. On the left is shown the simulation sample with the muons p_T between 10 and 100 GeV while on the right with muons p_T between 100 and 1000 GeV .



(a) Time resolution for a simulated sample of muons with $p_T \in [10, 100] GeV$. The data sample are collected using a threshold of $8 \times \sigma$ and peak time of 200 ns at the test beam. Results from the cosmic stand of Munich (LMU) are also shown (using a different type of electronics (APV25)).

(b) Time resolution for a simulated sample of muons with $p_T \in [10, 100] GeV$ and a time smearing of 10 ns. The data sample are collected using a threshold of $8 \times \sigma$ and peak time of 200 ns at the test beam. Results from the cosmic stand of Munich (LMU) are also shown (using a different type of electronics (APV25)).



(c) Time resolution for a simulated sample of muons with $p_T \in [10, 100] GeV$ and a time smearing of 20 ns. The data sample are collected using a threshold of $8 \times \sigma$ and peak time of 200 ns at the test beam. Results from the cosmic stand of Munich (LMU) are also shown (using a different type of electronics (APV25)).

Figure C.42: Time resolutions for a MicroMegas chamber as a function of the track angle. In blue shades are indicated the simulations values with different cuts on the strip charge while in the other colours are indicated the values obtained from data measured at the test beam and/or at the cosmic ray stands of the construction sites.

D Analysis validation tests

In this appendix the results of all the validation tests made on all the differential and double differential distributions are shown.

D.1 Internal bias tests with Poissonian fluctuations

Absolute distributions

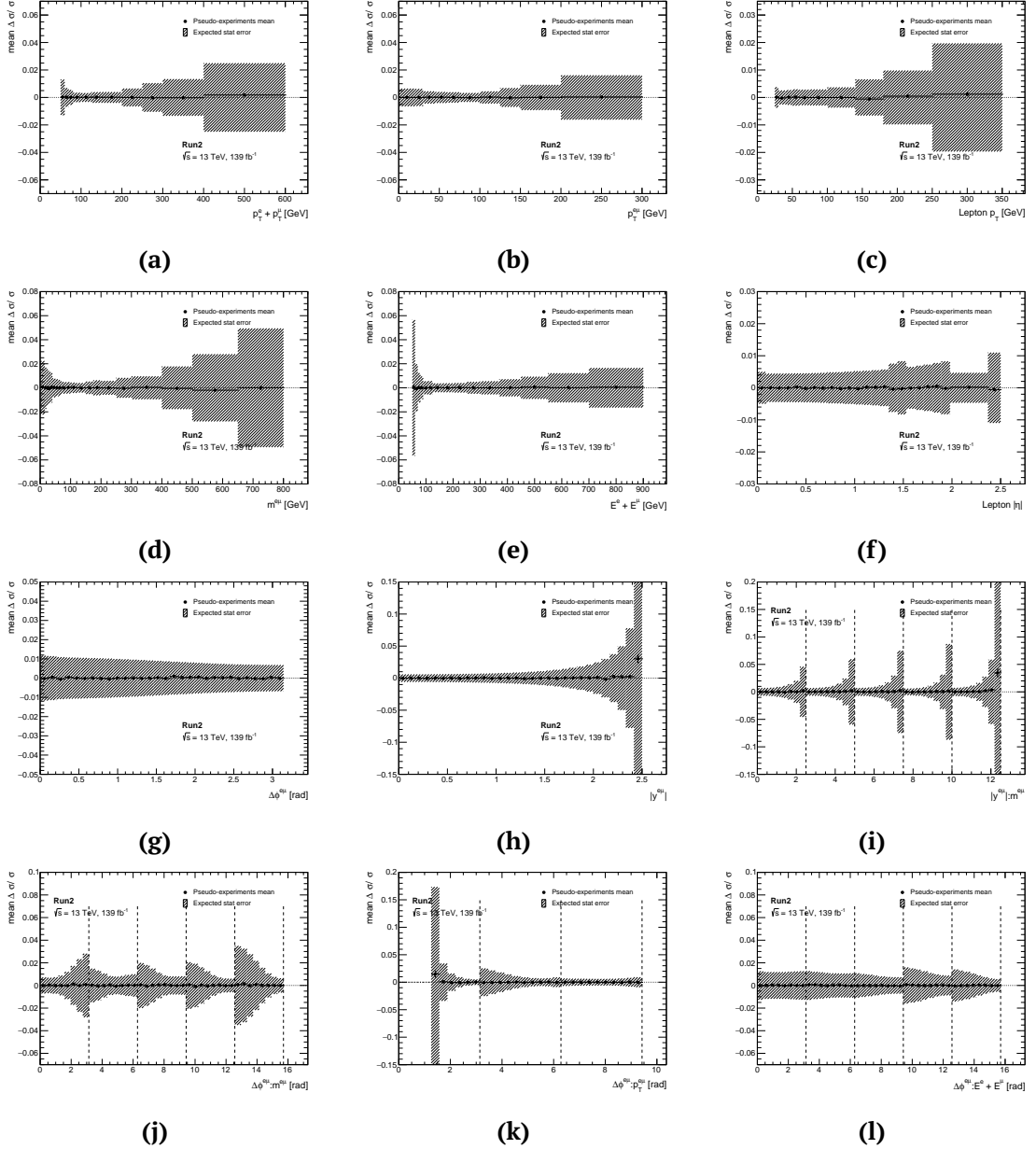


Figure D.43: Mean extracted for each bin of each (double) variable from the Poissonian fluctuations fitted to the 1000 internal bias tests pseudo-experiments results. The mean is in all cases consistent with zero within the standard deviation, demonstrating that the double tagging technique has no internal bias within the expected statistical sensitivity (gray shaded region).

Normalised distributions

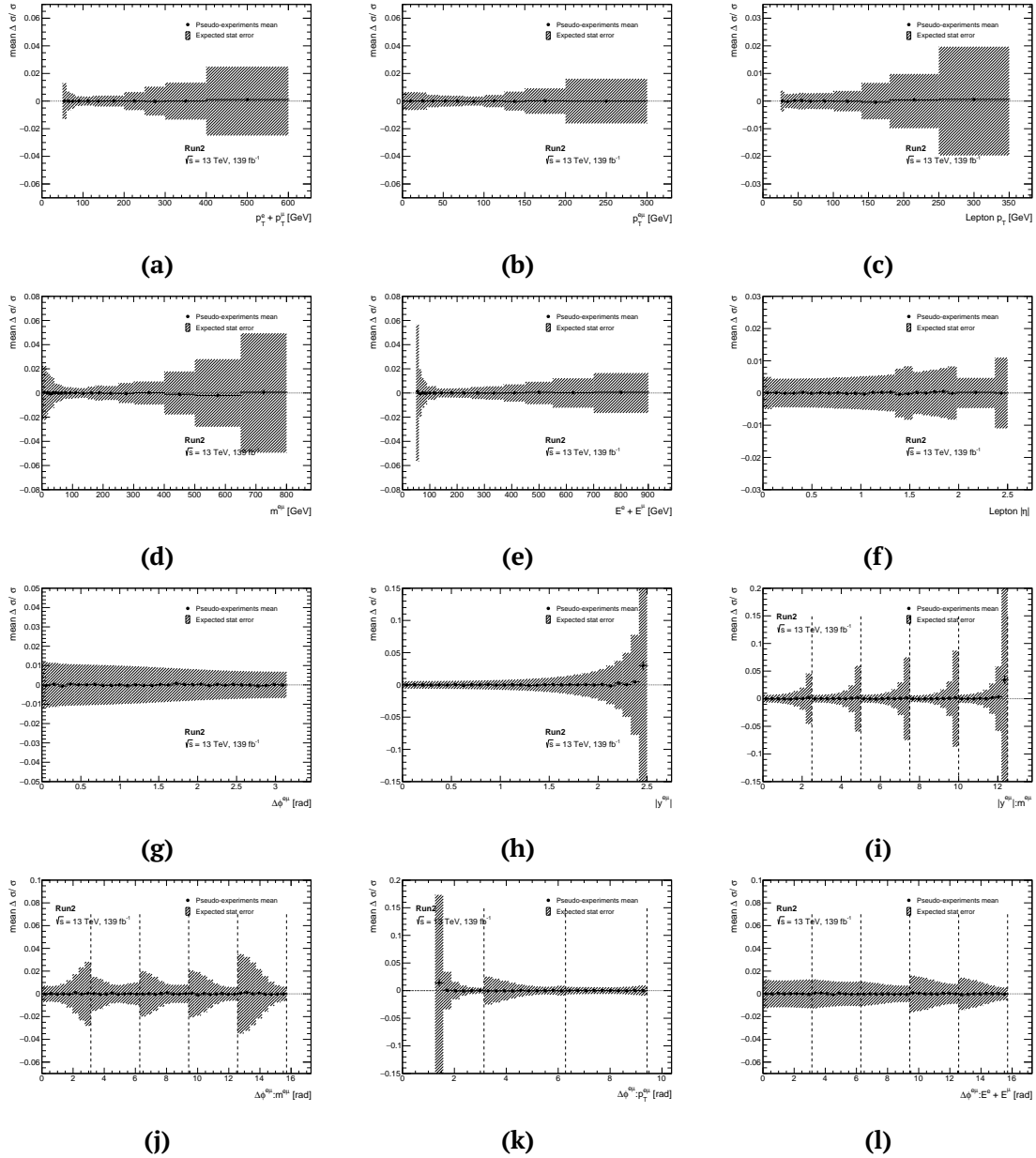


Figure D.44: Mean extracted for each bin of each normalised (double) variable from the Poissonian fluctuations fitted to the 1000 internal bias tests pseudo-experiments results. The mean is in all cases consistent with zero within the standard deviation, demonstrating that the double tagging technique has no internal bias within the expected statistical sensitivity (gray shaded region).

D.2 Stress tests

Absolute distributions

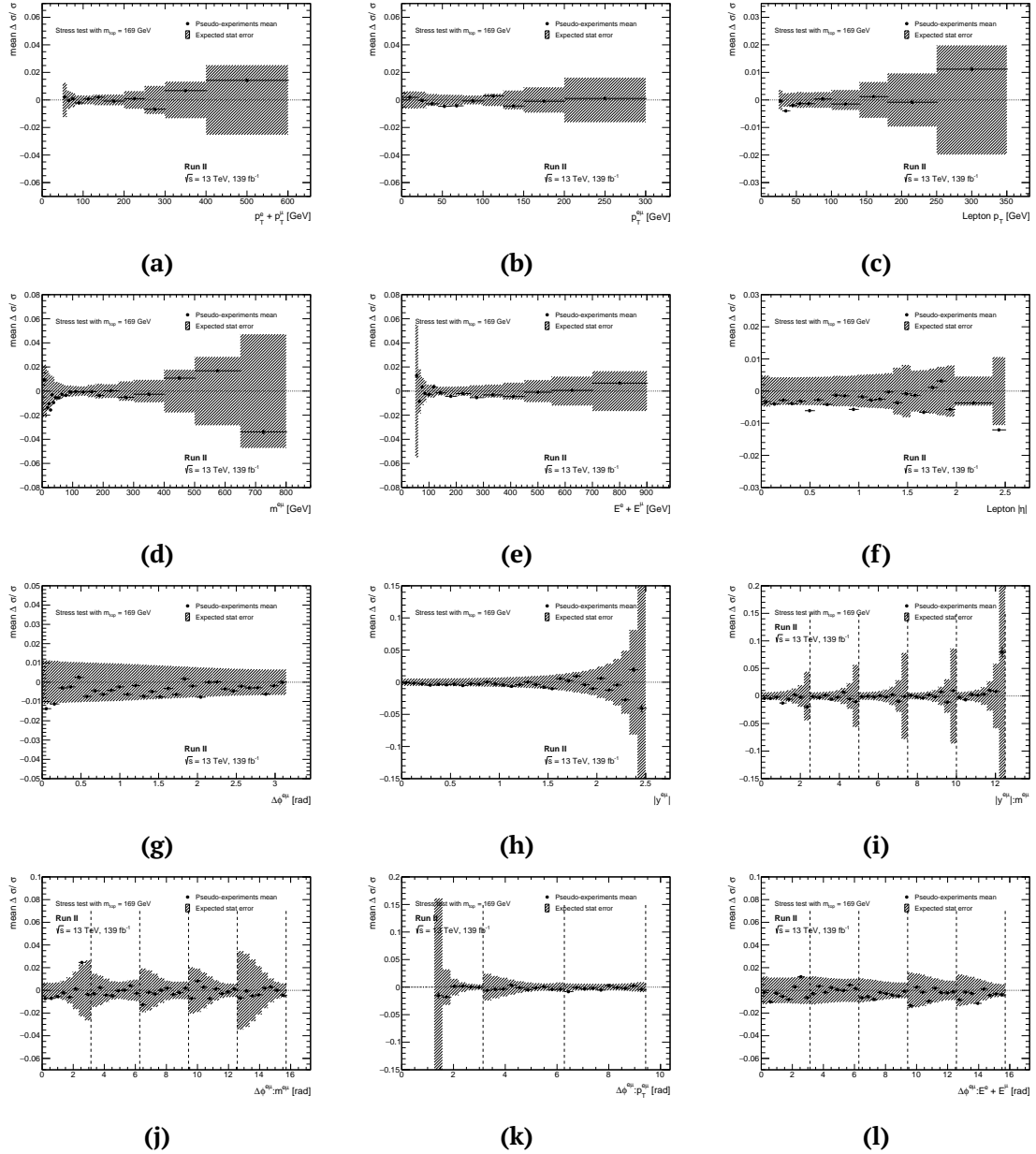


Figure D.45: Mean extracted for each bin of each (double) variable from the Poissonian fluctuations fitted to the 1000 stress tests (with the sample with a simulated $m_{top} = 169 \text{ GeV}$) pseudo-experiments results. The mean is in all cases consistent with zero within the standard deviation (in some cases more than 1 standard deviation ma still acceptable), demonstrating that the double tagging technique has no bias changing the truth distributions within the expect statistical sensitivity (gray shaded region).

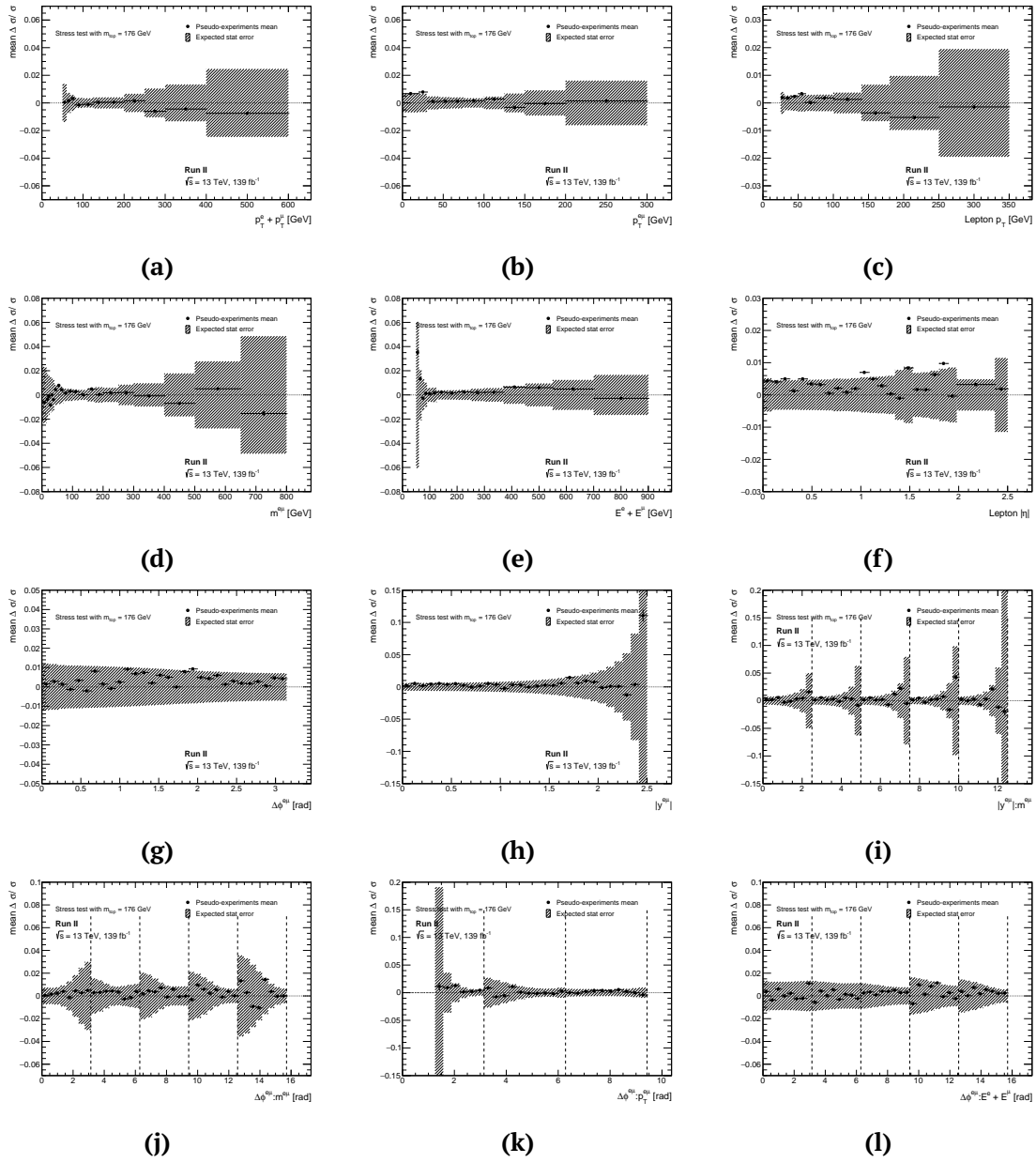


Figure D.46: Mean extracted for each bin of each (double) variable from the Poissonian fluctuations fitted to the 1000 stress tests (with the sample with a simulated $m_{top} = 176 \text{ GeV}$) pseudo-experiments results. The mean is in all cases consistent with zero within the standard deviation (in some cases more than 1 standard deviation ma still acceptable), demonstrating that the double tagging technique has no bias changing the truth distributions within the expect statistical sensitivity (gray shaded region).

Normalised distributions

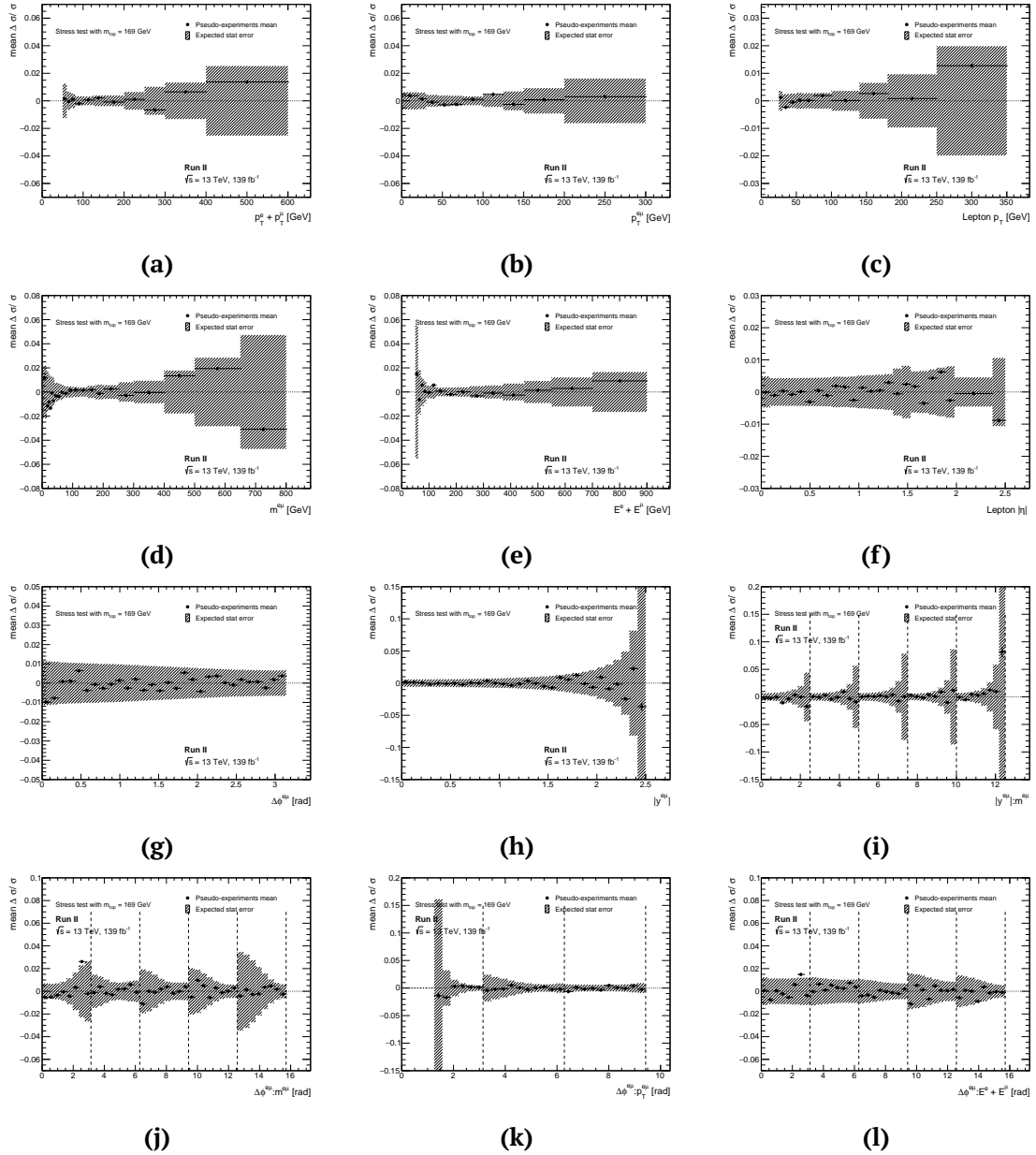


Figure D.47: Mean extracted for each bin of each normalised (double) variable from the Poissonian fluctuations fitted to the 1000 stress tests (with the sample with a simulated $m_{\text{top}} = 169 \text{ GeV}$) pseudo-experiments results. The mean is in all cases consistent with zero within the standard deviation (in some cases more than 1 standard deviation ma still acceptable), demonstrating that the double tagging technique has no bias changing the truth distributions within the expect statistical sensitivity (gray shaded region).

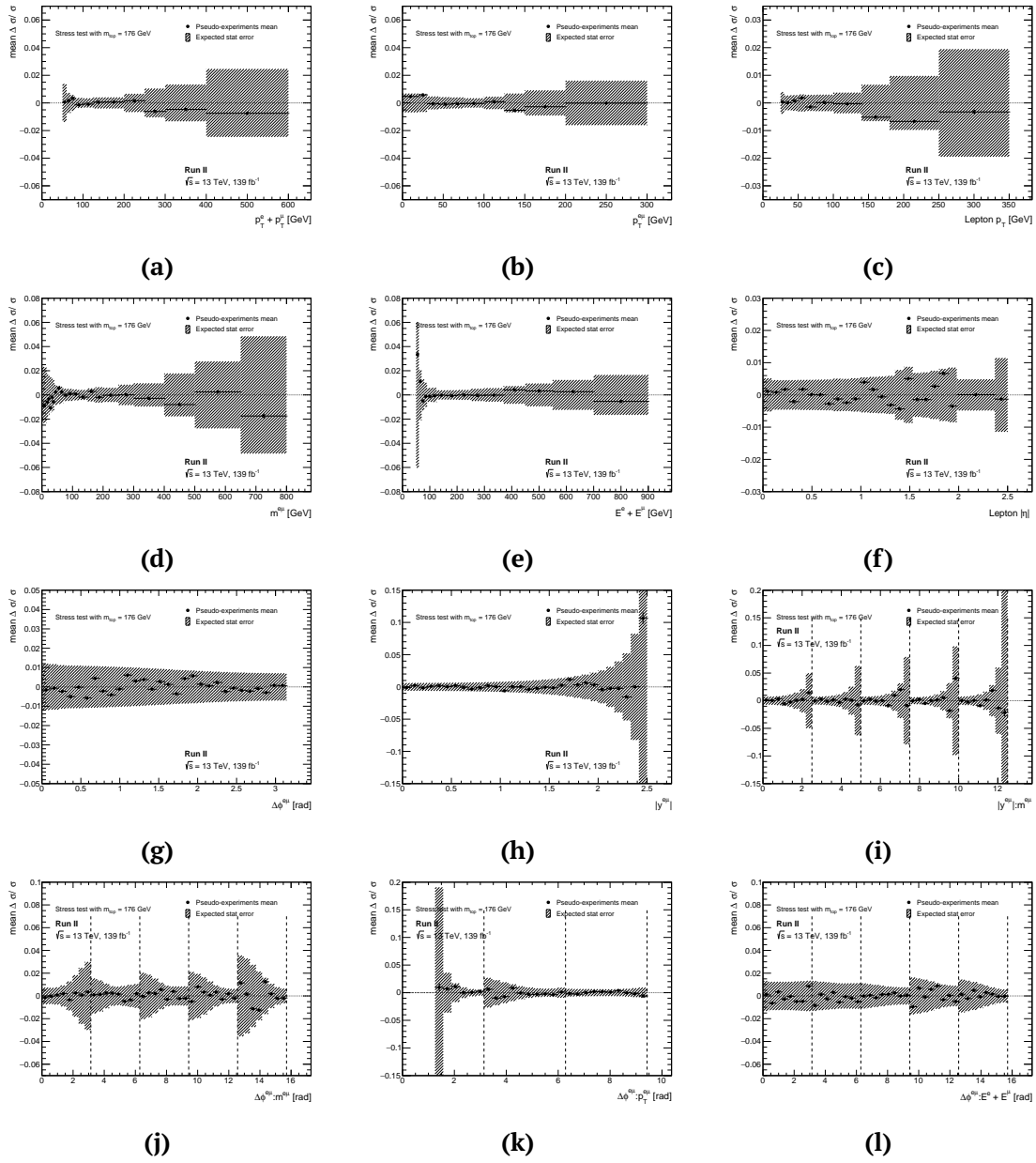


Figure D.48: Mean extracted for each bin of each normalised (double) variable from the Poissonian fluctuations fitted to the 1000 stress tests (with the sample with a simulated $m_{top} = 176 \text{ GeV}$) pseudo-experiments results. The mean is in all cases consistent with zero within the standard deviation (in some cases more than 1 standard deviation ma still acceptable), demonstrating that the double tagging technique has no bias changing the truth distributions within the expect statistical sensitivity (gray shaded region).

D.3 Ratio stress tests

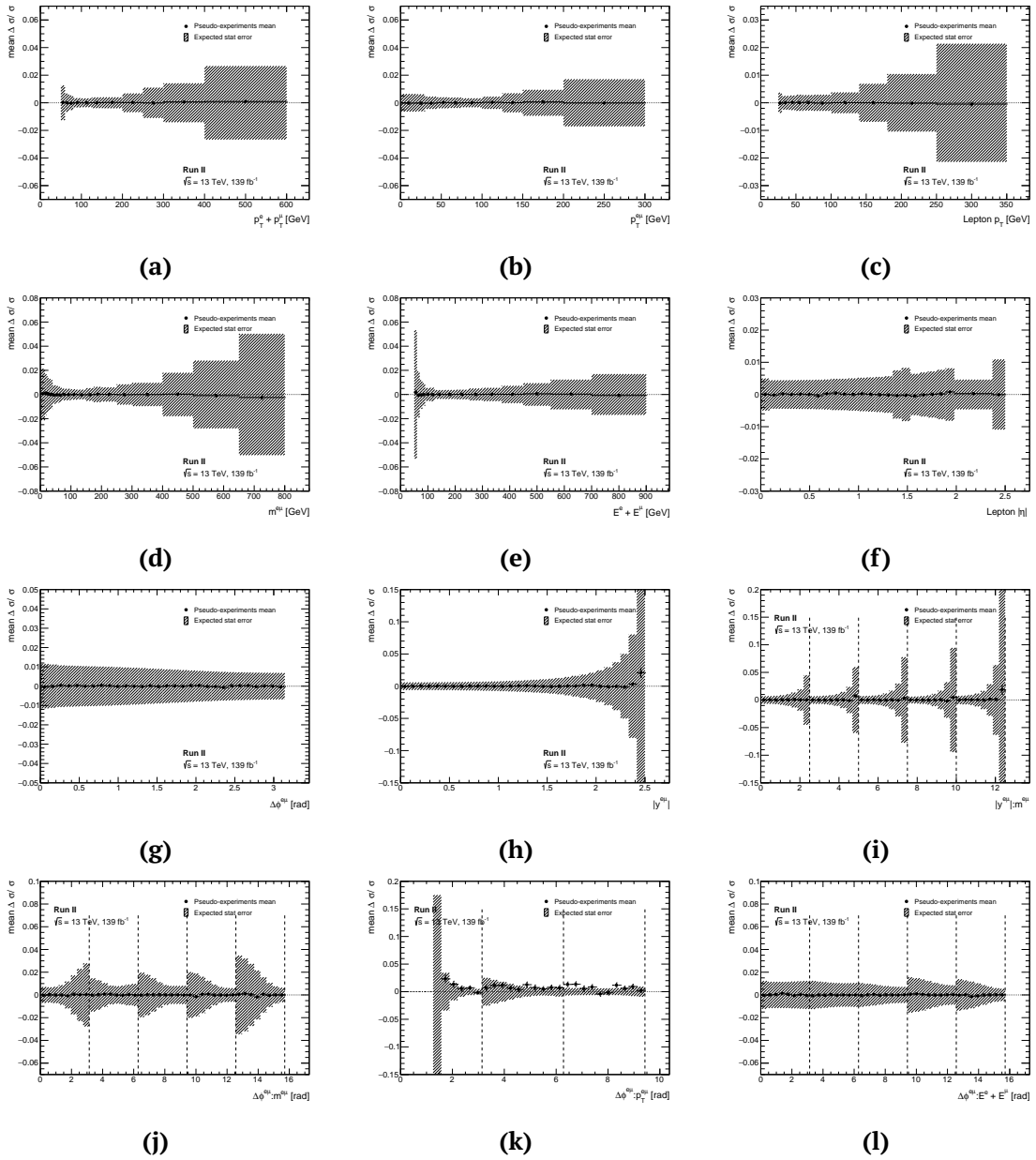


Figure D.49: Mean extracted for each bin of each (double) variable from the Poissonian fluctuations fitted to the 1000 ratio stress tests pseudo-experiments results. The mean is in all cases consistent with zero within the standard deviation, demonstrating that the double tagging technique has no bias, with a non perfect Data/MC ratio, within the expect statistical sensitivity (gray shaded region).

Normalised distributions

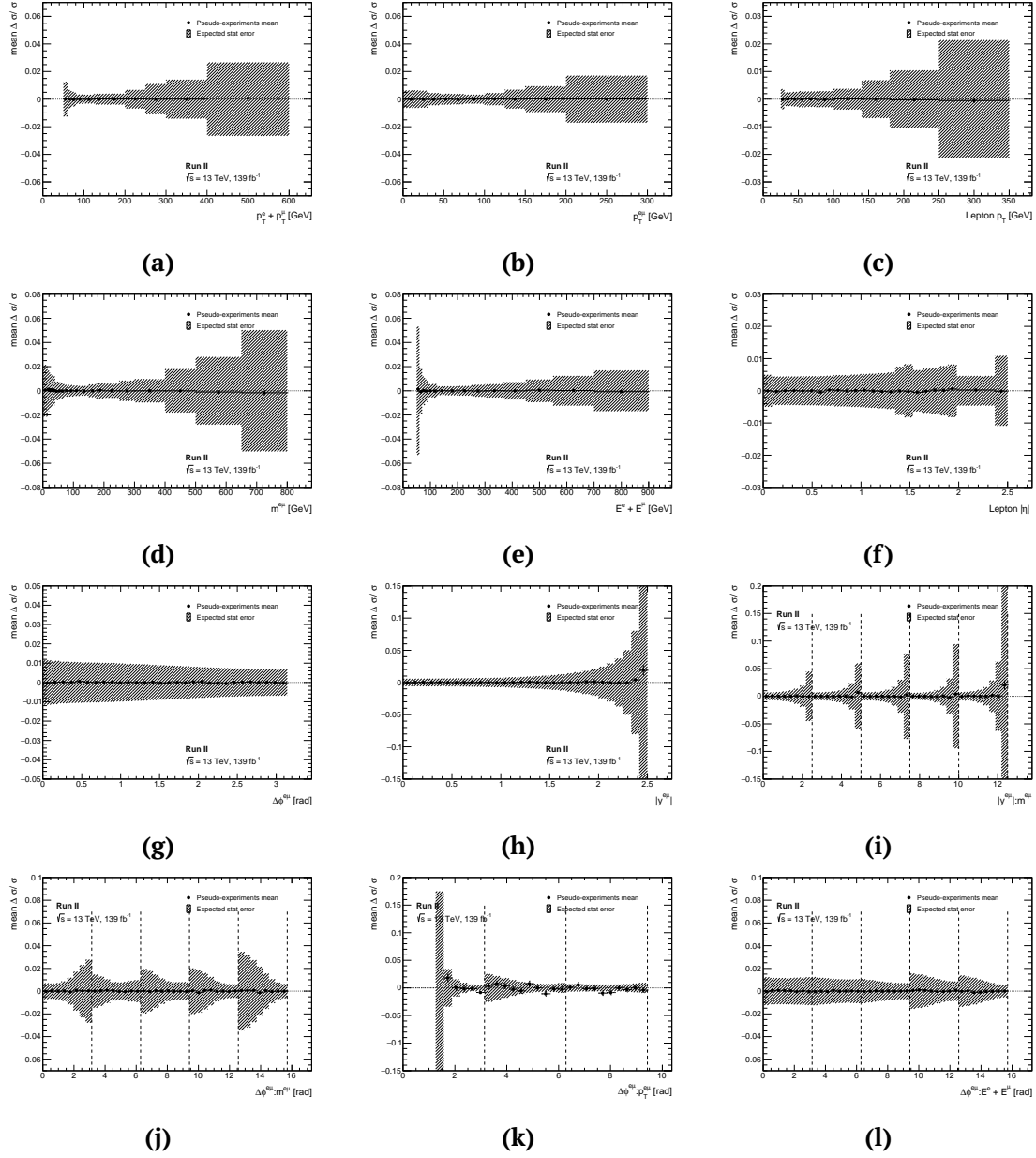


Figure D.50: Mean extracted for each bin of each normalised (double) variable from the Poissonian fluctuations fitted to the 1000 ratio stress tests pseudo-experiments results. The mean is in all cases consistent with zero within the standard deviation, demonstrating that the double tagging technique has no bias, with a non perfect Data/MC ratio, within the expect statistical sensitivity (gray shaded region).

D.4 Closure tests

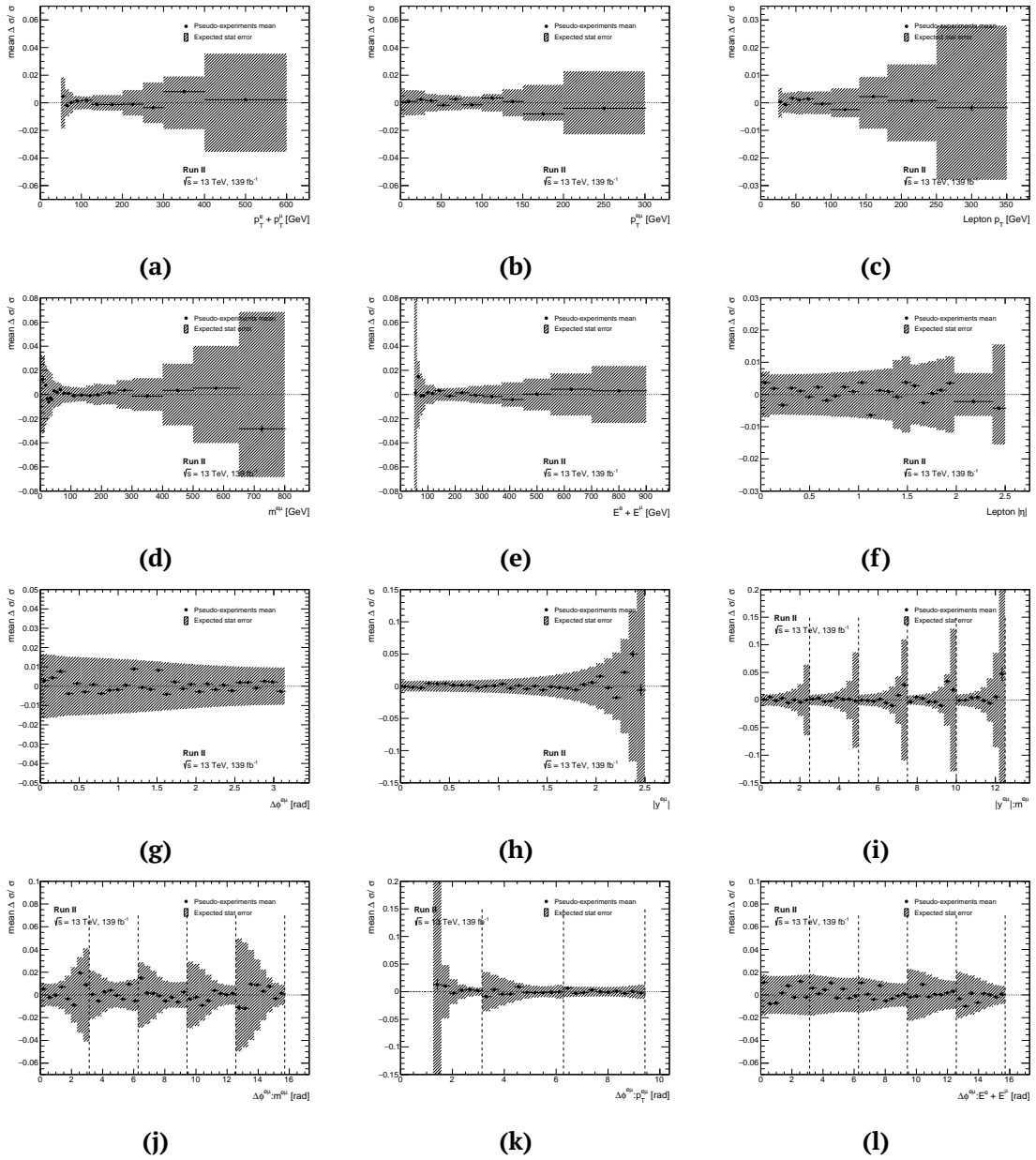


Figure D.51: Mean extracted for each bin of each (double) variable from the Poissonian fluctuations fitted to the 1000 closure tests pseudo-experiments results. The mean is in all cases consistent with zero within the standard deviation, demonstrating that the double tagging technique has no bias, using an independent sample, within the expect statistical sensitivity (gray shaded region).

Normalised distributions

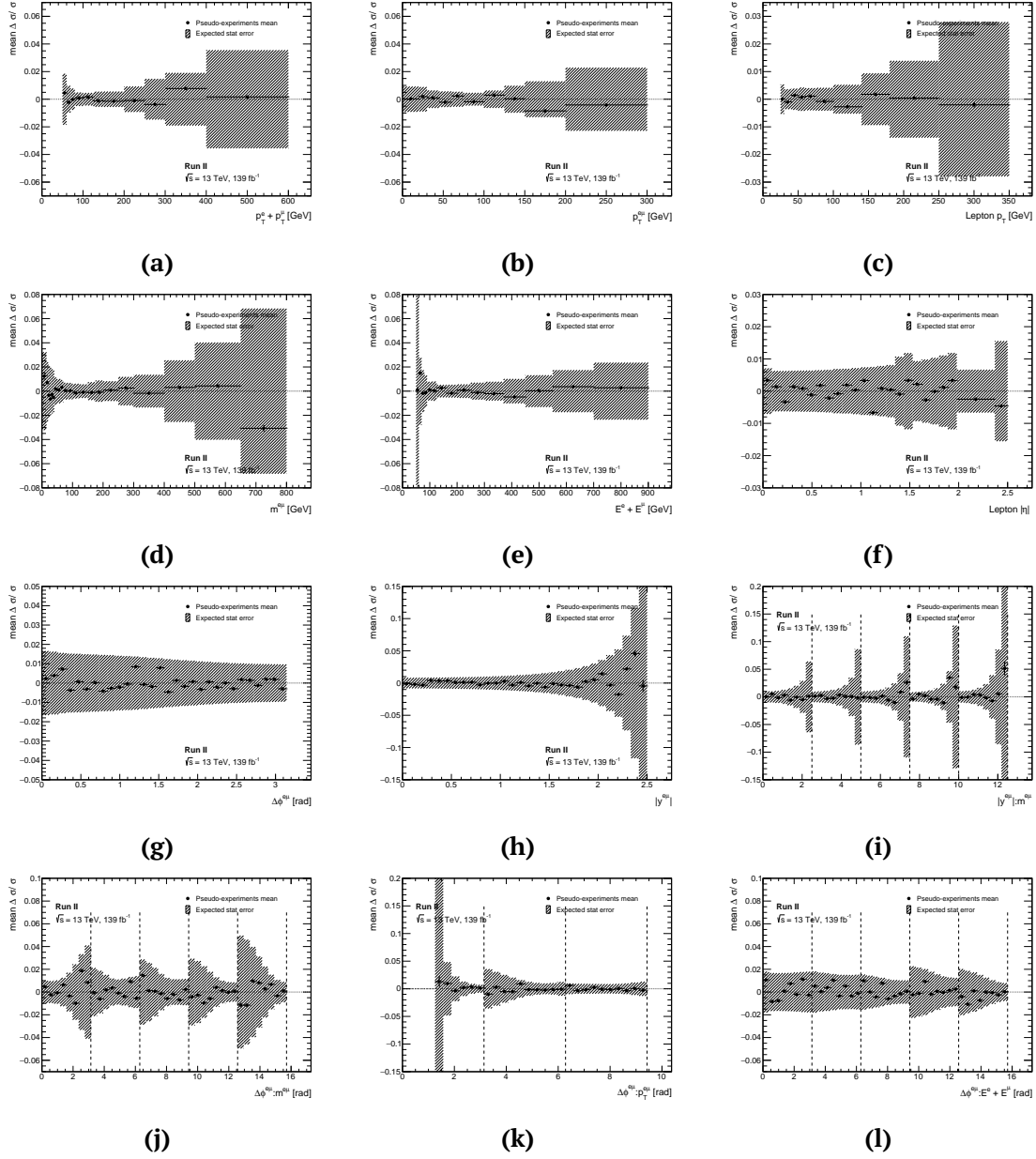


Figure D.52: Mean extracted for each bin of each normalised (double) variable from the Poissonian fluctuations fitted to the 1000 closure tests pseudo-experiments results. The mean is in all cases consistent with zero within the standard deviation, demonstrating that the double tagging technique has no bias, using an independent sample, within the expected statistical sensitivity (gray shaded region).

E Analysis uncertainties breakdown

E.1 Differential cross section

p_T^l bins	25.0- 30.0	30.0- 40.0	40.0- 50.0	50.0- 60.0	60.0- 75.0	75.0- 100.0	100.0- 140.0	140.0- 180.0	180.0- 250.0	250.0- 350.0
Cross section [fb/GeV]	465.7	437.0	360.1	279.6	198.9	110.1	42.1	13.0	3.19	0.512
Data statistics (%)	0.38	0.27	0.30	0.33	0.29	0.30	0.40	0.69	1.02	2.35
MC statistics (%)	0.11	0.07	0.07	0.07	0.07	0.07	0.09	0.17	0.28	0.65
Luminosity (%)	1.90	1.89	1.89	1.89	1.89	1.90	1.92	1.98	2.06	2.35
$\bar{t}\bar{t}$ (%)	0.30	0.43	0.35	0.48	0.41	0.55	0.50	0.90	0.59	0.97
Jets/ b -tagging (%)	0.11	0.11	0.11	0.12	0.15	0.15	0.17	0.20	0.26	0.40
Background (%)	0.76	0.70	0.67	0.70	0.70	0.88	1.26	2.22	4.20	12.89
Leptons (%)	1.09	0.87	0.74	0.74	0.74	0.82	0.96	1.42	1.86	4.23
Total uncertainty (%)	2.38	2.26	2.19	2.23	2.21	2.34	2.58	3.50	5.18	14.02

Table E.2: Differential absolute cross section for p_T^l .

$p_T^e + p_T^\mu$ bins	50.0- 60.0	60.0- 70.0	70.0- 80.0	80.0- 100.0	100.0- 125.0	125.0- 150.0	150.0- 200.0	200.0- 250.0	250.0- 300.0	300.0- 400.0	400.0- 600.0
Cross section [fb/GeV]	25.2	72.9	103.3	115.9	97.1	63.4	29.8	10.2	3.93	1.15	0.141
Data statistics (%)	1.24	0.66	0.52	0.33	0.33	0.39	0.41	0.65	1.09	1.42	2.84
MC statistics (%)	0.48	0.22	0.14	0.08	0.07	0.09	0.09	0.17	0.26	0.36	0.82
Luminosity (%)	1.90	1.90	1.88	1.88	1.88	1.89	1.92	1.97	2.01	2.05	2.26
$\bar{t}\bar{t}$ (%)	1.05	0.36	0.38	0.51	0.50	0.59	0.54	0.72	0.57	1.29	0.71
Jets/ b -tagging (%)	0.19	0.16	0.13	0.11	0.12	0.15	0.16	0.20	0.22	0.26	0.44
Background (%)	0.68	0.88	0.65	0.68	0.70	0.77	1.12	2.29	2.88	4.38	11.87
Leptons (%)	1.36	1.05	0.88	0.79	0.74	0.76	0.87	1.19	1.52	2.06	3.72
Total uncertainty (%)	2.97	2.47	2.28	2.24	2.23	2.30	2.49	3.40	4.03	5.61	13.01

Table E.3: Differential absolute cross section for $p_T^e + p_T^\mu$.

$p_T^{e\mu}$ bins	0.0- 20.0	20.0- 30.0	30.0- 45.0	45.0- 60.0	60.0- 75.0	75.0- 100.0	100.0- 125.0	125.0- 150.0	150.0- 200.0	200.0- 300.0
Cross section [fb/GeV]	32.8	69.7	88.2	111.9	122.1	94.0	48.9	19.9	5.78	0.873
Data statistics (%)	0.66	0.64	0.46	0.41	0.38	0.33	0.45	0.69	0.95	1.78
MC statistics (%)	0.21	0.17	0.11	0.09	0.09	0.07	0.10	0.16	0.23	0.48
Luminosity (%)	1.89	1.89	1.89	1.88	1.88	1.89	1.90	1.95	2.04	2.32
$\bar{t}\bar{t}$ (%)	0.37	0.51	0.48	0.59	0.51	0.56	0.60	0.69	0.82	1.61
Jets/ b -tagging (%)	0.19	0.22	0.18	0.15	0.14	0.12	0.15	0.21	0.28	0.35
Background (%)	0.86	0.74	0.70	0.69	0.62	0.70	1.03	2.02	3.62	12.08
Leptons (%)	0.79	0.78	0.78	0.79	0.79	0.78	0.89	1.20	1.62	2.63
Total uncertainty (%)	2.37	2.34	2.27	2.28	2.23	2.26	2.46	3.21	4.65	12.82

Table E.4: Differential absolute cross section for $p_T^{e\mu}$.

$E^e + E^\mu$ bins	50.0- 60.0	60.0- 70.0	70.0- 80.0	80.0- 90.0	90.0- 110.0	110.0- 125.0	125.0- 160.0	160.0- 200.0	200.0- 250.0	250.0- 300.0	300.0- 370.0	370.0- 450.0	450.0- 550.0	550.0- 700.0	700.0- 900.0
Cross section [fb/GeV]	1.40	9.11	20.7	31.0	44.0	51.7	52.0	43.6	31.8	21.1	12.9	6.99	3.48	1.43	0.622
Data statistics (%)	5.19	1.93	1.16	0.95	0.52	0.56	0.37	0.37	0.38	0.48	0.54	0.70	0.97	1.19	1.78
MC statistics (%)	3.72	0.88	0.37	0.28	0.15	0.13	0.09	0.09	0.09	0.11	0.13	0.16	0.22	0.29	0.44
Luminosity (%)	1.80	1.92	1.88	1.89	1.87	1.88	1.88	1.89	1.90	1.91	1.93	1.94	1.96	1.97	2.05
$\bar{t}\bar{t}$ (%)	1.90	0.55	0.84	0.53	0.97	0.36	0.35	0.40	0.29	0.48	0.54	0.77	0.83	0.72	1.95
Jets/ b -tagging (%)	1.06	0.38	0.14	0.17	0.13	0.12	0.12	0.13	0.11	0.15	0.13	0.15	0.17	0.16	0.27
Background (%)	5.63	1.23	0.97	0.70	0.68	0.74	0.70	0.66	0.72	1.05	1.31	1.62	1.90	2.28	3.53
Leptons (%)	1.56	1.10	0.96	0.88	0.80	0.75	0.73	0.74	0.78	0.84	0.93	1.07	1.29	1.61	2.47
Total uncertainty (%)	9.07	3.37	2.76	2.47	2.42	2.26	2.20	2.21	2.23	2.44	2.63	2.95	3.28	3.70	5.48

Table E.5: Differential absolute cross section for $E^e + E^\mu$.

$m^{\mu\mu}$ bins	0.0- 15.0	15.0- 20.0	20.0- 25.0	25.0- 30.0	30.0- 35.0	35.0- 40.0	40.0- 50.0	50.0- 60.0	60.0- 70.0	70.0- 85.0	85.0- 100.0	100.0- 120.0	120.0- 150.0	150.0- 175.0	175.0- 200.0	200.0- 250.0	250.0- 300.0	300.0- 400.0	400.0- 500.0	500.0- 650.0	650.0- 800.0
Cross section [fb/GeV]	8.28	19.0	23.7	29.3	35.3	38.6	45.9	56.6	69.1	77.4	77.1	67.9	51.2	35.0	24.0	13.8	6.79	2.60	0.741	0.212	0.068
Data statistics (%)	2.08	1.72	1.54	1.35	1.24	1.19	0.75	0.70	0.62	0.47	0.46	0.44	0.39	0.51	0.61	0.58	0.83	0.94	1.78	2.73	5.12
MC statistics (%)	0.47	0.36	0.33	0.30	0.28	0.25	0.18	0.21	0.20	0.13	0.10	0.09	0.09	0.12	0.15	0.13	0.20	0.23	0.43	0.67	1.25
Luminosity (%)	1.90	1.88	1.88	1.88	1.89	1.90	1.90	1.91	1.91	1.90	1.89	1.89	1.90	1.90	1.91	1.92	1.93	1.93	1.95	1.97	2.05
r_T (%)	1.83	0.65	0.60	0.89	0.54	0.41	0.23	0.30	0.38	0.60	0.36	0.34	0.51	0.43	0.41	0.33	0.64	0.68	0.65	1.24	1.30
Jets/ b -tagging (%)	0.14	0.12	0.12	0.09	0.09	0.09	0.10	0.11	0.11	0.11	0.12	0.13	0.13	0.14	0.17	0.16	0.18	0.21	0.26	0.27	0.39
Background (%)	1.48	0.70	0.65	1.17	0.73	0.83	0.85	0.79	0.77	0.78	0.72	0.75	0.76	0.84	1.01	1.49	1.68	2.67	3.66	2.78	7.61
Leptons (%)	0.90	0.85	0.84	0.84	0.85	0.84	0.84	0.85	0.84	0.80	0.77	0.75	0.75	0.78	0.84	0.91	1.08	1.31	1.70	2.22	3.26
Total uncertainty (%)	3.81	2.87	2.75	2.88	2.60	2.58	2.39	2.38	2.56	2.34	2.25	2.24	2.27	2.33	2.44	2.69	2.99	3.75	4.89	5.10	10.11

Table E.6: Differential absolute cross section for $m^{\mu\mu}$.

$ p $ bins	0.0 - 0.09	0.09 - 0.18	0.18 - 0.27	0.27 - 0.36	0.36 - 0.45	0.45 - 0.54	0.54 - 0.63	0.63 - 0.72	0.72 - 0.81	0.81 - 0.90	0.9 - 0.99	0.99 - 1.08	1.08 - 1.17	1.17 - 1.26	1.26 - 1.35	1.35 - 1.44	1.44 - 1.53	1.53 - 1.62	1.62 - 1.71	1.71 - 1.80	1.80 - 1.89	1.89 - 1.98	1.98 - 2.07	2.07 - 2.16	2.16 - 2.25	2.25 - 2.34	2.34 - 2.43	2.43 - 2.52	2.52 - 2.61	
Cross section [pb/unit $ p $]	12.9	12.9	12.8	12.7	12.5	12.3	12.0	11.6	11.2	11.0	10.5	9.91	9.55	9.16	8.65	8.07	7.47	7.24	6.56	5.95	5.54	5.04	3.85	2.69						
Data statistics (%)	0.56	0.52	0.52	0.50	0.50	0.52	0.51	0.52	0.54	0.54	0.55	0.57	0.58	0.59	0.59	0.51	0.56	0.42	0.45	0.48	0.53	0.54	0.51	0.79						
MC statistics (%)	0.12	0.12	0.11	0.12	0.12	0.11	0.11	0.12	0.12	0.12	0.12	0.14	0.13	0.13	0.14	0.19	0.22	0.15	0.18	0.18	0.18	0.20	0.12	0.25						
Luminosity (%)	1.90	1.90	1.90	1.90	1.90	1.89	1.90	1.90	1.90	1.90	1.90	1.90	1.90	1.90	1.90	1.90	1.91	1.91	1.91	1.92	1.92	1.92	1.91	1.91						
f (%)	0.50	0.47	0.49	0.47	0.52	0.45	0.56	0.47	0.44	0.57	0.40	0.39	0.26	0.31	0.60	0.38	0.88	0.66	0.43	0.69	0.52	0.52	0.70	0.70						
Jet b -tagging (%)	0.12	0.15	0.15	0.15	0.15	0.14	0.15	0.15	0.12	0.12	0.12	0.15	0.16	0.16	0.15	0.14	0.12	0.12	0.10	0.11	0.11	0.11	0.11	0.16						
Background (%)	0.75	0.80	0.84	0.85	0.76	0.66	0.75	0.92	0.76	0.80	0.74	0.94	0.79	0.83	0.82	0.81	1.08	0.83	0.99	0.94	1.12	1.18	1.01	0.82						
Leptons (%)	1.01	0.81	0.76	0.76	0.76	0.76	0.76	0.76	0.76	0.76	0.76	0.77	0.77	0.79	0.78	0.76	0.80	0.97	0.97	0.97	0.95	0.95	1.02	1.17						
Total uncertainty (%)	2.57	2.29	2.30	2.29	2.23	2.22	2.28	2.32	2.26	2.26	2.25	2.53	2.25	2.28	2.33	2.30	2.57	2.43	2.45	2.50	2.54	2.57	2.52	2.62						

Table E.7: Differential absolute cross section for $|p|$.

$\Delta\phi^{\mu}$ bins	0.00-0.10	0.10-0.21	0.21-0.31	0.31-0.42	0.42-0.52	0.52-0.65	0.65-0.73	0.73-0.84	0.84-0.94	0.94-1.05	1.05-1.15	1.15-1.26	1.26-1.36	1.36-1.47	1.47-1.57	1.57-1.68	1.68-1.78	1.78-1.88	1.88-1.99	1.99-2.09	2.09-2.20	2.20-2.30	2.30-2.41	2.41-2.51	2.51-2.62	2.62-2.72	2.72-2.83	2.83-2.95	2.95-3.04	3.04-3.14			
Cross section [pb/rad]	2.23	2.21	2.20	2.24	2.25	2.33	2.34	2.42	2.45	2.51	2.62	2.76	3.02	3.10	3.21	3.38	3.49	3.68	3.86	4.04	4.25	4.34	4.55	4.63	4.75	4.84	4.92	4.99	5.13	5.13			
Data statistics (%)	1.12	1.12	1.05	1.08	1.03	1.02	1.00	0.95	1.01	0.98	0.98	0.95	0.90	0.90	0.88	0.86	0.85	0.80	0.81	0.75	0.75	0.74	0.75	0.71	0.72	0.70	0.71	0.68	0.66	0.66			
MC statistics (%)	0.24	0.24	0.24	0.25	0.23	0.22	0.22	0.22	0.23	0.22	0.23	0.21	0.20	0.21	0.20	0.20	0.21	0.21	0.20	0.18	0.20	0.19	0.20	0.19	0.19	0.19	0.17	0.18	0.18	0.17	0.17		
Luminosity (%)	1.89	1.88	1.89	1.90	1.89	1.89	1.89	1.89	1.90	1.90	1.90	1.90	1.90	1.90	1.90	1.90	1.90	1.91	1.91	1.90	1.90	1.91	1.91	1.91	1.91	1.90	1.91	1.91	1.91	1.91	1.90	1.90	
β (%)	0.70	0.67	0.66	0.56	0.43	0.65	0.70	0.61	0.62	0.41	0.32	0.22	0.48	0.27	0.45	0.25	0.40	0.20	0.71	0.83	0.54	0.38	0.44	0.38	0.32	0.32	0.32	0.32	0.32	0.32	0.32	0.37	0.37
jets/ β -tagging (%)	0.11	0.10	0.10	0.08	0.10	0.09	0.12	0.10	0.10	0.11	0.11	0.09	0.10	0.11	0.12	0.12	0.14	0.13	0.13	0.13	0.13	0.17	0.16	0.17	0.16	0.18	0.19	0.19	0.18	0.19	0.19	0.19	
Background (%)	1.06	0.73	0.96	1.04	0.77	0.79	0.96	0.92	1.27	0.87	0.87	0.76	0.86	0.86	0.86	0.86	0.79	0.99	0.92	0.79	0.83	0.70	1.05	0.92	0.85	0.98	0.86	0.86	0.86	0.87	0.87	0.87	
Leptons (%)	0.84	0.84	0.84	0.85	0.84	0.84	0.84	0.83	0.83	0.82	0.83	0.82	0.81	0.80	0.81	0.80	0.80	0.79	0.79	0.79	0.79	0.79	0.79	0.80	0.80	0.81	0.81	0.82	0.83	0.83	0.83	0.83	
Total uncertainty (%)	2.69	2.56	2.61	2.60	2.49	2.53	2.60	2.54	2.72	2.50	2.46	2.41	2.48	2.44	2.56	2.39	2.48	2.42	2.47	2.49	2.42	2.55	2.47	2.42	2.42	2.39	2.49	2.45	2.49	2.39	2.39	2.39	

Table E.8: Differential absolute cross section for $\Delta\phi^{\mu}$.

$ \nu^{\mu\mu} $ bins	0.00 -	0.08 -	0.17 -	0.25 -	0.33 -	0.42 -	0.50 -	0.58 -	0.67 -	0.75 -	0.83 -	0.92 -	1.00 -	1.08 -	1.17 -	1.25 -	1.33 -	1.42 -	1.50 -	1.58 -	1.67 -	1.75 -	1.83 -	1.92 -	2.00 -	2.08 -	2.17 -	2.25 -	2.33 -	2.42 -	2.50 -
	0.08	0.17	0.25	0.33	0.42	0.50	0.58	0.67	0.75	0.83	0.92	1.00	1.08	1.17	1.25	1.33	1.42	1.50	1.58	1.67	1.75	1.83	1.92	2.00	2.08	2.17	2.25	2.33	2.42	2.50	
Gross section [pb/unit $ \nu^{\mu\mu} $]	8.02	8.05	7.96	7.85	7.71	7.54	7.28	7.04	6.76	6.48	6.05	5.78	5.45	5.01	4.59	4.15	3.78	3.57	2.99	2.56	2.15	1.77	1.52	1.15	0.892	0.675	0.445	0.246	0.132	0.045	
Data statistics (%)	0.59	0.57	0.61	0.56	0.60	0.61	0.64	0.65	0.65	0.66	0.68	0.69	0.76	0.80	0.86	0.89	1.02	1.05	1.15	1.27	1.43	1.58	1.81	2.04	2.55	2.87	3.70	4.63	7.91	26.25	
MC statistics (%)	0.15	0.14	0.14	0.14	0.14	0.15	0.15	0.15	0.16	0.16	0.17	0.17	0.18	0.19	0.20	0.23	0.24	0.27	0.28	0.35	0.57	0.45	0.43	0.57	0.71	0.75	1.00	1.58	2.25	3.66	
Luminosity (%)	1.89	1.89	1.89	1.89	1.90	1.90	1.89	1.90	1.90	1.90	1.90	1.90	1.90	1.90	1.91	1.91	1.91	1.91	1.92	1.95	1.95	1.95	1.94	1.96	1.97	1.99	2.00	2.01	2.04	1.88	
δ (%)	0.63	0.52	0.26	0.48	0.61	0.25	0.44	0.30	0.32	0.31	0.33	0.56	0.68	0.45	0.53	0.82	0.70	0.57	0.81	0.66	1.28	1.40	1.66	1.13	1.12	1.77	5.21	2.15	3.56	5.77	
jets/ b -tagging (%)	0.13	0.13	0.13	0.13	0.12	0.14	0.14	0.13	0.14	0.13	0.14	0.14	0.13	0.13	0.13	0.11	0.11	0.11	0.13	0.14	0.14	0.14	0.12	0.10	0.14	0.52	0.18	0.24	0.29	0.77	
Background (%)	0.75	0.79	0.69	0.96	0.90	0.88	0.80	0.81	0.79	0.85	0.95	0.88	0.95	0.94	1.11	0.85	0.78	0.96	0.91	0.94	1.20	1.35	1.06	1.10	1.48	2.68	1.62	2.06	3.59	7.67	
Lepton ID (%)	0.77	0.77	0.77	0.78	0.77	0.77	0.77	0.77	0.78	0.78	0.79	0.80	0.81	0.82	0.84	0.86	0.88	0.91	0.91	0.94	1.01	1.09	1.11	1.23	1.80	1.59	1.41	1.30	1.59	1.89	
Total uncertainty (%)	2.54	2.53	2.27	2.39	2.40	2.33	2.34	2.32	2.32	2.43	2.59	2.35	2.49	2.50	2.58	2.57	2.58	2.59	2.74	2.79	3.19	3.59	3.53	3.51	4.00	5.01	5.80	6.26	9.88	28.51	

Table E.9: Differential absolute cross section for $|\nu^{\mu\mu}|$.

p_T^l bins	25.0-30.0	30.0-40.0	40.0-50.0	50.0-60.0	60.0-75.0	75.0-100.0	100.0-140.0	140.0-180.0	180.0-250.0	250.0-350.0
Normalised cross section [$10^{-3}/\text{GeV}$]	21.9	20.5	16.9	13.1	9.34	5.17	1.98	0.608	0.150	0.024
Data statistics (%)	0.54	0.22	0.25	0.28	0.26	0.26	0.37	0.68	1.00	2.34
MC statistics (%)	0.10	0.06	0.06	0.07	0.06	0.07	0.09	0.17	0.28	0.66
Luminosity (%)	0.01	0.01	0.01	0.01	0.01	< 0.01	0.03	0.08	0.17	0.46
$\bar{t}\bar{t}$ (%)	0.15	0.21	0.08	0.12	0.08	0.26	0.25	0.56	0.26	0.60
Jets/ b -tagging (%)	0.07	0.04	0.02	0.02	0.02	0.04	0.08	0.13	0.20	0.35
Background (%)	0.24	0.30	0.29	0.21	0.21	0.18	0.65	1.70	3.72	12.45
Leptons (%)	0.55	0.21	0.19	0.25	0.25	0.20	0.43	0.92	1.41	3.89
Total uncertainty (%)	0.72	0.48	0.44	0.44	0.43	0.47	0.91	2.13	4.13	13.29

Table E.10: Normalised differential cross section for p_T^l .

$p_T^e + p_T^\mu$ bins	50.0-60.0	60.0-70.0	70.0-80.0	80.0-100.0	100.0-125.0	125.0-150.0	150.0-200.0	200.0-250.0	250.0-300.0	300.0-400.0	400.0-600.0
Normalised cross section [$10^{-3}/\text{GeV}$]	2.56	6.82	9.67	10.8	9.09	5.93	2.79	0.958	0.368	0.108	0.013
Data statistics (%)	1.22	0.62	0.49	0.29	0.29	0.56	0.37	0.63	1.08	1.42	2.83
MC statistics (%)	0.47	0.21	0.13	0.08	0.06	0.08	0.09	0.17	0.26	0.36	0.82
Luminosity (%)	0.01	0.01	0.02	0.02	0.02	0.01	0.02	0.07	0.12	0.16	0.37
$\bar{t}\bar{t}$ (%)	0.92	0.17	0.22	0.31	0.10	0.24	0.19	0.40	0.24	0.91	0.50
Jets/ b -tagging (%)	0.17	0.12	0.09	0.05	0.01	0.04	0.08	0.13	0.14	0.17	0.37
Background (%)	0.60	0.79	0.46	0.47	0.33	0.12	0.54	1.78	2.49	4.00	11.49
Leptons (%)	0.85	0.43	0.25	0.25	0.22	0.17	0.32	0.72	1.07	1.64	3.37
Total uncertainty (%)	1.92	1.13	0.77	0.69	0.50	0.49	0.77	2.07	2.94	4.66	12.35

Table E.11: Normalised differential cross section for $p_T^e + p_T^\mu$.

$p_T^{e\mu}$ bins	0.0-20.0	20.0-30.0	30.0-45.0	45.0-60.0	60.0-75.0	75.0-100.0	100.0-125.0	125.0-150.0	150.0-200.0	200.0-300.0
Normalised cross section [$10^{-3}/\text{GeV}$]	3.09	6.56	8.29	10.5	11.5	8.84	4.60	1.87	0.543	0.082
Data statistics (%)	0.64	0.61	0.42	0.37	0.35	0.29	0.43	0.67	0.93	1.77
MC statistics (%)	0.20	0.16	0.10	0.09	0.08	0.07	0.09	0.16	0.22	0.48
Luminosity (%)	0.01	0.01	0.01	0.02	0.02	0.01	0.01	0.05	0.14	0.42
$\bar{t}\bar{t}$ (%)	0.14	0.35	0.20	0.34	0.21	0.19	0.40	0.35	0.63	1.38
Jets/ b -tagging (%)	0.12	0.17	0.09	0.06	0.03	0.04	0.12	0.21	0.28	0.33
Background (%)	0.55	0.43	0.50	0.43	0.43	0.21	0.42	1.48	3.14	11.64
Leptons (%)	0.29	0.27	0.25	0.17	0.13	0.05	0.30	0.73	1.19	2.23
Total uncertainty (%)	0.95	0.90	0.74	0.69	0.61	0.42	0.80	1.84	5.56	12.09

Table E.12: Normalised differential cross section for $p_T^{e\mu}$.

$E^e + E^\mu$ bins	50.0-60.0	60.0-70.0	70.0-80.0	80.0-90.0	90.0-110.0	110.0-125.0	125.0-160.0	160.0-200.0	200.0-250.0	250.0-300.0	300.0-370.0	370.0-450.0	450.0-550.0	550.0-700.0	700.0-900.0
Normalised cross section [$10^{-3}/\text{GeV}$]	0.131	0.857	1.94	2.91	4.14	4.86	4.89	4.10	2.99	1.99	1.21	0.657	0.328	0.135	0.058
Data statistics (%)	5.19	1.91	1.15	0.93	0.50	0.54	0.33	0.35	0.35	0.46	0.52	0.68	0.95	1.17	1.75
MC statistics (%)	3.74	0.88	0.37	0.28	0.13	0.12	0.08	0.08	0.08	0.11	0.13	0.16	0.22	0.28	0.43
Luminosity (%)	0.10	0.03	0.04	0.03	0.04	0.04	0.03	0.01	< 0.01	0.02	0.04	0.06	0.08	0.10	0.19
$\bar{t}\bar{t}$ (%)	1.67	0.65	0.53	0.39	0.69	0.21	0.17	0.13	0.17	0.18	0.17	0.64	0.65	0.72	1.86
Jets/ b -tagging (%)	1.05	0.39	0.13	0.11	0.07	0.03	0.02	0.02	0.02	0.05	0.04	0.05	0.08	0.08	0.21
Background (%)	5.70	1.20	1.18	0.63	0.70	0.59	0.39	0.28	0.19	0.37	0.65	1.02	1.33	1.76	3.03
Leptons (%)	0.89	0.52	0.42	0.35	0.31	0.26	0.22	0.17	0.13	0.17	0.27	0.44	0.73	1.11	2.06
Total uncertainty (%)	8.84	2.59	1.82	1.27	1.15	0.87	0.59	0.50	0.47	0.65	0.90	1.46	1.91	2.51	4.49

Table E.13: Normalised differential cross section for $E^e + E^\mu$.

$m^{\mu\mu}$ bins	0.0-15.0	15.0-20.0	20.0-25.0	25.0-30.0	30.0-35.0	35.0-40.0	40.0-50.0	50.0-60.0	60.0-70.0	70.0-85.0	85.0-100.0	100.0-120.0	120.0-150.0	150.0-175.0	175.0-200.0	200.0-250.0	250.0-300.0	300.0-400.0	400.0-500.0	500.0-650.0	650.0-800.0	
Normalised cross section [$10^{-3}/\text{GeV}$]	0.777	1.78	2.22	2.75	3.13	3.62	4.31	5.32	6.49	7.27	7.24	6.38	4.81	3.28	2.25	1.30	0.657	0.244	0.070	0.020	0.006	
Data statistics (%)	2.06	1.70	1.54	1.32	1.23	1.18	0.74	0.68	0.60	0.44	0.43	0.40	0.36	0.49	0.59	0.56	0.81	0.93	1.76	2.72	5.12	
MC statistics (%)	0.47	0.36	0.32	0.30	0.28	0.25	0.18	0.20	0.19	0.12	0.10	0.09	0.09	0.11	0.15	0.13	0.20	0.23	0.45	0.67	1.25	
Luminosity (%)	0.01	0.02	0.02	0.05	0.02	0.01	0.01	0.01	0.01	0.01	0.02	0.01	0.01	0.01	0.03	0.03	0.04	0.06	0.09	0.09	0.19	
$f(\%)$	1.64	0.35	0.49	0.55	0.37	0.18	0.21	0.39	0.30	0.56	0.19	0.09	0.31	0.33	0.32	0.18	0.32	0.45	0.41	1.01	1.34	
lepton-tagging (%)	0.16	0.15	0.14	0.10	0.07	0.08	0.06	0.06	0.06	0.06	0.02	0.03	0.05	0.05	0.06	0.06	0.09	0.11	0.16	0.17	0.30	
Background (%)	1.41	0.69	0.55	1.13	0.67	0.57	0.67	0.57	0.44	0.53	0.38	0.19	0.12	0.22	0.51	0.96	1.15	2.21	3.21	2.49	7.26	
Leptons (%)	0.32	0.18	0.19	0.16	0.17	0.17	0.17	0.19	0.17	0.16	0.16	0.13	0.10	0.13	0.22	0.30	0.53	0.78	1.21	1.79	2.86	
Total uncertainty (%)	3.05	1.91	1.74	1.87	1.48	1.36	1.05	1.01	0.84	0.69	0.64	0.48	0.51	0.65	0.89	1.17	1.55	2.57	3.91	4.28	9.52	

Table E.14: Normalised differential cross section for $m^{\mu\mu}$.

$ \eta $ bins	0.0 - 0.09	0.09 - 0.18	0.18 - 0.27	0.27 - 0.36	0.36 - 0.45	0.45 - 0.54	0.54 - 0.63	0.63 - 0.72	0.72 - 0.81	0.81 - 0.90	0.90 - 0.99	0.99 - 1.08	1.08 - 1.17	1.17 - 1.26	1.26 - 1.35	1.35 - 1.44	1.44 - 1.53	1.53 - 1.62	1.62 - 1.71	1.71 - 1.80	1.80 - 1.89	1.89 - 1.98	1.98 - 2.07	2.07 - 2.16	2.16 - 2.25	2.25 - 2.34	2.34 - 2.43	2.43 - 2.52	2.52 - 2.61	2.61 - 2.70	2.70 - 2.79	2.79 - 2.88	2.88 - 2.97	2.97 - 3.06	3.06 - 3.15	3.15 - 3.24	3.24 - 3.33	3.33 - 3.42	3.42 - 3.51	3.51 - 3.60	3.60 - 3.69	3.69 - 3.78	3.78 - 3.87	3.87 - 3.96	3.96 - 4.05	4.05 - 4.14	4.14 - 4.23	4.23 - 4.32	4.32 - 4.41	4.41 - 4.50	4.50 - 4.59	4.59 - 4.68	4.68 - 4.77	4.77 - 4.86	4.86 - 4.95	4.95 - 5.04	5.04 - 5.13	5.13 - 5.22	5.22 - 5.31	5.31 - 5.40	5.40 - 5.49	5.49 - 5.58	5.58 - 5.67	5.67 - 5.76	5.76 - 5.85	5.85 - 5.94	5.94 - 6.03	6.03 - 6.12	6.12 - 6.21	6.21 - 6.30	6.30 - 6.39	6.39 - 6.48	6.48 - 6.57	6.57 - 6.66	6.66 - 6.75	6.75 - 6.84	6.84 - 6.93	6.93 - 7.02	7.02 - 7.11	7.11 - 7.20	7.20 - 7.29	7.29 - 7.38	7.38 - 7.47	7.47 - 7.56	7.56 - 7.65	7.65 - 7.74	7.74 - 7.83	7.83 - 7.92	7.92 - 8.01	8.01 - 8.10	8.10 - 8.19	8.19 - 8.28	8.28 - 8.37	8.37 - 8.46	8.46 - 8.55	8.55 - 8.64	8.64 - 8.73	8.73 - 8.82	8.82 - 8.91	8.91 - 9.00	9.00 - 9.09	9.09 - 9.18	9.18 - 9.27	9.27 - 9.36	9.36 - 9.45	9.45 - 9.54	9.54 - 9.63	9.63 - 9.72	9.72 - 9.81	9.81 - 9.90	9.90 - 9.99	9.99 - 10.08	10.08 - 10.17	10.17 - 10.26	10.26 - 10.35	10.35 - 10.44	10.44 - 10.53	10.53 - 10.62	10.62 - 10.71	10.71 - 10.80	10.80 - 10.89	10.89 - 10.98	10.98 - 11.07	11.07 - 11.16	11.16 - 11.25	11.25 - 11.34	11.34 - 11.43	11.43 - 11.52	11.52 - 11.61	11.61 - 11.70	11.70 - 11.79	11.79 - 11.88	11.88 - 11.97	11.97 - 12.06	12.06 - 12.15	12.15 - 12.24	12.24 - 12.33	12.33 - 12.42	12.42 - 12.51	12.51 - 12.60	12.60 - 12.69	12.69 - 12.78	12.78 - 12.87	12.87 - 12.96	12.96 - 13.05	13.05 - 13.14	13.14 - 13.23	13.23 - 13.32	13.32 - 13.41	13.41 - 13.50	13.50 - 13.59	13.59 - 13.68	13.68 - 13.77	13.77 - 13.86	13.86 - 13.95	13.95 - 14.04	14.04 - 14.13	14.13 - 14.22	14.22 - 14.31	14.31 - 14.40	14.40 - 14.49	14.49 - 14.58	14.58 - 14.67	14.67 - 14.76	14.76 - 14.85	14.85 - 14.94	14.94 - 15.03	15.03 - 15.12	15.12 - 15.21	15.21 - 15.30	15.30 - 15.39	15.39 - 15.48	15.48 - 15.57	15.57 - 15.66	15.66 - 15.75	15.75 - 15.84	15.84 - 15.93	15.93 - 16.02	16.02 - 16.11	16.11 - 16.20	16.20 - 16.29	16.29 - 16.38	16.38 - 16.47	16.47 - 16.56	16.56 - 16.65	16.65 - 16.74	16.74 - 16.83	16.83 - 16.92	16.92 - 17.01	17.01 - 17.10	17.10 - 17.19	17.19 - 17.28	17.28 - 17.37	17.37 - 17.46	17.46 - 17.55	17.55 - 17.64	17.64 - 17.73	17.73 - 17.82	17.82 - 17.91	17.91 - 18.00	18.00 - 18.09	18.09 - 18.18	18.18 - 18.27	18.27 - 18.36	18.36 - 18.45	18.45 - 18.54	18.54 - 18.63	18.63 - 18.72	18.72 - 18.81	18.81 - 18.90	18.90 - 18.99	18.99 - 19.08	19.08 - 19.17	19.17 - 19.26	19.26 - 19.35	19.35 - 19.44	19.44 - 19.53	19.53 - 19.62	19.62 - 19.71	19.71 - 19.80	19.80 - 19.89	19.89 - 19.98	19.98 - 20.07	20.07 - 20.16	20.16 - 20.25	20.25 - 20.34	20.34 - 20.43	20.43 - 20.52	20.52 - 20.61	20.61 - 20.70	20.70 - 20.79	20.79 - 20.88	20.88 - 20.97	20.97 - 21.06	21.06 - 21.15	21.15 - 21.24	21.24 - 21.33	21.33 - 21.42	21.42 - 21.51	21.51 - 21.60	21.60 - 21.69	21.69 - 21.78	21.78 - 21.87	21.87 - 21.96	21.96 - 22.05	22.05 - 22.14	22.14 - 22.23	22.23 - 22.32	22.32 - 22.41	22.41 - 22.50	22.50 - 22.59	22.59 - 22.68	22.68 - 22.77	22.77 - 22.86	22.86 - 22.95	22.95 - 23.04	23.04 - 23.13	23.13 - 23.22	23.22 - 23.31	23.31 - 23.40	23.40 - 23.49	23.49 - 23.58	23.58 - 23.67	23.67 - 23.76	23.76 - 23.85	23.85 - 23.94	23.94 - 24.03	24.03 - 24.12	24.12 - 24.21	24.21 - 24.30	24.30 - 24.39	24.39 - 24.48	24.48 - 24.57	24.57 - 24.66	24.66 - 24.75	24.75 - 24.84	24.84 - 24.93	24.93 - 25.02	25.02 - 25.11	25.11 - 25.20	25.20 - 25.29	25.29 - 25.38	25.38 - 25.47	25.47 - 25.56	25.56 - 25.65	25.65 - 25.74	25.74 - 25.83	25.83 - 25.92	25.92 - 26.01	26.01 - 26.10	26.10 - 26.19	26.19 - 26.28	26.28 - 26.37	26.37 - 26.46	26.46 - 26.55	26.55 - 26.64	26.64 - 26.73	26.73 - 26.82	26.82 - 26.91	26.91 - 27.00	27.00 - 27.09	27.09 - 27.18	27.18 - 27.27	27.27 - 27.36	27.36 - 27.45	27.45 - 27.54	27.54 - 27.63	27.63 - 27.72	27.72 - 27.81	27.81 - 27.90	27.90 - 27.99	27.99 - 28.08	28.08 - 28.17	28.17 - 28.26	28.26 - 28.35	28.35 - 28.44	28.44 - 28.53	28.53 - 28.62	28.62 - 28.71	28.71 - 28.80	28.80 - 28.89	28.89 - 28.98	28.98 - 29.07	29.07 - 29.16	29.16 - 29.25	29.25 - 29.34	29.34 - 29.43	29.43 - 29.52	29.52 - 29.61	29.61 - 29.70	29.70 - 29.79	29.79 - 29.88	29.88 - 29.97	29.97 - 30.06	30.06 - 30.15	30.15 - 30.24	30.24 - 30.33	30.33 - 30.42	30.42 - 30.51	30.51 - 30.60	30.60 - 30.69	30.69 - 30.78	30.78 - 30.87	30.87 - 30.96	30.96 - 31.05	31.05 - 31.14	31.14 - 31.23	31.23 - 31.32	31.32 - 31.41	31.41 - 31.50	31.50 - 31.59	31.59 - 31.68	31.68 - 31.77	31.77 - 31.86	31.86 - 31.95	31.95 - 32.04	32.04 - 32.13	32.13 - 32.22	32.22 - 32.31	32.31 - 32.40	32.40 - 32.49	32.49 - 32.58	32.58 - 32.67	32.67 - 32.76	32.76 - 32.85	32.85 - 32.94	32.94 - 33.03	33.03 - 33.12	33.12 - 33.21	33.21 - 33.30	33.30 - 33.39	33.39 - 33.48	33.48 - 33.57	33.57 - 33.66	33.66 - 33.75	33.75 - 33.84	33.84 - 33.93	33.93 - 34.02	34.02 - 34.11	34.11 - 34.20	34.20 - 34.29	34.29 - 34.38	34.38 - 34.47	34.47 - 34.56	34.56 - 34.65	34.65 - 34.74	34.74 - 34.83	34.83 - 34.92	34.92 - 35.01	35.01 - 35.10	35.10 - 35.19	35.19 - 35.28	35.28 - 35.37	35.37 - 35.46	35.46 - 35.55	35.55 - 35.64	35.64 - 35.73	35.73 - 35.82	35.82 - 35.91	35.91 - 36.00	36.00 - 36.09	36.09 - 36.18	36.18 - 36.27	36.27 - 36.36	36.36 - 36.45	36.45 - 36.54	36.54 - 36.63	36.63 - 36.72	36.72 - 36.81	36.81 - 36.90	36.90 - 36.99	36.99 - 37.08	37.08 - 37.17	37.17 - 37.26	37.26 - 37.35	37.35 - 37.44	37.44 - 37.53	37.53 - 37.62	37.62 - 37.71	37.71 - 37.80	37.80 - 37.89	37.89 - 37.98	37.98 - 38.07	38.07 - 38.16	38.16 - 38.25	38.25 - 38.34	38.34 - 38.43	38.43 - 38.52	38.52 - 38.61	38.61 - 38.70	38.70 - 38.79	38.79 - 38.88	38.88 - 38.97	38.97 - 39.06	39.06 - 39.15	39.15 - 39.24	39.24 - 39.33	39.33 - 39.42	39.42 - 39.51	39.51 - 39.60	39.60 - 39.69	39.69 - 39.78	39.78 - 39.87	39.87 - 39.96	39.96 - 40.05	40.05 - 40.14	40.14 - 40.23	40.23 - 40.32	40.32 - 40.41	40.41 - 40.50	40.50 - 40.59	40.59 - 40.68	40.68 - 40.77	40.77 - 40.86	40.86 - 40.95	40.95 - 41.04	41.04 - 41.13	41.13 - 41.22	41.22 - 41.31	41.31 - 41.40	41.40 - 41.49	41.49 - 41.58	41.58 - 41.67	41.67 - 41.76	41.76 - 41.85	41.85 - 41.94	41.94 - 42.03	42.03 - 42.12	42.12 - 42.21	42.21 - 42.30	42.30 - 42.39	42.39 - 42.48	42.48 - 42.57	42.57 - 42.66	42.66 - 42.75	42.75 - 42.84	42.84 - 42.93	42.93 - 43.02	43.02 - 43.11	43.11 - 43.20	43.20 - 43.29	43.29 - 43.38	43.38 - 43.47	43.47 - 43.56	43.56 - 43.65	43.65 - 43.74	43.74 - 43.83	43.83 - 43.92	43.92 - 44.01	44.01 - 44.10	44.10 - 44.19	44.19 - 44.28	44.28 - 44.37	44.37 - 44.46	44.46 - 44.55	44.55 - 44.64	44.64 - 44.73	44.73 - 44.82	44.82 - 44.91	44.91 - 45.00	45.00 - 45.09	45.09 - 45.18	45.18 - 45.27	45.27 - 45.36	45.36 - 45.45	45.45 - 45.54	45.54 - 45.63	45.63 - 45.72	45.72 - 45.81	45.81 - 45.90	45.90 - 45.99	45.99 - 46.08	46.08 - 46.17	46.17 - 46.26	46.26 - 46.35	46.35 - 46.44	46.44 - 46.53	46.53 - 46.62	46.62 - 46.71	46.71 - 46.80	46.80 - 46.89	46.89 - 46.98	46.98 - 47.07	47.07 - 47.16	47.16 - 47.25	47.25 - 47.34	47.34 - 47.43	47.43 - 47.52	47.52 - 47.61	47.61 - 47.70	47.70 - 47.79	47.79 - 47.88	47.88 - 47.97	47.97 - 48.06	48.06 - 48.15	48.15 - 48.24	48.24 - 48.33	48.33 - 48.42	48.42 - 48.51	48.51 - 48.60	48.60 - 48.69	48.69 - 48.78	48.78 - 48.87	48.87 - 48.96	48.96 - 49.05	49.05 - 49.14	49.14 - 49.23	49.23 - 49.32	49.32 - 49.41	49.41 - 49.50	49.50 - 49.59	49.59 - 49.68	49.68 - 49.77	49.77 - 49.86	49.86 - 49.95	49.95 - 50.04	50.04 - 50.13	50.13 - 50.22	50.22 - 50.31	50.31 - 50.40	50.40 - 50.49	50.49 - 50.58	50.58 - 50.67	50.67 - 50.76	50.76 - 50.85	50.85 - 50.94	50.94 - 51.03	51.03 - 51.12	51.12 - 51.21	51.21 - 51.30	51.30 - 51.39	51.39 - 51.48	51.48 - 51.57	51.57 - 51.66	51.66 - 51.75	51.75 - 51.84	51.84 - 51.93	51.93 - 52.02	52.02 - 52.11	52.11 - 52.20	52.20 - 52.29	52.29 - 52.38	52.38 - 52.47	52.47 - 52.56	52.56 - 52.65	52.65 - 52.74	52.74 - 52.83	52.83 - 52.92	52.92 - 53.01	53.01 - 53.10	53.10 - 53.19	53.19 - 53.28	53.28 - 53.37	53.37 - 53.46	53.46 - 53.55	53.55 - 53.64	53.64 - 53.73	53.73 - 53.82	53.82 - 53.91	53.91 - 54.00	54.00 - 54.09	54.09 - 54.18	54.18 - 54.27	54.27 - 54.36	54.36 - 54.45	54.45 - 54.54	54.54 - 54.63	54.63 - 54.72	54.72 - 54.81	54.81 - 54.90	54.90 - 54.99	54.99 - 55.08	55.08 - 55.17	55.17 - 55.26	55.26 - 55.35	55.35 - 55.44	55.44 - 55.53	55.53 - 55.62	55.62 - 55.71	55.71 - 55.80	55.80 - 55.89	55.89 - 55.98	55.98 - 56.07	56.07 - 56.16	56.16 - 56.25	56.25 - 56.34	56.34 - 56.43	56.43 - 56.52	56.52 - 56.61	56.61 - 56.70	56.70 - 56.79	56.79 - 56.88	56.88 - 56.97	56.97 - 57.06	57.06 - 57.15	57.15 - 57.24	57.24 - 57.33	57.33 - 57.42	57.42 - 57.51	57.51 - 57.60	57.60 - 57.69	57.69 - 57.78	57.78 - 57.87	57.87 - 57.96	57.96 - 58.05	58.05 - 58.14	58.14 - 58.23	58.23 - 58.32	58.32 - 58.41	58.41 - 58.50	58.50 - 58.59	58.59 - 58.68	58.68 - 58.77	58.77 - 58.86	58.86 - 58.95	58.95 - 59.04	59.04 - 59.13	59.13 - 59.22	59.22 - 59.31	59.31 - 59.40	59.40 - 59.49	59.49 - 59.58	59.58 - 59.67	59.67 - 59.76	59.76 - 59.85	59.85 - 59.94	59.94 - 60.03	60.03 - 60.12	60.12 - 60.21	60.21 - 60.30	60.30 - 60.39	60.39 - 60.48	60.48 - 60.57	60.57 - 60.66	60.66 - 60.75	60.75 - 60.84	60.84 - 60.93	60.93 - 61.02	61.02 - 61.11	61.11 - 61.20	61.20 - 61.29	61.29 - 61.38	61.38 - 61.47	61.47 - 61.56	61.56 - 61.65	61.65 - 61.74	61.74 - 61.83	61.83 - 61.92	61.92 - 62.01	62.01 - 62.10	62.10 - 62.19	62.19 - 62.28	62.28 - 62.37
---------------	------------	-------------	-------------	-------------	-------------	-------------	-------------	-------------	-------------	-------------	-------------	-------------	-------------	-------------	-------------	-------------	-------------	-------------	-------------	-------------	-------------	-------------	-------------	-------------	-------------	-------------	-------------	-------------	-------------	-------------	-------------	-------------	-------------	-------------	-------------	-------------	-------------	-------------	-------------	-------------	-------------	-------------	-------------	-------------	-------------	-------------	-------------	-------------	-------------	-------------	-------------	-------------	-------------	-------------	-------------	-------------	-------------	-------------	-------------	-------------	-------------	-------------	-------------	-------------	-------------	-------------	-------------	-------------	-------------	-------------	-------------	-------------	-------------	-------------	-------------	-------------	-------------	-------------	-------------	-------------	-------------	-------------	-------------	-------------	-------------	-------------	-------------	-------------	-------------	-------------	-------------	-------------	-------------	-------------	-------------	-------------	-------------	-------------	-------------	-------------	-------------	-------------	-------------	-------------	-------------	-------------	-------------	-------------	-------------	-------------	-------------	--------------	---------------	---------------	---------------	---------------	---------------	---------------	---------------	---------------	---------------	---------------	---------------	---------------	---------------	---------------	---------------	---------------	---------------	---------------	---------------	---------------	---------------	---------------	---------------	---------------	---------------	---------------	---------------	---------------	---------------	---------------	---------------	---------------	---------------	---------------	---------------	---------------	---------------	---------------	---------------	---------------	---------------	---------------	---------------	---------------	---------------	---------------	---------------	---------------	---------------	---------------	---------------	---------------	---------------	---------------	---------------	---------------	---------------	---------------	---------------	---------------	---------------	---------------	---------------	---------------	---------------	---------------	---------------	---------------	---------------	---------------	---------------	---------------	---------------	---------------	---------------	---------------	---------------	---------------	---------------	---------------	---------------	---------------	---------------	---------------	---------------	---------------	---------------	---------------	---------------	---------------	---------------	---------------	---------------	---------------	---------------	---------------	---------------	---------------	---------------	---------------	---------------	---------------	---------------	---------------	---------------	---------------	---------------	---------------	---------------	---------------	---------------	---------------	---------------	---------------	---------------	---------------	---------------	---------------	---------------	---------------	---------------	---------------	---------------	---------------	---------------	---------------	---------------	---------------	---------------	---------------	---------------	---------------	---------------	---------------	---------------	---------------	---------------	---------------	---------------	---------------	---------------	---------------	---------------	---------------	---------------	---------------	---------------	---------------	---------------	---------------	---------------	---------------	---------------	---------------	---------------	---------------	---------------	---------------	---------------	---------------	---------------	---------------	---------------	---------------	---------------	---------------	---------------	---------------	---------------	---------------	---------------	---------------	---------------	---------------	---------------	---------------	---------------	---------------	---------------	---------------	---------------	---------------	---------------	---------------	---------------	---------------	---------------	---------------	---------------	---------------	---------------	---------------	---------------	---------------	---------------	---------------	---------------	---------------	---------------	---------------	---------------	---------------	---------------	---------------	---------------	---------------	---------------	---------------	---------------	---------------	---------------	---------------	---------------	---------------	---------------	---------------	---------------	---------------	---------------	---------------	---------------	---------------	---------------	---------------	---------------	---------------	---------------	---------------	---------------	---------------	---------------	---------------	---------------	---------------	---------------	---------------	---------------	---------------	---------------	---------------	---------------	---------------	---------------	---------------	---------------	---------------	---------------	---------------	---------------	---------------	---------------	---------------	---------------	---------------	---------------	---------------	---------------	---------------	---------------	---------------	---------------	---------------	---------------	---------------	---------------	---------------	---------------	---------------	---------------	---------------	---------------	---------------	---------------	---------------	---------------	---------------	---------------	---------------	---------------	---------------	---------------	---------------	---------------	---------------	---------------	---------------	---------------	---------------	---------------	---------------	---------------	---------------	---------------	---------------	---------------	---------------	---------------	---------------	---------------	---------------	---------------	---------------	---------------	---------------	---------------	---------------	---------------	---------------	---------------	---------------	---------------	---------------	---------------	---------------	---------------	---------------	---------------	---------------	---------------	---------------	---------------	---------------	---------------	---------------	---------------	---------------	---------------	---------------	---------------	---------------	---------------	---------------	---------------	---------------	---------------	---------------	---------------	---------------	---------------	---------------	---------------	---------------	---------------	---------------	---------------	---------------	---------------	---------------	---------------	---------------	---------------	---------------	---------------	---------------	---------------	---------------	---------------	---------------	---------------	---------------	---------------	---------------	---------------	---------------	---------------	---------------	---------------	---------------	---------------	---------------	---------------	---------------	---------------	---------------	---------------	---------------	---------------	---------------	---------------	---------------	---------------	---------------	---------------	---------------	---------------	---------------	---------------	---------------	---------------	---------------	---------------	---------------	---------------	---------------	---------------	---------------	---------------	---------------	---------------	---------------	---------------	---------------	---------------	---------------	---------------	---------------	---------------	---------------	---------------	---------------	---------------	---------------	---------------	---------------	---------------	---------------	---------------	---------------	---------------	---------------	---------------	---------------	---------------	---------------	---------------	---------------	---------------	---------------	---------------	---------------	---------------	---------------	---------------	---------------	---------------	---------------	---------------	---------------	---------------	---------------	---------------	---------------	---------------	---------------	---------------	---------------	---------------	---------------	---------------	---------------	---------------	---------------	---------------	---------------	---------------	---------------	---------------	---------------	---------------	---------------	---------------	---------------	---------------	---------------	---------------	---------------	---------------	---------------	---------------	---------------	---------------	---------------	---------------	---------------	---------------	---------------	---------------	---------------	---------------	---------------	---------------	---------------	---------------	---------------	---------------	---------------	---------------	---------------	---------------	---------------	---------------	---------------	---------------	---------------	---------------	---------------	---------------	---------------	---------------	---------------	---------------	---------------	---------------	---------------	---------------	---------------	---------------	---------------	---------------	---------------	---------------	---------------	---------------	---------------	---------------	---------------	---------------	---------------	---------------	---------------	---------------	---------------	---------------	---------------	---------------	---------------	---------------	---------------	---------------	---------------	---------------	---------------	---------------	---------------	---------------	---------------	---------------	---------------	---------------	---------------	---------------	---------------	---------------	---------------	---------------	---------------	---------------	---------------	---------------	---------------	---------------	---------------	---------------	---------------	---------------	---------------	---------------	---------------	---------------	---------------	---------------	---------------	---------------	---------------	---------------	---------------	---------------	---------------	---------------	---------------	---------------	---------------	---------------	---------------	---------------	---------------	---------------	---------------	---------------	---------------	---------------

$\Delta\phi^{\mu}$ bins	0.00-0.10-	0.10-0.21-	0.21-0.31-	0.31-0.42-	0.42-0.52-	0.52-0.63-	0.63-0.73-	0.73-0.84-	0.84-0.94-	0.94-1.05-	1.05-1.15-	1.15-1.26-	1.26-1.36-	1.36-1.47-	1.47-1.57-	1.57-1.68-	1.68-1.78-	1.78-1.88-	1.88-1.99-	1.99-2.09-	2.09-2.20-	2.20-2.30-	2.30-2.41-	2.41-2.51-	2.51-2.62-	2.62-2.72-	2.72-2.83-	2.83-2.93-	2.93-3.04-	
	0.10	0.21	0.31	0.42	0.52	0.63	0.73	0.84	0.94	1.05	1.15	1.26	1.36	1.47	1.57	1.68	1.78	1.88	1.99	2.09	2.20	2.30	2.41	2.51	2.62	2.72	2.83	2.93	3.04	
Normalised cross section [$10^{-2}/\text{rad}$]	20.9	20.8	20.7	21.0	21.2	21.9	22.0	22.8	23.0	23.6	24.7	25.9	26.9	28.4	29.1	30.2	31.8	32.8	34.6	36.3	38.0	39.7	40.8	42.6	43.5	44.7	45.5	46.2	47.0	48.2
Data statistics (%)	1.11	1.11	1.04	1.07	1.02	1.01	0.99	0.95	1.00	0.97	0.96	0.92	0.89	0.89	0.88	0.86	0.85	0.85	0.79	0.79	0.74	0.73	0.71	0.71	0.69	0.69	0.68	0.69	0.67	0.65
MC statistics (%)	0.24	0.24	0.24	0.22	0.22	0.22	0.22	0.22	0.23	0.22	0.23	0.21	0.20	0.20	0.20	0.20	0.20	0.21	0.20	0.19	0.18	0.20	0.18	0.18	0.19	0.18	0.17	0.18	0.17	0.16
Luminosity (%)	0.02	0.02	0.01	0.01	0.02	0.01	0.01	<0.01	0.01	0.01	0.01	<0.01	<0.01	<0.01	<0.01	<0.01	<0.01	<0.01	0.01	0.01	<0.01	<0.01	<0.01	<0.01	0.01	0.01	0.01	0.01	0.01	0.01
f (%)	0.69	0.50	0.74	0.28	0.32	0.59	0.65	0.70	0.47	0.21	0.41	0.30	0.38	0.37	0.24	0.22	0.19	0.24	0.26	0.43	0.59	0.24	0.17	0.29	0.37	0.27	0.46	0.36	0.53	0.24
jets/ b -tagging (%)	0.13	0.11	0.12	0.10	0.08	0.09	0.10	0.08	0.08	0.06	0.07	0.06	0.07	0.09	0.04	0.03	0.04	0.07	0.03	0.03	0.03	0.06	0.06	0.06	0.08	0.07	0.09	0.09	0.08	0.13
Background (%)	0.41	0.43	0.83	0.36	0.44	0.34	0.57	0.48	0.60	0.15	0.34	0.26	0.27	0.48	0.21	0.45	0.13	0.40	0.19	0.20	0.13	0.23	0.50	0.40	0.16	0.16	0.30	0.31	0.32	0.23
Leptons (%)	0.14	0.13	0.13	0.14	0.13	0.12	0.12	0.11	0.11	0.10	0.11	0.09	0.08	0.07	0.06	0.06	0.04	0.05	0.02	0.03	0.03	0.05	0.05	0.06	0.08	0.09	0.10	0.12	0.13	0.14
Total uncertainty (%)	1.40	1.32	1.55	1.20	1.18	1.25	1.27	1.28	1.29	1.04	1.13	1.03	1.03	1.11	0.96	1.02	0.90	0.98	0.87	0.94	0.98	0.83	0.91	0.88	0.83	0.79	0.90	0.87	0.95	0.77

Table E.16: Differential normalised cross section for $\Delta\phi^{\mu}$.

$ \gamma^{6\mu} $ bins	0.00 - 0.08	0.08 - 0.17	0.17 - 0.25	0.25 - 0.35	0.35 - 0.42	0.42 - 0.50	0.50 - 0.58	0.58 - 0.67	0.67 - 0.75	0.75 - 0.85	0.85 - 0.92	0.92 - 1.00	1.00 - 1.08	1.08 - 1.17	1.17 - 1.25	1.25 - 1.35	1.35 - 1.42	1.42 - 1.50	1.50 - 1.58	1.58 - 1.67	1.67 - 1.75	1.75 - 1.85	1.85 - 1.92	1.92 - 2.00	2.00 - 2.08	2.08 - 2.17	2.17 - 2.25	2.25 - 2.35	2.35 - 2.42	2.42 - 2.50
Normalised cross section [10^{-3} unit $ \gamma^{6\mu} $]	754.8	756.2	749.6	739.6	726.5	710.1	685.2	665.1	656.5	610.2	569.6	544.1	512.9	472.0	452.5	391.0	356.0	317.8	282.1	240.6	202.4	167.0	142.7	108.4	84.0	65.6	41.9	25.2	12.4	4.27
Data statistics (%)	0.56	0.55	0.60	0.55	0.59	0.59	0.62	0.64	0.64	0.64	0.67	0.67	0.74	0.79	0.84	0.87	1.00	1.04	1.15	1.25	1.41	1.57	1.79	2.05	2.52	2.86	3.69	4.62	7.90	26.22
MC statistics (%)	0.14	0.14	0.14	0.13	0.14	0.14	0.15	0.16	0.16	0.16	0.16	0.16	0.17	0.19	0.20	0.23	0.23	0.26	0.28	0.35	0.37	0.45	0.42	0.56	0.71	0.75	1.00	1.58	2.25	3.67
Luminosity (%)	0.02	0.02	0.02	0.02	0.02	0.01	0.02	0.01	0.01	0.01	<0.01	0.01	<0.01	0.01	0.01	0.02	0.02	0.02	0.05	0.04	0.06	0.07	0.06	0.08	0.09	0.12	0.15	0.15	0.19	0.11
r (%)	0.43	0.35	0.30	0.21	0.41	0.27	0.35	0.11	0.23	0.21	0.09	0.22	0.40	0.25	0.23	0.57	0.57	0.28	0.41	1.21	1.27	1.56	1.05	1.23	1.78	3.10	2.04	3.41	6.07	6.09
jets/ τ -tagging (%)	0.02	0.05	0.02	0.05	0.02	0.05	0.02	0.05	0.02	0.05	0.04	0.04	0.05	0.02	0.05	0.06	0.04	0.07	0.14	0.08	0.06	0.10	0.09	0.10	0.10	0.28	0.19	0.24	0.53	0.69
Other (%)	0.14	0.14	0.14	0.14	0.14	0.14	0.14	0.14	0.14	0.14	0.14	0.14	0.14	0.14	0.14	0.14	0.14	0.14	0.14	0.14	0.14	0.14	0.14	0.14	0.14	0.14	0.14	0.14	0.14	0.14
Leptons (%)	0.15	0.15	0.14	0.14	0.13	0.12	0.11	0.11	0.09	0.08	0.07	0.08	0.06	0.08	0.09	0.15	0.17	0.21	0.29	0.36	0.43	0.51	0.59	0.67	0.75	0.86	0.88	0.96	1.01	1.45
Total uncertainty (%)	0.77	0.76	0.77	0.75	0.80	0.72	0.76	0.69	0.77	0.78	0.75	0.78	0.89	0.90	1.04	1.09	1.25	1.18	1.38	1.51	2.04	2.31	2.58	2.59	3.30	4.24	5.27	5.76	9.50	28.30

Table E.17: Differential normalised cross section for $|\gamma^{6\mu}|$.

E.2 Double differential cross section

$m^{\mu\mu}$ bins $ \gamma^{\mu\mu} $ bins	$0 \text{ GeV} \leq m^{\mu\mu} < 70 \text{ GeV}$				$70 \text{ GeV} \leq m^{\mu\mu} < 100 \text{ GeV}$											
	0.00 - 0.31 - 0.65 - 0.94 - 1.25 - 1.56 - 1.88 - 2.19 - 2.50	0.31 - 0.65 - 0.94 - 1.25 - 1.56 - 1.88 - 2.19 - 2.50	0.65 - 0.94 - 1.25 - 1.56 - 1.88 - 2.19 - 2.50	0.94 - 1.25 - 1.56 - 1.88 - 2.19 - 2.50	0.00 - 0.31 - 0.65 - 0.94 - 1.25 - 1.56 - 1.88 - 2.19 - 2.50	0.31 - 0.65 - 0.94 - 1.25 - 1.56 - 1.88 - 2.19 - 2.50	0.65 - 0.94 - 1.25 - 1.56 - 1.88 - 2.19 - 2.50	0.94 - 1.25 - 1.56 - 1.88 - 2.19 - 2.50								
Cross section [pb/GeV/unit] $ \gamma^{\mu\mu} $	1.71	1.65	1.46	1.25	0.989	0.688	0.373	0.087	1.64	1.55	1.36	1.16	0.872	0.540	0.243	0.054
Data statistics (%)	0.68	0.68	0.74	0.85	1.07	1.34	1.90	4.18	0.66	0.71	0.80	0.85	1.06	1.45	2.59	5.87
MC statistics (%)	0.19	0.18	0.20	0.22	0.29	0.38	0.58	1.40	0.17	0.17	0.19	0.21	0.29	0.41	0.66	1.38
Luminosity (%)	1.89	1.89	1.90	1.90	1.91	1.96	1.97	2.01	1.88	1.88	1.89	1.90	1.90	1.95	1.95	2.05
τ (%)	0.48	0.57	0.24	0.56	0.33	0.29	0.92	1.53	0.68	0.49	0.40	0.87	0.93	0.93	1.07	2.37
Jets/ b -tagging (%)	0.11	0.09	0.12	0.09	0.10	0.12	0.18	0.24	0.12	0.12	0.13	0.12	0.16	0.12	0.12	0.69
Background (%)	0.72	0.68	0.76	0.98	0.83	1.36	1.51	1.64	0.66	0.77	0.75	0.77	0.81	1.23	1.66	2.62
Leptons (%)	0.84	0.80	0.78	0.81	0.93	1.12	1.25	1.57	0.76	0.75	0.75	0.75	0.78	0.85	0.98	1.14
Total uncertainty (%)	2.35	2.35	2.33	2.51	2.56	2.99	3.54	5.52	2.34	2.35	2.35	2.35	2.52	2.67	3.06	7.42

Table E.18: Double differential cross section for $|\gamma^{\mu\mu}| : m^{\mu\mu}$.

m_H^H bins	$100 \text{ GeV} \leq m_H^H < 130 \text{ GeV}$										$130 \text{ GeV} \leq m_H^H < 200 \text{ GeV}$										$200 \text{ GeV} \leq m_H^H < \infty \text{ GeV}$									
$ \nu^{eH} $ bins	0.00 - 0.31	0.31 - 0.65	0.65 - 0.94	0.94 - 1.25	1.25 - 1.56	1.56 - 1.88	1.88 - 2.19	2.19 - 2.50	0.00 - 0.31	0.31 - 0.65	0.65 - 0.94	0.94 - 1.25	1.25 - 1.56	1.56 - 1.88	1.88 - 2.19	2.19 - 2.50	0.00 - 0.31	0.31 - 0.65	0.65 - 0.94	0.94 - 1.25	1.25 - 1.56	1.56 - 1.88	1.88 - 2.19	2.19 - 2.50						
Cross section [pb/GeV/unit $ \nu^{eH} $]	1.43	1.35	1.19	0.991	0.686	0.379	0.159	0.030	1.91	1.80	1.56	1.18	0.749	0.396	0.143	0.023	1.30	1.15	0.911	0.607	0.342	0.132	0.040	0.005						
Data statistics (%)	0.70	0.74	0.85	0.92	1.16	1.71	2.92	7.55	0.62	0.65	0.70	0.84	1.10	1.68	3.27	9.43	0.76	0.79	0.88	1.16	1.71	2.74	6.52	20.89						
MC statistics (%)	0.16	0.16	0.18	0.22	0.25	0.39	0.67	1.91	0.13	0.14	0.16	0.19	0.25	0.38	0.76	2.34	0.17	0.19	0.20	0.27	0.37	0.75	1.55	7.37						
Luminosity (%)	1.88	1.88	1.89	1.89	1.90	1.92	1.97	1.92	1.89	1.90	1.90	1.91	1.93	1.97	1.98	1.98	1.92	1.95	1.95	1.94	1.98	2.04	1.99	1.99						
f (%)	0.16	0.41	0.49	0.65	0.71	1.48	1.49	3.61	0.43	0.36	0.37	0.68	0.67	1.55	1.10	6.91	0.57	0.76	0.54	0.85	1.52	1.67	3.56	6.47						
jets/-tagging (%)	0.13	0.13	0.13	0.13	0.11	0.13	0.17	0.37	0.14	0.14	0.14	0.16	0.17	0.17	0.12	0.27	0.18	0.18	0.17	0.19	0.21	0.24	0.34	1.52						
Background (%)	0.70	0.72	0.93	1.12	0.88	1.33	1.33	2.59	0.73	0.78	0.95	1.06	0.96	1.00	1.65	2.69	1.80	2.06	1.98	2.07	1.59	2.40	4.13	6.08						
Leptons (%)	0.72	0.72	0.73	0.76	0.81	0.96	1.27	1.51	0.73	0.74	0.77	0.81	0.88	1.16	1.68	2.27	0.98	1.03	1.10	1.23	1.48	1.91	2.67	3.91						
Total uncertainty (%)	2.26	2.31	2.44	2.60	2.64	3.42	4.30	9.30	2.29	2.31	2.40	2.57	2.67	3.39	4.69	12.59	2.98	3.21	3.13	3.43	3.73	4.93	9.27	24.30						

Table E.19: Double differential cross section for $|\nu^{eH}| : m_H^H$.

$m^{\mu\mu}$ bins $\Delta\phi^{\mu\mu}$ bins	0.00 - 0.39 - 0.79 - 1.18 - 1.57 - 1.96 - 2.36 - 2.75 - 3.14	0.39 - 0.79 - 1.18 - 1.57 - 1.96 - 2.36 - 2.75 - 3.14	0.00 - 0.39 - 0.79 - 1.18 - 1.57 - 1.96 - 2.36 - 2.75 - 3.14	0.39 - 0.79 - 1.18 - 1.57 - 1.96 - 2.36 - 2.75 - 3.14	0.00 - 0.39 - 0.79 - 1.18 - 1.57 - 1.96 - 2.36 - 2.75 - 3.14	0.39 - 0.79 - 1.18 - 1.57 - 1.96 - 2.36 - 2.75 - 3.14	0.00 - 0.39 - 0.79 - 1.18 - 1.57 - 1.96 - 2.36 - 2.75 - 3.14	0.39 - 0.79 - 1.18 - 1.57 - 1.96 - 2.36 - 2.75 - 3.14								
Cross section [pb/GeV/rad]	1.54	1.50	1.34	0.979	0.556	0.292	0.177	0.123	0.292	0.366	0.568	0.935	1.10	1.02	0.858	0.761
Data statistics (%)	0.68	0.66	0.71	0.82	1.15	1.74	2.35	2.59	1.51	1.27	1.06	0.85	0.81	0.80	0.89	0.98
MC statistics (%)	0.15	0.15	0.16	0.20	0.39	0.81	1.28	1.73	0.33	0.28	0.24	0.18	0.18	0.21	0.26	0.29
Luminosity (%)	1.89	1.89	1.90	1.91	1.91	1.95	1.95	2.01	1.89	1.89	1.90	1.90	1.89	1.88	1.89	1.88
τ (%)	0.43	0.53	0.32	0.41	0.62	1.20	0.77	1.30	0.27	0.58	0.64	0.45	0.74	0.67	0.59	0.65
jets/ b -tagging (%)	0.09	0.09	0.10	0.12	0.14	0.29	0.40	0.47	0.11	0.11	0.14	0.11	0.15	0.16	0.16	0.22
Background (%)	0.70	0.82	0.95	0.75	0.95	1.00	1.50	1.80	1.57	0.92	0.92	0.80	0.79	0.78	0.97	1.00
Leptons (%)	0.83	0.82	0.82	0.85	0.92	1.04	1.10	1.20	0.84	0.82	0.82	0.78	0.77	0.80	0.83	0.84
Total uncertainty (%)	2.53	2.38	2.41	2.40	2.69	3.53	3.88	4.50	3.04	2.67	2.60	2.41	2.46	2.44	2.54	2.60

Table E.20: Double differential cross section for $\Delta\phi^{\mu\mu}$; $m^{\mu\mu}$.

p_T^{μ} bins $\Delta\phi^{\mu}$ bins	0 GeV $\leq p_T^{\mu} < 40$ GeV		40 GeV $\leq p_T^{\mu} < 65$ GeV		65 GeV $\leq p_T^{\mu} < \infty$ GeV		2.83 - 5.14	2.51 - 2.83	2.20 - 2.51	1.88 - 2.20	1.57 - 1.88	1.26 - 1.57	0.94 - 1.26	0.65 - 0.94	0.31 - 0.65	0.00 - 0.31	2.83 - 5.14	2.51 - 2.83	2.20 - 2.51	1.88 - 2.20	1.57 - 1.88	1.26 - 1.57	0.94 - 1.26	0.65 - 0.94	0.31 - 0.65	0.00 - 0.31
	1.57 - 1.88	2.20 - 2.51	1.88 - 2.20	2.51 - 2.83	1.26 - 1.57	1.57 - 1.88																				
Cross section [pb/GeV/rad]	0.006	0.106	0.450	1.14	2.20	3.13	0.200	0.256	0.343	0.516	0.819	1.18	1.52	1.66	1.40	0.984	2.01	2.02	2.06	2.12	2.17	2.09	1.92	1.58	1.15	0.910
Data statistics (%)	14.33	3.28	1.52	0.89	0.63	0.52	2.38	2.00	1.71	1.35	1.09	0.88	0.72	0.69	0.75	0.88	0.65	0.64	0.60	0.60	0.59	0.62	0.62	0.71	0.80	0.85
MC statistics (%)	3.91	1.23	0.51	0.29	0.18	0.14	0.53	0.42	0.38	0.31	0.25	0.25	0.18	0.15	0.17	0.22	0.15	0.15	0.14	0.13	0.13	0.14	0.15	0.17	0.21	0.23
Luminosity (%)	1.87	1.91	1.92	1.89	1.89	1.89	1.87	1.86	1.86	1.88	1.89	1.88	1.88	1.86	1.89	1.88	1.89	1.90	1.90	1.90	1.91	1.91	1.92	1.94	1.96	1.97
r (%)	7.80	0.90	1.37	0.41	0.32	0.46	0.71	0.82	0.83	0.85	0.82	0.82	0.83	0.86	0.86	0.85	0.86	0.86	0.86	0.86	0.86	0.86	0.86	0.86	0.86	0.86
jets/ b -tagging (%)	0.53	0.43	0.3	0.21	0.16	0.21	0.16	0.15	0.12	0.11	0.14	0.15	0.14	0.17	0.16	0.21	0.16	0.16	0.15	0.15	0.14	0.14	0.15	0.16	0.16	0.16
Background (%)	6.46	2.13	0.98	0.82	0.77	0.77	1.06	1.08	1.08	0.85	0.71	0.82	0.77	0.70	0.86	0.85	0.80	0.80	0.82	0.81	0.82	0.82	0.82	0.82	0.82	0.82
Leptons (%)	3.12	1.30	1.02	0.85	0.77	0.77	1.18	1.13	1.08	1.01	0.92	0.84	0.77	0.74	0.78	0.85	0.85	0.83	0.82	0.81	0.80	0.81	0.81	0.81	0.81	0.81
Total uncertainty (%)	18.27	4.75	3.19	2.46	2.51	2.30	3.54	3.28	3.18	2.74	2.51	2.49	2.42	2.33	2.39	2.46	2.38	2.46	2.46	2.36	2.39	2.51	2.63	2.80	3.01	3.41

Table E.22: Double differential cross section for $\Delta\phi^{\mu} : p_T^{\mu}$.

$m^{\mu\mu}$ bins $ y^{\mu\mu} $ bins	$0 \text{ GeV} \leq m^{\mu\mu} < 70 \text{ GeV}$										$70 \text{ GeV} \leq m^{\mu\mu} < 100 \text{ GeV}$																					
	0.00 - 0.31 - 0.63 - 0.94 - 1.25 - 1.56 - 1.88 - 2.19 - 2.50	0.31 - 0.63 - 0.94 - 1.25 - 1.56 - 1.88 - 2.19 - 2.50	1.61,0	152.9	137.1	117.1	92.9	64.6	35.0	8.20	153.6	145.3	127.9	108.8	81.9	50.7	22.8	5.11														
Normalised cross section [10^{-3} GeV/units $ y^{\mu\mu} $]	0.66	0.66	0.73	0.82	1.05	1.33	1.89	4.17	10.65	0.70	0.78	0.84	1.05	1.44	2.38	5.86	0.19	0.17	0.20	0.21	0.29	0.38	0.58	1.40	0.17	0.17	0.18	0.20	0.28	0.41	0.66	1.39
Data statistics (%)	0.19	0.17	0.20	0.21	0.29	0.38	0.58	1.40	0.17	0.17	0.18	0.20	0.28	0.41	0.66	1.39	0.04	0.03	0.02	0.01	0.01	0.06	0.08	0.14	0.03	0.03	0.02	0.01	0.01	0.04	0.07	0.15
MC statistics (%)	0.23	0.39	0.26	0.46	0.33	0.36	0.99	1.27	0.51	0.41	0.28	0.82	0.75	0.81	0.92	2.19	0.08	0.07	0.06	0.08	0.07	0.09	0.16	0.26	0.04	0.03	0.03	0.05	0.17	0.09	0.11	0.71
Luminosity (%)	0.60	0.52	0.55	0.81	0.54	1.13	1.34	1.26	0.32	0.30	0.46	0.44	0.52	0.75	1.31	2.49	0.22	0.21	0.21	0.19	0.29	0.55	0.72	0.84	0.21	0.21	0.19	0.18	0.22	0.37	0.60	0.73
r (%)	0.22	0.21	0.21	0.19	0.29	0.55	0.72	0.84	0.21	0.21	0.19	0.18	0.22	0.37	0.60	0.73	0.60	0.52	0.55	0.81	0.54	1.13	1.34	1.26	0.32	0.30	0.46	0.44	0.52	0.75	1.31	2.49
Jets/ b -tagging (%)	0.22	0.21	0.21	0.19	0.29	0.55	0.72	0.84	0.21	0.21	0.19	0.18	0.22	0.37	0.60	0.73	0.60	0.52	0.55	0.81	0.54	1.13	1.34	1.26	0.32	0.30	0.46	0.44	0.52	0.75	1.31	2.49
Background (%)	0.22	0.21	0.21	0.19	0.29	0.55	0.72	0.84	0.21	0.21	0.19	0.18	0.22	0.37	0.60	0.73	0.60	0.52	0.55	0.81	0.54	1.13	1.34	1.26	0.32	0.30	0.46	0.44	0.52	0.75	1.31	2.49
Leptons (%)	0.22	0.21	0.21	0.19	0.29	0.55	0.72	0.84	0.21	0.21	0.19	0.18	0.22	0.37	0.60	0.73	0.60	0.52	0.55	0.81	0.54	1.13	1.34	1.26	0.32	0.30	0.46	0.44	0.52	0.75	1.31	2.49
Total uncertainty (%)	0.97	0.97	1.00	1.28	1.30	1.90	2.69	4.84	10.95	0.91	0.99	1.29	1.45	1.90	3.01	6.95	0.97	0.97	1.00	1.28	1.30	1.90	2.69	4.84	10.95	0.91	0.99	1.29	1.45	1.90	3.01	6.95

Table E.25: Double differential normalised cross section for $|y^{\mu\mu}| : m^{\mu\mu}$.

P_T^{eH} bins $\Delta\phi^{eH}$ bins	$0 \text{ GeV} \leq P_T^{eH} < 40 \text{ GeV}$					$40 \text{ GeV} \leq P_T^{eH} < 65 \text{ GeV}$					$65 \text{ GeV} \leq P_T^{eH} < \infty \text{ GeV}$																
	0.00 - 1.57 1.57	1.57 - 1.88 1.88	1.88 - 2.20 2.20	2.20 - 2.51 2.51	2.51 - 2.83 2.83	0.00 - 0.31 0.31	0.31 - 0.63 0.63	0.63 - 0.94 0.94	0.94 - 1.26 1.26	1.26 - 1.57 1.57	1.57 - 1.88 1.88	1.88 - 2.20 2.20	2.20 - 2.51 2.51	2.51 - 2.83 2.83	0.00 - 0.31 0.31	0.31 - 0.63 0.63	0.63 - 0.94 0.94	0.94 - 1.26 1.26	1.26 - 1.57 1.57	1.57 - 1.88 1.88	1.88 - 2.20 2.20	2.20 - 2.51 2.51	2.51 - 2.83 2.83				
Normalised cross section [$10^{-3}/\text{GeV/rad}$]	0.59	9.97	40.4	106.6	206.6	293.3	18.8	24.0	32.2	48.4	76.9	110.3	143.1	155.9	131.0	92.3	189.0	189.7	193.8	198.6	203.9	195.8	179.9	148.6	108.1	85.4	
Data statistics (%)	14.32	3.27	1.50	0.87	0.59	0.49	2.37	1.98	1.69	1.34	1.07	0.86	0.70	0.68	0.74	0.87	0.63	0.62	0.58	0.58	0.58	0.60	0.61	0.69	0.78	0.94	
MC statistics (%)	3.94	1.24	0.51	0.28	0.17	0.13	0.53	0.42	0.39	0.31	0.25	0.22	0.18	0.15	0.16	0.21	0.14	0.13	0.13	0.13	0.13	0.13	0.14	0.16	0.16	0.20	0.23
Luminosity (%)	0.03	0.01	0.02	0.01	0.01	0.01	0.04	0.05	0.04	0.02	0.02	0.02	0.02	0.02	0.01	0.01	0.01	0.01	< 0.01	< 0.01	0.01	0.01	0.02	0.04	0.07	0.07	
f (%)	7.71	0.36	1.20	0.13	0.19	0.21	0.98	0.58	0.49	0.75	0.44	0.52	0.55	0.26	0.18	0.40	0.43	0.25	0.26	0.26	0.21	0.44	0.52	0.19	0.23	0.56	
jets/ b -tagging (%)	0.36	0.26	0.13	0.16	0.11	0.14	0.24	0.13	0.07	0.08	0.08	0.05	0.06	0.08	0.09	0.11	0.12	0.09	0.10	0.08	0.10	0.08	0.08	0.10	0.08	0.17	
Background (%)	5.95	1.85	0.88	0.75	0.59	0.47	0.97	1.34	1.50	0.99	0.59	0.49	0.67	0.70	0.33	0.37	0.36	0.25	0.48	0.13	0.43	0.54	0.65	0.91	1.16	1.57	
Leptons (%)	2.86	0.78	0.42	0.32	0.33	0.27	0.66	0.56	0.50	0.40	0.32	0.28	0.33	0.34	0.24	0.22	0.14	0.14	0.13	0.13	0.12	0.15	0.26	0.45	0.67	0.80	
Total uncertainty (%)	17.99	4.06	2.22	1.24	0.83	0.79	2.88	2.57	2.40	1.89	1.36	1.18	1.18	1.08	0.88	1.08	0.87	0.75	0.82	0.68	0.78	0.94	1.08	1.25	1.59	2.10	

Table E.29: Double differential normalised cross section for $\Delta\phi^{eH} : P_T^{eH}$.

$E^e + E^\mu$ bins $\Delta\phi^{e\mu}$ bins		$0 \text{ GeV} \leq E^e + E^\mu < 110 \text{ GeV}$	$110 \text{ GeV} \leq E^e + E^\mu < 140 \text{ GeV}$
		0.00 - 0.39 - 0.79 - 1.18 - 1.57 - 1.96 - 2.36 - 2.75 - 3.14	0.00 - 0.39 - 0.79 - 1.18 - 1.57 - 1.96 - 2.36 - 2.75 - 3.14
Normalised cross section [$10^{-3}/\text{GeV/rad}$]		45.4 45.9 45.6 46.6 46.3 44.5 43.6 41.5	39.1 41.0 44.3 48.2 49.6 52.5 50.9 51.2
Data statistics (%)		1.19 1.12 1.07 1.11 1.11 1.15 1.20 1.23	1.27 1.15 1.13 1.08 1.04 1.02 1.07 1.03
MC statistics (%)		0.27 0.24 0.26 0.27 0.31 0.43 0.44 0.50	0.27 0.26 0.24 0.24 0.27 0.25 0.26 0.26
Luminosity (%)		0.05 0.04 0.04 0.03 0.04 0.03 0.03 0.03	0.04 0.04 0.03 0.03 0.03 0.03 0.03 0.04
if (%)		0.35 0.79 0.46 0.54 0.95 1.06 0.62 0.81	0.78 0.38 0.21 0.16 0.95 0.53 0.63 0.36
jets/ b -tagging (%)		0.11 0.08 0.10 0.07 0.19 0.18 0.16 0.16	0.11 0.06 0.05 0.02 0.06 0.06 0.08 0.06
Background (%)		0.81 0.90 1.01 0.69 0.97 0.69 1.03 0.82	0.42 1.02 0.65 0.61 0.35 0.85 0.82 0.59
Leptons (%)		0.30 0.30 0.30 0.33 0.34 0.35 0.35 0.35	0.20 0.20 0.22 0.23 0.28 0.30 0.32 0.36
Total uncertainty (%)		1.54 1.69 1.60 1.48 1.82 1.80 1.80 1.80	1.59 1.61 1.56 1.29 1.51 1.49 1.55 1.32

Table E.30: Double differential normalised cross section for $\Delta\phi^{e\mu}$; $E^e + E^\mu$.

$E^e + E^{\mu}$ bins	140 GeV $\leq E^e + E^{\mu} < 200$ GeV										200 GeV $\leq E^e + E^{\mu} < 250$ GeV										250 GeV $\leq E^e + E^{\mu} < \infty$ GeV										
$\Delta\phi^{e\mu}$ bins	0.00 - 0.39		0.79 - 1.18		1.57 - 1.96		2.36 - 2.75		3.14		0.0 - 0.39		0.79 - 1.18		1.57 - 1.96		2.36 - 2.75		3.14		0.00 - 0.39		0.79 - 1.18		1.57 - 1.96		2.36 - 2.75		3.14		
	0.39	0.79	1.18	1.57	1.96	2.36	2.75	3.14			0.39	0.79	1.18	1.57	1.96	2.36	2.75	3.14			0.39	0.79	1.18	1.57	1.96	2.36	2.75	3.14			
Normalised cross section [$10^{-3}/\text{GeV/rad}$]	56.3	59.7	64.9	77.6	89.1	101.1	106.6	106.5	27.6	28.7	32.5	40.5	48.7	60.0	69.6	74.0	39.8	42.9	50.2	64.1	87.6	123.7	163.6	195.4							
Data statistics (%)	1.05	0.95	0.92	0.86	0.78	0.75	0.72	0.72	1.57	1.46	1.32	1.20	1.11	0.94	0.92	0.87	1.32	1.22	1.16	1.07	0.84	0.73	0.57	0.56							
MC statistics (%)	0.23	0.21	0.21	0.19	0.19	0.18	0.18	0.18	0.35	0.33	0.31	0.26	0.25	0.23	0.21	0.21	0.30	0.29	0.26	0.24	0.20	0.16	0.15	0.13							
Luminosity (%)	0.02	0.02	0.02	0.02	0.01	0.02	0.02	0.02	0.02	0.01	0.01	<0.01	<0.01	<0.01	<0.01	<0.01	0.06	0.05	0.05	0.05	0.05	0.04	0.05	0.05							
f (%)	0.61	0.40	0.52	0.42	0.25	0.46	0.34	0.49	0.59	1.43	0.49	0.64	0.93	0.42	0.17	0.69	0.76	0.82	0.73	0.47	0.95	0.40	0.20	0.25							
jets/ b -tagging (%)	0.12	0.09	0.11	0.06	0.04	0.10	0.08	0.08	0.18	0.11	0.10	0.12	0.05	0.02	0.05	0.17	0.19	0.16	0.11	0.15	0.11	0.07	0.06	0.12							
Background (%)	0.40	0.41	0.18	0.41	0.40	0.36	0.42	0.48	0.34	0.31	0.52	0.78	0.47	0.65	0.40	0.47	1.40	1.56	1.17	1.10	1.13	0.81	0.80	0.59							
Leptons (%)	0.17	0.15	0.16	0.15	0.18	0.25	0.28	0.29	0.24	0.24	0.20	0.15	0.14	0.15	0.24	0.25	0.50	0.51	0.47	0.47	0.45	0.38	0.37	0.40							
Total uncertainty (%)	1.31	1.15	1.11	1.07	0.95	1.00	0.96	1.05	1.77	2.11	1.55	1.60	1.55	1.24	1.07	1.26	2.16	2.25	1.89	1.70	1.77	1.24	1.08	0.96							

Table E.31: Double differential normalised cross section for $\Delta\phi^{e\mu} : E^e + E^{\mu}$.

Acknowledgements

I left the writing of this piece of thesis to the last. In some ways it was the most complicated part to write. I would like to thank and remember all the people who have been involved with me in some way during this period of more than three years. They have been part of this journey.

In primis vorrei ringraziare il mio supervisor ufficiale, Giuseppe Salamanna, per l'aiuto datomi, per le passeggiate peripatetiche, per avermi inserito nel mondo delle analisi di ATLAS ma anche per i momenti all'esterno dell'università come le (poche) partite a calcetto o gli aperitivi. Oltre a lui non posso non ringraziare Mauro Iodice che è stato il mio mentore per le MicroMegas e che mi ha seguito (e rotto abbastanza le scatole chiedendomi di fare mille mila cose :P) per tutto il dottorato. Ho imparato molto grazie a voi!

Grazie a tutti il gruppo ATLAS RomaTre che mi hanno accolto e fatto sentire subito a mio agio.

Grazie anche a tutti i dottorandi [Alberto, Ale, Anto, Cri, Davide, Ele, Fede, Filippo, Francesca, Giachomo, Giulio, Marco, Romana, Simone, Teresita e Valentina] che hanno condiviso con me le giornate in ufficio, i pranzi, le pause caffè e le uscite insieme!

Many thanks to all the colleagues who worked with me in MicroMegas group and in the Top Working Group: Theo Alexopoulos, Cesare Bini, Stelian Buda, Federica Fabbri, Paolo Iengo, Giada Mancini, Ioannis Maniatis, Paolo Massarotti, Maria Perganti, Marino Romano, Stefano Rosati and Patrick Scholer. In particular I want to tank Rosanna Ignazzi with whom I would have liked to work longer but who taught me so much. Many many thanks to Francesco Spanò and Stephanie Zimmermann who helped me so much and they also allowed me to work directly at CERN. Goodbye Stephanie!

Grazie alla saletta [Alfo, Giulia, Giulietta, Jaja, Justin, Leo, Limone, Maria, Pino, Pippo, Raffammerda, Sebbino, Scurcio, Tacchino, Valery e Vannico] con le asta del fanta lì dentro, le feste di Natale, il Marcantonio e il Pig, le missioni e le scuole insieme.

Grazie a tutti i ragazzi/e che ho conosciuto o con cui sono stato su al CERN. Tornerò su a scassarvi! :) In particolare ai ragazzi del Cinefellow [Alberto, Anita, Ago, Chiaretta, il Cholo, Dario, Fede, Friti, LoZuolo, MJ, Nico, Saverio e Tommaso] ma anche ai vari Adele, Arianna, Bibi, Dani, Giuliano, Giulia (vale doppio), Giuly, Marco, Milla, Peterinho e Tazio.

Grazie a Saretta, Giorgia e Francesca, le amiche di lunga data.

Grazie ad Ema e Max (Forza Roma, come non mettercelo in tesi) con i quali spero presto di tornare a giocare a calcetto e ad andare allo stadio!

Grazie mille al gruppo di amici che si muove attraverso le città europee (Amsterdam, Berlino, Civitavecchia, Enschede, Friburgo in Brisgovia, Ginevra, Firenze, Padova, Parigi, Sheffield, Roma, Torino e a breve anche Nizza e Postdam) ma che rimane sempre unito. Grazie per tutte le volte che ci sentiamo e vediamo nonostante tutto, grazie per esserci

sempre! Grazie Ele, Giulio, Lisa, Simo, Stefi, Teo e Vero.

La più profonda gratitudine va a voi due che mi avete amato e sostenuto (e criticato quando serviva) da quando sono nato. Vi devo tanto. Grazie mamma e papà.

Ho lasciato per ultimo un ringraziamento molto speciale. Quei 1000 e più km che ci hanno separato per buona parte di questo dottorato sono nulla in confronto a quanto sei tu per me. Grazie a te che riempi e riempi le mie giornate di gioia con il tuo sorriso, a te che sei stata il mio grande supporto, in questo percorso e in molte altre occasioni. Grazie Simi per avermi cambiato la vita! <3